



**Centrum
Badań Molekularnych
i Makromolekularnych
Polskiej Akademii Nauk**

DESIGN, SYNTHESIS, AND PROPERTIES OF BINARY SYSTEMS COMPRISING LINEZOLID

PhD thesis by:

Mehrnaz Khalaji

Supervisor:

Assoc. prof. dr hab. Marta Dudek

Structural Chemistry Department,
Centre of Molecular and Macromolecular Studies,
Polish Academy of Sciences

Thesis Submitted to the Scientific Council of Polish Academy of Sciences, in Fulfilment of the
Requirements for the Degree of Doctor of Philosophy

Łódź, 2025

Abstract of thesis presented to the Centre of Molecular and Macromolecular Studies
Polish Academy of Sciences, in fulfillment of the requirement for the degree of Doctor of
Philosophy (PhD)

DESIGN, SYNTHESIS, AND PROPERTIES OF BINARY SYSTEMS COMPRISING LINEZOLID

By

Mehrnaz Khalaji

Łódź, 2025

Supervisor: assoc. prof. dr hab. Marta Dudek

Structural Chemistry Division

The research presented in this thesis focuses on exploring cocrystals involving the antibiotic linezolid (LIN) with the ultimate aim of improving its suitability for drug delivery systems, particularly through using mesoporous silica nanoparticles (MSNs). The study begins with experimental mechanochemical screening, which led to the discovery of nine new crystal phases, including four neat cocrystals: linezolid-2,3-dihydroxybenzoic acid (LIN-2,3DHBA), linezolid-3,5-dihydroxybenzoic acid (LIN-3,5DHBA), linezolid-2,4-dihydroxybenzoic acid (LIN-2,4DHBA), linezolid-2,6-dihydroxybenzoic acid (LIN-2,6DHBA), and five cocrystal hydrates: linezolid-gallic acid hydrate (LIN-GA-H₂O), linezolid-2,4-dihydroxybenzoic acid hydrate (LIN-2,4DHBA-H₂O), linezolid-3,4-dihydroxybenzoic acid hydrate (LIN-3,4DHBA-H₂O), linezolid-2,5-dihydroxybenzoic acid hydrate (LIN-2,5DHBA-H₂O), and linezolid-p-aminobenzoic acid hydrate (LIN-PABA-H₂O). In addition, two cocrystals reported previously but without structural details, *i.e.* linezolid-benzoic acid (LIN-BA) and linezolid-p-hydroxybenzoic acid hydrate (LIN-PHBA-H₂O), were obtained. A comprehensive investigation into the factors influencing the formation of these phases was conducted, encompassing diverse experimental conditions, such as polymorphic forms of LIN and the presence of various solvents to create liquid-assisted grinding conditions. These experimental results were compared with predictions from the established

virtual cocrystal screening tools, including molecular complementarity, hydrogen bond propensity, and molecular electrostatic potential maps. It was observed that these predictive methods offer valuable insights into a molecule tendencies to form cocrystals with specific coformers, highlighting the role of molecular conformation.

To structurally characterize the obtained crystalline phases, the conducted research successfully produced five single crystals from cocrystals of this antibiotic. This enabled their characterization using single-crystal X-ray diffraction, further supplemented by solid-state NMR spectroscopy, powder X-ray diffraction, and differential scanning calorimetry. Each cocrystal exhibited distinct structural features, variations in water content, and different heterosynthons, revealing multiple intermolecular interactions preferred by the LIN molecule. Furthermore, based on the frequency of the observed supramolecular synthons, an intriguing hierarchy of hydrogen-bond acceptor sites for linezolid was established, along with a recognition of the significant role of aromatic-aromatic interactions in structure stabilization. Notably, some of these cocrystals displayed modified thermal properties, making them suitable candidates for drug delivery systems.

Addressing challenges related to solid microcrystalline powders, which hinder the usage of single-crystal X-ray diffraction for crystal structure determination, further research introduced an innovative approach to crystal structure determination by combining knowledge-based approach to narrow down the vast conformational space of LIN and some of the coformers with quantum chemical calculations, followed by high-resolution solid-state NMR experiments and crystal structure prediction (CSP) calculations. As a result, it was possible to overcome obstacles posed by molecules with substantial conformational flexibility. This combined protocol successfully elucidated the crystal structure of a LIN cocrystal with 2,3-dihydroxybenzoic acid and identified the most probable conformations of LIN within the LIN cocrystal with 2,4-dihydroxybenzoic acid, despite LIN cocrystals presenting complex conformational landscapes.

Investigating the factors and techniques that impact the incorporation of binary components into mesoporous materials, together with unveiling any unforeseen interactions, have a capacity to guide the identification of the optimal strategy for loading LIN cocrystals into MSNs. To do that, the loading process into MSNs of model binary systems comprising benzoic acid and fluorobenzoic acid was studied and followed by preliminary studies of loading LIN and its selected binary system into MSNs. By conducting these latter studies, employing both established and refined methodologies, the aim was to forge novel pathways towards

augmenting drug delivery systems *via* the judicious modification of APIs through cocrystallization.

The broader context of this research arises from the critical need for innovative drug delivery systems. Traditional administration of drugs faces limitations related to solubility, permeability, and targeting. Consequently, the utilization of MSNs as drug delivery systems has garnered significant attention due to their exceptional properties, including high loading capacity, biocompatibility, and ease of functionalization. This thesis contributes valuable insights into the development of LIN cocrystals with enhanced properties, holding promise for the future of drug delivery systems.

Streszczenie pracy przedstawionej w Centrum Badań Molekularnych i
Makromolekularnych Polskiej Akademii Nauk w ramach spełnienia wymogu uzyskania stopnia
naukowego doktora (PhD)

**PROJEKTOWANIE, SYNTEZA I WŁAŚCIWOŚCI UKŁADÓW BINARNYCH ZAWIERAJĄCYCH
LINEZOLID**

Mehrnaz Khalaji

Łódź, 2025

Promotor: dr hab. Marta Dudek, prof. CBMM

Dział Chemii Strukturalnej

Badania przedstawione w tej pracy skupiają się na eksploracji kokryształów zawierających antybiotyk linezolid (LIN), a ostatecznym ich celem jest możliwość jego zastosowania w systemach dostarczania leków, szczególnie poprzez wykorzystanie mezoporowatych nanocząstek krzemionki (MSN). Badanie rozpoczyna się od eksperymentalnych badań mechanochemicznych, które doprowadziły do odkrycia dziewięciu nowych faz krystalicznych, w tym czterech czystych kokryształów: z kwasem 2,3-dihydroksybenzoesowym, kwasem 2,4-dihydroksybenzoesowym, kwasem 3,5-dihydroksybenzoesowym i kwasem 2,6-dihydroksybenzoesowym, oraz pięciu hydratów kokryształów z kwasami: galusowym, 2,4-dihydroksybenzoesowym, 3,4-dihydroksybenzoesowym, 2,5-dihydroksybenzoesowym i p-

aminobenzoesowym. Dodatkowo, otrzymano dwa systemy binarne opisane w literaturze, ale bez szczegółowych danych strukturalnych, z kwasem benzoesowym i kwasem p-hydroksybenzoesowym. Przeprowadzono kompleksowe badania czynników wpływających na powstawanie tych faz, obejmujące różne warunki eksperymentalne, takie jak polimorficzne formy LIN i obecność różnych rozpuszczalników w celu stworzenia odpowiednich warunków mechanochemicznego ucierania wspomaganego cieczą. Wyniki eksperymentów porównano następnie z przewidywaniami za pomocą narzędzi do „wirtualnego poszukiwania” kokryształów, obejmującymi komplementarność molekularną, skłonność do tworzenia wiązań wodorowych i mapy molekularnego potencjału elektrostatycznego. Zaobserwowano, że te metody predykcyjne dostarczają cennych informacji na temat tendencji cząsteczki do tworzenia kokryształów z określonymi koformerami, podkreślając rolę konformacji molekularnej.

Aby scharakteryzować strukturalnie otrzymane kokryształy LIN podjęto wysiłek w celu otrzymania monokryształów odpowiedniej wielkości do badań krystalograficznych, co zakończyło się powodzeniem w przypadku pięciu faz. Te kokryształy dokładnie przeanalizowano przy użyciu szeregu technik, w tym dyfrakcji promieni rentgenowskich na monokryształach, spektroskopii NMR w ciele stałym, proszkowej dyfrakcji promieni rentgenowskich i różnicowej kalorymetrii skaningowej. Każdy kokryształ wykazywał odrębne cechy strukturalne, różnice w zawartości wody i różne heterosyntony, ujawniając liczne interakcje międzycząsteczkowe preferowane przez cząsteczkę LIN. Ponadto, ustalono intrygującą hierarchię miejsc akceptorowych wiązań wodorowych dla linezolidu oraz znaczącą rolę oddziaływań aromatyczno-aromatycznych w stabilizacji struktury. Warto zauważyć, że te kokryształy wykazywały zmodyfikowane właściwości termiczne, co czyniło je odpowiednimi kandydatami do zastosowania w systemach dostarczania leków.

Aby sprostać wyzwaniom związanym ze strukturalną charakterystyką substancji mikrokryсталicznych, dla których niemożliwe jest zastosowanie dyfrakcji promieniowania rentgenowskiego na monokryształach, w ramach badań wprowadzono innowacyjne podejście. Łącząc wysokiej rozdzielczości spektroskopię NMR w stanie stałym z obliczeniami przewidywania struktur krystalicznych (CSP) i oparte na wiedzy podejście pozwalające na zawężenie koniecznej do przeszukania przestrzeni konformacyjnej, w badaniu przezwyciężono przeszkody stwarzane przez cząsteczki o znacznej elastyczności konformacyjnej. Dzięki zastosowanemu podejściu z powodzeniem określono strukturę krystaliczną kokryształu LIN z kwasem 2,3-dihydroksybenzoesowym i zidentyfikowano najbardziej prawdopodobne konformacje LIN w kokryształach LIN z kwasem 2,4-dihydroksybenzoesowym, mimo bardzo dużej złożoności konformacyjnej układu.

Kolejnym krokiem były badania dotyczące wpływu czynników i metod wprowadzania substancji chemicznych w układach binarnych do porowatych nanokrzemionek, przeprowadzone w celu zidentyfikowania najkorzystniejszych dla LIN i jego kokryształów strategii ładowania do nośników krzemionkowych. W tym celu wykorzystano modelowe systemy binarne zawierające kwasy benzoesowy i fluorobenzoesowe, a następnie przeprowadzono badania nad ładowaniem LIN i jego wybranego kokryształu do porów krzemionek. Te ostatnie eksperymenty, obejmujące zarówno znane jak i nowo wprowadzone metody ładowania leków do nośników krzemionkowych, miały na celu wskazanie nowych ścieżek pozwalających na szersze zastosowanie systemu dostarczania leków poprzez celową modyfikację formy stałej leku (kokryształizację).

Szerszy kontekst tych badań podkreśla krytyczną potrzebę innowacyjnych systemów dostarczania leków. Tradycyjne podawanie leków napotyka ograniczenia związane z rozpuszczalnością, przepuszczalnością i terapią celowaną. W związku z tym wykorzystanie MSN jako systemów dostarczania leków wzbudziło duże zainteresowanie ze względu na ich wyjątkowe właściwości, w tym wysoką ładowność, biokompatybilność i łatwość funkcjonalizacji. Niniejsza praca wnosi cenne informacje na temat rozwoju kokryształów LIN o ulepszonych właściwościach, co może być obiecujące dla przyszłości systemów dostarczania leków z tym antybiotykiem.

Acknowledgments

I would like to dedicate my special thanks to:

my Ph.D. advisor prof. dr hab. Marta Dudek for the opportunity to carry out my scientific work, for the time spent, patience, and scientific support;

prof. dr hab. Marek Potrzebowski, prof. dr hab. Grzegorz D. Bujacz, for all the helpful discussions we have shared;

prof. dr hab. Alain Hedoux for hosting my research visit in UMET Lille, France, and for all the helpful discussions we have shared;

and all colleagues for discussions, invaluable advice, feedback on my research, for always being supportive of my work, and during preparing my thesis;

I would like to express my heartfelt gratitude to my parents and my brother for their unwavering support and encouragement throughout my academic journey and the completion of this thesis. Your love, understanding, and sacrifices have played a pivotal role in my success.

I would like to express my deepest gratitude to my husband for his unwavering support, love, and understanding throughout the journey of completing this thesis. Your encouragement and patience during the long hours of research, writing, and revisions have been invaluable.

I would like to acknowledge:

Financial support from the National Science Centre, Poland, under the OPUS grant No. UMO-2017/25/B/ST4/02684, Sonata grant No. UMO-2018/31/D/ST4/01995, Opus grant No. UMO-2018/31/B/ST4/01973. The Polish Infrastructure for Supporting Computational Science in the European Research Space (PL-GRID) for providing computational resources. A purchase of a Panalytical powder X-Ray diffractometer used to obtain results included in this thesis was supported by the funds from the EU Regional Operational Program of the Lodz Region, RPLD.01.01.00-10-0008/18. The financial support provided by Campus France (French Embassy in Poland) under the SSHN scholarship for a high-level scientific visit to UMET, Grant No. 148767Z.

Declaration

The work presented in this Dissertation entitled “DESIGN, SYNTHESIS, AND PROPERTIES OF BINARY SYSTEMS COMPRISING LINEZOLID” has been carried out by me under the guidance of assoc. prof. dr hab. Marta Dudek at the Centre of Molecular and Macromolecular Studies of Polish Academy of Sciences, Łódź, Poland.

This work has not been submitted in part or in full for a degree, a diploma, or a fellowship to any other university or institute. Whenever contributions of others are involved, every effort is made to indicate this clearly, with due acknowledgment of collaborative research and discussions. This Dissertation is a bonafide record of original work done by me, and all sources listed within have been detailed in the bibliography.

Mehrnaz Khalaji

Date:15/05/2025

Place: Łódź, Poland

Tables of Contents

Abstract (English)	II
Abstract (Polish)	V
Acknowledgements	VII
Declaration	IX
Tables of Contents	X
1.Introduction	1
2.State of knowledge	6
2.1.Cocrystals	6
2.2.Coformer selection	6
2.2.1.Molecular complementarity (MC)	7
2.2.2.Hydrogen Bonding Propensity (HBP)	8
2.2.3.Hansen Solubility Parameter (HSP)	9
2.2.4.The pKa-based tool	9
2.2.5.COSMO-RS	10
2.2.6.Gas-phase molecular electrostatic potential surfaces (MEPS).	11
2.2.7.Hot-stage microscopy	11
2.3.Methods of cocrystal preparation	12
2.3.1.Solvent Evaporation	12
2.3.2.Solid-State Grinding (Neat Grinding)	13
2.3.3.Liquid-Assisted Grinding (Solvent-Drop Grinding)	14
2.3.4.Other methods of cocrystallization	14
2.4.Properties enhancement of an API by cocrystallization	15
2.4.1.Melting Point	16
2.4.2.Solubility	17
2.4.3.Stability	18
2.4.4.Bioavailability	18
2.4.5.Permeability	19
2.5.Drug delivery systems (DDS) design	20
2.5.1.Mesoporous silica nanoparticles (MSNs)	20
2.5.2.Drug Confinement Methods	22
2.5.2.1.Solvent-Based Methods	23
2.5.2.1.1.Adsorption	23
2.5.2.1.2.Incipient Wetness Impregnation	24
2.5.2.1.3.Solvent Evaporation	24
2.5.2.1.4.Diffusion Supported Loading (DiSupLo)	24
2.5.2.1.5.Supercritical Fluid Technology (SCF)	25
2.5.2.1.6.Covalent Grafting	25
2.5.2.2.Solvent-free Methods	26
2.5.2.2.1.Thermal solvent free (TSF) (melt method)	26
2.5.2.2.2.Co-Milling (Mechanochemical Grinding)	26
2.6.Characterization methods	27
2.6.1.Single crystal X-ray diffraction	27
2.6.2.Powder X-ray diffraction (PXRD)	29
2.6.3.Solid state nuclear magnetic resonance spectroscopy (SSNMR)	31
2.6.3.1.1D High-Resolution SSNMR Experiments	33

2.6.3.2.Fast Magic Angle Spinning	34
2.6.3.3.High-Resolution ¹ H NMR MAS	34
2.6.3.4.2D SSNMR experiments	36
2.6.3.5.Multinuclear SSNMR	38
2.6.3.6.Applications of SSNMR in pharmaceutical analysis	38
2.6.3.7.NMR Crystallography	42
2.6.4.Raman spectroscopy	44
2.6.5.Thermal techniques	48
2.6.5.1.Differential scanning calorimetry (DSC)	48
2.6.5.2.Thermal gravimetry analysis (TGA)	52
2.6.6.Computational Methods	53
2.6.6.1.Density Functional Theory (DFT)	53
2.6.6.2.Lattice energy calculations	54
2.6.6.3.CSP and its combination with solid-state NMR measurements	55
3.Objectives of the thesis	57
4.Results and discussion	60
4.1.Coformer selection for linezolid cocrystallization (T1, Virtual Cocrystal Screening Methods as Tools to Understand the Formation of Pharmaceutical Cocrystals - A Case Study of Linezolid, a Wide-Range Antibacterial Drug, Khalaji, M., Potrzebowski, M.J., Dudek, M.K., <i>Crystal Growth and Design</i> , 2021, 21, pp. 2301–2314)	60
4.2.Crystal structure determination of linezolid cocrystals by single crystal X-ray diffraction (T2, Structural variety of heterosynthons in linezolid cocrystals with modified thermal properties, Khalaji, M., Wróblewska, A., Wielgus, E., G.D. Bujacz, Dudek, M.K., Potrzebowski, M.J., <i>Acta Crystallographica Section B: Structural Science, Crystal Engineering and Materials</i> , 2020, 76, pp. 892–912)	64
4.3.Crystal structure determination of linezolid cocrystals using an alternative CSP-NMR approach. (T3, Narrowing down the conformational space with solid-state NMR in crystal structure prediction of linezolid cocrystals, Khalaji, M., Paluch, P., Potrzebowski, M.J., Dudek, M.K., <i>Solid State Nuclear Magnetic Resonance</i> , 2022, 121, 101813)	67
4.4.Binary system confinement model (T4, Unexpected Factors Affecting the Kinetics of Guest Molecule Release from Investigation of Binary Chemical Systems Trapped in a Single Void of Mesoporous Silica Particles, Trzeciak, K. Wielgus, E. Kaźmierski, S., Khalaji M., Dudek, M.K., Potrzebowski, M.J., <i>ChemPhysChem</i> , 2023, 24, e202200884)	70
4.5.Confinement of linezolid and its cocrystal into mesopores of silica nanoparticles (T5, Developing appropriate conditions for loading LIN and its cocrystal with 2,3-dihydroxybenzoic acid into the pores of mesoporous silica materials. Mehrnaz Khalaji, Alain Heudoux, Marta K. Dudek. Unpublished work)	72
4.5.1.Materials and methods	73
4.5.2.Methods of linezolid and cocrystal confinement	75
4.5.2.1.Physical mixture	76
4.5.2.2.Mechanical neat grinding (MECHANO)	76
4.5.2.3.Mechanical liquid assistant grinding (MeLo)	76
4.5.2.4.Diffusion-supported loading (DiSupLo)	76
4.5.2.5.Thermal solvent free(TSF)	77

4.5.2.6. Thermal wet 1 (TW1)	77
4.5.2.7. Thermal wet 2 (TW2)	77
4.5.3. Evaluation of the confinement results	77
4.5.3.1. PXRD	77
4.5.3.2. DSC and TGA	77
4.5.3.3. Raman spectroscopy	78
4.5.4. Results and Discussion	79
4.5.4.1. Powder X-ray characterization of the confinement results of linezolid	79
4.5.4.2. Thermal characterization of the confinement results for linezolid	85
4.5.4.3. Raman spectroscopy characterization of the linezolid confined by MECHANO	88
4.5.4.4. Linezolid cocrystal 2,3DHBA-LIN confinement by TSF method	91
4.6. Conclusions	93
5. Final conclusions	95
6. Published side projects	99
7. Ongoing side project	100
8. Further outlooks	101
8.1. Release and Absorption Dynamics of Confined Linezolid and Its Cocrystals	101
8.2. Diversification of Bio-Applications for Linezolid Cocrystals	101
8.3. Comprehensive Study of Solubility Behavior	101
9. List of figures	103
10. List of publications connected with PhD thesis	105
11. List of publications connected with the side projects	105
12. List of lectures and posters connected with the PhD thesis	106
13. Academic biography EDUCATION	107
14. List of abbreviations used in the thesis	109
15. References	127
Appendix I – Published articles	
Appendix II - Declaratory statement from co-authors of the published results	

1. Introduction

Most currently available medications face challenges related to their limited water solubility, which leads to reduced absorption rates and diminished bioavailability [1,2]. The inadequate solubility of these drugs is primarily attributed to their high crystallinity, elevated melting point, and partition coefficient [2]. Solubility plays a crucial role in determining the effectiveness of medications, as it directly impacts their overall therapeutic potential. Owing to their poor solubility, drugs that are poorly soluble in water are often expelled rapidly from the gastrointestinal tract before they can fully dissolve and be absorbed into the bloodstream for systemic circulation [3]. This phenomenon results in diminished bioavailability and a lack of dose proportionality, often necessitating dose escalation to achieve the desired therapeutic blood concentration. However, such dose increases can sometimes lead to local toxicity within the gastrointestinal tract, thereby adversely affecting patient compliance.

Cocrystals represent a growing class of crystalline materials. They comprise two or more distinct molecules residing within the same crystal lattice, interconnected through non-ionic and non-covalent interactions. The formulation of challenging pharmaceutical compounds as cocrystals presents a pragmatic approach to manipulating their solid-state properties, facilitating innovation in new drug development and product reformulation. While research on cocrystals has experienced substantial growth over the past twenty years, the successful translation of cocrystals into clinical practice remains somewhat limited. It is crucial to recognize that the pharmaceutical characteristics of a cocrystal are unequivocally determined by the choice of cocrystal formers and the resultant crystal structure. This is followed by an exploration of the potential applications of cocrystals in the realm of medicinal products. Cocrystallization has emerged as a highly utilized method for obtaining novel crystalline forms of active pharmaceutical ingredients (APIs). This approach is particularly favored due to its capacity to yield crystalline forms with altered physicochemical properties [4-7]. Among these properties, water solubility stands out as a primary concern [8,9], although cocrystal formation can also impact other aspects such as solid form stability during manufacturing or melting points [10-13]. Consequently, well-designed cocrystals hold the potential to enhance the bioavailability of a drug. Cocrystals are on the brink of playing a crucial role in the evolving landscape of drug discovery and development, paving the way for enhancing drug delivery, exploring combination therapies, and pushing the boundaries of personalized medicine forward [14].

Another avenue for improving API bioavailability involves drug delivery systems, with a notable focus on mesoporous silica nanoparticles (MSNs) [15,16]. MSNs possess unique characteristics that make them an exceptional choice for drug delivery, particularly for

enhancing the solubility of poorly water-soluble drugs [17]. Their favorable bioavailability profile further renders them suitable for delivering drugs [18]. The spatial confinement of poorly soluble drug molecules within the mesopores of MSNs reduces lattice energy and the recrystallization of amorphous drugs, consequently enhancing their bioavailability and dissolution rates compared to crystalline drug forms, functioning as sustained-release systems that mitigate the risk of side effects linked to a sudden release of a high drug dose [18-21]. Additionally, the hydrophilic large surface areas of MSNs facilitate the dispersion and wetting of the encapsulated drugs, thereby augmenting the dissolution rate of the drug molecules and increasing their drug-loading capacities [22,23]. Several methods have been introduced for loading specific APIs into MSNs, including the solid-state thermal solvent-free approach [21,24-28]. This technique involves converting an API crystal into the molten phase in the presence of silica carriers, leading to drug recrystallization within the nanoparticle pores. A key advantage of this approach is the significantly higher drug loading efficiency compared to conventional solution-based methods. However, a noteworthy limitation is the requirement to melt the drug, which can be problematic for thermally sensitive or phase-transition-prone compounds.

To circumvent this limitation, the cocrystallization of a drug with a coformer from the generally recognized as safe (GRAS) list has been proposed [29], resulting in a cocrystal with a lower melting point that can be introduced into MSNs. Furthermore, there is a growing interest in modifying the thermal properties of pharmaceutical cocrystals and loading them into MSNs, stemming from previous observations that altering the composition of cocrystals within MSNs can influence the release rate of an API [27]. This has the potential to open up new avenues in therapeutic strategies.

One such drug grappling with poor water solubility and a heightened risk of mitochondrial toxicity is linezolid (LIN), Figure 1.1, a broad-spectrum antibiotic primarily used to combat infections caused by resistant strains of Gram-positive bacteria [30,31]. Presently, two polymorphic forms of LIN are known: orthorhombic form II [32], commercially available, and triclinic form III [33,34], occasionally mislabelled as form IV [35]. These two polymorphs exhibit enantiotropic phase transition, with stable form II transforming into metastable form III upon heating to temperatures between 120°C and 140°C for a specified duration [32,33,36,37]. This enantiotropic polymorphism presents challenges when applying the thermal solvent-free method to introduce LIN into MSNs unless alternative crystalline forms of the antibiotic are generated. Ideally, these new forms should possess lower melting points than the observed phase transition from form II to form III. Cocrystallization emerges as the method of choice to achieve this goal.

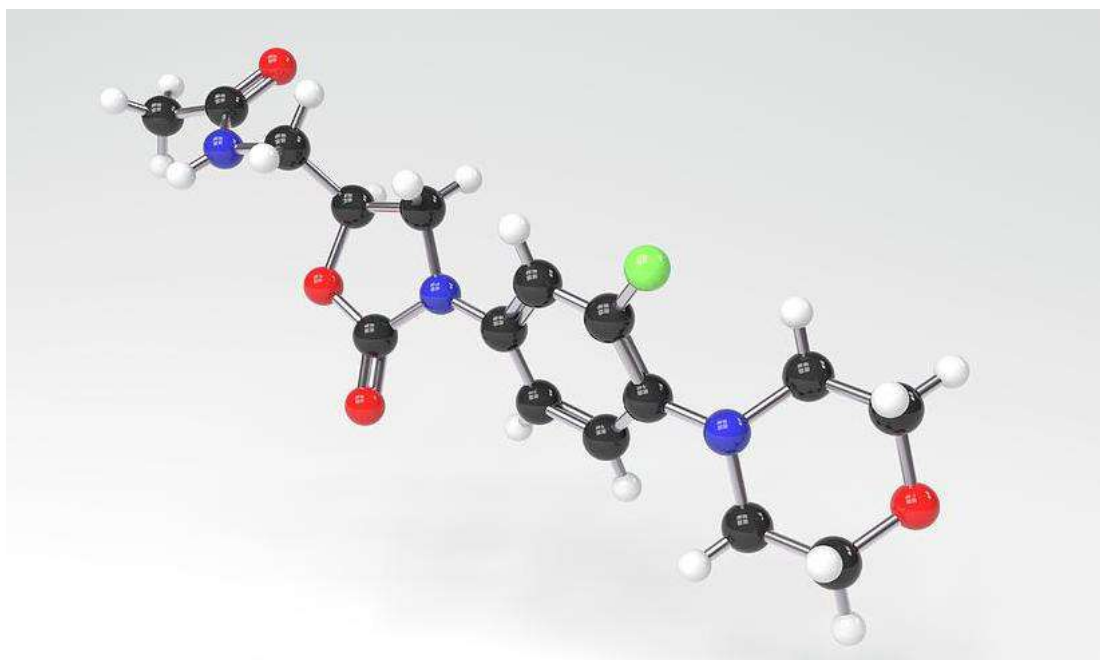


Figure 1.1. Linezolid (LIN) structure.

As indicated by a recent survey encompassing 774 cocrystals [38], approximately 27.7% of cocrystals exhibit lower melting points compared to their individual components. Consequently, the selection of coformers plays a pivotal role in attaining lower melting solid cocrystals of LIN. The available patent literature [39] suggests that LIN forms cocrystals with carboxylic aromatic acids. In the cited study, four LIN cocrystals were produced, with benzoic acid (BA), *p*-hydroxybenzoic acid (PHBA), 1,5-naphthalenedisulfonic acid, and salicylic acid. Among these cocrystals, only those with BA and PHBA demonstrated significantly lower melting temperatures (112°C and 76°C, respectively) than the temperature of the phase transition from LIN form II to LIN form III (approximately 150°C in DSC). Unfortunately, the crystal structures of these crystalline forms were not reported, limiting our understanding of the supramolecular synthon preferences exhibited by LIN.

To fill the above-mentioned gap in our knowledge, this study is focused on the structural characterization of crystalline binary phases of LIN, as well as on the search for new ones. For crystal structure characterization, the method of choice is single-crystal X-ray diffraction, provided that crystals of sufficient dimensions can be obtained. In numerous instances, solid materials crystallize into microcrystalline powders, rendering the application of single-crystal X-ray diffraction for structural elucidation unfeasible. In such scenarios, a combination of high-resolution solid-state NMR and crystal structure prediction (CSP) calculations can offer a

successful alternative. However, when dealing with molecules exhibiting significant conformational flexibility, the CSP-NMR protocol encounters substantial challenges, including uncertainties in NMR signal assignment and a conformational search space too vast to be comprehensively covered by computational methods within a reasonable timeframe.

CSP stands as an intriguing concept within modern computational chemistry, offering the promise of predicting, without any prior experimental knowledge, how a given molecule will crystallize and which crystal forms are most plausible [40-42]. Tremendous progress has been made in this field over the past three decades, enabling reliable predictions for relatively large and complex systems, including expansive organic cages [43], pharmaceutical-like compounds [44,45], and multi-component systems [46-49]. Despite these achievements, CSP has its limitations, particularly when dealing with flexible molecules, owing to the vast search space required for accurate predictions [50,51]. This challenge is amplified in multi-component systems, as is the case with cocrystals, which, by definition, consist of at least two components. In rigid CSP searches, where molecules are considered rigid during crystal structure generation, each combination of conformations of the components in a cocrystal must be independently explored. For highly flexible molecules, this can quickly become impractical. In the context of using CSP for crystal structure determination, these challenges can be mitigated by experimental techniques that help narrow down the search space. For that purpose, the NMR crystallography approach can be used. In its classical form, it integrates advanced solid-state NMR and diffraction-based experiments (mostly powder X-ray diffraction, PXRD) with quantum-mechanical calculations to construct, refine, and validate the most accurate structural model based on experimental data [52-54]. Each of the three methods involved serves distinct purposes. PXRD primarily provides information about the long-range order within the solid, including unit cell parameters, crystal system, and space group. Solid-state NMR data, conversely, offer insight into the local environment of specific nuclei, providing information on the number of molecules within an asymmetric unit of the crystallographic unit cell, molecular conformation, local disorder, and atom-atom proximity resulting from intermolecular interactions.

Together, these experimental data can be used to construct a structural model, which can then be refined and validated against experimental data using computational methods. However, in many cases, ambiguities may arise in interpreting experimental data, such as signal overlap in NMR or low crystallinity of samples. Consequently, the constraints extracted from experiments may not be conclusive enough to build a reliable structural model. In such instances, CSP calculations become especially valuable, as they can potentially yield structural

models regardless of experimental data. In this sense, the experimental and computational components of NMR crystallography and CSP calculations complement each other and compensate for each other's limitations.

Accounting for the presented background, this thesis has pursued the **primary objective of identifying suitable coformers to create novel cocrystals of linezolid with improved physicochemical characteristics**. These cocrystals are envisioned to play a pivotal role in enhancing the efficacy of loading of drug delivery systems, particularly when confined within mesoporous silica nanoparticles. The investigation involved a systematic exploration of various coformers and the application of mechanochemistry to facilitate cocrystal formation. Advanced analytical techniques such as NMR spectroscopy, differential scanning calorimetry (DSC), single crystal and powder X-ray diffraction, and solubility measurements were employed to characterize the resulting cocrystals thoroughly.

This research is poised to significantly advance the realms of cocrystallization and crystal engineering. **Through structural characterization of the obtained binary phases, deeper insights into LIN's propensity for forming cocrystals was sought for**, by establishing a hierarchy of hydrogen bonding acceptors, thus shedding light on the fundamental mechanisms underlying this phenomenon. By systematically evaluating the factors influencing the mechanochemical synthesis of cocrystals, such as varying the amount of solvent in liquid-assisted grinding (LAG) and the duration of grinding, we can elucidate the intricacies of this method and anticipate its outcomes more effectively.

Furthermore, the **evaluation of the selected physicochemical properties of cocrystals** enables us to explore avenues for optimizing API characteristics, potentially leading to more favorable properties. In the realm of powder binary components, demonstrating how the NMR-CSP combination can be utilized to ascertain the crystal structure of a cocrystal, or in more challenging scenarios, to indicate the correct conformation of LIN within the crystal, promises to enhance our understanding of these complex systems.

Studying the factors and methods influencing the loading of binary components into mesoporous materials, and uncovering unexpected interactions, will inform the selection of the most effective approach for loading LIN cocrystal into MSNs. Through **preliminary studies involving the loading of LIN and its cocrystal into MSNs** using developed and modified methods, we can potentially open up new avenues for enhancing drug delivery systems through cocrystal modifications of APIs.

2. State of knowledge

2.1. Cocrystals

The concept of "cocrystals" and the principles of hydrogen bonding in organic cocrystals were initially introduced by Etter [55,56]. A cocrystal is a solid-state compound composed of two or more different neutral molecular species that are typically crystalline solids under ambient conditions. Cocrystals have gained attention as promising alternative solid forms for drug development. Cocrystallization with pharmaceutically acceptable (GRAS) compounds is a proven method for improving the performance of pharmaceutical compounds. This process does not negatively impact the primary pharmacological activity of an API; instead, it offers enhancement in various physical properties. By engaging in cocrystallization, scientists can effectively modify solubility, thermal stability, hygroscopicity, compressibility behavior, and so on. As demonstrated through research, this technique is particularly valuable for drugs with poor solubility [55–60]. Cocrystallization arises from competing molecular interactions between similar molecules (homomers) and different molecules (heteromers) [57,58], mostly *via* hydrogen bonds. Hydrogen bonds are fundamental to molecular recognition phenomena in pharmaceutical systems, generating various molecular networks in the crystalline state, including single-component crystals, their polymorphs, and multiple-component crystals or cocrystals.

In a cocrystal, components combine in specific ratios through non-covalent interactions like hydrogen bonds and van der Waals forces. This approach improves drug properties, merging crystal engineering with pharmaceuticals [10,61]. Cocrystal formers can be excipients or other drugs, allowing for the development of new drug forms [62, 63]. Cocrystallization, especially useful for updating older drugs, complements biological products, promoting cost-effectiveness and patient access to therapy. The rise in novel cocrystals reflects its success, with patent submissions increasing seven-fold from 2004 to 2016 [10]. Pharmaceutical cocrystals offer inventors opportunities to extend drug lifecycles. Recent Food and Drug Administration guidelines recognize cocrystals as intermediates, streamlining their development [64].

2.2. Coformer selection

The process of selecting suitable cofomers for cocrystal development is a pivotal aspect of pharmaceutical research. Several factors come into play when determining the most appropriate cofomer for a specific API. These considerations include the type of functional group, pKa value, physical characteristics, and molecular size of the cofomer [65,66]. Cofomer

selection can be approached through three main methods: experimental, knowledge-based, and computational-based (theoretical) approaches. The experimental method relies on trial and error, wherein various coformers are empirically tested for cocrystal formation with the API. This approach necessitates confirming cocrystal formation using analytical techniques, such as PXRD and DSC. However, this method is often resource-intensive and time-consuming [65]. The knowledge-based methods offer the advantage of predicting cocrystal formation before experimental trials, thereby streamlining the coformer selection process. However, it is important to note that while these methods provide valuable guidance, they do not guarantee a successful cocrystallization of any API molecule and are typically used as complementary tools in the coformer selection process. Still, knowledge-based methods provide a more efficient means of coformer selection than trial-and-error experimental ones. They draw on various principles established from the so-far gained knowledge on cocrystallization to predict potential coformers based *e.g.* on their structural and chemical compatibility with the API. Some of the knowledge-based approaches include the pKa rule, molecular complementarity, hydrogen bond propensity (HBP), and Hansen Solubility Parameter (HSP). Theoretical methods for coformer selection in cocrystal formation involve a systematic and computational approach to identify potential coformers that can interact favorably with the target drug molecule. The computational-based methods are, among others, COSMO-RS and gas-phase molecular electrostatic potential surfaces (MEPS). Machine Learning approaches using molecular descriptors are difficult to classify as they seem to be on the border between theoretical and knowledge-based methods. However, none of these methods consider explicitly the crystal environment and its effects on the stability of a proposed cocrystal. This deficiency can be addressed to some extent by crystal structure prediction (CSP) methods, the reliability of which has increased significantly over the past 30 years [43,55]. However, the major limitation of CSP in the context of cocrystal prediction is their computational cost. In the following parts, some of the most important predictive tools for cocrystal formation are briefly characterized.

2.2.1. Molecular complementarity (MC)

MC, a knowledge-based method for predicting cocrystal formation, evaluates molecular shape and polarity. In its original application, it was observed that descriptors related to these aspects are pivotal in identifying the most likely coformers for a given molecule. The study emphasized the preference for molecules to form cocrystals with coformers of similar shapes. Geometrical descriptors like M/L ratio, S, and S/L ratio were introduced to quantify the geometrical shape, accounting for the lengths of the shortest (S), medium (M), and longest (L)

axes of a rectangular box enclosing the van der Waals volume. It is important to note that these descriptors may vary based on the molecular conformation of a coformer. Beyond geometry, MC considers the dipole moment magnitude, as well as the fraction of nitrogen and oxygen atoms in the molecules. The screening results are presented as a "pass" or "fail" if any of the descriptors do not match the established criteria of similarity, indicating the predicted success or failure of cocrystal formation for the evaluated coformers [67].

2.2.2. Hydrogen Bonding Propensity (HBP)

Supramolecular synthons, integral to cocrystal development, are structural units formed through intermolecular interactions, acting as building blocks for cocrystals [68]. Some of them, like carboxylic acid–pyridine and amide–amide, demonstrate high success rates in cocrystallization [69]. However, it is difficult to estimate whether under given circumstances the formation of supramolecular synthons stabilizing a cocrystal will prevail over synthons stabilizing parent crystal forms. Hydrogen bond propensity (HBP) is a predictive knowledge-based tool that evaluates the incidence of a given supramolecular synthon in the CSD database and estimates the likelihood of cocrystal formation based on the likelihood of this specific interaction to occur, in comparison with the likelihood of competitive interactions. The case of diacerein cocrystals exemplifies the practical application of supramolecular synthon methods, where coformers with specific functional groups were strategically chosen based on a Cambridge Structural Database (CSD) search, resulting in successful cocrystals [70]. The structural chemistry of six thiazole amides was investigated using both experimental crystallographic data and calculated hydrogen-bond propensities as proposed by Sandhu and colleagues. The strength and stability of the homosynthon in these compounds were evaluated by attempting to cocrystallize them with 20 different carboxylic acids. Through liquid-assisted grinding experiments, a total of 120 reactions were attempted, resulting in sixty successful cocrystals. HBP calculations were utilized to anticipate the outcomes of these reactions. A multi-component score (MC score) derived from the HBP calculations, when coupled with a cut-off value >0.0 , yielded a 77% agreement between prediction and experimental outcome (with 88% success for aliphatic acids and 67% for aromatic acids). By adjusting the MC score cut-off to ≥ -0.1 , the overall success rate for cocrystal prediction rose to 91%, notably reducing the occurrence of false negatives [71].

2.2.3. Hansen Solubility Parameter (HSP)

The prediction of the miscibility between a drug and a coformer using the Hansen Solubility Parameter (HSP) offers valuable insights into the potential for cocrystal formation. In principle, if the two substances are miscible, they are more likely to form a binary solid. The HSP is often estimated using group contribution methods, with well-known approaches by Fedors, Hoy, and Van Krevelen being commonly employed for this purpose [72-74].

According to Van Krevelen's criteria, compounds are considered to exhibit good miscibility when their total solubility parameter, the square root of the sum of the squared dispersion, polar, and hydrogen bonding components, ($\Delta\delta$) differs by less than 5 MPa^{0.5}. This parameter is recognized as one of the key indicators for predicting cocrystal formation [74]. Building upon this, Mohammad et al. later proposed that for an API and a coformer to form a cocrystal, their miscibility should extend to the molecular level with $\Delta\delta$ being less than 7 MPa^{0.5} [75].

The HSP has proven to be a valuable tool in various cocrystal screening studies, aiding in the selection of suitable coformers. For instance, it played a crucial role in the synthesis of itraconazole cocrystals [76]. Furthermore, systematic variations of solvents based on their HSP can significantly influence the outcomes of cocrystallization. For example, when crystallizing sulfamethazine–4-aminosalicylic acid from eight solvents with different HSPs and solubility parameters, it was observed that they are likely to interact differently with APIs, ultimately affecting cocrystallization, leading to the observation of distinct polymorphic forms, and highlighting the influence of solvent choice on cocrystal polymorphism [77].

2.2.4. The pKa-based tool

One of the most pressing and yet unsolved issues in selecting coformers is establishing whether a given molecule will indeed create a cocrystal with an API or a salt (in this latter instance the occurrence of a proton transfer from an acid to a base takes place). The pKa value characterizes the tendency of an acid or a conjugate acid of a base to release a proton. A key criterion proposed by the pKa rule is the value of ΔpK_a , which represents the difference between the pKa of the base (pKa_{base}) and the pKa of the acid (pKa_{acid}). When ΔpK_a is greater than 3, it predominantly indicates the formation of a salt. Conversely, when ΔpK_a is less than 0, it predicts the likelihood of cocrystal formation [78]. This prediction method has proven to be reliable in scenarios where ΔpK_a falls above or below these limits. However, the pKa rule encounters challenges when ΔpK_a falls within the intermediate range of 0 to 3. This is a common

occurrence, especially in cases involving cocrystal formers with functional groups such as COOH and pyridine [79–81]. In this intermediate range, the possibility arises for the formation of salts, cocrystals, or even complexes with shared protons or mixed ionization states. Further analysis of ΔpK_a in the context of 6465 crystalline complexes from the Cambridge Structural Database has revealed a linear relationship between ΔpK_a and the probability of proton transfer within the ΔpK_a range of -1 to 4 [82]. This observation highlights the complexity of the ΔpK_a parameter and its potential implications in various crystal formation scenarios. Despite its limitations in the intermediate ΔpK_a range, the pK_a rule remains a valuable and straightforward tool widely applied for the rational selection of coformers in preparing pharmaceutical cocrystals. However, its capacity is focused rather on differentiation between a salt and a cocrystal rather than indicating whether a binary solid will be formed at all. This approach has been successfully employed in developing pharmaceutical cocrystals, including examples such as AMG 517 and a phosphodiesterase-IV inhibitor [83,84].

2.2.5. COSMO-RS

Computational techniques for cocrystal screening have several advantages compared to experimental methods, particularly in terms of resource conservation. One such computational virtual cocrystal screening method is the conductor-like screening model for real solvents (COSMO-RS). COSMO-RS is a theory rooted in fluid-phase thermodynamics that assesses the compatibility of cocrystal-forming substances within a supercooled liquid phase [85]. This approach relies on quantifying the excess enthalpy (H_{ex}) between a mixture of an API and a coformer and the individual pure components to gauge their propensity for cocrystallization. COSMO-RS takes into account various modes of molecular interactions, encompassing electrostatic forces, hydrogen bonding, and van der Waals interactions, thus enhancing its precision in ranking coformers when compared to methods that solely focus on hydrogen bonding between molecules [86]. Furthermore, COSMO-RS offers dependable rankings for coformers to enhance the solubility of APIs. Recent applications of COSMO-RS have encompassed evaluating the likelihood of cocrystallization for various compounds, including salicylamide and ethebamide with aromatic carboxylic acids [87]. It has also been instrumental in guiding the selection of dicarboxylic acids for cocrystallization with phenylpiperazine derivatives [88].

2.2.6. Gas-phase molecular electrostatic potential surfaces (MEPS).

Another virtual cocrystal screening method relies on computed gas-phase molecular electrostatic potential surfaces (MEPS). This particular approach utilizes the identification and quantification of possible interaction points at the molecular surface (referred to as Surface Site Interaction Points or SSIPs) obtained from *ab initio* MEPS calculations for isolated molecules in the gas phase to pinpoint potential coformers. The idea is to use these points to compare whether it is more energetically feasible for a molecule to interact with the coformer or with itself. The effectiveness of this method has been validated using data from 18 experimental cocrystal screening studies. It was applied to assess the likelihood of nalidixic acid forming cocrystals, leading to the identification of 44 coformers with a high probability of success and the prediction of 7 potential cocrystals. Similar screening strategies were employed to uncover new cocrystals for spironolactone and griseofulvin [89].

2.2.7. Hot-stage microscopy

Hot-stage microscopy (HSM) is an example of the experimental screening techniques used for the selection of promising coformers. It involves the direct visualization of the sample as it is heated. When two components are heated together, a high melting point component typically melts and recrystallizes before the other molten component comes into contact with it, creating a distinct zone of mixing. This method allows researchers to identify the number of phases present in the system, making it a useful tool for cocrystal screening. By examining the thermodynamic landscape with the assistance of a binary phase diagram, researchers can improve the efficiency of cocrystal screening without the necessity to perform many separate crystallization experiments. For instance, researchers used hot-stage microscopy to screen for cocrystal formation involving nicotinamide as a coformer with various APIs. This method, also known as the Kofler contact method, proved effective in elucidating cocrystal formation and understanding the thermodynamic behavior of binary systems [90].

Despite the progress made with theoretical, knowledge-based, and experimental methods, each has its own set of strengths and limitations. The success rates of these methods vary depending on factors such as the nature of the drug molecule, the desired properties of the cocrystal, and the available computational or experimental resources, but in principle they fall somewhere between 30 and 80% [91]. Therefore, a holistic and synergistic approach that integrates these diverse methods is essential for overcoming the inherent challenges in coformer selection.

2.3.Methods of cocrystal preparation

Cocrystal preparation methods can be broadly categorized into two major categories: solution crystallization and solid-state crystallization. Various methods and techniques are employed for the preparation of pharmaceutical cocrystals, with each approach offering its own advantages and considerations. The choice of method depends on factors such as the specific coformers, the desired properties of a cocrystal, and the challenges presented by the system.

2.3.1. Solvent Evaporation

The technique described is one of the most commonly employed methods for generating cocrystals and crystals in general. Cocrystallization involves dissolving an API and a coformer in a shared solvent with an appropriate stoichiometric ratio and then allowing the solvent to completely evaporate. During the evaporation process, the molecules in the concentrated solution undergo the required conformational changes, leading to proper intermolecular interactions between different functional groups. This results in the production of a cocrystal product.

The choice of solvent is a crucial factor in this method as it influences the solubility of the components and may promote or inhibit certain intermolecular interactions. If the solubility of an API and a coformer in a solvent is not similar, the component with lower solubility tends to precipitate first. The preparation of cocrystals by solvent evaporation is typically conducted on a small scale and does not require complex equipment. This approach often yields cocrystals of high quality and purity.

Nevertheless, it comes with three notable drawbacks. Firstly, it necessitates the use of relatively large amounts of solvent, raising concerns about both environmental impact and cost-effectiveness. Secondly, the scalability of the method for producing larger quantities of cocrystals may be limited, rendering it less suitable for industrial-scale production. Thirdly, and particularly significant in the context of linezolid (LIN) cocrystallization, a substantial solubility disparity between an API and a coformer may occur. In the context of this thesis, the divergent solubility preferences of LIN and the coformers in various solvents introduce complexity to the cocrystal synthesis process, requiring careful consideration and optimization of solvent selection to achieve efficient cocrystal formation. Addressing all three mentioned challenges is pivotal for advancing the practical applicability and scalability of cocrystallization techniques in pharmaceutical manufacturing [63].

2.3.2. Solid-State Grinding (Neat Grinding)

This cocrystallization method is a solvent-free approach. It involves mixing solid materials in the appropriate stoichiometric ratios to create a desired cocrystal. The mixture is then subjected to mechanical forces using tools such as a mortar and pestle, a ball mill, or a vibratory mill. The typical grinding duration ranges from 30 to 60 minutes. This method allows for the efficient preparation of numerous cocrystals, and any failures, if they are not the result of the intrinsic properties of the systems, are usually attributed to inappropriate settings or conditions.

The reduction in particle size achieved through grinding increases the specific surface area available for interactions between the cocrystal-forming materials, facilitating the development of intermolecular bonds. This method offers the advantage of increased selectivity compared to cocrystallization through dissolution. It is a straightforward and rapid way to prepare the desired cocrystal. Moreover, experiments involving the mixing of cocrystals with other components that can potentially form cocrystals with an API have been conducted. In such cases, the cofomer can be replaced, which serves two purposes: it allows for the assessment of the stability of a cocrystal in the presence of other excipients, and it can reveal alternative modifications of a cocrystal. Some modifications that do not typically occur in the process of dissolution, such as the caffeine-trifluoroacetic acid cocrystal, were initially obtained only through grinding. Thus, this method has also been used to clarify hydrogen bond preferences. Mechanochemistry, specifically solid-state grinding, was employed in the patent application for the pterostilbene-caffeine cocrystal, highlighting its versatility and importance in cocrystal research [92]. Additionally, it is noteworthy that the first cocrystals of LIN were successfully obtained through grinding, showcasing the effectiveness of mechanochemical methods in the synthesis of pharmaceutical cocrystals [39].

Despite its advantages, mechanochemistry has some inherent disadvantages, particularly when considering scale-up processes. Moreover, the production of cocrystals through grinding can result in the formation of microcrystalline powders, making it challenging to analyze the crystal structure accurately. This limitation poses difficulties in obtaining detailed structural information, which is crucial for a comprehensive understanding of the material properties. Therefore, while mechanochemistry is a valuable tool in cocrystal research, addressing issues related to scale-up and structural analysis is essential for its broader application in the pharmaceutical industry [93].

2.3.3. Liquid-Assisted Grinding (Solvent-Drop Grinding)

This method is a modification of neat grinding, and it involves adding a small amount of solvent during the grinding process [59,92]. This technique has been employed to enhance supramolecular selectivity, both in terms of polymorphic and stoichiometric outcomes, in crystalline systems. The process entails mixing the two components and introducing a minimal quantity of solvent, typically a few tenths of an equivalent of solvent per mole of the component. It is important to note that the solvent used is usually not designed to be a part of the final product.

The effect of the solvent can be described as catalytic-like, as it accelerates the cocrystallization process but is not usually incorporated into the cocrystal structure. This method offers several advantages, including improved performance, greater control over polymorph production, and enhanced crystallinity of the final product. It is compatible with a wide range of coformers. Additionally, it significantly accelerates the cocrystallization rate, making it particularly useful for cases where cocrystal formation is slow when employing neat grinding for an extended duration. The usefulness of liquid-assisted grinding was demonstrated for example for the caffeine-glutaric acid (1:1) cocrystals, for which neat grinding predominantly resulted in form I contaminated with another polymorphic form, but liquid-assisted grinding with less polar solvents (*e.g.* cyclohexane or hexane) favored pure form I, while more polar solvents (*e.g.* water or acetonitrile) led to pure form II [95]. This capability allows for the interconversion between crystalline forms of polymorphic organic components, depending on the polarity of the solvent.

However, there are some limitations to liquid-assisted grinding. It is typically conducted on a small scale, consumes relatively high amounts of energy, and may have lower performance in terms of product purity compared to other methods. And although the crystallinity of the final product is usually higher than for neat grinding, microcrystalline powders are the most commonly expected outcomes of the process [59,94].

2.3.4. Other methods of cocrystallization

Other methods of cocrystallization entail a variety of solution or solid state methods. Below some of the more commonly used are very briefly characterized.

Among the solution methods, the slurring is a straightforward method that involves adding a crystallization solvent to create a suspension of an API and coformer, followed by

stirring, filtration, and drying. Notably applied in the celecoxib-venlafaxine cocrystal patent, it simplifies cocrystal synthesis [96]. Also conducted in solution is antisolvent cocrystallization, in which into a solution of dissolved API and coformer, a solvent in which the components are less soluble is introduced, promoting solid component precipitation. The main disadvantage of this method is that it exhibits lower performance compared to other methods and requires a relatively large volume of solvent [96]. An interesting approach to cocrystallization is offered by the use of supercritical fluids (SCF), such as CO₂, which combine gas and liquid characteristics, serving as an alternative to organic solvents. CO₂ can be used as a solvent, an anti-solvent, and an atomized anti-solvent. This method, including SCF CO₂ as an antisolvent crystallization and spray-drying crystallization, has been employed to produce pure indomethacin-saccharin cocrystals [97]. Finally, a spray drying technique is a process, in which a liquid or slurry is rapidly dried by exposure to hot gas, offering advantages in the formation of pure cocrystals. Unlike traditional solvent evaporation methods, solutions with components having significantly different saturation levels can yield pure cocrystals when spray-drying is employed. This approach facilitates kinetic monitoring and encompasses the influence of the material's glassy state in the process [98].

Among the solid phase cocrystallization methods, the innovative Resonant Acoustic Mixing® (RAM) technique utilizes a low-frequency acoustic field for non-contact mixing, reducing both mixing time and cost. Its most important advantage over other solid-state methods is its easier scalability. Successful applications, such as the carbamazepine-nicotinamide cocrystal, highlight its suitability for large-scale cocrystal production, delivering high-purity cocrystalline products [99,100]. Another well-scalable method is Twin-Screw Extrusion (TSE), which transforms raw materials into a uniform product using controlled conditions. It has been employed in pharmaceutical cocrystal preparation, demonstrated, for example in the patent for L-malic acid and L-tartaric acid cocrystallization. A huge advantage of TSE is that it can be applied as a part of the Matrix-Assisted Cocrystallization approach for the simultaneous production and formulation of numerous pharmaceutical cocrystals at the same time, resulting in high-quality cocrystals [90,101].

2.4. Properties enhancement of an API by cocrystallization

Cocrystals of pharmaceuticals have the potential to improve the physical and chemical characteristics of drugs. These enhancements include melting point, tablet formation, solubility, stability, bioavailability, and permeability, which will be illustrated with relevant examples.

2.4.1. Melting Point

The melting point is a fundamental physical property, representing the temperature at which a solid transitions into a liquid phase while maintaining thermodynamic equilibrium [83]. This property is crucial for assessing product purity, with sharp melting points and narrow ranges indicating high purity. A high melting point signifies the thermodynamic stability of new materials, offering enhanced thermal stability for an API through the selection of coformers with higher melting points [62]. The melting point of pharmaceutical cocrystals can be adjusted by carefully choosing the coformers.

When considering the factors that influence melting points, such as molecular arrangement within the crystal lattice, molecular symmetry, intermolecular interactions, and conformational degrees of freedom, it becomes apparent that drawing a strict line from a molecular structure to the crystalline lattice energy to the melting point can be challenging [102]. This complexity intensifies in multicomponent systems, as each component possesses distinct properties that can influence the environment and intermolecular interactions within the lattice [103]. The above considerations indicate that the melting point of an API can be changed through cocrystallization. For example, carbamazepine/nicotinamide (1:1) cocrystal has a melting point of 151–161 °C, while the raw drug and the coformer exhibit melting points at 192 and 128 °C, respectively [104]. Another cocrystal of carbamazepine with glutaric acid has a melting point of 124 °C, when their pure compounds have, respectively, 192 and 98 °C melting points [105]. Some drugs exist in a liquid state at room temperature due to their low melting points. Binding them in one crystal lattice with a solid component has the potential to alter the melting point of liquid drugs by incorporating a suitable coformer. Propofol is applied to induce and maintain general anaesthesia and sedation. It is formulated as an oil-in-water emulsion because its low melting point of 18 °C results in associated problems including instability, pain on injection, and hyperlipidemia. McKellar et al. adopted a binary system approach to obtain a novel solid form of propofol using isonicotinamide as the coformer. The propofol–isonicotinamide binary is a stable solid at room temperature due to the increased melting point 50 °C higher than that of the starting material [106]. Another study reported by Bacchi et al. showed that binaries of propofol–bipyridine and propofol–phenazine could convert liquid propofol into a crystalline phase [107].

2.4.2. Solubility

Solubility is a critical parameter for formulations of poorly soluble drugs. Various approaches have been employed to enhance drug solubility, including salt formation, solid dispersions, and particle size reduction, among others. Cocrystallization has also been explored by several researchers as a mean to improve solubility [108].

The solubility of cocrystals has been studied in diverse conditions and media, encompassing water, 0.1 N HCl, phosphate buffer, simulated gastric fluid (SGF), and simulated intestinal fluid (SIF). Most studies report powder dissolution data at multiple time points. Some studies controlled particle size through sieving, while others did not specify control measures, and some employed different particle size ranges for comparison. This variability highlights the flexibility of experimental variables that can be tailored to obtain specific information [109]. As an example of how solubility can be changed through binary system formation can serve that of cocrystals of epalrestat with betaine, in which a two-fold increase in solubility in comparison to pure API was observed. The reason was attributed to the formation of a layered structure between the drug and the coformer. As compared to epalrestat, betaine has higher water solubility with a higher tendency to go into solution, resulting in the formation of cocrystals with higher solubility. On contact with water, the rate of epalrestat dissolution is accelerated due to rapid dissolution of betaine, which was supported by the cocrystal having a 3.5-fold higher intrinsic dissolution rate compared to the parent drug [110]. Selection of a coformer of intermediate solubility directly influences cocrystal solubility, as it will lead to a prolonged parachute effect. This hypothesis is effectively highlighted by furosemide and 2-picolinamide sesquihydrate cocrystal [111]. Sustained super-saturation levels of the dissolved drug were maintained throughout 24 h. This was attributed to the fact that the coformer 2-picolinamide has intermediate solubility, which led to the gradual leaching of the drug. Such a phenomenon was described by a new term, the synthon-extended-spring-parachute effect. Further, the cocrystal with higher polarity composed of zwitterionic coformer will have a higher solubility and consequently higher dissolution rate compared to non-ionized ones. For example, for the non-ionic cocrystal of diclofenac with theophylline only a 1.6-fold increase in solubility was observed, whereas cocrystal of the same drug with zwitterionic conformer, L-proline, showed a 7.69-fold increase in solubility [112,113].

2.4.3. Stability

Stability studies play a pivotal role in the development of new dosage formulations, especially in the context of pharmaceutical cocrystals. Several crucial stability studies should be conducted, including investigations into relative humidity, stress, chemical stability, thermal stability, solution stability, and photostability.

In relative humidity stress tests, automated water sorption/desorption studies are undertaken to assess the impact of moisture on the formulation [83]. Cocrystallization can inhibit an unwanted hydration process, as happens *e.g.* in the case of anhydrous caffeine. In the cited study cocrystals of caffeine were synthesized with acid coformers, such as oxalic acid, glutaric acid, maleic acid, and malonic acid. The stability of the cocrystal towards hydration followed the order of strength of acid groups in coformers, where the oxalic acid cocrystal was stable while the glutaric acid, which has the weakest acidity groups, showed the lowest stability. It was hypothesized that the driving force for stabilization of cocrystals was achieved by employing the hydrogen bond donor such as the carboxylic acid group for the basic imidazole nitrogen of caffeine. This effectively prevents water incorporation into the lattice of a cocrystal [114]. Similar studies were conducted with etoricoxib, where stability enhancement was seen due to the strong hydrogen bonding between the coformer and API [115].

The chemical stability of adefovir dipivoxil was influenced by crystallizing it with acidic and basic coformers, saccharin and nicotinamide, respectively. The acidic coformer clearly enhanced the stability, while the basic coformer did not stabilize the structure to such an extent. The authors of the study hypothesized three reasons for this: (1) the acidic coformer provided a micro-acidic environment to the structure, inhibiting the hydrolysis, whereas the basic coformer enhanced the degradation; (2) the acidic coformer introduced into the crystal lattice inhibited the dimerization, which later may lead to degradation; (3) the strong hydrogen bond of an acidic coformer prevents the moisture attack on the functional groups of drugs which are prone to hydrolysis [116].

2.4.4. Bioavailability

Bioavailability refers to the rate and extent to which a pure drug enters the systemic circulation. The challenge of low oral bioavailability often arises in the development of new formulations for APIs, and can be improved by cocrystallization. For example, baicalein, a flavonoid which has antiproliferative effects on pulmonary artery smooth muscle cells and may have anti-cancer properties, has a very poor oral bioavailability. The formation of a cocrystal

with nicotinamide led to a remarkable improvement in this property. Studies showed that this cocrystal achieved a peak plasma concentration that was 2.49 times higher and an area under the curve that was 2.80 times greater compared to the pure drug when administered to rats [117]. Similarly, the cocrystal of meloxicam with aspirin, which are both non-steroid anti-inflammatory agents, demonstrated superior oral bioavailability compared to pure meloxicam. In experiments involving rats, it exhibited a 12-fold faster onset of action than pure meloxicam. Meloxicam–aspirin represents an informative case study, illustrating the ability of API–API cocrystals to improve API bioavailability. In a rat pharmacokinetic study, the oral bioavailability of meloxicam from meloxicam–aspirin cocrystal was higher than from meloxicam alone (69% versus 16%, respectively). Maximum plasma concentrations of meloxicam were also increased after administration of the cocrystal, although time to achieve maximum plasma concentration was similar versus the reference meloxicam. The authors of this study speculated that these effects could lead to a more rapid onset of analgesia, proposing that plasma levels of meloxicam after cocrystal administration might reach those required for therapeutic effect sooner than from reference meloxicam [118]. These findings underscore the valuable role of cocrystals in addressing the challenge of low oral bioavailability [59].

2.4.5. Permeability

Drug absorption and distribution within the body are significantly influenced by the permeability of drugs across biological membranes. The extent of drug permeability is closely related to the n-octanol/water partition coefficient, which is quantified using parameters like $\log P$ and $(C \log P)$ for the unaltered form of a drug. The presence of a coformer in a crystal lattice together with a drug has a capacity of influencing drug permeability, even though this process takes place after dissolution. For instance, the permeability of a Biopharmaceutics Classification System class-III drug, 5-fluorouracil (5FU), was effectively enhanced through cocrystallization with various coformers such as 3-hydroxybenzoic acid, 4-aminobenzoic acid, and cinnamic acid. This improvement in permeability was attributed to the formation of specific heterosynthron interactions between the drug and its coformer in a solution [119]. All of the cocrystals showed improved membrane permeability compared to free 5FU. The cumulative amount per unit area of permeated 5FU in the first ten hours for the first 1-3 rank cocrystals was increased by 41%, 70% and 83%, and the steady penetration rate of the first 1-3 rank cocrystals was increased by 38%, 66% and 79% respectively, as compared to pure drug [120]. Similarly, hydrochlorothiazide, another drug used to treat hypertension and swelling due to fluid build-up, was investigated for its permeability in cocrystal form with different coformers using

Franz diffusion cells [121]. In the studies, it was observed that the drug flux across membranes was consistently higher for the cocrystals in comparison to the pure drug, except for the succinamide cocrystal. This enhancement in permeability was again attributed to the formation of specific intermolecular interactions between the drug and its coformers [122].

2.5. Drug delivery systems (DDS) design

Drug nanoformulations have presented a persistent challenge to researchers, as the creation of safe and efficient systems that can deliver precise drug concentrations to target sites within the body, bypassing various *in vivo* barriers, remains a complex task. An appealing solution to address this challenge lies in the utilization of smart and intelligent drug delivery systems (DDS). Among these, mesoporous silica stands out as promising materials.

Mesoporous silica nanoparticles (MSNs), first discovered in the early 1990s, have seen wide-ranging applications across industries and scientific fields, including heterogeneous catalysis, electrochemistry, analytical chemistry, molecular biology, and more. The initial foray into pharmacy occurred in 2001 when Vallet-Regi introduced the use of MCM-41 silica in the release of ibuprofen [123]. This pivotal work marked the beginning of extensive research into the deployment of mesoporous particles as carriers within drug delivery systems.

Importantly, silica has received approval from the US Food and Drug Administration as "Generally Recognized as Safe" [124]. It is also authorized for use in cosmetics and as a food additive. Investigations conducted in simulated body fluids have revealed a three-stage degradation process of mesoporous silica nanoparticles following administration, which appears to facilitate drug release. Furthermore, *in vivo* studies assessing absorption, distribution, and excretion in mice following oral and intravenous MSN administration have indicated favorable tissue biocompatibility. However, intramuscular and subcutaneous administration posed challenges in MSN absorption. *In vivo* assessments, including mortality rates, clinical observations, pathological examinations, and blood chemistry analyses, have generally shown low toxicity of MSNs in mice. These silica nanoparticles tend to accumulate primarily in liver cells, from which they are gradually eliminated over approximately four weeks, although prolonged use at higher doses has been associated with a liver damage [125-128].

2.5.1. Mesoporous silica nanoparticles (MSNs)

Today, porous silica matrices have become widely adopted as carriers for active substances. In pharmaceutical applications, amorphous silica is particularly prevalent due to its

lower toxicity compared to the crystalline form [129-133]. Consequently, various types of silica have undergone extensive investigation, encompassing porous and non-porous silica, fumed silica, silica gels, and more. To further enhance the properties of porous silica materials, meticulous control of pore structural features has been employed, leading to the development of ordered mesoporous particles, currently the most commonly used, as evidenced by the extensive literature available [15-134]. These ordered mesoporous particles, characterized by their structured porous design (often featuring channels without interconnections), large surface area (exceeding 700 m²/g), and high pore volume (above 1 cm³/g), offer precise control over loading and drug release kinetics [135].

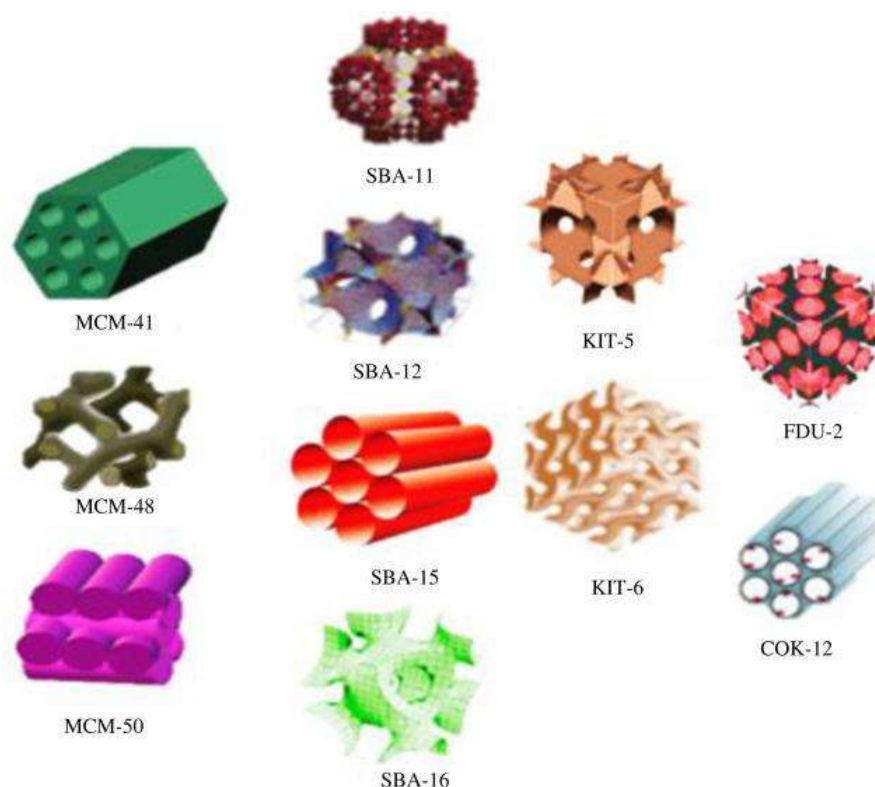


Figure 2.1. Types of mesoporous silica nanoparticles. Reprinted with permission from ref. [139]

MSNs possess two functional surfaces: an inner cylindrical surface formed by pores and an outer surface. Both of these surfaces can be selectively functionalized to enhance loading and release properties. Additionally, the outer surface can be modified to optimize drug delivery to specific targets within the body [136,137]. One of the most significant advantages, particularly from a pharmaceutical perspective, is the enhancement of the solubility of an API when loaded into mesoporous silica, resulting in the formation of drug-carrier dispersion

systems [138]. Figure 2.1 illustrates the most commonly utilized MSNs in drug formulation, showcasing differences in pore size and shape [139].

2.5.2. Drug Confinement Methods

The loading of drugs into the pores of mesoporous silica can be achieved through various methods, as summarized graphically in Figure 2.2 [140]. Generally, these methods are categorized into two primary approaches: solvent-free methods and solvent-based methods, often referred to as wet methods [138-141].

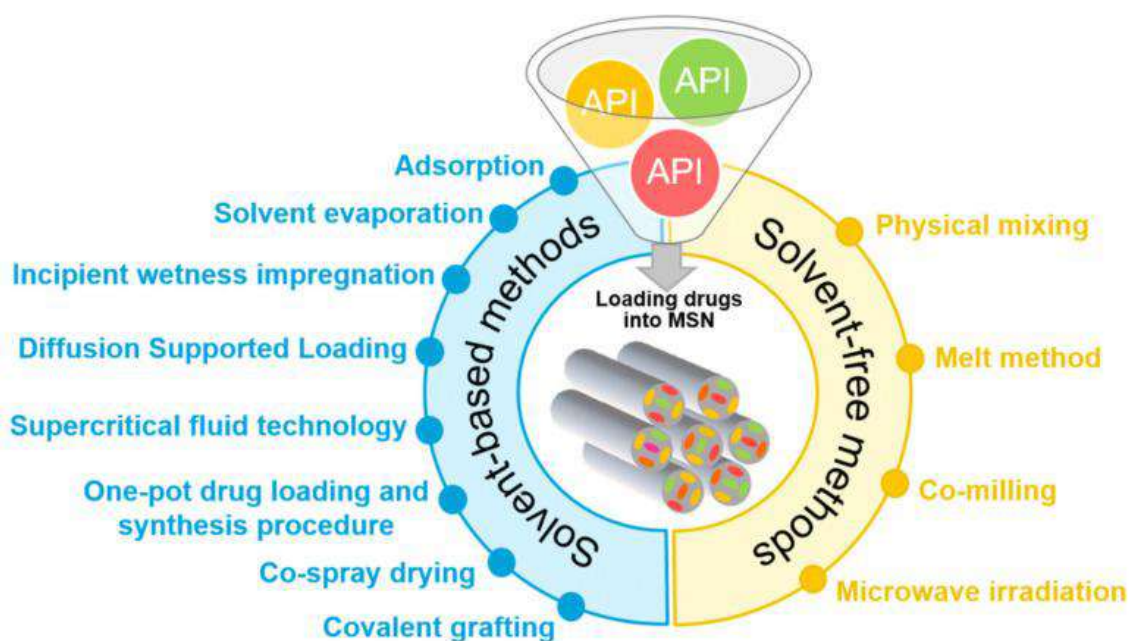


Figure 2.2. Drug confinement methods. Reprinted with permission from ref. [140].

The process of drug encapsulation entails the adsorption of drug molecules onto the inner and outer surfaces of mesoporous silica under conditions conducive to interactions between the drug and the carrier, including van der Waals forces, hydrogen bonding, electrostatic binding, or even covalent bonding [140]. Ideally, a drug loading process should rapidly confine a substantial quantity of a drug, which subsequently can be released in a controlled manner as per a desired release profile [141]. It is also desirable to minimize the fraction of the drug adsorbed on the external particle surface to prevent the risk of crystallization due to the absence of pore entrapment effects [143].

The extent of drug loading depends on several critical parameters. Foremost among these are the surface area of the mesoporous silica and the affinity of a drug for the silica substrate

[144,145]. In wet methods, the internal pore volume of the silica, the polarity of the solvent used, and the concentration of the drug in the solution also play pivotal roles [146]. The choice of the drug loading method has a significant impact on the degree of drug loading, the distribution of a drug within the silica, and the physicochemical properties of the loaded drug [131], although further studies are needed to fully recognize the influence each of the loading method have.

For the successful commercialization of any DDS, it is imperative to have an easy, cost-effective, and reproducible method for large-scale production. Since the encapsulation of APIs is a critical step in the application of mesoporous silica-based delivery systems, there is a pressing need to develop suitable large-scale drug-loading techniques. The most common methods of drug loading, their advantages and disadvantages are discussed below.

2.5.2.1. Solvent-Based Methods

There are several solvent-based approaches for loading drugs into mesoporous silica, each aiming to improve drug release by maintaining the API in an amorphous state within the MSN. In general, in wet methods, regardless of the specific procedure, it is essential to remove the solvent after the loading to acceptable levels in accordance with the guidelines of the International Conference on Harmonization (ICH) Q3 (R5) [147]. Therefore, whenever possible, it is recommended to use less toxic and safe solvents, such as ethanol or supercritical or near-critical CO₂, as alternatives to organic solvents in the drug loading process for human pharmaceutical applications [148-150]. It is also important to note that loading drugs using solvent-based methods can be challenging due to their often multi-stage and time-consuming processes, large solvent volumes, and difficulties in controlling the filling factor. The various wet-based loading methods offer different advantages and drawbacks, and their selection depends on the specific characteristics of a drug and the desired drug delivery system.

2.5.2.1.1. Adsorption

The adsorption method is a widely used and simple technique for loading drugs into the pores of MSNs. In this method, mesoporous silica is immersed in a concentrated drug solution. After sufficient time, drug molecules are adsorbed onto the pore walls. The drug-loaded MSNs are then separated from the solution through filtration or centrifugation, and the particles are typically dried to remove any residual solvent. However, in some cases, the drying step may be omitted. While the adsorption method can be employed for both hydrophilic and hydrophobic

drugs and is suitable for thermally sensitive substances, it often requires high drug concentrations to achieve significant drug loading, which can be challenging for poorly soluble drugs. Additionally, this method is time-consuming, and it is challenging to predict the degree of drug loading. Moreover, a considerable amount of the drug may be lost during the filtration or centrifugation process [151].

2.5.2.1.2. Incipient Wetness Impregnation

The incipient wetness impregnation method, commonly used for catalyst preparation, is also suitable for loading drugs into mesoporous materials. In this approach, a known volume of a concentrated drug solution, approximately equal to the pore volume of the MSN, is added dropwise to the silica. The wet powder, with the drug diffusing into the pores through capillarity, is then dried and quickly washed to remove excess drug coating on the external silica surface. This method is more efficient than traditional solvent immersion processes and takes advantage of the large pore volume of mesoporous silica. However, achieving a high degree of drug loading typically requires the use of highly concentrated drug solutions and repeated impregnations, extending the loading process. The uniformity of drug distribution can be challenging to control, and there is a risk of drug crystallization on the silica's external surface, potentially blocking mesopores [143].

2.5.2.1.3. Solvent Evaporation

The solvent evaporation method combines aspects of both adsorption and subsequent rapid solvent evaporation. In this approach, silica is dispersed in a volatile organic solution of a drug, such as ethanol or dichloromethane. The solvent is then rapidly evaporated, either using a rotary evaporator or heating, to obtain drug-loaded MSNs. Unlike the adsorption method, where solvent removal occurs through filtration, solvent evaporation may affect the physical state of the drug, its localization within the MSN, and the rate of release from the carrier. The solvent evaporation method provides more time for drug molecules to rearrange and aggregate inside the mesopores compared to the incipient wetness impregnation method, resulting in faster release kinetics [24].

2.5.2.1.4. Diffusion Supported Loading (DiSupLo)

Diffusion Supported Loading (DiSupLo) is an efficient method developed in the group of professor Potrzebowski for loading APIs into mesoporous silica. In this approach, a pre-

homogenized physical mixture of an API and MSNs, with desired proportions of both components, is placed in a closed vessel containing ethanol for a specific duration at room temperature, without direct solvent-solid contact. The ethanol vapor diffuses into the solid mixture, condenses, and dissolves the drug. The dissolved API is transported into the pores of the MSN through capillary forces. DiSupLo offers several advantages, including being a fast process requiring minimal amount of solvent, environmental friendliness, ease of use, and suitability for achieving high drug loading degrees. This technique is particularly beneficial for loading two or more components with specific API compositions, expanding the applicability of MSNs for multi-component systems [152]. Its main limitation is a limited scalability.

2.5.2.1.5. Supercritical Fluid Technology (SCF)

Supercritical Fluid technology, commonly used in the food and chromatography industries, is another method for loading drugs into mesoporous silicas. SCF technology has several advantages over traditional organic solvents, including the ability to efficiently impregnate drugs into solid matrices. Carbon dioxide is the most commonly used supercritical fluid due to its mild critical conditions, inertness, non-flammability, and non-toxicity. Additionally, SCF technology allows for the removal of residual solvent when the drug loading process is performed without a cosolvent, making it environmentally friendly. However, some drugs exhibit poor solubility in supercritical CO₂, which can be a limitation. Despite this, SCF technology offers potential benefits, including reduced processing time and avoidance of residual solvents [153,154].

2.5.2.1.6. Covalent Grafting

Covalent grafting involves linking the drug to functional groups present on the pore walls of mesoporous silica through covalent bonds. This approach prevents the leaching of the drug before it reaches the target site and allows for controlled drug release upon the breakage of the covalent bond. Commonly employed bonds for covalent attachment of drugs include amide, disulfide, ester, thiol, and carbamate bonds. Covalent grafting offers advantages such as slow drug release, improved biodistribution, therapeutic efficacy, and reduced systemic toxicity. However, this method may convert the API to an inactive form, so preserving the original molecular structure of the drug is essential. Additionally, the presence of sufficient functional groups on the carrier surface is not always guaranteed, which can affect colloidal stability and

surface charge. Steric hindrance of drug molecules crowded on the silica surface can also impact the formation and breaking of chemical bonds [155-166].

2.5.2.2. Solvent-free Methods

Solvent-free methods for loading drugs into mesoporous silica offer several advantages compared to wet methods. They are less time-consuming, allow for a high degree of drug loading, and are environmentally friendly as they do not require the use or removal of residual solvents from drug products.

2.5.2.2.1. Thermal solvent free (TSF) (melt method)

The melt method involves heating a physical mixture of the drug and mesoporous silica above the melting point of the drug, which, in a molten state, can enter the MSNs pores. This approach is highly efficient and significantly reduces the time required for drug incorporation into the mesoporous silica. However, it is most suitable for thermally stable drugs with low viscosity after melting. The viscosity of the molten drug can impact its penetration into the mesopores, and this method may not be suitable for all types of drugs [131,158].

2.5.2.2.2. Co-Milling (Mechanochemical Grinding)

Co-milling is a commonly used technique for producing submicrometric particles and solid-state amorphization. Recent studies have shown that milling, using a planetary ball mill, can be an effective solvent-free method for introducing organic compounds, such as benzoic acid and 4-fluorobenzoic acid, into the pores of MCM-41. This technique is simple, does not involve time-consuming steps, and can be scaled up for industrial applications. However, it is important to consider the resistance of nanocarriers to mechanical stress during ball milling processes. The duration of milling can also impact the crystallinity of mesoporous materials, with longer milling times leading to a loss of crystallinity [159-162]. This issue was well-recognized for MCM-41. Abu-Zied et al. investigated the effect of ball milling on the structure, texture, and morphological properties of mesoporous MCM-41 material [162]. Their results showed that by increasing the milling time, the amorphization process of mesoporous MCM-41 material accelerates. MCM-41 retains its initial crystallinity until 30 min of milling time. A serious loss of MCM crystallinity occurs after 1–2 h of milling, while the complete loss of crystallinity of this material is noticeable after four hours of ball milling [163].

The existing array of drug loading methods serves various applications but lacks universal applicability, often designed for specific contexts rather than easily transferable across different systems. This underscores the necessity for novel approaches in drug loading techniques. Consequently, the pursuit of introducing modifications into loading methods is warranted, aiming to address this limitation and enhance the versatility and effectiveness of drug delivery systems.

2.6. Characterization methods

After forming a binary system or a confined mesoporous material, one of the crucial steps is to identify the precise nature and purity of the system through appropriate analysis. This process is essential for pharmaceutical cocrystals, as the uniformity of the drug can significantly impact their physicochemical properties. Certainly, as the interest in utilizing mesoporous silica nanoparticles for drug delivery grows, there is a clear need to use suitable analytical tools for studying drug loading.

Several conventional analytical methods have been employed to study binary systems, offering various insights into their structure and behavior. These methods include techniques such as single crystal X-ray diffraction, a method of choice for crystal structure analysis, provided that a suitable crystal can be grown, powder X-ray diffraction, spectroscopy (NMR and Raman), and thermal analysis (DSC and TGA). Since each technique analyses different aspects of solid state structure, it often provides partial information, and usually only its combination is necessary to characterize the material comprehensively. Some widely used techniques, which were also utilized in this PhD thesis, are described below.

2.6.1. Single crystal X-ray diffraction

The primary technique for crystal structure determination, single crystal X-ray diffraction (SCXRD), is a technique to determine crystalline materials atomic and molecular structure by analyzing the interaction of X-rays with a crystal, providing detailed insights into the arrangement of atoms and their bonding within a material. SCXRD relies on the diffraction of X-rays by the periodic atomic planes in a crystal. When X-rays strike the crystal, they are scattered in specific directions based on the crystal internal structure. This phenomenon is governed by the Bragg's Law:

$$n\lambda = 2d \sin\theta$$

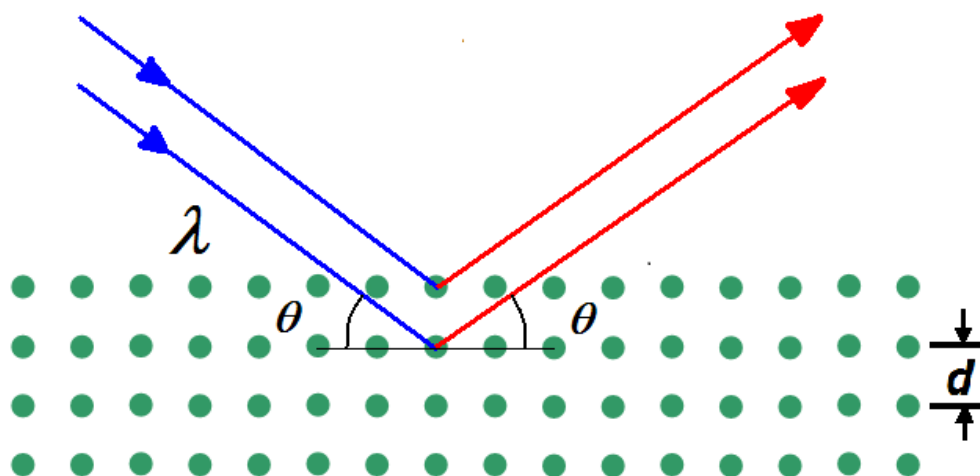


Figure 2.3. Bragg's Law, n is the order of diffraction, λ is the X-ray wavelength, d is the distance between atomic planes, and θ is the diffraction angle.

To conduct SCXRD, a high-quality single crystal is mounted on a goniometer and exposed to an X-ray beam. The resulting diffraction pattern, recorded by a detector, contains information about the electron density within the crystal. Computational analysis of these patterns reveals the positions of atoms, the structure geometry, and the crystal lattice symmetry.

SCXRD provides highly detailed structural information, including atomic positions, bond lengths, bond angles, and molecular geometry, with sub-angstrom precision. It is capable of resolving the structures of both small molecules and large macromolecules, such as proteins, making it invaluable across diverse scientific disciplines. The technique is also instrumental in identifying crystal symmetry and distinguishing between polymorphic forms, offering critical insights into material properties. Additionally, SCXRD enables researchers to map electron density, revealing bonding and chemical interactions within the crystal. As a minimally invasive method, it preserves the sample for further analysis, making it both precise and non-destructive.

Despite its exceptional capabilities, single-crystal X-ray diffraction has several limitations. The technique requires high-quality, defect-free single crystals of adequate size, which can be difficult (or indeed impossible in some cases) and time-consuming to produce. Similarly, in the case of binary systems like cocrystals, they are often prepared by mechanochemistry or desolvation, which leads to microcrystalline powders, while single-crystal growth from solution can be challenging due to differences in the solubility of the parent components. Analyzing large or disordered molecular systems poses challenges due to weak diffraction signals or complex

unit cells, while proper alignment and mounting of the crystal demand significant expertise. Furthermore, SCXRD relies on advanced instruments and powerful computational tools for accurate data collection and refinement. Additionally, because X-rays primarily interact with electrons, accurately locating light atoms such as hydrogen atoms often necessitates supplementary techniques, in particular when they are located between two electronegative atoms.

2.6.2. Powder X-ray diffraction (PXRD)

When SCXRD is not an option, alternative techniques such as powder X-ray diffraction become essential. While PXRD is a straightforward and elegant method, it often falls short of providing a complete description of a crystal structure.

The underlying physics of PXRD is the same as SCXRD (it is based on the interaction between X-rays and the periodic arrangement of atoms in a crystalline material described by the Bragg's law), with an exception that the experiment is performed for a powdered sample with a random orientation of crystallites. As a result, multiple diffraction peaks are observed, each corresponding to a different set of crystal planes from differently aligned crystallites. This "powder averaging" effect allows for the analysis of polycrystalline materials, which may not be suitable for SCXRD due to the lack of large, high-quality crystals. In PXRD the diffraction angles and intensities are measured to determine the spacing between atomic planes in the crystal.

SCXRD and PXRD are both diffraction-based techniques used to analyze crystalline materials, yet they differ fundamentally in their methodology, data acquisition, and structural resolution. SCXRD is employed to determine the precise three dimensional atomic arrangement of a single crystal. It involves the measurement of diffraction intensities from a well-ordered lattice, where each diffraction spot corresponds to a specific set of crystallographic planes. This technique enables the direct determination of unit cell parameters, atomic positions, and interatomic interactions with high accuracy. PXRD, in contrast, is used to analyze polycrystalline or powdered materials, where the random orientation of crystallites leads to diffraction signals that are averaged into a continuous diffraction pattern as a function of the scattering angle (2θ). Instead of discrete reflections, PXRD generates intensity profiles that correspond to the crystal structure symmetry and unit cell parameters. While PXRD is highly effective for phase identification, quantitative phase analysis, and microstructural characterization (e.g. crystallite size and strain *via* the Scherrer equation), it does not provide direct atomic coordinates. Structural refinement through Rietveld analysis can extract crystallographic information from

PXRD data, but with lower precision compared to SCXRD and only for high-quality experimental data.

PXRD primarily enables the identification of phases within the sample. By comparing the experimental diffraction pattern with known reference patterns, it becomes possible to determine the phases present in the material. This is important for assessing the composition and purity of the sample, as well as identifying any secondary phases or impurities that might be present, cocrystal formation, and drug confinement inside the drug carrier.

Furthermore, the sharpness of the diffraction peaks provides insights into the size of the crystallites in the powder sample. Broader peaks typically suggest smaller crystallites or structural defects, while sharper peaks indicate larger, well-ordered crystallites. By interpreting these diffraction features, PXRD offers a comprehensive understanding of the materials crystal structure, molecular arrangement, phase composition, and physical characteristics.

To refine the structural information derived from PXRD, techniques like Rietveld refinement are commonly employed [164]. This method involves fitting a calculated diffraction pattern to the experimental data, allowing for the precise determination of structural parameters such as atomic positions, thermal vibrations, and crystallite size.

Although it is not always possible to fully describe the analyzed phases by PXRD, this method has been successfully employed to resolve the crystal structures of various pharmaceutical compounds. The first demonstration of *ab initio* structure solution from PXRD data using conventional techniques was for cimetidine, a previously known molecular crystal. Other pharmaceutical compounds, including chlorothiazide, a clinically used diuretic, and polymorphic form V of sulfathiazole, an antibacterial agent, have also been structurally characterized using traditional PXRD approaches [165].

More commonly, direct-space techniques are employed for structure determination in pharmaceutical materials, particularly those containing conformationally flexible molecules. Examples include piracetam, a nootropic drug, for which the structure was found using the atom-atom potential method, and chloroxylenol, an antiseptic, which structure was solved through a combination of maximum-entropy and Monte Carlo methods [166]. Additionally, the structure of ibuprofen form I was determined using a genetic algorithm technique [167], while promazine hydrochloride and thiothixene, both anti-psychotics, were solved *via* simulated annealing. In the case of thiothixene, structural knowledge and conformational flexibility were incorporated into direct-space modeling by fixing the piperazine ring in a chair conformation

and constraining stereochemistry based on prior chemical knowledge, minimizing unnecessary flexibility in the model [168].

Beyond pharmaceutical applications, PXRD is widely used to study structural transformations associated with phase transitions and solid-state reactions. Its practical advantage lies in the ability to monitor structural changes in real time under varying external conditions, such as temperature, pressure, or different gaseous environments. In contrast, phase transitions and chemical reactions in single crystals often lead to a decline in crystal quality, such as twinning, fracturing, or conversion into a polycrystalline phase, limiting the effectiveness of SCXRD. Moreover, certain materials, such as clathrate hydrates, require synthesis and characterization under non-ambient conditions, making PXRD a more viable technique than single-crystal diffraction for structural analysis in these cases.

PXRD is instrumental in determining whether any changes in the drug polymorphic form occurred during the loading process. The absence of crystalline peaks in sufficient quantities suggests that the material has become amorphous or that it has entered the silica mesopores. For instance, the combination of DSC and PXRD demonstrated that mesopores transform the insoluble crystalline form of the angiotensin II receptor blocker, valsartan, into a more soluble amorphous state [169]. It is important to note that XRD data reflect the structural properties of crystal domains and not necessarily the entire particle. Therefore, when analyzing particle sizes, additional methods like microscopy are essential for obtaining accurate information [170,171].

2.6.3. Solid state nuclear magnetic resonance spectroscopy (SSNMR)

Solid state NMR spectroscopy is currently one of the preferred methods for studying the solid state structure of both new and commercially available synthetic drugs, as well as novel supramolecular complexes. SSNMR is a nondestructive, versatile technique that allows for the analysis of a broad range of parameters in a single measurement. It can be used on solid materials in various physical states, including crystalline and amorphous, and is effective for materials of varying complexity, such as pure APIs, excipients, solid dispersions, and even commercial pharmaceutical formulations [172-173]. SSNMR is used to probe solid material atomic-scale structure and dynamics. SSNMR exploits the Zeeman interaction at its core, where nuclear spins align in a strong external magnetic field B_0 , resulting in discrete energy levels according to the nuclear spin quantum number (Figure 2.3). The resonance condition is met when an applied radiofrequency RF pulse matches the energy difference between these levels, inducing transitions that can be detected as an NMR signal.

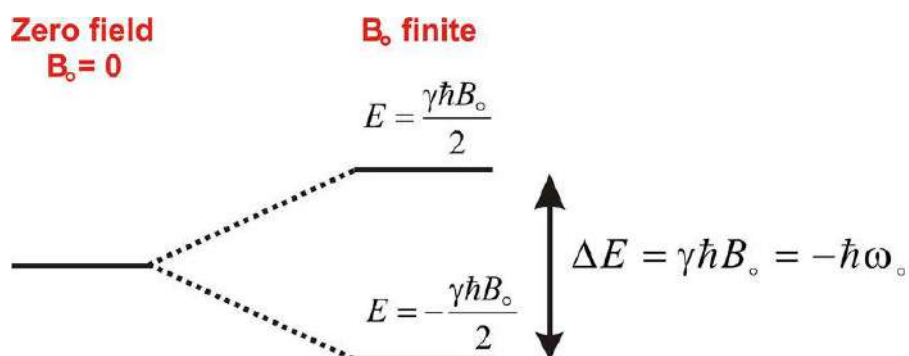


Figure 2.4. Zeeman interaction for spin $\frac{1}{2}$ nucleus. B_0 is the external static magnetic field, E is the energy of the spin states, γ is the gyromagnetic ratio of the nucleus, \hbar is the reduced Planck constant ($\hbar = h/2\pi$), ω_0 is the Larmor angular frequency, related by $\omega_0 = -\gamma B_0$.

Unlike solution-state NMR, where rapid molecular tumbling averages out anisotropic and dipolar interactions, solids exhibit strong dipolar couplings, chemical shift anisotropies (CSA), and quadrupolar interactions (for nuclei with spin $I > 1/2$). These interactions broaden NMR signals, making spectral interpretation practically impossible. To overcome this, various techniques are employed, with the most prominent one being magic-angle spinning (MAS), and additional ones include cross-polarization (CP), and decoupling sequences. MAS involves rapidly spinning the sample at an angle of 54.74° relative to B_0 , which effectively averages out anisotropic and dipolar interactions, leading to higher resolution spectra. Cross-polarization enhances sensitivity by transferring polarization from abundant high- γ (γ - gyromagnetic ratio) nuclei (*e.g.* ^1H) to low- γ nuclei (*e.g.* ^{13}C , ^{15}N). Decoupling techniques, such as high-power proton decoupling, minimize dipolar couplings, further sharpening spectral lines. For quadrupolar nuclei ($I > 1/2$), the nuclear quadrupole moment interacts with the local electric field gradient, producing additional splitting. Advanced techniques, such as multiple-quantum MAS (MQMAS) and satellite transition spectroscopy (STMAS), help resolve these broad interactions and extract structural information.

The following sections provide a detailed explanation of SSNMR pulse sequences, focusing on multinuclear 1D spectra, 2D techniques for retrieving homonuclear (*e.g.* Back-to-Back ^1H - ^1H) or heteronuclear correlations (HETCOR), used in the experiments performed within the framework of this PhD thesis, along with their practical applications.

2.6.3.1.1D High-Resolution SSNMR Experiments.

In the study and development of pharmaceutical compounds, acquiring high-resolution ^{13}C CPMAS spectra is one of the most essential and commonly performed experiments. The ^{13}C isotope, despite its low natural abundance of 1.1% and weak gyromagnetic ratio γ , is preferred over ^1H which has a natural abundance of 99.99% due to the absence of an extensive homonuclear interaction network. Sensitivity is enhanced through polarization transfer from ^1H to ^{13}C during the cross polarization step, where two simultaneous radio frequency (rf) fields are applied under the Hartmann–Hahn condition for a duration known as the contact time [173,176]. Moderate sample spinning speeds around 10 kHz at the magic angle help average out chemical shift anisotropy, enabling ^{13}C CPMAS spectra to be almost comparable to those obtained in solution state NMR. To further eliminate dipolar interactions with protons, a high-power decoupling rf field is applied during acquisition using different pulse sequences, like two pulse phase modulated (TPPM) or SPINAL-64, which help narrow the linewidth [177,178].

CPMAS efficiency can be improved by using a ramped pulse during the CP step [178], which provides better signal intensity compared to a constant rf irradiation step. Achieving an optimal signal to noise ratio requires careful adjustment of experimental parameters. Glycine is commonly used as an external reference and for setting the Hartmann–Hahn condition. The contact time, a crucial parameter for obtaining accurate signal intensities, is typically set to 1.5–2.5 ms to acquire a complete ^{13}C spectrum. However, if a pharmaceutical compound exhibits a relaxation time ^1H T_1 in the order of several seconds or longer, an appropriate repetition delay must be selected [180–183].

Spectral editing plays a significant role in characterizing new compounds. A key related experiment is the quaternary carbon editing spectrum, particularly the non-quaternary suppression (NQS) sequence. In this method, the ^1H and ^{13}C rf fields are turned off for approximately 40–70 μs after CP and before acquisition [172,173]. This delay allows magnetization to decay due to ^1H – ^{13}C dipolar coupling, effectively suppressing CH and CH_2 signals while retaining quaternary carbon and methyl group signals. Additionally, separate CH and CH_2 spectra can be obtained through CP–polarization inversion, which consists of a 40 μs CP step followed by a second step (typically 35 μs) with an inverted phase on the proton rf pulse [184].

High-resolution CPMAS spectra of ^{15}N , which has a natural abundance of 0.37% and a gyromagnetic ratio of $-0.101\gamma(^1\text{H})$, can also be obtained from naturally abundant samples. In this case, the contact time, which exhibits greater variability compared to ^{13}C , is generally set to

6 ms, and the number of repetitions (scans) is significantly higher, resulting in longer experimental times.

A limitation of the CPMAS technique is its non-quantitative nature, meaning that the signal areas under the observed resonances are not directly proportional to the number of resonating nuclei. Signal intensities depend heavily on the CP step, particularly the strength of dipolar interactions and relaxation times, especially the spin lattice relaxation time in the rotating frame ($T_{1\rho}$) for both involved nuclei. Several approaches have been proposed to enable quantitative analysis of pharmaceutical mixtures and tablets. For example, one method involves adding a known quantity of an internal standard to the sample for intensity comparison [185].

2.6.3.2. Fast Magic Angle Spinning

The orientation dependence of NMR spin interactions leads to pronounced line broadening in solid samples. [186,187]. MAS transforms the broad signal into a set of spinning sidebands spaced by the MAS frequency. As the spinning rate increases, these sidebands are pushed further apart, concentrating signal intensity into the isotropic center band and thereby enhancing both spectral resolution and sensitivity [188-190]. Ultra-fast MAS (up to 160 kHz) effectively suppresses heteronuclear dipolar couplings, allowing for the use of heteronuclear decoupling schemes that operate at lower radiofrequency field strengths, which in turn reduces the probe duty cycle and minimizes sample heating [191]. Additionally, fast MAS averages out homonuclear dipolar interactions, facilitating high-resolution ^1H solid-state NMR of protonated solids [189,192]. Beyond dipolar suppression and sensitivity improvements, fast MAS extends coherence lifetimes, which supports the use of more sophisticated pulse sequences. These developments have led to the commercial availability of probes capable of MAS rates up to 160 kHz [193,194].

2.6.3.3. High-Resolution ^1H NMR MAS

Solid-state ^1H NMR plays a vital role in the structural characterization of pharmaceutical compounds due to the high sensitivity of ^1H , high gyromagnetic ratio γ , its high natural abundance, and its widespread presence in organic solids. However, the strong dipolar interactions among protons lead to significant line broadening, often reaching tens of kHz under static conditions, which exceeds the relatively narrow ^1H chemical shift range of approximately 20 ppm [195]. Recent advancements, including fast MAS and improved homonuclear decoupling techniques, have significantly enhanced the resolution in organic compounds. These

improvements have made solid-state ^1H NMR particularly valuable for directly observing interactions such as strong and weak hydrogen bonding and π - π stacking, which are key determinants of molecular conformation and functionality.

In ^1H MAS NMR of organic solids, the extent of residual dipolar linewidth is inversely proportional to the MAS frequency. Moderate MAS spinning rates, below 10 kHz are generally insufficient to provide the resolution needed for obtaining well resolved peaks and site specific information in solid state ^1H spectra. The first approach to overcoming dipolar broadening and retrieving chemical shift information is to employ ultra fast MAS. The mid-1990s saw the introduction of 2.5 mm probes, enabling spinning speeds up to 35 kHz sufficient to average out many of the strongest proton-proton dipolar couplings, thereby revolutionizing solid state ^1H NMR. More recently, commercial availability of ultra fast MAS probes capable of spinning at 70, 100 or even 160 kHz, using 1.3, 0.7 and 0.4 mm rotors, respectively, and high field NMR spectrometers has expanded the potential applications of ^1H NMR spectroscopy [196].

A second approach to obtaining high resolution ^1H NMR spectra involves the application of homonuclear decoupling sequences, originally introduced by Lee, Goldberg, and Waugh [197,198]. These sequences effectively average out the spin components of ^1H - ^1H dipolar interactions, while mechanical sample rotation at the magic angle averages out anisotropic shielding interactions. This concept underpins the well established combined rotational and multi pulse spectroscopy (CRAMPS) technique, first introduced in the late 1970s for slow MAS regimes. More recently, advanced pulse sequences such as the decoupling using DUMBO optimization family and the phase-modulated Lee-Goldburg (PMLG) scheme have demonstrated the power of ^1H solid-state NMR for structural characterization and analysis [175,199].

Renewed interest in the CRAMPS approach over the past decade can be attributed to technological advancements in radio frequency console systems, which now offer improved reliability and precise phase, amplitude, and frequency switching. These developments have led to more stable experimental performance and the refinement of multiple pulse decoupling schemes that function effectively under moderate to fast MAS conditions. Notably, frequency-switched Lee-Goldburg (FSLG), PMLG, and DUMBO decoupling techniques have gained widespread use, further solidifying ^1H solid-state NMR as a powerful tool for structural characterization [195].

2.6.3.4. 2D SSNMR experiments

A widely used solid state NMR approach for obtaining structural information involves advanced 2D SSNMR experiments, where additional spectral dimensions introduce more detailed insights. In 2D NMR, specialized pulse sequences generate spectra that depend on two distinct time variables, enhancing the resolution and interpretability of complex data. These 2D spectra enable the direct observation of intermolecular and intramolecular interactions by establishing correlations between specific atomic sites, primarily mediated by homonuclear and heteronuclear dipolar couplings. As a result, 2D SSNMR facilitates improved spectral assignments and the extraction of crucial structural details, such as interatomic distances, molecular proximities, hydrogen bonding, π - π interactions, and ring currents.

One of the most commonly applied techniques in pharmaceutical research is the acquisition of ^1H - ^{13}C and/or ^1H - ^{15}N heteronuclear correlation (HETCOR) spectra. These experiments significantly enhance ^1H spectral resolution and assignment by leveraging the superior resolution of the $^{13}\text{C}/^{15}\text{N}$ dimension, which benefits from a broader chemical shift range and inherently sharper peaks. Various methodologies have been developed to acquire HETCOR spectra, typically requiring 8–12 hours and 10–20 mg of the sample at natural abundance [200]. Several pulse sequences have been optimized for different coherence transfer pathways in HETCOR experiments, including the FSLG-decoupled CP correlation method by van Rossum et al. [201], the MAS-J-HMQC approach by Lesage et al. [202], and the REPT-HSQC technique by Saalwächter et al. [203]. However, under the very fast MAS (above 50 kHz), it becomes feasible to use inverse proton detection, shortening the experimental time and increasing spectral resolution [204].

The primary objective of a ^1H - ^{13}C invHETCOR experiment is to determine and assign ^1H chemical shifts for protons directly bonded to specific carbon atoms. To achieve this, short CP contact times, ranging from 50 to 100 μs , are used, enabling the establishment of correlations between isotropic signals of heteronuclei through the detection of cross-peaks, which indicate close spatial proximity between the corresponding nuclei. To analyze longer range proximities, usually up to 4 Å, longer contact times of 2 to 3 ms can be used, enabling the assignment of quaternary carbon atoms and establishing inter- and intramolecular contacts (Figure 2.5 b,c).

Following the acquisition of a high resolution solid state ^1H NMR spectrum, to register ^1H - ^1H correlation experiment a method is required to not only maintain high ^1H resolution but also to provide access to dipolar coupling information. One effective technique for this purpose is 2D ^1H - ^1H double quantum – single quantum (DQ-SQ) MAS spectroscopy, where the key principle

is that double quantum coherence (DQC) can only be generated if a dipolar coupling exists between two protons [200]. However, MAS influences DQC excitation, necessitating the use of recoupling strategies to counteract sample rotation effects. Several recoupling methods commonly employed in homonuclear MAS NMR spectroscopy include, for example Back-to-Back (BaBa) [205]. The interpretation of a BaBa spectrum (Figure 2.5 d) allows for determining proton-proton proximities in a crystal.

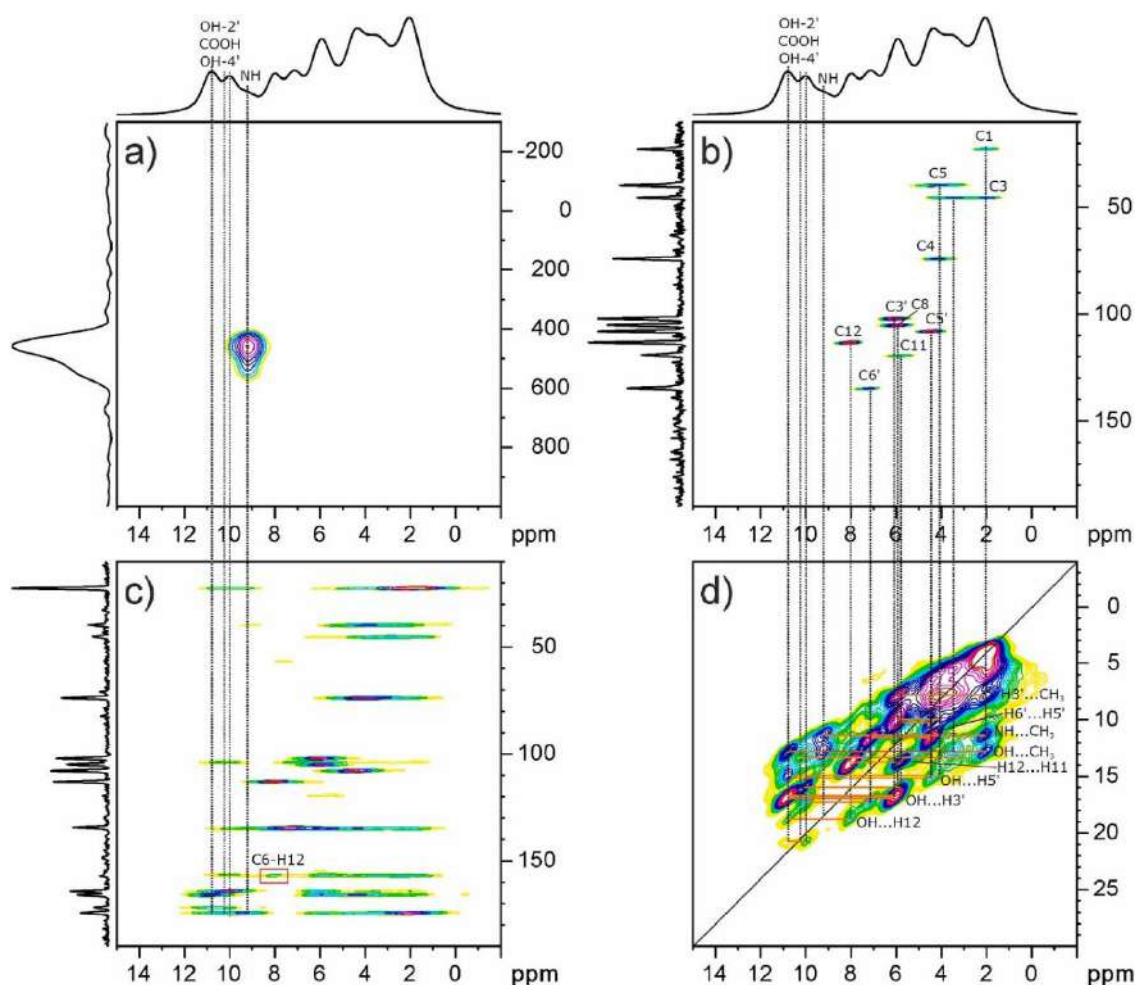


Figure 2.5. (a) ^1H - ^{14}N D-HMQC, (b), (c) ^1H - ^{13}C invHETCOR NMR with short (100 μs) (b) and long (3 ms) (c) second contact time, and (d) ^1H - ^1H SQ-DQ with Back-to-Back recoupling NMR spectra for LIN:2,4-DHBA cocrystal recorded with a spinning speed of 62.5 kHz; red rectangle marks one of the key H-C correlation; the C-H pairs are assigned in the HETCOR spectrum with short contact time [T3].

2.6.3.5. Multinuclear SSNMR

In addition to the commonly employed 1D and 2D NMR techniques using ^{13}C , ^1H , and ^{15}N , other nuclei play a crucial role in determining the structure of pharmaceuticals and their complexes. For instance, in fluorine containing compounds, ^{19}F is particularly advantageous due to its 100% natural abundance and high gyromagnetic ratio, making it second only to ^1H in receptivity. Furthermore, in the solid state, the relaxation properties of ^{19}F enable rapid spectral acquisition, typically within 15 minutes. Techniques such as 1D ^{19}F NMR, using direct polarization or a rotor-synchronized Hahn-echo pulse sequence with MAS, 2D ^{13}C - ^{19}F , and ^1H - ^{19}F HETCOR have been effectively utilized for identifying molecular correlations, interactions, and amorphous content in tablets, as well as analyzing complex mixtures [206-210]. Additionally, 2D experiments incorporating ^{19}F , such as ^1H - ^{19}F CPLG-HETCOR and ^{19}F CP-DARR which relies on magnetization transfer *via* spin diffusion, have been successfully applied to investigate solid dispersions of diflunisal, a non-steroidal anti-inflammatory drug [211].

The quadrupolar isotope ^{14}N is another useful probe in SSNMR of pharmaceuticals. Recent studies have demonstrated the capabilities of the ^{14}N - ^1H HMQC SSNMR experiment for characterizing intermolecular hydrogen bonding motifs, where ^{14}N - ^1H HMQC enables indirect detection of ^{14}N lineshapes through direct proton acquisition [212,213]. Coherence transfer occurs through heteronuclear dipolar couplings, with rotary resonance recoupling reintroducing these interactions. Fast MAS plays a crucial role in reducing strong proton homonuclear dipolar couplings and extending ^1H dephasing times. This approach has been applied to various pharmaceutical compounds, including cimetidine, an antiulcer drug [214], a nicotinamide-palmitic acid cocrystal, and an acetaminophen solid dispersion [215].

2.6.3.6. Applications of SSNMR in pharmaceutical analysis

Over the past decade, numerous publications [181,216] have highlighted the integration of several different SSNMR techniques for the comprehensive characterization of newly developed pharmaceuticals. For example, Bruno et al. [181] utilized ^{13}C CPMAS NMR to analyze tizoxanide, where differences in ^{13}C CPMAS and non-quaternary suppression spectra allowed for the identification of hydrogen bonding modifications. Their findings confirmed the transition from intramolecular to intermolecular hydrogen bonding. Similarly, Wawer et al. [217] applied ^{13}C CPMAS, ^1H , and ^{15}N SSNMR, to examine sildenafil base and sildenafil citrate (Viagra). Differences between solution and solid state ^{13}C chemical shifts provided insights into molecular rigidity and conformational changes, while ^{15}N CPMAS spectra revealed the presence of hydrogen bonds. The zwitterionic nature of certain compounds has also been confirmed *via*

SSNMR, as demonstrated by Olivera et al., who observed chemical shift variations in ^{13}C spectra of procainamide derivatives [218].

Further applications of SSNMR in structural analysis of pharmaceuticals include studies by Chattah et al. on norfloxacin and ciprofloxacin complexes with aluminum, synthesized using two different methodologies. Differences in solid state and solution state ^{13}C spectra enabled the confirmation of zwitterionic character, while ^{13}C CPMAS spectra confirmed the complete transformation of the pure drug into complexes. Additionally, $T_{1\rho}$ relaxation times indicated a biexponential behavior, suggesting the presence of at least two distinct phases within the complexes. Further insights were gained using ^{27}Al MAS NMR, where chemical shifts provided information on aluminum coordination [219].

When analyzing solid state molecular structures, Van der Waals interactions, hydrogen bonding, and π - π stacking are crucial for understanding molecular arrangements. Mafra et al. employed SSNMR and computational simulations to investigate the packing interactions in anhydrous (Form I) and hydrated (Form II) ciprofloxacin [220]. SCXRD was used to correlate SSNMR findings with packing interactions, while a complete assignment of ^1H and ^{13}C NMR spectra was performed using SSNMR experiments such as 2D ^1H - ^{13}C PRESTO-HETCOR, 1D ^1H wDUMBO, and 2D ^1H - ^1H DQ CRAMPS. These results allowed for the analysis of structurally related compounds where SCXRD was not feasible.

Alternative approaches include variable temperature SSNMR, as demonstrated by Apperley et al. for characterizing indomethacin and nifedipine. Changes in chemical shifts upon heating provided insights into hydrogen bond formation, polymorphism, and recrystallization behavior [221]. Similarly, Carignani et al. investigated ibuprofen dynamics using multi technique NMR, including ^{13}C chemical shifts, ^{13}C line shapes, and relaxation time measurements across different temperatures and frequencies. These experiments identified molecular motion regimes and provided activation energies for various rotational and π flipping motions [222].

Recent studies have also expanded the range of nuclei used in pharmaceutical SSNMR characterization. Vogt et al. explored a novel antibacterial benzoxaborole compound using ^{11}B SSNMR, where the boron signal chemical shift provided structural insights. Correlation experiments, such as ^1H - ^{11}B HETCOR, facilitated the unambiguous assignment of specific ^1H signals [223]. Similarly, Tatton et al. introduced a J-resolved ^{15}N - ^1H spectral editing method and a 2D ^{14}N - ^1H HMQC experiment, applied to cimetidine and tenoxicam, to probe nitrogen-hydrogen interactions [214].

Multicomponent pharmaceutical solids, including ionic complexes and salts, are often developed to improve solubility, stability, bioavailability, and organoleptic properties. A deeper understanding of solid state interactions can aid in the rational design of crystalline APIs. Romañuk et al. investigated a fluoroquinolone-saccharine (FQ-SAC) family, using ^{13}C CPMAS and ^1H - ^{13}C HETCOR to study the structural differences among various FQ-SAC salts. These analyses provided key insights into zwitterionic behavior, hydrogen bonding, and molecular interactions [224]. Their subsequent study identified a new polymorph of CIP-SAC (CIP-SAC II), exhibiting distinct crystallinity compared to the previously reported CIP-SAC I [225]. Garro Linck et al. further characterized these polymorphic forms using multinuclear SSNMR, including ^1H , ^{13}C , and ^{15}N NMR, as well as ^1H - ^1H BABA and ^1H - ^{13}C REPT-HSQC 2D experiments, to investigate local packing differences [226].

Vogt et al. utilized multinuclear 1D and 2D SSNMR techniques to investigate various cocrystals and complexes, including palmitic acid-nicotinamide, piroxicam-saccharin, fluoxetine HCl-succinic acid, and triphenylphosphine oxide-6-chloro-2-pyridone. As an example, their findings on the palmitic acid-nicotinamide cocrystal demonstrated that 1D ^1H and ^{13}C SSNMR spectra confirmed cocrystal formation. The presence of a hydrogen bond between the carboxylic group and the pyridine group was indicated by the change in the chemical shift of the proton involved. Additionally, 2D ^1H - ^{13}C HETCOR experiments verified the molecular-level association between nicotinamide and palmitic acid, while ^1H - ^1H DQ MAS experiments provided further insights into the cocrystal formation [227].

Similarly, Maruyoshi et al. studied the indomethacin-nicotinamide cocrystal, proposing four potential intermolecular arrangements. By employing ^1H - ^1H DQ MAS SSNMR and ^{14}N - ^1H HMQC experiments, they identified the intermolecular hydrogen bonding between the two compounds. This finding enabled them to determine the correct intermolecular arrangement involved in the cocrystal formation [228].

Tatton et al. also explored hydrogen bond interactions in the nicotinamide-palmitic acid cocrystal using ^{14}N - ^1H HMQC SSNMR. Their 2D spectrum of nicotinamide exhibited distinct cross peaks for both nitrogen sites, as illustrated in Fig. 2.6 a. In contrast, the 2D spectrum of the nicotinamide-palmitic acid cocrystal (Fig. 2.6 b) revealed a clear correlation between the nitrogen of nicotinamide (N1) and the carboxylic acid hydrogen in palmitic acid (H1), confirming the presence of an intermolecular hydrogen bond. The observed differences in the ^{14}N chemical shift between nicotinamide and the cocrystal were attributed to variations in the isotropic second-order quadrupolar shift [215].

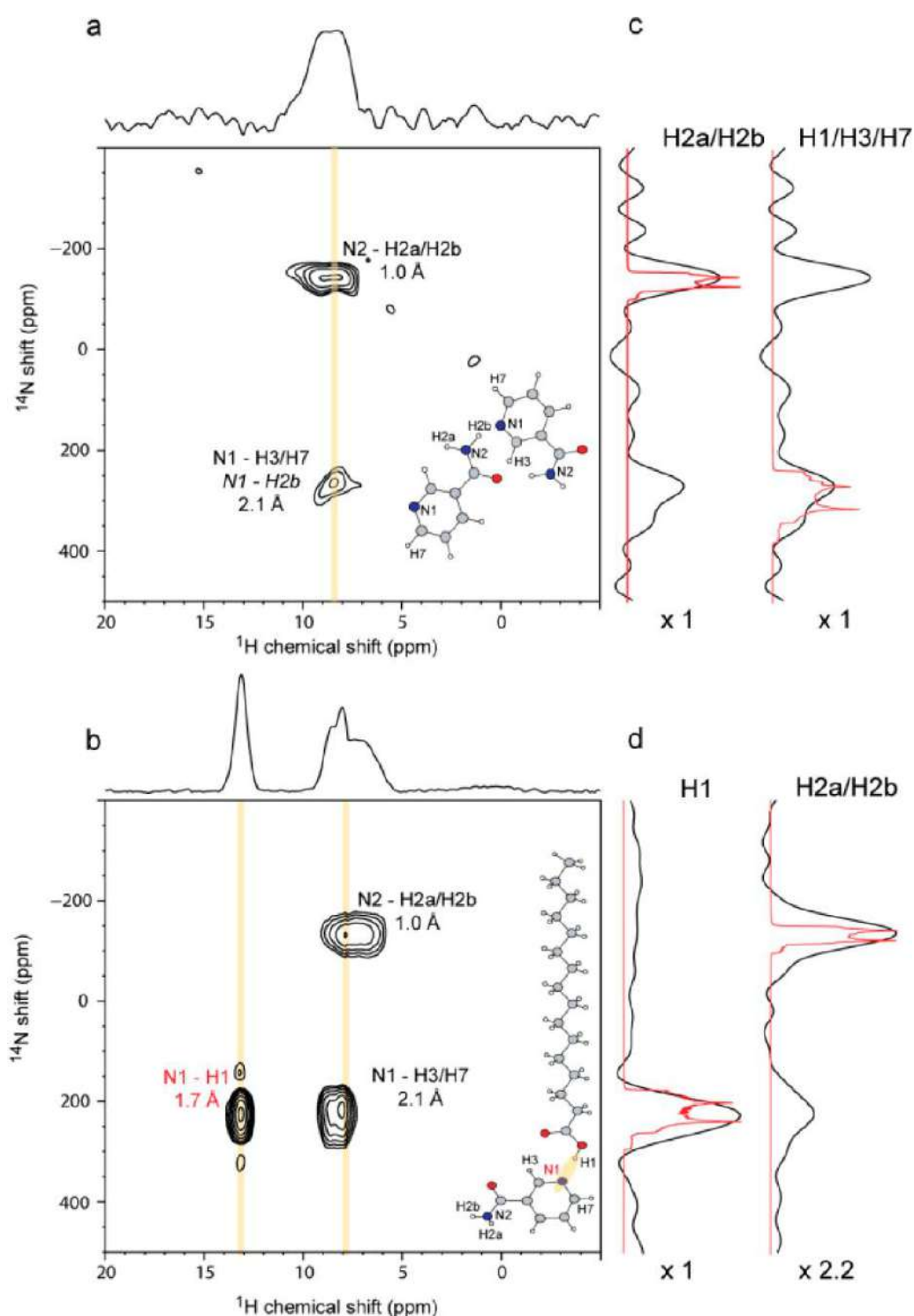


Figure 2.6. ^{14}N - ^1H HMQC spectra recorded at $\nu_0 = 850$ MHz and a MAS frequency of 60 kHz for a) nicotinamide and b) a nicotinamide-palmitic acid cocrystal; c) and d) ^{14}N columns taken through the highlighted area of the spectrum overlaid with lineshapes simulated using the SpinEvolution software. Reprinted with permission from ref. [215].

2.6.3.7. NMR Crystallography

X-ray studies result in knowledge about the distribution of electron density rather than providing direct information about the positions of atomic nuclei. Mainly, it requires long range order, something that amorphous solids do not fulfill. In addition, to give full crystallographic information, a single crystal is required, which is not available in many cases. Some of these problems are overcome by SSNMR, which is very sensitive to nearest neighbour interactions, giving information directly on the nuclei in question. Crystallographic information can be obtained from the use of SSNMR techniques, usually under MAS, making it possible to derive full crystal structures with the help of NMR data [228]. In general, NMR crystallography has followed two strategies: structure proposal and structure validation. In a review by Harris, properties of some solid pharmaceuticals are obtained through the measurement of chemical shifts in MAS NMR experiments [229]. For example, the number of molecules per asymmetric unit in calcium acetate monohydrate is obtained from ^{13}C CPMAS, and the detection of the nature of hydrogen bonding is given for cortisone acetate by observing spinning sidebands in ^{13}C CPMAS. A combination of computational analysis through chemical shift calculations using CASTEP and experimental approach comprising INADEQUATE experiment, the information about atomic connectivity were used for assigning the chemical shifts and comparing the α - and β form of testosterone I [231]. A similar study was performed for oxybuprocaine hydrochloride [232]. The calculations using GIPAW approach were used to contrast two different structures published in Crystal Structure Database (codes ZIVKAQ and ZIVKAQ01) for a bronchodilator used for asthma therapy, terbutaline sulphate form B (TBS Form B), and to obtain a full assignment of ^{13}C CPMAS spectrum. In addition, the determination of chemical shifts in the proton spectrum and hydrogen bonding was done by performing $^1\text{H}^{13}\text{C}$ HETCOR, DQ CRAMPS, and proton–proton spin diffusion. In particular, GIPAW results had significant implications giving an explicit identity to the labels of the carbons, with sites in the crystal structure (Fig 2.7 a and b) [233].

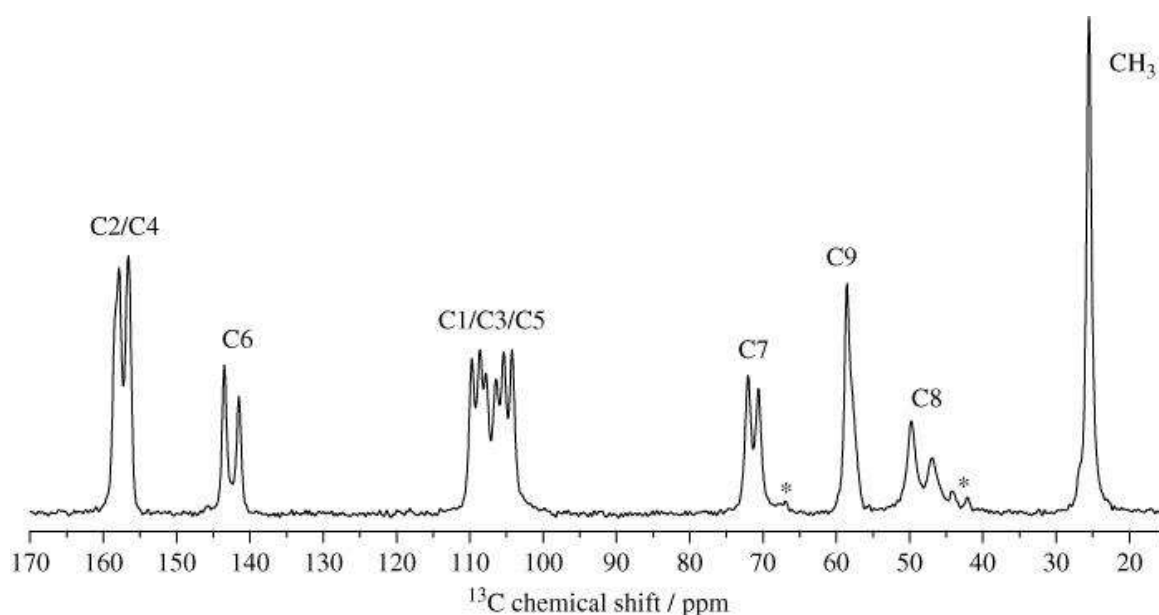


Figure 2.7. a) 125 MHz ^{13}C spectrum of TBS Form b) The asterisks (*) indicate spinning sidebands. Reprinted with permission from ref. [233].

Recently, the structure of diterbutaline sulphate diacetic acid solvate given in the Cambridge Crystallographic Database (code ZIYXAG), was checked by using ^{13}C solid-state NMR together with CASTEP calculations. An error in the geometry of one acetic acid molecule was found and confirmed by a new X-ray diffraction study. This study demonstrated that experimental solid-state NMR, combined with computational analysis, is a powerful technique to validate structures defined by X-ray diffraction [234]. Taking into account another approach, SMARTER crystallography (structure elucidation by combining magnetic resonance, computational modelling, and diffraction) has been applied recently to elucidate the structure of powdered amoxicillin trihydrate (a β -lactamic antibiotic). In this case, ^1H NMR chemical shifts have been used directly in the structure generation step and also in the refinement step [235]. The SMARTER crystallography approach makes use of a genetic algorithm approach for crystal structure determination. The algorithm is based on classical force fields and semi-empirical chemical shift approaches, making this approach faster than DFT calculations [236,237].

More recently, a combination of DFT methods and crystal structure prediction with SSNMR experiments that included ^{13}C CP MAS, ^1H MAS NMR, $^{13}\text{C}^{13}\text{C}$ INADEQUATE, and $^1\text{H}^{13}\text{C}$ HETCOR has been used to determine the crystal structures of four small drug molecules: cocaine, flufenamic acid, flutamide, and theophylline [238].

2.6.4. Raman spectroscopy

Raman spectroscopy is a vibrational spectroscopic technique based on inelastic scattering of monochromatic light, commonly from a laser source, by molecular vibrations, rotations, or other low-frequency excitations in a material. This inelastic scattering, known as the Raman effect, was first observed by C.V. Raman in 1928 and provides a fundamental tool for molecular characterization. When photons interact with a material, they predominantly undergo Rayleigh scattering, where the scattered photons retain the same energy (elastic scattering). However, a small fraction (approximately 1 in 10^6 photons) undergoes inelastic scattering, resulting in either a loss or gain of energy, leading to what is termed Stokes or anti Stokes Raman scattering, respectively. In Stokes scattering, the incident photon excites a molecule to a virtual energy state, and the scattered photon emerges with lower energy as the molecule transitions to a higher vibrational state. Conversely, in anti Stokes scattering, a molecule already in an excited vibrational state interacts with the incident photon, transferring energy to it, thereby resulting in a scattered photon of higher energy. The intensity of anti Stokes scattering is typically lower than that of Stokes scattering due to the Boltzmann distribution, which favors molecules in the ground state at ambient temperatures. The Raman effect can be described using quantum mechanics as a second-order light-matter interaction process. The interaction of the incident electromagnetic field with a molecule induces a temporary distortion in the electronic cloud, forming a virtual energy state. The probability of inelastic scattering depends on the polarizability tensor of the molecule, which is modulated by vibrational normal modes. The Raman activity of a vibrational mode is governed by the selection rule requiring a change in the molecular polarizability during vibration. This contrasts with infrared (IR) absorption spectroscopy, which requires a dipole moment change for a transition to be IR active.

In the classical description, the Raman effect is understood through the concept of molecular polarizability, which describes how an external electric field (such as light) induces a dipole moment in the molecule. If a molecule vibrates, its polarizability changes periodically. When an oscillating electric field from the incident light interacts with the molecule, it induces a time-dependent dipole moment that oscillates at the frequency of the light source. The re-emitted radiation contains components shifted in frequency due to this polarizability modulation, corresponding to the vibrational modes of the molecule.

The selection rules governing Raman spectroscopy are determined by group theory and symmetry considerations. Highly symmetric molecules tend to exhibit distinct Raman active modes, while centrosymmetric molecules obey the mutual exclusion principle, wherein vibrational modes active in IR spectroscopy are forbidden in Raman.

Raman spectra provide a molecular fingerprint of a substance, with peak positions corresponding to specific vibrational transitions. The intensity of the Raman peaks depends on the polarizability change and the concentration of the species, making it a powerful tool for quantitative analysis.

Due to its ability to provide detailed molecular insights, Raman spectroscopy is widely applied in materials science, chemistry, biology, and nanotechnology [239-241]. Raman spectroscopy, rooted in fundamental quantum and classical physics principles, is a crucial analytical technique for probing molecular structures and interactions, offering qualitative and quantitative insights into complex systems.

Variable temperature Raman spectroscopy studies offer extensive insight into molecular and lattice dynamics. A typical Raman spectrum spans a broad wavelength range (3600–10 cm^{-1}), exceeding in the lower range region the range typically covered by mid-IR spectroscopy (4000–400 cm^{-1}). This enables the analysis of lattice vibrations in organic compounds with high precision [242]. By systematically altering the sample temperature, variations in lattice energies can be examined, facilitating the characterization of the crystal lattice structure. Moreover, variable temperature Raman spectroscopy provides information analogous to that obtained from IR studies, such as phase transitions and solvate association mechanisms [243]. Heating ramps in Raman experiments are an essential tool for studying temperature-dependent changes in the structure and molecular dynamics of materials. In low-frequency Raman spectroscopy (LFRS), the effects of heating are evident through shifts in vibrational modes, peak broadening, and variations in quasielastic scattering (QES), which offer valuable insights into material properties and behaviors.

Firstly, heating allows researchers to track phase transitions such as crystallization, melting, or glass transitions. These structural changes are important for understanding how materials behave under varying temperature conditions. As temperature increases, molecules become more mobile, and molecular mobility can be observed through changes in the vibrational dynamics, revealing insights into molecular order and disorder. Additionally, heating enhances thermally activated molecular motions, contributing to QES, which provides crucial data on molecular dynamics in the low-frequency region.

Another key aspect of heating ramps is their role in the elimination of thermal distortions in the Raman spectra. Temperature fluctuations can impact the intensity of Raman signals, but controlled heating ensures consistent data collection. Corrections using the Bose factor can then

be applied to ensure an accurate interpretation of the spectra, minimizing the effects of thermal noise.

In the context of APIs confined within MSNs, heating ramps during LFRS provide unique insights into the behavior of APIs in confined environments. The molecular mobility of APIs confined in MSNs is typically restricted due to interactions with the nanopores. As temperature increases, molecular mobility may improve, which can be detected through changes in the QES region ($5\text{--}50\text{ cm}^{-1}$) of the Raman spectrum. A lack of significant changes in QES suggests strong confinement, whereas an increase in QES intensity may indicate partial or full release from the pores.

Heating ramps also allow for the study of phase transitions and structural rearrangements of the API within MSNs. Confined APIs may exhibit different polymorphic forms than their bulk counterparts. By monitoring changes in the vibrational density of states (V_{DOS}), researchers can track phase transitions, such as an amorphous-to-crystalline transformation. Characteristic peaks in the Raman susceptibility spectrum $\chi''(\omega)$ would emerge if an API transitions from an amorphous to crystalline state upon heating.

The interaction strength between the API and MSNs is another critical area that can be analyzed with heating ramps. APIs that are strongly bound to the silica surface, through hydrogen bonding or electrostatic interactions, will show minimal changes in their spectra with increasing temperature, indicating restricted motion. In contrast, weaker interactions may allow for greater molecular mobility, as evidenced by an increase in QES intensity with temperature. Heating ramps provide crucial insights into controlled drug release mechanisms. If the API begins to diffuse out of the MSNs during heating, changes in both the low-frequency and fingerprint regions of the Raman spectrum can indicate molecular desorption or solubilization. These observations are fundamental for understanding the release mechanism of the API from the MSNs, which is critical for optimizing drug delivery systems.

To investigate the structural state of an API using Raman spectroscopy, a comparative analysis is conducted between two key samples: pure crystalline API, and API-loaded MSNs. The Raman spectra of these samples are collected using a monochromatic laser, typically at wavelengths such as 532 nm or 785 nm, in a backscattering mode. The spectra of the API-loaded MSNs are then compared with the reference sample to detect changes in vibrational features.

The key indicators of amorphization in Raman spectra include peak broadening, reduced intensity, and the disappearance of lattice vibrational modes. If the API undergoes a transition

from a crystalline to an amorphous state within the MSNs, the sharp peaks characteristic of the crystalline structure diminish, giving way to broader bands that reflect molecular disorder. Additionally, peak shifts may be observed, indicating molecular interactions between the API and the silica surface, such as hydrogen bonding or van der Waals interactions. [244,245]

Raman spectroscopy enables the examination of three distinct categories of molecular motions within the framework of the rigid body model:

Collective vibrations, termed lattice vibrations or phonons in crystals, manifest as external motions detected below 150 cm^{-1} . These vibrations serve as a crystalline signature, with molecular disorder causing the broadening of phonon peaks, reflecting the overall disorder of the amorphous state. The low-frequency spectrum provides insights into short-range order. Terahertz spectroscopy complements this by offering information on collective motions, featuring specific selection rules linked to crystalline symmetry.

Internal motions, covering vibrations within the molecule, span the $500\text{--}1800\text{ cm}^{-1}$ region, revealing the molecular fingerprint, and the X–H stretching region (between 2800 and 3800 cm^{-1} , where $X = \text{C, N, O}$). This latter region offers valuable insights into H-bonding associations.

Semi-internal (or external) motions signify very low-frequency rotations of a group of atoms within the molecule or of the entire molecule.

The low-frequency spectrum of molecular materials contains a wealth of information resulting from the overlapping of external collective and semi-external motions. Nevertheless, accurately extracting information about these motion classes poses a challenge and depends on detecting the Raman signal at very low frequencies. Recent advancements in filters now enable routine spectrometers to capture the Raman signal at low frequencies [246]. Delving into the low-frequency realm provides rapid insights into identifying crystalline polymorphism, contributing to the advancement of low-frequency Raman investigations in pharmaceutical sciences [247-255].

Raman spectroscopy applied to porous silica materials can yield valuable insights into the characteristics of silicon nanostructures. These properties are highly dependent on factors such as symmetry, structural geometry, morphology, pore diameter, and backbone size. A commonly used approach in analyzing Raman scattering from porous silicon involves the first-order phonon entrapment model, which employs the calibration of the spectrometer at 521 cm^{-1} to analyze the shape of Raman scattering bands. This allows for the determination of the size of

crystallites embedded within the porous layer. Additionally, Raman spectroscopy can capture low-frequency acoustic vibrations exhibited by nano-sized particles [254].

The incorporation of poorly soluble drugs like indomethacin into mesoporous silica materials, specifically MCM-41 and SBA-15, was initially explored using Raman spectroscopy by Hellstem et al. [255]. Raman imaging proves to be especially valuable in the pharmaceutical industry because it provides insights into the spatial distribution of compounds within a sample and is sensitive to the crystallinity and polymorphism of these compounds. Despite certain challenges encountered during the analysis, such as fluorescence and sample combustion, this research offered significant information regarding drug distribution and the presence of unexpected solid forms like solvates or rare polymorphs of the model drug.

2.6.5. Thermal techniques

Thermal analysis encompasses a group of calorimetry techniques in which the properties of a sample are monitored concerning heat flow or mass reduction while the sample temperature within a specific atmosphere is altered. Combining data from thermo-analytical methods like differential scanning calorimetry (DSC) and thermogravimetry (TGA) enables the quantification and characterization of the physicochemical nature of drugs including neat polymorphs, cocrystals, solvates or drugs introduced into the pores of silica [256].

2.6.5.1. Differential scanning calorimetry (DSC)

Differential Scanning Calorimetry is a thermoanalytical technique that quantitatively measures the heat flow associated with physical and chemical transformations in a material as a function of temperature or time. It is widely used in materials science, polymer research, and pharmaceutical development to study phase transitions such as glass transition, melting, crystallization, and thermal degradation. The fundamental physics behind DSC is based on the first law of thermodynamics, which states that the change in the internal energy of a system is equal to the heat added and the work done. Since DSC operates under constant pressure conditions, the measured heat flow corresponds directly to the enthalpy of the process. The DSC instrument measures the difference in heat flow between a sample and an inert reference material (such as an empty aluminum pan) as both are heated or cooled at a controlled rate. The resulting heat flow is plotted against temperature or time, providing information about the thermal events occurring in the sample. The DSC thermogram provides direct information about

enthalpic changes during thermal events, which can be endothermic (heat absorption) or exothermic (heat release). Endothermic transitions occur when a sample absorbs heat, leading to a downward deviation in the DSC curve (or upward, depending on the convention). These transitions are indicative of processes in which a material moves to a higher energy state, typically accompanied by a phase change. One example of an endothermic transition is the glass transition, characterized by glass transition temperature (T_g), which is a second-order transition. Unlike first-order transitions, such as melting, the glass transition is characterized by a change in heat capacity rather than a sharp latent heat peak. At T_g , the amorphous material undergoes a change in its physical properties, transitioning from a brittle, glassy state to a more flexible, rubbery state, without involving a phase change between solid and liquid.

In contrast, the transition characterized by melting temperature (T_m) represents a first-order transition, where crystalline regions of a material absorb heat to convert from a solid to a liquid phase. This is reflected in the DSC curve as a distinct endothermic peak. The area under this peak is proportional to the enthalpy change associated with the melting process, allowing the calculation of the heat absorbed during the transition from solid to liquid.

Additionally, DSC can be used to study solvent evaporation or desolvation processes in which volatiles are lost from a solvated or hydrated sample. This is typically observed as an endothermic peak in the DSC curve, corresponding to the loss of solvent or water from the sample. The peak area in these cases reflects the amount of heat required to remove the solvent, providing useful information about the volatility and stability of the sample under thermal conditions [261-262]. Finally, an example of an endothermic transition before the melting point transition and not associated with a loss of a volatile compound is a solid-solid phase transition, associated with the change in the crystal structure of the analyzed molecule (polymorphic transition).

Exothermic transitions occur when a sample releases heat, leading to an upward deviation in the DSC curve (or downward, depending on the convention). These transitions are indicative of processes where the system moves from a higher energy state to a lower energy one. One common example is crystallization, where an ordered solid phase forms from an amorphous or supercooled liquid state. During crystallization, the release of latent heat results in a characteristic exothermic peak in the DSC thermogram. Similarly, crosslinking reactions in thermosetting polymers, which involve the formation of covalent bonds between polymer chains, also release heat, manifesting as exothermic transitions in the DSC curve. Another

example of exothermic behavior is oxidative degradation, where a sample decomposes in an oxygen-rich atmosphere, releasing heat as a part of the chemical breakdown process.

In addition to identifying exothermic and endothermic transitions, DSC is a powerful technique for measuring enthalpy changes associated with various thermal events. The area under the DSC peak is proportional to the heat released or absorbed, allowing for the quantification of enthalpy changes during phase transitions, chemical reactions, or other thermal processes. Furthermore, DSC can provide insights into a specific heat capacity of a material, which is essential for understanding how a substance responds to temperature changes. By examining these thermal behaviors, DSC offers valuable information on the materials stability, crystallization tendencies, and reactions to thermal stress, making it an indispensable tool for materials characterization in a wide range of scientific disciplines.

Differential Scanning Calorimetry is widely utilized in pharmaceutical science. Polymorphs of pharmaceutical compounds can exhibit distinct thermal properties, such as melting points and enthalpy changes, which can be differentiated using DSC. For example, polymorphs of ritonavir and carbamazepine display different melting points and heat capacities, enabling researchers to distinguish between these forms [257]. This differentiation is essential for selecting the most stable polymorph for drug formulation, ensuring consistency in therapeutic efficacy.

In the study of drug-excipient interactions, DSC plays a vital role by detecting shifts in melting points or the emergence of new exothermic peaks that may indicate incompatibility or degradation. For example, when paracetamol is mixed with lactose, DSC can reveal the thermal behaviors of both components, showing that lactose decomposes at a temperature higher than the melting point of paracetamol. If an early exothermic peak appears, it suggests an interaction between the drug and excipient that may lead to undesirable degradation [258]. Thus, DSC is an essential tool for ensuring the stability and compatibility of pharmaceutical formulations [259].

The analysis of cocrystals and amorphous drug systems is another key application of DSC. Cocrystals, which are engineered to improve the solubility and stability of active pharmaceutical ingredients, can be characterized using DSC by examining their distinct melting points compared to their individual components. For example, the 1:1 ibuprofen-nicotinamide cocrystal displays a melting point that differs from those of pure ibuprofen and nicotinamide. Also, DSC can help verify the stoichiometry of the cocrystal by comparing the melting points and enthalpy changes of the components, and any residual peaks indicate incomplete cocrystal formation [260]. Additionally, DSC is used to determine the glass transition temperature (T_g) and crystallization

behavior of amorphous drug forms, providing important information on the stability and dissolution properties of these systems [261].

DSC is also invaluable for detecting the presence of solvates and hydrates in pharmaceutical compounds, which can influence the stability, solubility, and bioavailability of drugs. By measuring solvent or water loss, DSC can distinguish between anhydrous and hydrated forms of a drug. For instance, cefuroxime axetil monohydrate exhibits an endothermic peak around 100°C corresponding to water loss, while the anhydrous form does not show this peak [262]. Similarly, ritonavir, when crystallized from ethanol, may contain residual ethanol in the crystal lattice, which can be detected by DSC through a characteristic thermal event peak around 70–100°C [263]. This ability to quantify hydrate and solvate content is crucial for ensuring consistent drug delivery and formulation stability.

DSC is also instrumental in determining the drug dispersion in binary systems. In the case of amorphous solid dispersions like the itraconazole-PVP system, DSC can confirm whether the drug is crystalline or fully dispersed in the polymer. If the melting peak of a drug is absent, this suggests that it is in an amorphous form, which is beneficial for improving solubility [264].

DSC is used to characterize the physical state and location of an API in a material by observing its melting point. It has been observed that when a drug is confined within the pores of mesoporous silica, its melting point and glass transition appear at lower temperatures than those of the crystalline state, and the melting occurs over a broader range. As the concentration of a drug in the mesoporous silica increases, the peak of the endothermic heat of fusion decreases. When all of the drug is loaded into the porous silica structure, the melting point peak of the drug is not observable, indicating that the incorporated substance is in an amorphous form and the mesoporous silica prevents it from recrystallizing. Conversely, the drug on the outer surfaces of the pores is considered a bulk material and does not exhibit a glass transition. Therefore, DSC analysis distinguishes the compound on the surface of mesoporous silica from the one contained within it. Additionally, DSC measurements can help determine the pore size distribution based on the observation of solid-liquid phase transformations inside the pores, such as melting/freezing points and enthalpies. The melting/freezing point depends on the pore size, and the transformation enthalpy depends on the pore volume. This method also provides information about the interaction between the porous and confined material [265].

Apart from the above, researchers have utilized DSC to quantify monomolecular loading capacity using a solvent-free melting approach during heat-cool-heat cycles. For instance, ibuprofen with good glass-forming ability was studied using this approach. The drug that fuses

into the pores of mesoporous silica during the first heating cycle becomes amorphous after cooling. In cases of easily glass-forming substances, no crystallization occurs after cooling. These particles are adsorbed and immobilized on the silica surface, resulting in no additional glass transition in the DSC. Consequently, their quantity can be determined after the silica is fully loaded by examining the change in heat capacity [266,268]. In five types of mesoporous silica with the same chemical composition but different surface area, diameter, and pore volume, the loading capacity of three model drugs: paracetamol, celecoxib, and cinnarizine was determined. Based on the heat-cool-heat DSC method, the loading capacity was compared with the theoretical capacity calculated from the surface area and amorphous density of drugs as well as the surface area and pore volume of silica. It was concluded that monomolecular loading ability increases with increasing surface area and decreasing pore volume [139].

2.6.5.2. Thermal gravimetry analysis (TGA)

This technique is valuable for assessing the changes in sample weight as a function of temperature over a specific duration. It provides precise information about the drying temperature during different stages of the reaction involving the components. Moreover, it is employed for predicting the stability, purity, compatibility, and presence of solvates or hydrates.

TGA helps determine the thermal stability of a material by analyzing weight loss as a function of temperature. The onset decomposition temperature (T_{onset}) indicates the resistance of a material to thermal degradation. Materials with a higher decomposition temperature are generally more thermally stable. Pure substances exhibit well-defined degradation profiles with sharp transitions at specific temperatures. Impurities or secondary phases may cause multiple degradation steps or deviations from expected mass loss patterns. In cocrystal or binary systems, TGA can detect interactions between components. If the degradation profile of a mixture differs significantly from the sum of individual components, it suggests chemical or physical interactions (e.g., degradation catalysis or stabilization) [269]. TGA is useful for identifying solvates/hydrates by monitoring weight loss at lower temperatures corresponding to solvent/water release. The stepwise loss of mass at specific temperature ranges distinguishes hydrates (bound water) and solvates (organic solvents) from free moisture/adsorbed content. This analysis allows also for the quantification of solvent molecules present in a solid form. In binary systems and cocrystals, the relative composition of components can be inferred by analyzing stepwise weight loss and residue fraction at different temperature stages. For example, if a cocrystal contains a volatile coformer, TGA can quantify its proportion by measuring the mass loss at its characteristic evaporation temperature. If a

polymer blend or a composite material undergoes selective degradation, the remaining residue can be correlated to the known degradation behavior of individual components to estimate their weight fractions [270].

In the context of API-MSNs systems, since the inorganic carrier is more thermally stable than the organic guest molecule, weight loss from drug degradation followed by desorption of volatile components can be observed by gradually increasing the sample temperature using TGA. The weight loss is proportional to the total drug content. The amount of solvent remaining in the pores after loading can also be determined by the same principle. However, thermogravimetric analysis may give erroneous results in determining whether all loaded material has left the carrier when thermostable compounds or the drug itself form strong connections to the mesoporous silica [271].

2.6.6. Computational Methods

The structural characterization of small powdered organic crystals plays an increasingly key role in organic chemistry in general, and in pharmaceutical chemistry in particular. Even though reference structures from single-crystal diffraction studies are commonly available, when the sample is in powder form, characterization becomes very difficult. The past decade has seen an increasing recognition of the power of a combined approach linking experimental solid-state NMR with first principles (i.e. density functional theory, DFT) calculations of NMR parameters. For example, the gauge-including projector augmented wave (GIPAW) [272] using the plane wave pseudopotential formalism within DFT has been widely applied for calculating NMR parameters of periodic solids. One of the codes offering an implementation of GIPAW is CASTEP. CASTEP has been used to obtain chemical shifts, energies, and properties of crystalline materials from first principles, incorporating crystallographic repetition [273].

2.6.6.1. Density Functional Theory (DFT)

Density Functional Theory is a quantum mechanical computational method used to study the electronic structure of molecules, materials, and condensed-phase systems. A good balance between accuracy and computational efficiency makes it widely used in chemistry, materials science, and physics. It is based on the Hohenberg-Kohn theorems, which state that the ground-state properties of a many-electron system are uniquely determined by its electron density. The Kohn-Sham approach introduces a system of non-interacting electrons that reproduces the

same density as the real interacting system, making calculations more feasible. Exchange-correlation functionals, such as LDA, GGA (PBE), and hybrid functionals (B3LYP, HSE06), are key components in improving accuracy.

In the context of cocrystals, DFT helps in quantifying non-covalent interactions such as hydrogen bonding and π - π stacking that, among other things, drive cocrystal formation. In favourable circumstances, DFT, often combined with dispersion corrections (denoted as DFT-D – dispersion-corrected DFT), can predict whether two molecules will form a stable cocrystal by calculating lattice energies and cohesive interactions. The relative stability of different polymorphic forms of cocrystals can also be assessed in this way. DFT calculations provide insights into the electronic structure of cocrystals, especially charge transfer between components, which is useful for optoelectronic and pharmaceutical applications. By analyzing phonon dispersion and elastic properties, DFT helps in understanding the mechanical stability of cocrystals, which is essential for designing robust pharmaceutical formulations.

In pharmaceutical sciences, DFT aids in understanding drug behavior at the molecular level by analyzing binding interactions between a drug molecule and excipients in drug formulations, optimizing stability, solubility, and predicting hydrogen bonding patterns. DFT calculations provide insight into how a drug interacts with its carrier, such as hydrophobic or hydrophilic interactions in polymer-based drug delivery systems. It helps design controlled-release formulations by evaluating the electronic structure changes upon interaction with solvents or biological media. DFT models adsorption energies and electronic interactions between drug molecules and nanocarriers like graphene oxide, metal-organic frameworks, and mesoporous silica for designing targeted drug delivery systems. DFT is used in predicting drug metabolism pathways by studying electron density distributions and reactivity indices (Fukui functions, HOMO-LUMO gap). It helps optimize the lipophilicity, stability, and reactivity of drug candidates [274,275].

2.6.6.2. Lattice energy calculations

Lattice energy is a thermodynamic quantity that represents the energy released when ions, atoms, or molecules in the gas phase come together to form a crystalline lattice. It is a crucial parameter in determining the stability and strength of a crystal structure, particularly in the context of ionic compounds, molecular crystals, and cocrystals, since the strength and nature of intermolecular interactions such as hydrogen bonding, π - π stacking, and van der Waals forces contribute significantly to its value. Lattice energy calculations are vital for

understanding the interactions between coformers in a crystallized system. A more exothermic (more negative) lattice energy typically indicates a more stable crystal. By comparing the lattice energies of different cocrystal candidates, one can predict the thermodynamic favorability of their formation. By calculating the lattice energies of different polymorphs of a cocrystal, researchers can predict the most stable form under certain conditions. Since cocrystals may offer improved solubility, dissolution rate, and bioavailability compared to the parent compound, the calculations of their lattice energies can reveal a correlation between the energetic features of given crystal forms and the observable physicochemical properties. Often, stronger lattice energies correlate with more robust mechanical properties and higher melting points. In cocrystal engineering, understanding these properties allows for the design of materials with specific thermal stability and mechanical resilience. In ionic crystals, the Born-Landé Equation relates lattice energy to the charges of the ions and the distance between them.

There are several approaches enabling the calculations of lattice energies. One of them is PIXEL method, which is a computational approach that estimates lattice energy by summing the various intermolecular interactions, electrostatic, polarization, and dispersion forces between molecules in the crystal. In many cases, however, it suffices to calculate the energy of a given crystal (for example using DFT), followed by the calculations (at the same level of theory) of isolated molecules building this crystal placed in a box large enough to ensure no interactions are influencing the results. The difference between these two values constitute an excellent estimation of the lattice energy [276].

2.6.6.3.CSP and its combination with solid-state NMR measurements

Crystal Structure Prediction (CSP) has emerged as a powerful computational tool for exploring the potential crystal structures of a given molecular compound. CSP methods generate a set of low-energy candidate crystal structures based on molecular conformations and packing considerations. However, ranking and identifying the correct structure among many plausible polymorphs remain challenging due to subtle energetic differences and the limitations of force fields or DFT in accurately capturing intermolecular interactions.

To overcome these challenges, experimental solid-state NMR spectroscopy can be integrated with CSP. SSNMR provides site-specific information on molecular environments, hydrogen bonding, and intermolecular interactions, making it an excellent complement to computational methods. By comparing experimental NMR chemical shifts with those computed

for the CSP-generated structures using advanced quantum chemical methods (such as GIPAW-DFT), one can validate and refine the predicted crystal structures.

This hybrid NMR-CSP approach is particularly valuable for systems where X-ray diffraction fails—such as in poorly crystalline, disordered, or amorphous-like materials. Nevertheless, several difficulties arise in the process. Firstly, CSP must generate a comprehensive and reliable landscape of possible structures, which can be computationally expensive or even prohibitively long. Secondly, SSNMR spectra interpretation requires high-resolution data and careful spectral assignment, which is non-trivial for complex systems. Finally, the accuracy of computed NMR chemical shifts depends on the chosen theoretical level, making establishing a good enough agreement between experiment and computation a non-trivial task. Despite these challenges, the synergy between CSP and SSNMR is increasingly proving to be a robust methodology for crystal structure determination [40,51].

3. Objectives of the thesis

One of the aims of pharmaceutical studies is to modify drug delivery with pharmaceutically acceptable molecules and tune the release ratio. To achieve this goal, this thesis aims to build upon the existing knowledge and address the solubility challenges associated with linezolid (LIN), an antibiotic agent. This objective is rooted in the understanding gleaned from the literature review, acknowledging the existing gaps and aiming to contribute solutions to enhance LIN solubility by cocrystal formation and using drug delivery systems.

One of the most important parts is **exploring coformer selection methods, used mostly to understand cocrystal formation, such as evaluating their predictive strength and their dependence on factors, such as molecular conformation, the presence of intramolecular hydrogen bonds, and lattice energy (T1)**. To achieve it, the performance of the three existing methods, molecular complementarity (MC), hydrogen bond propensity (HBP) and molecular electrostatic potential (MEP) maps, is evaluated here in terms of indicating promising coformers, and further used to design a useful strategy to select the candidates for cocrystal formation from among similar coformers (**lattice energy**). To enable the evaluation, **LIN cocrystals need to be created experimentally, so the experimental result can be compared with the predictions**.

Therefore, the next objective focuses on the **mechanochemical synthesis of pharmaceutical cocrystals with LIN (T1)**. The systematic investigation of various experimental conditions for mechanochemical reactions is guided by a deep understanding of cocrystallization methods, as outlined in the literature. By comparing experimental outcomes with predictions from virtual cocrystal screening tools, the objective emphasizes the impact of molecular conformation on predictive accuracy, with direct relevance to improving the method of cocrystal formation. **Additionally, the analysis of intermolecular energy contributions, particularly lattice energy, aims to unravel the factors influencing cocrystal formation**. Toward studying the influence of parameters used in mechanochemical grinding on the obtained results, various solvents used as LAGs, different grinding times, different amounts of solvent, the influence of grinding on the polymorphic form of both compounds, API, and coformers are taken into account as important factors in mechanochemical cocrystallization.

To fully understand the preferences of LIN interactions with coformers, it is needed to recognize their crystal structure (T2, T3). This objective delves into the **structural exploration and potential applications of LIN cocrystals**. The synthesis of cocrystals through mechanochemical grinding is informed by insights from the state of knowledge, guiding the

selection of coformers and experimental conditions. Generating single crystals for in-depth scrutiny, particularly using **single crystal X-ray diffraction**, aims to explore synthon preferences **(T2)**.

However, some LIN cocrystals did not successfully crystallize as monocrystals from nanopowder obtained after mechanochemical cocrystallization, due to different solubility between LIN and coformers, thus introducing **a new objective to search for alternative methods of crystal structure determination**. The third objective aims at **introducing an integrative approach for crystal structure determination**, focusing on overcoming challenges of characterization of microcrystalline powder by **using solid-state NMR and crystal structure prediction (CSP) calculations (T3)**. This approach, developed based on insights from the literature, directly addresses the challenge of CSP-NMR crystal structure determination of conformationally flexible LIN molecules and demonstrates the sensitivity of solid-state NMR parameters on the local environment in the crystal structure. Applying this novel method to LIN:2,3-DHBA and LIN:2,4-DHBA cocrystals is meant to advance the understanding of the preferences of LIN's molecular arrangements within challenging crystalline systems. This work also emphasizes the importance of geometry optimization in rigid CSP searches, which is particularly relevant to LIN and enhances the reliability of crystal structure predictions.

To have in hand cocrystals and characterize them structurally is a good starting point for MSNs application. Currently, there are not enough studies on the interactions of MSNs with two-component crystals, in particular in terms of selecting and evaluating the methods that are the best suited to introduce both components into the pores of MSNs. In the case of LIN, solution based methods are eliminated for obvious reasons, *i.e.*, because there is no cocrystal anymore in solution. The fourth objective is therefore to **examine the loading behavior of binary model systems into mesoporous silica using mainly solid-state-based methods (T4)**, aligning with the solubility enhancement potential. Investigation of loading behavior, using distinct loading methods, considers guest molecule interactions within the mesoporous framework to improve the delivery. Monitoring intermolecular contacts and phase changes using advanced techniques, such as MAS NMR and PXRD, provides insights into the loading mechanisms influencing release kinetics.

Finally, to gain knowledge on the LIN interaction with silica material, the loading of LIN itself into MSNs was studied. The final objective was **to introduce LIN and LIN cocrystals into MSNs to study the possibility of drug delivery systems formation (T5)**. First, the methods selected from the previous part were used to examine the loading of LIN itself. LIN loading was done for the first time. Also, based on the specific characteristics of LIN, like solubility and phase

transition during temperature increase, the modified loading method was introduced. The investigation into the thermal loading of LIN cocrystals within mesoporous silica nanoparticles considers various loading methods and ratios based on a deep understanding of LIN properties. Characterizing loaded samples using advanced analytical techniques, including PXRD, TGA, DSC, and Raman spectroscopy, provides an understanding of LIN and its cocrystal behavior within MSNs.

By anchoring each objective in the identified gaps and challenges outlined in the state of knowledge, this thesis aims to provide a coherent and innovative approach to enhancing LIN's solubility and studying its drug delivery potential through the strategic utilization of mechanochemistry and cocrystal engineering.

Below is the list of the experimental chapters that constitute the conducted research. Four of them were already published, while the fifth is yet unpublished. Therefore, the next part of the thesis gives a brief summary of works **T1-T4**, while **T5** is described in details in terms of experimental protocols as well as the obtained results.

T1. Virtual Cocrystal Screening Methods as Tools to Understand the Formation of Pharmaceutical Cocrystals - A Case Study of Linezolid, a Wide-Range Antibacterial Drug, Khalaji, M., Potrzebowski, M.J., Dudek, M.K., *Crystal Growth and Design*, 2021, 21, pp. 2301–2314

T2. Structural variety of heterosynthons in linezolid cocrystals with modified thermal properties, Khalaji, M., Wróblewska, A., Wielgus, E., G.D. Bujacz, Dudek, M.K., Potrzebowski, M.J., *Acta Crystallographica Section B: Structural Science, Crystal Engineering and Materials*, 2020, 76, pp. 892–912

T3. Narrowing down the conformational space with solid-state NMR in crystal structure prediction of linezolid cocrystals, Khalaji, M., Paluch, P., Potrzebowski, M.J., Dudek, M.K., *Solid State Nuclear Magnetic Resonance*, 2022, 121, 101813

T4. Unexpected Factors Affecting the Kinetics of Guest Molecule Release from Investigation of Binary Chemical Systems Trapped in a Single Void of Mesoporous Silica Particles, Trzeciak, K. Wielgus, E. Kaźmierski, S., Khalaji M., Dudek, M.K., Potrzebowski, M.J., *ChemPhysChem*, 2023, 24, e202200884.

T5. Developing appropriate conditions for loading LIN and its cocrystal with 2,3-dihydroxybenzoic acid into the pores of mesoporous silica materials. Mehrnaz Khalaji, Alain Heudoux, Marta K. Dudek. Unpublished work

4. Results and discussion

4.1. Coformer selection for linezolid cocrystallization (T1, Virtual Cocystal Screening Methods as Tools to Understand the Formation of Pharmaceutical Cocystals - A Case Study of Linezolid, a Wide-Range Antibacterial Drug, Khalaji, M., Potrzebowski, M.J., Dudek, M.K., *Crystal Growth and Design*, 2021, 21, pp. 2301–2314)

The selection of coformers is a major challenge in developing pharmaceutical cocrystals compatible with pharmaceutically active substances. The general strategy used in selecting coformers is a tactless experimental approach whereby a predetermined number of candidates from compounds listed in the generally regarded as safe list are used to form multicomponent crystals. A patent related to LIN cocrystals was identified as a promising starting point, leading to the selection of coformers with specific structural features. These features included hydrogen bond donors and acceptors, planarity or rigidity, appropriate molecular size and shape, and suitable polarity, all concluded to select aromatic acid derivatives (Figure 4.1). In addition, three representatives of non-aromatic acids were included in the list.

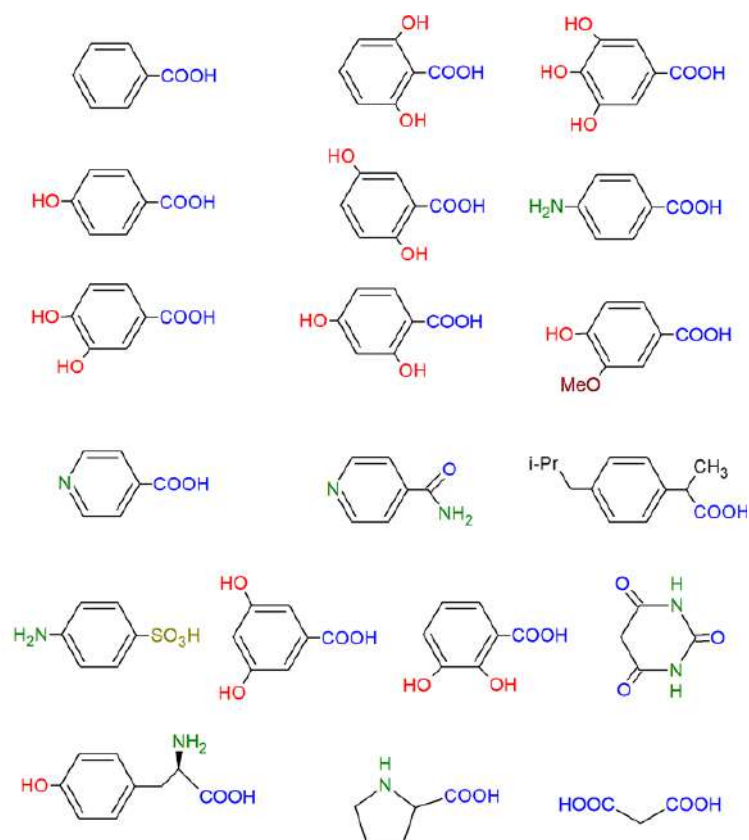


Figure 4.1. Chemical structure of selected coformers.

Mechanochemistry was chosen for the cocrystal formation due to several key factors. Differences in solubility between the pure compounds were exploited to avoid recrystallization of one of them instead of cocrystallization. Encouraging results from prior patent demonstrated the effectiveness of mechanochemical methods in producing cocrystals with desirable properties. Additionally, mechanochemistry was preferred for its environmentally friendly nature, as it typically involves fewer solvents and generates less chemical waste than conventional methods.

The investigation into the application of mechanochemistry as a versatile tool for synthesizing pharmaceutical cocrystals has experienced substantial growth in recent years. Within the context of this Ph.D. thesis, the primary emphasis has been on experimentally screening the selected coformers for the formation of binary crystals with LIN using mechanochemical methods. This research endeavour has yielded significant results, culminating in the identification of **nine novel crystal phases, comprising LIN-2,6DHBA, LIN-3,4DHBA-H₂O, LIN-GA-H₂O, LIN-2,3DHBA, LIN-3,5DHBA-H₂O, LIN-2,4DHBA, LIN-2,5DHBA-H₂O, LIN-2,4DHBA, and LIN-PABA-H₂O**, which was confirmed by powder X-ray diffraction and solid state NMR measurements (see Figure 2, paper T1, appendix I). Nineteen different coformers were screened.

The first important outcome of this work lies in deciphering the intricate factors that influence the formation of these diverse crystal phases. To achieve this, a systematic exploration of various experimental conditions for mechanochemical reactions was conducted. The polymorphic forms of LIN and the presence of different solvents, creating liquid-assisted grinding conditions, were carefully studied. As a result, I have discovered that a less thermodynamically stable form of LIN (form III) was more prone to form cocrystals with selected coformers, and that for some of the coformers, only one solvent was promoting binary phase formation. For example, p-aminobenzoic acid only formed cocrystal when water was used as a solvent but in the case of 3,4- dihydroxybenzoic acid cocrystal formed with all three solvents (toluene, water, methanol), while 2,6- dihydroxybenzoic acid was the only coformer which formed cocrystal by both neat and LAG grinding with all solvents. All screening results are gathered in Table 1 from paper T1 (see appendix I). In addition, manipulating the amount of solvent shows that the complete conversion to the respective cocrystals was possible only after adding a substantial amount of solvent, but an excess addition caused incomplete cocrystallization (see Figure 4, paper T1, appendix I, for NMR spectra used to monitor the cocrystallization reaction outcome with varying amount of solvents).

Concurrently, the outcomes of these experiments were compared with predictions from the three widely utilized virtual cocrystal screening tools: molecular complementarity (MC), hydrogen bond propensity (HBP), and molecular electrostatic potential (MEP) maps. The significance of these predictive tools became apparent in elucidating the preferences of a molecule like LIN to form cocrystals with specific coformers. Notably, the **impact of molecular conformation of both LIN and the coformers on predictive accuracy was carefully assessed**, which is usually neglected in similar studies. In this context, a nuanced comparison between the prediction methods revealed insightful observations, for example, that conformation of LIN has a significant influence on the MC predictive performance (see Table 3 in paper T1, appendix I), while if an intramolecular HB is present in a molecule, it can very much influence the MEP results (see Table 5 in paper T1, appendix I). Overall, while molecular electrostatic potential maps demonstrated higher consistency with experimental outcomes in the performed studies, it is suggested that this was because the examined coformers were preselected (most of them were aromatic carboxylic acids). However, the nuanced performance of these methods suggests a strategic approach. **Geometrical considerations and the propensity for specific supramolecular synthons**, as incorporated in molecular complementarity and hydrogen bond propensity approaches, appear pivotal in the **preliminary stages of coformer selection**. Meanwhile, **energy-based methods**, exemplified by molecular electrostatic potential maps, prove particularly advantageous when dealing with **coformers of similar size and hydrogen-bonding capabilities**.

An additional layer of understanding emerged from the analysis of intermolecular energy contributions, specifically lattice energy, to the total energy of crystal forms of coformers. In theory, the higher the lattice energy of a coformer, the more difficult it should be for mechanochemical forces to destroy this lattice, and since LIN is a constant reactant in all cocrystallization experiments, it was hypothesized that there will be a visible correlation between the coformer lattice energy and its ability to form cocrystals with LIN. Indeed, this parameter proved to be indicative of the feasibility of cocrystal formation, especially in cases where coformers exhibited a capacity to form similar supramolecular synthons (see table 6, paper T1, appendix I). As a result, it can serve as an additional new tool in virtual cocrystal screening for the selection among coformers with similar functional groups. Moreover, the incorporation of intermolecular energy considerations into prediction attempts not only delineates potential barriers to cocrystal formation but also identifies coformers more likely to engage in successful cocrystal formation. This insight assumes special significance in the context

of mechanochemical cocrystal formation, where the destruction of crystal lattices during the reaction necessitates a judicious understanding of the energy dynamics involved.

The overarching implication of this research extends beyond the immediate experimental context. It underscores the utility of virtual cocrystal screening tools not only in guiding the selection of promising coformers for experimental validation but also in comprehending the governing factors influencing cocrystal formation. In the case of a specific API like LIN, the comprehensive evaluation of multiple prediction methods—molecular complementarity, hydrogen bond propensity, and molecular electrostatic potential maps—revealed their collective efficacy in indicating why some of the tested coformers did not form binary phases with LIN, despite the structural similarity to those that did. The examples include 3,5-DHBA and 2,6-DHBA which both form cocrystals with LIN experimentally, despite failing the MC test due to the shape mismatch. HBP results favored 3,5-DHBA-LIN interactions, yet 2,6-DHBA formed cocrystals more readily, possibly due to its lower lattice energy. IBU, despite passing the MC test, did not form cocrystals with LIN due to insufficient energy gain. INN and INA were promising in MC and HBP but showed low cocrystal probability in MEP due to limited energy benefits. Generally, energy gain drives cocrystal formation with LIN, especially among similar compounds, while MC and HBP screenings are useful for early selection.

This research not only contributes to the expanding body of knowledge in the field of mechanochemical synthesis of binary phases, producing, in addition, **nine new cocrystals of LIN** but also establishes a **nuanced framework for the strategic utilization of virtual cocrystal screening tools**. The findings presented herein extend beyond the specific case of LIN, offering a valuable guide for researchers navigating the complex landscape of pharmaceutical cocrystal discovery. I contributed to the published article by conducting all mechanochemical experiments, designing and performing the experiments aimed at unveiling the role of the amount of solvent used to create LAG conditions, taking part in the coformer selection process, performing NMR analyses, taking part in interpreting them, and undertaking virtual cocrystal screening studies, as well as taking part in the writing of the manuscript. These results are published in the journal of *Crystal Growth and Design*, 2021, 21, pp. 2301–2314 published by the American Chemical Society (paper T1, appendix I). [T1]

4.2. Crystal structure determination of linezolid cocrystals by single crystal X-ray diffraction (T2, Structural variety of heterosynthons in linezolid cocrystals with modified thermal properties, Khalaji, M., Wróblewska, A., Wielgus, E., G.D. Bujacz, Dudek, M.K., Potrzebowski, M.J., *Acta Crystallographica Section B: Structural Science, Crystal Engineering and Materials*, 2020, 76, pp. 892–912)

Determining the crystal structure of a pharmaceutical binary phase is important because it reveals how two components interact at the molecular level, affecting key properties like solubility, stability, and dissolution rates. This understanding is vital for optimizing drug formulations, enhancing therapeutic efficacy, and ensuring consistent product quality. Also, avoiding issues like polymorphism, which can alter the drug performance. The second part of this PhD thesis focuses on crystallization and crystal structure determination of the obtained binary phases of LIN. To thoroughly analyse these structures, single crystals were successfully generated for five cocrystals, enabling in-depth scrutiny through state-of-the-art single crystal X-ray diffraction. It is worth noting, that crystallization of the binary phases of LIN is a difficult task because of the solubility difference between coformers and LIN, hence crystallization of single crystals appropriate for X-ray studies was possible only for some of the binaries.

The coformers for which crystallization attempts were successful were benzoic acid (BA), p-hydroxybenzoic acid (PHBA), protocatechuic acid (3,4DHBA), γ-resorcylic acid (2,6DHBA), and gallic acid (GA), two of which were reported before in the patent literature without any structural details, while the remaining three are new phases obtained within the framework of this PhD thesis. Their structural studies employed a multidimensional analytical approach, encompassing advanced techniques such as solid-state NMR spectroscopy, powder X-ray diffraction, and differential scanning calorimetry measurements, but the cornerstone of this investigation lay in the successful generation of single crystals for these phases, revealing the diverse landscape of interactions achievable with LIN.

Within each cocrystal, distinct structural features have surfaced, revealing variable water content and a spectrum of heterosynthons, despite the high structural similarity of the coformers. This diversity underscores the existence of more than one type of intermolecular interaction preferred by the LIN molecule. For example, cocrystals with BA and PHBA are stabilized by $\text{NH}_{\text{LIN}} \cdots \text{O}=\text{C}-\text{OH}_{\text{coformer}}$ and $\text{C}=\text{O}_{\text{amide_LIN}} \cdots \text{OH}_{\text{coformer}}$ synthons (see Figure 4.2 below and Figures 8a and 9a, paper T2, appendix II), while in the cocrystals with 3,4-DHBA and GA the only hydrogen bond interaction between LIN and a coformer is $\text{C}=\text{O}_{\text{amide_LIN}} \cdots \text{HO-Ar}$ (see Figures 11b and 12d, paper T2, appendix II). Notably, in these two cocrystals, dimeric

interactions between COOH groups from the coformers, one of the most pervasive dimeric interaction characteristic of aromatic acids, is preserved. In addition, out of the five cocrystals, three were found to be cocrystal hydrates LIN:GA, LIN:3,4-DHBA and LIN:PHBA, while LIN:BA and LIN:2,6-DHBA were neat cocrystals. As a result of a detailed analysis a proposed hierarchy of hydrogen-bond acceptor sites within LIN has been formulated based on the frequency of observed supramolecular synthons: $\text{C}=\text{O}_{\text{amide}} > \text{C}=\text{O}_{\text{oxazolidone}} > \text{C}-\text{O}-\text{C}_{\text{morpholine}} > \text{C}-\text{N}-\text{C}_{\text{morpholine}} > \text{C}-\text{O}-\text{C}_{\text{oxazolidone}}$ (see Table 2, paper T2, appendix II). Additionally, in all examined cocrystals aromatic–aromatic interactions have been identified as crucial stabilizing factors. Quantum–chemical calculations have corroborated the energetically favourable nature of cocrystal formation, with negative stabilization energies obtained for all five cocrystals (see Table 3, paper T2, appendix II). Interestingly, it was found that in the cocrystal with 2,6-DHBA LIN molecule assumes quite an unfavourable conformation in terms of its energy, indicating that in this case, the intermolecular energy contribution to the lattice energy has to be significant. Finally, it is worth mentioning that among the cocrystal hydrates, one was found to be a non-stoichiometric hydrate, the one formed with 3,4-DHBA. In this case, several structural solutions with somewhat varying amounts of water were obtained, with the best one showing 0.625 H₂O per one LIN and one 3,4-DHBA molecule. The possibility of the same crystal structure containing different amounts of water was also confirmed by ¹H NMR experiments (see Figure 5, paper T2, appendix II).

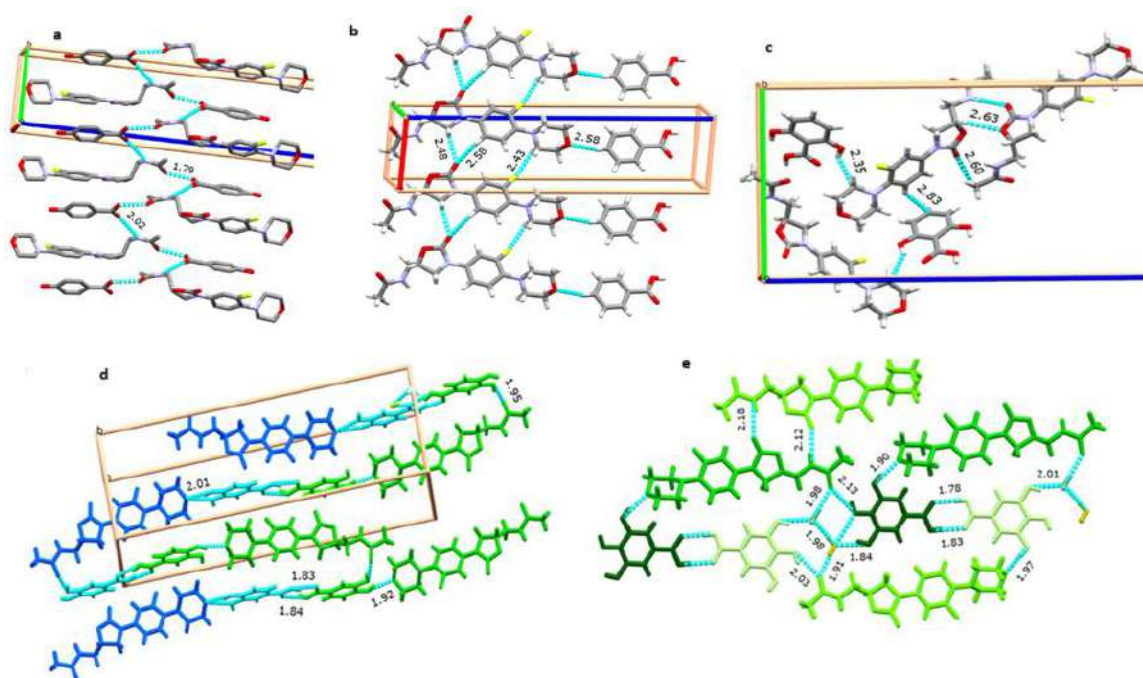


Figure 4.2. The most pervasive supramolecular synthon between LIN and aromatic acid coformers found in the analysed cocrystals.

The analysed cocrystals were examined in terms of their thermal properties. This is of importance for the future design of the drug delivery systems comprising LIN and its binary phases. Introducing LIN with a coformer as a cocrystal into MSN expects the possibility of manipulating its release ratio. However, LIN and its coformers have different solubility, so introducing cocrystals using wet methods would be pointless, but by using solvent-free approaches, like the thermal solvent-free (TSF) method, the solubility barrier can be overcome. The only issue regarding the TSF method is to avoid heating the sample above the phase transition from LIN II to LIN III (141°C), and so the cocrystals with a melting point below this phase transition are the key solution. The modified thermal properties of the obtained cocrystals are noteworthy, with four of them exhibiting melting points lower than the temperature of the phase transition from LIN form II to LIN form III. This shift in physicochemical properties opens avenues for the potential application of melting-based techniques in introducing LIN into drug delivery systems.

The impact of cocrystallization on the water solubility of LIN has also been meticulously evaluated (see Figure 14, paper T2, appendix II). Interestingly, it was found that only in two cases solubility of a binary phase was higher in comparison to LIN form II. In particular, a significant 43% improvement in solubility for LIN:3,4-DHBA:H₂O cocrystal was found, while LIN:BA cocrystal demonstrated a 10% increase. In contrast, the water solubility of LIN:2,6-DHBA was comparable to that of LIN II, while for the remaining two cocrystals, a 23-32% decrease was observed. Although these results may be viewed as somewhat disappointing, as not all cocrystals exhibited better water solubility, they still demonstrate well the influence crystal phase can have on the physicochemical properties of a solid, including water solubility.

In summary, this research, augmented by the successful generation of single crystals for five distinct cocrystals, not only expands our understanding of cocrystal formation with linezolid but also paves the way for tailored drug design strategies. The identified trends in intermolecular interactions offer valuable insights into the rational design of cocrystals, providing a foundation for enhanced pharmaceutical applications of linezolid in the evolving landscape of drug delivery systems. My role in the published article was the mechanochemical formation, crystallization, and preliminary characterization (PXRD, NMR, and DSC measurements) of all five cocrystals, taking part in the crystal structure analysis, interpretation of the obtained results, and writing the preliminary draft of the manuscript. This work has been published in the journal of *Acta Crystallographica Section B: Structural Science, Crystal Engineering and Materials*, 2020, 76, pp. 892–912 (paper T2, appendix II). [T2]

4.3. Crystal structure determination of linezolid cocrystals using an alternative CSP-NMR approach. (T3, Narrowing down the conformational space with solid-state NMR in crystal structure prediction of linezolid cocrystals, Khalaji, M., Paluch, P., Potrzebowski, M.J., Dudek, M.K., *Solid State Nuclear Magnetic Resonance*, 2022, 121, 101813)

As indicated above, only five out of all eleven binary phases of LIN (nine new ones and two already reported) produced appropriate single crystals for X-ray diffraction studies. The remaining ones were crystalline according to PXRD, but crystallized only as fine powders. To explore such crystal structures, alternative approaches have to be sought. One of them is based on the combined use of high-resolution solid-state NMR, powder X-ray diffraction experiments, and crystal structure prediction (CSP) calculations, and is often referred to as CSP-enhanced NMR crystallography and abbreviated as NMR-CPSX. However, when dealing with molecules characterized by significant conformational freedom, particularly when it concerns multicomponent crystals, the joint CSP-NMR protocol faces challenges such as NMR signal assignment ambiguities and the vast conformational search space that computational methods struggle to navigate efficiently.

This section of this doctoral thesis introduces a novel strategy to overcome these challenges, leveraging the synergistic potential of solid-state NMR and CSP in demanding circumstances. The investigation focuses on two distinct cocrystals of LIN with 2,3-dihydroxybenzoic acid (2,3-DHBA) and 2,4-dihydroxybenzoic acid (2,4-DHBA). The two examined cases can be viewed as a straightforward one (LIN:2,3-DHBA), for which the experimental data indicated a high degree of similarity of this structure with the one of known LIN:2,6-DHBA cocrystal, and a much more demanding one (LIN:2,4-DHBA), with no counterparts in any of the known crystal forms of LIN.

In the straightforward case, the solid-state NMR spectra showed very similar chemical shifts for LIN in LIN:2,3-DHBA cocrystal to those in LIN:2,6-DHBA cocrystal (Figure 4.3e and Figure 2e, paper T3, appendix III). This indicated that the conformation of LIN in both forms is very similar (or indeed, identical). Further, the similarity in intermolecular interactions was demonstrated by ^1H - ^{13}C *inv*HETCOR and ^1H DQ MAS NMR experiments (Figure 4.3). Based on these results, two methods were approached: (1) utilizing LIN:2,6-DHBA cocrystal, replacing the coformer present with that of 2,3-DHBA and geometry optimizing the resulting crystal, (2) *de novo* CSP using molecular conformation of LIN extracted from LIN:2,6-DHBA cocrystal. Among these, the latter approach was shown to yield the best agreement with the PXRD and solid state

NMR experimental data (see Figure 3b and Table 1, paper T3, appendix III), producing a very good structural model for LIN:2,3-DHBA cocrystal.

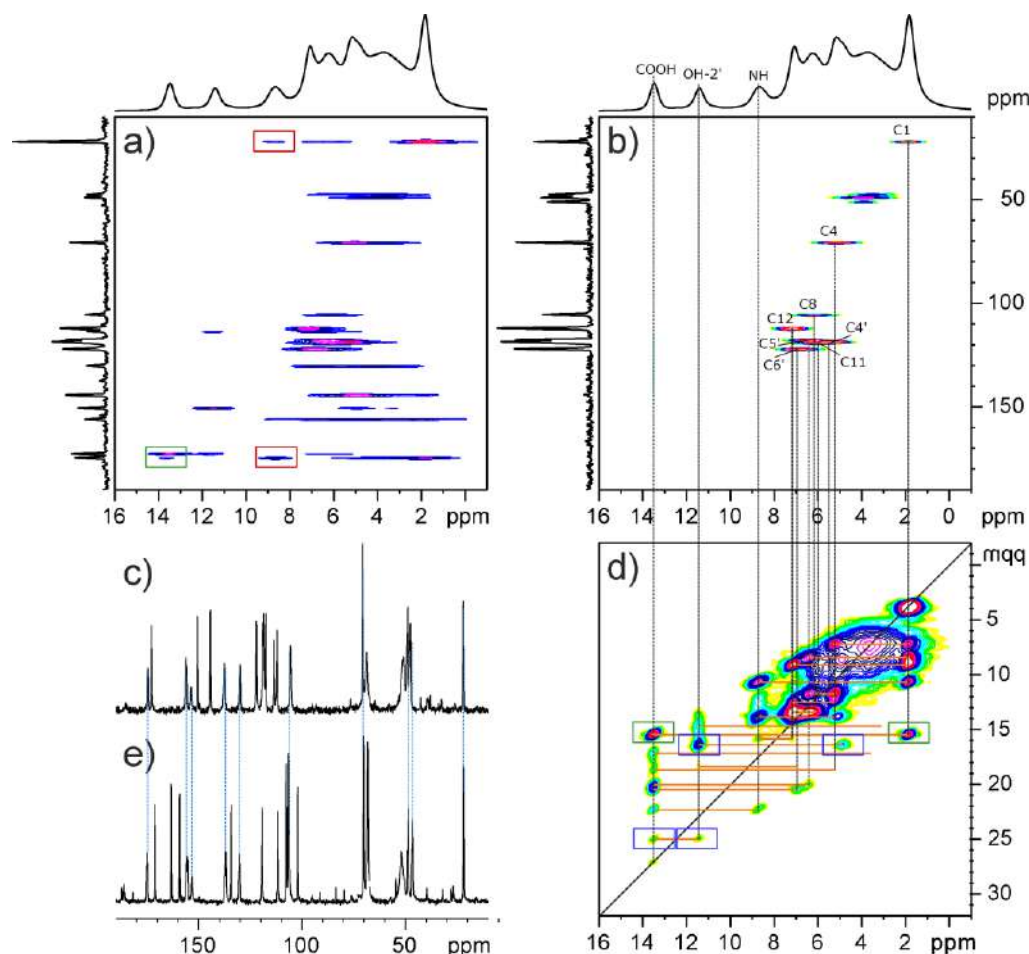


Figure 4.3. (a) and (b) ^1H - ^{13}C *inv*HETCOR NMR spectrum recorded with a contact time of 3 ms (a) and 100 μs (b), and (d) ^1H - ^1H DQ-SQ MAS with ^1H - ^1H Back-to-Back (BaBa) recoupling spectrum for LIN:2,3-DHBA cocrystal; (c) and (e) a comparison of the ^{13}C CPMAS NMR spectra recorded for LIN:2,3-DHBA and LIN:2,6- DHBA cocrystals. The 2D spectra were recorded with a sample spinning speed of 62.5 kHz; color rectangles mark some of the main correlation signals. In 1D spectra the dotted light blue lines correspond to the resonances originating from LIN and indicate the similarity of chemical environment of LIN molecules in both crystals.

The heightened complexity with the LIN:2,4-DHBA cocrystal arises from LIN inherent conformational flexibility and a 'floppy' side-chain capable of assuming numerous conformations. The substantial conformational search space, compounded by the flexibility of both LIN and 2,4-DHBA, made traditional NMR crystallography approaches impractical in this study. To address these challenges, a methodology was introduced, integrating knowledge-

based data (Mogul search), conformational exploration, and structural constraints extracted from high-resolution solid-state NMR spectra. This innovative approach tentatively narrowed down the search space, identifying a subset of conformations for CSP calculations. In this case, a curated set of 27 LIN conformations was selected and combined with two possible conformations of 2,4-DHBA. These conformations were used to generate trial crystal structures in CSP calculations. The calculations were limited to generating only a small set of structures. The idea standing behind this approach stems from the fact that NMR data are sensitive primarily to molecular conformation and less so to the long-range order in the crystal. Hence, a correct conformation in a crystal should produce a reasonable agreement with the experimental NMR data, even if the molecular packing is not exactly right.

The comparison of theoretical NMR data for the selected 27 components conformational set with experimental NMR data for LIN facilitated the further reduction of potential LIN conformations to five, which were then used in a more thorough CSP search (see Figure 9, paper T3, appendix III). Ultimately, the identified crystal structures corresponding to these selected conformations revealed the two most probable molecular arrangements of LIN. Remarkably, one of these arrangements exhibited exceptional agreement with experimental NMR parameters, encompassing both ^1H and ^{13}C chemical shifts. Admittedly, the conducted calculations did not lead to the generation of the unambiguously final structural model of LIN:2,4-DHBA cocrystal, but nevertheless, they are an important step forward in dealing with complex, conformationally flexible systems in CSP-NMRX.

An additional observation that arose from the performed calculations was that in the realm of rigid CSP searches, a thorough geometry optimization of generated structures is a prerequisite before comparing calculated and experimental NMR data. For some of the structures, the agreement with NMR data prior and after the geometry optimization changed remarkably. This precaution ensures the comprehensive consideration of relevant crystal structures.

In summary, this research not only introduces a nuanced approach to address the complexities of conformationally flexible molecules but also emphasizes the significance of integrative methodologies in advancing our understanding of molecular arrangements within challenging crystalline systems. In the published article, I played a role in conducting conformational searches, Mogul search, taking part in quantum-chemical calculations, analysing NMR and PXRD results, and comparing them with predicted data. Additionally, I contributed to the writing of a section in the manuscript draft. This work has been published in journal of *Solid State Nuclear Magnetic Resonance*, 2022, 121, 101813 (paper 3, appendix III). [T3]

4.4. Binary system confinement model (T4, Unexpected Factors Affecting the Kinetics of Guest Molecule Release from Investigation of Binary Chemical Systems Trapped in a Single Void of Mesoporous Silica Particles, Trzeciak, K. Wielgus, E. Kaźmierski, S., Khalaji M., Dudek, M.K., Potrzebowski, M.J., *ChemPhysChem*, 2023, 24, e202200884)

In this part of the thesis, the focus is on a preliminary study of the loading of well-defined binary systems (a cocrystal and a solid solution) and untreated materials (physical mixtures) into the voids of MCM-41 mesoporous silica particles as a model to unlock the mixing knowledge before loading LIN and its cocrystal. Utilizing three distinct filling methods, namely Diffusion Supported Loading (DiSupLo), mechanical ball-mill loading (MeLo, earlier referred to as Co-milling), and thermal solvent-free loading (TSF), it was aimed to investigate the loading behavior of guest molecules within the MCM-41 pores. The chosen model systems for this investigation involve benzoic acid (BA), perfluorobenzoic acid (PFBA), and 4-fluorobenzoic acid (4-FBA) as probes, allowing for exploration of binary system interactions.

Magic Angle Spinning NMR Spectroscopy techniques and Powder X-ray Diffraction were employed to monitor the intermolecular contacts and phase changes of the guest molecules within the MCM-41 pores. Given the common application of mesoporous silica materials in drug delivery systems, special emphasis was placed on factors influencing guest release kinetics. Findings highlight that not only the content and composition of binary systems but also the loading technique significantly impact the rate of guest release.

The study introduces innovative methods for visualizing differences in release kinetics, confirming the complex nature of MCM-41 porosity. The material exhibits at least two distinct areas with free spaces (voids) where guest particles can reside, namely, the interstitial space and internal pore space. For chemical entities with a high affinity for forming binary systems, the presence of MCM-41 does not hinder the spontaneous formation of such systems, retaining a subtle binary structure stabilized by non-covalent interactions. For example, for a sample obtained by MeLo it was shown using solid-state NMR spectroscopy (specifically, ^{19}F - ^{19}F NOESY MAS and ^1H - ^{19}F HOESY MAS NMR experiments, see Figure 4.4 and Figure 4, paper T4, appendix IV) that both compounds interact with themselves inside the voids of MCM in a manner similar to that observed in a crystal lattice. This important finding shows that pervasive interactions present in a crystal may be preserved in a drug delivery system.

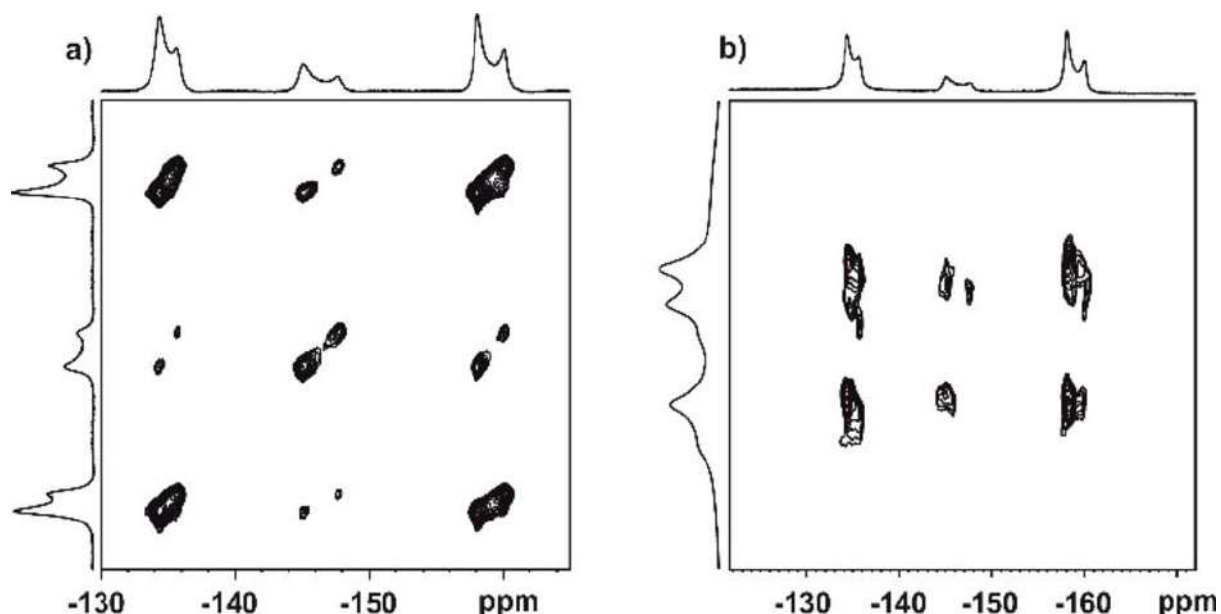


Figure 4.4. a) ^{19}F - ^{19}F NOESY MAS and b) ^1H - ^{19}F HOESY MAS spectra of BA : PFBA cocrystal embedded in MCM-41 (1 : 2 by weight) using the MeLo method (without LA) recorded at 12.5 kHz MAS with a mixing time of 20 ms and 350 ms, respectively.

Additionally, the investigation reveals that the selection of coformers has a substantial impact on the release rates of media located in MCM-41 voids. The study of BA:PFBA and BA:4-FBA systems demonstrates apparent differences in release profiles. Surprisingly, the analysis of the release ratio of guests loaded using different methods indicates that the chosen loading method can significantly influence the release profile of guest particles in the MCM-41 voids. For example, for BA:PFBA system an extended release of both components was observed from samples obtained with MeLo in comparison with the material from DiSupLo and TSF (see Figure 16, paper T4, appendix IV). This unexpected result suggests that both coformer selection and loading method jointly serve as a powerful tool for steering the amount and rate of release. Further exploration is required to delve into the nuances of the mechanical loading method and its potential impact on particle location within MCM-41 voids.

This preliminary study sheds light on the intricate interplay between binary system composition, loading methods, and their collective influence on the release dynamics within mesoporous silica particles. These findings not only expand our understanding of drug delivery design but also open avenues for fine-tuning release kinetics, offering valuable insights for future pharmaceutical applications. My role in this project was to synthesize the binary systems, to prepare the confined and physically mixed samples, and to take part in the PXRD and SSNMR experiments. This work has been published in the journal of *ChemPhysChem*, 2023, 24, e202200884 (paper T4, appendix VI). [T4]

4.5. Confinement of linezolid and its cocrystal into mesopores of silica nanoparticles

(T5, Developing appropriate conditions for loading LIN and its cocrystal with 2,3-dihydroxybenzoic acid into the pores of mesoporous silica materials. Mehrnaz Khalaji, Alain Heudoux, Marta K. Dudek. Unpublished work)

This doctoral thesis section presents the development and study of confinement of linezolid and one selected linezolid cocrystal with a pharmaceutically acceptable coformer into mesoporous silica nanoparticles. This work marks the first instance of utilizing linezolid in a drug delivery system based on the findings from the binary models. The focus of this research is twofold. Firstly, **to examine and optimize the loading of linezolid itself, and to investigate how the drug confinement within the delivery system can be fine-tuned**. Secondly, to study the possibility of **loading the newly developed cocrystal system, and to analyse how the cocrystallization influences the overall loading efficiency**. By exploring both the individual confinement of linezolid and its integration within cocrystal, this research aims to study the effectiveness and precision of drug delivery for linezolid.

This study delves into the realm of cocrystallization as a promising strategy for pharmaceutical optimization, with a specific objective: **the selection of a linezolid cocrystal demonstrating reduced melting under the phase transition temperature of commercial linezolid and using it in an attempt to introduce it into the pores of MSNs**. This investigation transcends conventional approaches by centring on thermal solvent free (TSF) loading within mesoporous silica nanoparticles. In addition, other loading methods, including mechanical neat grinding (MECHANO), diffusion-supported loading (DiSupLo) introduced in our laboratory, and mechanochemical grinding with LAG (MeLo), were evaluated for the confinement of linezolid, alongside introducing two new modified thermal wet methods, thermal wet 1 (TW1) and thermal wet 2 (TW2), tailored for this research.

The preliminary exploration based on the findings of the binary model study spans different loading ratios (1:1, 2:1, and 3:1) of linezolid within two selected mesoporous materials, namely MCM-41 and SBA-15, selected because of the different pore sizes. The diversity of the tested loading ratios facilitates a comprehensive understanding of their impact on the loading process. Furthermore, the TSF is applied to investigate linezolid cocrystal confinement within mesoporous silica nanoparticles, enabling a comparative analysis of cocrystal and non-cocrystal drug loading.

Characterization of the loaded samples emerges as a crucial facet of this study. Powder X-ray Diffraction was used to analyse the crystalline structure of substances, facilitating the

identification of changes induced by loading and offering insights into the efficacy of each loading method. Thermogravimetric analysis and differential scanning calorimetry were employed to assess the thermal stability and phase transitions of loaded samples, providing valuable information for understanding the behaviour of linezolid within the mesoporous carriers. Furthermore, Raman spectroscopy served as a powerful tool for structural analysis of the studied systems. This sensitive technique yields detailed information on interactions within the loaded samples, offering additional insights into the efficiency of cocrystal loading and its impact on the internal structure of the mesoporous carriers.

This comprehensive investigation aims to advance the understanding of linezolid and linezolid cocrystal loading inside mesoporous silica nanoparticles. Through the examination of established and innovative loading methods, as well as different loading ratios for neat linezolid, the study endeavours to identify the most effective strategies for optimizing drug delivery systems. The outcomes of this research have the potential to significantly contribute to the development of advanced pharmaceutical formulations, addressing challenges associated with the solubility of linezolid. These results are not yet published and are described in detail below.

4.5.1. Materials and methods

Mesoporous silica nanoparticles have been carefully chosen as carriers for drug delivery applications, emphasizing the critical aspect of confinement. Specifically, MCM-41 and SBA-15, characterized by two different hexagonal pore morphology channel types [277] shown in Figure 4.5 and respective pore sizes 4 and 12 nm, and particle size <100 nm and <150 μm , were selected based on their favourable attributes. These nanoparticles were procured from Sigma Aldrich and utilized in both their commercial and calcinated forms across various confinement methodologies and their results characterization.

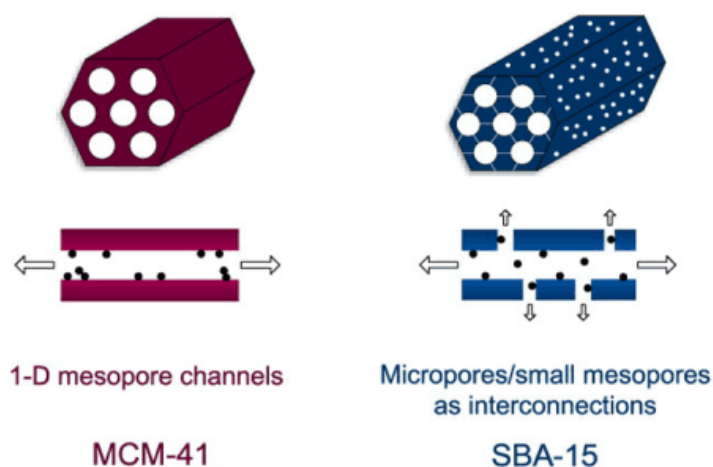


Figure 4.5. The two selected mesoporous silica nanoparticles [277].

The stable form II of commercial linezolid, purchased from ABCR GmbH (Germany), was employed for the confinement process of neat linezolid. Form III of linezolid is excluded from confinement due to its susceptibility to undergo form changes under varying conditions during milling and heating by the confinement process. This cautious selection ensures the stability and reliability of the chosen drug carrier system. Out of the newly synthesized cocrystals of LIN, one system was selected for loading study, from among the anhydrous binary forms. Two key considerations guided the decision. Firstly, the preference was given to linezolid cocrystals with lower melting points to minimize the potential for phase transition of linezolid during the TSF confinement, particularly after the cocrystal lattice experiences disruption. Figure 4.6 features the thermograms of the obtained linezolid cocrystals in comparison with the phase transition and the melting point of linezolid II and III.

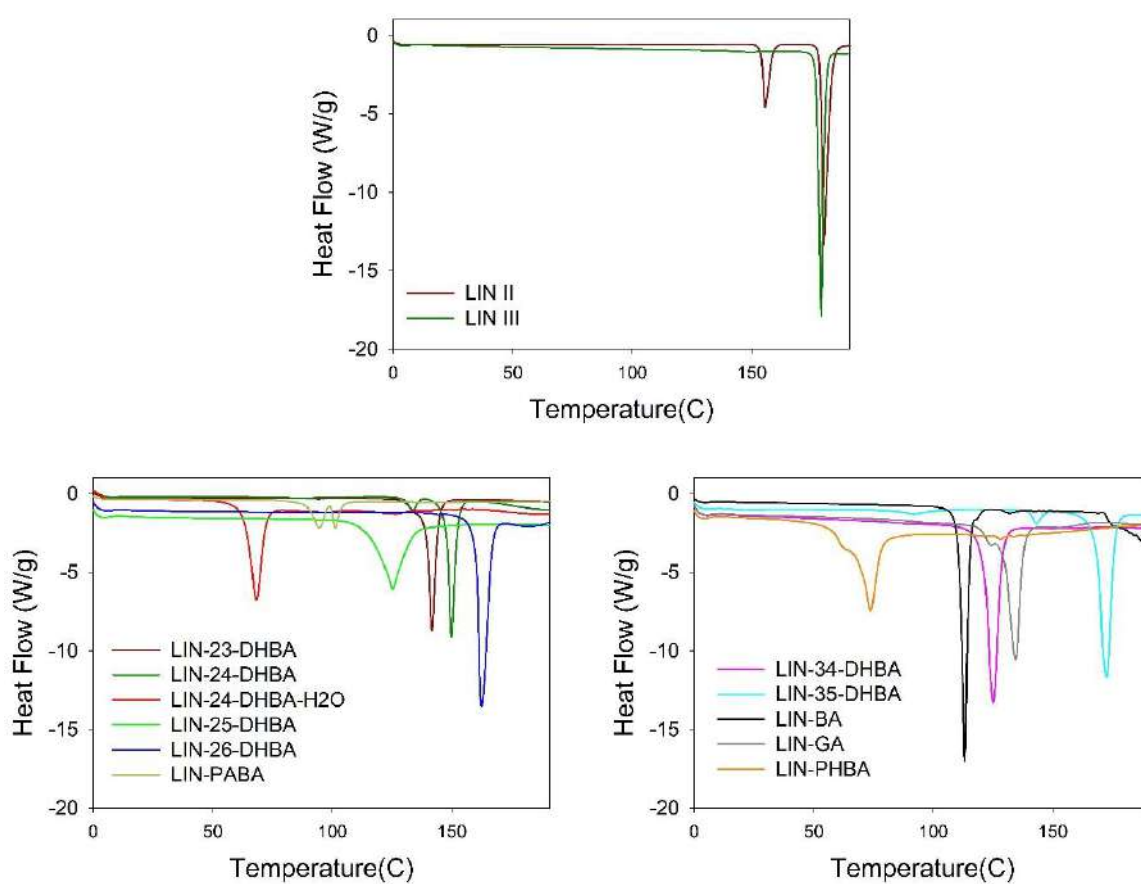


Figure 4.6. DSC curves for linezolid II and III and their cocrystals.

LIN:2,3-DHBA cocrystal has a melting point of 141°C, which is lower than the II \rightarrow III phase transition of LIN at 154°C. Secondly, despite some hydrate cocrystals having lower melting points, their complexity and introduction of an additional component in the considerations

(water) prompted their exclusion from this study. Finally, cocrystal with established crystal structures was given preference. Based on these reasons LIN:23DHBA was selected for confinement studies.

4.5.2. Methods of linezolid and cocrystal confinement

In optimizing drug delivery systems, the selection of loading methods plays a crucial role in determining their effectiveness [T4]. In the case of linezolid, several challenges arise that can significantly impact the confinement process, particularly as this is the first attempt to confine the drug. Therefore, it is essential to identify the most suitable approach.

The primary challenge stems from the limited solubility of linezolid. To address this issue, we introduce two novel wet methods that do not require preparing highly concentrated solutions of linezolid. Instead, we systematically design a step-by-step confinement process that combines wet and thermal methods. Additionally, we employ a mechanochemical approach, utilizing mechanical force to incorporate the API into the system.

A second challenge is the dissolution of the linezolid cocrystal in wet methods. It is important to emphasize that isolating and embedding a crystalline unit cell of a cocrystal within MSNs is not feasible. Any method used for loading components into MSNs inherently disrupts the crystal lattice. However, additional complexity arises in maintaining the precise 1:1 ratio of API and coformer when solubilizing a cocrystal. If dissolution occurs, there is a risk that one component—either the API or the coformer—may enter the MSNs independently, leading to an undefined or inconsistent linezolid:coformer:carrier ratio. Also, the reason behind the cocrystal confinement is to use the enhanced thermal stability of linezolid and avoid changing form during thermal confinement by its cocrystallization, therefore, we use only TSF for the confinement of linezolid cocrystal.

Beyond enhancing drug delivery efficacy, this research also prioritizes environmental sustainability by minimizing the toxicity risks associated with solvent use in traditional wet methods. Conventional wet techniques often leave solvent residues, potentially compromising the biocompatibility and safety of the drug delivery system. Moreover, reducing solvent consumption benefits the environment. By utilizing thermal, mechanochemical, and innovative wet methods that operate with little amount of solvent, this study aligns with eco-friendly principles, contributing to the development of sustainable pharmaceutical formulations with a reduced environmental footprint. All confinement methods are described in detail as follows.

4.5.2.1. Physical mixture

A freshly prepared physical mixture of LIN with the proper weight ratio of separated components was placed together in one pot and homogenized. The calcinated MSNs were separately homogenized before mixing, and then the components were gently mixed together. The mixture was prepared for the comparison purposes and investigation of a spontaneous loading of LIN.

4.5.2.2. Mechanical neat grinding (MECHANO)

The samples were obtained by using the planetary ball mill PM 200. 100 mg of homogenous physical mixture with a proper weight ratio of silica material and LIN were added to a 50 ml stainless-steel jar with 10 steel balls (5 mm diameter). The grinding was performed for 45 minutes with 5 minutes interval after 15 minutes of milling to avoid overheating at 450 Hz frequency. For these experiments MCM-41 and SBA-15 silica were calcined at 300°C for 1 h before grinding to remove water.

The samples used for Raman studies were prepared in plastic Eppendorf vials with a capacity of 200 ml, and one steel ball, 5 mm diameter, due to the necessity of elimination of high induced fluorescence. The proper weight ratio of API and MSNs was added to fill the vial completely then ground with an MM200 mixing mill at 10 Hz for 1 hour with 5-minute intervals every 10 minutes for mixing the content at the ends of the vials to avoid blocking accessibility of the material. SBA-15 silica was used here without calcination to avoid induced fluorescence due to prolonged heating.

4.5.2.3. Mechanical liquid assistant grinding (MeLo)

The samples obtained by MeLo were prepared according to the procedure described earlier for MECHANO, using a planetary ball mill with the addition of ethanol (20 µl) as a liquid assistant (LA).

4.5.2.4. Diffusion-supported loading (DiSupLo)

The homogenized physical mixture with the proper weight ratio of linezolid to MSNs was placed in an open jar with a capacity of 20 ml (the mixture filled one fifth of the jar's volume), inside the closed vessel of 50 ml containing 15 ml of ethanol for 3 hours. There was no direct contact between the solid mixture and the liquid solvent. The diffusing vapours of ethanol penetrated the whole volume of the vessel, and the API dissolved in the minimal volume of solvent was transported to the pores of MSNs.

4.5.2.5. Thermal solvent free(TSF)

The homogenized physical mixture of the selected weight ratio of API (linezolid or cocrystal) and calcinated mesoporous silica was heated at approximately 7 °C above the melting point or phase transition of the starting cocrystal or API for 70 minutes. The heating temperature for LIN and LIN-2,3DHBA binary was 161°C and 148°C, respectively.

4.5.2.6. Thermal wet 1 (TW1)

In this method 10 mg of linezolid was added to the proper amount of ethanol to dissolve completely and added to 100 mg of MSNs as a 10 percent by weight ratio to SBA-15 was added to the container, and heated above the boiling point of ethanol to ensure thorough drying before the next API portion was added, for example, doing this procedure twice resulted in 20 percent weight ratio linezolid to SBA-15. The entire container was maintained under vacuum at a temperature exceeding the boiling point of ethanol to eliminate any residual solvent within the pores.

4.5.2.7. Thermal wet 2(TW2)

The API was introduced to SBA-15 similarly as in TW1, and then the container was kept at a temperature 5 degrees above the phase transition of linezolid for 70 minutes.

4.5.3. Evaluation of the confinement results

4.5.3.1. PXRD

Powder X-ray diffraction experiments were conducted using a Panalytical Empyrean diffractometer operating in Bragg-Brentano reflection mode and employing zero-background silicon sample holders. The diffractometer was equipped with a PIXcel3D detector featuring all 255 active channels, and Cu K α radiation ($\lambda=1.5419$ Å) was utilized. The incident beam employed 0.02 Soller slits, a 1/8° divergence slit, and a 10 mm beam mask. For the diffracted beam, 0.02 large Soller slits and a 7.5 mm mask were employed. Diffractograms were recorded over a 2θ range of 3.0 to 50.0°, utilizing a step size of 0.0131°.

4.5.3.2. DSC and TGA

Differential scanning calorimetry measurements were conducted with a 2920 MDSC V2.6A instrument from TA Instruments. Hermetically sealed aluminum pans were utilized, and

a nitrogen flow of 50 mL was maintained. Temperature calibration was performed using tin and indium as reference points in a two-point calibration. The heating rate was set at 10 K/min. Thermogravimetric analysis measurements were executed with a 2950 TGA HR V5.4A instrument from TA Instruments. Platinum pans were employed, and a nitrogen flow of 60 mL was maintained. The heating rate for TGA measurements was also set to 10 K/min.

4.5.3.3. Raman spectroscopy

Low-frequency Raman spectroscopy investigations were conducted using the high-dispersive XY-Dilor spectrometer, featuring three gratings (1800 gr/mm) and equipped with a Cobolt laser emitting at 660 nm. The slits were maintained at 150 μm to enable the detection of a Raman signal down to 5 cm^{-1} in a high-resolution configuration (less than 1 cm^{-1}). The samples were loaded into spherical Pyrex cells, which were hermetically sealed.

Sample temperature regulation was achieved using an Oxford nitrogen flux device, ensuring temperature fluctuations within 0.1 $^{\circ}\text{C}$. Low-frequency Raman spectra (LFRS) were collected between 5 and 350 cm^{-1} in 1 min, in situ during the heating ramp at 1 $^{\circ}\text{C}/\text{min}$. The analysis of the LFRS required specific processing [249,278], addressing spectrum distortion induced by temperature *via* the Bose factor, particularly crucial at very low frequencies.

To obtain the low-frequency spectrum independent of temperature fluctuations, the Raman intensity $I_{\text{Raman}}(\omega, T)$ was converted into reduced intensity $I_r(\omega)$ using the formula:

$$I_r(\omega) = I_{\text{Raman}}(\omega, T) / [n(\omega, T) + 1]\omega$$

where $n(\omega, T)$ is the Bose factor. This representation of the LFRS is commonly used to highlight molecular disorders corresponding to fast molecular motions, thermally activated, and detected in the low-frequency region (5–50 cm^{-1}), contributing to the LFRS as quasielastic intensity (I_{QES}). In disordered molecular systems, the structural information is contained in the pure vibrational spectrum, obtained by removing the contribution of the quasielastic intensity from the $I_r(\omega)$ -spectrum, which is then converted into Raman susceptibility according to [279-281]:

$$\chi''(\omega) = \omega \cdot I_r(\omega) = (C(\omega) \cdot \omega) / G(\omega)$$

where $C(\omega)$ is the coupling coefficient between light and vibration, and $G(\omega)$ is the vibrational density of states (V_{DOS}). $\chi''(\omega)$ is recognized to be a representation very close to the V_{DOS} [282-284].

In this investigation, the low-frequency spectra of multi-component systems are presented using Raman susceptibility, while the temperature dependencies of low-frequency

Raman spectra are illustrated through reduced intensity to monitor phenomena associated with disordering.

4.5.4. Results and Discussion

The main challenge in studying a system after introducing it into a drug delivery system is the characterization of a confined API and establishing whether indeed the API was loaded inside the pores. Linezolid was confined for the first time, with containment methods used to solve the problem of low solubility. The confinement can affect the thermal stability and the interaction at the molecular level inside the pores. The results obtained with four different experimental methods (PXRD, Raman spectroscopy, and two thermal methods, DSC and TGA) used in this regard are discussed in the subsequent chapters.

4.5.4.1. Powder X-ray characterization of the confinement results of linezolid

After the confinement process, the initial parameter to be assessed is whether the components entered the MSNs, which can be observed by examining the crystallinity of the binary system. Successful confinement should result in a reduced amount of crystalline sample compared to the starting material. In interpreting these results, it is essential to note that comparing the abundance of crystalline LIN residues across different samples is inherently qualitative rather than quantitative. Direct comparisons of crystalline LIN leftovers are limited by factors such as slight variations in the sample amount placed on the plate and differing signal to noise ratios. These factors mean that while qualitative differences can be observed between methods, it is not accurate to conclude which method introduced the largest amount of LIN based on these measurements alone.

In this study, the influence of the API-to-mesoporous particle ratio was initially examined, along with an exploration of the impact of channel type and pore size of the nanoparticles.

Figure 4.7 illustrates the effect of the ratio of LIN to MCM-41 used in the DiSupLo method of confinement. As anticipated, a higher ratio of API to nanoparticles demonstrates a higher intensity of the reflexes originating from LIN in the crystalline phase, indicating that it has not been fully loaded inside the pores. A detailed analysis of the intensity of a reflex at $2\theta=17^\circ$ (top of Figure 4.7) reveals a higher signal for a 1:1 ratio and a larger quantity of linezolid remaining outside of MCM-41 pores or interacting with external subphases. Hence, in all further studies 3:1 ratio of silica to API was used.

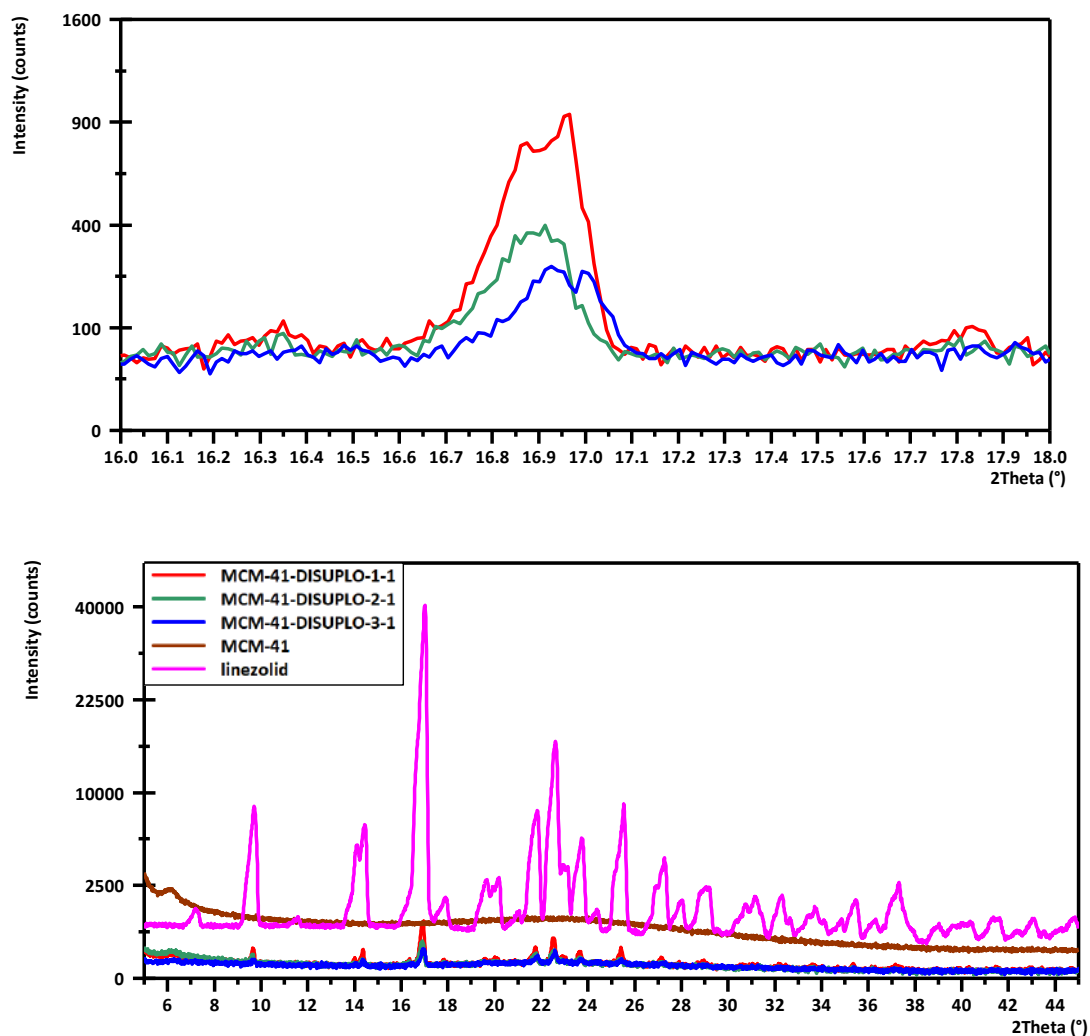


Figure 4.7. PXRD of samples of LIN introduced to MCM-41 in the ratio of 1:1,1:2 and 1:3 using a DiSupLo method. and the expansion of the 16-18° 2 θ range

The influence of the type of mesopores is not as pronounced as the effect of the ratio between linezolid and mesoporous nanoparticles. The results obtained from utilizing a different type of MSNs (SBA-15) are illustrated in Figure 4.8. A detailed analysis reveals only a slight variation in the intensity of reflexes. However, somewhat lower reflexes intensity implies that SBA-15 could be a more advantageous choice as a nanocarrier for introducing both linezolid and linezolid cocrystal into the MSNs pores, in particular if both cocrystal components are to be introduced into the same space.

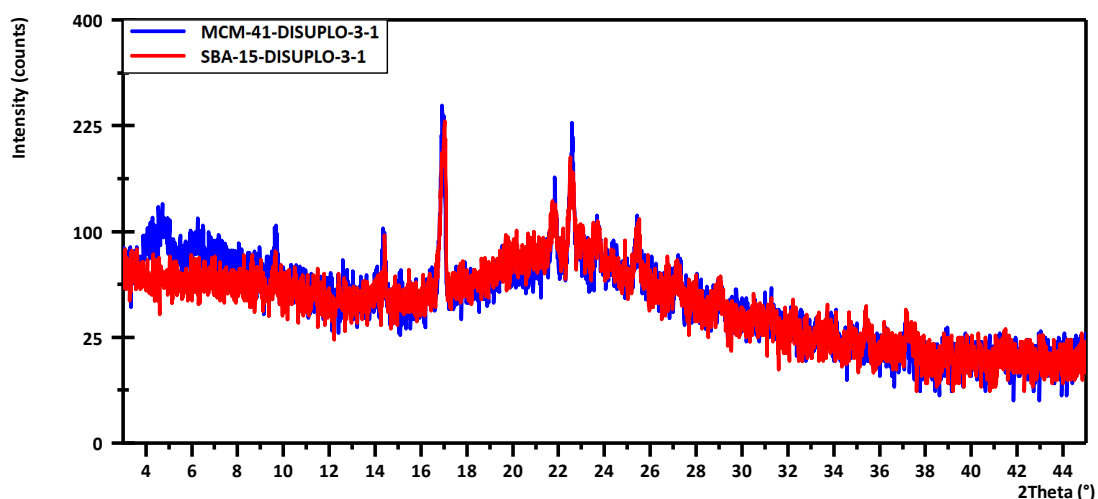


Figure 4.8. A comparison of PXDR diffractograms for linezolid confined into SBA-15 and MCM-41 by DiSupLo method in 1:3 ratio.

Another crucial aspect of this study is evaluating the impact of different loading methods on confinement efficiency. Among the six tested approaches, two were completely solvent-free, MECHANO and TSF methods. Two other methods, DiSupLo and MeLo, utilized only microliter-scale amounts of solvent. Additionally, two newly developed methods, TW1 and TW2 (for which introduction the rationale is given further) employed milliliter-scale solvent volumes. This classification highlights the varying degrees of solvent involvement in the confinement process, which has implications for both drug loading efficiency and environmental sustainability.

To compare the four solvent-free or solvent-usage-limiting approaches the commercial form of linezolid was introduced to SBA-15 with a weight ratio of 3:1 of mesopores to API. The larger pores MSNs were selected for this purpose so that the influence of the small size of the pores of MCM-41 is eliminated from the considerations. The PXRD results reveal that the method employing thermal force through the melting of the API exhibits the lowest amount of crystalline phase present after the confinement compared to the other methods. Additionally, the dissipation of the reflex at 17° 2θ indicates the phase transition of the linezolid phase when using thermal solvent-free loading (Figure 4.9). Once again, this underscores the importance of introducing linezolid in the form of its cocrystal with a melting point below the phase transition temperature of commercial linezolid.

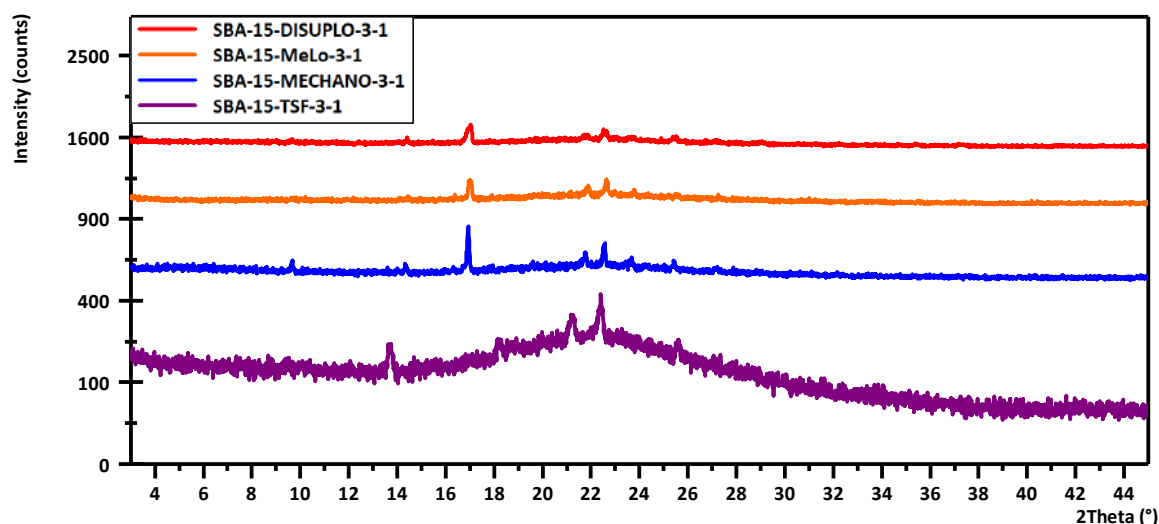


Figure 4.9. The PXRD diffractograms of linezolid introduced to SBA-15 (1:3) with DiSupLo, MeLo, MECHANO and TSF.

The qualitative PXRD data indicate that none of the methods tested achieved complete confinement of LIN within the SBA-15 mesopores. The persistent presence of crystalline LIN reflexes across the tested approaches, as shown in Figure 4.8, suggests that each method leaves a portion of LIN outside the SBA-15 structure. This finding prompts a critical assessment of whether the issues arise from the mass ratio of LIN to the mesoporous material or whether these specific methodologies are inherently inadequate for a fully effective LIN confinement. These results underline the need for optimization in terms of method selection and sample ratios, reinforcing the rationale behind the proposed innovative approach discussed in subsequent sections. In light of published results on confining large molecular APIs [24], wet methods have demonstrated superior outcomes. Drawing inspiration from the modified incipient wetness impregnation, two new confinement methods were devised, TW1 and TW2, bearing in mind that the employment of the classic incipient wetness approach is burdened with the earlier mentioned limitations.

A primary challenge of employing wet methods for introducing linezolid lies in its low solubility. To address this limitation, a small amount of API was dissolved in a minimal ethanol portion—a biocompatible solvent. This solution was then gradually introduced into SBA-15. In each step, a 10 percent by weight ratio to SBA-15 was added to the container, and heated above the boiling point of ethanol to ensure thorough drying before the next API portion was added (TW1). The entire container was maintained under vacuum at a temperature exceeding the boiling point of ethanol to eliminate any residual solvent within the pores. The second invented method combines a thermal and a wet method and is named TW2. In this method, the API is

introduced to SBA-15 in a similar manner as in TW1, and then the container is additionally kept at a temperature 5 degrees above the melting point of the API. These novel approaches serve two main purposes: first, the solvent aids in breaking down the crystal lattice energy barrier and weakening API-API interactions, and second, during the heating process, the solvent evaporates, facilitating the sweep of API particles inside the pores. Dissolving the linezolid sample in ethanol before introducing it into the SBA-15 pores effectively eliminates concerns related to the LIN phase transition, which can occur in less controlled deposition methods. This dissolution approach has a distinct advantage over the incipient wetness method, as it ensures that the entirety of the dissolved LIN is evenly introduced into the mesopores, enhancing the loading efficiency and uniformity of LIN distribution.

In these new methods, based on the linezolid solubility in ethanol studied before [285], the total amount of LIN dissolved in ethanol was calibrated to achieve a precise mass ratio of MSNs to LIN, maximizing the pore-loading capacity without oversaturation. This step-by-step approach in the new methods makes it possible to introduce linezolid in the amount used in other methods without hesitation over poor solubility or oversaturation when using the minimum amount of solvent. The innovative dissolution approach combines the rapid initiation efficiency of DiSupLo with the sustained functionality of TSF, enabling an efficient and prolonged introduction of linezolid within the SBA-15 structure.

The PXRD results, as shown in Figure 4.10, indicate that indeed the TW1 method surpasses the other previously used methods. The purple line, notably, lacks any crystallinity signal.

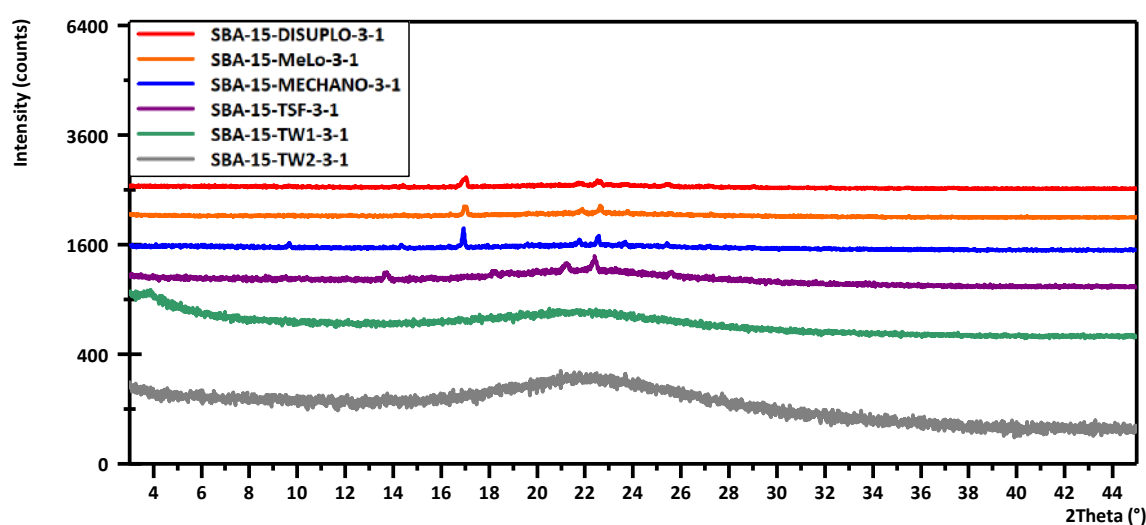


Figure 4.10. PXRD SBA-15:LIN (3:1) wight ratio,by DiSupLo,MeLo, MECHANO, TSF, TW1, TW2.

For an in-depth investigation of two recently developed methods and to explore the impact of spontaneous loading, previously examined in our laboratory in the binary model systems of cocrystals of benzoic acid and fluorinated benzoic acids [T4], a blend of linezolid and SBA-15 was meticulously prepared and sealed in a container for four days. Figure 4.11 presents the PXRD patterns of samples prepared using TW1 and TW2, along with a physical mixture containing 20 percent linezolid to SBA-15 after storage. This lower API to MSN ratio was selected to make it easier to track the possibility of spontaneous loading to compare the higher ratio that we selected before for studying the loading efficiency.

In both of the newly devised methods, TW1 and TW2, the entirety of the linezolid was successfully confined within the SBA-15, as opposed to the physical mixture where at least some of the linezolid crystals are outside also the comparison between the pattern for a physical mixture registered immediately after preparation shows that most probably for LIN there is no spontaneous loading.

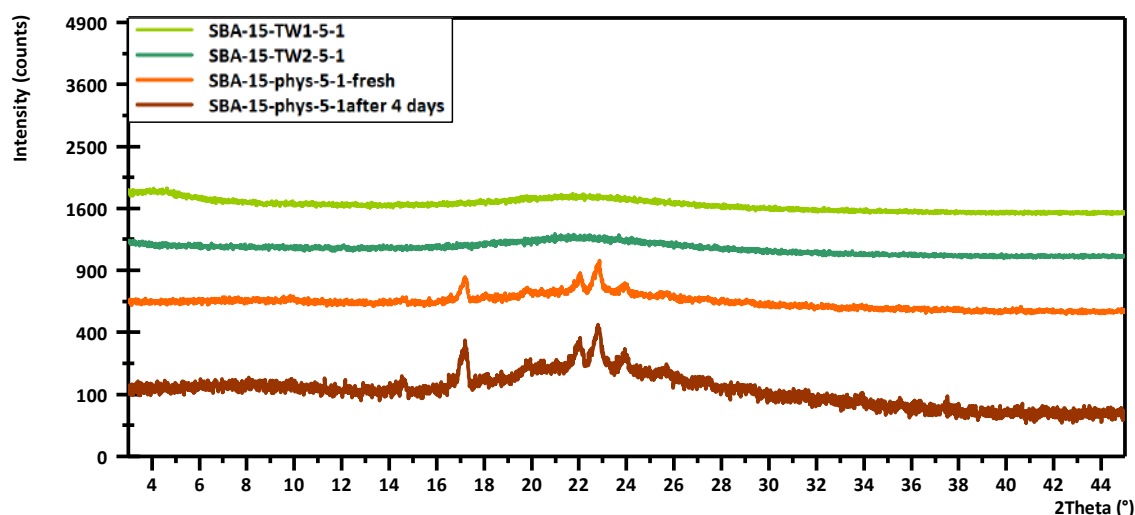


Figure 4.11. PXRD for SBA15:LIN(20%) prepared by TW1 and TW2 and for the stored physical mixture.

To summarize this part, the PXRD studies hint that for confinement of LIN SBA-15 with a bigger pore size is a better option. Applying different ratio of API to mesoporous silica shows ratio-dependent amount of API is left after the loading, making the study more precise with PXRD as a nonquantitative approach. All the solvent-free and microsolvent methods show some crystallinity in the PXRD, which comes from the leftover API outside of the mesoporous nanoparticle or the part of the API that interacts with the outer surface. This justifies further evaluation of confinement with other methods. Two new methods, TW1 and TW2, show there is no crystallinity left after the process, indicating a full confinement. It is worth to stress that

LIN experienced a phase transition during the TSF method application, which justifies the necessity of using cocrystal for the TFS method of loading in the case of API with thermal phase transition. Finally, the PXRD study of a physical mixture with a lower weight ratio eliminates the possibility of spontaneous LIN confinement.

4.5.4.2. Thermal characterization of the confinement results for linezolid

The samples of LIN confined in SBA-15, maintaining a 20 percent weight ratio of commercial linezolid to SBA-15, confined using three selected approaches, namely, MECHANO, TW1, and TW2 methods, were studied by thermal analysis. Additionally, a physical mixture with an equivalent ratio was prepared to facilitate a comparative thermal treatment analysis.

For this study, the three confinement methods were excluded, as the samples were analyzed in their as-prepared state without further processing. Residual solvents in the MeLo and DiSupLo samples complicated the thermal analysis. In addition, as previously mentioned, PXRD confirmed the phase transition of crystalline linezolid during TSF, indicating that TSF is not a suitable confinement method for linezolid as an API due to thermal phase transformation upon heating. In addition, the phase transformation effect would be difficult to separate from the confinement effect in the interpretation of the obtained results. Therefore, the remaining three confinement methods were analyzed with this approach.

The absence of the recrystallization or melting peak of the API in the DSC plots indicates a successful loading process, with the substance maintained in an amorphous form within the mesoporous silica structure. Conversely, the drug residing on the external surfaces of the pores behaves akin to a bulk material without displaying a glass transition, but with a clear melting point peak present.

TGA serves as a valuable tool for observing weight loss attributed to drug degradation and/or the desorption of volatile components with increasing sample temperature. This weight loss corresponds to the total drug content, and the determination of solvent remnants in the pores post-loading is also feasible. It is crucial, however, to exercise caution in interpreting TGA results, especially in cases involving thermounstable compounds or when robust connections are formed between the drug and mesoporous silica, as these interactions can lead to incomplete volatilization or degradation of the drug during heating. Such strong interactions may prevent the drug from desorbing fully at the temperatures typically used in TGA, potentially leading to an underestimation of the drug content or misinterpretation of the thermal profile.

The DSC plot, which compares commercial linezolid and a confined API utilizing various methods (Figure 4.12), unveils insightful observations. The absence of visible peaks in

comparison to pure linezolid at 150°C and 180°C related to LIN form II -> LIN form III phase transition and LIN form III melting point, respectively, across all methods besides physical mixture underscores the successful confinement within the mesoporous pores. In a comparative analysis with the physical mixture, a very small endotherm around 150°C reveals that MECHANO introduces a portion of linezolid outside the pores or probably in interaction with the outer surface of SBA-15, as recognized in further study done with Raman spectroscopy and explained in details in the next section. Notably, the application of the thermal method (TW2) prompts API in the outer surface to undergo a phase transition to linezolid form III, as visible from a very small peak at 180°C, instead of at 150°C (red lines), whereas sample after MECHANO (blue lines) does not show any melting event at 180 °C for the residual LIN or LIN interacting with the outer silica surface.

The green line in the DSC plot, corresponding to the physical mixture, sheds light on the impact of the heating ramp on the confinement of bulk linezolid outside the pores. The absence of a signal at ca. 180°C (the melting point of linezolid form III), together with a presence of a phase transition event at 150°C, suggest that at higher temperatures bulk linezolid, pre-melting, seamlessly integrates into the mesoporous pores. For further exploration, consideration of variable heating temperatures in Thermal Solvent Free loading is recommended, particularly for APIs undergoing phase transitions due to thermal treatments.

Despite selecting a 20 percent API-to-nanoparticle ratio for thermal studies to ensure a complete confinement, the MECHANO sample exhibited a small endothermic peak at 150°C, indicating the presence of crystalline linezolid interacting with the outer surface or outside of the pores. This crystalline phase linezolid led to the exclusion of the sample from TGA analysis, which is intended to study the stability of linezolid confined within the mesoporous particles.

An added advantage of drug delivery design involving the introduction of API inside mesoporous silica is evident in the heightened thermal stability of the confined API. This holds particular significance for APIs sensitive to temperature or undergoing phase transitions with increasing temperature. Thermogravimetric analysis can show a higher degradation temperature for the API when encapsulated within the silica particle, indicating a protective effect. The confinement within the mesopores creates a stable microenvironment that limits API mobility, restricting its exposure to heat and thus preserving its stability. These results collectively support the enhanced thermal stability of APIs when delivered through mesoporous silica carriers, making them more suitable for applications involving heat-sensitive compounds [138].

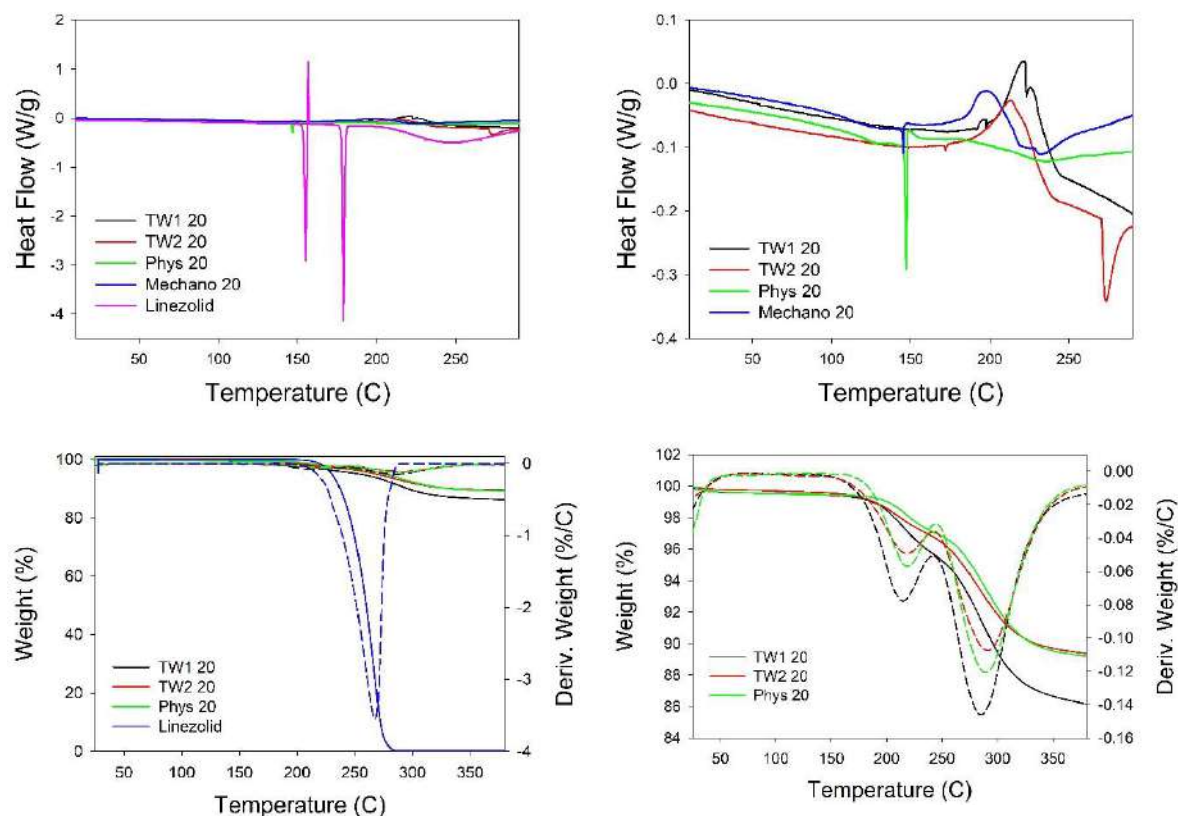


Figure 4.12. DSC (up) and TGA (down) plots for the physical mixture of LIN and SBA-15, as well as confined LIN into SBA-15 with MECHANO, TW1 and TW2 method of loading.

The TGA results for LIN presented in Figure 4.12 (right panel) illustrate the weight loss behavior of the samples confined using the TW1 and TW2 methods (at 20% loading), compared to the physical mixture. The degradation of pure linezolid begins around 200 °C and reaches a complete decomposition by approximately 270 °C. The physical mixture, which did not undergo any confinement treatment and was only subjected to the heating ramp during the TGA measurement, exhibits less than 0.5% weight loss below 100 °C—attributed to moisture release—followed by a 2.5% weight loss between 190 °C and 245 °C, and an additional 8% around 290°C, with a sharp degradation peak.

The sample confined using TW2 method shows a similar degradation pattern but with a few notable differences. It exhibits a slight weight loss of 0.3% before the ethanol evaporation point and demonstrates a second-stage degradation peak approximately 5°C higher than that of the physical mixture, indicating enhanced thermal stability. Overall, the total weight loss in this sample reached 15%. The TW1-confined sample, which experienced only moderate heating up to the ethanol evaporation point during the loading process, exhibited a 0.4% weight loss around the ethanol evaporation temperature. It showed a first-stage weight loss of 3.85%, with

a degradation peak at 213 °C—about 5 °C lower than in the TW2 sample—and a second-stage loss of 9.7%.

The two distinct mass loss events observed in confined samples represent two degradation regimes of the API within the mesoporous structure. As reported in previous studies [T4], the first degradation event (after solvent evaporation) corresponds to linezolid molecules located in the central part of the mesopores, with minimal interaction with the pore walls. In contrast, the second degradation event represents the confined API interacting with the internal surfaces of the mesoporous material, leading to improved thermal stability.

Comparison of the physical mixture and TW2 indicates that confinement at elevated temperature (as in TW2) results in a 5°C increase in the degradation temperature of the second regime, suggesting improved thermal resistance. Moreover, applying a controlled heating ramp rather than direct exposure to high temperature appears to further enhance the overall thermal stability, as evidenced by the lower total weight loss (physical mixture). Specifically, the second-stage weight loss follows the trend: physical mixture (7.9%) < TW1 (9.7%) < TW2 (10.7%), suggesting that the degree of interaction between linezolid and the inner pore surfaces is greater in samples where drug molecules enter the pores more gradually—either through thermal ramping or vapor-phase diffusion.

The total residual mass at 400°C was 89% for the physical mixture, 85.9% for TW1, and 85.1% for TW2, confirming that thermal treatment during the confinement process enhances the most the thermal stability of the drug. Interestingly, since the physical mixture also shows confinement-like effects during TGA, it indicates that solid-state NMR studies may be better suited to reliably probe drug–mesoporous silica interactions, without the influence of thermal conditions during the measurements.

Based on the thermal studies conducted on confined linezolid, the complexity of the results, and the likelihood of API confinement during thermal analysis (DSC and TGA measurements), it was decided to further investigate the studied systems using Raman spectroscopy. The confinement of the binary system added complexity to the TGA analysis, and predicting their interactions within the matrix necessitated a more powerful analytical tool. Raman spectroscopy with a heating ramp was therefore chosen as the preferred method at this stage.

4.5.4.3. Raman spectroscopy characterization of the linezolid confined by MECHANO

In this part of the study, the linezolid sample confined using the MECHANO method was analyzed to investigate whether the small amount of crystalline content observed was a residual

unconfined drug or the result of interactions with the outer surface of mesoporous silica nanoparticles. A drug-to-carrier weight ratio of 35% (linezolid:SBA-15) was selected to optimize the presence of crystalline domains potentially interacting with the outer surface of the MSNs. For comparison, pure linezolid was used as a reference.

Both the confined sample and pure linezolid were investigated using low-frequency Raman spectroscopy under a controlled heating ramp of 1 °C/min. As detailed in the Methods section, LFRS enables monitoring of phase transitions during heating. If linezolid resides outside the pores, it may exhibit phase transitions similar to the pure drug, transitioning between crystalline polymorphs (*i.e.*, from Form II to Form III). In contrast, interaction with the internal or external MSN surfaces often disrupts crystallinity, leading to an amorphous state. Unconfined particles typically exhibit a glass transition, and crystalline phases can be identified by phonon peaks below 25 cm⁻¹.

Figure 4.13a shows the LFRS of pure linezolid undergoing a typical phase transition from Form II to Form III during heating. Figures 4.13b and 4.13c present the LFRS of the MECHANO-prepared linezolid–MSN sample during the first and second heating ramps, respectively. Phonon peaks below 25 cm⁻¹ observed during the first heating indicate the presence of nanocrystals within the mesopores. The corresponding temperature-dependent quasielastic intensities (I_{QES}) derived from the Raman spectra are shown in Figure 4.14.

The first heating cycle was conducted from room temperature to 160 °C to induce the melting of these nanocrystals. The system was then cooled to –40 °C, followed by a second heating cycle up to 120 °C to examine whether a glass transition occurred, indicating the transformation of melted nanocrystals into an amorphous phase. As seen in Figure 4.13c, the absence of a glass transition confirmed that the linezolid nanocrystals were effectively confined within the pores. Moreover, the lack of phonon peaks in the second heating spectra suggests no recrystallization, further supporting that the nanocrystals were located inside the pores. If the crystals were out of the MSNs, recrystallization would be expected during cooling or the second heating ramp.

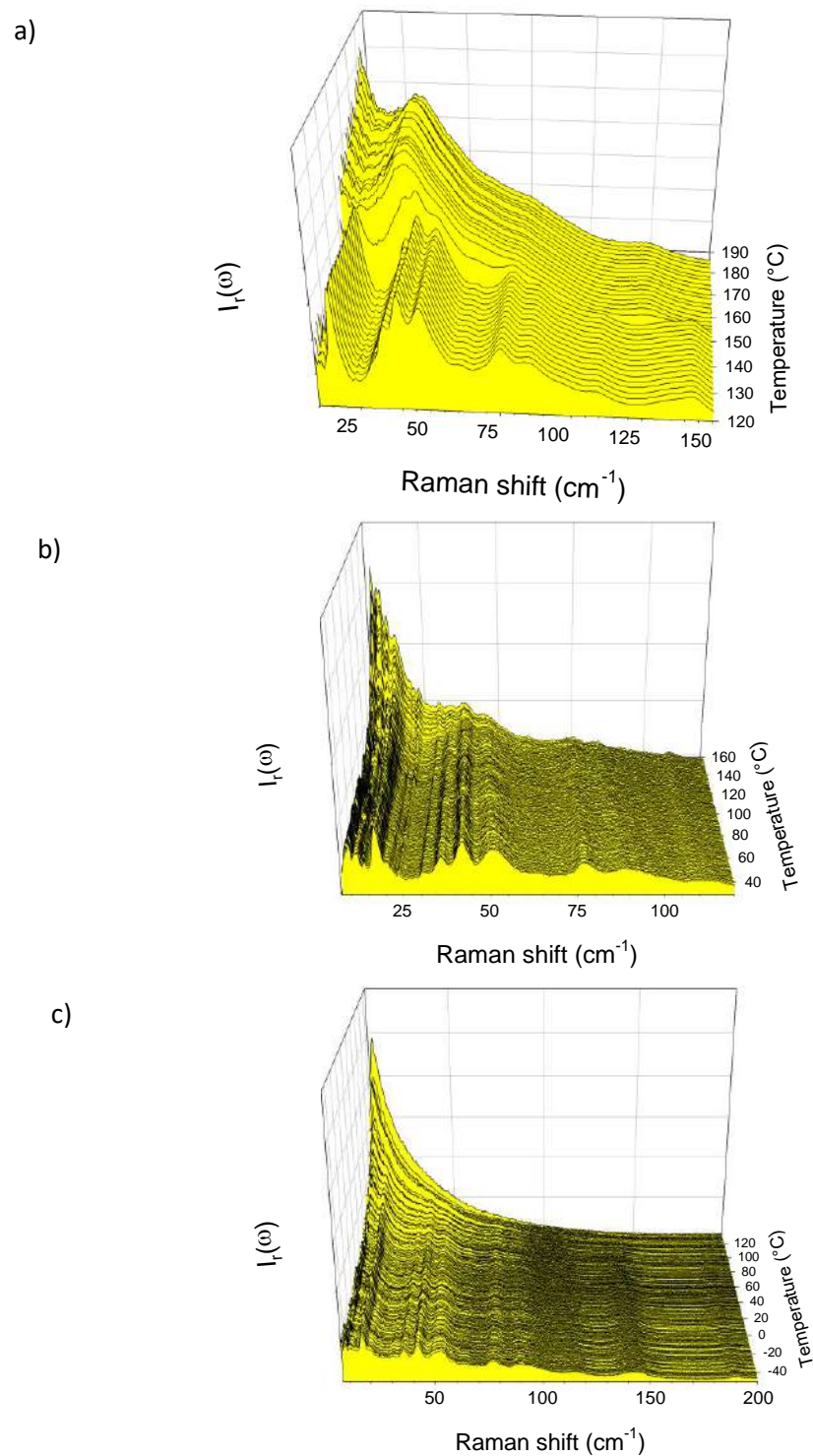


Figure 4.13. Low-frequency Raman spectra of the (a) linezolid; b) first heating LIN35%:SBA-15 confined by MECHANO at 10 Hz collected upon heating at 1 °C/min heating from room temperature up to 160 °C ; (c) second heating of the confined linezolid from –40 °C to 120 °C.

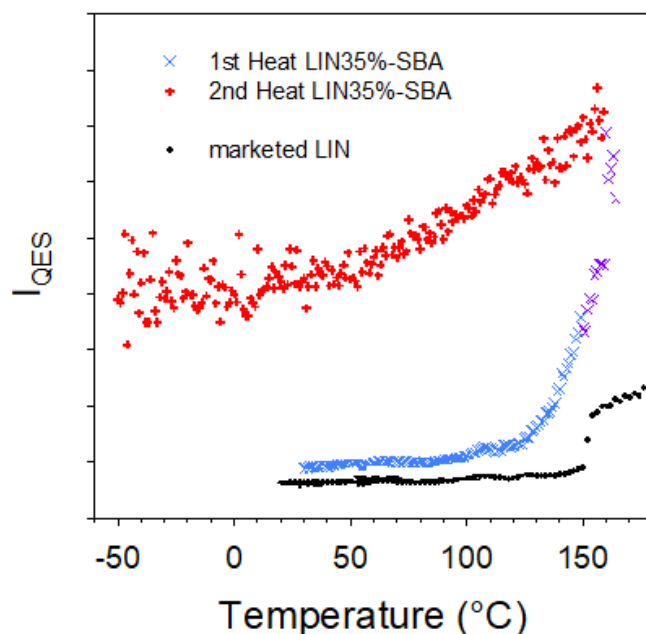


Figure 4.14. Temperature dependence of the quasielastic intensity (I_{QES}) of the composite prepared by MECHANO at 10 Hz; I_{QES} (LIN35%:SBA-15) calculated in the first (blue) and second (red) heating runs in compression with I_{QES} of bulk LIN heating runs (black)

This thermal cycling approach—heating, cooling, and reheating—has previously been used to assess pore loading and nanocrystal behavior in MECHANO-processed systems [286,287]. The broad melting range observed during the first heating implies a wide size distribution of nanocrystals and reduced stability of the smallest ones.

As shown in Figure 4.14, the I_{QES} during the first heating of the MECHANO sample showed slightly higher intensity at low temperatures compared to bulk crystalline linezolid (between 120–150 °C), indicating the coexistence of nanocrystalline and amorphous forms in the confined sample. During the second heating, the $I_{QES}(T)$ curve exhibited a change in slope slightly above the glass transition temperature (T_g) of bulk amorphous linezolid. This smoother transition, relative to bulk glassy linezolid, indicates that confinement *via* the MECHANO method leads to partial or complete amorphization of the drug.

4.5.4.4. Linezolid cocrystal 2,3DHBA-LIN confinement by TSF method

Based on the results from linezolid confinement, the SBA-15 was selected for cocrystal confinement, and 2,3DHBA-LIN cocrystal was chosen to study the possibility of linezolid cocrystal confinement by application of the TSF method to benefit from the lower melting point

of cocrystal compared to the pure linezolid and avoiding phase transformation caused during the heating in this method. As before the first evaluation of the ternary system was done by PXRD as shown in Figure 4.15. The comparison between pure linezolid, its cocrystal, and the confined cocrystal into the SBA-15 shows almost no crystallinity as seen by the very low intensity reflexes originating from both linezolid and the coformer. This suggests that at least some portion of the cocrystal was introduced into the MSN particle. Also, the DSC results (Figure 4.16), obtained in the next step, confirm the loading was succesful, as seen by the absence of either a phase transition or a melting event of the cocrystal.

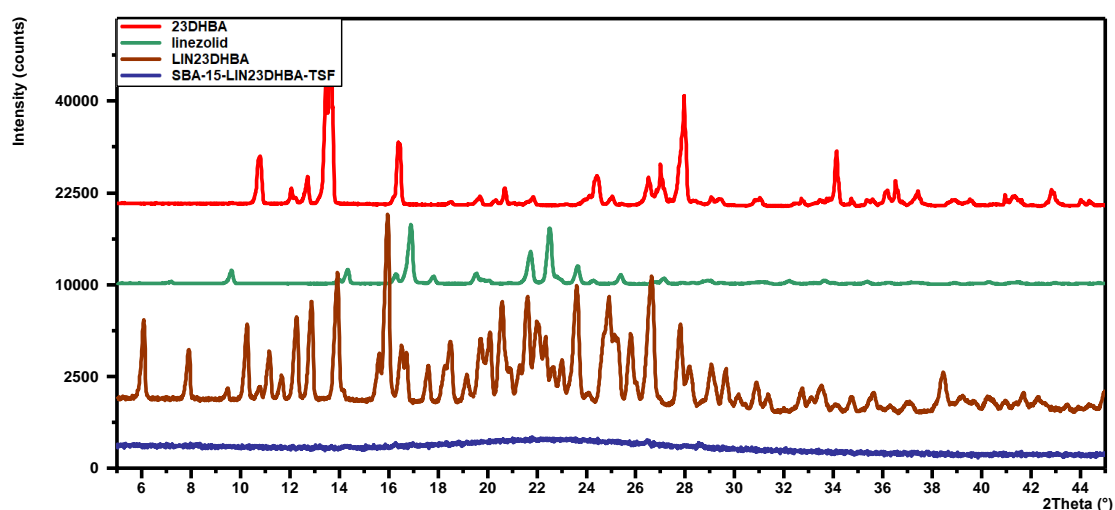


Figure 4.15. PXRD (LIN-23DHBA30%:SBA-15) prepared by TSF and LIN23DHBA cocrystal, linezolid and 23DHBA.

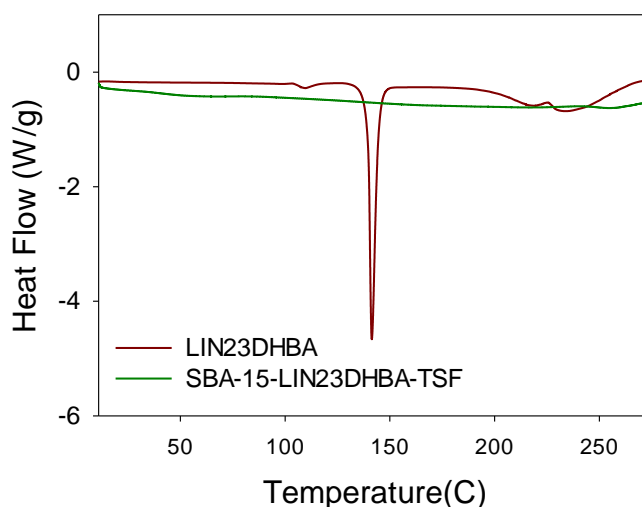


Figure 4.16. DSC (LIN-23DHBA30%:SBA-15) prepared by TSF and LIN23DHBA cocrystal.

Finally, the LFR spectra captured at room temperature for a cocrystal system confined through the TSF method and featuring the LIN:23DHBA cocrystal are illustrated in Figure 4.17a. The observed increase in intensity below 50 cm^{-1} signifies the amorphization effect resulting from cocrystal confinement. The presence of phonon peaks, shown in Figure 4.17a, serves as a signature of nanocrystals within the pore. Figure 4.17b depicts the temperature-dependent quasielastic intensity calculated from the specified spectral region under 25 cm^{-1} .

The wide temperature range of melting, spanning from 80 to 150°C , indicates a diverse distribution of nanocrystal sizes and the low stability of the smallest nanocrystals, a consequence of confinement. This phenomenon is further emphasized by the initiation of cocrystal melting beyond 150°C . This result unambiguously confirms the successful cocrystal confinement into MSNs.

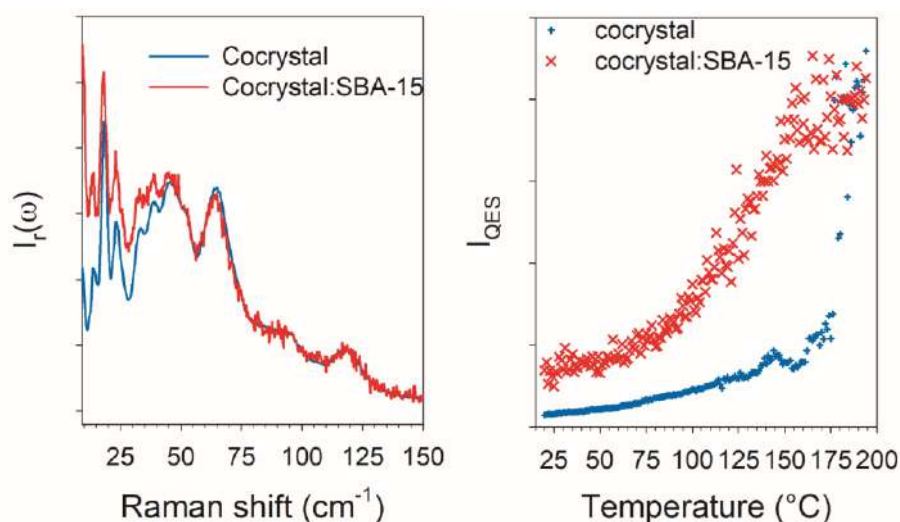


Figure 4.17. Right; Low-frequency Raman spectra of the (LIN-23DHBA30%:SBA-15) prepared by TSF and LIN23DHBA cocrystal; left; Temperature dependence of the quasielastic intensity (I_{QES}) of the binary system prepared by TSF; I_{QES} (LIN-23DHBA-30%:SBA-15) calculated in (red) and LIN-23DHBA (blue) heating runs.

4.6. Conclusions

In this study, linezolid and one of its new cocrystals were, for the first time, successfully confined within mesoporous nanoparticles. The solubility limitations of pure linezolid necessitated the elimination of the wet method and the introduction of new wet-thermal methods, while phase changes during heating introduced uncertainties when using the thermal solvent-free (TSF) method, and cocrystallization solved this problem. The findings demonstrate

that MECHANO is a reliable and effective approach for confining pure linezolid, as confirmed by Raman spectroscopy, which indicated that linezolid penetrated the mesoporous pores. However, questions remain regarding the interactions of linezolid with itself and with the mesoporous matrix inside the nanoparticles. Solid-state NMR is expected to be a valuable tool for further investigation.

For the cocrystal confinement, the study shows that the TSF method can be a dependable approach after addressing the phase transition issues of the active pharmaceutical ingredient through cocrystallization. Avoiding phase transitions upon heating was a critical step forward that enabled a proper interpretation of the DSC results. The registered Raman experiments unambiguously proved a successful confinement of LIN:2,3-DHBA cocrystal inside the SBA-15 mesopores. Nevertheless, to extend this research to other binaries of LIN, the influence of the third component in hydrate cocrystals and the interactions of individual binary particles within the mesoporous pores require further exploration by the use of a variety of linezolid cocrystals.

The primary aim of this research was to investigate the feasibility of loading linezolid into mesoporous nanoparticles by appropriate methods and solving the thermal stability issue through cocrystallization. Future studies should focus on detailed evaluations of solubility and release profiles of the confined systems to better understand and optimize them.

5. Final conclusions

This research advances the mechanochemical synthesis of linezolid cocrystals by systematically investigating coformer selection and their structural interactions with LIN to enhance solubility and its physicochemical properties through cocrystallization. Additionally, for the first time, this study explores the potential of using a drug delivery system by confining linezolid and carefully selected one of its cocrystals within mesoporous silica nanoparticles.

Through experimental screening, **nine novel LIN-based cocrystals** were successfully identified, highlighting the influence of coformer structure, solvent selection, and reaction conditions on cocrystal formation. All of the coformers with which the cocrystals were obtained belong to a group of aromatic carboxylic acids and include 2,6-DHBA, 2,5-DHBA, 2,4-DHBA, 2,3-DHBA, 3,4-DHBA, 3,5-DHBA, BA, PABA, GA. The study demonstrated that **mechanochemistry is a highly effective** and environmentally friendly **approach** for synthesizing cocrystals, in particular, when API has a different solubility than a coformer, and also minimizing solvent use and waste production.

For the obtained cocrystals the performed analysis showed a diversity of coformer influence on the observed physicochemical property. **Thermal analysis** indicated that eight of the eleven cocrystals exhibit melting points below the phase transition of LIN form II to form III, making them suitable candidates for solvent-free drug formulation approaches such as the thermal solvent-free method. Moreover, **solubility assessments** highlighted the impact of cocrystallization on water solubility of LIN, with five cocrystals demonstrating improved solubility, particularly LIN:3,4-DHBA:H₂O, which showed a notable 43% increase. Despite some cocrystals exhibiting reduced solubility, the findings emphasize the role of crystal phase modification in tuning drug properties.

A key contribution of the first part of the work is also the **integration of virtual cocrystal screening tools**—molecular complementarity (MC), hydrogen bond propensity (HBP), and molecular electrostatic potential (MEP) maps—which provided **valuable insights into the predictive modeling of cocrystal formation**. The results underscore the **importance of considering intermolecular energy contributions**, particularly lattice energy, in assessing the feasibility of new cocrystals. The findings also reveal that while energy-based methods like MEP maps show strong predictive power, structural and supramolecular factors captured by MC and HBP play a crucial role in the initial selection process.

For all cocrystals, many attempts were undertaken to establish their crystal structures. **The determination of the crystal structures** of linezolid cocrystals **through single-crystal X-ray diffraction** has provided essential insights into the intermolecular interactions governing their

stability and physicochemical properties. The successful growth of single crystals of five distinct cocrystals—formed with benzoic acid, p-hydroxybenzoic acid, protocatechuic acid, γ-resorcylic acid, and gallic acid—demonstrates the **structural diversity** achievable with LIN and highlights the complexity of cocrystallization due to solubility differences between LIN and its coformers. The study revealed **a range of hydrogen-bonding motifs**, with distinct supramolecular synthons governing the stability of each cocrystal. Additionally, the identification of **aromatic–aromatic interactions** as key stabilizing factors, along with quantum-chemical calculations confirming negative stabilization energies, underscores the thermodynamic favorability of cocrystal formation. Notably, LIN molecule in LIN:2,6-DHBA cocrystal presented an energetically unfavorable conformation, suggesting that strong intermolecular interactions play a crucial role in compensating for intramolecular strain.

Despite significant effort, it was not possible to grow single crystals for some of the new crystalline phases. Hence, **approaches alternative to SCXRD** were sought for. This research demonstrates the value of employing these alternative methodologies, particularly the CSP-NMR approach, in determining the crystal structures of LIN cocrystals when traditional single-crystal X-ray diffraction is not feasible. By **integrating** high-resolution solid-state **NMR**, **PXRD**, and **CSP** techniques, the crystal structures of two additional cocrystals—LIN:2,3-DHBA and LIN:2,4-DHBA— were successfully described, **overcoming challenges posed by molecular flexibility and ambiguous NMR signal assignments**. For LIN:2,3-DHBA cocrystal, structural similarity with the previously determined structure of LIN:2,6-DHBA enabled an efficient CSP-based approach, which yielded a reliable structural model with strong agreement between computational and experimental data. In contrast, LIN:2,4-DHBA cocrystal presented a greater challenge due to the conformational flexibility of both LIN and the coformer and no structural analogues known. To address this, an innovative strategy incorporating conformational filtering and CSP calculations was introduced, significantly narrowing down the search space and identifying two most probable molecular arrangements. Although a fully definitive crystal structure was not established, the approach represents a significant advancement in applying CSP-NMR to complex multicomponent systems.

An additional conclusion from the conducted CSP-NMR studies is the established necessity of **thorough geometry optimizations** in CSP-based rigid searches to ensure meaningful comparisons with experimental NMR data. The findings contribute valuable insights into the structural landscape of LIN cocrystals, reinforcing the importance of hybrid methodologies in the rational design of pharmaceutical solids.

After having successfully synthesized nine new cocrystals and structurally characterized most of them, the final step of the work should entail an approach to embed the cocrystals into the mesoporous silica nanoparticles. However, since not much was understood about the mechanism of cocrystal confinement into the silica mesopores and the rational selection of the loading method, I took part in a project involving the study of a binary model systems, which provides a **foundational understanding of the confinement behavior of well-defined cocrystals** within MCM-41 mesoporous silica and offers valuable insights into drug delivery applications. By investigating different loading techniques—Diffusion Supported Loading, mechanical ball-mill loading, and thermal solvent-free loading—it was demonstrated that both the method of loading and the composition of the binary system significantly influence guest molecule behavior, including their interactions, spatial distribution, and release kinetics.

The findings highlight that mesoporous silica particles contain at least **two distinct confinement regions**—interstitial space and internal pore space—where guest molecules can reside. Importantly, for binary systems with a strong tendency to form intermolecular interactions, the structural integrity of these interactions can be maintained within MCM-41 voids. This was exemplified by solid-state NMR analysis of the MeLo-loaded BA:PFBA system, where the interactions mirrored those found in crystalline phases. Furthermore, the study revealed that both **the choice of coformer and the loading technique** act as crucial parameters in modulating release profiles. The extended release observed in the MeLo-loaded BA:PFBA system compared to DiSupLo and TSF underscores the potential of mechanical loading as a tool for a controlled drug release. The results open new possibilities for tailoring drug release kinetics through precise control of material composition and processing techniques, paving the way for further advancements in pharmaceutical delivery systems.

The last part of my study successfully demonstrated the **confinement of pure linezolid and its new cocrystal within mesoporous nanoparticles**, marking a significant advancement in addressing the solubility and thermal stability challenges associated with linezolid. For **pure linezolid**, the introduction of **two new wet-thermal methods** proved essential in overcoming the limitations of traditional wet methods. **Raman spectroscopy** confirmed the **successful penetration** of linezolid into mesoporous pores, highlighting the effectiveness of MECHANO as a confinement technique. However, the nature of molecular interactions between linezolid and the mesoporous matrix remains unresolved, necessitating further exploration using solid-state NMR techniques.

For cocrystal confinement, this research demonstrated that the **TSF method is a viable option once phase transition issues are resolved through cocrystallization**. The avoidance of

phase changes during heating represents a crucial breakthrough, leading to a **successful loading of the cocrystal** into the MSNs. Future studies should focus on assessing the solubility and release profiles of these confined systems, ultimately contributing to the optimization of mesoporous-based drug delivery strategies for linezolid and its cocrystals.

6. Published side projects

During doctoral research, two side projects on the structural transformations of linezolid was conducted, which resulted in two publications exploring its polymorphic and polyamorphic behaviors. These studies provided critical insights into the molecular ordering processes and thermally induced transformations of linezolid in various solid-state forms.

The first study, titled **"Description of an original molecular ordering process into a disordered crystalline form: the atypical low-temperature transformation of the disordered form III of linezolid"** investigated the structural stability and transformation mechanisms of linezolid form III upon cooling. Using a combination of low- and high-frequency Raman spectroscopy, differential scanning calorimetry, and powder X-ray diffraction, it was observed that form III remained stable down to 0°C, but transformed at lower temperatures. Raman spectroscopy revealed a soft mode indicative of new intermolecular hydrogen-bond interactions, suggesting a continuous transformation with both displacive and order-disorder characteristics. PXRD analysis confirmed the absence of symmetry breaking but showed significant Bragg peak broadening, indicating a distribution of frozen molecular conformations [288].

The second publication, **"Low-frequency Raman signatures of a transient polyamorphic situation in Linezolid: A competition between conformational polymorphs"** identified two first-order transformations within disordered form III, revealing a transient amorphous state distinct from the glassy state. This intermediate phase resulted from the competition between a locally preferred ordered structure and the long-range disorder characteristic of form III. Additionally, it was discovered that the rapid heating of the stable crystalline form II to form III involved a transient liquid state, an uncommon feature in polymorphic transitions. These findings underscored the role of thermally activated conformational motions and high energy barriers in kinetic hindering of these transformations, which were detectable only through the rapid acquisition capability of low-frequency Raman spectroscopy [289].

Together, these investigations shed light on the complex solid-state behavior of linezolid, providing valuable knowledge on the interplay between molecular conformation, polymorphism, and polyamorphism in pharmaceutical compounds. It is worth mentioning that this project was conducted under the supervision of Professor Alain Hedoux in his research group at the University of Lille, France, and was financed by the SSHN scholarship from the French embassy in Poland.

7. Ongoing side project

As a side project of this thesis, during the initial phase of the study and the preparation of the experimental section on coformer selection for linezolid cocrystal formation, various coformers were tested under different grinding conditions. Additionally, the impact of mechanochemical processes on the pure coformer was evaluated.

During this investigation, grinding one specific coformer, 3,5-DHBA (3,5-dihydroxybenzoic acid), led to the discovery of a previously unknown hydrate form. Further analysis revealed that the method of preparation significantly influenced the dehydration process and the stability of this higher hydrate.

Two methodologies to crystallize this new hydrate, vapour diffusion exposure and MECHANO with varying amounts of liquid assistant in LAG, were employed. Notably, the quantity of solvent in LAG played a critical role in the outcome. Smaller amounts of water resulted in the formation of a known hemihydrate with extended stability, whereas increasing the water content led to the formation of a higher hydrate with shorter stability. In contrast, preparation using vapour diffusion exposure exclusively produced the higher hydrate.

Efforts to grow single crystals of the higher hydrate were successful only under low-temperature conditions in a refrigerated environment. A batch of the higher hydrate, initially prepared *via* mechanochemical methods, was fully dissolved and subsequently seeded with a small amount of the higher hydrate before being stored in the fridge. Interestingly, each time a single crystal was selected from this batch and analyzed using single-crystal X-ray diffraction, it revealed a new crystal form distinct from previously analyzed single crystals. The timeframe for monocrystal selection ranged from two days to two weeks.

Determining the structure of this newly identified hydrate(s) has proven challenging and remains an ongoing process. Furthermore, the influence of the preparation method on the stability of the higher hydrate was systematically examined using powder X-ray diffraction under varying temperature and humidity conditions.

8. Further outlooks

The ongoing research into the pharmacological and pharmaceutical applications of linezolid and its cocrystals presents several promising avenues for future exploration. The primary outlooks of these studies focus on understanding the release and absorption dynamics of confined linezolid, diversifying its bio-applications, and conducting a comprehensive study of its solubility behavior. Each of these areas is critical to advancing the utility of linezolid in drug delivery systems, and they are outlined below.

8.1. Release and Absorption Dynamics of Confined Linezolid and Its Cocrystals

A key focus of ongoing research is the in-depth analysis of the release kinetics and absorption patterns of linezolid and its cocrystals within various drug delivery systems. This research aims to elucidate how the confinement of linezolid within different carriers influences its pharmacokinetics, particularly concerning controlled release mechanisms and absorption characteristics. By exploring these dynamics, researchers can better understand how to optimize the delivery and efficacy of linezolid, potentially leading to more effective and targeted therapeutic outcomes.

8.2. Diversification of Bio-Applications for Linezolid Cocrystals

Another significant area of interest is the exploration of new therapeutic applications for linezolid cocrystals beyond their well-established antibiotic uses. This research seeks to identify potential synergistic effects or novel therapeutic roles that could arise when linezolid is formulated as a cocrystal. For example, some of the conducted preliminary research showed, that a cocrystal with 2,4-DHBA statistically significantly enhanced the c-Fos expression and that the observed effect was stronger than the effect originating from a simple sum of components action. By broadening the scope of linezolid pharmaceutical utility, such research could pave the way for new treatments and broaden the range of conditions that linezolid can effectively address.

8.3. Comprehensive Study of Solubility Behavior

To support the optimization of linezolid cocrystals in drug delivery systems, a systematic investigation into the solubility behavior of these compounds is underway. This research examines the influence of various factors, including pH, surfactants, ion concentration, co-formers, and molecular arrangements, on the solubility of linezolid cocrystals. By analyzing

release ratios under diverse conditions, researchers aim to provide a comprehensive understanding of how these factors impact the effectiveness of drug delivery systems, ultimately enhancing the performance and reliability of linezolid-based therapies.

9. List of figures

Figure 1.1. Linezolid (LIN) structure.

Figure 2.1. Types of mesoporous silica nanoparticles. Reprinted with permission from ref. [139]

Figure 2.2. Drug confinement methods. Reprinted with permission from ref. [140].

Figure 2.3. Bragg's Law, n is the order of diffraction, λ is the X-ray wavelength, d is the distance between atomic planes, and θ is the diffraction angle.

Figure 2.4. Zeeman interaction for spin $\frac{1}{2}$ nucleus. B_0 is the external static magnetic field, E is the energy of the spin states, γ is the gyromagnetic ratio of the nucleus, \hbar is the reduced Planck constant ($\hbar = h/2\pi$), ω_0 is the Larmor angular frequency, related by $\omega_0 = -\gamma B_0$.

Figure 2.5. (a) ^1H - ^{14}N D-HMQC, (b), (c) ^1H - ^{13}C invHETCOR NMR with short (100 μs) (b) and long (3 ms) (c) second contact time, and (d) ^1H - ^1H SQ-DQ with Back-to-Back recoupling NMR spectra for LIN:2,4-DHBA cocrystal recorded with a spinning speed of 62.5 kHz; red rectangle marks one of the key H-C correlation; the C-H pairs are assigned in the HETCOR spectrum with short contact time [T3].

Figure 2.6. ^{14}N - ^1H HMQC spectra recorded at $\nu_0 = 850$ MHz and a MAS frequency of 60 kHz for a) nicotinamide and b) a nicotinamide-palmitic acid cocrystal; c) and d) ^{14}N columns taken through the highlighted area of the spectrum overlaid with lineshapes simulated using the SpinEvolution software. Reprinted with permission from ref. [215].

Figure 2.7. a) 125 MHz ^{13}C spectrum of TBS Form b) The asterisks (*) indicate spinning sidebands. Reprinted with permission from ref. [233].

Figure 4.1. Chemical structure of selected coformers.

Figure 4.2. The most pervasive supramolecular synthon between LIN and aromatic acid coformers found in the analysed cocrystals.

Figure 4.3. (a) and (b) ^1H - ^{13}C invHETCOR NMR spectrum recorded with a contact time of 3 ms (a) and 100 μs (b), and (d) ^1H - ^1H DQ-SQ MAS with ^1H - ^1H Back-to-Back (BaBa) recoupling spectrum for LIN:2,3-DHBA cocrystal; (c) and (e) a comparison of the ^{13}C CPMAS NMR spectra recorded for LIN:2,3-DHBA and LIN:2,6- DHBA cocrystals. The 2D spectra were recorded with a sample spinning speed of 62.5 kHz; color rectangles mark some of the main correlation signals. In 1D spectra the dotted light blue lines correspond to the resonances originating from LIN and indicate the similarity of chemical environment of LIN molecules in both crystals.

Figure 4.4. a) ^{19}F - ^{19}F NOESY MAS and b) ^1H - ^{19}F HOESY MAS spectra of BA : PFBA cocrystal embedded in MCM-41 (1 : 2 by weight) using the MeLo method (without LA) recorded at 12.5 kHz MAS with a mixing time of 20 ms and 350 ms, respectively.

Figure 4.5. The two selected mesoporous silica nanoparticles [277].

Figure 4.6. DSC curves for linezolid II and III and their cocrystals.

Figure 4.7. PXRD of samples of LIN introduced to MCM-41 in the ratio of 1:1,1:2 and 1:3 using a DiSupLo method. and the expansion of the 16-18° 2 θ range

Figure 4.8. A comparison of PXDR diffractograms for linezolid confined into SBA-15 and MCM-41 by DiSupLo method in 1:3 ratio.

Figure 4.9. The PXRD diffractograms of linezolid introduced to SBA-15 (1:3) with DiSupLo, MeLo, MECHANO and TSF.

Figure 4.10. PXRD SBA-15:LIN (3:1) wight ratio,by DiSupLo,MeLo, MECHANO, TSF, TW1, TW2.

Figure 4.11. PXRD for SBA15:LIN(20%) prepared by TW1 and TW2 and for the stored physical mixture.

Figure 4.12. DSC (up) and TGA (down) plots for the physical mixture of LIN and SBA-15, as well as confined LIN into SBA-15 with MECHANO, TW1 and TW2 method of loading.

Figure 4.13. Low-frequency Raman spectra of the (a) linezolid; b) first heating LIN35%:SBA-15 confined by MECHANO at 10 Hz collected upon heating at 1 °C/min heating from room temperature up to 160 °C ; (c) second heating of the confined linezolid from -40 °C to 120 °C.

Figure 4.14. Temperature dependence of the quasielastic intensity (IQES) of the composite prepared by MECHANO at 10 Hz; IQES (LIN35%:SBA-15) calculated in the first (blue) and second (red) heating runs in compression with IQES of bulk LIN heating runs (black)

Figure 4.15. PXRD (LIN-23DHBA30%:SBA-15) prepared by TSF and LIN23DHBA cocrystal, linezolid and 23DHBA.

Figure 4.16. DSC (LIN-23DHBA30%:SBA-15) prepared by TSF and LIN23DHBA cocrystal.

Figure 4.17. Right; Low-frequency Raman spectra of the (LIN-23DHBA30%:SBA-15) prepared by TSF and LIN23DHBA cocrystal; left; Temperature dependence of the quasielastic intensity (IQES) of the binary system prepared by TSF; IQES (LIN-23DHBA-30%:SBA-15) calculated in(red) and LIN-23DHBA(blue) heating runs.

10. List of publications connected with PhD thesis

T1. Virtual Cocystal Screening Methods as Tools to Understand the Formation of Pharmaceutical Cocystals - A Case Study of Linezolid, a Wide-Range Antibacterial Drug, Khalaji, M., Potrzebowski, M.J., Dudek, M.K., *Crystal Growth and Design*, 2021, 21(4), pp. 2301–2314

T2. Structural variety of heterosynthons in linezolid cocystals with modified thermal properties, Khalaji, M., Wróblewska, A., Wielgus, E., G.D. Bujacz, Dudek, M.K., Potrzebowski, M.J., *Acta Crystallographica Section B: Structural Science, Crystal Engineering and Materials*, 2020, 76, pp. 892–912

T3. Narrowing down the conformational space with solid-state NMR in crystal structure prediction of linezolid cocystals, Khalaji, M., Paluch, P., Potrzebowski, M.J., Dudek, M.K., *Solid State Nuclear Magnetic Resonance*, 2022, 121, 101813

T4. Unexpected Factors Affecting the Kinetics of Guest Molecule Release from Investigation of Binary Chemical Systems Trapped in a Single Void of Mesoporous Silica Particles, Trzeciak, K. Wielgus, E. Kaźmierski, S., Khalaji M., Dudek, M.K., Potrzebowski, M.J., *ChemPhysChem*, 2023, 24(7), e202200884

T5. Developing appropriate conditions for loading LIN and its cocystal with 2,3-dihydroxybenzoic acid into the pores of mesoporous silica materials. Mehrnaz Khalaji, Alain Heudoux, Marta K. Dudek. Unpublished work.

11. List of publications connected with the side projects

1. Description of an original molecular ordering process into a disordered crystalline form: the atypical low-temperature transformation of the disordered form III of linezolid, Khalaji Mehrnaz, Dudek Marta Katarzyna, Paccou Laurent, Danède Florence, Guinet Yannick, Hédoux Alain, *Phys. Chem. Chem. Phys.*, 26, 20709-20716, **2024**.
2. Low-frequency Raman signatures of a transient polyamorphic situation in Linezolid: A competition between conformational polymorphs, Mehrnaz Khalaji, Laurent Paccou, Yannick Guinet, Alain Hédoux, *J. Chem. Phys.* 162, 074501 **2025**.

3. Tunable Micromechanics and Morphology of Plasticized Polyhydroxyalkanoate: Roles of Structural Interactions and Crystallization in Solvents, Mehrnaz Khalaji, Ramin Hosseinneshad, Dhanumalayan Elumalai, Iurii Vozniak, and Fahmi Zaïri, *ACS Applied Polymer Materials*, 7 (9), 5333-5338, **2025**.

12. List of lectures and posters connected with the PhD thesis

1. Pharmaceutical and physicochemical properties enhancement of linezolid by mechanochemical cocrystallization and drug delivery design, XIII Sesja Magistrantów i Doktorantów Łódzkiego Środowiska Chemików 24 Jun, 2022, Lodz, Poland
2. The pharmaceutical and phytochemical properties enhancement of linezolid by mechanochemical cocrystallization and drug delivery design, IX Doctoral Symposium on Chemistry 19-20 May 2022, Lodz, Poland
3. Linezolid co-crystals structure elucidation by joint use of high-resolution solid state NMR and crystal structure prediction (CSP) calculations, Central European NMR Symposium & Bruker users meeting 21st to 23rd September, 2022 Warsaw, Poland
4. Application of solid-state NMR in Mechanochemistry of linezolid co-crystals 2ed International Conference YUPPAS NMR, Lodz, Poland, Jun 17-18, 2019 – poster.
5. Joint use of mechanochemistry and solid-state NMR in the synthesis and structural characterization of pharmaceutical cocrystals, International Conference 15th EURO - 21st ISMAR, Berlin, Germany- August 25-30, 2019-poster
6. NMR crystallography; the synergy of high-resolution solid-state NMR and crystal structure prediction (CSP) calculations, Doctoral Symposium On Chemistry 18th to 19th May 2023, Lodz, Poland, poster

13. Academic biography EDUCATION

- MS, Chemical Engineering 2011-2014 Sahand University of Technology, Iran

Thesis: "Upgrading the API unit of Shazand refinery, using lamella settler" Advisor: Prof.

Sirous Ebrahimi

- BS, Chemical Engineering 2006-2010 University of Tabriz, Iran

Project: Feasibility study of designing suitable process to recover carbon dioxide from hydrogen unit of refinery, converting it to ethanol and mixing it with gasoline to reduce MTBE consumption.

WORK/ TEACHING/ RESEARCH EXPERIENCE:

- The Centre of Molecular and Macromolecular Studies, Poland 2018 to current Position: Scientific Research Specialist; Mechanochemical synthesis of cocrystals, running solid-state NMR experiments, analysis of DSC and TGA results, analysis of PXRD result, running PXRD experiments, running computational calculations
- University of Applied Science and Technology, Iran 2015 to 2018, Position: Lecturer, Courses: Petrochemical Industries , Chemical Industries, Material and Energy Balance, Mass Transfer, Reactor design, Unit Operations, Process Control, Unit Operations lab, Process Control lab
- Azma Negin Khazar, Iran 2017 to 2018, Position: Technical Manager
- High-level scientific research visit, Université Lille Nord de France, France 2023

HONORS AND AWARDS

- SSHN scholarship for a high-level scientific research visit in France- French embassy 2023
- Co-investigator: Opus 15; Mesoporous and self-organizing molecular transporters as carriers of drugs and other low molecular chemical entities. NCN 2018/31/B/ST4/01973, 2019-2022
- Best PhD freshman 2019
- Best PhD sophomore 2020
- Best PhD junior 2021
- Best PhD senior 2022
- The scholarships were granted by CMMS PAS under the support of the Ministry of Science and Higher Education, Poland
- The article "Low-frequency Raman signatures of a transient polyamorphic situation in Linezolid: A competition between conformational polymorphs, Mehrnaz

Khalaji, Laurent Paccou, Yannick Guinet, Alain Hédoux, *J. Chem. Phys.* 162, 074501, 2025.” featured in the special collection “International Women’s Day 2025 Collection of Physical Chemistry Chemical Physics (PCCP)”, the high-quality research led by women as first author in the fields of physical chemistry, chemical physics, and biophysical chemistry.

14. List of abbreviations used in the thesis

active pharmaceutical ingredients (APIs)
area under the curve (AUC)
Back-to-Back (BaBa)
benzoic acid (BA)
Biopharmaceutics Classification System (BCS)
chemical shift anisotropy (CSA)
combined rotational and multi pulse spectroscopy (CRAMPS)
Conference on Harmonization (ICH)
cross polarization (CP)
Crystal Structure Prediction (CSP)
CSP-supported NMR crystallography (NMR-CPSX)
density functional theory (DFT)
differential scanning calorimetry (DSC)
diffusion supported loading (DiSupLo)
double quantum – single quantum (DQ-SQ)
double quantum coherence (DQC)
drug delivery systems (DDS)
4-fluorobenzoic acid (4-FBA)
frequency-switched Lee–Goldburg (FSLG)
gauge-including projector augmented wave (GIPAW)
molecular electrostatic potential surfaces (MEPS)
generally recognized as safe (GRAS)
Hansen solubility parameter (HSP)
heteronuclear correlation (HETCOR)
hot-stage microscopy (HSM)
hydrogen bond propensity (HBP)
infrared (IR)
liquid-assisted grinding (LAG)
liquid assistant (LA)
linezolid (LIN)
linezolid-2,3-dihydroxybenzoic acid cocrystal (LIN-2,3DHBA)
linezolid-2,4-dihydroxybenzoic acid cocrystal (LIN-2,4DHBA)

linezolid-2,4-dihydroxybenzoic acid cocrystal hydrate (LIN-2,4DHBA-H₂O)
linezolid-2,5-dihydroxybenzoic acid cocrystal hydrate (LIN-2,5DHBA-H₂O)
linezolid-2,6-dihydroxybenzoic acid cocrystal (LIN-2,6DHBA)
linezolid-3,4-dihydroxybenzoic acid cocrystal hydrate (LIN-3,4DHBA-H₂O)
linezolid-3,5-dihydroxybenzoic acid cocrystal (LIN-3,5DHBA)
linezolid-galic acid hydrate cocrystal (LIN-GA-H₂O)
linezolid-p-aminobenzoic acid cocrystal hydrate (LIN-PABA-H₂O)
linezolid-p-hydroxybenzoic acid cocrystal hydrate (LIN-PHBA-H₂O)
linezolid-benzoic acid cocrystal (LIN-BA)
low-frequency Raman spectroscopy (LFRS)
magic-angle spinning (MAS)
matrix-Assisted Cocrystallization (MAC)
mechanochemical neat grinding loading (MECHANO)
mechanochemical grinding with LAG loading (MeLo)
mesoporous silica nanoparticles (MSNs)
molecular complementarity (MC)
multiple-quantum MAS (MQMAS)
non-quaternary suppression (NQS)
p-hydroxybenzoic acid (PHBA)
perfluorobenzoic acid (PFBA)
pharmacokinetic (PK)
phase-modulated Lee–Goldburg (PMLG)
powder X-ray diffraction (PXRD)
quasielastic scattering (QES)
radiofrequency RF
resonant Acoustic Mixing® (Ram)
satellite transition spectroscopy (STMAS)
simulated gastric fluid (SGF)
simulated intestinal fluid (SIF)
single crystal X-ray diffraction (SXRD)
solid state nuclear magnetic resonance spectroscopy (SSNMR)
supercritical Fluid Technology (SCF)
surface Site Interaction Points (SSIPs)
thermal solvent free (TSF)

thermal wet 1 (TW1)
thermal wet 2(TW2)
thermogravimetry (TGA)
two pulse phase modulated (TPPM)
twin-Screw Extrusion (TSE)

15. Reference

1. Hauss DJ. *Adv. Drug Deliv. Rev.* 59, 667-676, 2007.
2. Savjani KT, Gajjar AK, Savjani JK. *Int. Sch. Res. Not.*, 195727, 2012.
3. Bodor N.J. *Pharm. Sci.*, 1984.
4. Douroumis D, Ross SA, Nokhodchi A. *Adv. Drug Deliv. Rev.* 117, 178–195, 2017.
5. Palanisamy V, Sanphui P, Prakash M, Chernyshev V. *Acta Cryst. C*75, 1102–1117, 2019.
6. Kaur R, Cavanagh KL, Rodríguez-Hornedo N, Matzger AJ. *Cryst. Growth Des.* 17, 5012–5016, 2017.
7. Putra OD, Umeda D, Nugraha IP, Furuishi T, Nagase H, Fukuzawa K, Uekusa H, Yonemochi E. *CrystEngComm*, 19, 2614–2622, 2017.
8. Lipinski, C. A. *Curr. Drug. Discov.* 4, 17–19, 2001.
9. Jain S, Patel N, Lin S. *Drug Dev. Ind. Pharm.* 41, 875–887, 2015.
10. Schultheiss N, Newman A. *Cryst. Growth Des.* 9, 2950–2967, 2009.
11. Stanton MK, Tufekcic S, Morgan C, Bak A. *Cryst. Growth Des.* 9, 1344–1352, 2009.
12. Sun CC, Hou H. *Cryst. Growth Des.* 8, 1575–1579, 2008.
13. Karki S, Friščić T, Fábíán L, Laity PR, Day GM, Jones W. *Adv. Mater.* 21, 3905–3909, 2009.
14. Wong SN, Chen YCS, Xuan B, Sun CC, Chow SF. *CrystEngComm*. 23. 7005-7038, 2021.
15. Bharti C, Nagaich U, Pal AK, Gulat, N. *Int. J. Pharm. Investig.* 5, 124–133, 2015.
16. Narayan R, Nayak UY, Raichur AM, Garg S. *Pharmaceutics*, 10, 118, 2018.
17. Hong EJ, Choi DG, Shim MS. *Acta. Pharm. Sin. B* 6, 297-307, 2016.
18. Zhang Y, Wang J, Bai X, Jiang T, Zhang Q, Wang S. *Mol. Pharm.* 9, 505-513, 2012.
19. Zhao Q, Wang T, Wang J, Zheng L, Jiang T, Cheng G, Wang S. *J. Non-Cryst. Solids* 358, 229-235, 2012.
20. Manzano M, Vallet-Regí M. *Chem. Commun.* 55, 2731–2740, 2019.

21. Jafari S, Derakhshankhah H, Alaei L, Fattahi A, Varnamkhasti BS, Saboury AA. *Biomed. Pharmacother.* 109, 1100–1111, 2019.
22. Hu Y, Zhi Z, Wang T, Jiang T, Wang S. *Eur. J. Pharm. Biopharm.* 79, 544–551, 2011.
23. Mohseni M, Gilani K, Mortazavi SA. *Iran. J. Pharm. Res.* 14, 27–34, 2015.
24. Mellaerts R, Jammaer JAG, Speybroeck VM, Chen H, Humbeeck JV, Augustijns P, Mooter VDG, Martens JA. *Langmuir*, 24, 8651–8659, 2008.
25. Limnell T, Santos HA, Mäkilä E, Heikkilä T, Salonen J, Murzin DY, Kumar N, Laaksonen T, Peltonen L, Hirvonen J. *J. Pharm. Sci.* 100, 3294–3306, 2011.
26. Skorupska E, Jeziorna A, Potrzebowski MJ. *J. Phys. Chem. C*, 120, 13169–13180, 2016.
27. Skorupska E, Kaźmierski S, Potrzebowski MJ. *Mol. Pharm.* 14, 1800–1810, 2017.
28. Skorupska E, Paluch P, Jeziorna A, Potrzebowski MJ. *J. Phys. Chem. C*, 119, 8652–8661, 2015.
29. Food and Drug Administration, Guidance for Industry, 2019.
30. Moellering RC. *Ann. Intern. Med.* 138, 135–142, 2003.
31. Abou Hassan OK, Karnib M, El-Khoury R, Nemer G, Ahdab-Barmada M, BouKhalil P. *Front. Pharmacol.* 7, 325, 2016.
32. Maccaroni E, Alberti E, Malpezzi L, Masciocchi N, Vladiskovic C. *Int. J. Pharm.* 351, 144–151, 2008.
33. Rao DM, Reddy PK. *International Patent WO 2005/035530 A1*, 2005.
34. Tanaka R, Hirayama N. *Anal. Sci.* X, 24, 43–44, 2008.
35. Wielgus E, Paluch P, Frelek J, Szczepek WJ, Potrzebowski MJ. *J. Pharm. Sci.* 104, 3883–3892, 2015.
36. Bergren MS. *US Patent 6559305 B1*, 2003.
37. Frelek J, Górecki M, Łaszcz M, Suszczyńska A, Vass E, Szczepek WJ. *Chem. Commun.* 48, 5295–5297, 2012.
38. Perlovich GL. *CrystEngComm*, 19, 2870–2883, 2017.
39. Devarakonda SN, Thaimattam R, Muppidi VK, Kanniah SL, Duggirala NK. *International Patent WO 2009/140466 A2*, 2009.
40. Price SL. *Chem. Soc. Rev.* 43 2098–2111, 2014.

41. Woodley SM, Catlow R. *Nat. Mater.* 7, 937–946, 2008.
42. Day GM. *Crystallogr. Rev.* 17, 3–52, 2011.
43. Pulido A, Chen L, Kaczorowski T, Holden D, Little MA, Chong SY, Slater BJ, McMahon DP, Bonillo B, Stackhouse CJ, Stephenson A, Kane CM, Clowes R, Hasell T, Cooper AI, Day GM, *Nature* 543, 657–664, 2017.
44. Hoja J, Ko HY, Neumann MA, Car R, DiStasio RA, Tkatchenko A. *Sci. Adv.* 5, 2019.
45. Bhardwaj RM, McMahon JA, Nyman J, Price LS, Konar S, Oswald IDH, Pulham CR, Price SL, Reutzel-Edens SM. *J. Am. Chem. Soc.* 141, 13887–13897, 2019.
46. Braun DE, Karamertzanis PG, Price SL. *Chem. Commun.* 47, 5443–5445, 2011.
47. Braun DE, Orlova M, Griesser UJ. *Cryst. Growth Des.* 14, 4895–490, 2014.
48. Dudek MK, Day GM. *CrystEngComm* 21, 2067–2079, 2019.
49. Pakhnova M, Kruglov I, Yanilkin A, Oganov AR. *Chem. Phys.* 22, 16822–16830, 2020.
50. Braun DE, McMahon JA, Bhardwaj RM, Nyman J, Neumann MA, van de Streek J, Reutzel-Edens SM, *Cryst. Growth Des.* 19, 2947–2962, 2019.
51. Dudek MK, Druzbecki K. *CrystEngComm* 24, 1665–1678, 2022.
52. Bryce DL. *IUCrJ* 4, 350–359, 2017.
53. Ashbrook SE, McKay D. *Chem. Commun.* 52, 7186–7204, 2016.
54. Hodgkinson P. *Prog. Nucl. Magn. Reson. Spectrosc.* 118–119, 10–53, 2020.
55. Etter MC. *Acc Chem Res*, 23, 120-6, 1990.
56. Etter MC. *J Phys Chem*, 95 4601-10, 1991.
57. Zaworotko M. *Acta Cryst A* 64:C11-C12, 2008.
58. Rodríguez-Hornedo N, Nehm SJ, Jayasankar A. In *Encyclopedia of Pharmaceutical Technology*, 3rd Edition, Taylor & Francis, London, 615-635, 2007.
59. Babu NJ, Reddy LS, Aitipamula S, Nangia A. *Chem Asian J* 3, 1122-1133, 2008.
60. Desiraju GR. *Angew Chem Int Ed Engl* 46(44), 8342-56, 2007.
61. Tiekink ERT, Vittal JJ. John Wiley & Sons, 25-50, 2006.
62. Fleischman SG, Kuduva SS, McMahon JA, Moulton B, Walsh RB, Rodriguez-Hornedo N, Zaworotko MJ. *Cryst Growth Des* 3, 909-919, 2003.

63. McNamara DP, Childs SL, Giordano J, Iarriccio A, Cassidy J, Shet MS, Mannion R, O'Donnell E, Park A. *Pharma Res*, 23, 1888-1897, 2006.
64. Hisada N, Takano R, Takata N, Shiraki K, Ueto T, Tanida S. *Eur J Pharm Biopharm* 103, 192-9, 2016.
65. Manin AN, Drozd KV, Churakov AV, Perlovich GL. *Cryst. Growth Des.* 18, 5254–5269, 2018.
66. Dhondale MR, Thakor P, Nambiar AG, Singh M, Agrawal AK, Shastri NR, Kumar D. *Pharmaceutics*, 15, 189, 2023.
67. Fábián L, *Cryst. Growth Des.*, 9, 3, 1436–1443, 2009.
68. Desiraju GR. *Angew. Chem., Int. Ed. Engl.*, 34(21), 2311–2327, 1995.
69. Jagia M, Daptardar R, Patel K, Bansal AK, Patel S. *Mol. Pharmaceutics*, 16(11), 4610–4620, 2019.
70. Tomar S, Chakraborti S, Jindal A, Grewal MK, Chadha R. *Int. J. Pharm.*, 574, 118942, 2020.
71. Sandhu B, McLean A, Sinha AS, Desper J, Sarjeant AA, Vyas S, Reutzel-Edens SM, Aakeröy CB, *Crystal Growth & Design*, 18 (1), 466-478, 2018.
72. Fedors RF. *Polym. Eng. Sci.* 14(2), 147–154. 82, 1974.
73. Hoy KL. Union Carbide Corporation, Chemicals and Plastics Research and Development, South Charleston, WV, 1975.
74. Van Krevelen DW, Nijenhuis KT. Elsevier, 2009.
75. Mohammad MA, Alhalaweh A, Velaga SP. *Int. J. Pharm.*, 407(1–2), 63–71, 2011.
76. Shete A, Murthy S, Korpale S, Yadav A, Sajane S, Sakhare S, Doijad R. *J. Drug Delivery Sci. Technol.*, 28, 46–55, 2015.
77. Hagymási A, Vörös-Horváth B, Šafarik T, Balić T, Szabó P, Gósi F, Nagy S, Pál S, Kunsági-Máté S, Széchenyi A. *Eur. J. Pharm. Sci.*, 156, 105599, 2021.
78. Childs SL, Stahly GP, Park A. *Mol. Pharmaceutics*, 4(3), 323–338, 2007.
79. Berry DJ, Steed JW. *Adv. Drug Delivery Rev.*, 117, 3–24, 2017.
80. Desiraju GR. RSC Publishing, Cambridge, UK, pp. 1–8, 2011.
81. Tothadi S, Shaikh TR, Gupta S, Dandela R, Vinodand CP, Nangia AK. *Cryst. Growth Des.* 21(2), 735–747, 2021.
82. Cruz-Cabeza AJ. *CrystEngComm*, 14(20), 6362–6365, 2012.

83. Stanton MK, Bak A. *Cryst. Growth Des.* 8(10), 3856–3862, 2008.
84. Variankaval N, Wenslow R, Murry J, Hartman R, Helmy R, Kwong E, Clas SD, Dalton C, Santos I. *Cryst. Growth Des.* 6(3), 690–700, 2006.
85. Abramov YA, Loschen C, Klamt A. *J. Pharm. Sci.*, 101(10), 3687–3697, 2012.
86. Klamt A. *Comput. Mol. Sci.*, 1(5), 699–709, 2011.
87. Przybyłek M, Ziółkowska D, Mroczyńska K, Cysewski P. *Eur. J. Pharm. Sci.*, 85, 132–140, 2016.
88. Cysewski P, *J Mol Model*, 23(4):136, 2017.
89. Grecu T, Adams H, Hunter CA, McCabe JF, Portell A, Prohens R, *Crystal Growth & Design*, 14 (4), 1749-1755, 2014.
90. Jain A, Yang G, Yalkowsky S, *H Ind Eng Chem Res*, 43, 7618–7621, 2004.
91. Alshehri AS, Gani R, You F, *Computers and Chemical Engineering* 141, 107005, 2020.
92. US 8,513,236 B2 10, 2013
93. Colacino E, Isoni V, Crawford D, García F, *Trends in Chemistry*, 3, 5, 335-339, 2021.
94. Vishweshwar P, McMahon JA, Peterson ML, Hickey MB, Shattock TR, Zaworotko MJ. *Chem Commun.* 4601-4603, 2005.
95. Mukherjee A, Rogers RD, Myerson AS, *CrystEngComm*, 20, 3817-3821, 2018.
96. Ramon C, Salaman P, Cés SV, Tesson N, Castano MT, EP2340818A1, 2009.
97. Pando C, Cabañas A, Cuadra IA. *RSC Advances*, 6, 71134-71150, 2016.
98. Liu N, Duan B, Lu X, Mo H, Xu M, Zhang Q, Wang B, *CrystEngComm*, 20, 2060-2067, 2018.
99. Ende DJ, Anderson SR, Salan JS, *Organic Process Research & Development*, 18 (2), 331-341, 2014.
100. Sheikh AY, Rahim SA, Hammond RB, Roberts KJ, *CrystEngComm*, 11, 501-509, 2009.
101. Medina C, Daurio D, Nagapudi K, Alvarez-Nunez F. *J Pharm Sci*, 99, 4, 1693-1696, 2010.
102. R. J. C. Brown and R. F. C. Brown, *Journal of Chemical Education*, 77 (6), 724, 2000.
103. Schultheiss N, Newman A, *Crystal Growth & Design*, 9 (6), 2950-2967, 2009.

104. Chieng N, Hubert M, Saville D, Rades T, Aaltonen J, *Cryst. Growth Des.*, 9, 5, 2377–2386, 2009.
105. Kalantri SS, Yadav MD, *Cryst. Res. Technol*, 59, 2300296, 2024.
106. Scott C. McKellar, Alan R. Kennedy, Neil C. McCloy, Eileen McBride, Alastair J. Florence, *Cryst. Growth Des.*, 14, 5, 2422–2430, 2014.
107. Bacchi A, Capucci D, Giannetto M, Mattarozzi M, Pelagatti P, Rodriguez-Hornedo N, Rubini K, Sala A, *Cryst. Growth Des.*, 16, 11, 6547–6555, 2016.
108. Sareen S, Mathew G, Joseph L, *Int J Pharm Investig.* 2(1):12-7, 2012.
109. Karagianni A, Malamataris M, Kachrimanis K, *Pharmaceutics*, 10(1):18, 2018.
110. Kalofonos I, Stahly PG, Martin-DoyleDimitris W, Stults KS, Houston TL. WO2010011926A2.
111. Banik M, Gopi SP, Ganguly S, Desiraju GR, *Cryst. Growth Des.*, 16, 9, 5418–5428, 2016.
112. Surov AO, Voronin AP, Manin AN, Manin NG, Kuzmina LG, Churakov AV, Perlovich GL, *Mol. Pharmaceutics* 2014, 11, 10, 3707–3715, 2014.
113. Nugrahani I, Utami D, Ibrahim S, Nugraha YP, Uekus H, *European Journal of Pharmaceutical Sciences*. Volume 117, 2018, Pages 168-176, 2018.
114. Alsirawan MHDB, Vangala VR, Kendrick J, Leusen FJJ, Paradkar A, *Cryst. Growth Des.*, 16, 6, 3072–3075, 2016.
115. Alzweiri M, Sallam M, Al-Zyoud W, Aiedeh K, *Symmetry*, 10(7), 288, 2018.
116. Gao Y, Gao J, Liu Z, Kan H, Zu H, Sun W, Zhang J, Qi S, *International Journal of Pharmaceutics*, 438, 1–2, 327-335, 2012.
117. Huang Y, Zhang B, Gao Y, Zhang J, Shi L, *Journal of Pharmaceutical Sciences*, 103, 8, 2330-2337, 2014.
118. Cheney ML, Weyna DR, Shan N, Hanna M, Wojtas L, Zaworotko MJ, *JOURNAL OF PHARMACEUTICAL SCIENCES*, 100, 6, 2011.
119. Dai XL, Li S, Chen JM, Lu TB, *Cryst. Growth Des.*, 16, 8, 4430–4438, 2016.
120. Dai XL, Voronin AP, Gao W, Perlovich GL, Lu TB, Chen JM, *CrystEngComm*, 21, 5095-5105, 2019.
121. Gopi SP, Banik M, Desiraju GR, *Cryst. Growth Des.*, 17, 1, 308–316, 2017.
122. M. K. Chaitanya Mannava, Abhijit Garai, and Ashwini K. Nangia, *Molecular Pharmaceutics*, 20 (5), 2293-2316, 2023.

123. Vallet-Regí M, Ramila A, del Real RP, Perez-Pariente J. *Chem. Mater*, 13, 308–311, 2001.
124. Garcia-Bennett AE. *Nanomedicine* 6, 867–877, 2011.
125. Liu TL, Li LL, Teng X, Huang XL, Liu HY, Chen D, Ren J, He JQ, Tang FQ. *Biomaterials* 32, 1657–1668, 2011.
126. He, Q.J., Shi, J.L., Zhu, M., Chen, Y., Chen, F. *Micropor. Mesopor. Mater.*, 131, 314–320, 2010.
127. Fu CH, Liu TL, Li LL, Liu HY, Chen D, Tang FQ. *Biomaterials*. 34, 2565–2575, 2013
128. Tang FQ, Li LL, Chen D. *Adv. Mater.* 24, 1504–1534, 2012.
129. Kinnari P, Makila E, Heikkila T, Salonen J, Hirvonen J, Santos HA. *Int. J. Pharm.* 414, 148–156, 2011.
130. Buyuktimkin T, Wurster DE. *Int. J. Pharm.* 478, 164–171, 2015.
131. McCarthy CA, Ahern RJ, Dontireddy R, Ryan KB, Crean AM. *Drug Deliv.* 13, 93–108, 2016.
132. Jeelani PG, Mulay P, Venkat R, Ramalingam C. *Silicon* 12, 1337–1354, 2020.
133. Miura H, Kanebako M, Shirai H, Nakao H, Inagi T, Terada K. *Eur. J. Pharm. Biopharm.*, 76, 215–221, 2010.
134. Carvalho GC, Sábio RM, de Cássia Ribeiro T, Monteiro AS, Pereira DV, Ribeiro SJL, Chorilli M. *Pharm. Res.*, 37, 191, 2020.
135. Chircov C, Spoiala A, Paun C, Craciun L, Ficai D, Ficai A, Andronescu E, Turculet SC. *Molecules*, 25, 3814, 2020.
136. Zid L, Zelenak V, Almasi M, Zelenakova A, Szucsova J, Bednarcik J, Sulekova M, Hudak A, Vahovska L. *Molecules*, 25, 4722–4738, 2020.
137. Natarajan SK, Selvaraj S. *RSC Adv.* 4, 14328–14334, 2014.
138. Le TT, Elyafi AKE, Mohammed AR, Al-Khattawi A. *Pharmaceutics*, 11, 269, 2019.
139. Tella JO, Adekoya JA, Ajanaku KO. *R Soc Open Sci.* 8, 9(6):220013, 2022.
140. Trzeciak K, Chotera-Ouda A, Bak-Sypien II, Potrzebowski MJ. *Pharmaceutics*. 24, 13(7), 950. 2021.
141. Seljak KB, Kocbek P, Gašperlin M. *J. Drug Deliv. Sci. Technol.*, 59, 101906, 2020.

142. Li Z, Zhang YT, Feng NP. *Expert Opin. Drug Deliv.* 16, 219–237, 2019.
143. Maleki A, Kettiger H, Schoubben A, Rosenholm JM, Ambrogi V, Hamidi M. J. *Control. Release*, 262, 329–347, 2017.
144. Andersson J, Rosenholm J, Areva S, Lindén M. *Chem. Mater.*, 16, 4160–4167, 2004.
145. Singh A, Worku ZA, Van den Mooter G. *Expert Opin. Drug Deliv.* 8, 1361–1378, 2011.
146. Prestidge CA, Barnes TJ, Lau CH, Barnett C, Loni A, Canham L. *Expert Opin. Drug Deliv.* 4, 101–110, 2007.
147. ICH Guideline Q3C (R6), 2021.
148. Eren ZS, Tunçer S, Gezer G, Yildirim LT, Banerjee S, Yilmaz A. *Micropor. Mesopor. Mater.* 235, 211–223, 2016.
149. Hillerström A, van Stam J, Andersson M. *Green Chem.*, 11, 662–667, 2009.
150. Belhadj-Ahmed F, Badens E, Llewellyn P, Denoyel R, Charbit G. J. *Supercrit. Fluids*, 51, 278–286, 2009.
151. Lehto VP, Riikonen J. Santos, H.A., Ed.; Woodhead Publishing: Cambridge, UK, pp. 337–355, 2014.
152. Trzeciak K, Kaźmierski S, Wielgus E, Potrzebowski MJ. *Micropor. Mesopor. Mater.* 308, 110506, 2020.
153. Ahern RJ, Crean AM, Ryan KB. *Int. J. Pharm.*, 439, 92–99, 2012.
154. Kompella UB, Koushik K. *Crit. Rev. Ther. Drug Carr. Syst.* 18, 173–199, 2001.
155. Yuan L, Chen W, Hu J, Zhang JZ, Yang, D. *Langmuir*, 29, 734–743, 2013.
156. Xie X, Li F, Zhang H, Lu Y, Lian S, Lin H, Gao Y, Jia L. *Eur. J. Pharm. Sci.*, 83, 28–35, 2016.
157. Wang N, Cheng X, Li N, Wang H, Chen H. *Adv. Healthcare Mater.* 8, 2019.
158. Waters LJ, Bedford S, Parkes GMB. *AAPS PharmSciTech*, 12, 1038–1043, 2011.
159. Hampsey JE, Castro CM, McCaughey B, Wang D, Mitchell B, Lu Y. J. *Am. Ceram. Soc.*, 87, 1280–1286, 2004.
160. Willart JF, Descamps M. *Mol. Pharm.*, 5, 905–920, 2008.
161. Trzeciak K, Kaźmierski S, Druźbicki K, Potrzebowski MJ. *J. Phys. Chem. C* 125, 10096–10109, 2021.

162. Abu-Zied BM, Schwieger W, Asiri AM. *Micropor. Mesopor. Mater.* 218, 153–159, 2015.
163. Cheney ML, Weyna DR, Shan N, Hanna M, Wojtas L, Zaworotko MJ. *J Pharm Sci* 100, 2172–81, 2011.
164. H. M. Rietveld, 2, 2, 65–71, 1969.
165. Mohd R. Abu Bakar, Zoltan K. Nagy, Chris D. Rielly, Sandy E. Dann, *International Journal of Pharmaceutics*, Volume 414, Issues 1–2, Pages 86–103, 2011.
166. S. Mat, S. Municio, J. L. Alonso, E. R. Alonso, I. León, *ChemistryOpen*, e202400490–99, 2025.
167. K. Shankland, W.I.F. David, T. Csoka, L. McBride, *International Journal of Pharmaceutics*, 165, 1, 117–126, 1998.
168. David WIF, Shankland K, Shankland N, *Chem. Commun.*, 931–932, 1998.
169. Biswas N. *Eur. J. Pharm. Sci.* 99, 152–160, 2017.
170. Kijac AZ, Li Y, Sligar SG, Rienstra CM. *Biochemistry* 46, 13696–703, 2007.
171. Bolla G, Chernyshev V, Nangia A. *IUCrJ* 4, 206–14, 2017.
172. Geppi M, Mollica G, Borsacchi S, Veracini CA. *Appl. Spectrosc. Rev.* 43, 202–302, 2008.
173. Robin Kingsley Harris, Longman Scientific & Technical, 260, 1986.
174. D.D. Laws, H.-M.L. Bitter, A. Jerschow, *Angew. Chem. Int. Ed.* 41 (17), 3096–3129, 2002.
175. A. Lesage, *Phys. Chem. Chem. Phys.* 11 (32), 6876–6891, 2009.
176. K. Paradowska, I. Wawer, *J. Pharm. Biomed. Anal.* 93, 27–42, 2014.
177. A.E. Bennett, C.M. Rienstra, M.I. Auger, K.V. Lakshmi, R.G. Griffin, *J. Chem. Phys.* 103 (16), 6951–6958, 1995.
178. B.M. Fung, A.K. Khitrin, K. Ermolaev, *J. Magn. Reson.* 142 (1), 97–101, 2000.
179. G. Metz, X.L. Wu, S.O. Smith, *J. Magn. Reson. A* 110 (2), 219–227, 1994.
180. B.N. Nelson, L.J. Schieber, D.H. Barich, J.W. Lubach, T.J. Offerdahl, D.H. Lewis, et al., *Solid State Nucl. Magn. Reson.* 29 (1–3), 204–213, 2006.
181. F.P. Bruno, M.R. Caira, E.C. Martin, G.A. Monti, N.R. Sperandeo, *J. Mol. Struct.* 1036, 318–325, 2013.

182. F.P. Bruno, M.R. Caira, G.A. Monti, D.E. Kassuha, N.R. Sperandeo, *J. Mol. Struct.* 984 (1–3), 51–57, 2010.
183. C. Garnero, A.K. Chattah, M. Longhi, *Carbohydr. Polym.* 94 (1), 292–300, 2013.
184. X.L. Wu, K.W. Zilm, *J. Magn. Reson. A* 104 (1), 119–122, 1993.
185. R.K. Harris, P. Hodgkinson, T. Larsson, A. Muruganantham, *J. Pharm. Biomed. Anal.* 38 (5), 858–864, 2005.
186. J. Schaefer and E. O. Stejskal, *J. Am. Chem. Soc.*, 98, 1031–1032, 1976.
187. E. R. Andrew, A. Bradbury and R. G. Eades, *Nature*, 182, 1659, 1958.
188. M. Deschamps, *Annu. Rep. NMR Spectrosc.*, 81, 109–144, 2014.
189. Y. Nishiyama, *Solid State Nucl. Magn. Reson.*, 78, 24–36, 2016.
190. Y. Nishiyama, G. Hou, V. Agarwal, Y. Su and A. Ramamoorthy, *Chem. Rev.*, 123, 918–988, 2023.
191. M. Ernst, A. Samoson and B. H. Meier, *Chem. Phys. Lett.*, 348, 293–302, 2001.
192. Y. Ishii and R. Tycko, *J. Magn. Reson.*, 142, 199–204, 2000.
193. Y. Ishii, N. P. Wickramasinghe and S. Chimon, *J. Am. Chem. Soc.*, 125, 3438–3439, 2003.
194. J. Blahut, L. Benda, A. L. Lejeune, K. J. Sanders, B. Burcher, E. Jeanneau, D. Proriot, L. Catita, P.-A. R. Breuil, A. A. Quoineaud, A. J. Pell and G. Pintacuda, *RSC Adv.*, 11, 29870–29876, 2021.
195. S.P. Brown, *Solid State Nucl. Magn. Reson.* 41, 1–27, 2012.
196. K. Yazawa, F. Suzuki, Y. Nishiyama, T. Ohata, A. Aoki, K. Nishimura, et al., *Chem. Commun.* 48 (91), 11199–11201, 2012.
197. J. Waugh, L. Huber, U. Haeberlen, *Phys. Rev. Lett.* 20 (5), 180–182, 1968.
198. M. Lee, W.I. Goldberg, *Phys. Rev.* 140 (4A), 1261–1271, 1965.
199. C. Coelho, J. Rocha, P.K. Madhu, L. Mafra, *J. Magn. Reson.* 194 (2), 264–282, 2008.
200. S.P. Brown, H.W. Spiess, *Chem. Rev.* 101 (12), 4125–4156, 2001.
201. B.J. van Rossum, H. Forster, H.J.M. de Groot, *J. Magn. Reson.* 124 (2), 516–519, 1997.

202. A. Lesage, D. Sakellariou, S. Steuernagel, L. Emsley, J. Am. Chem. Soc. 120 (50), 13194–13201, 1998.
203. K. Saalwachter, R. Graf, H.W. Spiess, J. Magn. Reson. 140 (2), 471–476, 1999.
204. Andrew G.M. Rankin, Julien Trébosc, Piotr Paluch, Olivier Lafon, Jean-Paul Amoureux, Journal of Magnetic Resonance, 303, 28–41, 2019.
205. Sommer W, Gottwald J, Demco DE, Spiess HW. J. Magn. Reson. A 113, 131–134, 1995.
206. Vogt FG, Strohmeier M. Mol. Pharm. 9, 3357–3374, 2012.
207. Brus J, Urbanova M, Sedenkova I, Brusova H. Int. J. Pharm. 409, 62–74, 2011.
208. Urbanova M, Brus J, Sedenkova I, Policianova O, Kobera L. Acta A Mol. Biomol. Spectrosc. 100, 59–66, 2013.
209. Yu J-X, Hallac RR, Chiguru S, Mason RP. Prog. Nucl. Magn. Reson. Spectrosc. 70, 25–49, 2013.
210. Petzoldt C, Bley O, Byard SJ, Andert D, Baumgartner B, Nagel N, et al. Eur. J. Pharm. Biopharm. 86, 337–350, 2014.
211. Pham TN, Watson SA, Edwards AJ, Chavda M, Clawson JS, Strohmeier M, et al. Mol. Pharm. 7, 1667–1691, 2010.
212. Cavadini S. Prog. Nucl. Magn. Reson. Spectrosc. 56, 46–77, 2010.
213. Gan Z, Amoureux JP, Trébosc J. Chem. Phys. Lett. 435, 163–169, 2007.
214. Tatton AS, Pham TN, Vogt FG, Iuga D, Edwards AJ, Brown SP. CrystEngComm 14, 2654–2659, 2012.
215. Tatton AS, Pham TN, Vogt FG, Iuga D, Edwards AJ, Brown SP. Mol. Pharm. 10, 999–1007, 2013.
216. Kuminek G, Rauber GS, Riekes MK, Campos CEM, Monti GA, Bortoluzzi AJ, et al. J. Pharm. Biomed. Anal. 78–79, 105–111, 2013.
217. I. Wawer, M. Pisklak, Z. Chilmonczyk, J. Pharm. Biomed. Anal. 38 (5) 865–870, 2005.
218. Olivera ME, Ramírez Rigo MV, Chattah AK, Levstein PR, Baschini M, Manzo RH. Eur. J. Pharm. Sci. 18, 337–348, 2003.

219. Chattah AK, Garro Linck Y, Monti GA, Levstein PR, Breda SA, Manzo RH, et al. *Magn. Reson. Chem.* 45, 850–859, 2007.
220. Mafra L, Santos SM, Siegel R, Alves I, Almeida Paz FA, Dudenko D, et al. *J. Am. Chem. Soc.* 134, 71–74, 2012.
221. Apperley DC, Forster AH, Fournier R, Harris RK, Hodgkinson P, Lancaster RW, et al. *Magn. Reson. Chem.* 43, 881–892, 2005.
222. Carignani E, Borsacchi S, Geppi M. *ChemPhysChem* 12, 974–981, 2011.
223. F.G. Vogt, G.R. Williams, R.C.B. Copley, *J. Pharm. Sci.* 102 (10), 3705–3716, 2013.
224. Romañuk CB, Manzo RH, Linck YG, Chattah AK, Monti GA, Olivera ME. *J. Pharm. Sci.* 98, 3788–3801, 2009.
225. Romañuk CB, Garro Linck Y, Chattah AK, Monti GA, Cuffini SL, Garland MT, et al. *Int. J. Pharm.* 391, 197–202, 2010.
226. Garro Linck Y, Chattah AK, Graf R, Romañuk CB, Olivera ME, Manzo RH, et al. *Phys. Chem. Chem. Phys.* 13, 6590–6596, 2011.
227. Vogt FG, Clawson JS, Strohmeier M, Edwards AJ, Pham TN, Watson SA. *Cryst. Growth Des.* 9, 921–937, 2008.
228. Maruyoshi K, Iuga D, Antzutkin ON, Alhalaweh A, Velaga SP, Brown SP. *Chem. Commun.* 48, 10844–10846, 2012.
229. Taulelle F. *NMR Crystallogr.* 6, 1053–1057, 2004.
230. Harris RK. *NMR Crystallogr.* 6, 1025–1037, 2004.
231. Harris RK, Joyce SA, Pickard CJ, Cadars S, Emsley L. *Phys. Chem. Chem. Phys.* 8, 137–143, 2006.
232. Harris RK, Cadars S, Emsley L, Yates JR, Pickard CJ, Jetti RKR, et al. *Phys. Chem. Chem. Phys.* 9, 360–368, 2007.
233. Harris RK, Hodgkinson P, Zorin V, Dumez J-N, Elena-Herrmann B, Emsley L, et al. *Magn. Reson. Chem.* 48, 103–112, 2010.
234. Apperley DC, Batsanov AS, Clark SJ, Harris RK, Hodgkinson P, Jochym DB. *J. Mol. Struct.* 1015, 192–201, 2012.
235. Santos SM, Rocha J, Mafra L. *Cryst. Growth Des.* 13, 2390–2395, 2013.
236. Martineau C, Cadiou A, Bouchevreau B, Senker J, Taulelle F, Adil K. *Dalton Trans.* 41, 6232–6241, 2012.

237. Brouwer DH. J. Magn. Reson. 194, 136–146, 2008.
238. Baías M, Widdifield CM, Dumez J-N, Thompson HPG, Cooper TG, Salager E, et al. Phys. Chem. Chem. Phys. 15, 8069–8080, 2013.
239. Achibat T, Boukenter A, Duval E. J. Chem. Phys. 99, 2046–2051, 1993.
240. Bugay DE. Adv. Drug Deliv. Rev. 48, 43–65, 2001.
241. Hédoux A, Guinet Y, Descamps M. Int. J. Pharm. 417, 17–31, 2011.
242. Hédoux A. Adv. Drug Deliv. Rev. 100, 133–146, 2016.
243. Larkin PJ, Dabros M, Sarsfield B, Chan E, Carriere J, Smith BC. Appl. Spectrosc. 68, 758–776, 2014.
244. Larkin P, Wasylyk J, Raglione M. Appl. Spectrosc. 69, 1217–1228, 2015.
245. Ruggiero M, Sutton J, Fraser-Miller S, Zaczek A, Korter T, Gordon K, Zeitler J. Cryst. Growth Des. 18, 6513–6520, 2018.
246. Otaki T, Tanabe Y, Kojima T, Miura M, Ikeda Y, Koide T, Fukami T. Int. J. Pharm. 542, 56–65, 2018.
247. Nemtsov I, Mastai Y, Tischler Y, Aviv H. ChemPhysChem 19, 3116–3121, 2018.
248. Lipiainen T, Fraser-Miller S, Gordon K, Strachan CJ. J. Pharm. Biomed. Anal. 149, 343–350, 2018.
249. Iwata K, Karashima M, Ikeda Y, Inoue M, Fukami T. CrystEngComm, 20(14), 1928–1934, 2018.
250. Walker G, Romann P, Poller B, Lobmann K, Grohgan H, Rooney J, Huff G, Smith G, Rades T, Gordon K. Mol. Pharm. 14, 4675–4684, 2017.
251. Berzins K, Fraser-Miller S, Gordon K. Int. J. Pharm. 592, 120034, 2021.
252. Shibata T, Mori T, Kojima S. Spectrochim. Acta A 150, 207–211, 2015.
253. Inoue M, Hisada H, Koide T, Carriere J, Heyler R, Fukami T. Org. Process Res. Dev. 21, 262–265, 2017.
254. Rahman MM, Aznan M, Yusof AM, Ansaryr H, Siddiqi MJ, Yusan S. Orient. J. Chem. 33, 611–621, 2017.
255. Hellstaen S, Qu HY, Heikkila T, Kohonen J, Reinikainen SP, Louhi-Kultanen M. CrystEngComm 14, 1582–1587, 2012.
256. Wu TK, Lin SY, Lin HL, Huang YT. Bioorg. Med. Chem. Lett. 21, 3148–3151, 2011.

257. Yao X, Henry RF, Zhang GGZ. *J. Pharm. Sci.* 112, 237–242, 2023.
258. Telford R, Seaton CC, Clout A, Buanz A, Gaisford S, Williams GR, Prior TJ, Okoye CH, Munshi T, Scowen IJ, *Chem. Commun.*, 52, 12028–12031, 2016
259. Chadha R, Bhandari S. *J. Pharm. Biomed. Anal.* 87, 82–97, 2014.
260. M. Guerain, Y. Guinet, N.T. Correia, L. Paccou, F. Danède, A. Hédoux, *International Journal of Pharmaceutics*, 584, 119454, 2020.
261. Alhalaweh A, Alzghoul A, Mahlin D, Bergström CA.S, *International Journal of Pharmaceutics*, 495, 1, 312–317, 2015.
262. Talaczynska A, Mizera M, Szybowicz M, Nowicka AB, Garbacki P, Paczkowska M, Zalewski P, Kozak M, Oszczapowicz I, Jelinska A, Cielecka-Piontek J, *Acta Pol Pharm. S*, 73(5), 1299–1309, 2016.
263. Bauer J, Spanton S, Henry R, Quick J, Dziki W, Porter W, Morris J, *Pharmaceutical Research*, Vol. 18, No. 6, 2001.
264. Pore YV, Shinde VR, Rao JV, *Journal of Applied Pharmaceutical Science*, 6 (10), 037–044, 2016.
265. Shilyaeva Y, Volovlikova O, Poyarkov K, Yuditskaya S, Gavrilov S. *Int. J. Nanoscience.*, 18, 1940073–1940077, 2019.
266. Hempel NJ, Brede K, Olesen NE, Genina N, Knopp MM, Lobmann K. *Int. J. Pharm.*, 544, 153–157, 2018.
267. Lehto VP, Vaha-Heikkilä K, Paski J, Salonen J. *J. Therm. Anal. Calorim.* 80, 393–397, 2005.
268. Bavnhoj CG, Knopp MM, Madsen CM, Lobmann K. *Int. J. Pharm. X*, 1, 1000082–1000087, 2019.
269. Dana E. Moseson, Madison A. Jordan, Dishan D. Shah, Isaac D. Corum, Benedito R. Alvarenga Jr., Lynne S. Taylor, *International Journal of Pharmaceutics*, 590, 30, 119916, 2020.
270. van der Wel PC. *Emerg Top Life Sci*, 2, 57–67, 2018.
271. Nassimbeni LR, Ba'thori NB, Atwood JL. Elsevier: Burlington, MA, USA, p. 3–21, 2017.
272. C. Pickard, F. Mauri, *Phys. Rev. B* 63, 24, 245101–245113, 2001.
273. R.K. Harris, P. Hodgkinson, C.J. Pickard, J.R. Yates, V. Zorin, *Magn. Reson. Chem.* 45 (S1), S174–S186, 2007.

274. Ludeña EV, Arroyo D, Salazar EX, Vallejo J, *Advances in Quantum Chemistry*, 76, 59-78, 2018.
275. Kryachko ES, Ludeña EV, *Physics Reports* 544, 2, 123-239, 2014.
276. Taylor CR, Day GM. *Cryst. Growth Des.*, 18, 2, 892–904, 2018.
277. Yang, X., Li, Z., Liu, Y., Xing, Y., Wei, J., Yang, B., Zhang, C., Yang, R.T., and Tsai, C.J. *Aerosol Air Qual. Res.* 19: 911-924, 2019.
278. D. A. Long, *Raman Spectroscopy*, McGraw-Hill International Book Company, 1977.
279. M. H. Brooker, O. F. Nielsen, and E. Praestgaard, *J. Raman Spectrosc.* 19, 71–78, 1988.
280. F. L. Galeener and P. N. Sen, *Phys. Rev. B* 17(4), 1928–1933, 1978.
281. R. Shuker and R. W. Gammon, *Phys. Rev. Lett.* 25(4), 222–225, 1970.
282. A. P. Sokolov, A. Kisliuk, D. Quitmann, and E. Duval, *Phys. Rev. B* 48, 7692–7695, 1993.
283. E. Duval, A. Boukenter, and T. Achibat, *J. Phys.: Condens. Matter* 2(51), 10227–10234, 1990.
284. N. V. Surovtsev, S. V. Adichtchev, E. Rossler, and M. A. Ramos, *J. Phys.: Condens. Matter* 16, 223–230, 2004.
285. A. Fontana, F. Rocca, M. P. Fontana, B. Rosi, and A. J. Dianoux, *Phys. Rev. B* 41(6), 3778–3785, 1990.
286. Zheng S, Han Y, Zhang J, Li W, *Fluid Phase Equilibria*, 432, 18e27, 2017.
287. Moutamenni B, Tabary N, Mussi A, Dhainaut J, Ciotonea C, Fadel A, Paccou L, Dacquin J-P, Guinet Y, Hédoux A. *Pharmaceutics.*, 15(2):390, 2023.
288. Khalaji M, Dudek MK, Paccou L, Danède F, Guinet Y, Hédoux A, *Phys. Chem. Chem. Phys.*, 26, 20709-20716, 2024.
289. Khalaji M, Paccou L, Guinet Y, Hédoux A, *J. Chem. Phys.* 162, 074501 2025.

Appendix I

T1:

Virtual Cocystal Screening Methods as Tools to Understand the Formation of Pharmaceutical Cocystals - A Case Study of Linezolid, a Wide-Range Antibacterial Drug, Khalaji, M., Potrzebowski, M.J., Dudek, M.K., *Crystal Growth and Design*, 2021, 21, pp. 2301–2314

T2:

Structural variety of heterosynthons in linezolid cocystals with modified thermal properties, Khalaji, M., Wróblewska, A., Wielgus, E., G.D. Bujacz, Dudek, M.K., Potrzebowski, M.J., *Acta Crystallographica Section B: Structural Science, Crystal Engineering and Materials*, 2020, 76, pp. 892–912

T3:

Narrowing down the conformational space with solid-state NMR in crystal structure prediction of linezolid cocystals, Khalaji, M., Paluch, P., Potrzebowski, M.J., Dudek, M.K., *Solid State Nuclear Magnetic Resonance*, 2022, 121, 101813

T4:

Narrowing down the conformational space with solid-state NMR in crystal structure prediction of linezolid cocystals, Khalaji, M., Paluch, P., Potrzebowski, M.J., Dudek, M.K., *Solid State Nuclear Magnetic Resonance*, 2022, 121, 101813

T1:

Virtual Cocrystal Screening Methods as Tools to Understand the Formation of Pharmaceutical Cocrystals - A Case Study of Linezolid, a Wide-Range Antibacterial Drug, Khalaji, M., Potrzebowski, M.J., Dudek, M.K., Crystal Growth and Design, 2021, 21, pp. 2301–2314

Virtual Cocrystal Screening Methods as Tools to Understand the Formation of Pharmaceutical Cocrystals—A Case Study of Linezolid, a Wide-Range Antibacterial Drug

Mehrnaz Khalaji, Marek J. Potrzebowski, and Marta K. Dudek*



Cite This: <https://dx.doi.org/10.1021/acs.cgd.0c01707>



Read Online

ACCESS |



Metrics & More

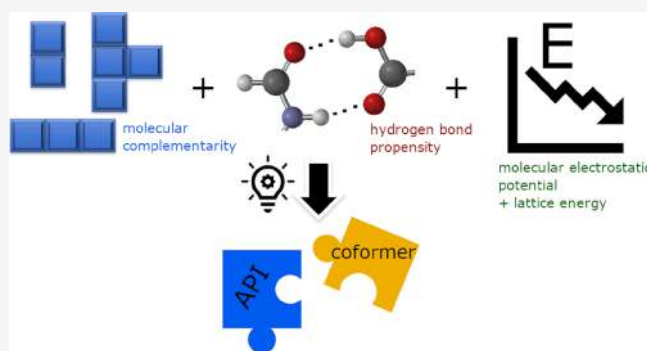


Article Recommendations



Supporting Information

ABSTRACT: Experimental mechanochemical screening of cocrystals with linezolid (LIN) resulted in the formation of six new crystal phases, including three neat cocrystals and three cocrystal hydrates, in addition to seven previously described cocrystals. In an attempt to understand the factors governing the formation of these phases, different experimental conditions of the mechanochemical reactions (polymorphic forms of LIN and presence of different solvents to create liquid-assisted grinding conditions) were tested and the results were compared with the predictions from three commonly used virtual cocrystal screening tools: molecular complementarity, hydrogen bond propensity, and molecular electrostatic potential maps. It is shown that these three methods can be used to help understand a molecule's preferences to form cocrystals with particular coformers. The influence of molecular conformation on the outcome of the predictions is also evaluated. A comparison between the prediction methods indicates that while considering a set of similar coformers, the approach based on molecular electrostatic potential maps seems to be more consistent with the experimental results than molecular complementarity and hydrogen bond propensity tools. Instead, these two latter approaches are recommended at the early stages of coformer selection. In addition, intermolecular energy contribution (lattice energy) to the total energy of crystal forms of coformers was found to be indicative of the feasibility of cocrystal formation in the case of coformers capable of forming similar supramolecular synthons.



INTRODUCTION

Recent years have witnessed an enormous interest in pharmaceutical cocrystal formation,^{1–6} including introducing several drugs into the market in their cocrystal forms (among them a cocrystal of ertugliflozin and L-pyrogutamic acid sold under the brand name of Steglatro,⁷ a drug–drug cocrystal containing valproic acid and sodium valproate marketed as Depakote,⁸ and a cocrystal of celecoxib and tramadol awaiting Food and Drug Administration evaluation⁹). This is because appropriately designed and performed cocrystallization of an active pharmaceutical ingredient (API) can offer improved solubility, better stability, modified thermal properties, and in the case of drug–drug cocrystals, enhanced biological action. This “appropriate” design is not a trivial task and in conjunction with an effort to understand the formation of a particular crystalline form of a substance of interest is at the heart of crystal engineering.

Crystal engineering focuses on the existence^{10–14} and the ways to crystallize^{15–17} different polymorphic forms, the propensity of a molecule to form solvates and/or hydrates,^{18–21} as well as the likelihood of synthesizing cocrystals with desired physicochemical properties.^{22–24} Among the mentioned crystal forms, cocrystals seem to offer the most

possibilities in terms of actual engineering as there are numerous cocrystal formers (coformers), which can be utilized to create desired solids. As it often happens, the variety of coformers is at the same time a blessing and a curse for cocrystal design because it is often difficult to predict a priori which of the coformers will constitute the best cocrystal former. This is true in terms of both a propensity of a given molecule to form certain intermolecular interactions under the given experimental conditions (and hence to form a cocrystal) as well as of the physicochemical properties of a future crystalline form. As a result, significant experimental efforts are needed to find the best coformer, and this is often associated with many unsuccessful attempts. It is therefore not surprising that the number of works dealing with the possibility of predicting the outcome of cocrystallization has been growing noticeably over the last two decades.

Received: December 18, 2020

Revised: February 16, 2021

One of the main works in this field was undoubtedly made by Desiraju and his idea of implementing the concept of supramolecular synthons to crystal engineering.²⁵ On the other hand, in the case of multiple possibilities of forming different intermolecular interactions, it may not be that easy to indicate the correct synthon preferences, as illustrated recently by Corpinot et al. on a series of cocrystals of theophylline with fluorobenzoic acids.²⁶ Among other approaches developed as fast virtual screening tools, the most prominent ones include approaches involving molecular complementarity,²⁷ hydrogen bond propensity,²⁸ and molecular electrostatic potential maps.²⁹ The first one of these methods is based on molecular descriptors associated with the shape and size of the considered molecules, their dipole moments, as well as the fraction of nitrogen and oxygen atoms.^{27,30,31} As a consequence of being associated with a molecule's shape, the results of molecular complementarity screening will depend to some extent on the conformation of the considered chemicals. Contrarily, the hydrogen bond propensity approach is a knowledge-based method, which relies on the analysis of the occurrence of certain intermolecular interactions of a given functional group in the Cambridge Structural Database (CSD), regardless of its spatial arrangement. Such an analysis can be performed for each functional group present in a molecule of interest as well as in a potential coformer, giving as a result an estimated likelihood of a given intermolecular interaction between both compounds to be formed. This likelihood can then be juxtaposed to the likelihood of the formation of intermolecular interactions between the same molecules, thus indicating a probability of cocrystal formation.^{32–36} Finally, the method based on molecular electrostatic potential maps provides an estimate of the energy gain upon possible intermolecular interactions between the two considered molecules.^{29,37–41} Apart from these three methods, there are also other approaches that may be used for the prediction of cocrystal formation, such as the one based on the Hansen solubility approach,⁴² machine learning methods,⁴³ a conductor-like screening model for real solvents (COSMO-RS) approach,⁴⁴ or crystal structure prediction calculations.^{45–47} While all these methods have their own benefits, some of them are more suitable for solution crystallization experiments (Hansen solubility method), while others require a large training data set (machine learning approach) or expensive calculations (CSP-based methods).

Each of the three briefly characterized above methods of cocrystal prediction focuses on a slightly different aspect of cocrystal formation, starting with more Tetris-like (geometrical) considerations (molecular complementarity), through the experimentally observed propensities of functional groups toward the formation of certain supramolecular synthons (hydrogen bond propensity), and ending with an emphasis on the energetic aspects of the expected interactions (molecular electrostatic potential maps). In this work, we use all three virtual screening methods to predict and understand the formation of cocrystals of an antibacterial agent, linezolid (LIN, Figure 1). This wide-range antibiotic has been identified

by the World Health Organization as an essential medicine reserved to treat infections caused by multidrug resistant microbes.⁴⁸ Although its oral bioavailability is excellent,⁴⁹ cocrystallization of LIN may offer other benefits including the modification of its release rate⁵⁰ and possibility of use of thermal-based methods to introduce it into drug delivery systems.⁵¹

In our recent work, we have structurally characterized five cocrystals and cocrystal hydrates of LIN obtained via mechanochemical grinding, demonstrating the tendency of LIN to form a variety of different intermolecular interactions, despite forming crystals with coformers having the same functional groups (benzoic acid and its hydroxy derivatives).⁵² In the current work, we use LIN and an extended list of the considered coformers of 19 different compounds (Table 1) as a model system to demonstrate a combined experimental and theoretical approach, which allows for a better understanding of the conditions that have to be met by a coformer to successfully form a cocrystal with a fairly complex and flexible API, possessing multiple possible interaction sites. We exploit different virtual screening tools for cocrystal prediction, which helps to identify the most important factors for the successful cocrystal design of LIN. We tested different experimental conditions for the formation of the cocrystals, staying however within the boundaries of mechanochemical reactions (with the reasons for such a limitation given below in the Results and Discussion section). Within this, the influence of the polymorphic form of LIN taken for grinding is examined together with the presence of three different solvents used to create liquid-assisted grinding (LAG) conditions, as well as the amount of the solvent used. The outcome of all of these experiments together as well as of each of them separately is juxtaposed with the virtual screening predictions to better understand the limitations of the applied approaches. Finally, we propose inclusion of intermolecular energy of the tested coformers as a tool that may indicate the tendency of a coformer to form a cocrystal with a given API.

LIN crystallizes in one of two well-characterized polymorphic anhydrous forms, namely, form II and form III.^{53–56} Form II is more thermodynamically stable than form III and is characterized as having one LIN molecule in an asymmetric part of a crystallographic unit cell in contrast to LIN form III, which crystallizes with two symmetric independent molecules in an asymmetric part of a unit cell. In our grinding experiments, both forms were tested for the cocrystal formation with the considered coformers and the influence of the polymorphic form taken for the reaction on its outcome is described in one of the following sections. In our previous work, we obtained and characterized five cocrystals of LIN, all of them with aromatic acid derivatives, namely, benzoic acid (BA), *p*-hydroxybenzoic acid (PHBA), 2,6-dihydroxybenzoic acid (2,6-DHBA), 3,4-dihydroxybenzoic acid (3,4-DHBA), and 3,4,5-trihydroxybenzoic acid (gallic acid, GA).⁵² Here, we test these coformers again using different grinding conditions and extend our coformer list to other hydroxybenzoic acid derivatives (2,5-dihydroxybenzoic acid, 2,5-DHBA, 2,4-dihydroxybenzoic acid, 2,4-DHBA, 2,3-dihydroxybenzoic acid, 2,3-DHBA, and 3,5-dihydroxybenzoic acid, 3,5-DHBA) to evaluate the hypothesis that all –OH- and –COOH-containing aromatic entities will be attractive coformers for LIN. We also test a variety of other coformers including aromatic acid derivatives with other functional groups (*p*-aminobenzoic acid, PABA, vanillic acid, VA, sulfanilic acid, SA, isonicotinic acid,

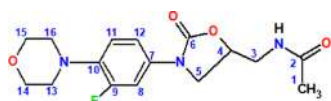
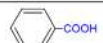
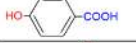
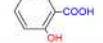
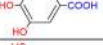
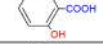
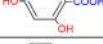
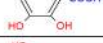
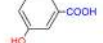

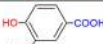

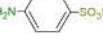
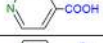

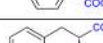

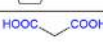
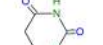
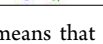


Figure 1. Chemical structure and carbon atom numbering of LIN.

Table 1. Summary of the Coformers Tested for the Formation of Cocrystals with LIN Together with the Grinding Conditions with Respect to the Polymorphic Form of LIN and Addition of a Solvent to Form LAG Conditions (Tol—Toluene, MeOH—Methanol, and H₂O—Water)^{a,b,c}

coformer	structure	name	grinding conditions					
			LIN_II	LIN_III	LIN_II Tol	LIN_II MeOH	LIN_II H ₂ O	
		benzoic acid (BA)	x	v	v	v	v	
		p-hydroxybenzoic acid (PHBA)	x	x/v	x	v	v	
		2,6-dihydroxybenzoic acid (2,6-DHBA)	y*	v	v	v	v	
		3,4-dihydroxybenzoic acid (3,4-DHBA)	x	v	v	v	v	
		2,5-dihydroxybenzoic acid (2,5-DHBA)	x	x	x	v	v	
		2,4-dihydroxybenzoic acid (2,4-DHBA)	x	x	x	v	v**	
		2,3-dihydroxybenzoic acid (2,3-DHBA)	x	x	v	v	v	
		3,5-dihydroxybenzoic acid (3,5-DHBA)	x	x	x	v	x	
		gallic acid (GA)	x	v	x/v	v	v	
		vanillic acid (VA)	x	x	x	x	x	
		p-aminobenzoic acid (PABA)	x	x	x	x	v	
		sulfanilic acid (SA)	x	x	x	x	x	
		isonicotinic acid (INA)	x	x	x	x	x	
		isonicotinamid (INN)	x	x	x	x	x	
		ibuprofen (IBU)	x	x	x	x	x	
		L-tyrosine (TYR)	x	x	x	x	x	
		L-proline (PRO)	x	x	x	x	x	
		malonic acid (MAL)	x	x	x	x	x	
		barbituric acid (BARB)	x	x	x	x	x	

^av means that under the given conditions, a cocrystal with LIN was obtained, x indicates no cocrystal formation, whereas x/v means that the cocrystal was formed but the conversion of the starting material was not complete. ^bThe reaction was completed after 3 h of grinding. ^cDifferent cocrystals were formed than in the presence of methanol as a liquid assistant.

INA, isonicotinamide, INN, and ibuprofen, IBU) as well as two amino acids, aromatic and aliphatic ones (L-tyrosine, TYR, and L-proline, PRO), an aliphatic dicarboxylic acid (malonic acid, MAL), and an amide of an aliphatic acid (barbituric acid, BARB).

EXPERIMENTAL SECTION

Materials. LIN form II was purchased from ABCR GmbH (Germany) and used without any further purification. Its phase identity was determined using ¹³C cross polarization/magic angle spinning nuclear magnetic resonance (CPMAS NMR) spectrum and differential scanning calorimetry (DSC) measurements. LIN form III was prepared from LIN form II by heating the sample to 130 °C for 12 h in an oven, as described previously.^{55,57} 2,3-DHBA, 2,4-DHBA, 2,5-DHBA, 2,6-DHBA, 3,4-DHBA, 3,5-DHBA, PHBA, PABA, GA, VA, SA, INN, BARB, and TYR were purchased from Sigma-Aldrich. BA, INA, and IBU were purchased from TCI Chemicals (Japan). MAL was purchased from Fluka AG (USA). PRO was purchased from Reanal Labor LLC (Hungary). All coformers were used as is unless otherwise stated.

Mechanochemical Grinding. In all mechanochemical reactions, 100 mg of LIN_II or LIN_III was ground using a ball mill (Retsch MM 200 mixer mill) with an appropriate amount of a coformer in a stoichiometric ratio of 1:1. If an experiment was conducted in the presence of a liquid assistant (LAG), a small amount of water, methanol, or toluene (up to 250 μ L, typically 80 μ L) was added to the reaction mixture. The ball mill was set to 25 Hz and the typical reaction time was 1 h, unless otherwise stated. All experiments were performed in 5 mL agate jars using one agate ball.

Nuclear Magnetic Resonance (NMR) Spectroscopy. Solid-state NMR spectroscopy was used each time to evaluate the outcome of the mechanochemical reactions. To that purpose, ¹³C CPMAS NMR spectra were recorded for pure components and for each of the reaction mixtures using a Bruker Avance III spectrometer, with ¹H and ¹³C resonating frequencies of 400.13 and 100.90 MHz, respectively. A typical experimental setup used a contact time of 2.5 ms, a repetition delay of 10 s (with a few exceptions given in detail in the Supporting Information), and an acquisition time of 45 ms.

The solution ¹H NMR spectra in anhydrous acetone-*d*₆ (dried over molecular sieves for 48 h) were recorded in order to evaluate the presence of solvents in crystal lattices of the obtained cocrystals. The spectra were recorded using a 500 MHz Bruker Avance III spectrometer and calibrated at the residual solvent signal. In order to estimate the amount of water present in the crystal, all ¹H signals were integrated and an integral value of 1 was assigned to a well-resolved signal at 4.78 ppm, originating from one LIN hydrogen atom. Water in acetone resonates at ca. 2.9 ppm, so its amount was estimated from the integral value of ¹H signals found at this resonating frequency. For all acquired ¹H NMR solution spectra, see Supporting Information Figure S15.

Powder X-Ray Diffraction (PXRD). All powder X-ray diffractograms were collected using a Bruker D8 Advance or a Panalytical AERIS diffractometer using a Cu K α radiation source (λ = 1.5406 Å) in the Bragg–Brentano horizontal geometry. The data were acquired in the 2 θ range of 4–50° with a step of 0.0297°. The diffractograms were analyzed with GSAS II software.⁵⁸

Thermogravimetric Analysis (TGA) and DSC Measurements. The DSC measurements were performed using a 2920 MDSC V2.6A instrument (TA Instruments) using hermetically closed aluminum pans and a nitrogen flow of 50 mL. A two-point temperature calibration on tin and indium was used. The heating rate was set to 10 K/min. The TGA measurements were carried out using 2950 TGA HR V5.4A equipment (TA Instruments) using platinum pans and a nitrogen flow of 60 mL. The heating rate was set to 10 K/min. All DSC and TGA plots were prepared using Matplotlib⁵⁹ in Python 2.7.

Virtual Cocrystal Screening Methods and Theoretical Calculations. *Molecular Complementarity (MC).* A MC survey was conducted using Mercury 4.3.1 software.⁶⁰ To create the .xyz files, five different conformations of LIN present in its known crystal structures were taken in turns as an active substance (LIN_II, LIN_III, LIN:BA cocrystal, LIN:PHBA cocrystal hydrate, and LIN:2,6-DHBA cocrystal) and evaluated against all tested coformers (each in one conformation only; the conformations were retrieved from a crystal structure taken for mechanochemical grinding, see evaluation of the coformer solid forms in the Supporting Information, and converted

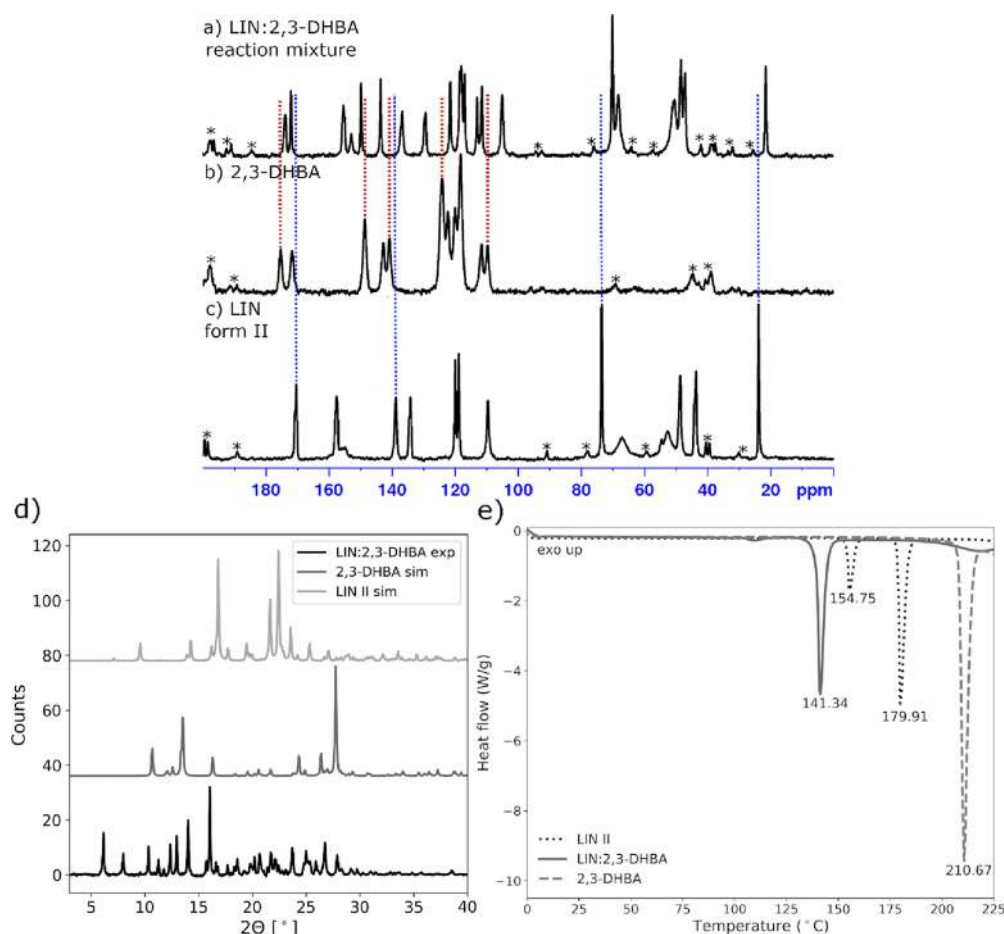


Figure 2. (a–c) ^{13}C CPMAS NMR spectra recorded at a spinning speed of 8 kHz for the reaction mixture obtained after mechanochemical grinding of LIN form II in the presence of H_2O (LAG) with 2,3-DHBA (a) as well as the spectra recorded for the respective pure compounds: (b) 2,3-DHBA and (c) LIN form II. Dotted lines show a shift of the ^{13}C resonances of LIN form II and 2,3-DHBA, indicating the formation of the LIN:2,3-DHBA cocrystal; asterisks indicate spinning sidebands; (d) experimental PXRD diffractogram of the LIN:2,3-DHBA reaction mixture and simulated PXRD diffractograms of LIN form II and 2,3-DHBA triclinic polymorph; (e) DSC thermograms of the LIN:2,3-DHBA reaction mixture, LIN form II, and triclinic polymorph of 2,3-DHBA.

into a .xyz file). All main molecular descriptors (M/L axis ratio, S/L axis ratio, S axis, dipole moment magnitude, and fraction of N and O atoms) were used.

Hydrogen Bond Propensity (HBP). The HBP calculations were performed using Mercury 4.3.1 software⁶⁰ for preparing the .mol files as for the MC survey, with the exception of LIN, for which only one conformation (from LIN form II) was tested. Each time, the functional groups suggested by Mercury were accounted for, and for each of them, a training set on the basis of at least 350 crystal structures was created. The quality of each of the obtained models (the level of discrimination) is expressed as the area under the receiver operating characteristics (ROC) curve and is given together with the prediction results listed in Table 4. From each of the obtained models, a multicomponent score was calculated by subtracting the highest propensity for the homodimeric interaction (either between two molecules of LIN or between two molecules of a coformer) from the highest heterodimeric propensity (LIN–coformer interaction). Values of multicomponent score ≥ 0 suggest that a heterodimeric interaction will be preferred over a homodimeric one.

Molecular Electrostatic Potential (MEP) Maps. In MEP map calculations, different conformations of LIN and cofomers present in their known solid forms were accounted for. Each time, a conformation was retrieved from the crystal structure of a considered molecule after geometry optimization of this structure under periodic boundary conditions (see details of the geometry optimization below). For the geometry-optimized molecules, MEP maps were calculated using Gaussian16 software⁶¹ and B3LYP/6-311G(d,p)⁶²

electron density. The density and potential cubes were calculated using 100^3 grid points per side and visualized and analyzed with GaussView4 software. The energy values on the respective maxima and minima points from each MEP map were recalculated to the α or β parameter for a given site using the equations derived by Musumeci et al.:²⁹ $\alpha = 0.0000162 \text{ MEP}_{\text{max}}^2 + 0.00962 \text{ MEP}_{\text{max}}$ and $\beta = 0.000146 \text{ MEP}_{\text{min}}^2 - 0.00930 \text{ MEP}_{\text{min}}$. All values were then used for the estimation of homo- and heterodimeric interaction energies as explained in Results and Discussion section. For all the obtained numerical values, see Table S4, Supporting Information.

Intermolecular Energy Calculations. To calculate the intermolecular energy of each of the cofomers and LIN, the respective crystal structures of the solid forms taking part in the mechanochemical reaction were first geometry-optimized under periodic boundary conditions with the CASTEP 19 code,⁶³ keeping all cell parameters fixed and allowing for all atoms to relax. A k -point grid of 0.07 \AA^{-1} and an energy cutoff of 600 eV was used, together with the PBE⁽⁶⁴⁾ functional with the Grimme D2 dispersion correction scheme.⁶⁵ The energy value obtained after geometry optimization is the total energy value for a given solid form and was each time expressed as the amount of energy per molecule in an asymmetric unit cell. All symmetry-unrelated molecules in a given solid form were retrieved from the geometry-optimized structure and put into a 20 \AA box (so that no intermolecular interactions were observed) and their energies were calculated at the same level of theory as above. The values obtained from these calculations are the intramolecular energies of each of the species and can be subtracted from the total energy values

to obtain the intermolecular energy term (sometimes referred to as lattice energy), E^{inter} . The final values of E^{inter} are expressed in kJ/mol of molecules. All numerical values from CASTEP calculations are listed in Table S5, Supporting Information.

RESULTS AND DISCUSSION

Experimental Screening Results. Experimental Determination of Cocrystal Formation. In our experimental screening, mechanochemical formation of cocrystals was selected as a method of choice for two main reasons. First, in the majority of cases, there is a notable difference in the solubilities of LIN and the tested coformers in water and many organic solvents.⁵² As a result, many classic solution crystallization attempts failed, with pure components precipitating separately from the solvents used, not because of a lack of tendency to form cocrystals but because of the mentioned solubility differences. Also because of this reason, we were not able to obtain XRD-quality single crystals for the new crystalline forms reported in this work. Second, the use of a solvent as a crystallization environment introduces large quantities of a new entity to the studied system, and the energy of the interactions of API and coformers with this entity (solvent) should be additionally accounted for (including a possibility of assuming different conformations, sometimes significantly different from those present in the solid phase). In contrast, in mechanochemical reactions, solid phases interact with each other, with the solvent–solid interactions (in the case of the LAG method) limited to a minimum. This exclusion of solvent–solid interactions allows us to gain a better understanding of the extent to which the energetic factors (energy of particular intermolecular interactions as well as all intermolecular interactions present in a given solid and expressed as the intermolecular or lattice energy of this solid) govern the formation of cocrystals under the studied conditions.

The outcome of the performed mechanochemical grinding was evaluated each time by ^{13}C CPMAS NMR spectroscopy. For the case of the five coformers previously shown to form cocrystals with LIN, the obtained spectra were compared with the ones recorded before for the respective cocrystals.⁵² In all other cases, if the NMR spectra indicated possible formation of a cocrystal, PXRD, DSC, and TGA experiments were performed. Figure 2 shows the ^{13}C CPMAS NMR spectra, PXRD diffractograms, and DSC thermograms of pure LIN form II, triclinic polymorph of 2,3-DHBA, and LIN:2,3-DHBA reaction mixture as an example of the case in which the formation of the cocrystal was observed. The exemplary experimental data for the case of VA, in which the outcome of the reaction was negative, are shown in Figure 3. All the other ^{13}C CPMAS NMR spectra, PXRD diffractograms, DSC thermograms, and TGA results are shown in Figures S1–S35 (Supporting Information).

Figure 2 shows how the outcome of a mechanochemical reaction can be elucidated on the basis of the ^{13}C CPMAS NMR spectra. After mechanochemical grinding of 2,3-DHBA with LIN form II in the presence of water to create LAG conditions (Figure 2a), most of the ^{13}C resonances in the solid-state NMR spectra were shifted in comparison to pure components (Figure 2b,c), which indicates that changes in crystal lattices took place for both compounds. This is particularly obvious when comparing the ^{13}C CPMAS NMR spectrum of pure 2,3-DHBA with that of the reaction mixture. In the first instance, the number of ^{13}C resonances is

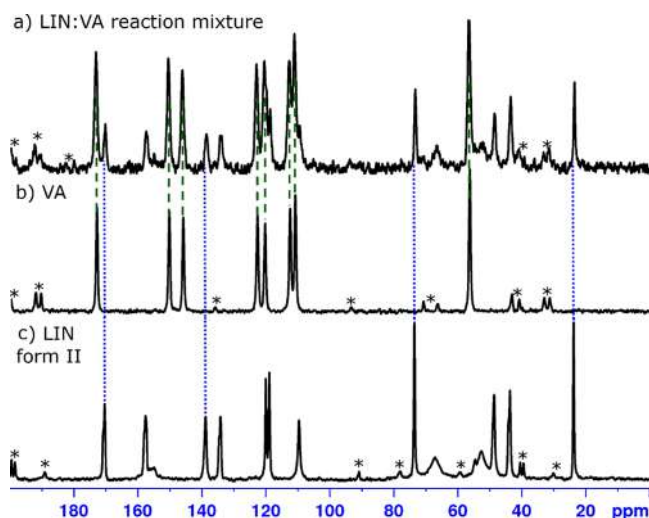


Figure 3. ^{13}C CPMAS NMR spectra recorded at a spinning speed of 8 kHz for the reaction mixture obtained after mechanochemical grinding of LIN form II in the presence of H_2O (LAG) with VA (a) as well as the spectra recorded for the respective pure compounds: (b) VA and (c) LIN form II. Dotted lines show that no shift of the ^{13}C resonances of LIN form II and VA took place after grinding, indicating a negative outcome of the cocrystallization attempt; asterisks indicate spinning sidebands.

doubled in comparison to the number of carbon atoms present in this molecule. This is in agreement with the crystal structure of the triclinic polymorph of 2,3-DHBA, crystallizing with two molecules present in the asymmetric part of a crystallographic unit cell.⁶⁶ Upon grinding with LIN, however, the number of carbon resonances in the NMR spectrum of the reaction mixture corresponds to the sum of the number of carbon atoms in one LIN and one 2,3-DHBA molecule. Since grinding 2,3-DHBA alone in the presence of water does not result in any changes to its crystalline phase, as determined from ^{13}C CPMAS NMR experiments, the change observed after grinding with LIN in both compounds indicates the formation of a new crystalline form, that is, a cocrystal. PXRD data obtained for the same reaction mixture confirm the formation of a new crystalline phase, which is different from either of the pure components and their other polymorphic forms. The formation of the LIN:2,3-DHBA cocrystal is further corroborated by the results of the DSC measurements, featuring one sharp endothermic event at ca. 141.3 °C, corresponding to the melting of a new crystal phase and clearly distinguishable from the DSC events present in the thermograms of pure components. The TGA results did not show any loss of mass before the endothermic event associated with melting; hence, this cocrystal does not contain any solvent molecules. This lack of solvent molecules in the crystal lattice of the cocrystal is further confirmed by the solution ^1H NMR measurements in anhydrous acetone- d_6 (see Figure S15, Supporting Information).

Contrarily to the example of LIN:2,3-DHBA, in the ^{13}C CPMAS NMR spectrum of the reaction mixture obtained after grinding LIN form II with VA in the presence of water to create LAG conditions (Figure 3), no changes were detected in the chemical shifts of all ^{13}C resonances for both pure components (spectra shown in Figure 3b,c). This alone may suggest that the cocrystallization attempt was unsuccessful. This is further corroborated by a clear difference in the signal

intensities of the ^{13}C resonances originating from LIN and VA, despite the molar ratio of both components in the reaction being 1:1. This difference arises from the differences in the ^1H relaxation times for both crystalline forms. LIN is known to have a rather long relaxation time and therefore requires a longer repetition time during the recording of the solid-state NMR spectra (even as long as 120 s).⁵³ In contrast, the experimental relaxation time for VA is much shorter. Since it is known that compounds bound together in one crystal lattice have similar ^1H relaxation times, the differences observed here further confirm that a cocrystal between LIN and VA was not formed.

In such a manner, based primarily on the analysis of the ^{13}C CPMAS NMR spectra recorded for all pure components and reaction mixtures obtained after mechanochemical grinding with LIN under different conditions, the formation of LIN cocrystals was evaluated, and if confirmed by the NMR results, corroborated with PXRD, DSC, and TGA measurements. All these experimental data are provided in the [Supporting Information](#). In total, the formation of 11 cocrystals was confirmed: five of them were previously characterized cocrystals and cocrystal hydrates with BA, PHBA, 2,6-DHBA, 3,4-DHBA, and GA and another six are new, previously not reported crystal phases formed by LIN with 2,3-DHBA, 3,5-DHBA, 2,4-DHBA, 2,5-DHBA and water, 2,4-DHBA and water, and PABA and water. The determination of the crystal structures of these six new cocrystals is beyond the scope of this work, especially that all our crystallization attempts to obtain monocystals suitable for single-crystal X-ray diffraction failed. As a result, their structural determination requires further studies, possibly using the NMR crystallography approach. Such studies will be continued in our laboratory.

Structural Features of the Coformers Forming Cocrystals with LIN. Table 1 lists the summary of the outcomes of the performed mechanochemical reactions including the conditions necessary for a particular coformer to form cocrystals with LIN. The formation of cocrystals with LIN was observed for BA and all hydroxybenzoic acid derivatives under at least one of the tested conditions. Overall, the coformers tending to form cocrystals with LIN under the tested conditions have an acidic group ($-\text{COOH}$) directly substituted to an aromatic ring. This, however, does not suffice to ensure successful cocrystal formation as there are cases in which this condition is fulfilled and yet no cocrystal is formed under either of the tested conditions. This occurs in VA, INA, and SA, compounds with only small structural differences with respect to coformers found to form the cocrystals: VA differs from 3,4-DHBA only in the presence of one $-\text{OCH}_3$ group instead of a $-\text{OH}$ group, INA has a pyridine ring instead of a benzene ring present in BA, while in SA, the sulfonyl group is attached to a benzene ring in *para* position to an amino group, in contrast to PABA, which contains a carbonyl group and *p*-amino substituent. Clearly, the sole possibility of forming similar supramolecular synthons is not enough to a priori indicate cocrystal-forming coformers. This is perhaps not surprising in the light of the recently published crystal structures of five of these cocrystals,⁵² showing no clear tendency of LIN to form one particular supramolecular synthon.

Interestingly, there is also a difference in the propensity toward the formation of cocrystals with LIN between six isomeric dihydroxybenzoic acids. 2,6-DHBA and 3,4-DHBA form cocrystals very easily, with 2,6-DHBA being the least demanding coformer among all tested chemicals and the sole

one forming cocrystals with LIN regardless of the conditions used during mechanochemical grinding. In comparison, 2,3-DHBA requires addition of any of the tested solvents to create LAG conditions, but 2,4-DHBA and 2,5-DHBA require addition of substantial amounts of polar solvents (water or methanol) as liquid assistants. Finally, 3,5-DHBA forms cocrystals with LIN only in the presence of methanol. In addition, 2,4-DHBA was found to form two different cocrystals: a neat one obtained after grinding the coformer with LIN in the presence of methanol and the other, a cocrystal hydrate, obtained after grinding the coformer with LIN in the presence of water.

Influence of the Polymorphic Form of LIN on the Reaction Outcome. In all cases but one neat mechanochemical grinding of LIN_II with the tested coformers failed to produce cocrystals, the only exception being LIN_II and 2,6-DHBA, which required 3 h of neat grinding to obtain full conversion to the cocrystal. Contrarily, neat grinding with LIN_III produced cocrystals with BA, 2,6-DHBA, 3,4-DHBA, GA, and PHBA, although in this last case a full conversion to the cocrystal was not achieved, even under a prolonged reaction time. Interestingly, grinding LIN_III alone or in the presence of a small amount of water or methanol always led to a phase transition to LIN_II. This indicates the lower room temperature stability of LIN_III in comparison to LIN_II and explains the easier formation of cocrystals when using LIN_III as a starting material. This conclusion is partially supported by quantum chemical calculations performed for both crystal forms of neat LIN. The total energy difference between the geometry-optimized crystal structures of both polymorphic forms calculated at the PBE-D2 level of theory is equal to only 1 kJ/mol of molecules, with form II being more stable. Note, however, that this value is within the uncertainty limits of PBE-D2 predictions. This total energy is the sum of the intramolecular energy contribution (the gas phase energy of a molecule in the conformation present in a crystal lattice) and the intermolecular energy contribution (sometimes referred to as the lattice energy, arising only from intermolecular interactions between the molecules in a crystal). The energy difference between the polymorphs of LIN in terms of this latter term, that is, intermolecular energy E^{inter} , is much more significant than the total energy difference and is equal to 7 kJ/mol of molecules (see Table S3, Supporting Information for the numerical values of the obtained energy and its components). Such a difference may explain the reason behind LIN_III being more susceptible to the breaking of its crystal lattice, which in turn can lead to easier formation of the cocrystals, especially if no significant change to the conformation of LIN molecules is necessary.

Apart from the influence of the polymorphic form of LIN on the outcome of grinding, we also noticed the influence of the coformers on the mechanochemical transformation of LIN form III to LIN form II. LIN form III alone was easily transformable to form II during grinding (see Figure S50, Supporting Information, for ^{13}C CPMAS NMR spectra of pure LIN_II and LIN_III as well as LIN_III after 30 and 60 min of grinding). However, in the presence of the majority of the coformers for which neat grinding with LIN_III did not produce cocrystals, the ^{13}C NMR signals originating from this form of LIN were clearly visible in the reaction mixture even after 60 min of grinding (see Supporting Information, Figures S25–S34). This means that the sole presence of these coformers inhibited LIN_III \rightarrow LIN_II transformation or

even prevented it entirely (see for example the NMR spectra of the reaction mixture of LIN_III and MAL, Figure S34, Supporting Information). We did not notice such an effect only in the case of BARB and INA. One of the possible explanations for the observed inhibition is that when both components are present, the collision energy is distributed evenly to the coformer and LIN, and hence, less mechanic energy is transferred to LIN alone. On the other hand, some other effects such as stabilization of LIN_III by certain coformers cannot be excluded, especially that the observed degree of inhibition of LIN_III to LIN_II transformation was different for different coformers.

Influence of the Presence of Solvent (LAG Conditions) on the Reaction Outcome. In comparison to neat grinding, LAG using methanol or water (both polar solvents) was always more efficient in producing LIN cocrystals. In four cases (2,4-DHBA, 2,5-DHBA, 3,5-DHBA, and PABA), the cocrystals were produced only when one of these solvents was used as liquid assistants. In contrast, the usage of toluene as a liquid assistant was not always beneficial. This method of cocrystal preparation did not lead to cocrystals of LIN with PHBA (in contrast to neat grinding of LIN form III with PHBA) and was only partially effective in the case of the LIN:GA cocrystal, even after 3 h of grinding. This poor performance of toluene as a liquid assistant may be associated with low solubility of LIN and most of the coformers in this solvent, in contrast to methanol and water, which are able to dissolve the studied chemicals, although in some cases rather poorly. It is worth noting that there is no direct correlation between the solubility of a given coformer in either methanol or water and the efficiency of a given solvent as a liquid assistant. For example, the LIN:PABA cocrystal was produced only in the presence of water, despite much better solubility of PABA in methanol than in water.

To further investigate the influence of the amount of solvent addition on the outcome of mechanochemical synthesis of the studied cocrystals, we selected two “difficult” coformers, that is, PHBA and 2,5-DHBA, for which the complete conversion to the respective cocrystals was possible only after adding a substantial amount of a liquid assistant. Figure 4 shows the ^{13}C CPMAS NMR spectra recorded for the reaction mixtures obtained after grinding PHBA, LIN_II, and different amounts of methanol (Figure 4a) as well as 2,5-DHBA, LIN_II, and different amounts of water (Figure 4b). Conversion of a starting material to a cocrystal can be easily observed in both cases by monitoring the ^{13}C signal originating from the methyl group of LIN (the most right-hand side signal) as its chemical shift is slightly different in LIN_II and in the respective cocrystals. This signal is marked in Figure 4a,b with a red dotted line. As can be seen in the case of both coformers, equimolar amounts of solvents with respect to LIN were not nearly enough to obtain full conversion to cocrystals. For 2,5-DHBA, the smallest amount of the solvent needed for the cocrystal signals to be observable was equal to 2 molar equivalents with respect to LIN and 2,5-DHBA, and increasing this amount to 4 molar equivalents was enough to obtain full conversion, with only slightly better crystallinity (narrower ^{13}C resonances) obtained upon further increase to 6 molar equivalents. Note that any further increase above 6 molar equivalents did not cause changes to the reaction outcome. In contrast, to obtain full conversion of PHBA and LIN_II to a cocrystal, as much as 21 molar equivalents of methanol was necessary. Perhaps the most interesting observation is that a

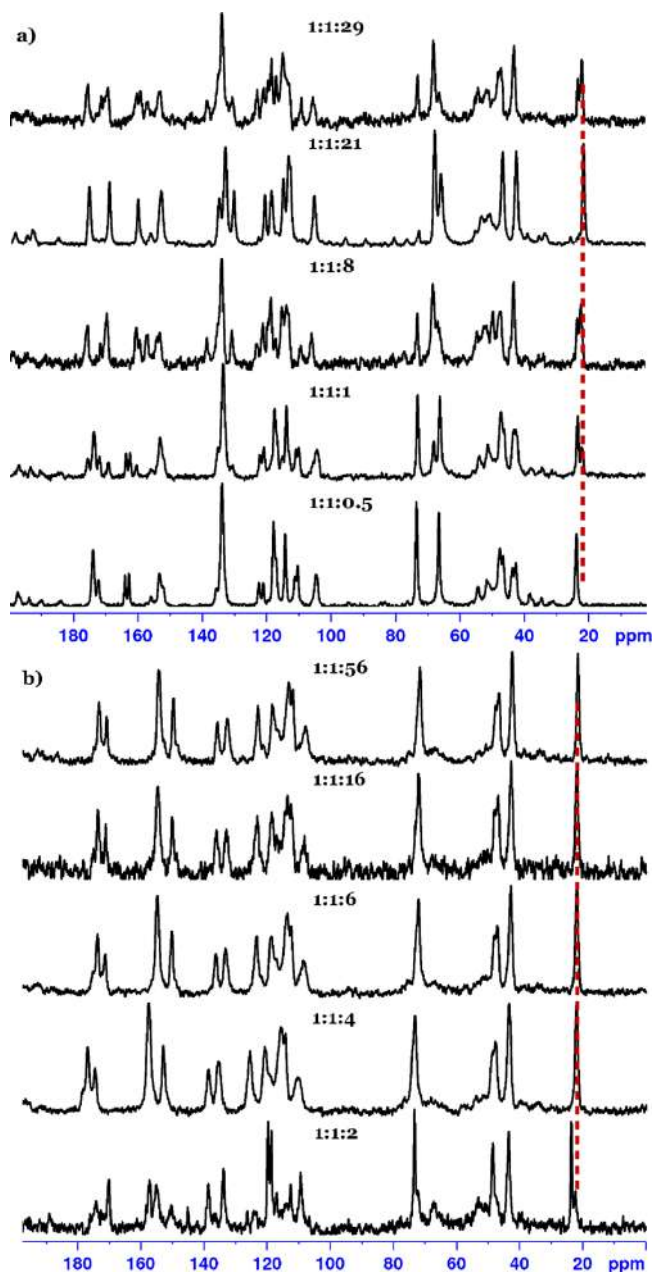


Figure 4. ^{13}C CPMAS NMR spectra of reaction mixtures obtained after grinding LIN_II with PHBA (a) and 2,5-DHBA (b) with varying amounts of methanol and water, respectively. The amount of the solvent is given in each spectrum in a molar ratio with respect to LIN and the coformer. The red dotted line denotes the emerging ^{13}C signal originating from the respective cocrystals.

further increase in the amount of solvent seems to yield worse results. This may be due to the fact that such an amount of solvent led to full dissolution of one of the components of the reaction mixture, which could result in recrystallization of the neat form upon evaporation of the solvent.

The Understanding Gained from the Prediction Methods Used in Virtual Cocrystal Screening. MC. MC is one of the knowledge-based methods used for the prediction of cocrystal formation, with its main focus being the molecular shape and polarity.²⁷ In the original paper regarding MC, it was found that the molecular descriptors concerning those two features seem to be the most decisive in the identification of

the most probable cofomers for a given molecule. It was shown in ref.²⁷ that molecules tend to form cocrystals with cofomers similar in shape. Three geometrical descriptors were introduced, M/L ratio, S, and S/L ratio, where S, M, and L are the lengths of the shortest, medium, and longest axes of a rectangular box enclosing the van der Waals volume of a molecule, all numerically describing the geometrical shape of the analyzed molecule and of the molecules present in a set of potential cofomers. Descriptors defined in such a way will therefore vary (sometimes significantly) depending on the molecular conformation of a cofomer, as also noticed very recently by Costa et al.⁶⁷ but often disregarded in many works exploiting MC as a cocrystal prediction tool. Apart from purely geometrical considerations, MC tests and compares also the dipole moment magnitude and fraction of nitrogen and oxygen atoms for the considered molecules. After calculating the molecular descriptors for a cofomer and the molecule of interest, the results of MC screening are given as a “pass” or “fail” flag for the cofomers for which the successful formation of a cocrystal is predicted or not, respectively. A “fail” flag means that a cofomer and a substance of interest were found incompatible in at least one of the considered descriptors.

For the majority of cofomers used in this study, changes to their conformation do not alter their S, M, and L parameters significantly. This, however, is not the case for LIN. Figure 5

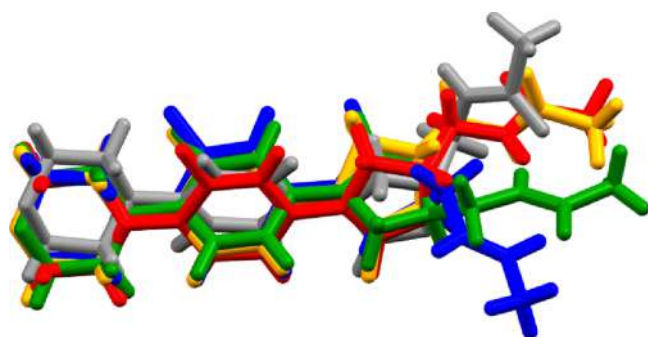


Figure 5. Molecular overlay of five distinct conformations of LIN found in its five different crystal structures. For the color description, see Table 2.

shows the molecular overlay of five different conformations of LIN found in its five different crystal structures, LIN_II, LIN_III, LIN:2,6-DHBA, LIN:BA, and LIN:PHBA:H₂O, while in Table 2, the molecular descriptors of each conformation used in the MC evaluation are listed. The five conformations of LIN differ mainly in terms of the M/L axis ratio and this is

Table 2. Molecular Descriptors Used in the MC Approach for Different Conformations of LIN

conformation	color in Figure 5	M/L axis ratio	S axis (Å)	S/L axis ratio	dipole moment magnitude(D)
LIN_II (1)	yellow	0.414	5.763	0.307	2.337
LIN_III ^a (2)	green	0.413	5.887	0.314	4.012
LIN:BA (3)	gray	0.543	5.821	0.339	5.859
LIN:2,6-DHBA (4)	red	0.416	6.629	0.358	3.696
LIN:PHBA:H ₂ O (5)	blue	0.554	5.936	0.350	5.836

^aNote that in LIN_III, two distinct conformations of LIN are present but their molecular descriptors are almost the same.

mostly due to the differences in the position of the methylacetamide chain. The observed differences are significant enough to influence the outcome of the MC screening; hence, all five conformations of LIN were accounted for in the evaluation. Table 3 summarizes the results obtained for each conformation together with a color-coded reason for getting a “fail” flag (if applicable).

Table 3. Results of MC Evaluation and their Comparison with the Experimental Results^a

molecule	conformation of LIN					cocrystal observed experimentally?
	1	2	3	4	5	
BA	pass	fail	pass	pass	pass	yes
PHBA	pass	pass	pass	pass	pass	yes
2,6-DHBA	fail	fail	fail	fail	fail	yes
3,4-DHBA	pass	pass	pass	pass	pass	yes
2,5-DHBA	fail	fail	pass	fail	pass	yes
2,4-DHBA	fail	fail	pass	fail	pass	yes
2,3-DHBA	fail	fail	pass	fail	pass	yes
3,5-DHBA	fail	fail	fail	fail	fail	yes
GA	fail	fail	pass	fail	pass	yes
VA	fail	fail	fail	fail	fail	no
PABA	pass	pass	pass	pass	pass	yes
SA	fail	fail	fail	fail	fail	no
INA	fail	fail	pass	fail	pass	no
INN	fail	fail	pass	fail	pass	no
IBU	pass	pass	pass	pass	pass	no
TYR	fail/fail	fail/fail	fail/fail	fail/fail	fail/fail	no
PRO	fail/fail	fail/fail	fail	fail/fail	fail	no
MAL	fail	fail	fail	fail	fail	no
BARB	fail	fail	fail	fail	fail	no
success rate						
overall	12/19	11/19	14/19	12/19	14/19	
NG LIN_II	12/19	13/19	6/19	12/19	6/19	
NG LIN_III	15/19	14/19	11/19	15/19	11/19	
LAG Tol	13/19	12/19	10/19	13/19	10/19	
LAG MeOH	11/19	10/19	13/19	11/19	13/19	
LAG H ₂ O	13/19	12/19	15/19	13/19	15/19	

^aIf a given system received a “fail” flag in the MC evaluation, the reason for the lack of complementarity is color-coded: M/L ratio is denoted as red, S/L ratio as blue, and dipole moment magnitude as yellow. If there is more than one reason for a “fail” flag, both are marked in the respective colors. NG—neat grinding with either LIN form II or LIN form III.

The successful prediction of cocrystal formation was obtained in 32–79% of cases depending on the considered conformation of LIN and the method of cocrystal synthesis accounted for in comparison with the prediction results. Overall, the most frequent reason for getting a “fail” flag because of a lack of complementarity was the M/L axis ratio between LIN and cofomers. That is why two conformations of LIN having a methylacetamide chain deviated from the longest axis of a molecule were found to have a better complementarity with many cofomers than the conformations with this chain positioned along the L axis. As a result, the success rate of cocrystal prediction was notably improved for these two conformations. These results underline the benefits of accounting for different molecular conformations, which can be present in crystalline forms of a studied molecule.

Table 4. HBP Results Expressed as the Highest Propensities toward the Formation of either Heterodimeric or Homodimeric Hydrogen Bond Interactions (with Statistical Uncertainties), Multicomponent Score, and Area under the ROC Curve, Expressing the Trustworthiness of the Predictive Model^a

molecule	highest propensity		multicomponent score	area under the ROC curve	cocrystal observed experimentally?
	heterodimer	homodimer			
BA	0.70 ± 0.10	0.69 ± 0.07	0.01	0.853	yes
PHBA	0.67 ± 0.10	0.67 ± 0.07	0.00	0.861	yes
2,6-DHBA	0.67 ± 0.10	0.68 ± 0.07	−0.01	0.861	yes
3,4-DHBA	0.69 ± 0.10	0.66 ± 0.08	0.03	0.856	yes
2,5-DHBA	0.67 ± 0.10	0.65 ± 0.07	0.02	0.857	yes
2,4-DHBA	0.71 ± 0.09	0.69 ± 0.07	0.02	0.862	yes
2,3-DHBA	0.69 ± 0.10	0.68 ± 0.07	0.01	0.857	yes
3,5-DHBA	0.68 ± 0.10	0.65 ± 0.08	0.03	0.857	yes
GA	0.71 ± 0.10	0.70 ± 0.07	0.01	0.860	yes
VA	0.63 ± 0.10	0.66 ± 0.07	−0.03	0.858	no
PABA	0.87 ± 0.06	0.65 ± 0.08	0.22	0.865	yes
SA	0.94 ± 0.06	0.99 ± 0.01	−0.05	0.911	no
INA	0.70 ± 0.08	0.66 ± 0.10	0.04	0.844	no
INN	0.76 ± 0.17	0.64 ± 0.21	0.08	0.814	no
IBU	0.51 ± 0.10	0.55 ± 0.07	−0.04	0.848	no
TYR	0.84 ± 0.07	0.94 ± 0.02	−0.10	0.877	no
PRO	0.77 ± 0.07	0.93 ± 0.02	−0.16	0.886	no
MAL	0.61 ± 0.09	0.56 ± 0.07	0.05	0.851	no
BARB	0.77 ± 0.18	0.77 ± 0.18	0.00	0.822	no

^aBolded positions indicate incorrect prediction by HBP.

It is also interesting to note that the success rate of the MC approach can be significantly different for different reaction conditions used during cocrystal preparation. For example, due to the generally lower reactivity of LIN_II, the outcome of neat grinding of this form with the studied coformers agrees with the MC predictions in only 32% for two of the considered conformations. It should therefore be stressed that a lack of agreement with the prediction results may not only be the fault of the prediction method but also of the limits put on the reaction conditions used for comparing the screening results.

HBP. HBP is another knowledge-based approach for cocrystal prediction that analyzes and ranks possible hydrogen-bonded supramolecular synthons according to the probability of their formation. This probability is estimated from the occurrence of a given interaction in a set of crystal structures published in the CSD and referred to as the propensity of this interaction.²⁸ Although the method itself was developed to assess the risk of polymorphism of a molecule, it is also useful in the evaluation whether the tendency to form heterodimeric interactions in a cocrystal will prevail over the tendency to form homodimeric interactions in pure forms.³³ Used in such a way, the HBP calculations return a multicomponent score, which is the difference between the highest propensity obtained for a heterodimer and the highest propensity obtained for a homodimer. Therefore, any positive value of the multicomponent score suggests the potential tendency for cocrystal formation.

As the HBP method primarily accounts for the specific functional groups present in an analyzed molecule, its molecular conformation should not, as a rule, influence the HBP predictions, although some steric effects around potential donors and acceptors of hydrogen bonds are included in the predictive model. Because of this, the HBP calculations were performed only for one conformation of LIN. Table 4 summarizes the highest homo- and heterodimeric hydrogen bond propensities with statistical uncertainties and multi-

component scores obtained for each of the studied systems together with the respective values of the area under the ROC curves, representing the level of discrimination in each case (i.e., the quality of the predictive model—the higher the value, the more trustworthy the predictions).²⁸ For the vast majority of the tested systems, the obtained values of the multicomponent score were close to 0, suggesting that the formation of the respective cocrystals is not excluded but also that it is not very favorable in terms of offering an attractive hydrogen bonding alternative in comparison with neat forms. Out of our list of 19 coformers, only one received a multicomponent score with LIN well above 0, *p*-aminobenzoic acid (PABA). At the same time, this is the only case with a positive multicomponent score even for the border cases (i.e., limits of the statistical uncertainties). Overall, assuming that the cutoff value of the multicomponent score indicating possible cocrystal formation is equal to or higher than 0 (as recommended by the authors of the method, see ref.³³), the HBP calculations successfully predicted the formation of cocrystals in 74% of cases. It is, however, worth stressing that there was only one case of false negative indication (regarding LIN and 2,6-DHBA) and it was not a very strong one (even more so, accounting for the statistical uncertainties of the established propensities), with the value of the multicomponent score obtained for this system equal to −0.01. Therefore, it may be concluded that the LIN–coformer interactions will, in a majority of cases, be at least competitive with LIN–LIN or coformer–coformer interactions.

MEP Maps. HBP calculations account only for the best hydrogen bond donor–acceptor pair, which is probably the most common reason for unsuccessful predictions of cocrystal formation by this model. More often than not crystals are stabilized by a sum of different intermolecular interactions, formation of which may be more favorable than the formation of one particular interaction, albeit a strong one. In contrast, MEP maps consider all possible pairs of electrostatic

interactions. In this method, for each possible interacting site, α or β value is calculated, reflecting the strength and direction of its interaction with a unit charge (α values represent hydrogen bond-donating sites, whereas β values represent hydrogen bond-accepting ones). Then, all sites are paired according to the strength of their interactions so that the overall energy gain from all possible electrostatic interactions between two given molecules can be calculated.²⁹ As a result, MEP maps give an estimate of the energy gain upon cocrystal formation. In this case, each molecule is treated as a whole, and therefore, its molecular conformation may influence the obtained results significantly. This, in particular, is the case for molecules capable of forming intramolecular hydrogen bonds. Such interactions can noticeably change the propensity of a given site to act as a hydrogen bond donor or acceptor. Because of this, we decided to calculate MEP maps for all conformations of the tested cofomers present in their known crystal forms. The same was also done for the LIN molecule.

As stated above, in the MEP-based method, α and β values are paired together according to their values (the highest donor with the highest acceptor, the second highest donor with the second highest acceptor, and so on) to calculate the interaction energy between two given molecules according to the equation

$$E = -\sum_i \alpha_i^* \beta_i$$

This is done for the molecule of interest as well as for each of the cofomers. Then, α and β values for the molecule of interest and for a given cofomer are combined together, ordered according to their values, and again the interaction energy is calculated. Finally, the possible energy gain (ΔE , kJ/mol) upon cocrystal formation is calculated according to the below equation

$$\Delta E = E^{\text{cocrystal}} - (E^{\text{linezolid}} + E^{\text{coformer}})$$

in which each of the energies denotes the interaction energies calculated from α and β values. Table 5 summarizes the obtained ($-\Delta E$) values for five conformations of LIN and all considered cofomers, including their conformations, if applicable. The higher the absolute value of ΔE , the most probable the cocrystal formation, with the threshold of 11 kJ/mol being established as a value denoting more than 50% probability that a given cocrystal will be formed.²⁹ As this is not a simple “yes” or “no” answer, establishing the prediction success rate is tricky, but it is clear from the inspection of Table 5 that the obtained $-\Delta E$ values are higher than 8 for at least one of the conformation of the considered cofomers experimentally forming cocrystals with LIN, with one exception of BA. In the case of the cofomers that did not form cocrystals with LIN in neither of the tested conditions, the $-\Delta E$ values were in the range of 0–7, suggesting a much lower probability of cocrystal formation. No cases of false-positive indications occurred (understood as indicating a probability of cocrystal formation higher than 50%). It is worth noting that the MEP-based approach is the only one among the tested methods not yielding any false-positive result. Note that in the case of TYR and PRO, the $-\Delta E$ values were calculated for neutral forms of these amino acids, while in all known crystal structures, both molecules exist in their zwitterionic forms. Accounting for such forms would require establishing a new $-\Delta E$ threshold, which requires a lot of computational effort and is beyond the scope of this work.

Table 5. $-\Delta E$ Values (in kJ/mol) Calculated from MEP Maps for Five Conformations of LIN and all Considered Cofomers

molecule	conformation of LIN				cocrystal observed experimentally?
	1	2	3/5 ^a	4	
BA	2	2	1	1	yes
PHBA-1	8	8	8	8	yes
PHBA-2	8	8	8	8	
2,6-DHBA-1	1	1	2	1	yes
2,6-DHBA-2	9	9	9	9	
3,4-DHBA	10	10	10	10	yes
2,5-DHBA	10	11	9	11	yes
2,4-DHBA	9	10	9	10	yes
2,3-DHBA	9	9	9	9	yes
3,5-DHBA-1	12	13	11	12	yes
3,5-DHBA-2	13	13	12	13	
3,5-DHBA-3	13	14	12	13	
GA-1	16	17	16	16	yes
GA-2	17	17	16	16	
GA-3	17	17	17	16	
GA-4	17	17	17	16	
VA	4	5	4	4	no
PABA	7	8	8	7	yes
SA	5	5	5	5	no
INA	2	2	1	2	no
INN	1	1	1	1	no
IBU-1	2	2	1	2	no
IBU-2	2	2	1	2	
IBU-3	1	1	0	1	
TYR ^b	2	2	2	1	no
PRO ^b	1	0	2	0	no
MAL	5	5	4	5	no
BARB	7	7	6	5	no

^aThe results obtained for LIN conformations 3 and 5 were identical.

^bThe results are given for neutral molecules; in their crystal structures, PRO and TYR tend to be present in zwitterionic forms.

In the original work on virtual cocrystal screening using MEP maps, only the most stable conformation in the gas phase was considered, which is a fair approximation.²⁹ However, because of that there are no data showing how molecular conformation can influence the prediction outcome. Our analysis indicates that the conformation of LIN did not change significantly the obtained results. The differences in the $-\Delta E$ values between different conformations of LIN are at most equal to 2. The same applies for the majority of the cofomers with the exception of 2,6-DHBA. The reason for this exceptional behavior of 2,6-DHBA lies in the fact that the conformational differences in this molecule result in different arrangements and strengths of intramolecular hydrogen bonds. Figure 6 shows two MEP maps together with the respective α and β values obtained for two different conformations of 2,6-DHBA, each present in the crystal structure of one of the polymorphs of this molecule. As can be seen, the maps differ not only in the location of the strongest donating and accepting sites but also, what is more important for cocrystal prediction using MEP distribution, in the α and β values themselves. This, in particular, is the case of the β parameter, with the highest value obtained for the first conformation equaling to 6.4, whereas for the second conformation, only to 3.5. Such significant differences directly translate into the

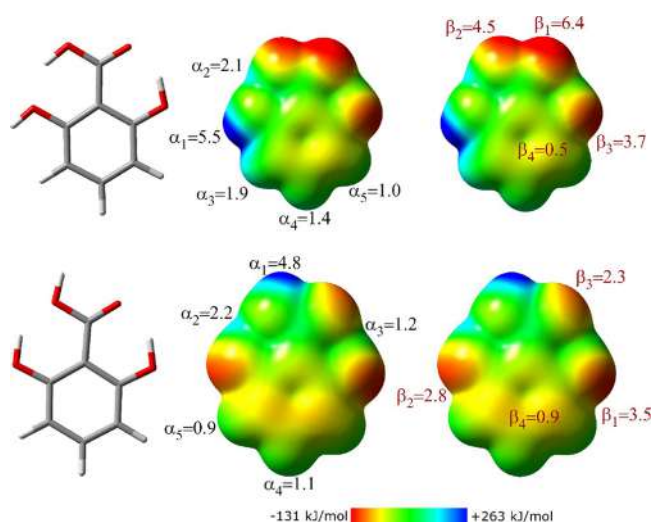


Figure 6. MEP maps calculated for two different conformations of 2,6-DHBA together with the calculated α and β values, representing the strength of the hydrogen bond-donating and hydrogen bond-accepting sites, respectively.

results of the estimated energy of the considered α – β interactions, as shown in Table 5. As a result, it may be concluded that it is safe to consider only one lowest energy conformation as long as there are no significant differences in the intramolecular interactions between the conformers.

Intermolecular Energy of Cofomers. In a very rough estimation, for a given cofomer with an ability to form the same (or similar) supramolecular synthon(s), the intermolecular energy of this cofomer (i.e., energy contribution to the total energy of a crystal arising only from intermolecular interactions) can be viewed as the energy barrier that need to be overcome in order for this cofomer to form a cocrystal with a given API. This would mean that if a molecular conformation of a cofomer remains unchanged during cocrystal formation, the tendency to form a given cocrystal should correlate with the above mentioned energy barrier posed by intermolecular interactions of a cofomer. If these assumptions are true, in a thermodynamically driven formation of cocrystals (and this concerns ca. 95% of cases⁶⁸), solid cofomers with a lower intermolecular energy will be easier to transform into the respective cocrystals. In our case, the majority of the considered cofomers have an acidic group (–COOH or –SO₃H), which are able to form C/S=O_{COF}...H–N_{LIN} and O/N–H_{COF}...O=C_{LIN} hydrogen bonds with a LIN amide moiety. Table 6 lists the intermolecular energies calculated for 15 tested cofomers possessing a free –COOH or –SO₃H group, together with a brief summary of their experimental tendency to form cocrystals with LIN. As can be seen, there is a trend for the crystal forms of cofomers having a lower intermolecular energy to form cocrystals with LIN more easily. Although the size of our data set is not nearly enough to establish any reliable correlation, these preliminary results show that intermolecular energy may be a promising indicator in virtual cocrystal screening. Its usage may be particularly advantageous in conjunction with the HBP method, which does not account for the energy of a given interaction. For example, the HBP method predicted cocrystal formation with LIN for MAL and INA as these cofomers have functional groups forming preferable intermolecular interactions with LIN. However, the intermolecular energy calculated for these

Table 6. Intermolecular Energies Calculated for 15 Cofomers Possessing –COOH or –SO₃H Groups and their Comparison with the Observed Experimental Tendency to Form Cocrystals with LIN Via Mechanochemical Grinding

coformer	intermolecular energy [kJ/mol]	ease of cocrystal formation with LIN
BA	–115	easily—with LIN_III without LAG
3,4-DHBA (hydrate)	–115	easily—with LIN_III without LAG
2,3-DHBA	–127	fairly easy—with LAG addition, possibly also with LIN_III
GA (hydrate)	–128	easily—with LIN_III without LAG
2,6-DHBA	–134	easily—with LIN_II and LIN_III without LAG
2,5-DHBA	–138	difficult—only with significant addition of LAG
PABA	–143	difficult—only with significant addition of LAG
VA	–144	no cocrystals are formed
PHBA	–144	difficult—only with significant addition of LAG
2,4-DHBA	–145	difficult—only with significant addition of LAG
MAL	–148	no cocrystals are formed
IBU	–152	no cocrystals are formed
INA	–159	no cocrystals are formed
3,5-DHBA	–174	difficult—only with significant addition of LAG
SA (hydrate)	–231	no cocrystals are formed
SA	–397	no cocrystals are formed

coformers is noticeably higher than for many others from the tested set and may constitute a too high energetic barrier for the predicted supramolecular synthons to be formed.

Virtual Cocrystal Screening Methods as Tools for Understanding the Formation of LIN Cocrystals. Each of the virtual screening methods used for cocrystal prediction focuses on a different aspect of a solid form formation. When performed together, these methods may not only yield a better prediction but can also help to understand the reasons behind the success and failure of the tested cofomers. In the case of LIN and the tested cofomers, it seems that the geometrical considerations are less important than the energetic ones. The same can be said about the preferred HB interactions as for most of the cofomers, heteromolecular interactions were found to be competitive with the homomolecular ones. This can be well illustrated using the examples of 3,5-DHBA, 2,6-DHBA, and IBU. Cocrystals of both 2,6-DHBA and 3,5-DHBA with LIN were obtained experimentally, but both cofomers received a “fail” flag in the MC survey because of a lack of complementarity in molecular shape. The HBP results indicated that the interactions between 3,5-DHBA and LIN will be preferred over LIN–LIN or 3,5-DHBA–3,5-DHBA interactions. This, however, was not the case for 2,6-DHBA, despite this cofomer having the same functional groups as 3,5-DHBA. It is worth recalling that the homomolecular interactions in the case of 2,6-DHBA were only slightly preferred in the HBP predictions over the heteromolecular ones. In the MEP map approach, both cofomers received $-\Delta E$ values indicating a good probability of cocrystal formation, with 3,5-DHBA showing a somewhat higher probability. Yet, experimentally, it was 2,6-DHBA which showed the highest tendency to form cocrystals with LIN, and this was actually the only cofomer that did react with LIN

form II without any solvent assistant. Perhaps this can be partly explained in the light of intermolecular energy results, according to which a less energy is needed to break the crystal lattice of 2,6-DHBA than 3,5-DHBA. Contrarily to the two dihydroxybenzoic acids, IBU passed the MC test but failed to produce cocrystals with LIN because of a lack of energy gain upon cocrystal formation, as indicated by the MEPS results as well as (partially) by intermolecular energy calculations. In this case also, the HBP results suggest that the formation of a hydrogen bond between IBU and LIN will be less favorable than LIN–LIN interactions. Another example is the case of INN and INA, which according to MC and HBP screening could be valid coformers to form cocrystals with LIN. Only the MEP-based approach indicates low probability for cocrystal formation due to an insufficient energy gain upon forming specific heteromolecular interactions. In the case of INA also, a relatively high value of intermolecular energy may disfavor the formation of a binary system with LIN. Only in the case of BARB and MAL, their incompatibility with LIN in terms of the molecular shape may be of higher importance. These coformers show a relatively good propensity toward the formation heteromolecular interactions with LIN (multi-component scores of 0.05 and 0.00 for MAL and BARB, respectively) and do not show severe disadvantages in terms of the energy gain upon cocrystal formation (with the maximum $-\Delta E$ values of 5 and 7 kJ/mol for MAL and BARB, respectively). Both, however, failed the MC test because of their very small sizes in comparison with LIN. Overall, it seems that for our list of coformers, the most important aspect that decides the formation of binary systems with LIN is the energy gain upon such a reaction. It should be noted, however, that ours is a preselected list of compounds quite similar in size and (in many cases) with very similar functional groups. A more diverse selection of coformers could have yielded different results, indicating that MC and HBP approaches may be more beneficial at the early stages of potential coformer selection, while energy-based criteria (MEP maps and intermolecular energy differences) can be more decisive for similar compounds.

CONCLUSIONS

Virtual cocrystal screening tools have attracted a lot of scientific attention with potential for rationalizing the choice of the most appropriate coformers for a given molecule of interest. Our work shows that they may be useful not only to indicate the most viable coformers worth to be tested experimentally but can also help to understand the factors governing the formation of cocrystals in the case of a particular API.

The overall performance of all tested methods for the prediction of cocrystal formation (i.e., MC, HBP, and MEPS) using LIN as a model API was satisfactory, indicating the usefulness of all three methods. On the other hand, our results indicate that geometrical aspects and the propensity of the formation of particular supramolecular synthons, as implemented into MC and HBP approaches, seem to be more important at the preliminary stages of the selection of coformers from a list of chemicals varying in size and functional groups. Meanwhile, when having a list of coformers similar in size and capable of forming similar hydrogen bonds, one may benefit more from the energy-based methods of prediction, such as MEPS. Additionally, accounting for the intermolecular energy of a coformer in the prediction attempt

may indicate the energy barrier that needs to be overcome for the successful formation of a cocrystal and hence may also point to the coformers more likely to form cocrystals. This could be of special importance for mechanochemical formation of cocrystals as in this case crystal lattices of the parent crystals need to be destroyed during the reaction, presumably consuming the energy delivered by mechanical grinding.

ASSOCIATED CONTENT

Supporting Information

The Supporting Information is available free of charge at <https://pubs.acs.org/doi/10.1021/acs.cgd.0c01707>.

Physicochemical data (PXRD, DSC, TGA, and solution ^1H NMR spectra) for new cocrystals of LIN, solid-state NMR spectra for all reaction mixtures and pure components, PXRD, DSC, and NMR data for pure coformers, and numerical data from CASTEP and MEPS calculations (PDF)

AUTHOR INFORMATION

Corresponding Author

Marta K. Dudek – Centre of Molecular and Macromolecular Studies of Polish Academy of Sciences, Lodz 90-363, Poland; orcid.org/0000-0003-3412-0177; Phone: +48 42 6803306; Email: mdudek@cbmm.lodz.pl

Authors

Mehrnaz Khalaji – Centre of Molecular and Macromolecular Studies of Polish Academy of Sciences, Lodz 90-363, Poland
Marek J. Potrzebowski – Centre of Molecular and Macromolecular Studies of Polish Academy of Sciences, Lodz 90-363, Poland

Complete contact information is available at: <https://pubs.acs.org/doi/10.1021/acs.cgd.0c01707>

Notes

The authors declare no competing financial interest.

ACKNOWLEDGMENTS

The Polish National Science Center is gratefully acknowledged for financial support under the OPUS grant UMO-2017/25/B/ST4/02684. The authors are also grateful to The Polish Infrastructure for Supporting Computational Science in the European Research Space (PL-GRID) for providing computational resources.

REFERENCES

- (1) Hornedo, N. R. Cocrystals: Molecular Design of Pharmaceutical Materials. *Mol. Pharmaceutics* **2007**, *4*, 299–300.
- (2) Duggirala, N. K.; Perry, M. L.; Almarsson, Ö.; Zaworotko, M. J. Pharmaceutical Cocrystals: along the Path to Improved Medicines. *Chem. Commun.* **2016**, *52*, 640–655.
- (3) Surov, A. O.; Manin, A. N.; Voronin, A. P.; Boycov, D. E.; Magdysyuk, O. V.; Perlovich, G. L. New Pharmaceutical Cocrystal Forms of Flurbiprofen: Structural, Physicochemical, and Thermodynamic Characterization. *Cryst. Growth Des.* **2019**, *19*, S751–S761.
- (4) Rai, S. K.; Gunnam, A.; Mannava, M. K. C.; Nangia, A. K. Improving the Dissolution Rate of the Anticancer Drug Dabrafenib. *Cryst. Growth Des.* **2020**, *20*, 1035–1046.
- (5) Costa, R. N.; Reviglio, A. L.; Siedler, S.; Cardoso, S. G.; Linck, Y. G.; Monti, G. A.; Carvalho, A. M. G.; Resende, J. A. L. C.; Chaves, M. H. C.; Rocha, H. V. A.; Choquesillo-Lazarte, D.; Infantes, L.; Cuffini, S. L. New Multicomponent Forms of the Antiretroviral Nevirapine

with Improved Dissolution Performance. *Cryst. Growth Des.* **2020**, *20*, 688–698.

(6) Martin, F.; Pop, M.; Kacso, I.; Grosu, I. G.; Miclăuş, M.; Vodnar, D.; Lung, I.; Filip, G. A.; Olteanu, E. D.; Moldovan, R.; Nagy, A.; Filip, X.; Bâldea, I. Ketoconazole-p-aminobenzoic Acid Cocrystal: Revival of an Old Drug by Crystal Engineering. *Mol. Pharmaceutics* **2020**, *17*, 919–932.

(7) Santra, R.; Bhogala, B. K. R.; Khanduri, C. H. *Ertugliflozin Co-Crystals And Process For Their Preparation*. WO2016189463 patent, 2016.

(8) Sherman, C. B. *Solid Substances Comprising Valproic Acid And Sodium Valproate*. WO1996023491 patent, 1996.

(9) Almansa, C.; Mercè, R.; Tesson, N.; Farran, J.; Tomàs, J.; Plata-Salamán, C. R. Co-crystal of Tramadol Hydrochloride–Celecoxib (ctc): A Novel API–API Co-crystal for the Treatment of Pain. *Cryst. Growth Des.* **2017**, *17*, 1884–1892.

(10) Price, S. L. Computed Crystal Energy Landscapes for Understanding and Predicting Organic Crystal Structures and Polymorphism. *Acc. Chem. Res.* **2009**, *42*, 117–126.

(11) Nauha, E.; Bernstein, J. “Predicting” Crystal Forms of Pharmaceuticals Using Hydrogen Bond Propensities: Two Test Cases. *Cryst. Growth Des.* **2014**, *14*, 4364–4370.

(12) Mortazavi, M.; Hoja, J.; Aerts, L.; Quéré, L.; van de Streek, J.; Neumann, M. A.; Tkatchenko, A. Computational Polymorph Screening Reveals Late Appearing and Poorly-Soluble Form of Rotigotine. *Commun. Chem.* **2019**, *2*, 70.

(13) Bhardwaj, R. M.; McMahon, J. A.; Nyman, J.; Price, L. S.; Konar, S.; Oswald, I. D. H.; Pulham, C. R.; Price, S. L.; Reutzle-Edens, S. M. A. Prolific Solvate Former, Galunisertib, under the Pressure of Crystal Structure Prediction, Produces Ten Diverse Polymorphs. *J. Am. Chem. Soc.* **2019**, *141*, 13887–13897.

(14) Neumann, M. A.; van de Streek, J. How Many Ritonavir Cases are There Still out There? *Faraday Discuss.* **2018**, *211*, 441–458.

(15) Thomas, L. H.; Wales, C.; Wilson, C. C. Selective Preparation of Elusive and Alternative Single Component Polymorphic Solid Forms Through Multi-Component Crystallisation Routes. *Chem. Commun.* **2016**, *52*, 7372–7375.

(16) Beckmann, W. Seeding the Desired Polymorph: Background, Possibilities, Limitations, and Case Studies. *Org. Process Res. Dev.* **2000**, *4*, 372–383.

(17) Friščić, T.; MacGillivray, L. R. Engineering Cocrystal and Polymorph Architecture via Pseudoseeding. *Chem. Commun.* **2009**, 773–775.

(18) Braun, D. E.; Karamertzanis, P. G.; Price, S. L. Which, if any, Hydrates Will Crystallise? Predicting hydrate formation of two dihydroxybenzoic acids. *Chem. Commun.* **2011**, *47*, 5443–5445.

(19) Braun, D. E.; Griesser, U. J. Why Do Hydrates (Solvates) Form in Small Neutral Organic Molecules? Exploring the Crystal Form Landscapes of the Alkaloids Brucine and Strychnine. *Cryst. Growth Des.* **2016**, *16*, 6405–6418.

(20) Dudek, M. K.; Day, G. M. Explaining Crystallization Preferences of Two Polyphenolic Diastereoisomers by Crystal Structure Prediction. *CrystEngComm* **2019**, *21*, 2067–2079.

(21) Braun, D. E.; Gelbrich, T.; Griesser, U. J. Experimental and Computational Approaches to Produce and Characterise Isostructural Solvates. *CrystEngComm* **2019**, *21*, 5533–5545.

(22) Mapp, L. K.; Coles, S. J.; Aitipamula, S. Design of Cocrystals for Molecules with Limited Hydrogen Bonding Functionalities: Propyphenazone as a Model System. *Cryst. Growth Des.* **2017**, *17*, 163–174.

(23) Putra, O. D.; Umeda, D.; Nugraha, Y. P.; Furuishi, T.; Nagase, H.; Fukuzawa, K.; Uekusa, H.; Yonemochi, E. Solubility Improvement of Epalrestat by Layered Structure Formation via Cocrystallization. *CrystEngComm* **2017**, *19*, 2614–2622.

(24) Bučar, D.-K. Engineering Molecular Crystals: Backbreaking, yet Gratifying. *Cryst. Growth Des.* **2017**, *17*, 2913–2918.

(25) Desiraju, G. R. Supramolecular Synthons in Crystal Engineering – A New Organic Synthesis. *Angew. Chem., Int. Ed. Engl.* **1995**, *34*, 2311–2327.

(26) Corpinot, M. K.; Stratford, S. A.; Arhangelskis, M.; Anka-Lufford, J.; Halasz, I.; Judáš, N.; Jones, W.; Bučar, D.-K. On the Predictability of Supramolecular Interactions in Molecular Cocrystals – the View from the Bench. *CrystEngComm* **2016**, *18*, 5434–5439.

(27) Fábíán, L. Cambridge Structural Database Analysis of Molecular Complementarity in Cocrystals. *Cryst. Growth Des.* **2009**, *9*, 1436–1443.

(28) Galek, P. T. A.; Fábíán, L.; Motherwell, W. D. S.; Allen, F. H.; Feeder, N. Knowledge-based Model of Hydrogen-Bonding Propensity in Organic Crystals. *Acta Cryst.* **2007**, *63*, 768–782.

(29) Musumeci, D.; Hunter, C. A.; Prohens, R.; Scuderia, S.; McCabe, J. F. Virtual Cocrystal Screening. *Chem. Sci.* **2011**, *2*, 883–890.

(30) Karki, S.; Friščić, T.; Fábíán, L.; Jones, W. New Solid Forms of Artemisinin Obtained through Cocrystallisation. *CrystEngComm* **2010**, *12*, 4038–4041.

(31) Pallipurath, A. R.; Civati, F.; Eziashi, M.; Omar, E.; McArdle, P.; Erxleben, A. Tailoring Cocrystal and Salt Formation and Controlling the Crystal Habit of Diflunisal. *Cryst. Growth Des.* **2016**, *16*, 6468–6478.

(32) Delori, A.; Galek, P. T. A.; Pidcock, E.; Jones, W. Quantifying Homo- and Heteromolecular Hydrogen Bonds as a Guide for Adduct Formation. *Chem. – Eur. J.* **2012**, *18*, 6835–6846.

(33) Wood, P. A.; Feeder, N.; Furlow, M.; Galek, P. T. A.; Groom, C. R.; Pidcock, E. Knowledge-based Approaches to Co-crystal Design. *CrystEngComm* **2014**, *16*, 5839–5848.

(34) Majumder, M.; Buckton, G.; Rawlinson-Malone, C. F.; Williams, A. C.; Spillman, M. J.; Pidcock, E.; Shankland, K. Application of Hydrogen-Bond Propensity Calculations to an Indomethacin–Nicotinamide (1 : 1) Co-crystal. *CrystEngComm* **2013**, *15*, 4041–4044.

(35) Delori, A.; Galek, P. T. A.; Pidcock, E.; Patni, M.; Jones, W. Knowledge-based Hydrogen Bond Prediction and the Synthesis of Salts and Cocrystals of the Anti-Malarial Drug Pyrimethamine with Various Drug and GRAS Molecules. *CrystEngComm* **2013**, *15*, 2916–2928.

(36) Sarkar, N.; Aakeröy, C. B. Evaluating Hydrogen-Bond Propensity, Hydrogen-Bond Coordination and Hydrogen-Bond Energy as Tools for Predicting the Outcome of Attempted Co-Crystallisations. *Supramol. Chem.* **2020**, *32*, 81–90.

(37) Barbas, R.; Font-Bardia, M.; Paradkar, A.; Hunter, C. A.; Prohens, R. Combined Virtual/Experimental Multicomponent Solid Forms Screening of Sildenafil: New Salts, Cocrystals, and Hybrid Salt–Cocrystals. *Cryst. Growth Des.* **2018**, *18*, 7618–7627.

(38) Grecu, T.; Hunter, C. A.; Gardiner, E. J.; McCabe, J. F. Validation of a Computational Cocrystal Prediction Tool: Comparison of Virtual and Experimental Cocrystal Screening Results. *Cryst. Growth Des.* **2014**, *14*, 165–171.

(39) Aakeröy, C. B.; Epa, K.; Forbes, S.; Schultheiss, N.; Desper, J. Ranking Relative Hydrogen-Bond Strengths in Hydroxybenzoic Acids for Crystal-Engineering Purposes. *Chem. – Eur. J.* **2013**, *19*, 14998–15003.

(40) Aakeröy, C. B.; Wijethunga, T. K.; Desper, J. Molecular Electrostatic Potential Dependent Selectivity of Hydrogen Bonding. *New J. Chem.* **2015**, *39*, 822–828.

(41) Grecu, T.; Prohens, R.; McCabe, J. F.; Carrington, E. J.; Wright, J. S.; Brammer, L.; Hunter, C. A. Cocrystals of Spironolactone and Griseofulvin Based on an in Silico Screening Method. *CrystEngComm* **2017**, *19*, 3592–3599.

(42) Mohammad, M. A.; Alhalaweh, A.; Velaga, S. P. Hansen Solubility Parameter as a Tool to Predict Cocrystal Formation. *Int. J. Pharm.* **2011**, *407*, 63–71.

(43) Wicker, J. G. P.; Crowley, L. M.; Robshaw, O.; Little, E. J.; Stokes, S. P.; Cooper, R. I.; Lawrence, S. E. Will they Co-crystallize? *CrystEngComm* **2017**, *19*, 5336–5340.

(44) Abramov, Y. A.; Loschen, C.; Klamt, A. Rational Coformer or Solvent Selection for Pharmaceutical Cocrystallization or Desolvation. *J. Pharm. Sci.* **2012**, *101*, 3687–3697.

- (45) Sun, G.; Jin, Y.; Li, S.; Yang, Z.; Shi, B.; Chang, C.; Abramov, Y. A. Virtual Coformer Screening by Crystal Structure Predictions: Crucial Role of Crystallinity in Pharmaceutical Cocrystallization. *J. Phys. Chem. Lett.* **2020**, *11*, 8832–8838.
- (46) Karamertzanis, P. G.; Kazantsev, A. V.; Issa, N.; Welch, G. W. A.; Adjiman, C. S.; Pantelides, C. C.; Price, S. L. Can the Formation of Pharmaceutical Cocrystals Be Computationally Predicted? 2. Crystal Structure Prediction. *J. Chem. Theory Comput.* **2009**, *5*, 1432–1448.
- (47) Issa, N.; Barnett, S. A.; Mohamed, S.; Braun, D. E.; Copley, R. C. B.; Tocher, D. A.; Price, S. L. Screening for Cocrystals of Succinic Acid and 4-Aminobenzoic Acid. *CrystEngComm* **2012**, *14*, 2454–2464.
- (48) World Health Organization. *The Selection and Use of Essential Medicines. Report of the WHO Expert Committee on Selection and Use of Essential Medicines*, 2019. WHO Technical Report Series, No. 1021
- (49) Roger, C.; Roberts, J. A.; Muller, L. Clinical Pharmacokinetics and Pharmacodynamics of Oxazolidinones. *Clin. Pharmacokinet.* **2018**, *57*, 559–575.
- (50) Skorupska, E.; Kaźmierski, S.; Potrzebowski, M. J. Solid State NMR Characterization of Ibuprofen:Nicotinamide Cocrystals and New Idea for Controlling Release of Drugs Embedded into Mesoporous Silica Particles. *Mol. Pharmaceutics* **2017**, *14*, 1800–1810.
- (51) Skorupska, E.; Jeziorna, A.; Potrzebowski, M. J. Thermal Solvent-Free Method of Loading of Pharmaceutical Cocrystals into the Pores of Silica Particles: A Case of Naproxen/Picolinamide Cocrystal. *J. Phys. Chem. C* **2016**, *120*, 13169–13180.
- (52) Khalaji, M.; Wróblewska, A.; Wielgus, E.; Bujacz, G. D.; Dudek, M. K.; Potrzebowski, M. J. Structural Variety of Heterosynthons in Linezolid Cocrystals with Modified Thermal Properties. *Acta Cryst.* **2020**, *76*, 892–912.
- (53) Maccaroni, E.; Alberti, E.; Malpezzi, L.; Masciocchi, N.; Vladiskovic, C. Polymorphism of Linezolid: a Combined Single-crystal, Powder Diffraction and NMR Study. *Int. J. Pharm.* **2008**, *351*, 144–151.
- (54) Tanaka, R.; Hirayama, N. Crystal Structure of Linezolid. *X-Ray Struct. Anal. Online* **2008**, *24*, x43–x44.
- (55) Wielgus, E.; Paluch, P.; Frelek, J.; Szczeppek, W. J.; Potrzebowski, M. J. Full Characterization of Linezolid and Its Synthetic Precursors by Solid-State Nuclear Magnetic Resonance Spectroscopy and Mass Spectrometry. *J. Pharm. Sci.* **2015**, *104*, 3883–3892.
- (56) Frelek, J.; Górecki, M.; Łaszczyńska, A.; Vass, E.; Szczeppek, W. J. Distinguishing between polymorphic forms of linezolid by solid-phase electronic and vibrational circular dichroism. *Chem. Commun.* **2012**, *48*, 5295–5297.
- (57) Rao, D. M.; Reddy, P. K. Crystalline Form of Linezolid. US 7,718,799 B2 patent, 2010.
- (58) Toby, B. H.; Von Dreele, R. B. GSAS-II: the Genesis of a Modern Open-Source All Purpose Crystallography Software Package. *J. Appl. Crystallogr.* **2013**, *46*, 544–549.
- (59) Hunter, J. D. Matplotlib: A 2D Graphics Environment. *Comput. Sci. Eng.* **2007**, *9*, 90–95.
- (60) Macrae, C. F.; Sovago, I.; Cottrell, S. J.; Galek, P. T. A.; McCabe, P.; Pidcock, E.; Platings, M.; Shields, G. P.; Stevens, J. S.; Towler, M.; Wood, P. A. Mercury 4.0: from Visualization to Analysis, Design and Prediction. *J. Appl. Crystallogr.* **2020**, *53*, 226–235.
- (61) Frisch, M. J.; Trucks, G. W.; Schlegel, H. B.; Scuseria, G. E.; Robb, M. A.; Cheeseman, J. R.; Scalmani, G.; Barone, V.; Petersson, G. A.; Nakatsuji, H.; Li, X.; Caricato, M.; Marenich, A. V.; Bloino, J.; Janesko, B. G.; Gomperts, R.; Mennucci, B.; Hratchian, H. P.; Ortiz, J. V.; Izmaylov, A. F.; Sonnenberg, J. L.; Williams-Young, D.; Ding, F.; Lipparini, F.; Egidi, F.; Goings, J.; Peng, B.; Petrone, A.; Henderson, T.; Ranasinghe, D.; Zakrzewski, V. G.; Gao, J.; Rega, N.; Zheng, G.; Liang, W.; Hada, M.; Ehara, M.; Toyota, K.; Fukuda, R.; Hasegawa, J.; Ishida, M.; Nakajima, T.; Honda, Y.; Kitao, O.; Nakai, H.; Vreven, T.; Throssell, K.; Montgomery, J. A., Jr.; Peralta, J. E.; Ogliaro, F.; Bearpark, M. J.; Heyd, J. J.; Brothers, E. N.; Kudin, K. N.; Staroverov,
- V. N.; Keith, T. A.; Kobayashi, R.; Normand, J.; Raghavachari, K.; Rendell, A. P.; Burant, J. C.; Iyengar, S. S.; Tomasi, J.; Cossi, M.; Millam, J. M.; Klene, M.; Adamo, C.; Cammi, R.; Ochterski, J. W.; Martin, R. L.; Morokuma, K.; Farkas, O.; Foresman, J. B.; Fox, D. J. *Gaussian 16, Revision B.01*, Gaussian, Inc., Wallingford CT, 2016.
- (62) Becke, A. D. Density-Functional Thermochemistry. III. The Role of Exact Exchange. *J. Chem. Phys.* **1993**, *98*, 5648–5652.
- (63) Clark, S. J.; Segall, M. D.; Pickard, C. J.; Hasnip, P. J.; Probert, M. J.; Refson, K.; Payne, M. C. First Principles Methods using CASTEP. *Z. Kristallogr.* **2005**, *220*, 567–570.
- (64) Perdew, J. P.; Burke, K.; Ernzerhof, M. Generalized Gradient Approximation Made Simple. *Phys. Rev. Lett.* **1996**, *77*, 3865–3868.
- (65) Grimme, S. Semiempirical GGA-Type Density Functional Constructed with a Long-Range Dispersion Correction. *J. Comput. Chem.* **2006**, *27*, 1787–1799.
- (66) Okabe, N.; Kyoyama, H. 2,3-Dihydroxybenzoic Acid. *Acta Cryst.* **2001**, *E57*, o1224–o1226.
- (67) Costa, R. N.; Choquesillo-Lazarte, D.; Cuffini, S. L.; Pidcock, E.; Infantes, L. Optimization and Comparison of Statistical Tools for the Prediction of Multicomponent Forms of a Molecule: the Antiretroviral Nevirapine as a Case Study. *CrystEngComm* **2020**, *22*, 7460–7474.
- (68) Taylor, C. R.; Day, G. M. Evaluating the Energetic Driving Force for Cocrystal Formation. *Cryst. Growth Des.* **2018**, *18*, 892–904.

Supporting Information

to

Virtual cocrystal screening methods as tools to understand the formation of pharmaceutical co-crystals - A case study of linezolid, a wide-range antibacterial drug

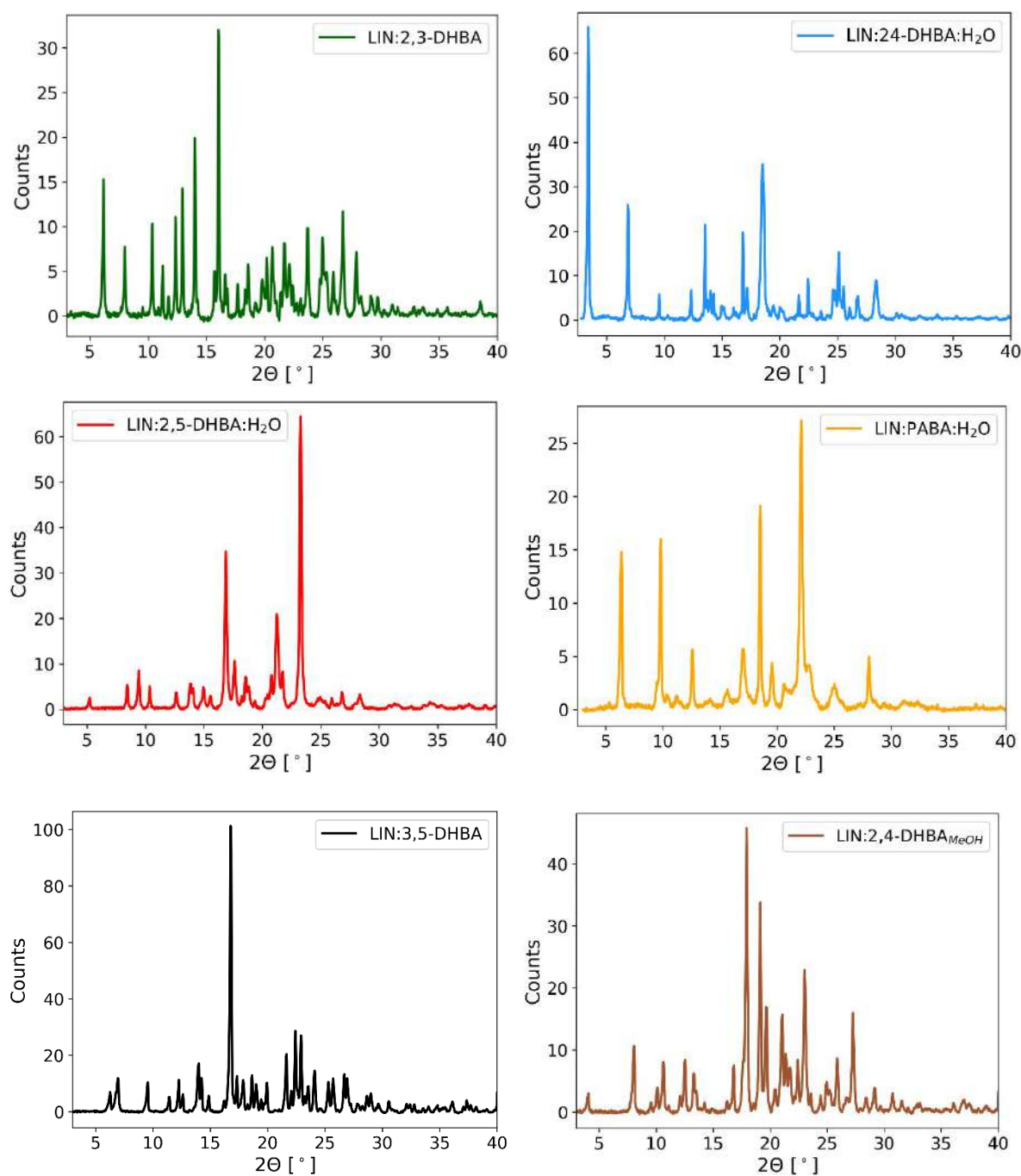
Mehrnaz Khalaji, Marek J. Potrzebowski and Marta K. Dudek *

Centre of Molecular and Macromolecular Studies of Polish Academy of Sciences, Sienkiewicza 112, 90-363 Lodz, Poland

1. Physicochemical data for six new cocrystals of LIN.....	2
1.1. PXRD data	2
1.2. Comparison of the PXRD data for the new cocrystals of LIN with the simulated PXRD diffractograms for pure forms.....	3
1.3. DSC & TGA data	7
1.4. Solution ¹ H NMR data.....	13
2. Solid-state NMR spectra registered for pure components and the reaction mixtures obtained after grinding.....	14
3. Determination of the coformers polymorphic forms	34
4. Numerical values from CASTEP and MEP calculations	49
5. References	52

1. Physicochemical data for six new cocrystals of LIN

1.1. PXRD data



Figures S1. PXRD data for six new crystal phases of LIN with 2,3-DHBA, 2,4-DHBA, 3,5-DHBA, 2,4-DHBA and water, 2,5-DHBA and water, and PABA and water.

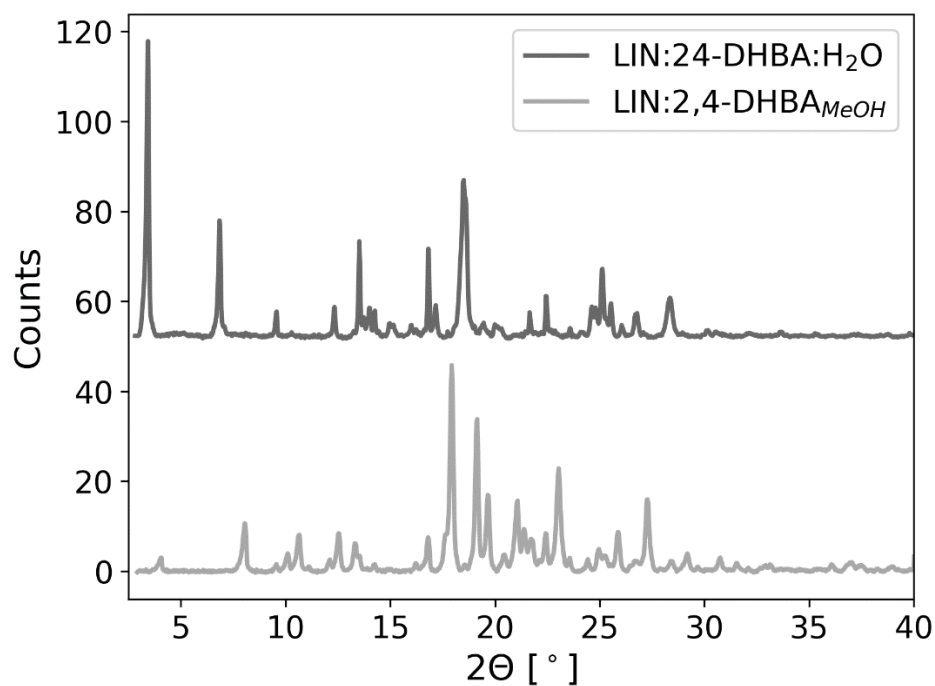


Figure S2. Comparison of PXRD data for LIN:2,4-DHBA and LIN:2,4-DHBA:H₂O crystals

1.2. Comparison of the PXRD data for the new cocrystals of LIN with the simulated PXRD diffractograms for pure forms

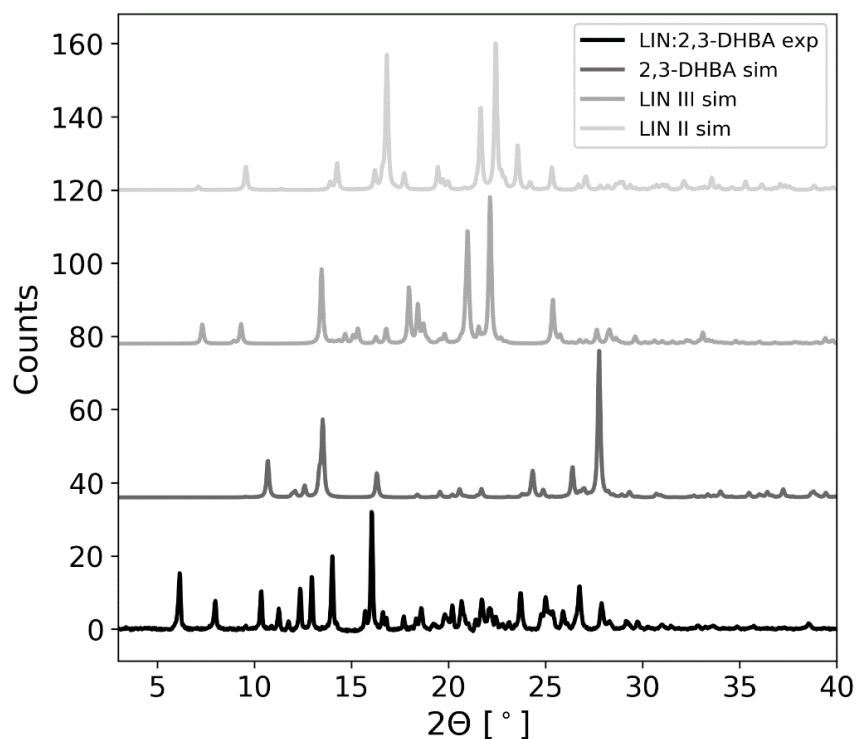


Figure S3. A comparison of simulated PXRD for pure LIN forms II and III and 2,3-DHBA triclinic form with the experimental PXRD for LIN:2,3-DHBA cocrystal

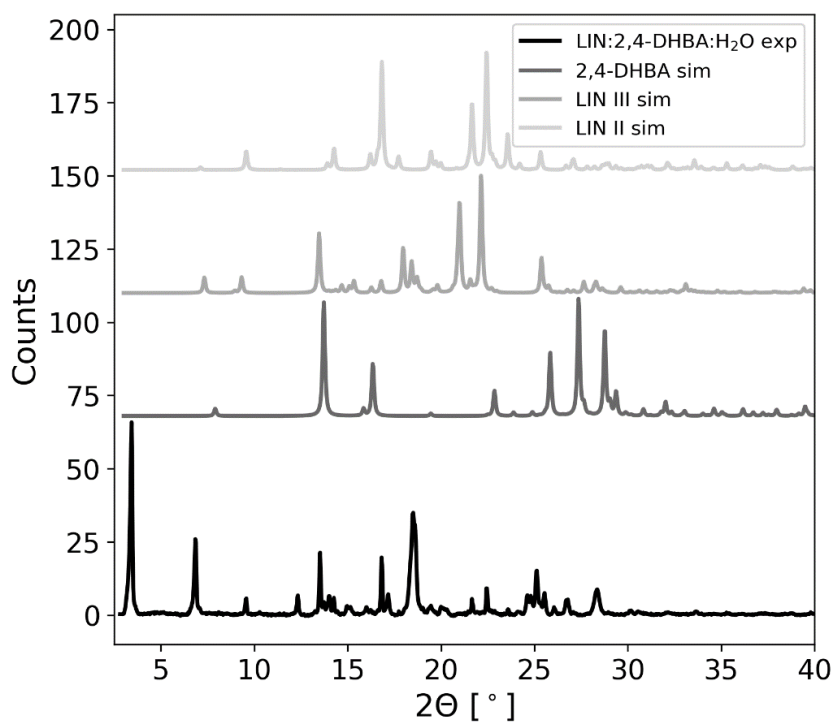


Figure S4. A comparison of simulated PXRD for pure LIN forms II and III and 2,4-DHBA form II with the experimental PXRD for LIN:2,4-DHBA cocrystal hydrate.

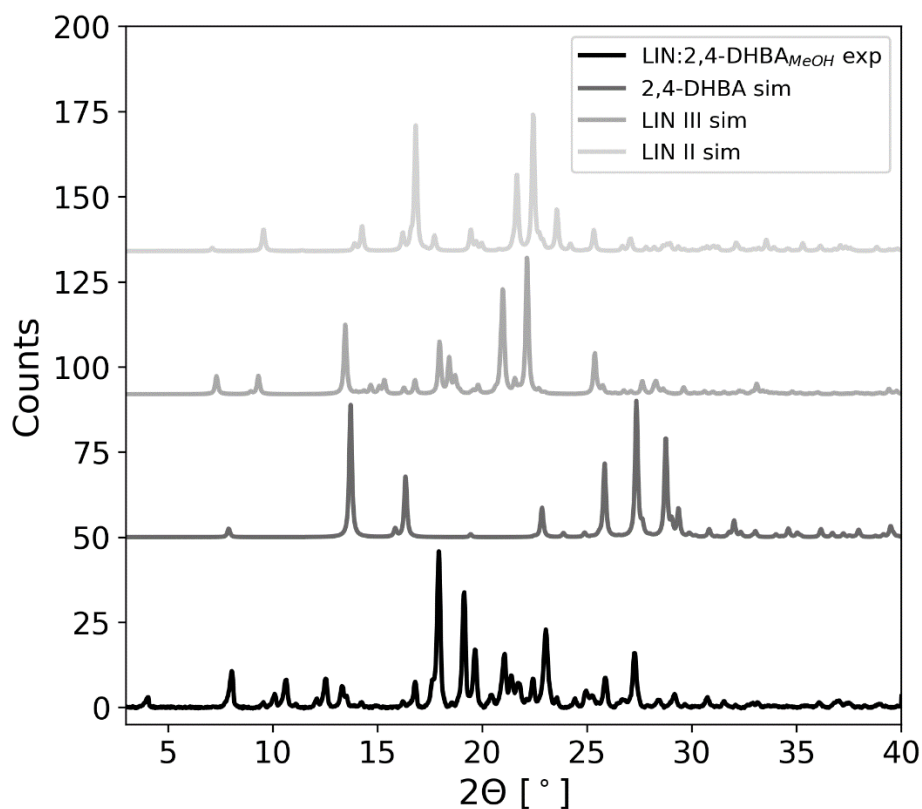


Figure S5. A comparison of simulated PXRD for pure LIN forms II and III and 2,4-DHBA form II with the experimental PXRD for LIN:2,4-DHBA cocrystal.

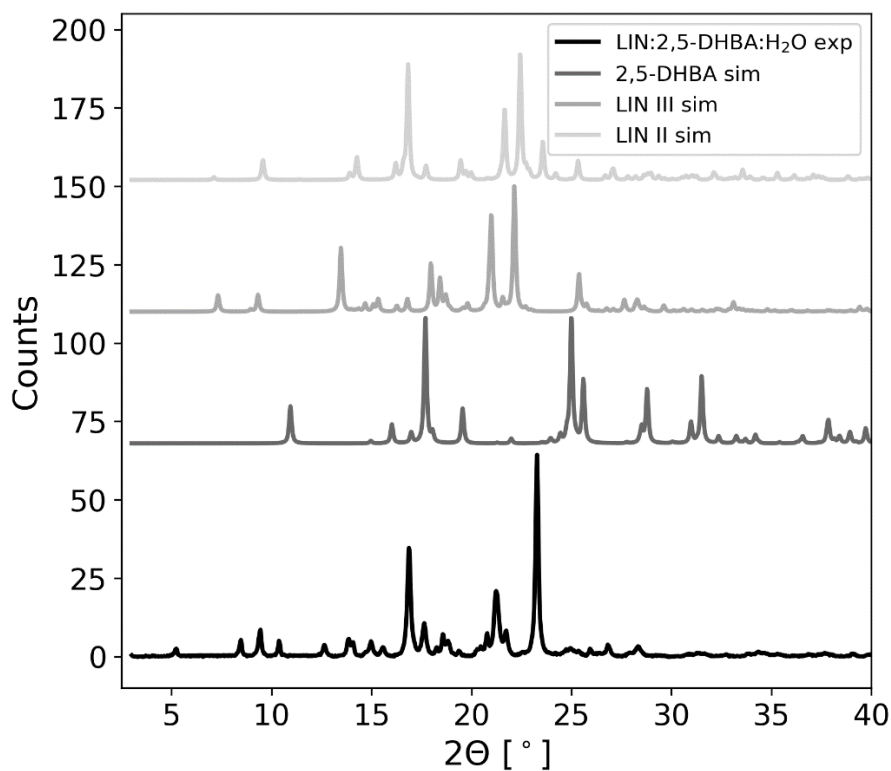


Figure S6. A comparison of simulated PXRD for pure LIN forms II and III and 2,5-DHBA form I with the experimental PXRD for LIN:2,5-DHBA cocrystal hydrate.

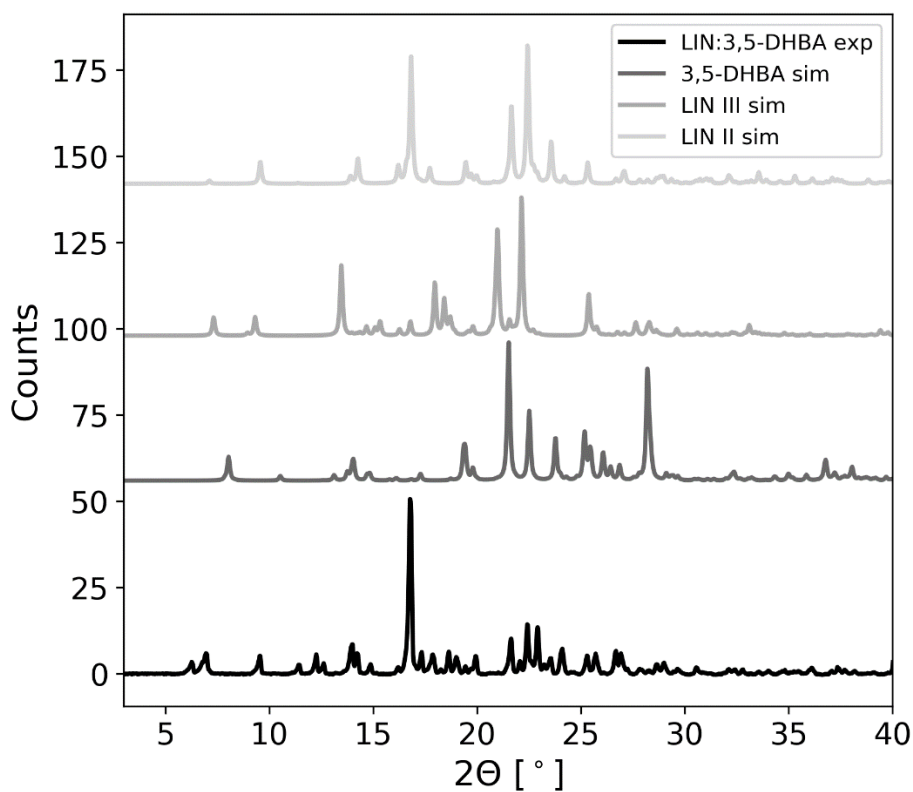


Figure S7. A comparison of simulated PXRD for pure LIN forms II and III and 3,5-DHBA form II with the experimental PXRD for LIN:3,5-DHBA cocrystal.

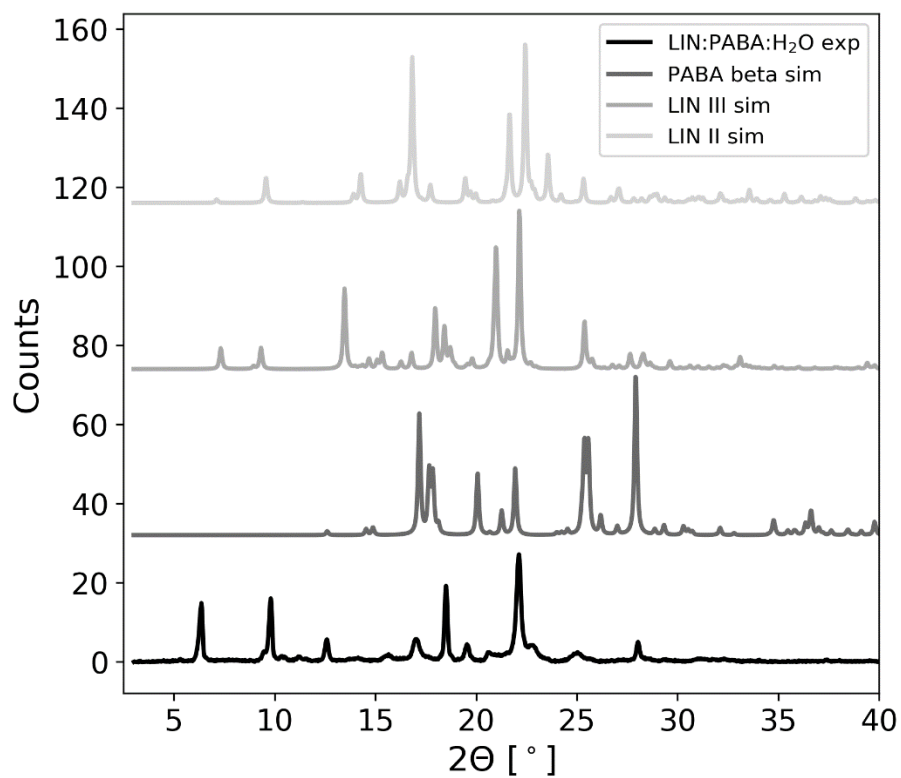


Figure S8. A comparison of simulated PXRD for pure LIN forms II and III and PABA form β with the experimental PXRD for LIN:PABA cocrystal hydrate.

1.3. DSC & TGA data

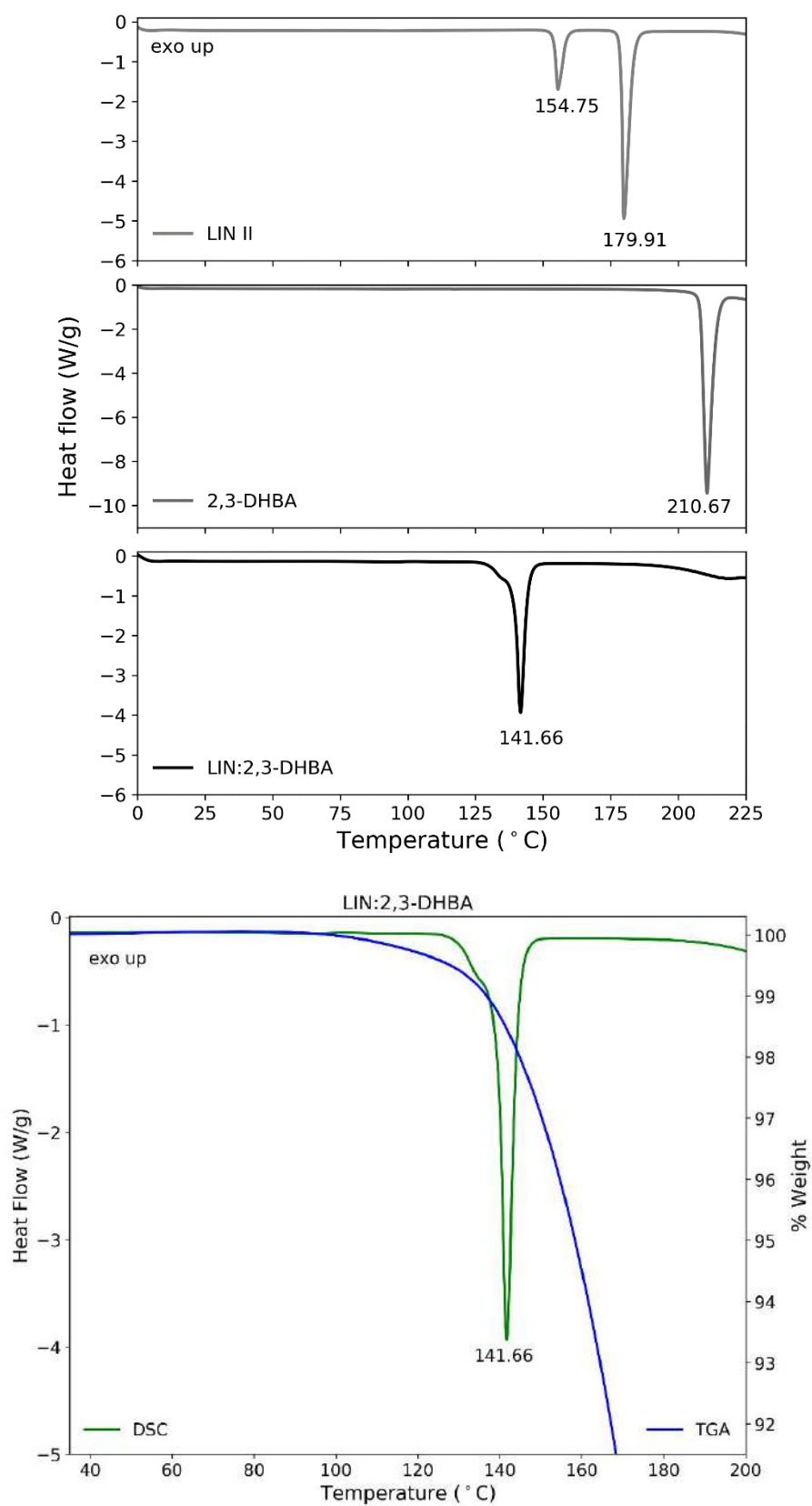


Figure S9. DSC thermograms for LIN:2,3-DHBA cocrystal, LIN form II and pure 2,3-DHBA, as well as TGA results for LIN:2,3-DHBA cocrystal.

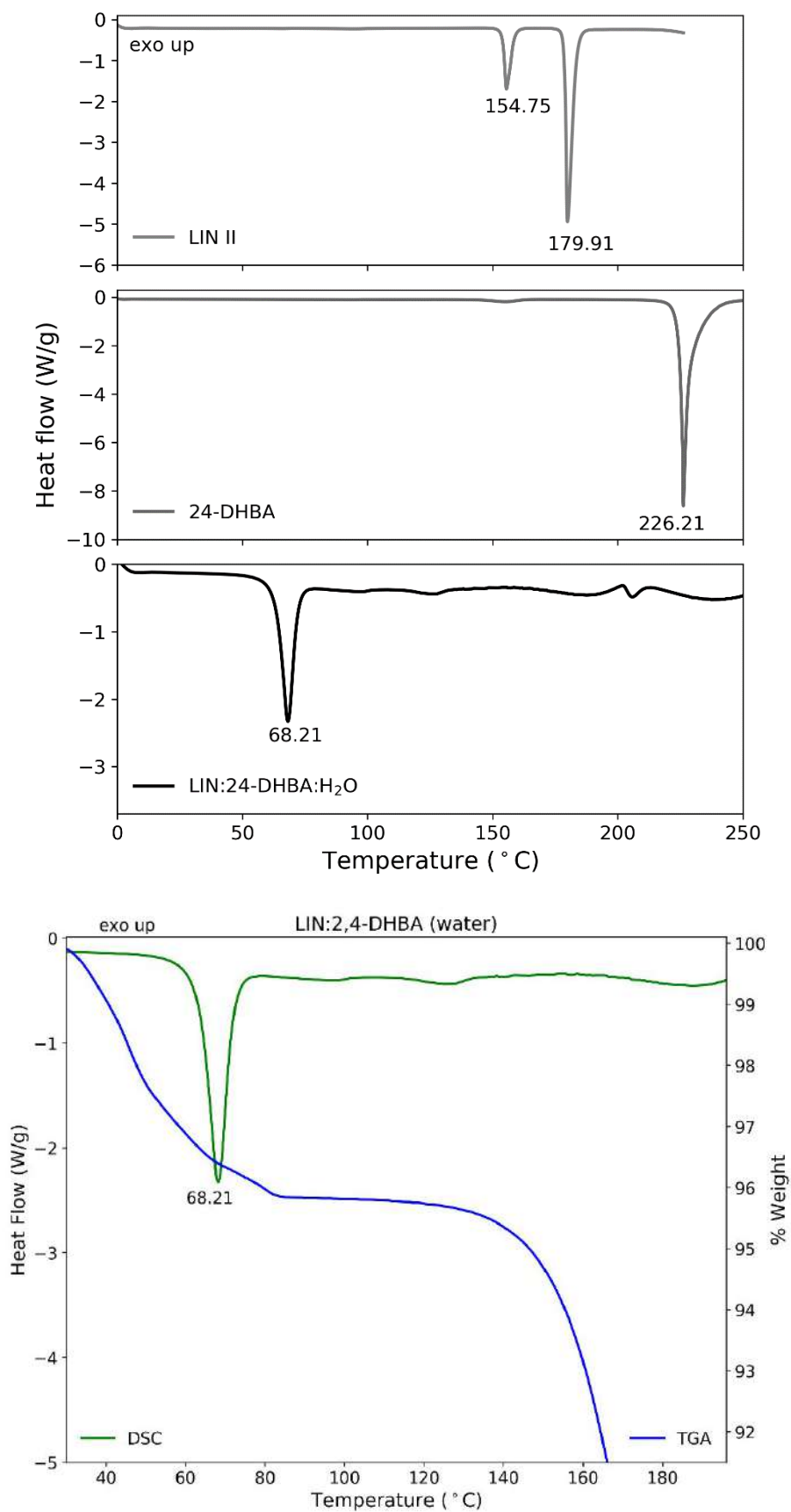


Figure S10. DSC thermograms for LIN:2,4-DHBA cocrystal hydrate, LIN form II and pure 2,4-DHBA, as well as TGA results for LIN:2,4-DHBA cocrystal hydrate.

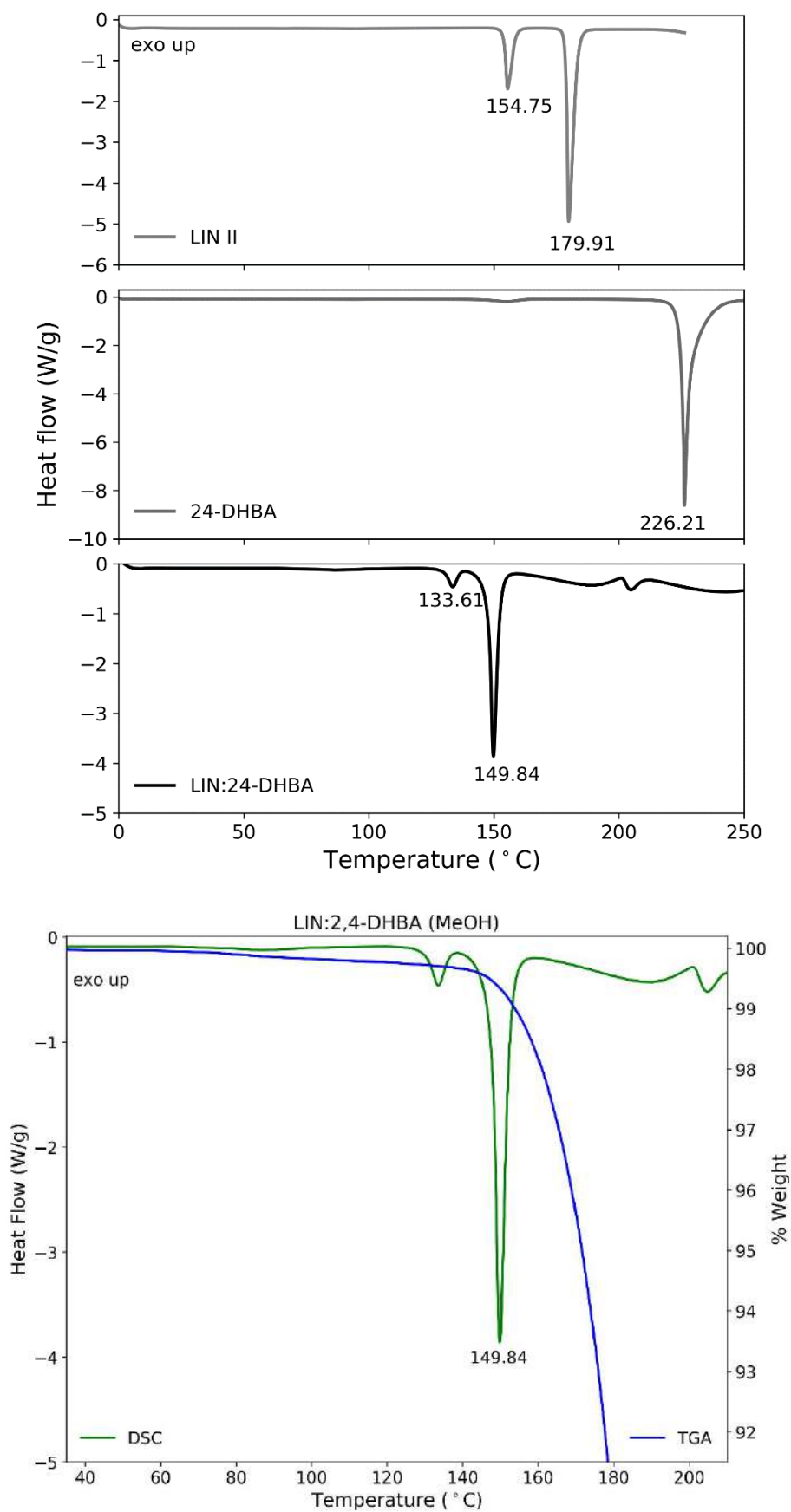


Figure S11. DSC thermograms for LIN:2,4-DHBA cocrystal, LIN form II and pure 2,4-DHBA, as well as TGA results for LIN:2,4-DHBA cocrystal.

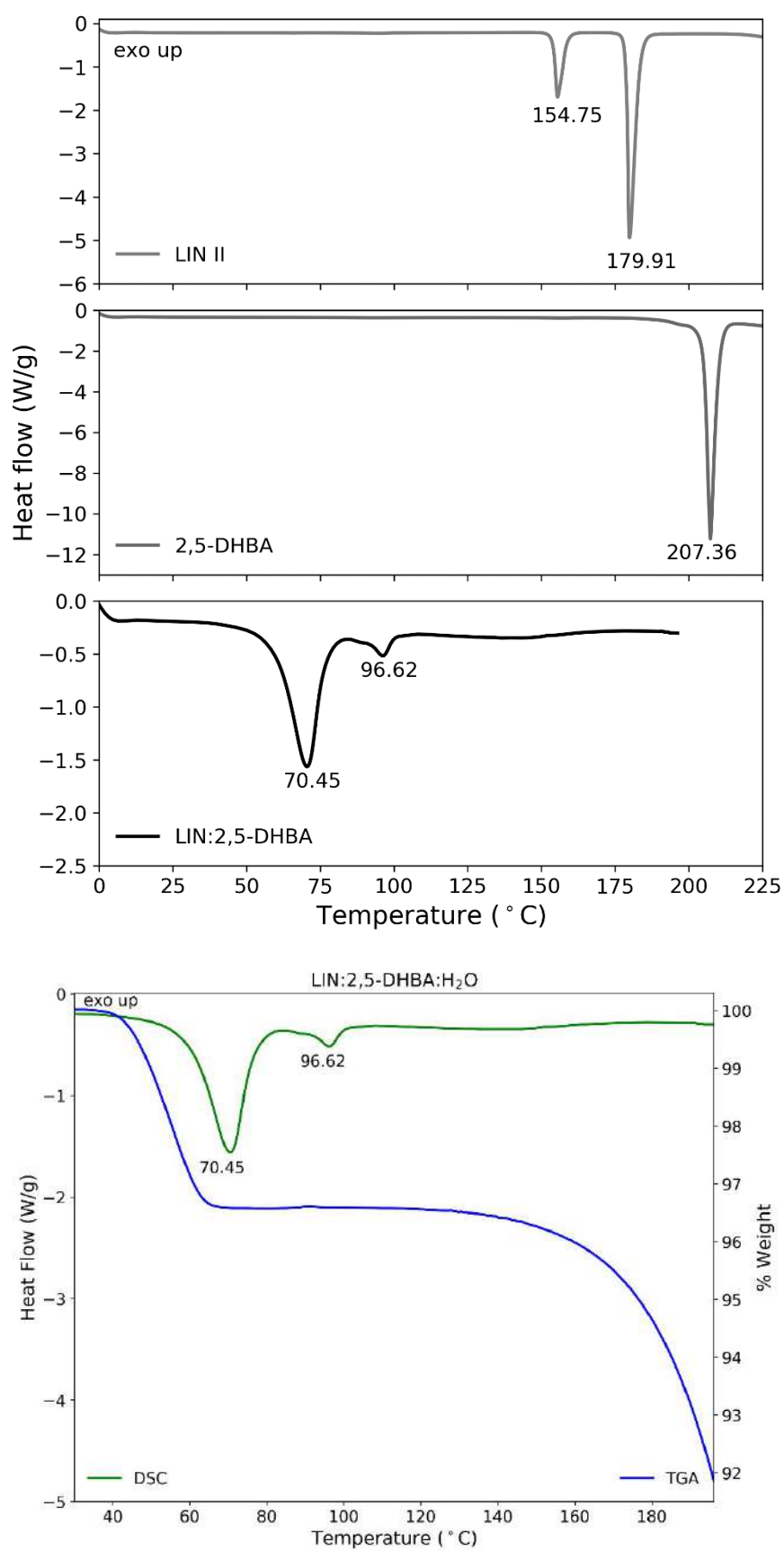


Figure S12. DSC thermograms for LIN:2,5-DHBA cocrystal hydrate, LIN form II and pure 2,5-DHBA, as well as TGA results for LIN:2,5-DHBA cocrystal hydrate.

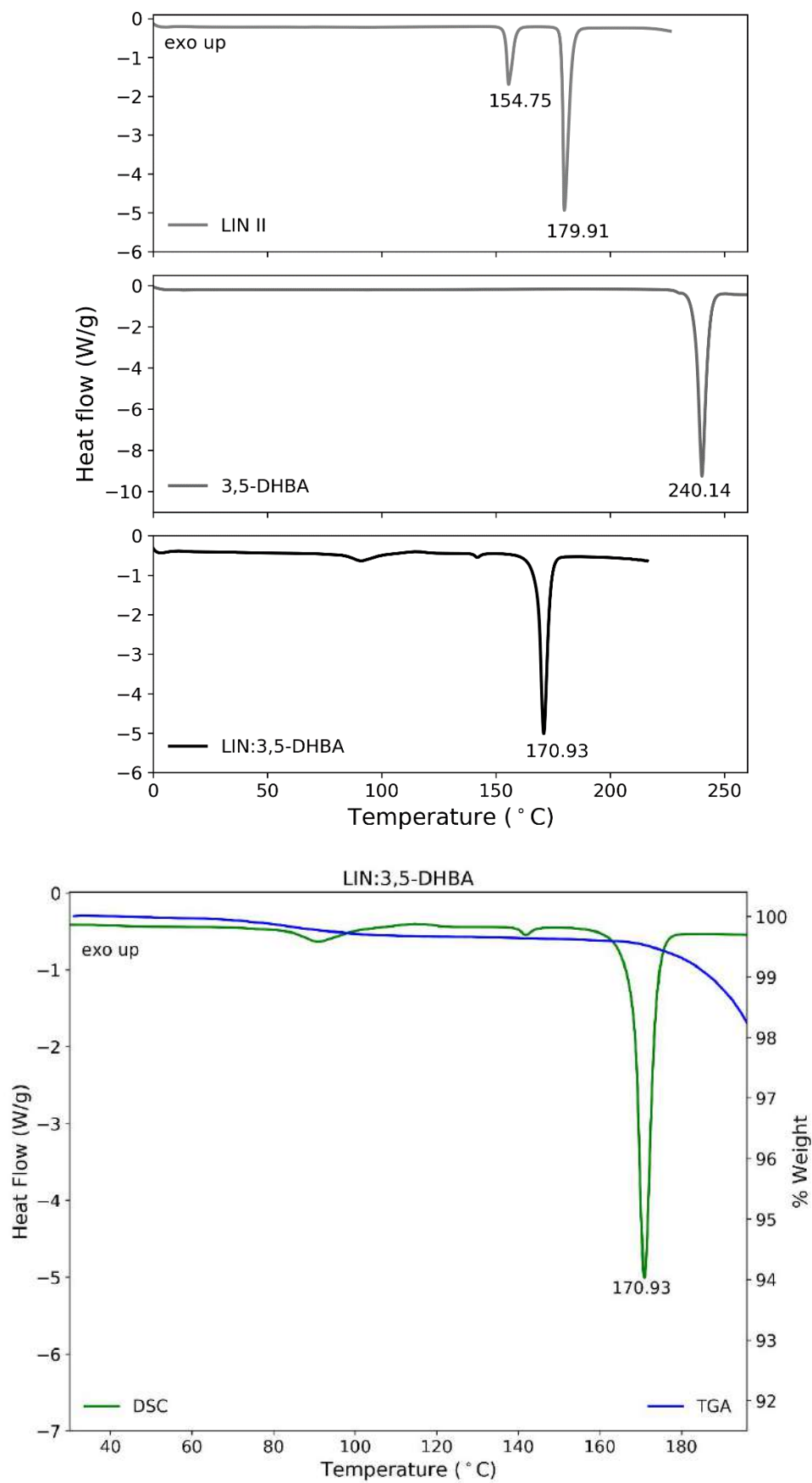


Figure S13. DSC thermograms for LIN:3,5-DHBA cocrystal, LIN form II and pure 3,5-DHBA, as well as TGA results for LIN:3,5-DHBA cocrystal.

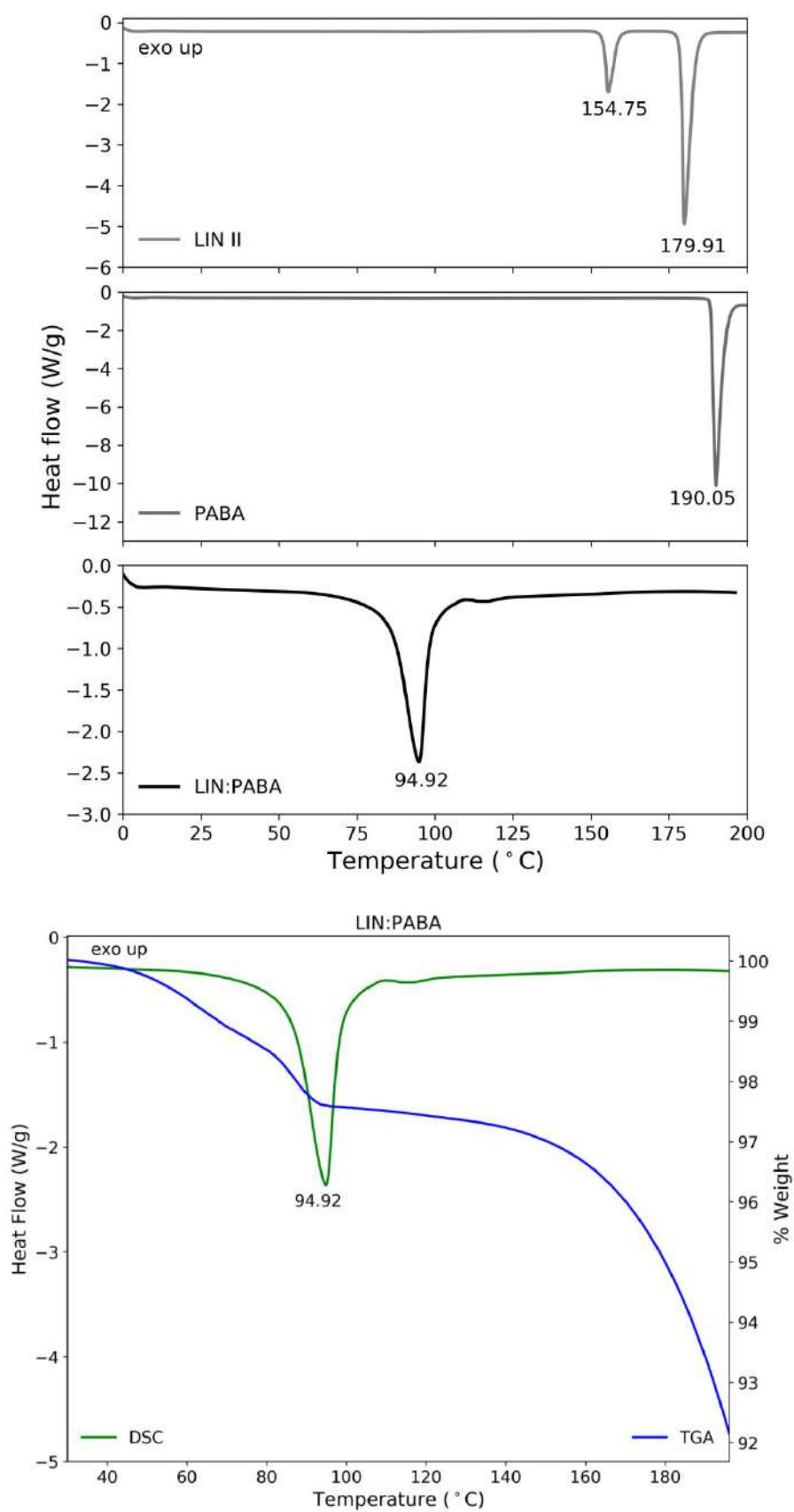


Figure S14. DSC thermograms for LIN:PABA cocrystal hydrate, LIN form II and pure PABA, as well as TGA results for LIN:PABA cocrystal hydrate.

1.4. Solution ^1H NMR data

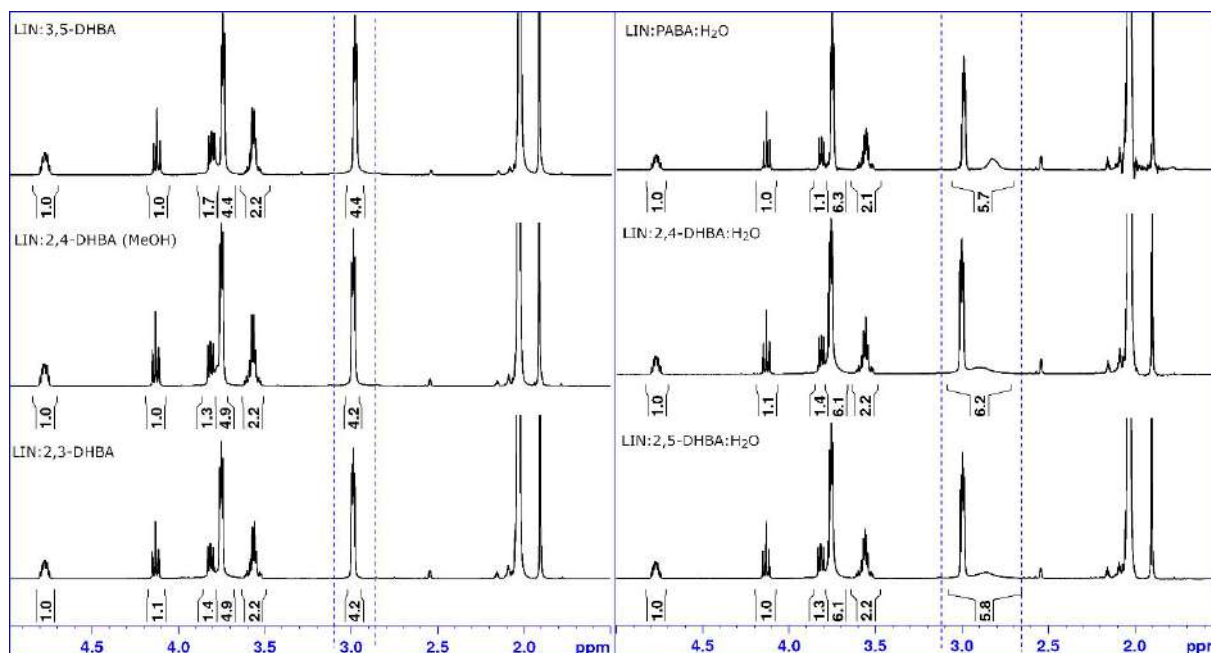


Figure S15. ^1H solution NMR spectra of the obtained cocrystals, registered in anhydrous acetone- d_6 in order to determine (if present) the amount of water present in the respective crystal structures. All ^1H signals were integrated in respect to a well-resolved LIN signal at 4.78 ppm. The left-hand side panel shows spectra of neat cocrystals, i.e. without the presence of water resonances, which is visible as a lack of ^1H resonances at ca. 2.8-2.9 ppm. Instead, only ^1H signals originating from 4 hydrogen atoms of LIN are visible (see a rectangle marked with the dashed lines at the left-hand side panel). The right-hand side panel shows ^1H NMR spectra for cocrystal hydrates – in these cases broadened ^1H resonances are visible at ca. 2.8-2.9 ppm, resulting in the integral value of ca. 2. This suggest that in each case one molecule of water is present in each crystal lattice.

2. Solid-state NMR spectra registered for pure components and the reaction mixtures obtained after grinding

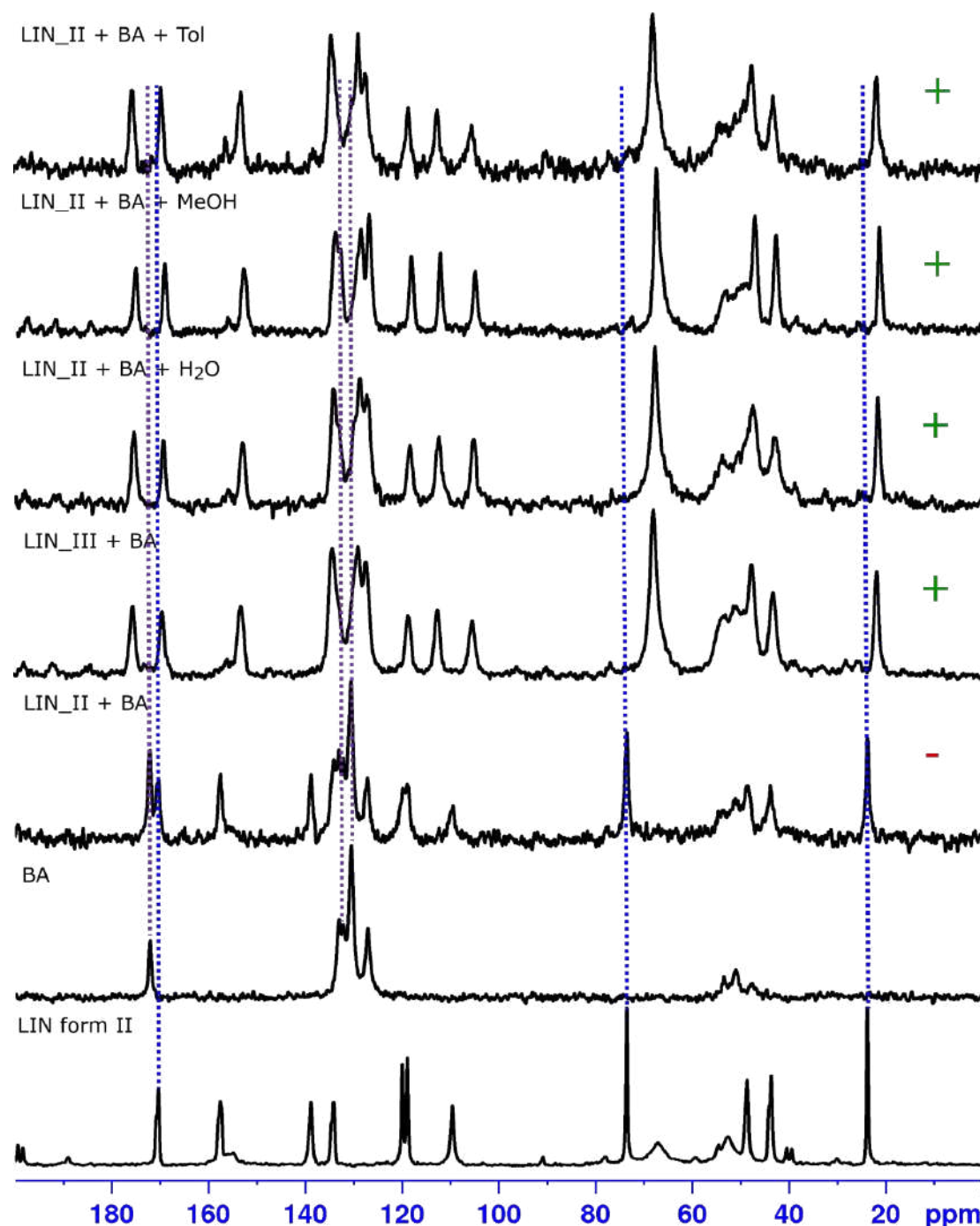


Figure S16. ^{13}C CPMAS NMR spectra for LIN form II, BA and various reaction mixtures obtained after grinding LIN_II or LIN_III with BA without any solvent and in the presence of water, methanol or toluene to create LAG conditions. Dashed lines indicate the positions of ^{13}C signals originating from pure reagents, 'plus' or 'minus' signs indicate whether a cocrystal was formed in given reaction conditions.

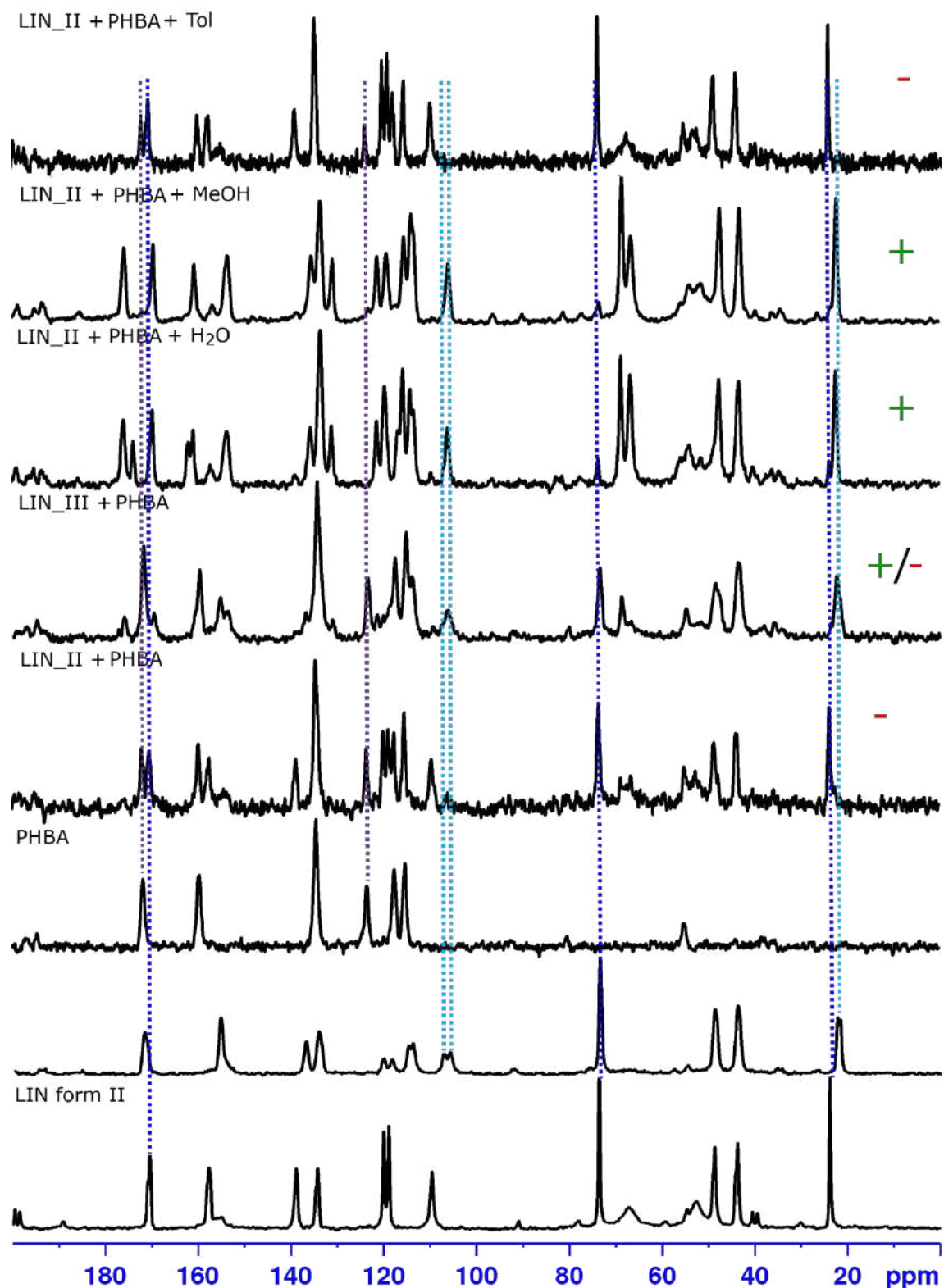


Figure S17. ^{13}C CPMAS NMR spectra for LIN form II, LIN form III, PHBA and various reaction mixtures obtained after grinding LIN_II or LIN_III with PHBA without any solvent and in the presence of water, methanol or toluene to create LAG conditions. Dashed lines indicate the positions of ^{13}C signals originating from pure reagents, ‘plus’ or ‘minus’ signs indicate whether a cocrystal was formed in given reaction conditions.

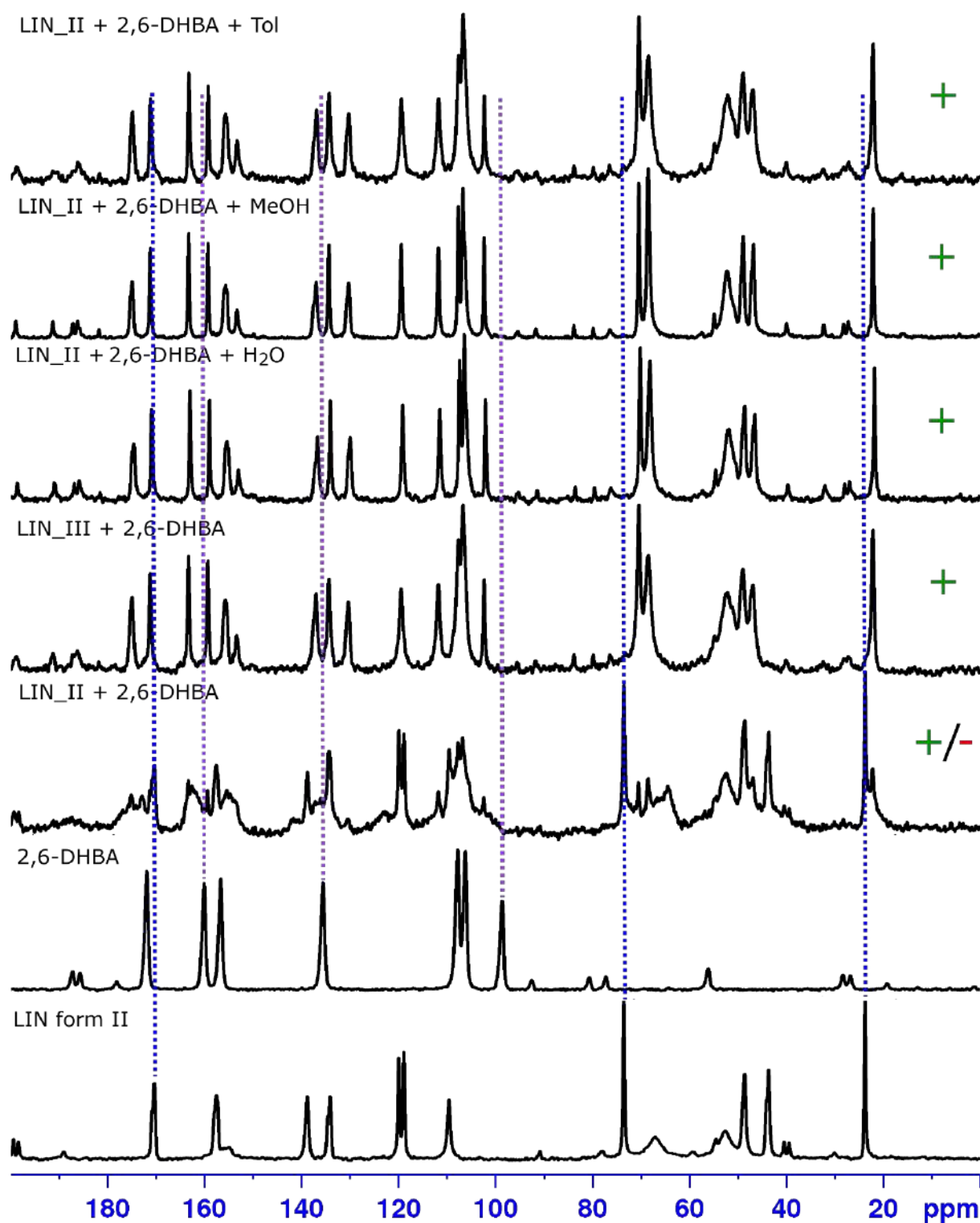


Figure S18. ^{13}C CPMAS NMR spectra for LIN form II, 2,6-DHBA and various reaction mixtures obtained after grinding LIN_II or LIN_III with 2,6-DHBA without any solvent and in the presence of water, methanol or toluene to create LAG conditions. Dashed lines indicate the positions of ^{13}C signals originating from pure reagents, 'plus' or 'minus' signs indicate whether a cocrystal was formed in given reaction conditions.

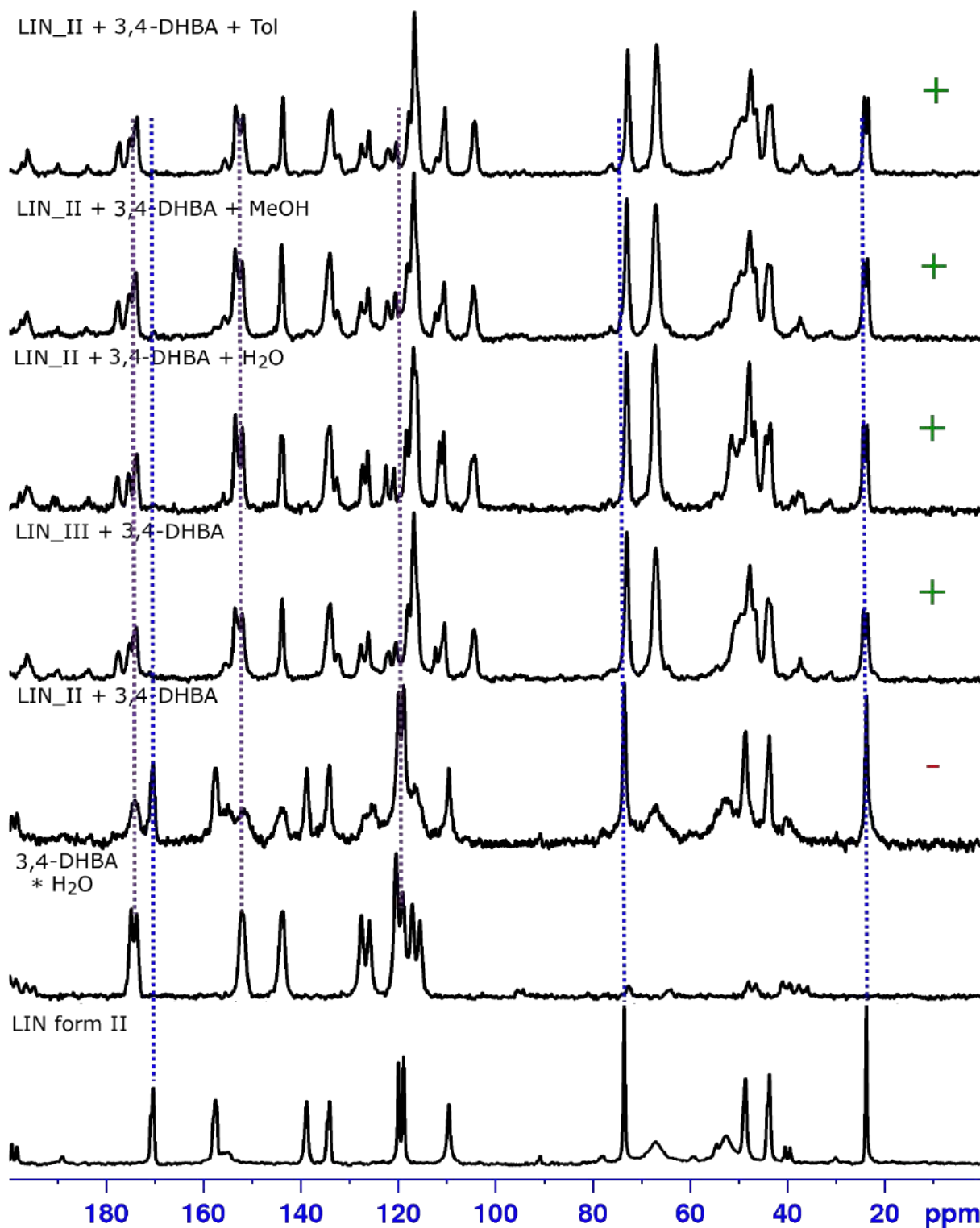


Figure S19. ^{13}C CPMAS NMR spectra for LIN form II, 3,4-DHBA*H₂O and various reaction mixtures obtained after grinding LIN_II or LIN_III with 3,4-DHBA*H₂O without any solvent and in the presence of water, methanol or toluene to create LAG conditions. Dashed lines indicate the positions of ^{13}C signals originating from pure reagents, 'plus' or 'minus' signs indicate whether a cocrystal was formed in given reaction conditions.

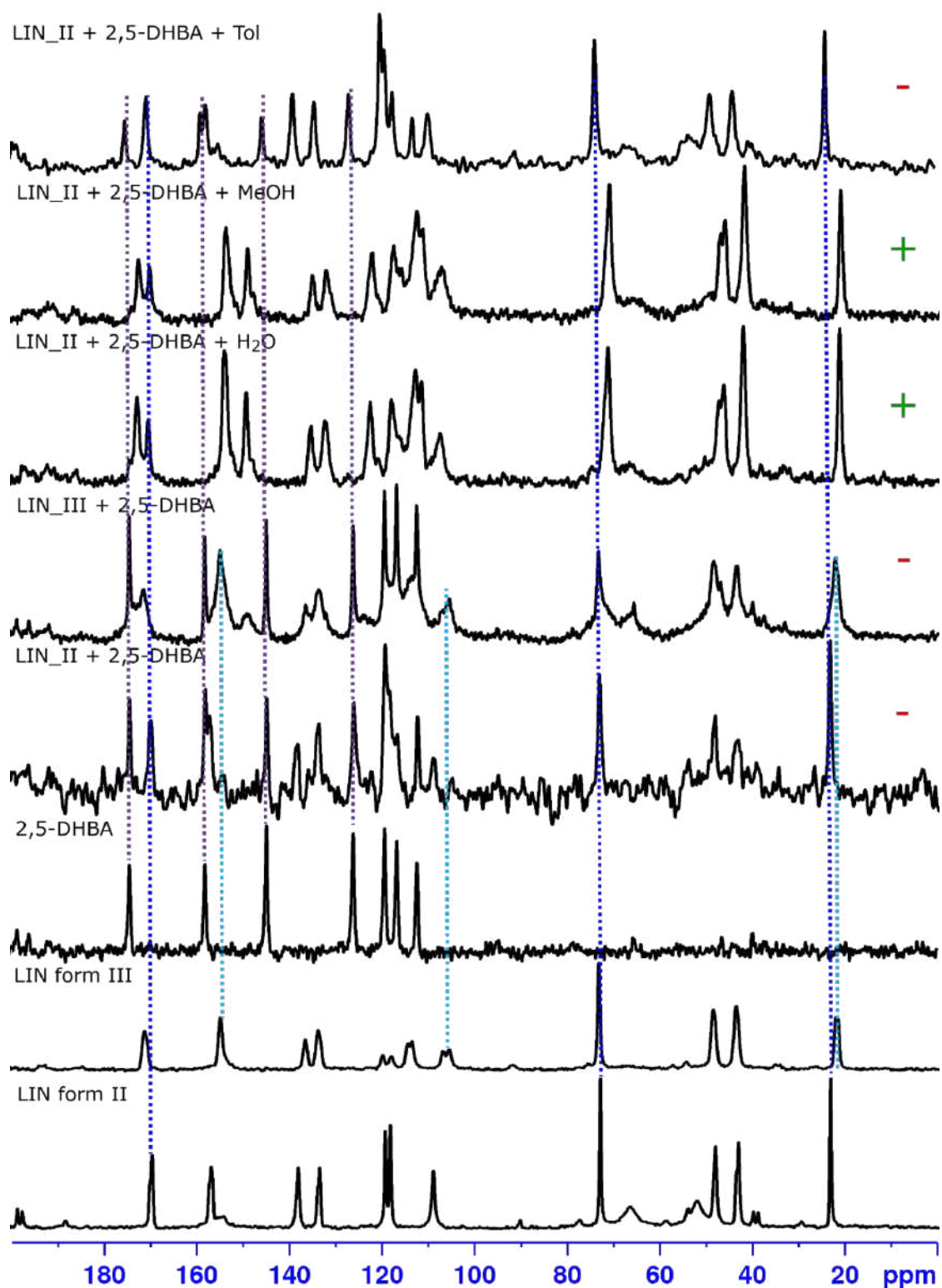


Figure S20. ^{13}C CPMAS NMR spectra for LIN form II, LIN form III, 2,5-DHBA and various reaction mixtures obtained after grinding LIN_II or LIN_III with 2,5-DHBA without any solvent and in the presence of water, methanol or toluene to create LAG conditions. Dashed lines indicate the positions of ^{13}C signals originating from pure reagents, 'plus' or 'minus' signs indicate whether a cocrystal was formed in given reaction conditions.

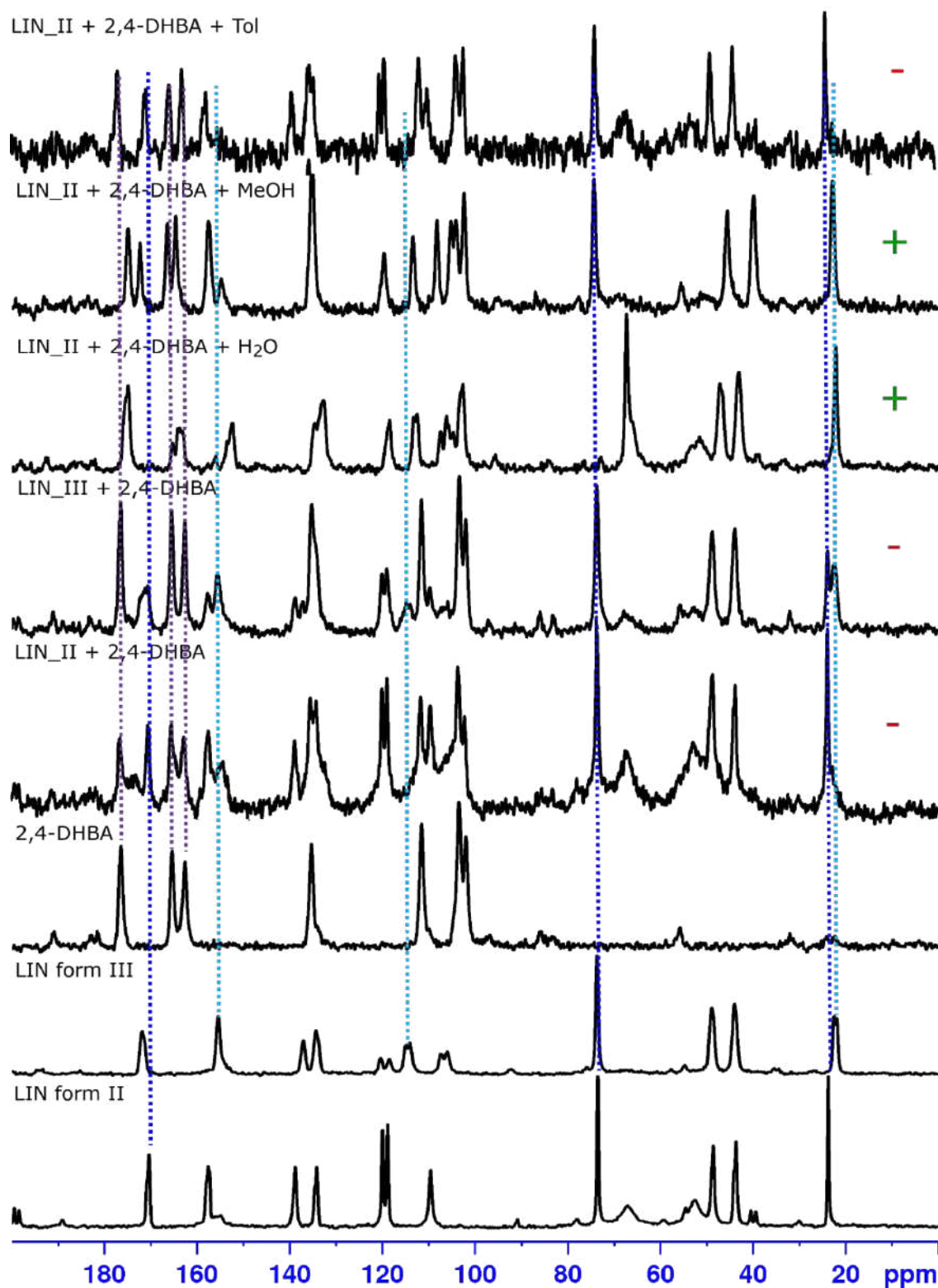


Figure S21. ^{13}C CPMAS NMR spectra for LIN form II, LIN form III, 2,4-DHBA and various reaction mixtures obtained after grinding LIN_II or LIN_III with 2,4-DHBA without any solvent and in the presence of water, methanol or toluene to create LAG conditions. Dashed lines indicate the positions of ^{13}C signals originating from pure reagents, 'plus' or 'minus' signs indicate whether a cocrystal was formed in given reaction conditions.

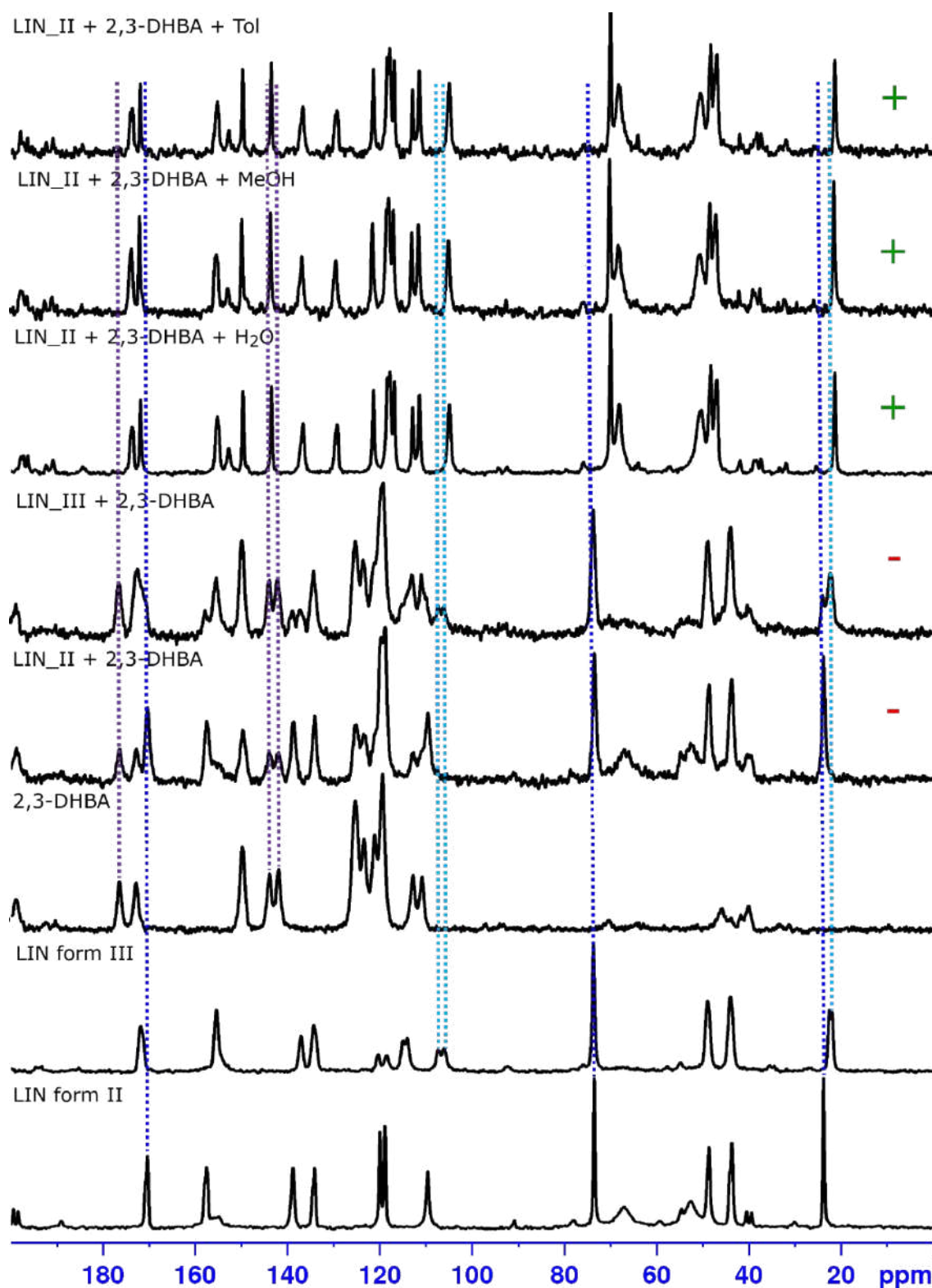


Figure S22. ^{13}C CPMAS NMR spectra for LIN form II, LIN form III, 2,3-DHBA and various reaction mixtures obtained after grinding LIN_II or LIN_III with 2,3-DHBA without any solvent and in the presence of water, methanol or toluene to create LAG conditions. Dashed lines indicate the positions of ^{13}C signals originating from pure reagents, 'plus' or 'minus' signs indicate whether a cocrystal was formed in given reaction conditions.

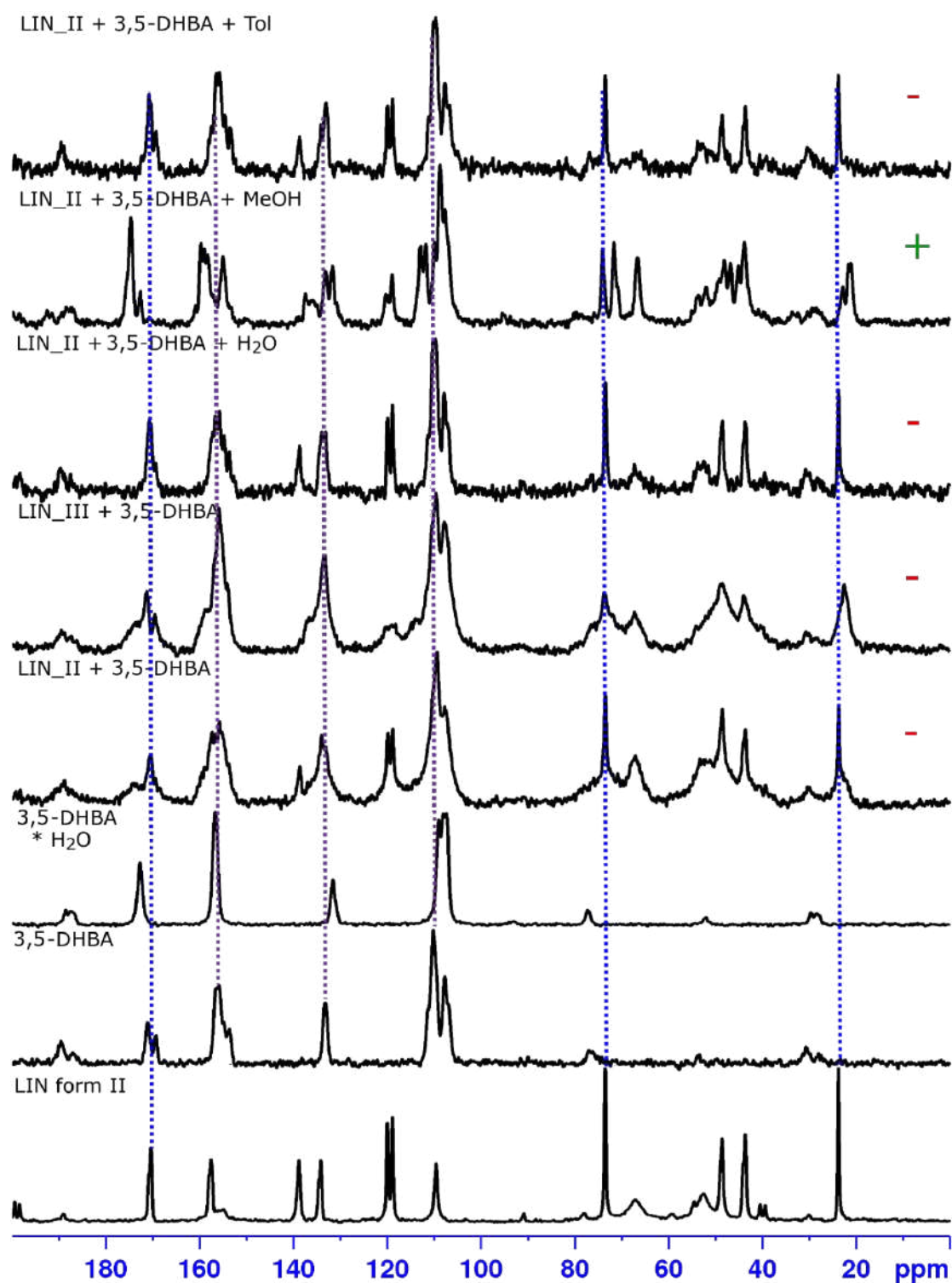


Figure S23. ^{13}C CPMAS NMR spectra for LIN form II, 3,5-DHBA, 3,5-DHBA* H_2O and various reaction mixtures obtained after grinding LIN_II or LIN_III with 3,5-DHBA without any solvent and in the presence of water, methanol or toluene to create LAG conditions. Dashed lines indicate the positions of ^{13}C signals originating from pure reagents, ‘plus’ or ‘minus’ signs indicate whether a cocrystal was formed in given reaction conditions.

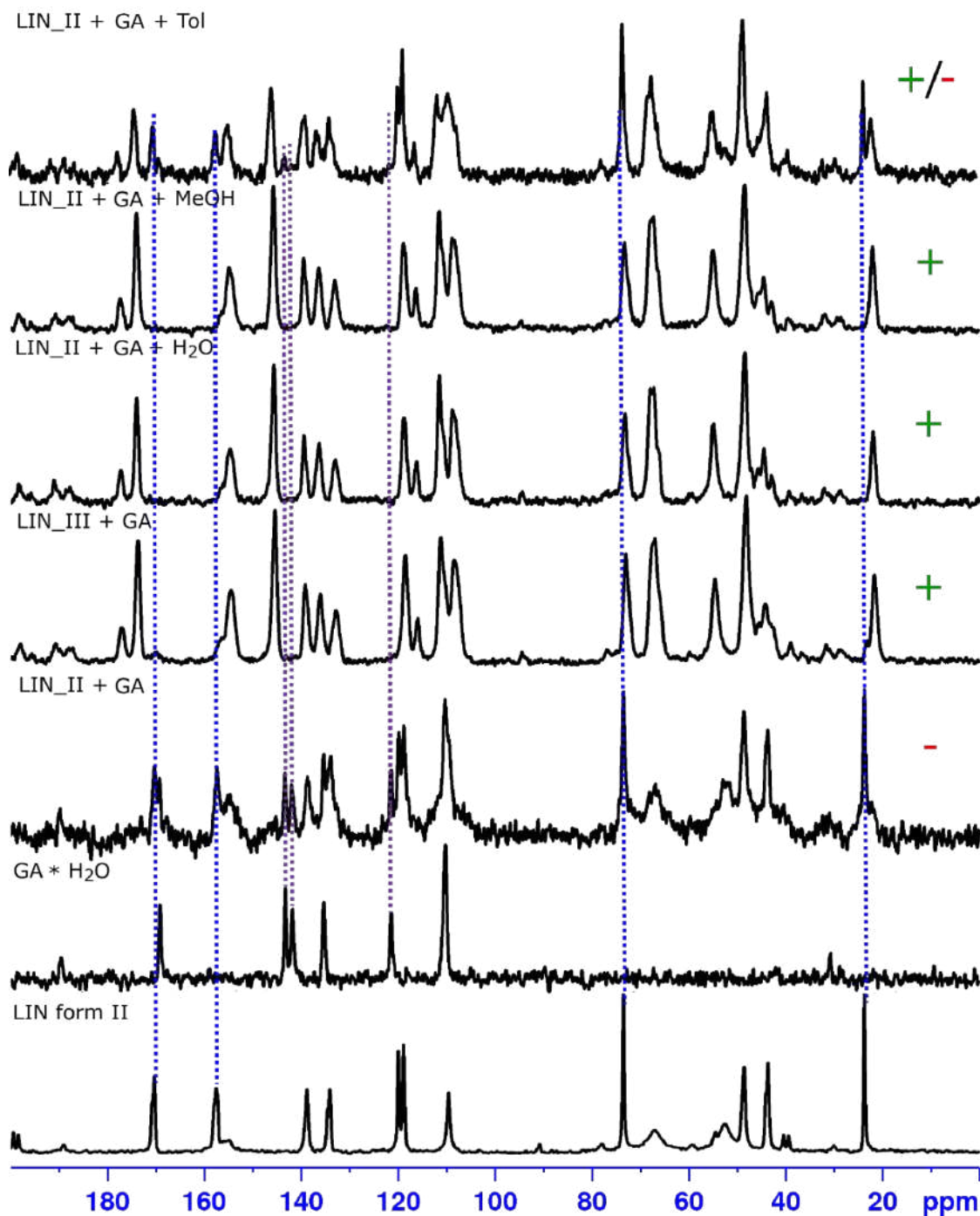


Figure S24. ^{13}C CPMAS NMR spectra for LIN form II, $\text{GA} \cdot \text{H}_2\text{O}$ and various reaction mixtures obtained after grinding LIN_II or LIN_III with GA without any solvent and in the presence of water, methanol or toluene to create LAG conditions. Dashed lines indicate the positions of ^{13}C signals originating from pure reagents, 'plus' or 'minus' signs indicate whether a cocystal was formed in given reaction conditions.

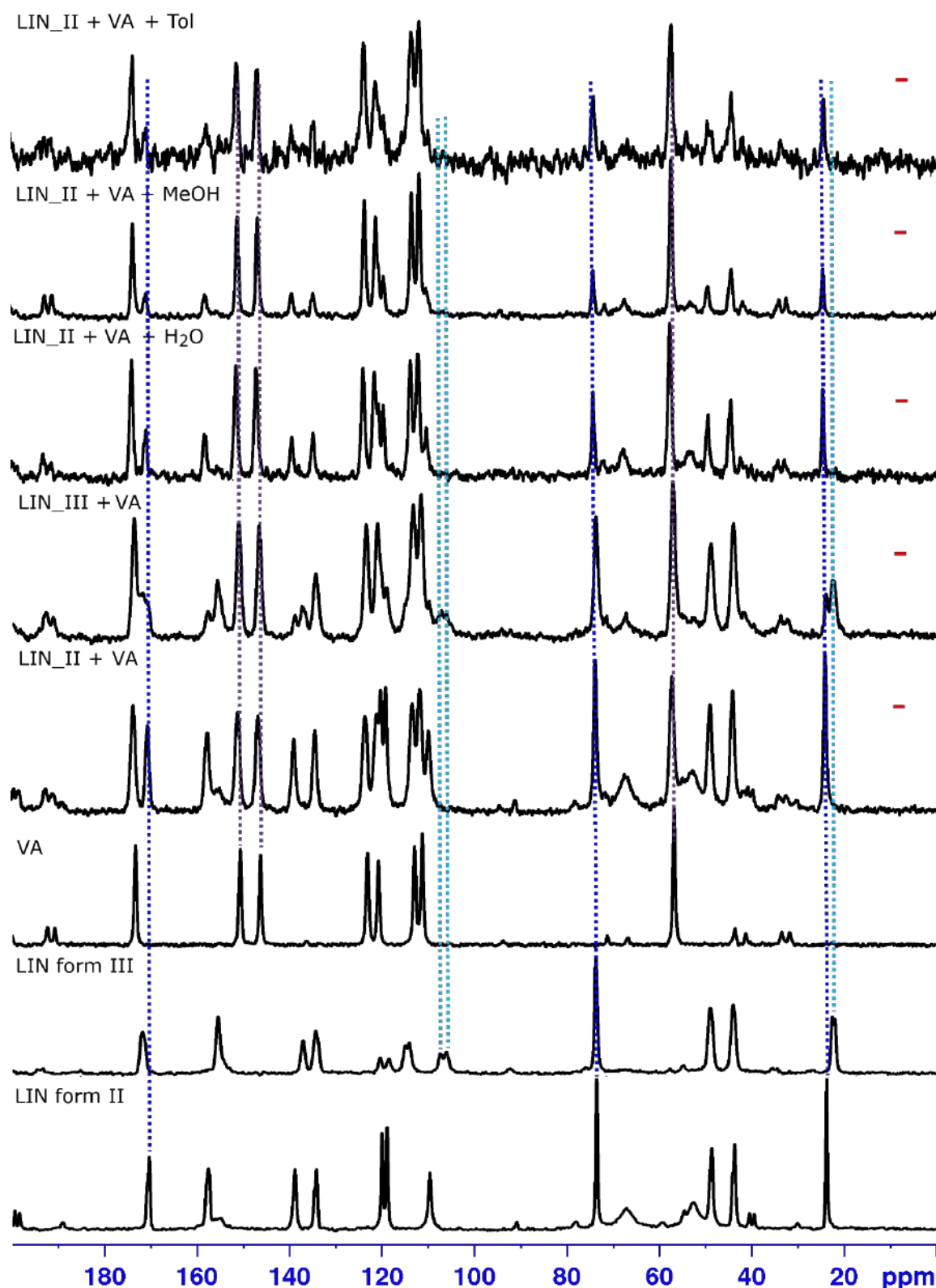


Figure S25. ^{13}C CPMAS NMR spectra for LIN form II, LIN form III, VA and various reaction mixtures obtained after grinding LIN_II or LIN_III with VA without any solvent and in the presence of water, methanol or toluene to create LAG conditions. Dashed lines indicate the positions of ^{13}C signals originating from pure reagents, 'minus' sign indicates a lack of cocrystal formation in given reaction conditions.

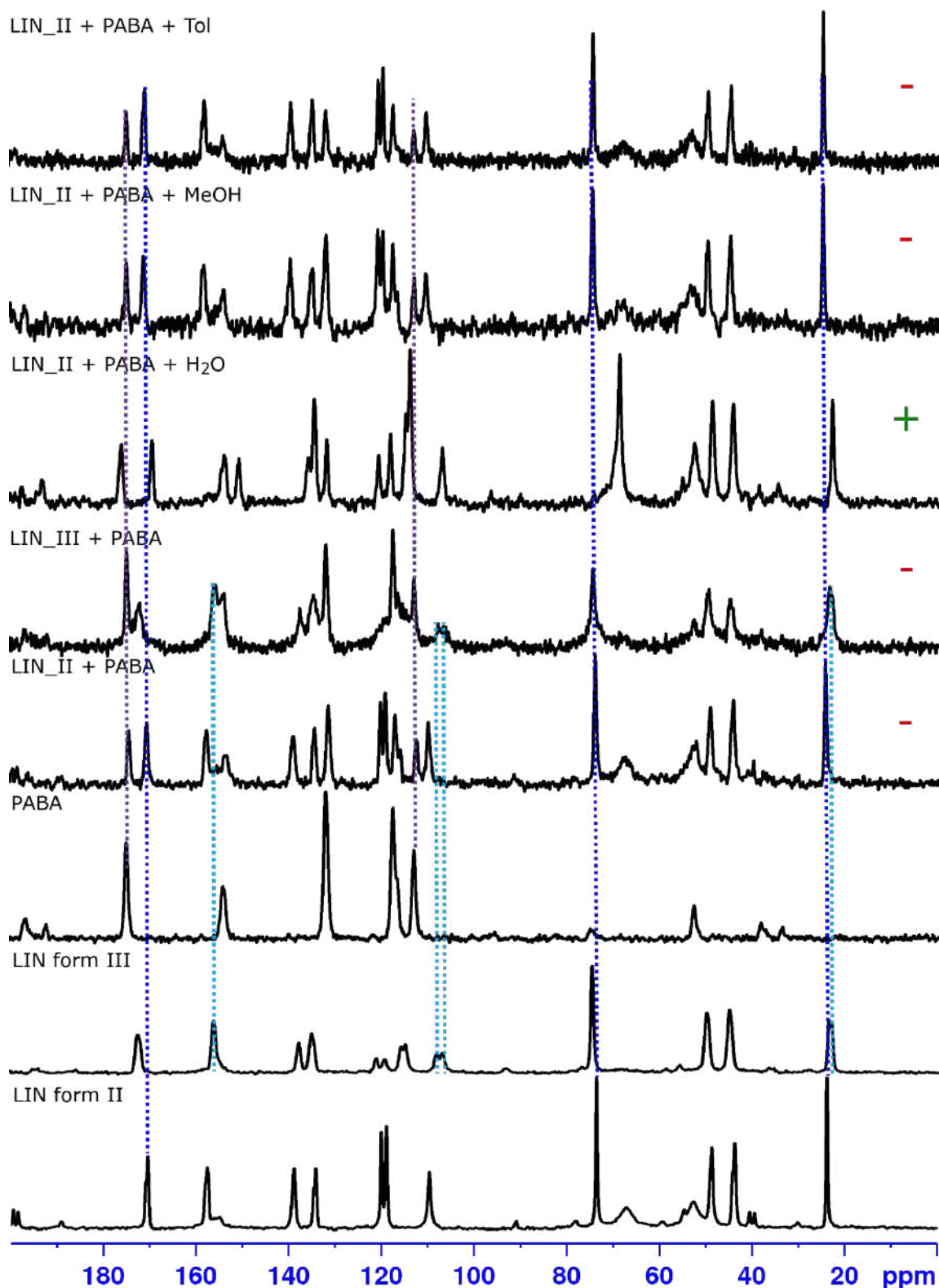


Figure S26. ^{13}C CPMAS NMR spectra for LIN form II, LIN form III, PABA and various reaction mixtures obtained after grinding LIN_II or LIN_III with PABA without any solvent and in the presence of water, methanol or toluene to create LAG conditions. Dashed lines indicate the positions of ^{13}C signals originating from pure reagents, 'plus' or 'minus' signs indicate whether a cocystal was formed in given reaction conditions.

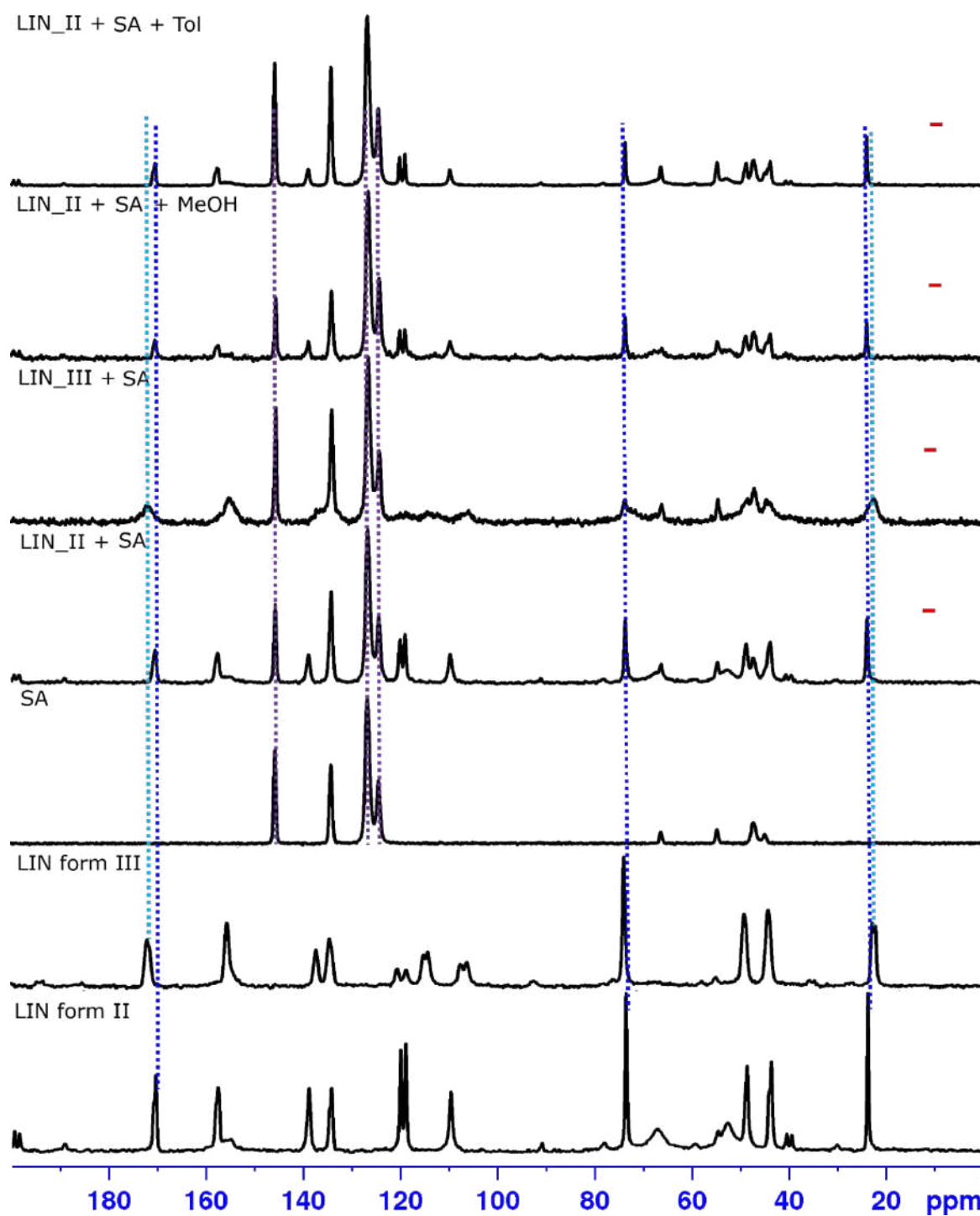


Figure S27. ^{13}C CPMAS NMR spectra for LIN form II, LIN form III, SA and various reaction mixtures obtained after grinding LIN_II or LIN_III with SA without any solvent and in the presence of water, methanol or toluene to create LAG conditions. Dashed lines indicate the positions of ^{13}C signals originating from pure reagents, 'minus' sign indicates a lack of cocrystal formation in given reaction conditions.

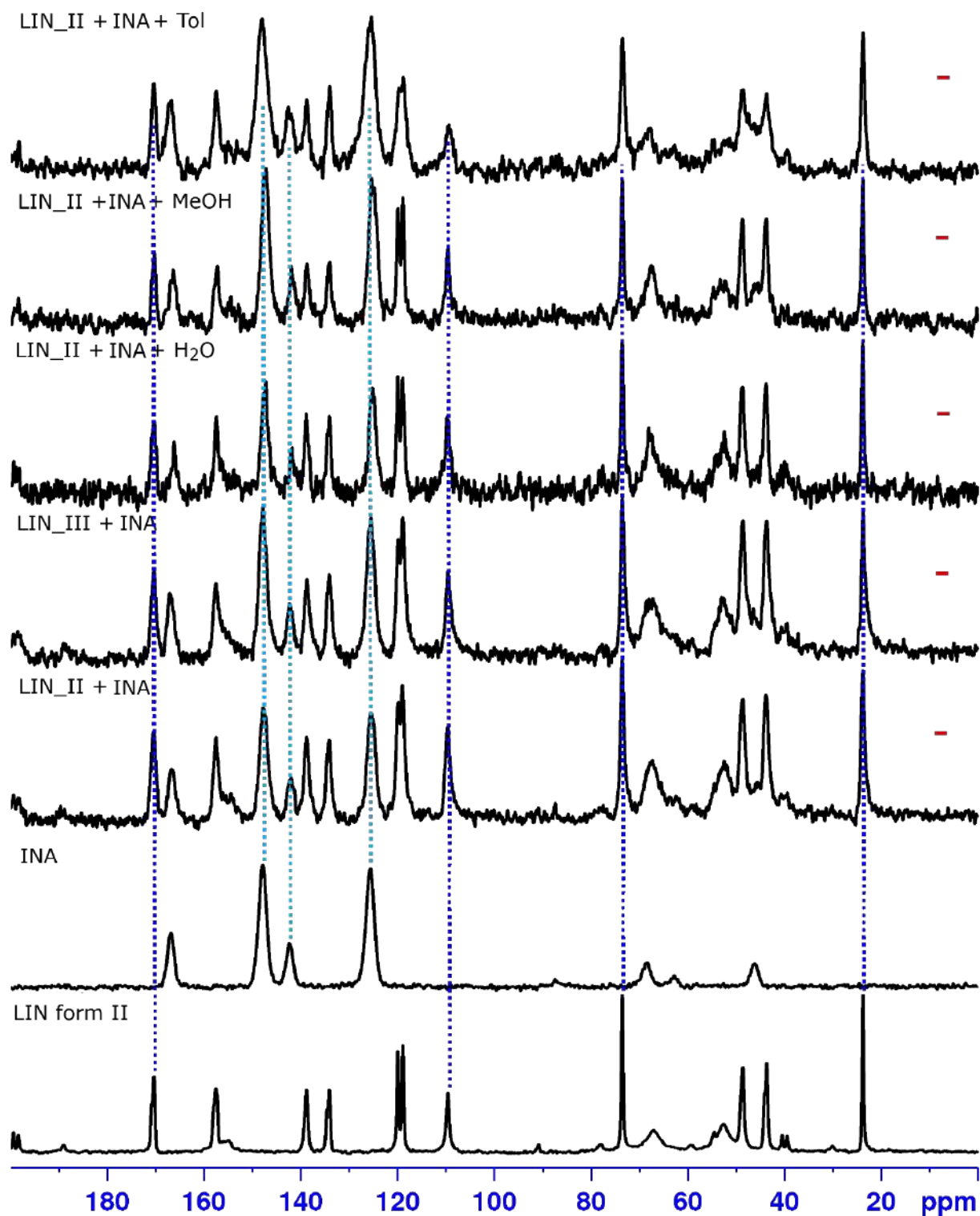


Figure S29. ^{13}C CPMAS NMR spectra for LIN form II, INA and various reaction mixtures obtained after grinding LIN_II or LIN_III with INA without any solvent and in the presence of water, methanol or toluene to create LAG conditions. Dashed lines indicate the positions of ^{13}C signals originating from pure reagents, ‘minus’ sign indicates a lack of cocrystal formation in given reaction conditions.

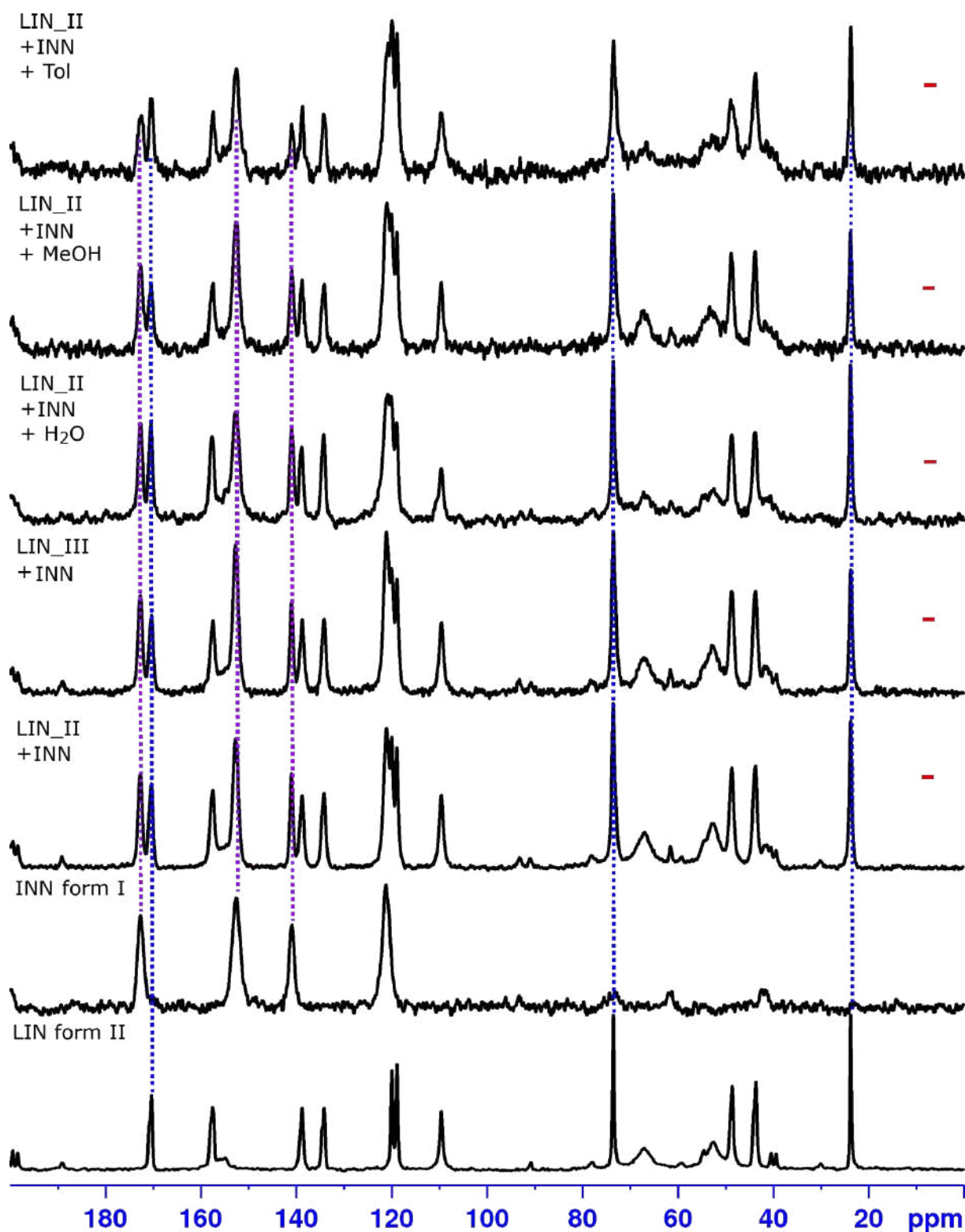


Figure S30. ^{13}C CPMAS NMR spectra for LIN form II, INN form I and various reaction mixtures obtained after grinding LIN_II or LIN_III with INN without any solvent and in the presence of water, methanol or toluene to create LAG conditions. Dashed lines indicate the positions of ^{13}C signals originating from pure reagents, 'minus' sign indicates a lack of cocrystal formation in given reaction conditions.

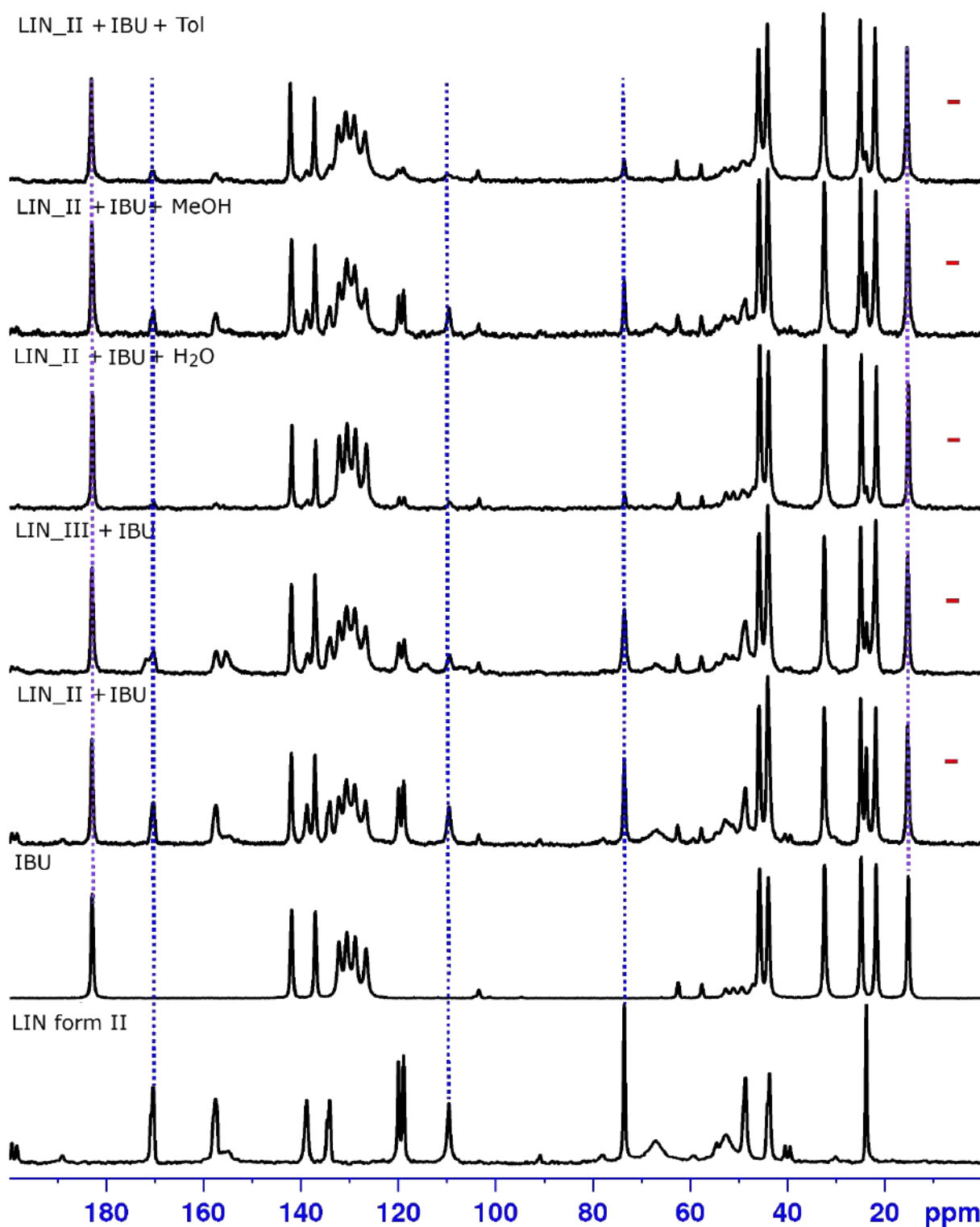


Figure S31. ^{13}C CPMAS NMR spectra for LIN form II, IBU and various reaction mixtures obtained after grinding LIN_II or LIN_III with VA without any solvent and in the presence of water, methanol or toluene to create LAG conditions. Dashed lines indicate the positions of ^{13}C signals originating from pure reagents, ‘minus’ sign indicates a lack of cocrystal formation in given reaction conditions.

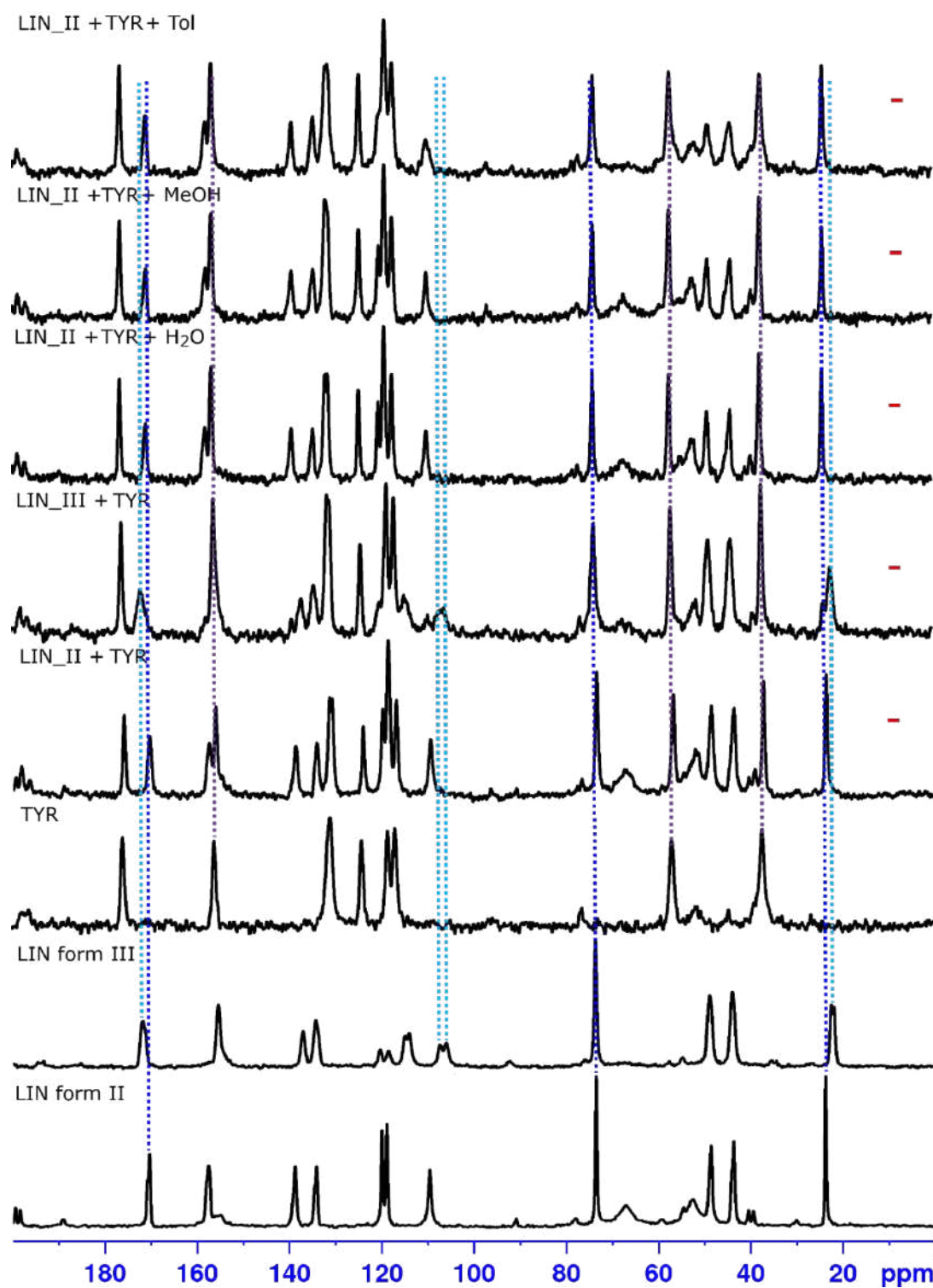


Figure S32. ^{13}C CPMAS NMR spectra for LIN form II, LIN form III, TYR and various reaction mixtures obtained after grinding LIN_II or LIN_III with TYR without any solvent and in the presence of water, methanol or toluene to create LAG conditions. Dashed lines indicate the positions of ^{13}C signals originating from pure reagents, 'minus' sign indicates a lack of cocrystal formation in given reaction conditions.

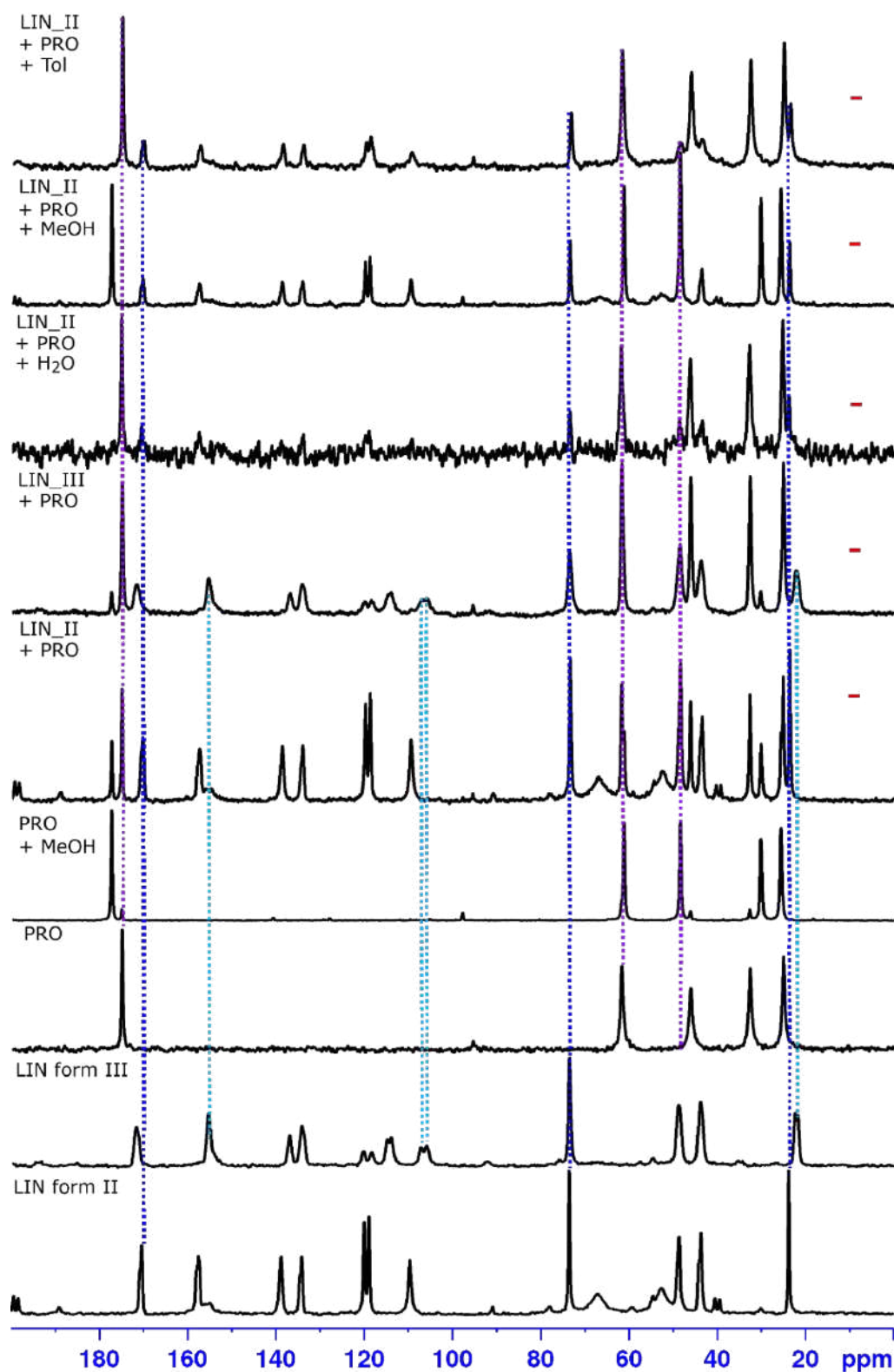


Figure S33. ^{13}C CPMAS NMR spectra for LIN form II, LIN form III, PRO and various reaction mixtures obtained after grinding LIN_II or LIN_III with PRO without any solvent and in the presence of water, methanol or toluene to create LAG conditions, as well as after grinding PRO with methanol. Dashed lines indicate the positions of ^{13}C signals originating from pure reagents, ‘minus’ sign indicates a lack of cocrystal formation in given reaction conditions.

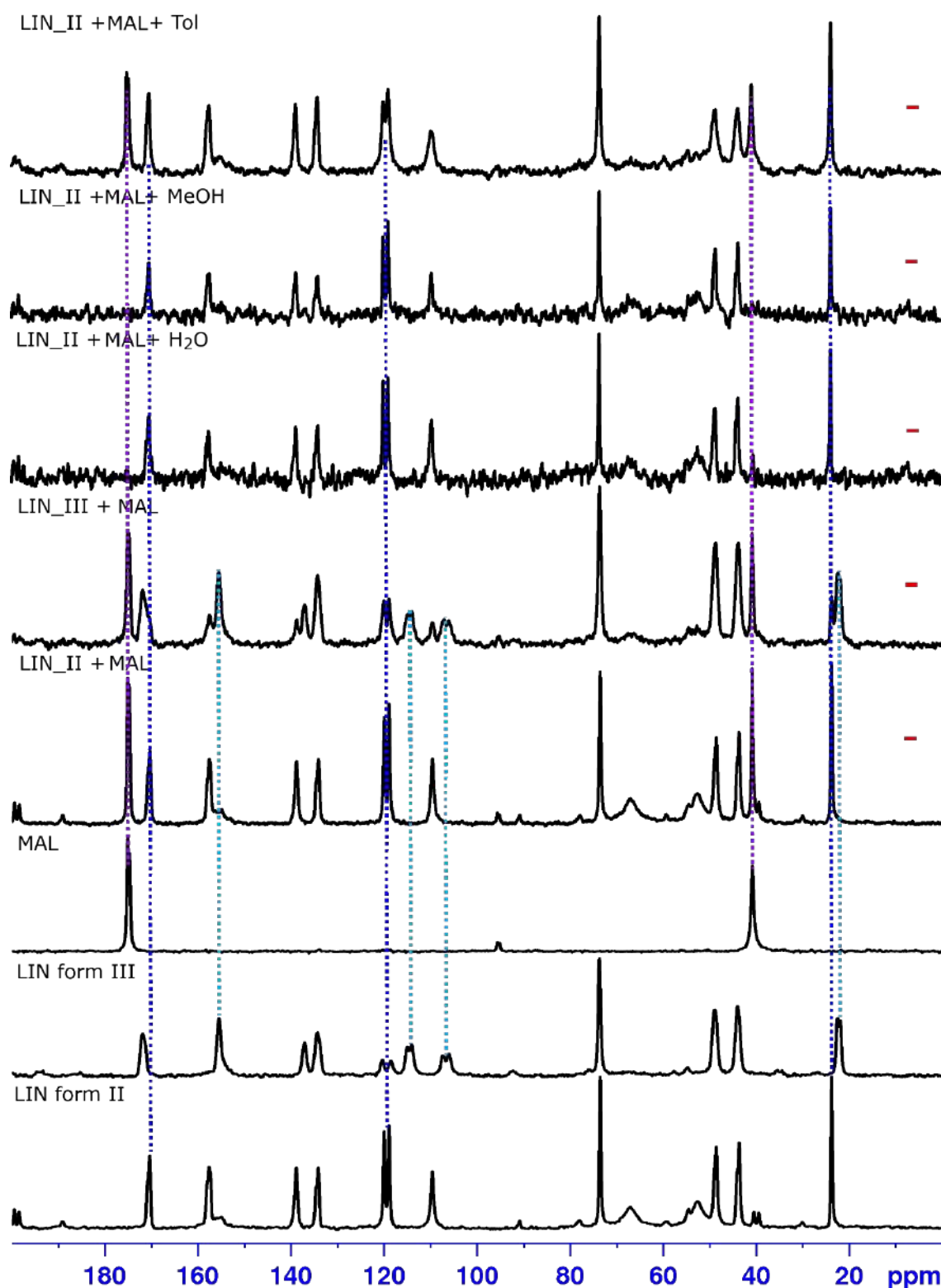


Figure S34. ^{13}C CPMAS NMR spectra for LIN form II, LIN form III, MAL and various reaction mixtures obtained after grinding LIN_II or LIN_III with MAL without any solvent and in the presence of water, methanol or toluene to create LAG conditions. Dashed lines indicate the positions of ^{13}C signals originating from pure reagents, 'minus' sign indicates a lack of cocrystal formation in given reaction conditions.

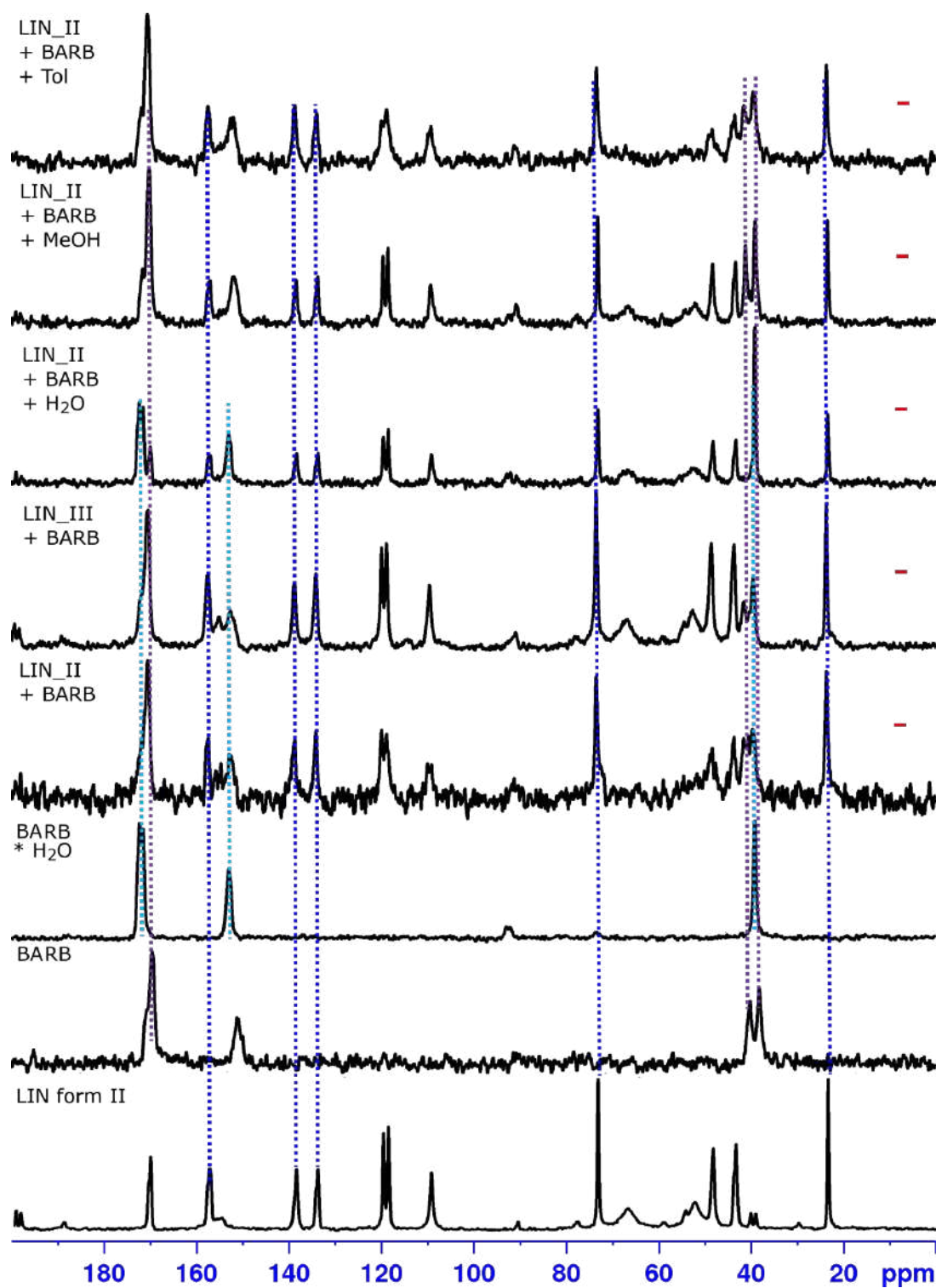


Figure S35. ^{13}C CPMAS NMR spectra for LIN form II, BARB, BARB* H_2O and various reaction mixtures obtained after grinding LIN_II or LIN_III with BARB without any solvent and in the presence of water, methanol or toluene to create LAG conditions. Dashed lines indicate the positions of ^{13}C signals originating from pure reagents, 'minus' sign indicates a lack of cocrystal formation in given reaction conditions.

3. Determination of the cofomers polymorphic forms

Benzoic acid (BA) crystallizes in one polymorphic $P2_1/c$ monoclinic form (CSD refcode BENZAC). For all calculations BENZAC13¹ crystal structure from the CSD database was used.

2,3-dihydroxybenzoic acid (2,3-DHBA) has two known polymorphic forms: triclinic P-1 (CSD refcode CACDAM)² and monoclinic $P2_1/n$ (CSD refcode CACDAM01).³ Of these, only the triclinic form is a $Z'=2$ structure, in agreement with the ¹³C CPMAS NMR spectrum registered for our sample of this cofomer (see Figure S36). Therefore the crystal structure of this triclinic form was accounted for in the calculations.

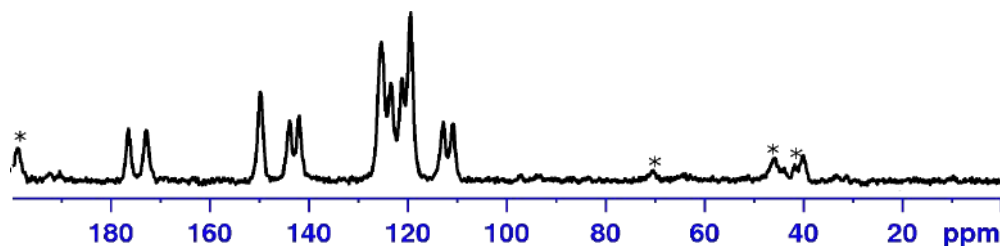


Figure S36. ¹³C CPMAS NMR spectrum of commercial 2,3-DHBA sample. The number of ¹³C resonances indicates a $Z'=2$ structure, which corresponds to a triclinic form of 2,3-DHBA. The repetition delay for this spectrum was equal to 300 s. Asterisks mark spinning sidebands.

2,4-dihydroxybenzoic acid (2,4-DHBA) exists in two monoclinic forms, form I (CSD refcode ZZZEEU08)⁴ and form II (CSD refcode ZZZEEU01).⁵ The forms are enantiotropically related, with form II being more stable at room temperature and showing in the DSC a phase transition to form I at ca. 155-160 °C.⁶ The DSC plot registered for the commercial sample of 2,4-DHBA shows an endothermic transition corresponding to this phase change (Figure S37). Therefore it was form II of 2,4-DHBA that was taking part for mechanochemical reactions.

2,4-DHBA is also known to form two hydrates: a hemihydrates (CSD refcode QIVTUK01)⁴ and a monohydrate (CSD refcode YUXGUV).⁷ In our conditions neither of these forms were observed. Even after grinding 2,4-DHBA with water or methanol no hydrate formation was observed, as indicated by a lack of any change in the ¹³C CPMAS NMR spectra of 2,4-DHBA before and after grinding with water or methanol (see Figure S37).

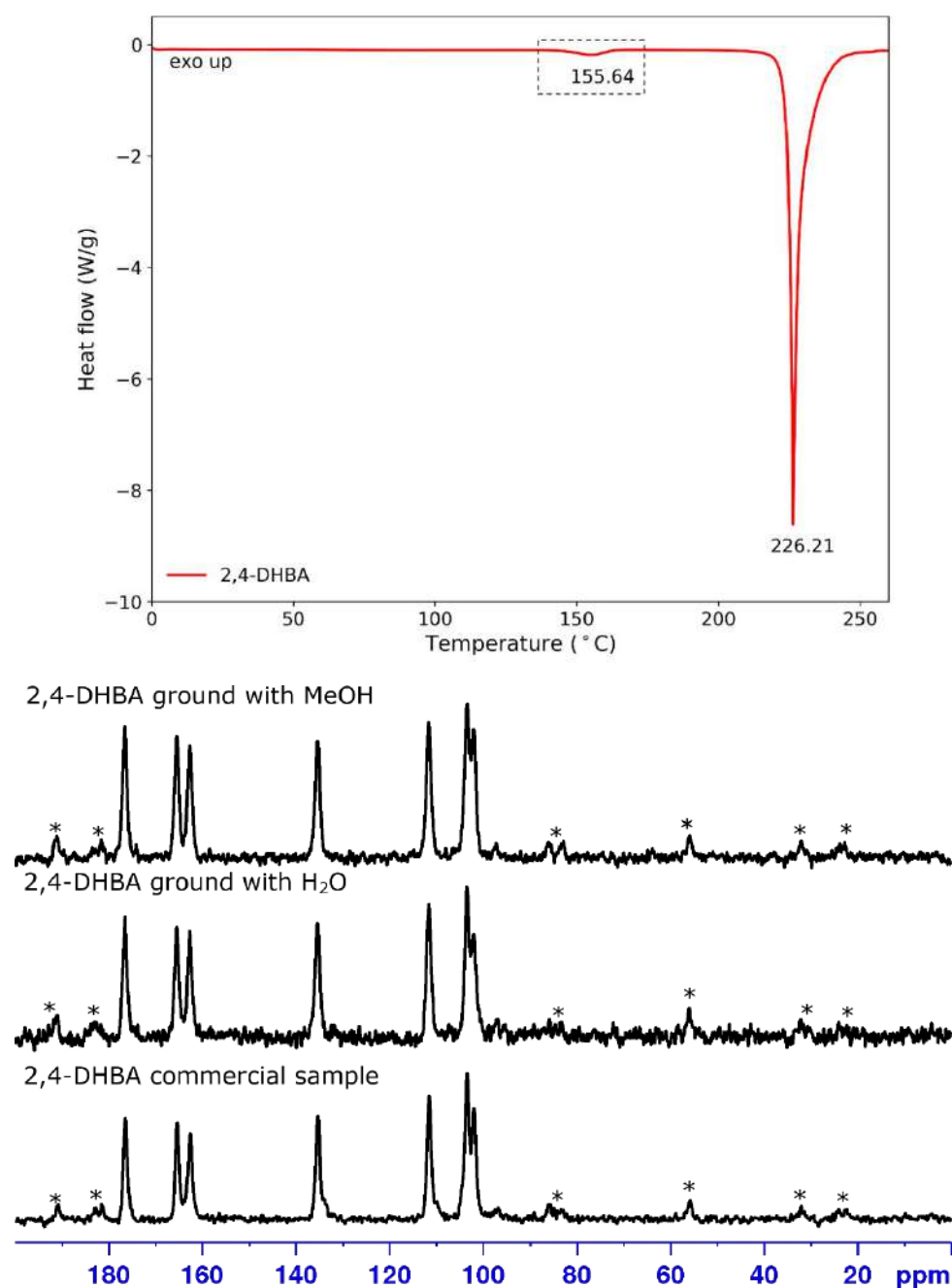


Figure S37. Upper: the DSC curve for a commercial sample of 2,4-DHBA with a phase transition from form II to form I marked by a dashed-lined rectangle; lower: ^{13}C CPMAS NMR spectra registered for a commercial sample of 2,4-DHBA and the same sample after grinding with water or methanol. Asterisks mark spinning sidebands.

2,5-dihydroxybenzoic acid (2,5-DHBA) has also two known polymorphic forms (both monoclinic): form I (CSD refcode BESKAL02)⁸ and form II (CSD refcode BESKAL03).⁸ The ^{13}C CPMAS NMR spectrum registered for the commercial sample of 2,5-DHBA indicated that it is a mixture of two polymorphic forms, which was deduced from the presence of additional small intensity signals apart from those detected for the major form present in the sample. The DSC measurements confirmed the presence of two polymorphs, as indicated by two separate melting events at temperatures corresponding to the melting points of form I (207.7 °C) and II

(203.6 °C), respectively.⁶ After recrystallization of this sample from 2-propanol/methanol only one set of signals was visible in the ^{13}C CPMAS spectrum of this sample and only one endothermic event on the DSAC curve corresponding to the melting point of form I (see Figure S38). In the grinding experiments with LIN form I of 2,5-DHBA was used.

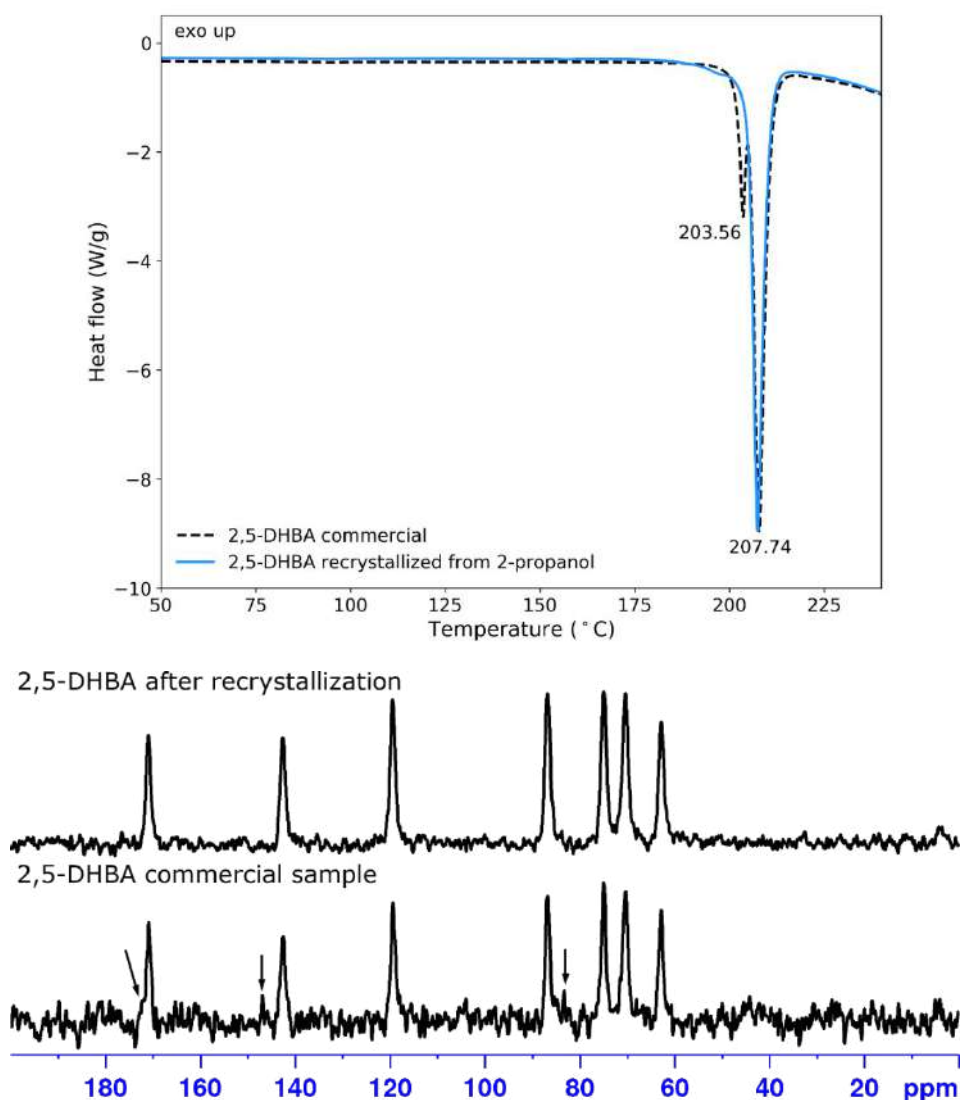


Figure S38. The DSC curves (upper) and ^{13}C CPMAS NMR spectra (lower) registered for a commercial sample of 2,5-DHBA and the same sample after recrystallization from 2-propanol/methanol. Arrows in the NMR spectrum of commercial 2,5-DHBA mark additional signals originating from form II.

2,6-dihydroxybenzoic acid (2,6-DHBA) crystallizes in two neat polymorphic forms: orthorhombic $Pna2_1$ form (CSD refcode LEZJAB)⁹ and monoclinic $P2_1/c$ form (CSD refcode LEZJAB01),¹⁰ in addition to a monohydrate $Pnma$ form (CSD refcode LEZJEF).⁹ The ^{13}C CPMAS NMR spectrum registered for commercial sample of 2,6-DHBA indicates the presence of a mixture of polymorphic forms, as indicated by small intensity signals marked in Figure S39 by arrows. This is further corroborated by the PXRD measurements, which suggest that the commercial sample contains $Pna2_1$ form with an admixture of the monohydrate form (see Figure S39 for reflexes originating from both forms clearly identifiable in the PXRD

diffractogram of 2,6-DHBA sample). The DSC curve for the commercial sample of 2,6-DHBA indicates the presence of the monoclinic form, with the melting point of ca. 164 °C, in agreement with the literature values (165-167 °C),¹¹ with a small endothermic event at ca. 95 °C in the DSC associated with a loss of water from a monohydrate form.

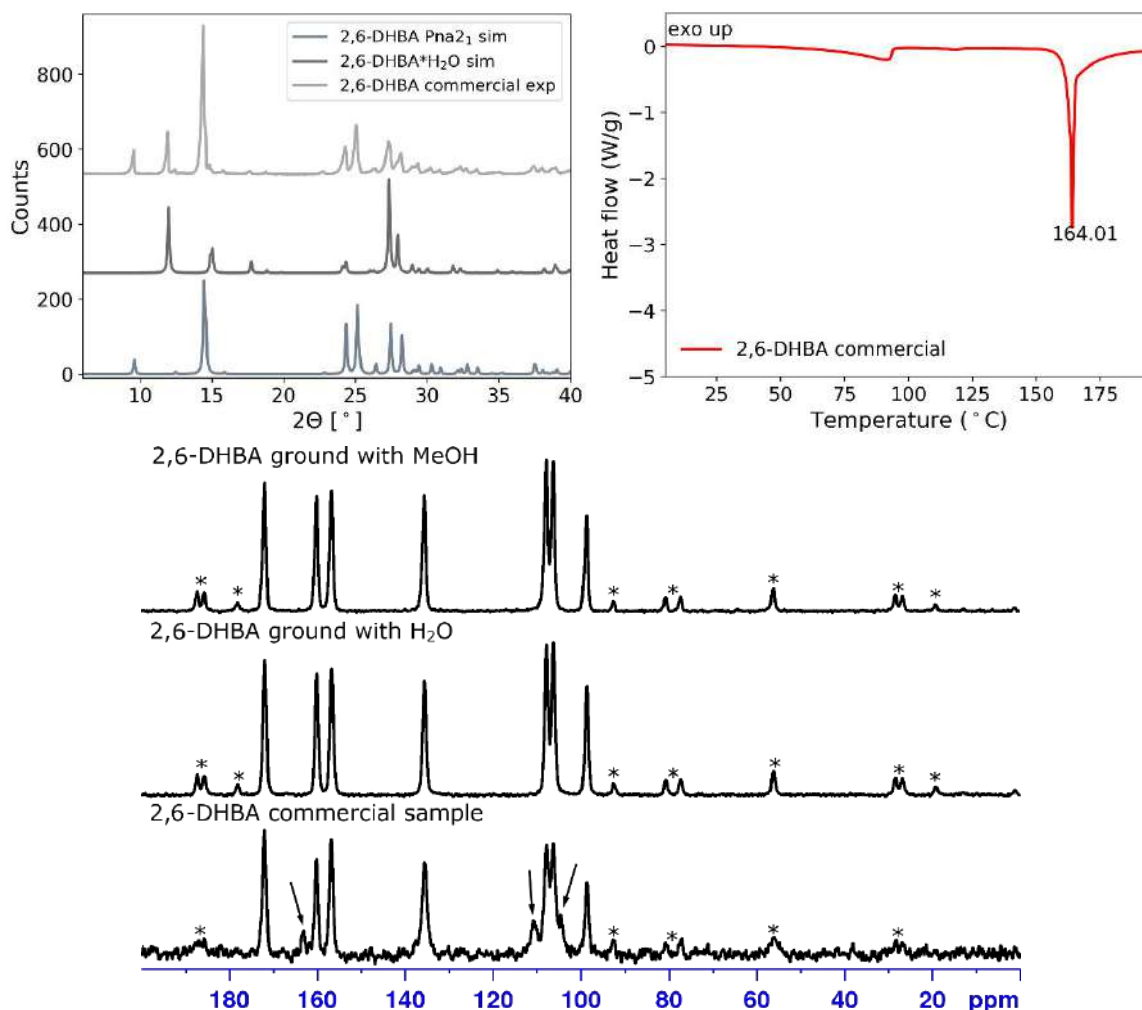


Figure S39. Upper left: experimental PXRD data for the commercial sample of 2,6-DHBA and simulated PXRD patterns for its orthorhombic form (LEZJAB), as well as its monohydrate (LEZJEF); upper right: the DSC curve for a commercial sample of 2,6-DHBA; lower: ¹³C CPMAS NMR spectra registered for a commercial sample of 2,6-DHBA and the same sample after grinding with water or methanol. Asterisks mark spinning sidebands, while arrows indicate additional signals originating from a monohydrate form of 2,6-DHBA.

Surprisingly, after grinding 2,6-DHBA sample with methanol or water the small intensity signals visible in the NMR spectrum of the commercial sample and originating from the monohydrate form are no longer detectable. Instead, only signals originating from the orthorhombic form are visible. Therefore, this form was designated as the one taking part in the mechanochemical reactions with LIN.

3,4-dihydroxybenzoic acid (3,4-DHBA) has only one neat crystal structure published in the CSD database, which was crystallized from the melt (CSD refcode WUYNUA), and three

crystal structures of 3,4-DHBA monohydrates: two triclinic forms (CSD refcodes BIJDON03¹² and BIJDON04)³ and one monoclinic form (CSD refcode BIJDON05)¹³. The ¹³C CPMAS NMR spectrum of commercial 3,4-DHBA shows very broad resonances (Figure S40) suggesting the presence of at least partially amorphous form. Mechanochemical grinding of this sample in the presence of water, as well as its crystallization from water yielded a form with two sets of ¹³C resonances in the solid-state NMR spectrum (Figure S40), indicating a $Z'=2$ structure, *i.e.* triclinic rhombic monohydrate form of 3,4-DHBA (BIJDON03). This form was used in all grinding experiments.

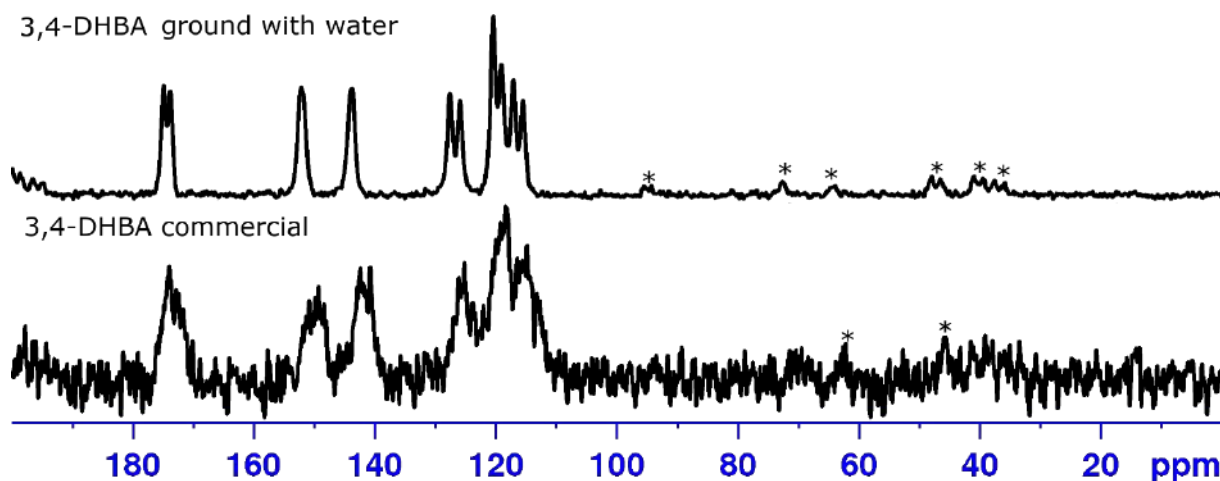


Figure S40. ¹³C CPMAS NMR spectra of the commercial sample of 3,4-DHBA and the same sample after grinding with water.

3,5-dihydroxybenzoic acid (3,5-DHBA) has two neat polymorphic forms: form 1 (CSD refcode WUYPOW)³ and form 2 (CSD refcode WUYPOW01),³ in addition to a hemihydrate (CSD refcode OKEMAT).¹⁴ The DSC curve for the commercial sample of 3,5-DHBA do not show any endothermic events that might be associated with a loss of crystalline water (see Figure S13). Therefore this is an anhydrous form. Its ¹³C CPMAS NMR spectrum indicates the presence of at least two sets of ¹³C resonances (possibly three, see Figure S41), indicating that this is form 2 of 3,5-DHBA. The presence of form 2 in the commercial sample is further confirmed by the PXRD data (see Figure 41). This form was used in the grinding experiments with LIN.

Grinding form 2 of 3,5-DHBA with methanol did not change its ¹³C CPMAS NMR spectrum, but upon grinding with water a different form of 3,5-DHBA emerged with only one set of ¹³C resonances (in contrast to the known hemihydrate, which is a $Z'=2$ structure). The PXRD diffractogram registered for this form indicated that this is a different from the published hemihydrate, in agreement with the NMR data. As this form does not easily yield crystals for single-crystal X-Ray measurements, establishing its crystal structure is beyond the scope of this work and will be in the future.

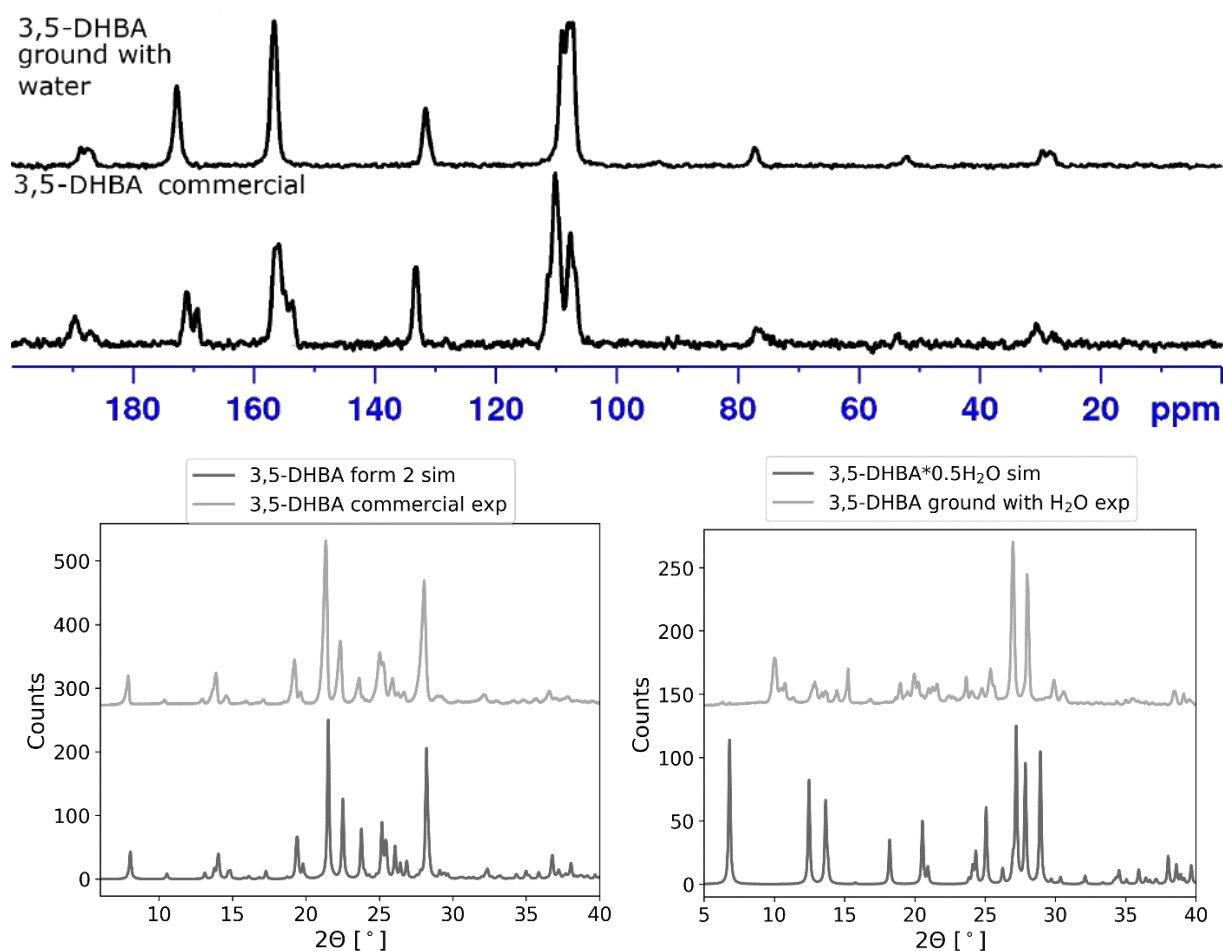


Figure S41. Upper: ^{13}C CPMAS NMR spectra registered for a commercial sample of 3,5-DHBA and the same sample after grinding with methanol or water. In the case of methanol no phase change was observed to the sample, but grinding with water yielded a different phase. Lower left: experimental PXRD data for the commercial sample of 3,5-DHBA and its comparison with the simulated powder pattern for form 2 of 3,5-DHBA (WUYPOW01). Lower right: comparison of the experimental PXRD data for 3,5-DHBA sample ground with water and the simulated PXRD pattern for a known hemihydrate of 3,5-DHBA.

p-hydroxybenzoic acid (PHBA) has two neat crystal structures published in the CSD in $P2_1/a$ (CSD refcode JOZZIH, form I)¹⁵ and $P2_1/n$ monoclinic space groups (CSD refcode JOZZIH01, form II),¹⁶ in addition to a monohydrate (CSD refcode PHBZAC02).¹⁷ The DSC registered for a commercial sample of PHBA (Figure S42) indicates that this form is not a hydrate. Grinding the commercial sample with water or methanol does not cause any changes to the phase of the commercial sample, as indicated by the ^{13}C CPMAS NMR measurements (Figure S42). The PXRD patterns for both neat polymorphs of PHBA are very similar, as both structures share some common features. Nevertheless, the comparison of the simulated PXRD data with the experimental diffractogram for commercial PHBA indicates that it is rather form I, with the positions of the diffraction peaks being closer to this form than to form II (see Figure S42).

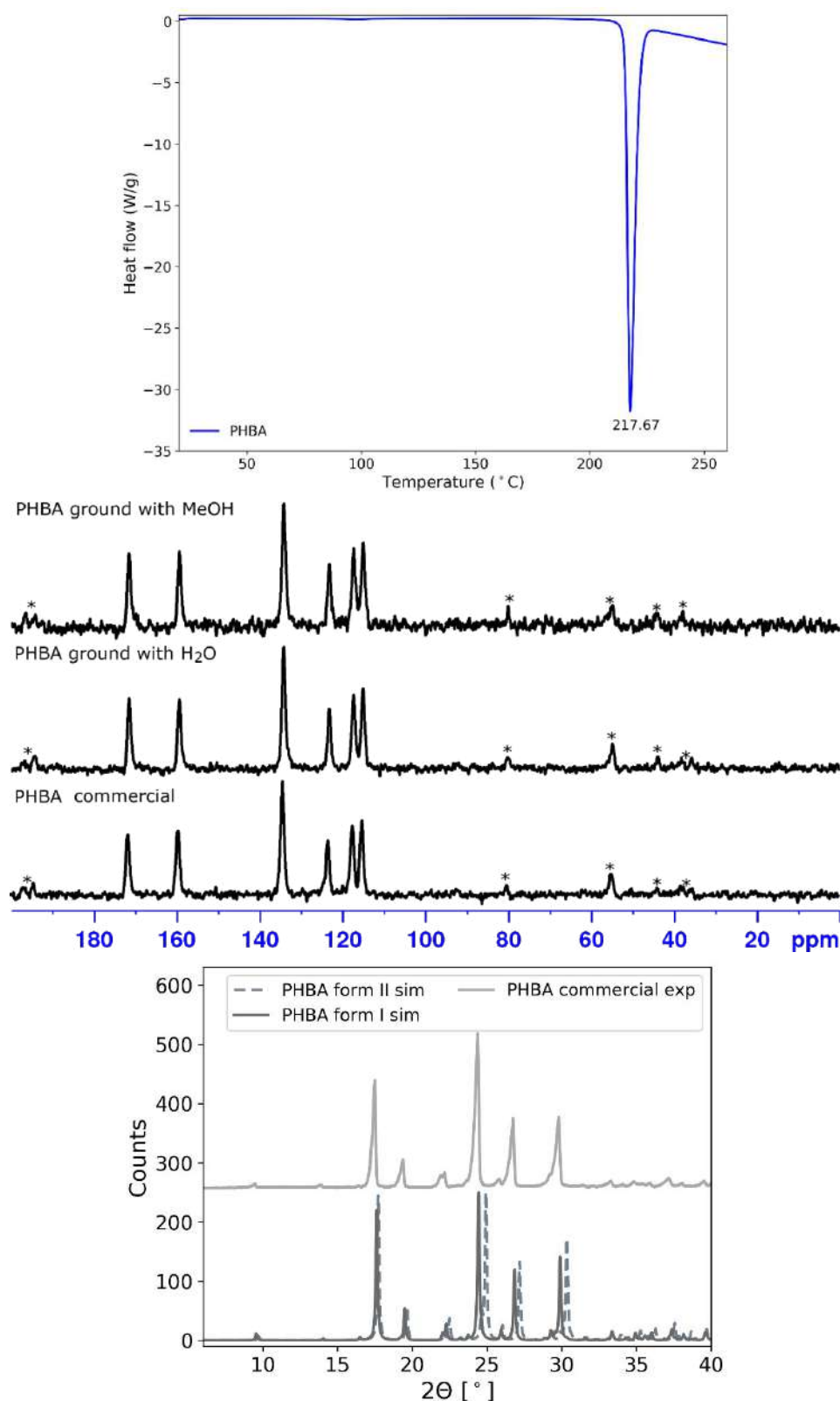


Figure S42. Upper: DSC curve for commercial sample of PHBA. Middle: ¹³C CPMAS NMR spectra registered for a commercial sample of PHBA and the same sample after grinding with methanol or water. No phase change was observed upon grinding. Asterisks mark spinning sidebands. Lower: experimental PXRD data registered for the commercial sample of PHBA and its comparison with the simulated PXRD patterns for two polymorphic forms of this coformer.

p-aminobenzoic acid (PABA) has four neat polymorphic forms with known crystal structures: form alpha I (CSD refcode AMBNAC06),¹⁸ form beta IV (CSD refcode AMBNAC10),^{Error! Bookmark not defined.} high pressure form delta (CSD refcode AMBNAC14)¹⁹ and orthorhombic form V (CSD refcode AMBNAC09).²⁰ The DSC measurement for commercial sample of PABA shows the melting event at ca. 190 °C (Figure S14), which is in good agreement with the literature melting point for the alpha I form. The presence of this form is also indicated by the PXRD data registered for the commercial sample (see Figure S43).

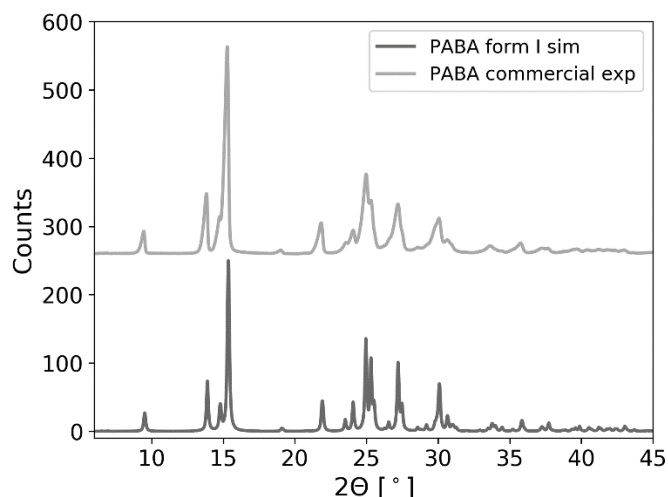


Figure S43. Experimental PXRD data registered for the commercial sample of PABA and its comparison with the simulated PXRD pattern for the α polymorph of PABA.

Gallic acid (GA) used for grinding experiments was in its monohydrate form. There are six polymorphs of GA monohydrate in the CSD, of which five are monoclinic polymorph and one is a triclinic polymorph. These are: $P2_1/c$ form I (CSD refcodes KONTIQ),²¹ $P2_1/n$ form II (CSD refcode KONTIQ01),²² triclinic $P-1$ form III (CSD refcode KONTIQ04),²³ $P2_1/c$ form IV (CSD refcode KONTIQ05),²³ $P2_1/c$ form V (CSD refcode KONTIQ06),²⁴ and $P2_1/c$ form VI (CSD refcode KONTIQ08).²⁵ The PXRD data indicate that the sample used for grinding experiments with LIN contains form II of GA monohydrate (see Figure S44). Upon grinding of the commercial form with water or methanol no changes to the ¹³C CPMAS NMR spectra are observed (Figure S44), indicating a lack of a phase change.

Vanillic acid (VA) has only one known crystal structure in the CSD, with the CSD refcode CEHGUS.²⁶ The ¹³C CPMAS NMR spectrum registered for a commercial sample of this coformer (see Figure S25) confirms that it is crystalline, with sharp resonances indicating $Z'=1$ structure, in agreement with the reported crystal structure.

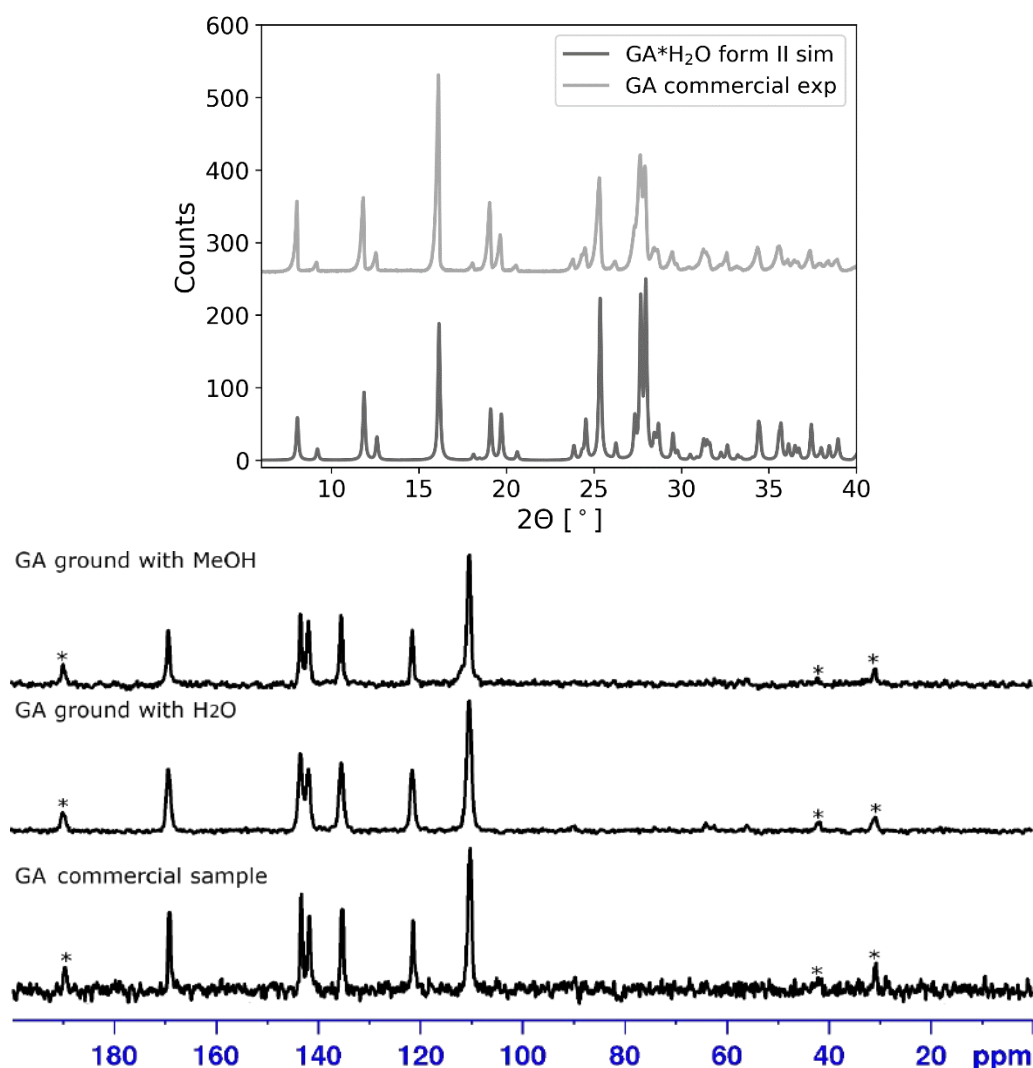


Figure S44. Upper: experimental PXRD data registered for the commercial sample of GA monohydrate and its comparison with the simulated PXRD pattern for the polymorphic form II of GA monohydrate; lower: ^{13}C CPMAS NMR spectra registered for a commercial sample of GA and the same sample after grinding with methanol or water. No phase change was observed upon grinding. Asterisks mark spinning sidebands.

Sulfanilic acid (SA) crystallizes in two neat polymorphic forms, orthorhombic $Pca2_1$ form (CSD refcode AFAZEM)²⁷ and monoclinic $P2_1/c$ form (AFAZEM01),²⁸ and in both of them it is in zwitterionic form. In addition there are four known hydrates, two monohydrates with SA as a zwitterion, a $P2_1/c$ monoclinic form (CSD refcode SANACM)²⁹ and a $P2_12_12_1$ orthorhombic form (CSD refcode SANACM01),³⁰ as well as one monohydrate (CSD refcode ISESEG)³¹ and one dihydrate (CSD refcode NESVOZ)³² with SA in its neutral form. The PXRD data for the commercial sample of SA indicates that it is a $Pca2_1$ polymorph (Figure S45). Upon grinding this sample with water a phase change is observed, consistent with the formation of the $P2_1/c$ monohydrate form, as also indicated by the PXRD pattern registered for SA sample after grinding with water.

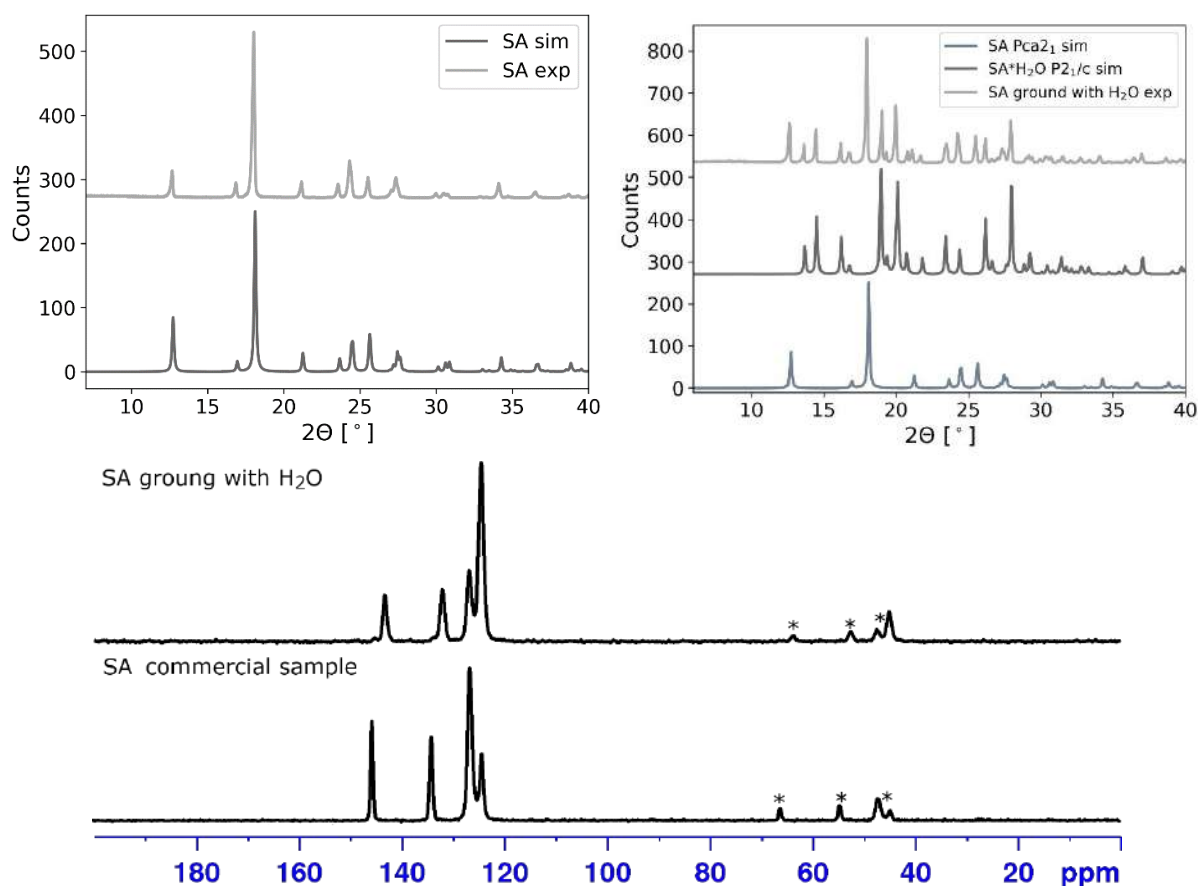


Figure S45. Upper left: experimental PXRD data registered for the commercial sample of SA and its comparison with the simulated PXRD pattern for the orthorhombic polymorph of SA (AFAZEM); upper right: experimental PXRD data registered for SA sample ground with water and its comparison with the simulated PXRD pattern for the $P2_1/c$ polymorph of SA monohydrate (SANACM); lower: ¹³C CPMAS NMR spectra registered for a commercial sample of SA and the same sample after grinding with water. A phase change upon grinding is readily observable. Asterisks mark spinning sidebands.

Isonicotinic acid (INA) has only one known crystal structure in the CSD, found in triclinic $P\bar{1}$ space group (CSD refcode ISNICA).³³ The ¹³C CPMAS NMR spectrum of the commercial sample indicates it is crystalline (see Figure S29).

Isonicotinamide (INN) is known to crystallize in as many as six neat polymorphic forms: monoclinic $P2_1/c$ form I (CSD refcode EHOWIH), monoclinic $P2_1/c$ form II (CSD refcode EHOWIH02), orthorhombic $Pbca$ form III (CSD refcode EHOWIH03),³⁴ monoclinic Pc form IV (CSD refcode EHOWIH04),³⁵ monoclinic $P2_1/c$ form V (CSD refcode EHOWIH05)³⁵ and recently discovered orthorhombic $Pca2_1$ form VI (CSD refcode EHOWIH06).³⁶ In addition to this reach variety of neat polymorphs, there are two monoclinic crystal structures of INN monohydrates, a $P2_1/c$ form (CSD refcode MOVITB01)³⁷ and Pc form (CSD refcode MOVBIT02).³⁷

The ¹³C CPMAS NMR spectrum of the commercial sample of INN indicates that this sample contains one of the three forms having $Z'=1$ structure (see Figure S30), *i.e.* form I, form III or form V, while PXRD data registered for this sample proves the presence of form I (Figure S46).

Grinding INN with water or methanol does not cause any changes to its phase according to the ^{13}C CPMAS NMR spectrum.

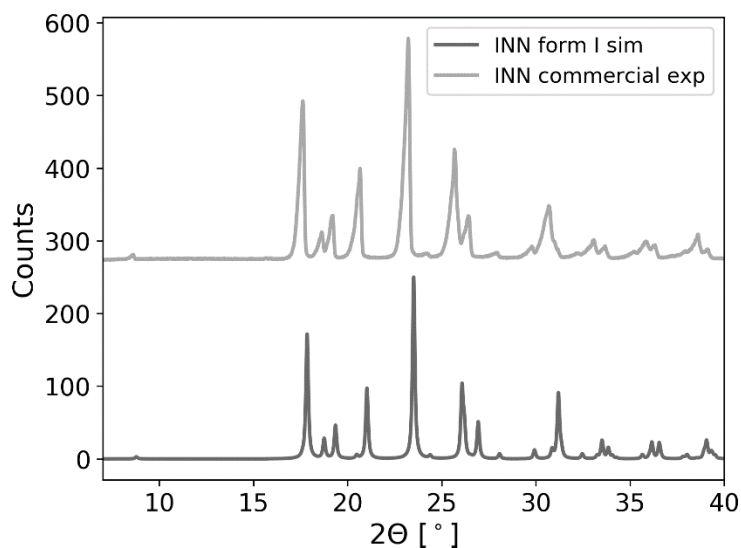


Figure S46. Experimental PXRD data registered for the commercial sample of INN and its comparison with the simulated PXRD pattern for the polymorphic form II of INN (EHOWIH).

Ibuprofen (IBU) commercial sample used for grinding experiments is a racemic mixture of R/S forms. The racemate of IBU is known to crystallize in either of the two $P2_1/c$ monoclinic forms, form 1 (CSD refcode IBPRAC01)³⁸ and form 2 (CSD refcode IBPRAC04).³⁹ The ^{13}C CPMAS NMR spectrum registered for the commercial sample of IBU (see Figure S31) is consistent with its form 1.

L-tyrosine (TYR) has in the CSD only one structure, that of $P2_12_12_1$ orthorhombic form (CSD refcode LTYROS11).⁴⁰ The ^{13}C CPMAS spectrum of the commercial sample (see Figure S32) confirms it is in a crystalline state.

L-proline (PRO) crystallizes in two neat polymorphic forms, orthorhombic $P2_12_12_1$ form I (CSD refcode PROLIN02)⁴¹ and triclinic $P1$ form II (CSD refcode PROLIN04),⁴¹ in addition to a monohydrate (CSD refcode RUWGEV)⁴² crystallizing in monoclinic $C2$ space group. The two neat forms of PRO are easily discernible by ^{13}C CPMAS NMR, as the second form is a $Z'=2$ structure. The solid-state NMR spectrum register for the commercial sample indicate that it is a $Z'=1$ structure and therefore most probably form I. Grinding this form in the presence of water or methanol yields a new form, with only small amounts of the commercial form present in the sample after the grinding. This new form was identified on the basis of its PXRD pattern as PRO monohydrate (see comparison of PXRD diffractograms in Figure S47). Interestingly, grinding PRO alone also leads to the formation of small amounts of the same monohydrate form, as shown by the ^{13}C CPMAS NMR spectra registered for the commercial sample and this same sample after grinding it alone, as well as in the presence of methanol (Figure S47). Also PXRD data registered for PRO ground in a ball mill alone shows the presence of a small amount

of PRO monohydrate. As a result both forms, PRO form I and PRO monohydrate should be considered as possible forms taking part in the mechanochemical reactions.

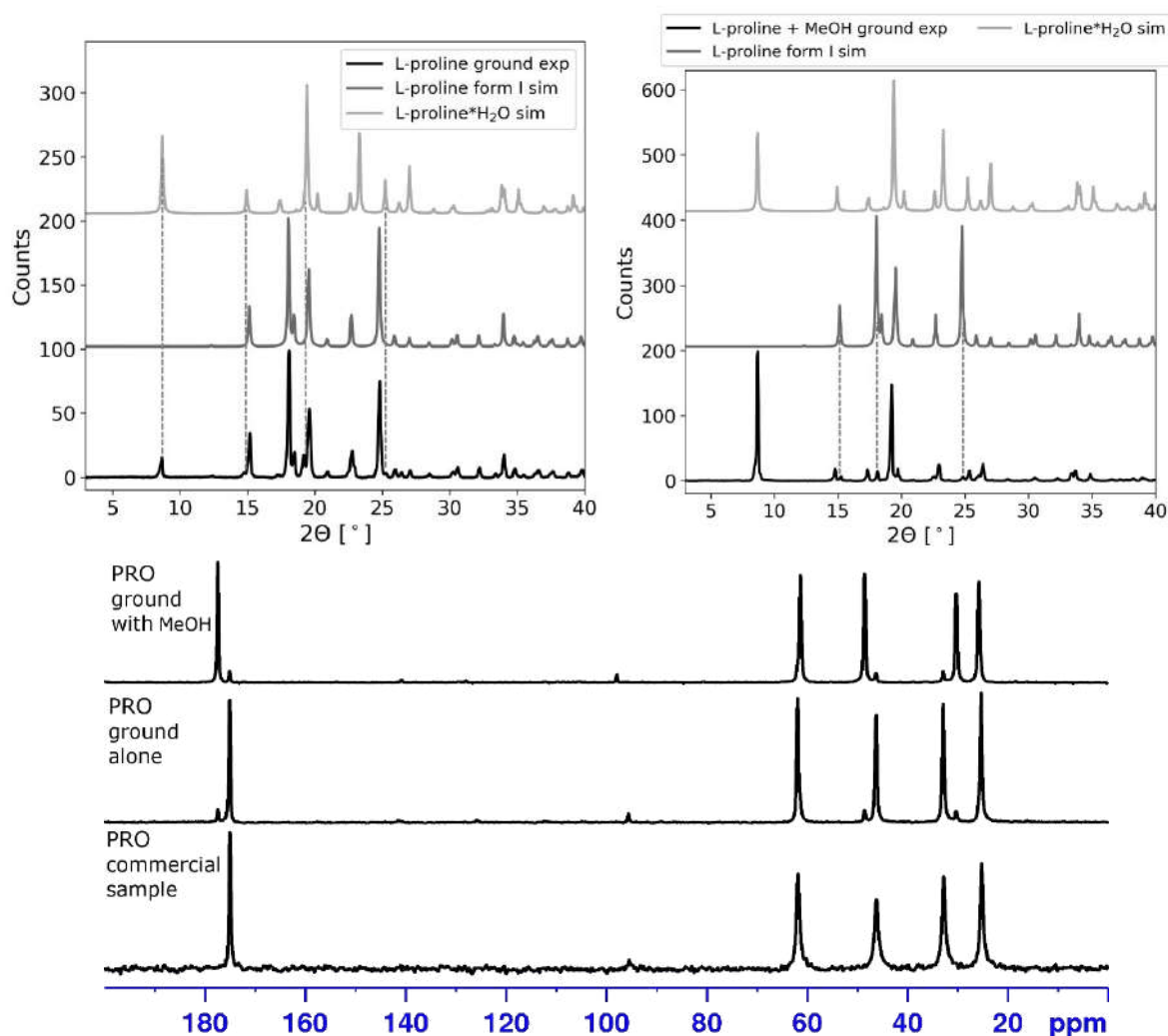


Figure S47. Upper: a comparison of the experimental PXRD data registered for the commercial sample of PRO ground alone for 1h in a ball mill (left) and for the commercial sample of PRO ground in a ball mill with methanol for 1h with the simulated powder patterns for PRO form I (PROLIN02) and PRO monohydrate (RUWGEV) (right); lower: ¹³C CPMAS NMR spectra registered for a commercial sample of PRO and the same sample after grinding it alone or with methanol in a ball mill. In both cases after grinding a new form emerges, with the difference in the quantity of this form.

Malonic acid (MAL) can crystallize in either of the three polymorphic forms: orthorhombic *Pbcn* form alpha, for which the only published crystal structure contains perdeuterated compound (CSD refcode MALNAC03), triclinic *P*-1 form beta (CSD refcode MALNAC02) and monoclinic *P*2₁/*n* epsilon form (CSD refcode MALNAC10). The PXRD data indicates that the commercial sample contains form β of MAL (Figure S48).

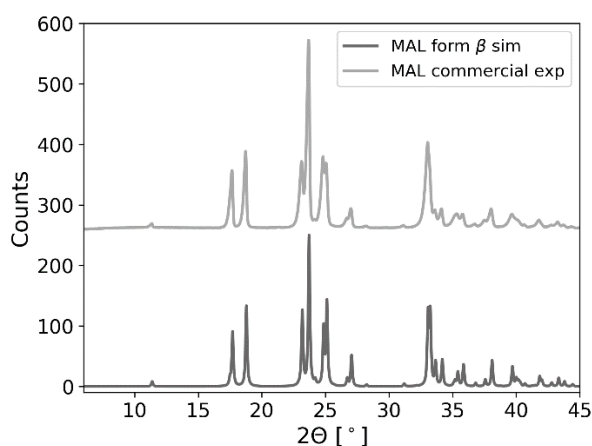


Figure S48. Experimental PXRD data registered for the commercial sample of MAL and its comparison with the simulated PXRD pattern for the polymorphic form β of MAL (MALNAC02).

Barbituric acid (BARB) can crystallize as one of the four known polymorphic forms, monoclinic $P2_1/c$ form I (CSD refcode BARBAC01),⁴³ monoclinic $P2_1/c$ form II with two BARB molecules in an asymmetric unit cell (CSD refcode BARBAC02),⁴³ high temperature monoclinic $C2/c$ form III (CSD refcode BARBAC03),⁴⁴ and monoclinic $P2_1/n$ form IV (CSD refcode IYAQOP).⁴⁵ In the forms I-III BARB is present in its keto form, whereas in form IV it exist as an enol. The commercial sample contains form II of BARB, which is evidenced from the characteristic ^{13}C CPMAS NMR spectrum of this sample (Figure S49), showing two well-separated resonances for CH_2 group, a feature characteristic for form II. Although there are reports in the literature that grinding BARB leads to the formation of form IV, we did not observed such effect after 1h of grinding of BARB alone or in the presence of methanol. However, upon grinding with water, a new form was formed, with the ^{13}C CPMAS NMR spectrum (Figure S49) consistent with the orthorhombic $Pnma$ polymorph of BARB dihydrate (CSD refcode BARBAD03)⁴⁶ (the monoclinic $P2_1/n$ dihydrate polymorph of BARB, BARBAD02, is a low-temperature form, stable below 220 K).⁴⁶

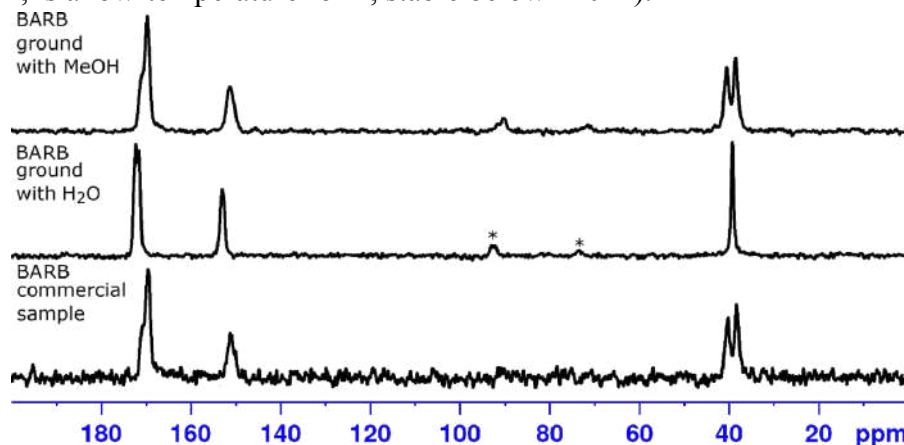


Figure S49. ^{13}C CPMAS NMR spectra registered for a commercial sample of BARB and the same sample after grinding with methanol or water. No phase change was observed upon grinding with methanol, grinding with water yielded BARB dihydrate. Asterisks mark spinning sidebands.

Table S2 summarizes the data on the known polymorphic forms of the studied coformers and on their hydrates and indicates which forms were accounted for as taking part in the mechanochemical grinding with LIN.

Table S2. Summary of the known polymorphic forms of the coformers used in this study. Bolded positions indicate crystal forms taking part in the mechanochemical grinding.

coformer	CSD refcode	SG	Z'	form
BA	BENZAC13	$P2_1/c$	1	monoclinic
2,3-DHBA	CACDAM	$P-1$	2	triclinic
	CACDAM01	$P2_1/n$	1	monoclinic
2,4-DHBA	ZZZEEU01	$P2_1/n$	1	form II
	ZZZEEU08	$P2_1/a$	1	form I
	QIVTUK01	$P-1$	2	hemihydrate
	YUXGUV	$P-1$	1	monohydrate
2,5-DHBA	BESKAL03	$P2_1/n$	1	form II – DSC
	BESKAL02	$P2_1/c$	1	form I
2,6-DHBA	LEZJAB	$Pna2_1$	1	orthorhombic
	LEZJAB01	$P2_1/c$	1	monoclinic
	LEZJEF	$Pnma$	0.5	monohydrate
3,4-DHBA	WUYNUA	$P-1$	3	crystallized from the melt
	BIJDON03	$P-1$	2	triclinic rhombic monohydrate
	BIJDON04	$P2_1/n$	1	monoclinic needle monohydrate
	BIJDON05	$P-1$	4	triclinic 2 monohydrate
3,5-DHBA	WUYPOW	$C2/c$	0.5	form 1
	WUYPOW01	$C2/c$	3	form 2
	OKEMAT	$P2_1$	2	hemihydrate
PHBA	JOZZIH	$P2_1/a$	1	monoclinic form I
	JOZZIH01	$P2_1/n$	1	monoclinic form II
	PHBZAC02			monohydrate
PABA	AMBNAC06	$P2_1/n$	2	form alpha I
	AMBNAC10	$P2_1/n$	1	form beta IV
	AMBNAC09	$Pna2_1$	2	form V
	AMBNAC14	Pn	1	high pressure form delta

GA	KONTIQ	$P2_1/c$	1	monohydrate, $P2_1/c$ form I
	KONTIQ01	$P2/n$	1	monohydrate $P2/n$ form II
	KONTIQ04	$P-1$	4	monohydrate triclinic form III
	KONTIQ05	$P2_1/c$	1	monohydrate monoclinic form IV
	KONTIQ06	$P2_1/c$	1	monohydrate form V
	KONTIQ08	$P2_1/c$	3	monohydrate form VI
VA	CEHGUS	$P2_1/c$	1	
SA	AFAZEM	$Pca2_1$	1	$Pca2_1$
	AFAZEM01	$P2_1/c$	1	$P2_1/c$
	ISESEG	$Pbca$	1	monohydrate
	NESVOZ	$P2_1/n$	1	dihydrate
	SANACM	$P2_1/c$	1	zwitterionic monohydrate $P2_1/c$ form
	SANACM01	$P2_12_12_1$	1	zwitterionic monohydrate $P2_12_12_1$ form
INA	ISNICA	$P-1$	1	
INN	EHOWIH	$P2_1/c$	1	form I
	EHOWIH02	$P2_1/c$	2	form II
	EHOWIH03	$Pbca$	1	form III (Iso3)
	EHOWIH04	Pc	3	monoclinic Pc form IV
	EHOWIH05	$P2_1/c$	1	monoclinic $P2_1/c$ form V
	EHOWIH06	$Pca2_1$	2	$Pca2_1$ form VI
	MOVTIB01	$P2_1/n$	2	monohydrate
	MOVTIB02	Pc	8	monohydrate
IBU	IBPRAC01	$P2_1/c$	1	racemate form 1
	IBPRAC04	$P2_1/c$	1	racemate form 2
TYR	LTYROS11	$P2_12_12_1$	1	
PRO	PROLIN02	$P2_12_12_1$	1	zwitterionic form I
	PROLIN04	$P1$	2	zwitterionic high-temp. form II
	RUWGEV	$C2$	1	zwitterionic monohydrate
MAL	MALNAC02	$P-1$	1	beta triclinic
	MALNAC03	$Pbcn$	0.5	alpha orthorhombic
	MALNAC10	$P2_1/n$	3	epsilon
BARB	BARBAC01	$P2_1/c$	1	form I
	BARBAC02	$P2_1/c$	2	form II
	BARBAC03	$C2/c$	0.5	form III
	IYAQOP-03	$P2_1/n$	1	enol form IV
	BARBAD03	$Pnma$	0.5	dihydrate orthorhombic form
	BARBAD02	$P2_1/n$	1	dihydrate monoclinic low-temp. form

Linezolid (LIN) has two known polymorphic forms: $P2_12_12_1$ form II ($Z'=1$) and $P-1$ form III ($Z'=2$, sometimes also referred to in the literature as form IV). Figure S50 shows the ^{13}C CPMAS NMR spectra of these two forms, together with the NMR spectra of form III after 30 and 60 minutes of grinding in a ball mill. It is clear, that during grinding a phase transition LIN III \rightarrow LIN II takes place, indicating higher room temperature stability of form II. After 30 min of grinding signals originating from LIN form II start to appear in the NMR spectrum but form III is still a dominant form, while after 60 minutes the resonances from LIN form III are no longer detectable.

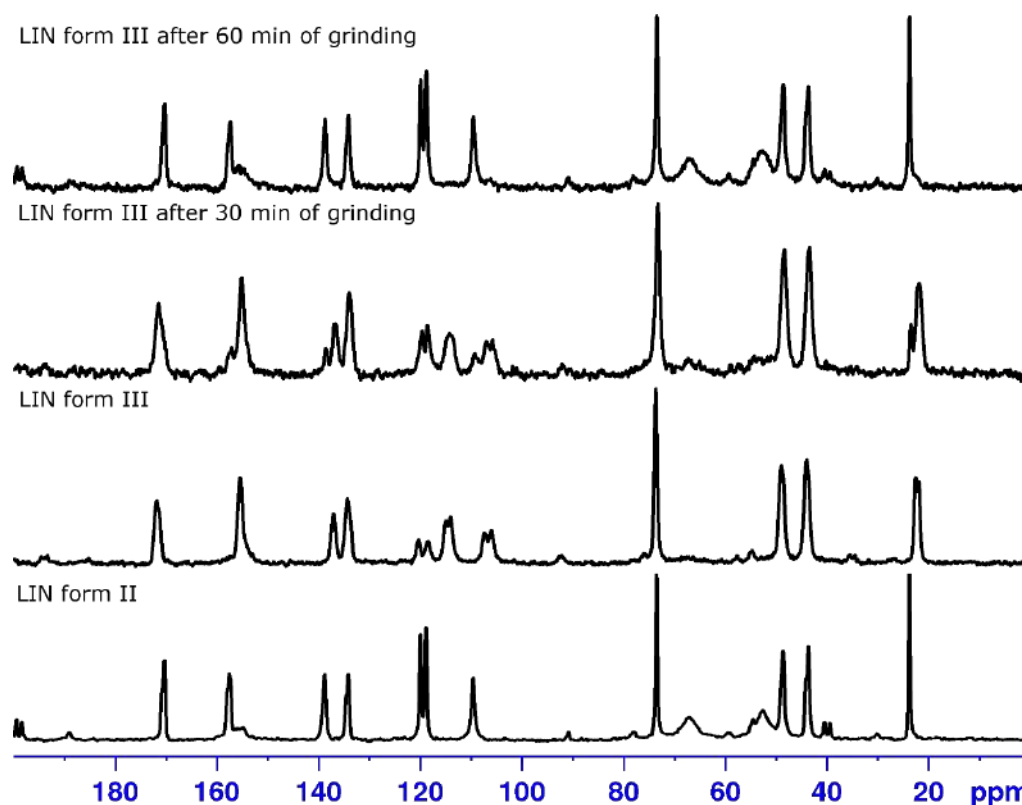


Figure S50. ^{13}C CPMAS NMR spectra of LIN form II and form III, as well as LIN form III after 30 and 60 min of grinding in a ball mill. The spectra were registered with a repetition time of 120 s.

4. Numerical values from CASTEP and MEP calculations

Table S3. Total, intramolecular and intermolecular energies of LIN_II and LIN_III (in kJ/mol) calculated under periodic boundary conditions at PBE-D2 level of theory and expressed per one LIN molecule.

Crystal form	E_{total}	$E_{\text{intramolecular}}$	$E_{\text{intermolecular}}$
LIN_II	-588031	-587709	-321
LIN_III_1	-588030	-587718	-314
LIN_III_2		-587713	

Table S4. Numerical α and β values (in kJ/mol) obtained from MEP calculations.

molecule	α values					β values				
	1	2	3	4	5	1	2	3	4	5
BA	3.64	1.16	1.12	1.08	0.90	5.04	1.41	0.62	0.59	0.00
PHBA-1	4.35	3.49	1.60	0.99	0.87	5.38	2.29	1.65	0.64	0.00
PHBA-2	4.37	3.49	1.64	0.99	0.94	5.50	2.31	1.55	0.68	0.00
2,6-DHBA-1	5.51	2.08	1.91	1.39	0.97	6.43	4.54	3.72	0.47	0.29
2,6-DHBA-2	4.77	2.22	1.21	1.08	0.86	3.52	2.80	2.33	0.84	0.81
3,4-DHBA	4.89	3.46	3.04	1.69	0.93	5.80	3.51	1.64	0.74	0.44
2,5-DHBA	4.13	4.04	1.32	1.13	1.00	3.73	3.02	2.77	0.71	0.67
2,4-DHBA	4.34	3.94	1.59	1.07	1.03	3.90	3.40	2.54	1.05	0.75
2,3-DHBA	4.21	2.77	1.48	1.02	0.96	3.31	2.67	1.20	0.95	0.81
3,5-DHBA-1	4.08	3.95	3.80	1.21	0.87	4.48	2.89	2.80	1.07	0.66
3,5-DHBA-2	4.15	4.07	3.68	1.41	1.24	5.29	3.12	2.29	1.16	0.77
3,5-DHBA-3	4.12	4.02	3.64	1.43	0.87	4.70	2.83	2.38	1.66	0.71
GA-1	4.61	3.62	3.50	3.01	0.90	5.02	3.36	1.90	0.82	0.78
GA-2	4.52	3.96	3.60	2.99	1.12	5.42	4.91	1.32	0.67	0.64
GA-3	4.73	3.64	3.53	2.98	1.19	5.74	3.64	1.27	0.85	0.83
GA-4	4.64	3.84	3.60	3.01	1.24	5.48	5.01	1.23	0.69	0.63
VA	3.46	3.03	1.47	1.26	0.86	5.71	2.97	1.36	0.89	0.30
PABA	3.19	2.90	2.89	1.23	1.19	6.29	2.15	2.05	1.21	0.00
SA	4.04	3.27	3.26	1.54	1.52	6.16	6.06	3.13	1.26	0.86
INA	4.14	1.22	1.10	1.05	1.01	5.48	3.88	0.78	0.00	0.00
INN	3.42	2.85	1.74	1.13	0.95	5.93	5.76	0.61	0.38	0.00
IBU-1	3.53	0.95	0.92	0.89	0.83	4.95	2.30	1.27	1.04	0.00
IBU-2	3.52	0.98	0.95	0.91	0.89	4.95	2.31	1.27	0.10	0.00
IBU-3	3.59	0.90	0.89	0.87	0.85	5.47	1.50	1.35	1.53	0.00
TYR*	4.07	2.74	1.85	1.66	1.57	7.70	5.38	3.03	1.09	0.00

PRO*	2.69	1.57	1.21	1.19	1.09	8.36	5.60	0.00	0.00	0.00
MAL	4.10	3.83	1.44	1.34	0.00	4.74	4.36	1.91	1.26	0.00
BARB	3.36	3.36	1.78	1.75	0.00	3.71	3.70	3.57	0.00	0.00
LIN-1	2.83	1.78	1.69	1.32	1.11	6.47	5.70	4.42	2.31	2.27
LIN-2	2.82	1.65	1.61	1.54	1.32	6.43	5.88	4.40	2.43	1.81
LIN-3/5**	3.71	1.77	1.62	1.32	1.32	6.86	5.74	4.43	3.94	2.47
LIN-4	2.82	1.78	1.69	1.59	1.52	6.48	5.74	4.41	2.32	2.27

* the results are given for neutral molecules; in its crystal forms PRO and TYR tends to be present in zwitterionic forms

** the results obtained for LIN conformations 3 and 5 were identical

Table S5. Energy values (in kJ/mol of molecules) obtained from calculations under periodic boundary conditions at PBE-D2 level of theory for the crystal forms of the coformers taking part in mechanochemical reaction with LIN.

coformer	crystal form (CSD refcode)	E _{total}	E _{intramolecular}	E _{intermolecular}
BA	<i>P</i> 2 ₁ /c (BENZAC13)	-200617	-200503	-115
3,4-DHBA * H ₂ O	<i>P</i> -1 triclinic (BIJDON03)	-165441	-165326	-115
2,3-DHBA	<i>P</i> -1 form (CACDAM)	-285345	-285218	-127
GA * H ₂ O	<i>P</i> 2 ₁ /n form II (KONTIQ01)	-186624	-186496	-128
2,6-DHBA	<i>P</i> na2 ₁ form (LEZJAB)	-285350	-285217	-134
2,5-DHBA	<i>P</i> 2 ₁ /c form I (BESKAL02)	-285346	-285208	-138
PABA	<i>P</i> 2 ₁ /n form α (AMBNAC06)	-228922	-228779	-143
VA	<i>P</i> 2 ₁ /c form (CEHGUS)	-303639	-303496	-144
PHBA	<i>P</i> 2 ₁ /a form I (JOZZIH)	-242991	-242847	-144
2,4-DHBA	<i>P</i> 2 ₁ /n form II (ZZZEEU01)	-285369	-285224	-145
MAL	<i>P</i> -1 form β	-221416	-221268	-148

(MALNAC02)				
IBU	<i>P</i> 2 ₁ /c racemate form I (IBPRAC01)	-310739	-310587	-152
INA	<i>P</i> -1 form (ISNICA)	-210518	-210359	-159
3,5-DHBA	<i>C</i> 2/c form 2 (WUYPOW01)	-285351	-285177	-174
SA * H ₂ O	<i>P</i> 2 ₁ /c form (SANACM)	-165425	-165194	-231
SA	<i>P</i> ca2 ₁ form AFAZEM	-285310	-284912	-397

5. References

- ¹ W. Cai, A. Katrusiak. Pressure effects on H-ordering in hydrogen bonds and interactions in benzoic acid. *CrystEngComm* 2012, 14, 4420–4424.
- ² N. Okabe, H. Kyoyama. 2,3-Di-hydroxy-benzoic acid. *Acta Cryst.* 2001, E57, o1224–o1226.
- ³ B. Sarma, P. Sanphui, A. Nangia. Polymorphism in Isomeric Dihydroxybenzoic Acids. *Cryst. Growth Des.* 2010, 10, 2388–2399.
- ⁴ D. E. Braun, P. G. Karamertzanis, J.-B. Arlin, A. J. Florence, V. Kahlenberg, D. A. Tocher, U. J. Griesser, S. L. Price. Solid-State Forms of β -Resorcylic Acid: How Exhaustive Should a Polymorph Screen Be? *Cryst. Growth Des.* 2011, 11, 210–220.
- ⁵ A. Parkin, M. Adam, R. I. Cooper, D. S. Middlemiss, C. C. Wilson. Structure and hydrogen bonding in 2,4-dihydroxybenzoic acid at 90, 100, 110 and 150 K; a theoretical and single-crystal X-ray diffraction study. *Acta Cryst.* 2007, B63, 303–308.
- ⁶ D. E. Braun, P. G. Karamertzanis, S. L. Price. Which, if any, hydrates will crystallise? Predicting hydrate formation of two dihydroxybenzoic acids. *Chem. Commun.* 2011, 47, 5443–45445.
- ⁷ B. Sridhar. Synthon preference in a hydrated [β]-resorcylic acid structure and its cocrystal with thymine. *Acta Cryst.* 2015, C71, 1042–1047.
- ⁸ D. E. Cohen, J. B. Benedict, B. Morlan, D. T. Chiu, B. Kahr. Dyeing Polymorphs: The MALDI Host 2,5-Dihydroxybenzoic Acid. *Cryst. Growth Des.* 2007, 7, 492–495.
- ⁹ M. Gdaniec, M. Gilski, G. S. Denisov. γ -Resorcylic acid, its monohydrate and its pyridinium complex. *Acta Cryst. C* 1994, C50, 1622–1626.
- ¹⁰ L. R. MacGillivray, M. J. Zaworotko. Crystal and molecular structure of 2,6-dihydroxybenzoic acid. *J. Chem. Cryst.* 1994, 24, 703–705.
- ¹¹ Y. Wang, Y. Chen, P. Zhu, Y. Bao, C. Xie, J. Gong, X. Jiang, B. Hou, W. Chen. Measurement and Correlation of the Solubility of 2,6-Dihydroxybenzoic Acid in Alcohols and Binary Solvents. *J. Chem. Eng. Data* 2017, 62, 3009–3014.
- ¹² V. Horneffer, K. Dreisewerd, H.-C. Lüdemann, F. Hillenkamp, M. Läge, K. Strupat. Is the incorporation of analytes into matrix crystals a prerequisite for matrix-assisted laser desorption/ionization mass spectrometry? A study of five positional isomers of dihydroxybenzoic acid. *Int. J. Mass Spectrom. Ion. Process.* 1999, 185, 859–870.
- ¹³ S. W. Ng. A triclinic modification of 3,4-dihydroxy-benzoic acid monohydrate. *Acta Cryst.* 2011, E67, o2476.
- ¹⁴ S. Varughese, G. R. Desiraju. Using Water as a Design Element in Crystal Engineering. Host–Guest Compounds of Hydrated 3,5-Dihydroxybenzoic Acid. *Cryst. Growth Des.* 2010, 10, 4184–4196.
- ¹⁵ E. A. Heath, P. Singh, Y. Ebisuzaki. Structure of p-hydroxybenzoic acid and p-hydroxybenzoic acid-acetone complex (2/1). *Acta Cryst.* 1992, C48, 1960–1965.
- ¹⁶ J. J. Du, S. A. Stanton, P. A. Williams, J. A. Ong, P. W. Groundwater, J. Overgaard, J. A. Platts, D. E. Hibbs. Using Electron Density to Predict Synthon Formation in a 4-Hydroxybenzoic Acid: 4,4'-Bipyridine Cocrystal. *Cryst. Growth Des.* 2018, 18, 1786–1798.

- ¹⁷ T.-J. Hsieh, C.-C. Su, C.-Y. Chen, C.-H. Liou, L.-H. Lu. Using experimental studies and theoretical calculations to analyze the molecular mechanism of coumarin, p-hydroxybenzoic acid, and cinnamic acid. *J. Mol. Struct.* 2005, 741, 193–199.
- ¹⁸ S. Athimoolam, S. Natarajan. 4-Carboxy-anilinium (2R,3R)-tartrate and a redetermination of the [alpha]-polymorph of 4-amino-benzoic acid. *Acta Cryst.* 2007, C63, o514–o517.
- ¹⁹ M. R. Ward, S. Younis, A. J. Cruz-Cabeza, C. L. Bull, N. P. Funnell, I. D. H. Oswald. Discovery and recovery of delta p-aminobenzoic acid. *CrystEngComm* 2019, 21, 2058–2066.
- ²⁰ R. Benali-Cherif, R. Takouachet, E.-E. Bendeif, N. Benali-Cherif. The structural properties of a noncentrosymmetric polymorph of 4-amino-benzoic acid. *Acta Cryst.* 2014, C70, 323–325.
- ²¹ R.-W. Jiang, D.-S. Ming, P. P. H. But, T. C. W. Mak. Gallic acid monohydrate. *Acta Cryst.* 2000, C56, 594–595.
- ²² N. Okabe, H. Kyoyama, M. Suzuki. Gallic acid monohydrate. *Acta Cryst.* 2001, E57, o764–o766.
- ²³ H. D. Clarke, K. K. Arora, Ł. Wojtas, M. J. Zaworotko. Polymorphism in Multiple Component Crystals: Forms III and IV of Gallic Acid Monohydrate. *Cryst. Growth Des.* 2011, 11, 964–966.
- ²⁴ D. E. Braun, R. M. Bhardwaj, A. J. Florence, D. A. Tocher, S. L. Price. Complex Polymorphic System of Gallic Acid—Five Monohydrates, Three Anhydrides, and over 20 Solvates. *Cryst. Growth Des.* 2013, 13, 19–23.
- ²⁵ A. A. Hoser, I. Sovago, A. Lanzac, A. Ø. Madsen. A crystal structure prediction enigma solved: the gallic acid monohydrate system – surprises at 10 K. *Chem. Commun.* 2017, 53, 925–928.
- ²⁶ B. Kozlevčar, D. Odlazek, A. Golobič, A. Pevec, P. Strauch, P. Šegedin. Complexes with lignin model compound vanillic acid. Two different carboxylate ligands in the same dinuclear tetracarboxylate complex [Cu₂(C₈H₇O₄)₂(O₂CCH₃)₂(CH₃OH)₂]. *Polyhedron* 2006, 25, 1161–1166.
- ²⁷ J. N. Low, C. Glidewell. A quasi-diamondoid hydrogen-bonded framework in an-hydro-us sulfanilic acid. *Acta Cryst.* 2002, C58, o209–o211.
- ²⁸ S. K. Callear, M. B. Hursthouse. University of Southampton, Crystal Structure Report Archive 2008, 552, doi:10.5258/ecrystals/552
- ²⁹ A. I. M. Rae. E. N. Maslen. The crystal structure of sulphanilic acid monohydrate. *Acta Cryst.* 1962, 15, 1285–1291.
- ³⁰ A. Banu, G. M. Golzar Hossain. A new polymorph of sulfanilic acid monohydrate. *Acta Cryst.* 2006, E62, o2252–o2253.
- ³¹ Q. Wang, CSD Communication 2016
- ³² S. Langenstück, C. Zhao, U. Englert. The ephemeral dihydrate of sulfanilic acid. *Acta Cryst.* 2018, C74, 7–12.
- ³³ F. Takusagawa, A. Shimada. Isonicotinic acid. *Acta Cryst.* 1976, B32, 1925–1927.
- ³⁴ J. Li, S. A. Bourne, M. R. Caira. New polymorphs of isonicotinamide and nicotinamide. *Chem. Commun.* 2011, 47, 1530–1532.
- ³⁵ K. S. Eccles, R. E. Deasy, L. Fábán, D. E. Braun, A. R. Maguire, S. E. Lawrence. Expanding the crystal landscape of isonicotinamide: concomitant polymorphism and co-crystallisation. *CrystEngComm* 2011, 13, 6923–6925.
- ³⁶ A. I. Vicatos, M. R. Caira. A new polymorph of the common coformer isonicotinamide. *CrystEngComm* 2019, 21, 843–849.
- ³⁷ N. B. Báthori, A. Lemmerer, G. A. Venter, S. A. Bourne, M. R. Caira. Pharmaceutical Co-crystals with Isonicotinamide—Vitamin B₃, Clofibric Acid, and Diclofenac—and Two Isonicotinamide Hydrates. *Cryst. Growth Des.* 2011, 11, 75–87.
- ³⁸ N. Shankland, A. J. Florence, P. J. Cox, D. B. Sheen, S. W. Love, N. S. Stewart, C. C. Wilson. Crystal morphology of ibuprofen predicted from single-crystal pulsed neutron diffraction data. *Chem. Commun.* 1996, 855–856.
- ³⁹ P. Derollez, E. Dudognon, F. Affouard, F. Danède, N. T. Correia, M. Descamps. Ab initio structure determination of phase II of racemic ibuprofen by X-ray powder diffraction. *Acta Cryst.* 2010, B66, 76–80.
- ⁴⁰ M. N. Frey, T. F. Koetzle, M. S. Lehmann, W. C. Hamilton. Precision neutron diffraction structure determination of protein and nucleic acid components. X. A comparison between the crystal and molecular structures of L-tyrosine and L-tyrosine hydrochloride. *J. Chem. Phys.* 1973, 58, 2547.
- ⁴¹ N. Tumanova, N. Tumanov, K. Robeyns, F. Fischer, L. Fusaro, F. Morelle, V. Ban, G. Hautier, Y. Filinchuk, J. Wouters, T. Leyssens, F. Emmerling. Opening Pandora's Box: Chirality, Polymorphism, and Stoichiometric Diversity in Flurbiprofen/Proline Cocrystals. *Cryst. Growth Des.* 2018, 18, 954–961.
- ⁴² J. Janczak, P. Luger. L-Proline Monohydrate at 100 K. *Acta Cryst.* 1997, C53, 1954–1956.
- ⁴³ T. C. Lewis, D. A. Tocher, S. L. Price. An Experimental and Theoretical Search for Polymorphs of Barbituric Acid: The Challenges of Even Limited Conformational Flexibility. *Cryst. Growth Des.* 2004, 4, 979–987.
- ⁴⁴ D. M. Többsen, J. Glinneman, M. R. Chierotti, J. van de Streek, D. Sheptyakov. On the high-temperature phase of barbituric acid. *CrystEngComm* 2012, 14, 3046–3055.

-
- ⁴⁵ M. U. Schmidt, J. Brüning, J. Glinnemann, M. W. Hützler, P. Mörschel, S. N. Ivashevskaya, J. van de Streek, D. Braga, L. Maini, M. R. Chierotti, R. Gobetto. The Thermodynamically Stable Form of Solid Barbituric Acid: The Enol Tautomer. *Angew. Chem. Int. Ed.* 2011, 50, 7924–7926.
- ⁴⁶ G. S. Nichol, W. Clegg. A variable-temperature study of a phase transition in barbituric acid dihydrate. *Acta Cryst.* 2005, B61, 464–472.

T2:

Structural variety of heterosynthons in linezolid cocrystals with modified thermal properties,
Khalaji, M., Wróblewska, A., Wielgus, E., G.D. Bujacz, Dudek, M.K., Potrzebowski, M.J., *Acta
Crystallographica Section B: Structural Science, Crystal Engineering and Materials*, 2020, 76, pp.
892–912



Structural variety of heterosynthons in linezolid cocrystals with modified thermal properties

Mehrnaz Khalaji,^a Aneta Wróblewska,^a Ewelina Wielgus,^a Grzegorz D. Bujacz,^b Marta K. Dudek^{a*} and Marek J. Potrzebowski^{a*}

^aCentre of Molecular and Macromolecular Studies of Polish Academy of Sciences, Sienkiewicza 112, Lodz, 90-363, Poland, and ^bInstitute of Technical Biochemistry, Technical University of Lodz, Stefanowskiego 4/10, Lodz, 90-924, Poland. *Correspondence e-mail: mdudek@cbmm.lodz.pl, marekpot@cbmm.lodz.pl

Received 22 June 2020
Accepted 7 August 2020

Edited by A. Katrusiak, Adam Mickiewicz University, Poland

Keywords: linezolid; cocrystals; X-ray diffraction; supramolecular synthons; thermal properties.

CCDC references: 1993998; 1993999; 1994000; 1994001; 1997194

Supporting information: this article has supporting information at journals.iucr.org/b

In a search for new crystalline forms of linezolid with modified thermal properties five cocrystals of this wide range antibiotic with aromatic acids were obtained *via* mechanochemical grinding and analyzed with single crystal X-ray diffraction, solid-state NMR spectroscopy, powder X-ray diffraction and DSC measurements. The coformers used in this study were benzoic acid, *p*-hydroxybenzoic acid, protocatechuic acid, *γ*-resorcylic acid and gallic acid. In each of the cocrystals distinct structural features have been found, including a variable amount of water and different heterosynthons, indicating that there is more than one type of intermolecular interaction preferred by the linezolid molecule. Basing on the frequency of the observed supramolecular synthons, the proposed hierarchy of the hydrogen-bond acceptor sites of linezolid (LIN) is C=O_{amide} > C=O_{oxazolidone} > C—O—C_{morpholine} > C—N—C_{morpholine} > C—O—C_{oxazolidone}. In addition, aromatic–aromatic interactions were found to be important in the stabilization of the analyzed structures. The obtained cocrystals show modified thermal properties, with four of them having melting points lower than the temperature of the phase transition from linezolid form II to linezolid form III. Such a change in this physicochemical property allows for the future application of melting-based techniques of introducing linezolid into drug delivery systems. In addition a change in water solubility of linezolid upon cocrystallization was evaluated, but only in the case of the cocrystal with protocatechuic acid was there a significant (43%) improvement in solubility in comparison with linezolid.

1. Introduction

In recent years cocrystallization has been one of the most exploited methods to obtain new crystalline forms of active pharmaceutical ingredients (APIs). This is because cocrystal formation offers a possibility of producing crystalline forms with different physicochemical properties (Douroumis *et al.*, 2017; Palanisamy *et al.*, 2019; Kaur *et al.*, 2017; Putra *et al.*, 2017). Among these water solubility seems to be of primary importance (Lipinski, 2001; Jain *et al.*, 2015), but other properties such as stability of a solid form during manufacturing or melting point can also be affected by cocrystal formation (Schultheiss & Newman, 2009; Stanton *et al.*, 2009; Sun & Hou, 2008; Karki *et al.*, 2009). As a result, appropriately designed cocrystals may enhance the bioavailability of a drug.

Another way of improving the bioavailability of APIs is through drug delivery systems based, in particular, on mesoporous silica nanoparticles (MSNs) (Bharti *et al.*, 2015; Narayan *et al.*, 2018). MSNs may increase drug solubility and/or change its pharmacokinetics, as well as serve as sustained release systems, decreasing the risk of side-effects caused by



© 2020 International Union of Crystallography

one-time release of a high dosage of a drug (Manzano & Vallet-Regí, 2019; Jafari *et al.*, 2019). To load a given API into MSNs a number of methods have been introduced, including the solid-state based thermal solvent-free approach (Mellaerts *et al.*, 2008; Linnell *et al.*, 2011; Skorupska *et al.*, 2015, 2016). It is based on transforming a crystal of an API into the melt phase in the presence of silica carriers, which leads to recrystallization of a drug inside the pores. The main advantage of this approach is a much higher filling factor of the silica nanocarriers with the drug in comparison to the most commonly used solution-based methods. On the other hand, the most serious limitation of this method is the necessity of melting the drug in order to introduce it into MSNs. This is particularly disadvantageous for thermally labile drug molecules and those which undergo phase transition upon heating. To overcome this limitation, the cocrystallization of a drug with a coformer from the generally regarded as safe (GRAS) list may be used (Food & Drug Administration, 2019), leading to a lower melting point of a crystal introduced into MSNs. Additional motivation and interest in modifying the thermal properties of pharmaceutical cocrystals and loading them into the pores of MSNs is associated with our previous observations that by changing the composition of cocrystals embedded into MSNs it is possible to control the release rate of an API (Skorupska *et al.*, 2017). This can open new possibilities in therapeutic strategies.

One of the drugs suffering from poor water solubility and associated with an increased risk of mitochondrial toxicity is linezolid (LIN, Fig. 1), a wide-range antibiotics used mainly to treat infections caused by resistant strains of Gram-positive bacteria (Moellering, 2003; Abou Hassan *et al.*, 2016). To date, crystal structures of two polymorphic forms of LIN are known, orthorhombic form II (Maccaroni *et al.*, 2008), which is a commercially available form, and triclinic form III (Rao & Reddy, 2005; Tanaka & Hirayama, 2008), which is also mistakenly referred to in the literature as form IV (Wielgus *et al.*, 2015). These two polymorphs are enantiotropic, with the stable form II undergoing transformation to the metastable form III by heating to a temperature between 120°C and 140°C for the appropriate amount of time (Maccaroni *et al.*, 2008; Bergren, 2003; Rao & Reddy, 2005; Frelek *et al.*, 2012). The existence of such enantiotropic polymorphism precludes the application of the thermal solvent-free method of introducing LIN into the pores of MSNs, unless other crystalline forms of this antibiotic are produced. Such new forms should

preferably have lower melting points than the observed phase transition from form II to form III. To achieve this purpose cocrystallization seems to be the method of choice. According to a recent survey of 774 cocrystals (Perlovich, 2017) the melting point of a cocrystal is lower than that of pure components in 27.7% of cases. This means that an appropriate selection of coformers has to be made in order to achieve lower melting solid cocrystals of LIN.

The available patent literature (Devarakonda *et al.*, 2009) suggests that LIN forms cocrystals with carboxylic aromatic acids. In the cited study four cocrystals of LIN were obtained, with benzoic acid (BA), *p*-hydroxybenzoic acid (PHBA), 1,5-naphthalenedisulfonic acid and salicylic acid. Among the cocrystals, only those with BA and PHBA have significantly lower melting temperature (112°C and 76°C, respectively) than the temperature of the phase transition from LIN form II → LIN form III (around 150°C). The crystal structures of these crystalline forms were not reported, which limits our understanding about supramolecular synthon preferences exhibited by LIN.

In this work we report the mechanochemical preparation and crystal structure determination of five cocrystals of LIN and carboxylic aromatic acids with the aim to produce cocrystals exhibiting improved thermal properties. First, we repeated the experiments reported in the patent literature, leading to the cocrystals with BA and PHBA, and put a special effort to obtain single crystals suitable for X-ray diffraction experiments. This was done in order to understand the preferences of LIN in respect of supramolecular synthon formation. Then, we designed, synthesized and characterized three new cocrystals of LIN with 2,6-dihydroxybenzoic acid (γ -resorcylic acid, 2,6-DHBA), 3,4-dihydroxybenzoic acid (protocatechuic acid, 3,4-DHBA) and gallic acid (GA, 3,4,5-trihydroxybenzoic acid) (Fig. 1). All five cocrystals were obtained using mechanochemical grinding, which is an efficient and environmentally friendly way of producing new solid forms (Do & Frišćić, 2017; Tröbs & Emmerling, 2014; Dudek *et al.*, 2019). In addition to structural characterization of the obtained cocrystals, their thermal behaviour as well as water solubility were analyzed and compared with their structural features. Finally, lattice energy calculations gave an insight into thermodynamic stability of the cocrystals.

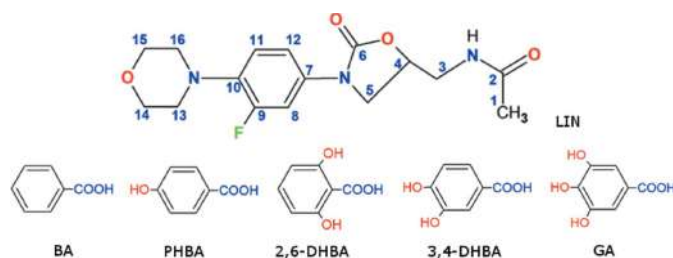


Figure 1
Chemical structure of LIN (with carbon atom labelling) and coformers used in this study.

2. Experimental

2.1. Materials

Linezolid form II (LIN) was purchased from ABCR GmbH (Germany) and used as is after evaluating its identity and purity by ^{13}C CPMAS NMR spectroscopy. BA, PHBA, 2,6-DHBA, GA and 3,4-DHBA were purchased from Sigma Aldrich and used without further purification, unless otherwise stated. All solvents were of analytical grade and were purchased from POCh (Poland).

2.2. Preparation of the cocrystals and subsequent recrystallization

For the preparation of cocrystals LIN (100 mg, ~ 0.3 mmol) was ground with the appropriate amount of coformers, corresponding to 1:1 molar ratio in a ball mill set to 25 kHz frequency for 1 h or 3 h, depending on the coformer (1 h reaction time was needed to obtain cocrystals with BA, 3,4-DHBA, 2,6-DHBA, and GA, while for form LIN:PHBA 3 h reaction time was used). In all cases, an addition of a small amount of methanol or water (up to 250 μ l) was used to create liquid-assisted grinding (LAG) conditions. Both solvents were found to be effective in facilitating the formation of the cocrystals, while without the presence of a solvent no cocrystals were formed. Every time the reaction outcome was tested with ^{13}C CPMAS NMR experiments and when no signals originating from pure compounds were observed in the NMR spectra, powder X-ray diffraction measurements were performed in order to confirm the phase purity of the obtained cocrystals.

The cocrystals prepared *via* mechanochemistry were subsequently used to obtain X-ray quality single crystals. To that purpose 100 mg of a given cocrystal was dissolved in methanol and left for slow evaporation of the solvent. All solutes were seeded with the appropriate cocrystals, to prevent the precipitation of pure components, which was often observed without the seeding.

2.3. NMR spectroscopy

Solid-state NMR measurements were performed on a Bruker Avance III spectrometer operating at 400.13 and 100.90 MHz frequencies for ^1H and ^{13}C , respectively. The studied samples were spun in 4 mm zirconia rotors with a spinning speed of 8 kHz. For all experiments, a cross-polarization contact time of 2.5 ms and SPINAL decoupling (Fung *et al.*, 2000) during acquisition were used. The repetition delays varied between experiments, from 10 s for the cocrystals obtained after mechanochemical grinding to 120 s for pure LIN forms II and III.

Solution NMR experiments were carried out in order to determine the content of water in the obtained cocrystals. The measurements were performed with a Bruker Avance III spectrometer operating at a resonating frequency of 500 MHz for ^1H , equipped with a 5 mm probe head and using anhydrous acetone- d_6 as a solvent. The solvent was dried prior to the experiments using 3 Å molecular sieves for 48 h and checked for the content of water by ^1H NMR measurements. For water content determination in the samples of cocrystals all proton signals were integrated and an integral value of a signal resonating at ~ 2.90 – 2.95 p.p.m. (originating from water protons) was referenced to ^1H signals of linezolid, in particular to the well resolved ^1H signal at 4.78 p.p.m. For all recorded proton spectra together with the obtained integral values see Fig. S3 in supporting information.

2.4. Single crystal X-ray diffraction measurements

Single crystal X-ray diffraction experiments for all cocrystals were carried out at room temperature using an Oxford SuperNova single-crystal diffractometer with micro-source Cu $K\alpha$ radiation ($\lambda = 1.5418$ Å) and a Titan detector. These conditions were chosen deliberately to be comparable to those present in the solid-state NMR experiments. In the case of all crystal structures the nonhydrogen atoms were present in the direct methods solution. The hydrogen atoms connected with carbon and nitrogen atoms were set geometrically and refined as riding with $U_{\text{iso}}(\text{H}) = 1.2U_{\text{eq}}(\text{parent atom})$. The hydrogen atoms at oxygens were found on the difference Fourier map and refined with geometrical restraints and with $U_{\text{iso}}(\text{H}) = 1.5U_{\text{eq}}(\text{O})$.

Diffraction data collection, cell refinement, data reduction, and absorption correction were performed using the *CrysAlis PRO* software (Oxford Diffraction). Structures were solved by direct methods (*SHELXS*; Sheldrick, 2008) and then refined using full-matrix least-squares methods (*SHELXL2015*; Sheldrick, 2015) implemented in the *OLEX2* package (Dolomanov *et al.*, 2009).

The crystal structures were deposited in the Cambridge Structural Database under the deposition numbers CCDC 1993998, CCDC 1993999, CCDC 1994000, CCDC 1994001 and CCDC 1997194 for LIN:BA, LIN:GA:H₂O, LIN:3,4-DHBA:H₂O, LIN:2,6-DHBA, and LIN:PHBA:H₂O cocrystals, respectively.

The diffraction data of LIN:PHBA:H₂O cocrystal were collected for more than a dozen of crystals and for all of them showed pseudo-merohedral twinning. Although for some of them the data could be indexed on an orthorhombic unit cell with one very long unit-cell dimension, we were able to find a reasonable solution only in the monoclinic space group $P2_1$ with two molecules of each of LIN, PHBA and water in the asymmetric unit. Reflections corresponding to four lattices were assigned on diffraction images and the fraction of twin components was refined. The refined model contained all atoms, but the conformation of two LIN molecules differed, with atoms in both of them showing large displacement parameters and R values of around 20%. For four best crystals of LIN:PHBA:H₂O the diffraction data collection was repeated in 100 K. These data allowed solution and refinement of the structure in space group $P2_12_12_1$, consistent with the metric unit cell. The refinement was performed using diffraction data (HKL5) from four twin components, as the introduction of the fifth and sixth components did not improve the model and the refinement parameters. The asymmetric unit contains one molecule each of LIN, PHBA and water.

In the LIN:3,4-DHBA:H₂O structure, first isotropic displacement parameters for water O atoms were calculated, and the water occupancies were refined. The occupancy of the first water molecule, located in a general position, refined close to unity. The second water molecule, located on the twofold rotation axis, refined to an occupancy of approximately 0.25 (the maximum occupancy of this site is 0.5). We fixed the occupancies at these values and implemented anisotropic

displacement parameters for both water molecules. In the next cycle of refinement the positions of the attached hydrogens were determined from a difference Fourier map, although the peaks corresponding to the hydrogen atoms at the partially occupied water were much lower. This crystallographic solution was obtained for a freshly crystallized sample. All crystallographic data obtained for the analysed crystals are presented in Table 1.

2.5. Powder X-ray diffraction measurements

Powder X-ray diffractograms were recorded with a Bruker D8 Advance diffractometer equipped with a LynxEye detector using Cu $K\alpha$ radiation ($\lambda = 1.5406 \text{ \AA}$). Diffraction data were collected in the Bragg–Brentano ($\theta/2\theta$) horizontal geometry between 2° and 40° (2θ) in 0.0297° steps.

2.6. DSC measurements

DSC measurements were recorded using a DSC 2920 system (TA Instruments). For all samples, the heating rate was set to 10 K min^{-1} , and the temperature was calibrated at two points using tin and indium.

2.7. Solubility measurements

The samples for solubility measurement were prepared by adding 10 mg of each solid (tested cocrystals and pure linezolid) in 300 μL of Milli-Q water, so that in each case a precipitate was visible. The obtained suspensions were constantly stirred at room temperature for 12 h, 24 h, 36 h and 48 h. After filtrations through a $0.22 \mu\text{m}$ PTFE syringe filter the filtrates were diluted with water to obtain an appropriate concentration of solution (in the range of UPLC-MS calibration).

The concentration of linezolid was determined by ACQUITY UPLC I-Class chromatography system coupled with SYNAPT G2-Si mass spectrometer equipped with an electrospray source and quadrupole-Time-of-Flight mass analyser (Waters Corp., Milford, MA, USA). ACQUITY BEH C18 column ($100 \times 2.1 \text{ mm}$, $1.7 \mu\text{m}$) maintained at 40°C temperature was used for the chromatographic separation of an analyte. A gradient program was employed with the mobile phase combining solvent A (1% formic acid in water) and solvent B (1% formic acid in acetonitrile) as follows: 20% B (0–0.5 min), 20–95% B (0.5–1.5 min), 95–95% B (1.5–2.2 min), 95–20% B (2.2–2.3 min) and 20–20% B (2.3–4 min). The flow rate was 0.35 ml min^{-1} , and the injection volume was $0.8 \mu\text{L}$.

For mass spectrometric detection, the electrospray source was operated in a positive resolution mode. The optimized source parameters were: capillary voltage 2.5 kV, cone voltage 20 V, desolvation gas flow 900 L h^{-1} with the temperature 350°C , nebulizer gas pressure 6.5 bar, source temperature 110°C . Mass spectra were recorded over an m/z range of 100 to 1200. Mass spectrometer conditions were optimized by direct infusion of the standard solution. The system was controlled with *MassLynx* software (Version 4.1) and the data processing (peak area integration, construction of the calibration curve) was performed with *TargetLynxTM* program.

The initial stock calibration solution of linezolid was created with a concentration of approximately 10 mg ml^{-1} in water and stored at 4°C . The stock solution was serially diluted with water to obtain working solutions at several concentration levels. Two calibration curves were prepared at seven different concentrations of LIN solutions. The calibration curves were linear over a concentration range from 10 ng ml^{-1} to 1000 ng ml^{-1} with the correlation coefficients of >0.995 and 0.997 , respectively (for calibration curves see Fig. S10, for numerical data used to calculate water solubility of the cocrystals see Table S1).

The determined concentrations of LIN (dissolved from the pure form and from the tested cocrystals) were reported as an average of two replicated experiments for each sample. The injections for each sample were repeated four times.

2.8. CASTEP calculations

To calculate stabilization energies of the obtained cocrystals their crystal structures taken from single-crystal X-ray measurements were used as inputs and geometry optimization in the *CASTEP* code (Clark *et al.*, 2005) was performed. For each crystal form, the experimental crystal structure was geometry optimized under periodic boundary conditions, keeping cell parameters fixed at the experimental values, and allowing all atomic positions to relax. In each case, PBE (Perdew *et al.*, 1996) functional with Grimme's dispersion correction scheme (Grimme, 2006) and ultrasoft pseudopotentials were used. The plane wave energy cut-off was set to 600 eV, while k-points separation was set to 0.07 \AA^{-1} . In the case of LIN:3,4-DHBA: H_2O cocrystal a structure with one water molecule in the asymmetric unit was taken for the calculations (which corresponds to 0.5 H_2O molecules per one LIN molecule). Note that in the experimental crystal structure 1.25 molecules of water per asymmetric unit were found. Such a fractional value, however, is difficult to be accounted for in the periodic DFT calculations; therefore, the approximation of the water content to the closest integer was applied. Then, in each case the same geometry optimization procedure was repeated for crystal structures of the coformers used to prepare the cocrystals. The following crystal structures were used: linezolid form II (CSD refcode TIYQAU01) (Maccaroni *et al.*, 2008), linezolid form III (CSD refcode TIYQAU) (Tanaka & Hirayama, 2008), benzoic acid (CSD refcode BENZAC13) (Cai & Katrusiak, 2012), *p*-hydroxybenzoic acid (CSD refcode JOZZIH01) (Du *et al.*, 2018), monoclinic polymorph of 2,6-dihydroxybenzoic acid (CSD refcode LEZJAB01) (MacGillivray & Zaworotko, 1994), triclinic polymorph of monohydrate of 3,4-dihydroxybenzoic acid (CSD refcode BIJDON03) (Horneffer *et al.*, 1999), monohydrate form I of gallic acid (CSD refcode KONTIQ01) (Okabe *et al.*, 2001). In each case stabilization energy was calculated as a difference between total energy of a cocrystal and a sum of total energies of pure components in the respective stoichiometric ratios. The final values were expressed in kJ mol^{-1} per cocrystal formula unit and in

kJ mol^{-1} per molecules. The numerical data used to calculate stabilization energies are given in Table S2.

For energetic evaluation of the conformation of LIN in its crystalline forms, the quantum-chemical calculations with the CASTEP code were performed using the parameters as specified above. After the optimization, all individual symmetry-independent molecules were placed in a 20 \AA cube and their energies were calculated at the same level of theory as stated above to give an intramolecular contribution to the total energy of each crystal.

To validate the crystal structures of the cocrystals and linezolid form III, as well as to assign ^{13}C solid-state NMR chemical shifts, for the geometry optimized crystal structures NMR parameters were calculated under periodic boundary conditions, using GIPAW approach (Pickard & Mauri, 2001; Yates *et al.*, 2007) and the same level of theory as stated above. The theoretical shielding constants (σ_{calc}) were recalculated to chemical shifts (δ_{calc}) using the following equation: $\delta_{\text{calc}} = (\sigma_{\text{calc}} - b)/a$, where a and b are the slope and intercept, respectively, calculated for the linear regression curve of the δ_{exp} versus σ_{calc} plot. To demonstrate the agreement between calculated and experimental ^{13}C data, root-mean-square deviation (RMSD) was calculated for each data set. All experimental and calculated values of δ_{exp} and σ_{calc} can be found in Tables S3 and S4.

3. Results and discussion

3.1. Solid-state NMR and CASTEP calculations as a tool for the determination of cocrystals formation and changes to the solid forms

Fig. 2 features ^{13}C CPMAS spectra of pure forms II and III of LIN, together with the assignment of the ^{13}C resonances. Form III was obtained from the commercially available form II by heating this latter solid for 12 h in an oven set to 130°C , which was confirmed to be an appropriate method to produce pure form III (Rao & Reddy, 2008). Note, however, that shorter heating times at this temperature led to a mixture of forms II and III. The assignment in the presented spectra was done on the basis of the literature data (Wielgus *et al.*, 2015), and validated against the calculated ^{13}C shielding constants for both forms of LIN (see Table S3 and Fig. S11 for the calculated values and regression curves showing the agreement between experimental and theoretical data). In the spectrum of form II resonances originating from morpholine ring carbon atoms (C13–C16) are significantly broadened, whereas in the spectrum of form III they are not observed. This was observed before and associated with temperature-dependent molecular dynamics of this ring present in both analyzed forms (Wielgus *et al.*, 2015). In addition, in the spectrum of form II the resonance originating from C9 is also broadened and has significantly lower intensity, which can be attributed to the coupling between ^{13}C and ^{19}F nuclei. In contrast to the spectrum of form II, in which each of the ^{13}C sites is represented by a single ^{13}C signal, some resonances in the spectrum of form III are split (see magnified regions in Fig. 2). This is the result of the

presence of two symmetry-independent molecules in the asymmetric unit of form III.

For the preparation of the cocrystals in each case LIN form II was used as a starting material. However, to make sure no phase transition of LIN form II occurs while grinding in a ball mill, we performed mechanochemical grinding of this form in the presence of methanol and water (solvents used to create LAG conditions) for 1 h. No apparent changes to the solid-state NMR spectra were noticeable after the grinding. In particular, no resonances originating from LIN form III appeared, which confirmed that LIN form II is still present after the grinding.

Similar experiments were performed for the analyzed cofomers. In the case of BA, PHBA, 2,6-DHBA and GA no changes to their ^{13}C CPMAS NMR spectra were observed after the mechanochemical grinding in the presence of methanol or water. In contrast, for 3,4-DHBA ground with water noticeable changes to the crystal form were observed by solid-state NMR. The ^{13}C CPMAS spectrum of anhydrous 3,4-DHBA before grinding (Fig. S1) features broad resonances, associated with some degree of amorphicity of this sample. After the grinding, narrow and well resolved resonances were observed. In addition, the number of the ^{13}C signals is doubled, which indicates that in the resulting crystal form there are two symmetry independent molecules in the asymmetric unit. Among the known crystalline forms of 3,4-DHBA, its monohydrate crystallizes in such a manner. To confirm the identity of the obtained crystalline form of 3,4-DHBA with its monohydrate, crystallization of this compound from water was performed, a procedure which leads to the triclinic polymorph of 3,4-DHBA monohydrate (Vilas-Boas *et al.*, 2018). The ^{13}C

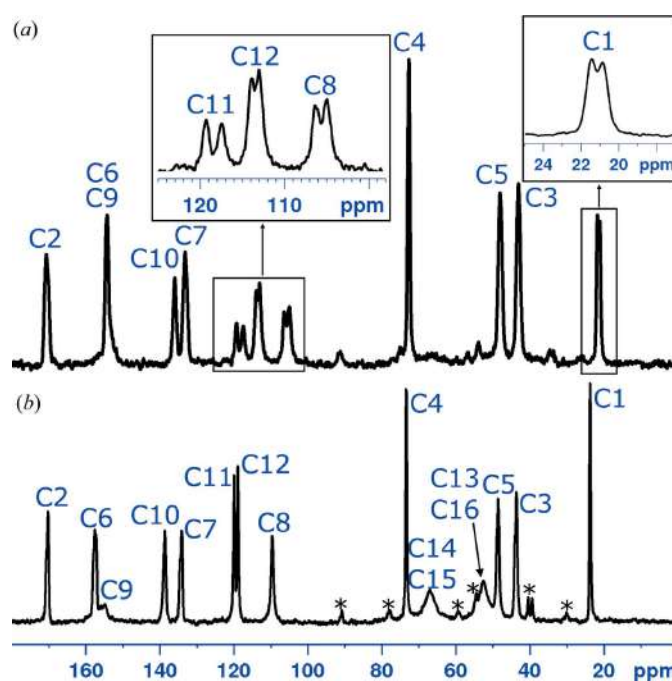


Figure 2
 ^{13}C CPMAS NMR spectra of LIN form III (a) and II (b) together with the assignment of the ^{13}C resonances.

CPMAS spectrum of the resulting solid was identical with the one for the sample obtained after mechanochemical grinding of the starting 3,4-DHBA with water (see Fig. S1). This confirms that mechanochemical grinding of anhydrous 3,4-DHBA in the presence of water leads to the formation of the monohydrate of 3,4-DHBA.

In the next step, cocrformers in their commercial forms were ground in a ball mill with LIN in the presence of water or methanol. Fig. 3 shows ^{13}C CPMAS NMR spectra recorded for the reaction mixtures obtained after the grinding. In each case a shift in the positions of ^{13}C resonances originating from LIN form II is clearly visible. This shift is not consistent with the formation of LIN form III. In addition, a shift in the position of the ^{13}C resonances originating from the cocrformers is noticeable in each case. Therefore, the formation of LIN cocrystals may be postulated.

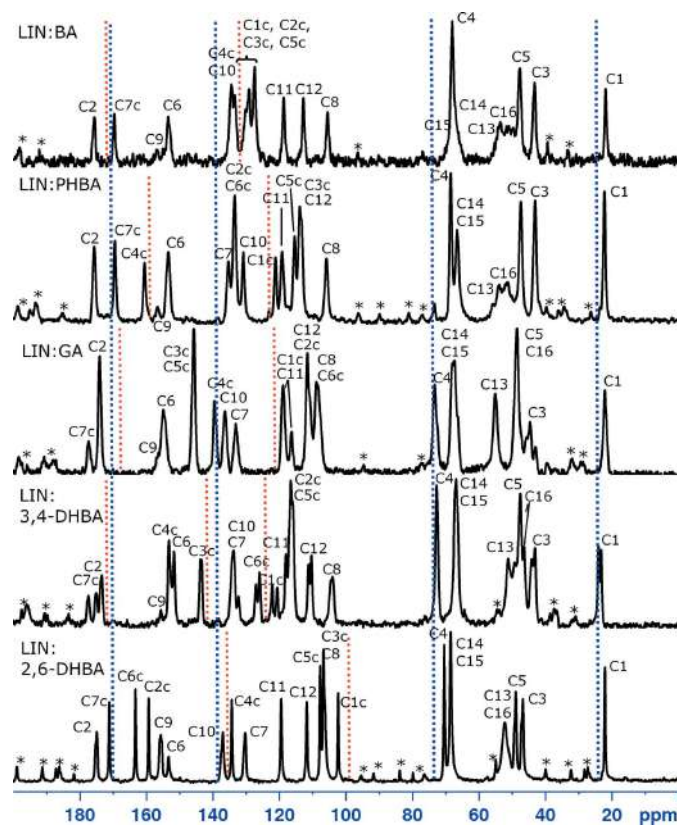


Figure 3
 ^{13}C CPMAS NMR spectra recorded with a spinning speed of 8 kHz for the reaction mixture obtained after mechanochemical grinding of LIN form II with BA, PHBA, GA, 3,4-DHBA and 2,6-DHBA. The assignment of the ^{13}C resonances was made on the basis of the calculated ^{13}C shielding constants for the respective crystal structures, letter 'c' given after the carbon atom number denotes a cocrformer molecule. Blue dotted lines show the original positions of the selected ^{13}C resonances of LIN form II, the red dotted lines mark the original positions of the selected ^{13}C resonances of the respective cocrformers in their crystal forms used for the mechanochemical grinding, while the asterisks mark spinning sidebands. For the ^{13}C solid-state NMR spectra of the cocrformers before grinding see Fig. S2.

In two cases, namely for the reaction mixture with 3,4-DHBA and with GA, some of the ^{13}C resonances originating from LIN are doubled or significantly broadened. This suggests that in these crystalline forms there may be more than one symmetry-independent molecule of LIN in an asymmetric unit. Another interesting feature noticeable in the presented ^{13}C CPMAS NMR spectra is a significant narrowing of the ^{13}C signals originating from the morpholine ring of LIN in comparison to these signals present in the spectrum of LIN form II. In particular, this concerns the resonances originating from C14 and C15 carbon atoms, and to a lesser extent these attributable to C13 and C16 atoms. The change is visible in all new solids to a different extent. It is the most pronounced in the product of grinding of LIN form II with 3,4-DHBA monohydrate and GA monohydrate, and the least so in the product of grinding of LIN with BA. The observed narrowing of the ^{13}C signals of the morpholine ring may be associated with a decrease in the molecular dynamics of this ring in the new solids. It can originate from at least two effects: (i) there is less accessible space for the ring to move in the newly obtain forms, and (ii) if the formation of the cocrystals is confirmed, a hydrogen-bonding interactions between a cocrformer and an oxygen atom from the morpholine ring of LIN could be formed.

In order to confirm the formation of new crystalline phases postulated by solid-state NMR results, powder X-ray diffraction experiments were performed for the obtained solids. Fig. 4

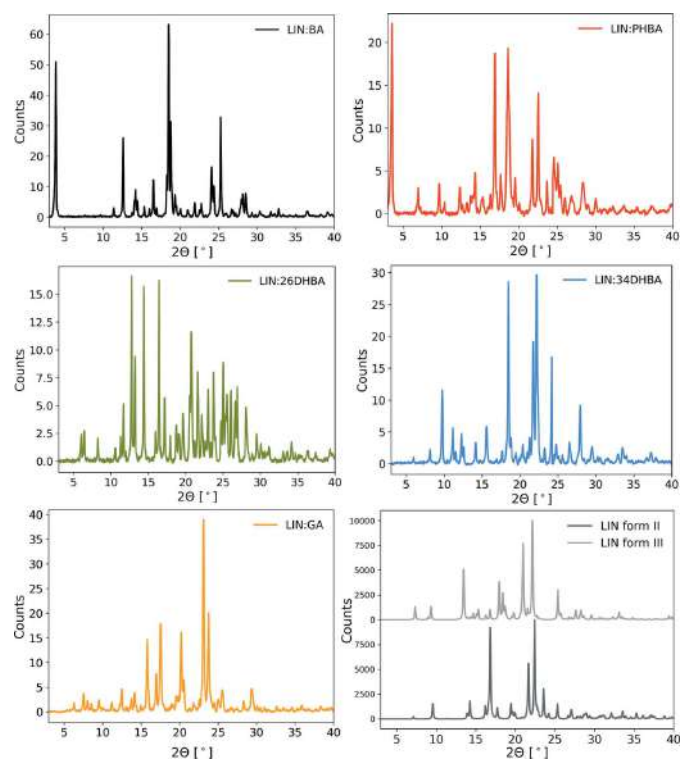


Figure 4
Experimental powder X-ray diffractograms for samples obtained after mechanochemical grinding of LIN:BA, LIN:PHBA, LIN:2,6-DHBA, LIN:3,4-DHBA and LIN:GA, as well as simulated PXRD patterns for LIN forms II and III.

Table 1
Experimental details.

For all structures: multi-scan absorption correction (*CrysAlis PRO*). Empirical absorption correction using spherical harmonics, implemented in SALE3 ABSPACK scaling algorithm.

	LIN:BA	LIN:PHBA:H ₂ O	LIN:2,6-DHBA
Crystal data			
Chemical formula	C ₁₆ H ₂₀ FN ₃ O ₄ ·C ₇ H ₆ O ₂	C ₁₆ H ₂₀ FN ₃ O ₄ ·C ₇ H ₆ O ₃ ·H ₂ O	C ₁₆ H ₂₀ FN ₃ O ₄ ·C ₇ H ₆ O ₄
<i>M_r</i>	459.47	492.47	491.47
Crystal system, space group	Monoclinic, <i>P</i> ₂ ₁	Orthorhombic, <i>P</i> ₂ ₁ 2 ₁ 2 ₁	Orthorhombic, <i>P</i> ₂ ₁ 2 ₁ 2 ₁
Temperature (K)	293	100	293
<i>a</i> , <i>b</i> , <i>c</i> (Å)	6.49617 (9), 7.41888 (18), 23.5870 (4)	6.428 (3), 6.987 (3), 52.001 (9)	4.7535 (3), 15.8010 (6), 29.8550 (11)
α , β , γ (°)	90, 92.9418 (13), 90	90, 90, 90	90, 90, 90
<i>V</i> (Å ³)	1135.26 (4)	2335.5 (15)	2242.42 (17)
<i>Z</i>	2	4	4
<i>D_x</i> (Mg m ^{−3})	1.344	1.401	1.456
Radiation type	Cu <i>K</i> α	Cu <i>K</i> α	Cu <i>K</i> α
μ (mm ^{−1})	0.87	0.95	0.99
Crystal size (mm)	0.63 × 0.40 × 0.10	0.5 × 0.15 × 0.09	0.47 × 0.09 × 0.05
Data collection			
Diffractionmeter	SuperNova, Dual, Cu at zero, TitanS2	SuperNova, Dual, Cu at zero, TitanS2	SuperNova, Dual, Cu at zero, TitanS2
<i>T_{min}</i> , <i>T_{max}</i>	0.211, 1.000	0.809, 1.000	0.269, 1.000
No. of measured, independent and observed [<i>I</i> > 2σ(<i>I</i>)] reflections	18 906, 4213, 4032	8325, 8325, 6511	29 271, 4581, 3744
<i>R_{int}</i>	0.048	0.187	0.087
(sin θ /λ) _{max} (Å ^{−1})	0.625	0.599	0.633
Refinement			
<i>R</i> [<i>F</i> ² > 2σ(<i>F</i> ²)], <i>wR</i> (<i>F</i> ²), <i>S</i>	0.037, 0.103, 1.03	0.143, 0.397, 1.65	0.042, 0.122, 1.02
No. of reflections	4213	8325	4581
No. of parameters	301	320	321
No. of restraints	1	0	0
H-atom treatment	H-atom parameters constrained	H-atom parameters constrained	H-atom parameters constrained
$\Delta\rho_{\max}$, $\Delta\rho_{\min}$ (e Å ^{−3})	0.18, −0.15	1.48, −0.82	0.17, −0.14
Absolute structure	Flack <i>x</i> determined using 1576 quotients [(<i>I</i> ⁺) − (<i>I</i> [−])] / [(<i>I</i> ⁺) + (<i>I</i> [−])] (Parsons <i>et al.</i> , 2013)	Classical Flack method preferred over Parsons because s.u. lower	Flack <i>x</i> determined using 1310 quotients [(<i>I</i> ⁺) − (<i>I</i> [−])] / [(<i>I</i> ⁺) + (<i>I</i> [−])] (Parsons <i>et al.</i> , 2013)
Absolute structure parameter	0.07 (9)	1.5 (6)	−0.13 (11)
CCDC number	1993998	1997194	1994001
	LIN:3,4-DHBA:H ₂ O	LIN:GA:H ₂ O	
Crystal data			
Chemical formula	2(C ₁₆ H ₂₀ FN ₃ O ₄)·2(C ₇ H ₆ O ₄)·1.25(H ₂ O)	C ₁₆ H ₂₀ FN ₃ O ₄ ·C ₇ H ₆ O ₅ ·H ₂ O	
<i>M_r</i>	1005.45	525.48	
Crystal system, space group	Orthorhombic, <i>P</i> ₂ ₁ 2 ₁ 2	Monoclinic, <i>P</i> ₂ ₁	
Temperature (K)	293	293	
<i>a</i> , <i>b</i> , <i>c</i> (Å)	30.3989 (2), 16.10240 (15), 9.66944 (7)	16.78184 (17), 15.4762 (2), 19.59820 (18)	
α , β , γ (°)	90, 90, 90	90, 105.7581 (10), 90	
<i>V</i> (Å ³)	4733.14 (7)	4898.74 (9)	
<i>Z</i>	4	8	
<i>D_x</i> (Mg m ^{−3})	1.411	1.425	
Radiation type	Cu <i>K</i> α	Cu <i>K</i> α	
μ (mm ^{−1})	0.97	1.00	
Crystal size (mm)	0.33 × 0.15 × 0.09	0.43 × 0.18 × 0.07	
Data collection			
Diffractionmeter	SuperNova, Dual, Cu at zero, TitanS2	SuperNova, Dual, Cu at zero, TitanS2	
<i>T_{min}</i> , <i>T_{max}</i>	0.790, 1.000	0.651, 1.000	
No. of measured, independent and observed [<i>I</i> > 2σ(<i>I</i>)] reflections	61 242, 9687, 9333	79 440, 19 039, 18 059	
<i>R_{int}</i>	0.027	0.042	
(sin θ /λ) _{max} (Å ^{−1})	0.627	0.628	
Refinement			
<i>R</i> [<i>F</i> ² > 2σ(<i>F</i> ²)], <i>wR</i> (<i>F</i> ²), <i>S</i>	0.044, 0.134, 1.02	0.043, 0.123, 1.04	
No. of reflections	9687	19 039	
No. of parameters	684	1366	
No. of restraints	0	1	

Table 1 (continued)

	LIN:3,4-DHBA:H ₂ O	LIN:GA:H ₂ O
H-atom treatment	H atoms treated by a mixture of independent and constrained refinement	H-atom parameters constrained
$\Delta\rho_{\max}$, $\Delta\rho_{\min}$ (e Å ⁻³)	0.47, -0.33	0.26, -0.21
Absolute structure	Flack x determined using 3979 quotients [$(I^+)-(I^-)$]/[$(I^+)+(I^-)$] (Parsons <i>et al.</i> , 2013)	Flack x determined using 7590 quotients [$(I^+)-(I^-)$]/[$(I^+)+(I^-)$] (Parsons <i>et al.</i> , 2013)
Absolute structure parameter	0.05 (3)	-0.01 (5)
CCDC number	1994000	1993999

Computer programs: *CrysAlis PRO* (Rigaku Oxford Diffraction, 2020), *SHELXS* (Sheldrick, 2008), *SHELXL* (Sheldrick, 2015), *OLEX2* (Dolomanov *et al.*, 2009).

shows the obtained experimental powder X-ray diffractograms, as well as the two simulated ones for LIN form II and III. In all cases different crystalline phases are present, with no detectable peaks originating from either of the LIN polymorphs. In addition, a comparison of the obtained PXRD patterns for samples of LIN:BA and LIN:PHBA with the patterns published in the patent literature confirms that in these two cases cocrystals of LIN were obtained.

In an attempt to determine whether solvent molecules used as liquid assistants during the grinding (water or methanol) are present after the reaction in the obtained solids, solution ¹H NMR measurements in anhydrous acetone-*d*₆ were performed. Such a method was used before to determine the water content in hydrates of catechin with a variable amount of water present in the crystals (Dudek *et al.*, 2016). The obtained exemplary ¹H NMR spectra are shown in Fig. 5, while all ¹H solution NMR spectra can be found in Fig. S3.

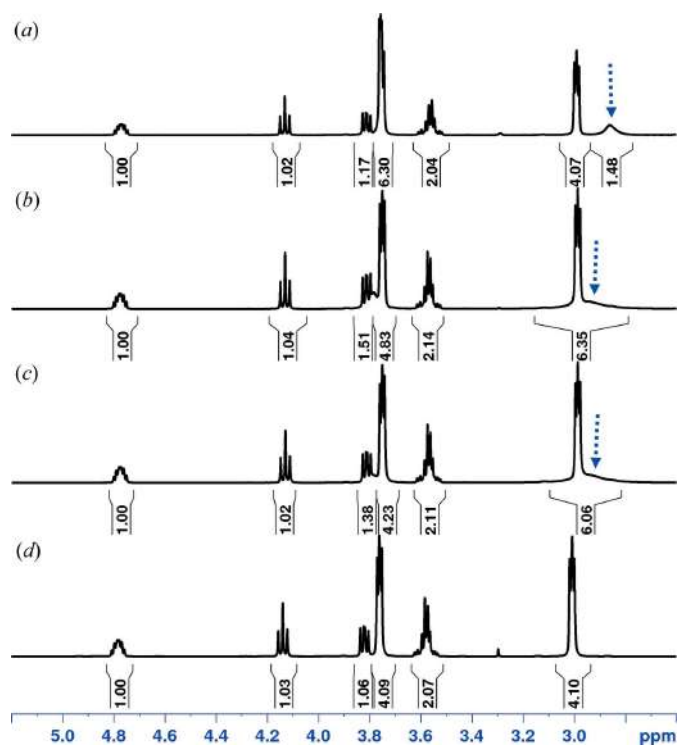


Figure 5

¹H NMR spectra in anhydrous acetone-*d*₆ registered for samples obtained after grinding LIN with 3,4-DHBA (*a* and *b*), GA (*c*), and 2,6-DHBA (*d*). Blue arrows indicate signal originating from water.

Water signal in acetone-*d*₆ has a chemical shift of ~2.90–2.95 p.p.m., while methanol should have two resonances, at 3.31 p.p.m. from CH₃ group and at 3.12 p.p.m. from OH group (Gottlieb *et al.*, 1997). As can be seen in Fig. 4 and Fig. S3 in none of the samples signals originating from methanol are present, but in some of them there are broad resonances at *ca* 2.90 p.p.m., assignable to water. No such signals were detected in two of the obtained solids, namely in LIN:BA and LIN:2,6-DHBA samples [Fig. 5(*d*)]. In the sample of LIN:PHBA and LIN:GA the estimated amount of water present in the analysed material was found to be equal to 1.25 and 1 molecule of water per one linezolid molecule, respectively. The last sample, obtained after grinding of LIN with 3,4-DHBA, turned out to be the most problematic. In this case, the amount of water found in the first experiment was equal to 0.75 H₂O molecules per linezolid molecule [Fig. 5(*a*)]. In order to check whether this is a fixed and repeatable amount, two more samples of LIN and 3,4-DHBA were ground and had ¹H NMR spectra in anhydrous acetone-*d*₆ measured. Each one of them gave the same spectral picture in the ¹³C CPMAS NMR measurements, and yet the content of water in each of the samples varied from 1.15 to 0.45 H₂O molecules per linezolid molecule. It is therefore possible that this crystal is a non-stoichiometric hydrate, with varying amount of water present. Interestingly, the amount of water found in LIN:3,4-DHBA by solution NMR measurements did not depend on whether methanol or water was used to create LAG conditions.

To summarize this part, solid-state NMR and PXRD experiments indicate that five cocrystals of LIN with BA, PHBA, 2,6-DHBA, 3,4-DHBA and GA were obtained, and in at least two of them (LIN:3,4-DHBA and LIN:GA) hydrogen-bond interaction between a coformer and a morpholine ring is expected. In addition, according to solution ¹H NMR measurements LIN:BA and LIN:2,6-DHBA cocrystals do not contain any solvent molecules, LIN:PHBA and LIN:GA cocrystals are 1.25-hydrate and a monohydrate, respectively, and LIN:3,4-DHBA is a non-stoichiometric hydrate. The assignment of the ¹³C resonances for the analyzed solids was performed on the basis of the CASTEP calculations of ¹³C shielding constants, using as a starting point the crystal structures determined by single crystal X-ray diffraction measurements, and comparing the calculated values with the experimental ¹³C chemical shifts. The assigned values can be found in Table S4 and Fig. S12.

3.2. Single crystal X-ray diffraction studies

To fully characterize the newly obtained solid forms of LIN, as well as to recognize the preferences of LIN for heterosynthons formation, we put a special effort into recrystallizing the crystals prepared *via* mechanochemistry. This task turned out to be a difficult one, as in the majority of crystallization attempts crystals of pure LIN form II or form III precipitated from a solution. Only after the appropriate seeding using mechanochemically prepared cocrystals were we able to obtain single crystals suitable for single crystal X-ray diffraction measurements. Unfortunately, in the case of the LIN:PHBA cocrystal the obtained solution is not of a very high quality due to the twinning of crystals (see *Experimental* for details), while Fig. S4 shows the simulated powder patterns for the obtained crystal solutions and their comparison with the experimental PXRD diffractograms. In the case of LIN:BA, LIN:26-DHBA, LIN:3,4-DHBA:H₂O and LIN:GA:H₂O the experimental PXRD diffractograms are in perfect agreement with the ones simulated for the crystal structures solved from single-crystal X-ray diffraction measurements. This indicates the phase purity of the mechanochemically ground samples. In the case of LIN:PHBA:H₂O some differences between the simulated and experimental PXRD patterns are noticeable, which can be attributed to the differences in the temperature in which both experiments were carried out. Note, that this is the only sample for which crystal structure was solved from the single crystal X-ray diffraction experiments measured at 100 K (in contrast to room temperature for PXRD experiment).

In the following section, a comparison of intermolecular interactions and packing arrangements present in the crystal structures of polymorphic forms of LIN and in the obtained

cocrystals is presented. In particular, we focused our attention to supramolecular synthons in each of the analyzed crystal structures to determine which of the possibilities offered by LIN molecules will be exploited to stabilize crystal lattices of the cocrystals. LIN is capable of forming a variety of supramolecular synthons, as it has at least four hydrogen-bond acceptor sites (two C=O groups, and two C—O—C groups in the morpholine and 2-oxazolidone rings), but only one site capable of acting as a hydrogen-bond donor, *i.e.* secondary amide group. It also has a fluorine atom substituted to the benzene ring, which can act as an acceptor for weaker C—H...F interactions, while the presence of aromatic rings and CH₃ group creates the possibility of formation of aromatic–aromatic and CH₃–aromatic interactions. All hydrogen-bond lengths in Figs. 6–12 are the distances between a hydrogen atom and a hydrogen-bond acceptor, while a full list of the observed hydrogen bonds with donor–acceptor distances and donor–hydrogen–acceptor angles are given in Table S5. Aromatic–aromatic interactions are recognized if the distance between the centroids of the interacting rings is less than 7 Å (Burley & Petsko, 1985).

3.3. Linezolid form II

Molecules of LIN in its polymorphic form II, solved in orthorhombic space group $P2_12_12_1$, are interacting mainly *via* C=O...H—N hydrogen bonds, forming chains consisting of LIN molecules, arranged alternately along the *b* direction [Fig. 6(a)]. The length of this bond is equal to 2.12 Å, which places it in moderate hydrogen bonds region. The C=O group engaged in this bond comes from the 2-oxazolidone ring, leaving the C—O—C acceptor site from this ring free. The chains formed by hydrogen-bonded LIN molecules are

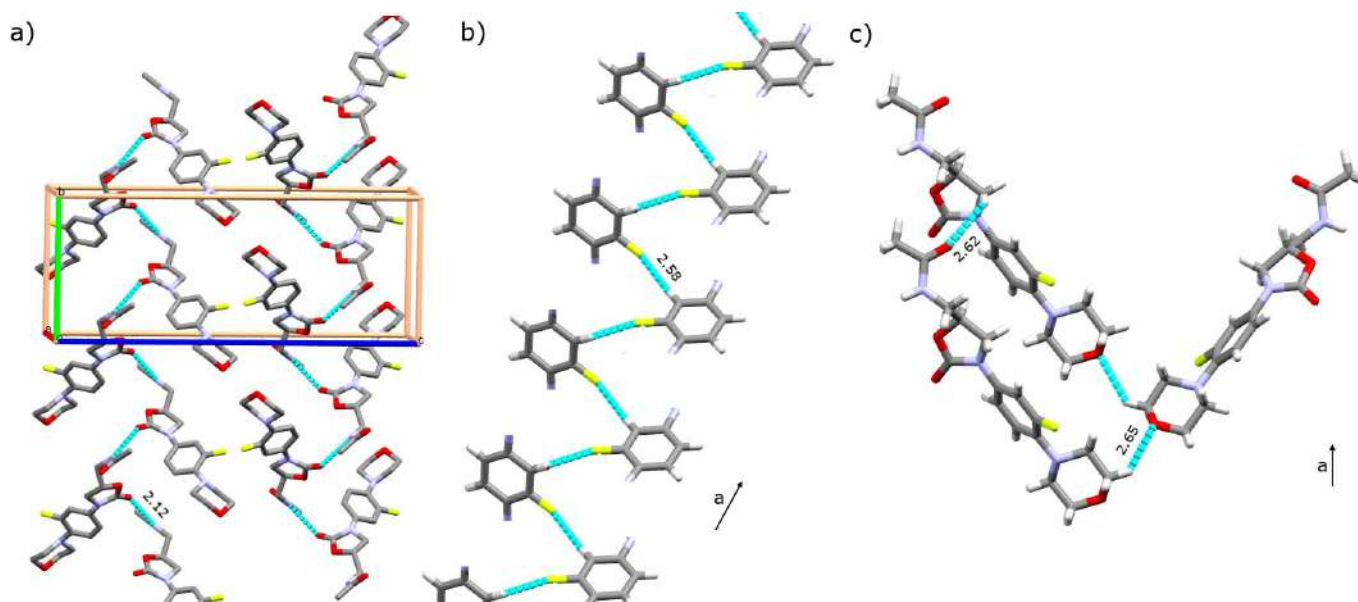


Figure 6
Packing arrangement and intermolecular interactions together with the distances between the interacting atoms found in LIN form II (TIYQAU01): (a) hydrogen-bonding network, (b) C—H...F interactions, and (c) C—H...O short contacts (van der Waals radii < −0.05 Å). In (a) and (b), the H atoms and parts of the LIN molecule, respectively, are omitted for clarity.

mutually interacting *via* $C-H \cdots F$ contacts [Fig. 6(b)], which were found to have similar behaviour and energy to weak hydrogen bonds (D'Oria & Novoa, 2008). The observed supramolecular $C-H \cdots F$ synthon is similar in topology to the $C-H \cdots O$ synthon and is one of the most common of the type present in fluorobenzene derivatives (Thalladi *et al.*, 1998; Thakur *et al.*, 2010). The remaining hydrogen-bond acceptor sites, the amide $C=O$ group and the $C-O-C$ morpholine ring group, form weak $C-H \cdots O$ interactions [Fig. 6(c)].

3.4. Linezolid form III

Form III of LIN (space group $P\bar{1}$) is characterized by the presence of two symmetry-independent molecules in the asymmetric unit. These molecules interact *via* the same type of $C=O \cdots HN$ hydrogen bond as in LIN form II, but forming a different (dimeric) supramolecular homosynthon [Fig. 7(a)]. The lengths of these bonds are shorter than in LIN form II, with the $H \cdots O$ distances equal to 2.07 and 2.04 Å. The two symmetry independent molecules assume different conformations [Fig. 7(b)], differing mainly in the values of the torsion angles about the single bonds between the 2-oxazolidone and fluorophenyl rings, and between the fluorophenyl and morpholine rings (for the exact values of the torsion angles of different LIN conformations see Table S6). This results in the RMSD value between atomic positions of the heavy atoms of 0.732 Å. The conformational differences propagate to the different intermolecular interactions, in particular those involving the fluorine atom and the $C-O-C$

group of the morpholine ring [Fig. 7(c)]. In molecule A none of these sites is engaged in short contact interactions, whereas in molecule B both sites interact *via* $C-H \cdots O$ and $C-H \cdots F$ interactions, respectively, with the methylene groups from the morpholine ring. In contrast, both molecules are engaged in $C_{Ar}-H \cdots O=C-NH$ short contacts with the $O \cdots H$ lengths of 2.26 and 2.50 Å, thus forming another dimeric homosynthon.

3.5. LIN:BA cocrystal

In the LIN:BA cocrystal, solved in monoclinic space group $P2_1$, LIN molecules do not interact *via* hydrogen bonds with other LIN molecules. Instead, the LIN amide group is engaged both as a donor and an acceptor of hydrogen bonds for the molecule of BA [Fig. 8(a)]. This is possible due to the alternating arrangement of BA and LIN molecules in the *b* direction. The $H \cdots O$ distances in the observed hydrogen bonds are equal to 1.81 and 2.04 Å for $C=O_{LIN} \cdots H-O_{BA}$ and $C=O_{BA} \cdots H-N_{LIN}$, respectively. Instead of the classical hydrogen bonds, LIN molecules interact with each other through $C=O \cdots H-C$ and $C-H \cdots F$ short contacts, forming planes of interacting molecules [Fig. 8(b)], with an additional $C-O_{morph} \cdots H-C_{Ar}$ short contact between LIN and BA molecules. The arrangement of the molecules in this crystal allows also for the formation of aromatic-aromatic interactions, absent in LIN forms II and III. These interactions, however weak, are formed between the aromatic rings of BA and LIN [Fig. 8(c)], with the distances between the centroids

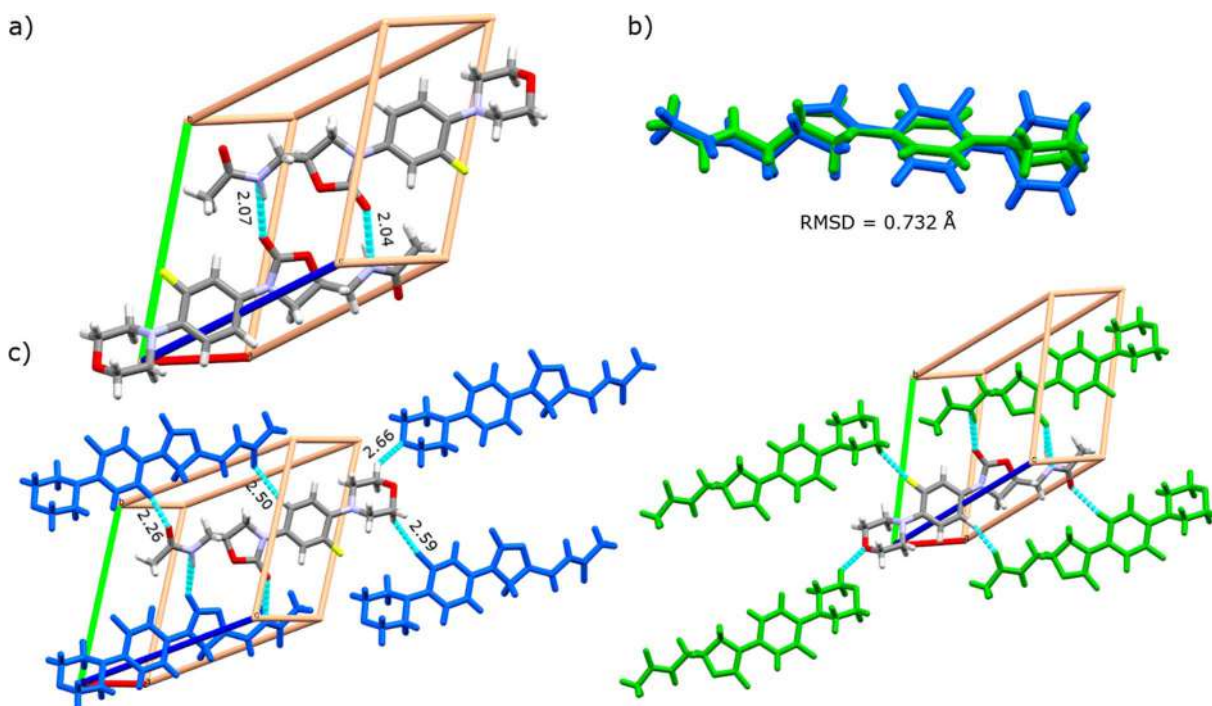


Figure 7
Packing arrangement and intermolecular interactions together with the distances between the interacting atoms found in LIN form III (TIYQAU): (a) hydrogen-bond interacting dimers, (b) the comparison of two symmetry independent LIN molecules, together with the RMSD value reflecting the differences in the atomic positions between the conformations, and (c) short $CH \cdots O$ and $CH \cdots F$ interactions (van der Waals radii < -0.05 Å) found for two symmetry-independent molecules of LIN. Different colours denote symmetry-independent molecules. All distances are given in Å.

of the interacting rings equal to 5.02 and 5.03 Å. There is also a weak parallel aromatic aromatic interactions between BA molecules [Fig. 8(d)], with the distance between the centroids of the BA rings equal to 6.50 Å. This is a rather long distance for recognizing aromatic–aromatic interactions, but still it matches the established criteria for them (< 7 Å). In addition, this interaction concerns aromatic rings aligned parallel, and, as was recently shown, a large horizontal distance between interacting aromatic rings may actually be energetically beneficial (Ninković *et al.*, 2020). The molecular conformation of the LIN molecule in this cocrystal is different from any of the conformations found in LIN forms II and III. Here, the conformational differences are the most pronounced not only in the mutual arrangements of the LIN rings, but primarily in the position of the amide group (see Table S6 for the detailed values of the main torsion angles of LIN), which is possibly associated with making both NH and C=O sites of this group easily accessible for the hydrogen-bonding interaction with BA molecule.

3.6. LIN:PHBA:H₂O cocrystal

LIN:PHBA:H₂O crystallizes as a hydrate, which was already suggested by the solution NMR experiments, in orthorhombic

space group $P2_12_12_1$. Its third lattice constant, c , is unusually large for small organic molecules and equals to *ca* 52.0 Å. The supramolecular synthons found in this cocrystal are very similar to those in LIN:BA cocrystal, with the strongest hydrogen bonds found between $\text{HN}-\text{C}=\text{O}_{\text{LIN}} \cdots \text{H}-\text{O}-\text{C}=\text{O}_{\text{PHBA}}$ and $\text{C}=\text{O}_{\text{PHBA}} \cdots \text{H}-\text{N}_{\text{LIN}}$, with the lengths of 1.79 and 2.02 Å, respectively [Fig. 9(a)]. Apart from these hydrogen bonds, there are also three others formed between the water molecule and the 4-OH group from PHBA (here water oxygen atom acts as hydrogen-bond acceptor), as well as between water acting as a hydrogen-bond donor and one O atom and one N atom from the morpholine ring of LIN [see Fig. 9(b)]. As before in the case of LIN:BA, linezolid molecules do not interact with each other *via* classical hydrogen bonds in this cocrystal, but form a number of short $\text{CH} \cdots \text{O}$ and $\text{CH} \cdots \text{F}$ contacts [Fig. 9(c)]. Three of these contacts are the same as in LIN:BA, with an additional one formed between C–O–C from the 2-oxazolidone ring of LIN and CH₃ group from another LIN molecule. Thus, in this cocrystal all hydrogen-bond acceptor sites of LIN are utilized. There are also strong similarities to LIN:BA in the aromatic–aromatic interactions found in LIN:PHBA:H₂O [Figs. 9(d) and 9(e)], with the distances between the centroids of the interacting aromatic moieties being shorter than in LIN:BA. Overall, it

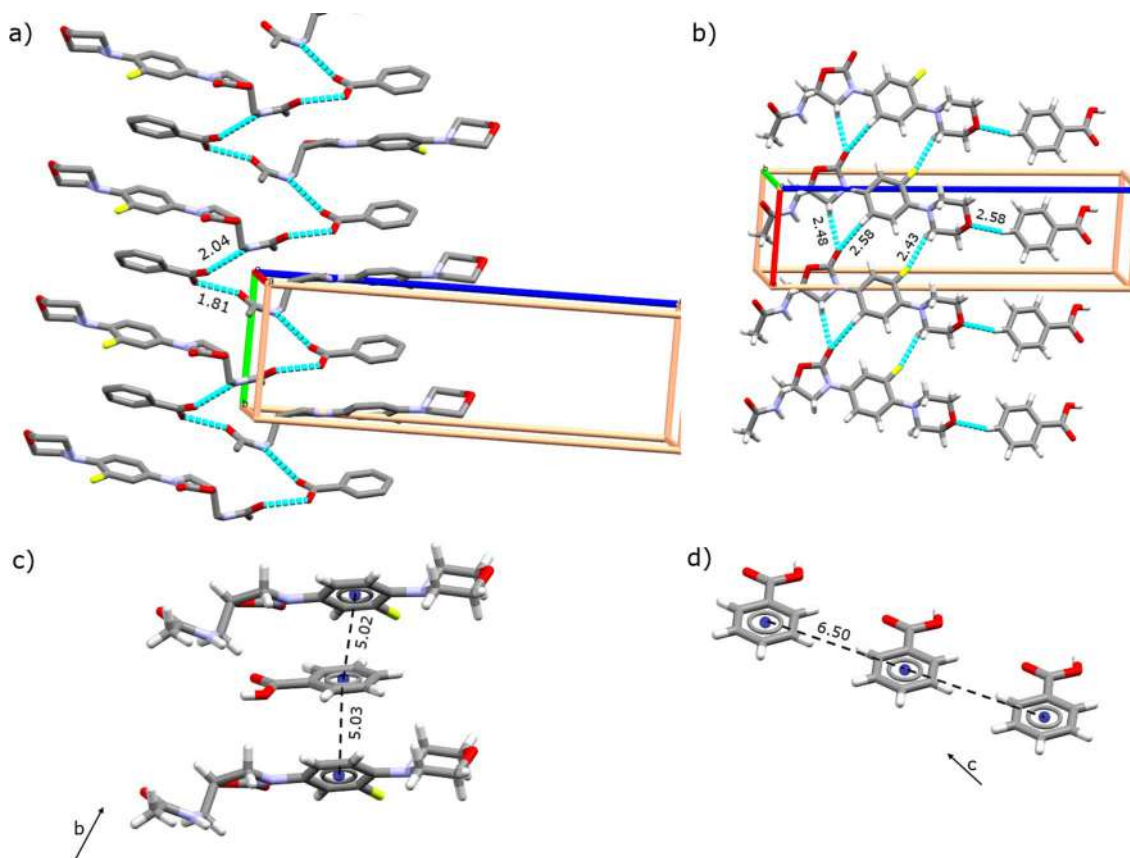


Figure 8 Packing arrangement and intermolecular interactions together with the distances between the interacting atoms found in LIN:BA cocrystal (CCDC deposition number 1993998): (a) hydrogen-bonding network, (b) $\text{CH} \cdots \text{O}$ and $\text{CH} \cdots \text{F}$ short contacts (van der Waals radii < -0.05 Å), (c) aromatic–aromatic interactions between BA and LIN, and (d) aromatic–aromatic interactions between BA molecules. In (a) hydrogen atoms are omitted for clarity. All distances are given in Å.

seems that this cocrystal is characterized by shorter interatomic distances between interacting molecules, with more hydrogen bonds and short contacts than it was found in LIN:BA. Hence, higher stabilization energy for this cocrystal can be expected. Molecular conformation of LIN in LIN:PHBA:H₂O is similar to that found in LIN:BA, with the only difference being the arrangement of the morpholine ring in respect to the fluorophenyl ring (see Table S6), a difference possibly enforced by the directional hydrogen-bonding interaction of nitrogen and oxygen atoms from this ring with water.

On the basis of the intermolecular interactions identified in LIN:BA and LIN:PHBA:H₂O cocrystals it seems that apart from carboxylic group, which readily interacts with NH and C=O groups of LIN, an additional hydroxyl group in PHBA offers a possibility of utilizing more hydrogen-bond acceptor sites of LIN. Also, aromatic–aromatic interactions seem to play a role in cocrystals stabilization. As a result, aromatic hydroxycarboxylic acids present as the best choice to act as coformers for LIN. To prepare new cocrystals, we selected

2,6-DHBA, 3,4-DHBA and GA. Two of these coformers have hydroxyl group at the C-4 position of the benzene ring, as did PHBA. In contrast, 2,6-DHBA does not have a hydroxyl group at the C-4 position, but it exhibits quite low melting temperature of 164°C, which gives hope for the formation of the cocrystal with desired properties.

3.7. LIN:2,6-DHBA cocrystal

In contrast to the two previous cases, in which LIN molecules interact with each other only through short contacts, while the hydrogen-bonding sites are engaged in the interactions with coformer molecules, in LIN:2,6-DHBA cocrystal there is a hydrogen bond between NH_{LIN}...O=C_{LIN} [Fig. 10(a)]. The carbonyl group participating in this bond comes from the 2-oxazolidone ring. Therefore, this synthon is the same as in LIN form II, though the mutual arrangement of LIN molecules is somewhat different. LIN interacts also with 2,6-DHBA *via* a hydrogen bond, located between amide

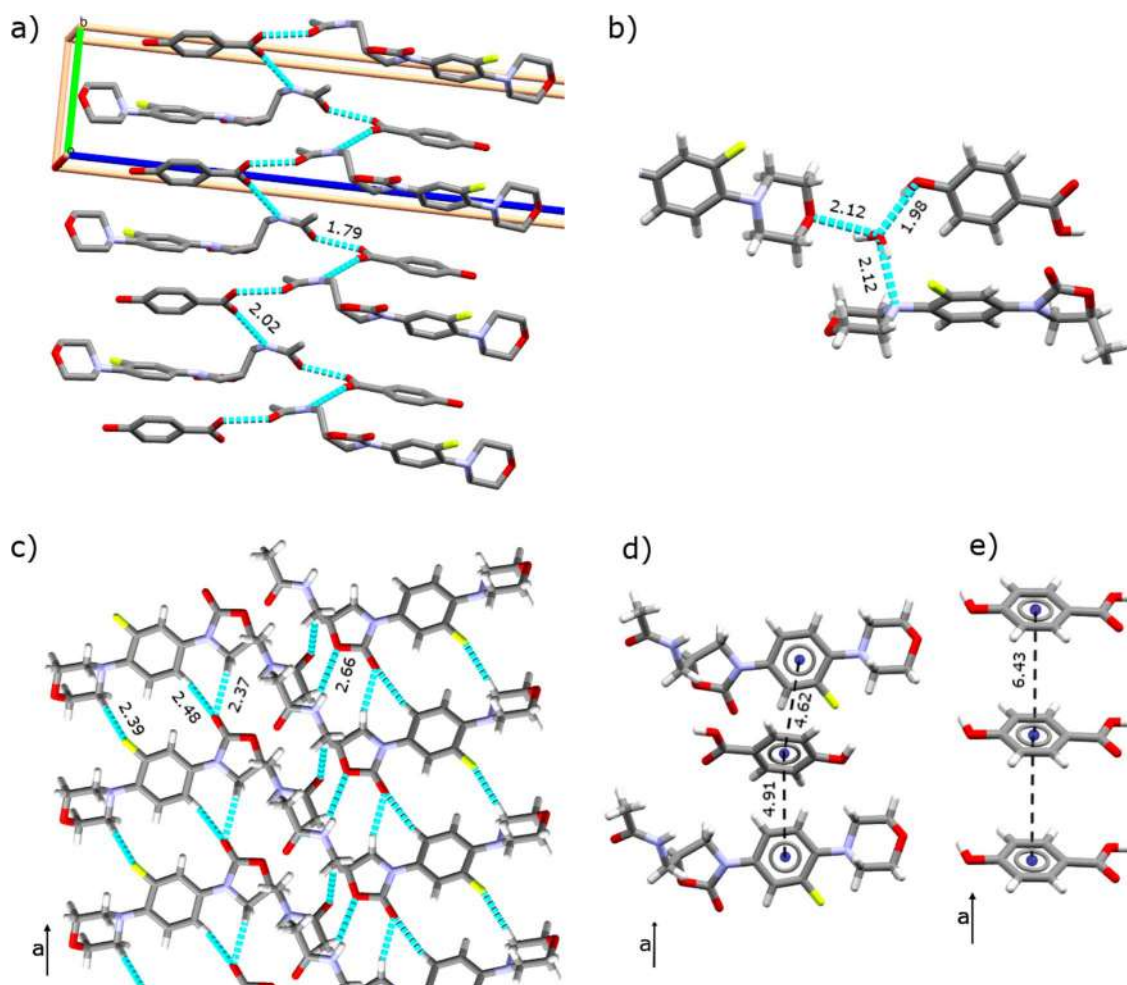


Figure 9

Packing arrangement and intermolecular interactions together with the distances between the interacting atoms found in LIN:PHBA:H₂O cocrystal (CCDC deposition number 1997194): (a) and (b) hydrogen-bonding network, (c) CH...O and CH...F short contacts (van der Waals radii < −0.05 Å), (d) aromatic–aromatic interactions between PHBA and LIN, and (e) aromatic–aromatic interactions between PHBA molecules. In (a) hydrogen atoms and in (b) parts of LIN molecules are omitted for clarity. All distances are given in Å.

$\text{C}=\text{O}_{\text{LIN}}$ group and acidic $\text{OH}_{2,6\text{-DHBA}}$ group [Fig. 10(c)]. This bond is a strong one, with the $\text{O}\cdots\text{H}$ distance equal to only 1.75 Å. Two other hydroxyl groups from 2,6-DHBA are engaged in the intramolecular hydrogen bonds with carboxyl

$\text{C}=\text{O}$ and OH group [Fig. 10(c)], in addition to a weak intermolecular $\text{OH}\cdots\text{O}$ short contact between two OH groups of 2,6-DHBA [Fig. 10(b)]. The additional stabilization of the crystal is provided by a number of short $\text{CH}\cdots\text{O}$ contacts

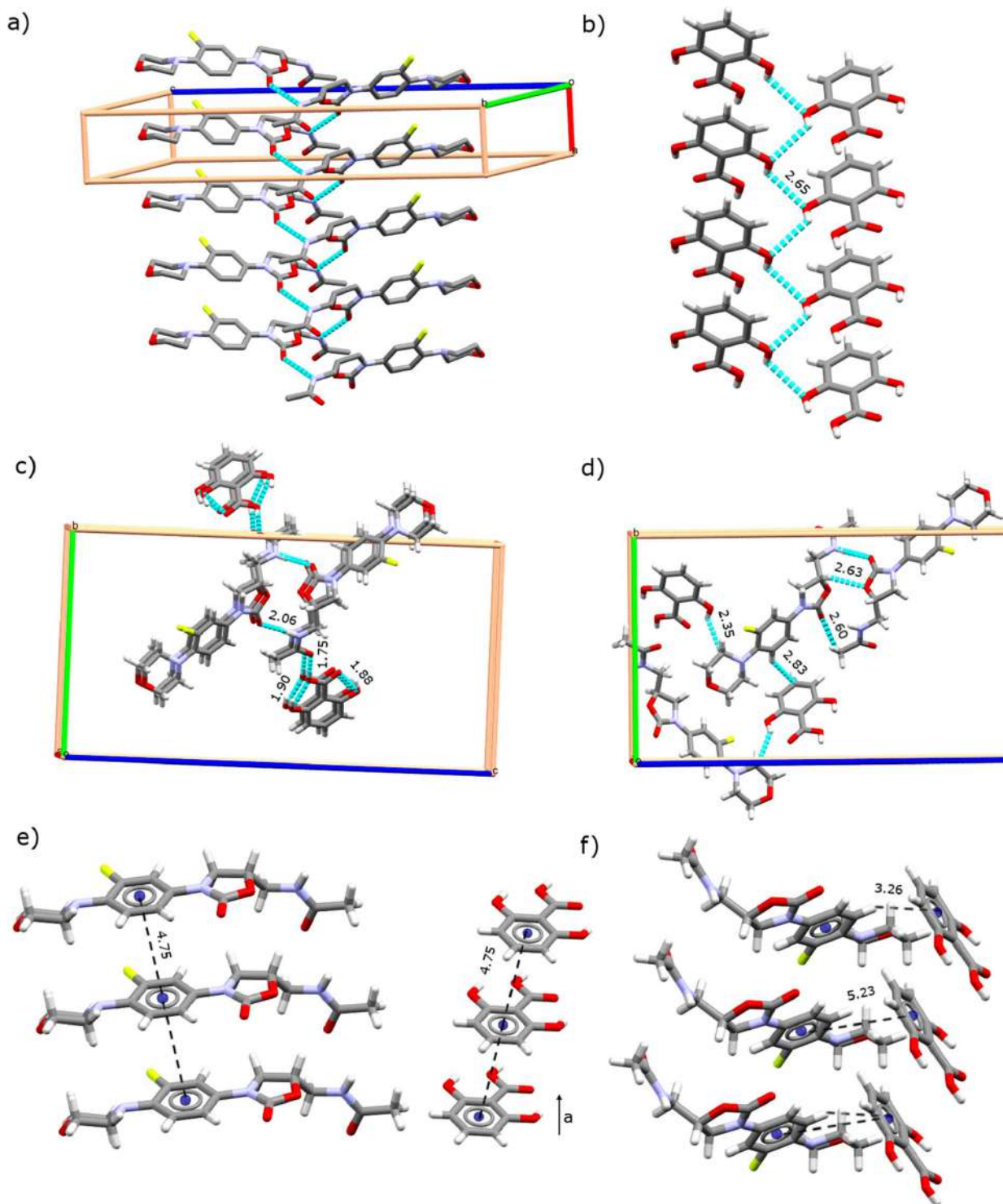


Figure 10

Packing arrangement and intermolecular interactions together with the distances between the interacting atoms found in LIN:2,6-DHBA cocrystal (CCDC deposition number 1994001): (a)–(c) hydrogen-bonding network, (d) $\text{CH}\cdots\text{O}$ short contacts (van der Waals radii < -0.05 Å aromatic interactions between 2,6-DHBA molecules, as well as between LIN molecules, and (f) T-shaped aromatic–aromatic interactions between 2,6-DHBA and LIN molecules. In (a) hydrogen atoms are omitted for clarity. All distances are given in Å.

[Fig. 10(d)], but the $\text{CH}\cdots\text{F}$ interactions are not present. Instead, both LIN and 2,6-DHBA are engaged in aromatic–aromatic homomolecular interactions with the distances between the centroids of the interacting rings equal to 4.75 Å [Fig. 10(e)], as well as with each other through a T-shaped interaction shown in Fig. 10(f), with the $\text{CH}\cdots\text{O}$ distances marked in Fig. 10(d). The T-shaped aromatic ring interactions are characterized by the distance of 5.23 Å between the centroids of the interacting rings, while the distance between the closest hydrogen atom of LIN pointing towards the 2,6-DHBA ring to the centroid of this latter ring equal to 3.26 Å. The conformation of LIN in this cocrystal again differ significantly from all the other conformations found in LIN form II and III, as well as from those in LIN:BA and LIN:PHBA:H₂O, and is the most similar to the one of molecule B from LIN form III, differing from it by one torsion angle value between the 2-oxazolidone and the fluorophenyl rings (Table S6).

3.8. LIN:3,4-DHBA:H₂O cocrystal

As indicated by solid-state NMR measurements, the cocrystal of LIN with 3,4-DHBA, solved in orthorhombic space group $P2_12_12_1$, has two symmetry-independent formula units and it is a hydrate. There are two positions of water molecules, and the best solution for this cocrystal was found after refining one of the possible positions of water with a full occupancy, whereas the second one, located at the symmetry axis, had its occupancy refined as a quarter. This means that the amount of water found in LIN:3,4-DHBA:H₂O is equal to 0.625 H₂O per linezolid molecule in a freshly crystallized sample. However, the structure determined for the crystal kept for a week on a Petri dish showed lower water occupancy (data not shown). This is in agreement with solution and solid-state NMR measurements for this crystal, which indicated that the amount of water in the crystals of LIN:3,4-DHBA:H₂O may vary, while preserving the same crystalline form. Often

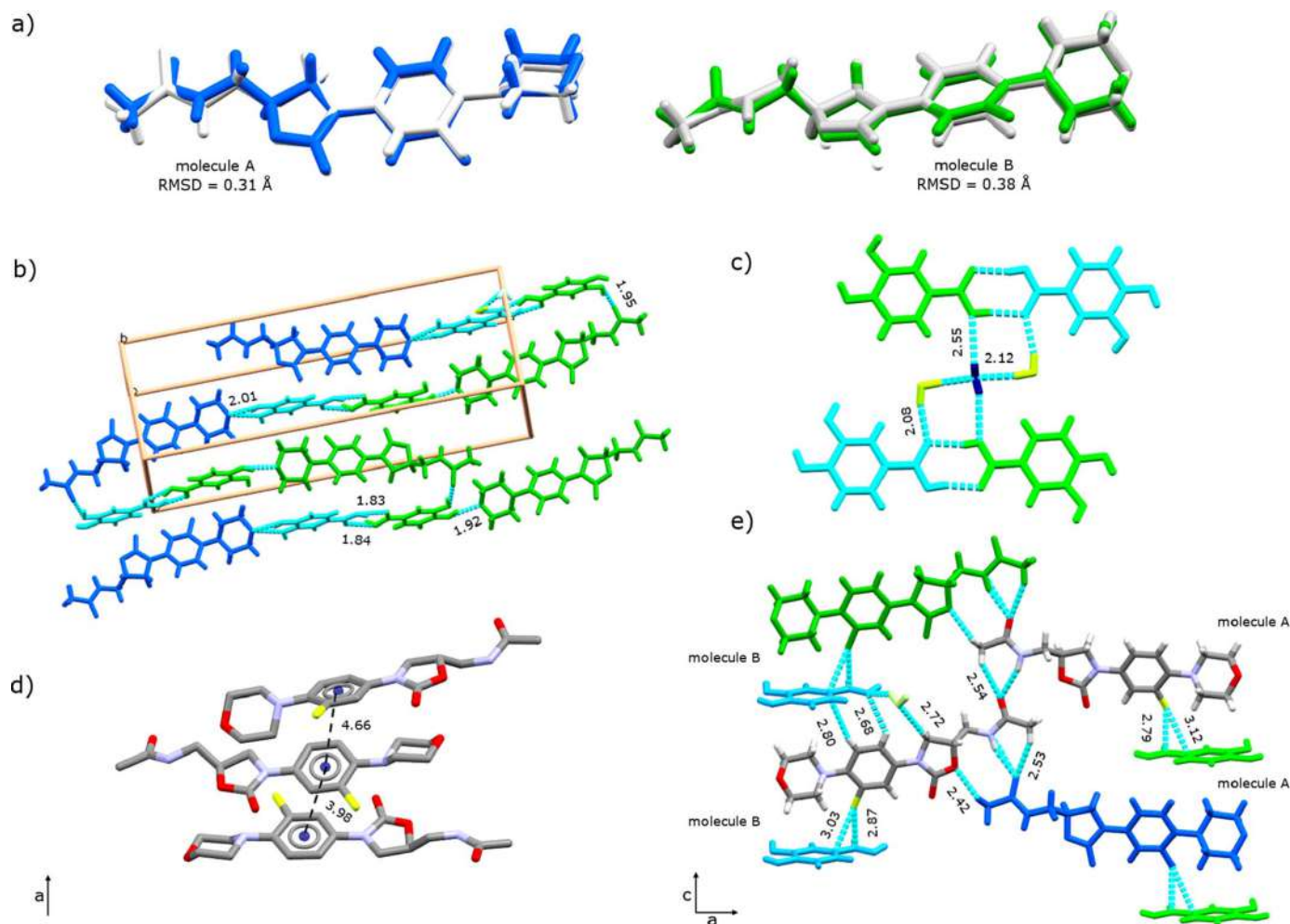


Figure 11 Packing arrangement, intermolecular interactions together with the distances between interacting atoms and conformations of LIN found in LIN:3,4-DHBA:H₂O cocrystal hydrate (CCDC deposition number 1994000): (a) comparison of two conformations of LIN (blue and green) with the ones found in LIN form III, (b) and (c) hydrogen-bonding network, (d) aromatic–aromatic interactions between LIN molecules, and (e) $\text{CH}\cdots\text{O}$ short contacts (van der Waals radii < −0.05 Å) and T-shaped aromatic–aromatic interactions between 3,4-DHBA and LIN molecules. Different colours denote non-symmetry equivalent molecules. All distances are given in Å.

such non-stoichiometric hydrates are channel hydrates, in which water molecules may be loosely bound and as a result they are easily removable (Braun & Griesser, 2018; Tieger *et al.*, 2016; Dudek *et al.*, 2016). This however is not the case of LIN:3,4-DHBA:H₂O cocrystal. Although in this crystal structure water molecules are located together forming small reservoirs, in which they are interacting with each other, these reservoirs are not propagated along any of the crystallographic axes.

The two symmetry-independent molecules of LIN found in this crystal structure differ slightly in conformation, mainly in respect to the mutual positions of the fluorophenyl and the morpholine ring. Interestingly, these two conformations are very similar to the ones found in LIN form III, with the RMSD values for the atomic positions obtained after molecular

overlay of the respective conformations found to be equal to 0.31 and 0.38 Å [Fig. 11(a) and Table S6]. For one of two molecules of LIN a disorder in the position of —O—C=O group of the 2-oxazolidone ring was observed, with the refined occupancy at the two positions equal to 0.63:0.37. For the two molecules of LIN both classical hydrogen bonding and weak CH...O hydrogen bonds are similar in number and in length. They interact with each other through NH_A...O=C—NH_B hydrogen bonds [Fig. 11(b)], aromatic–aromatic interactions [Fig. 11(d)] and short CH...O contacts [Fig. 11(e)]. For each of them there are two hydrogen-bonding interactions with 3,4-DHBA molecules, that is between the oxygen atom from the morpholine ring and the hydroxyl group at C4 position of 3,4-DHBA (with the *D*—H...*A* distances of 1.92 and 2.01 Å for LIN molecules B and A, respectively) and between the

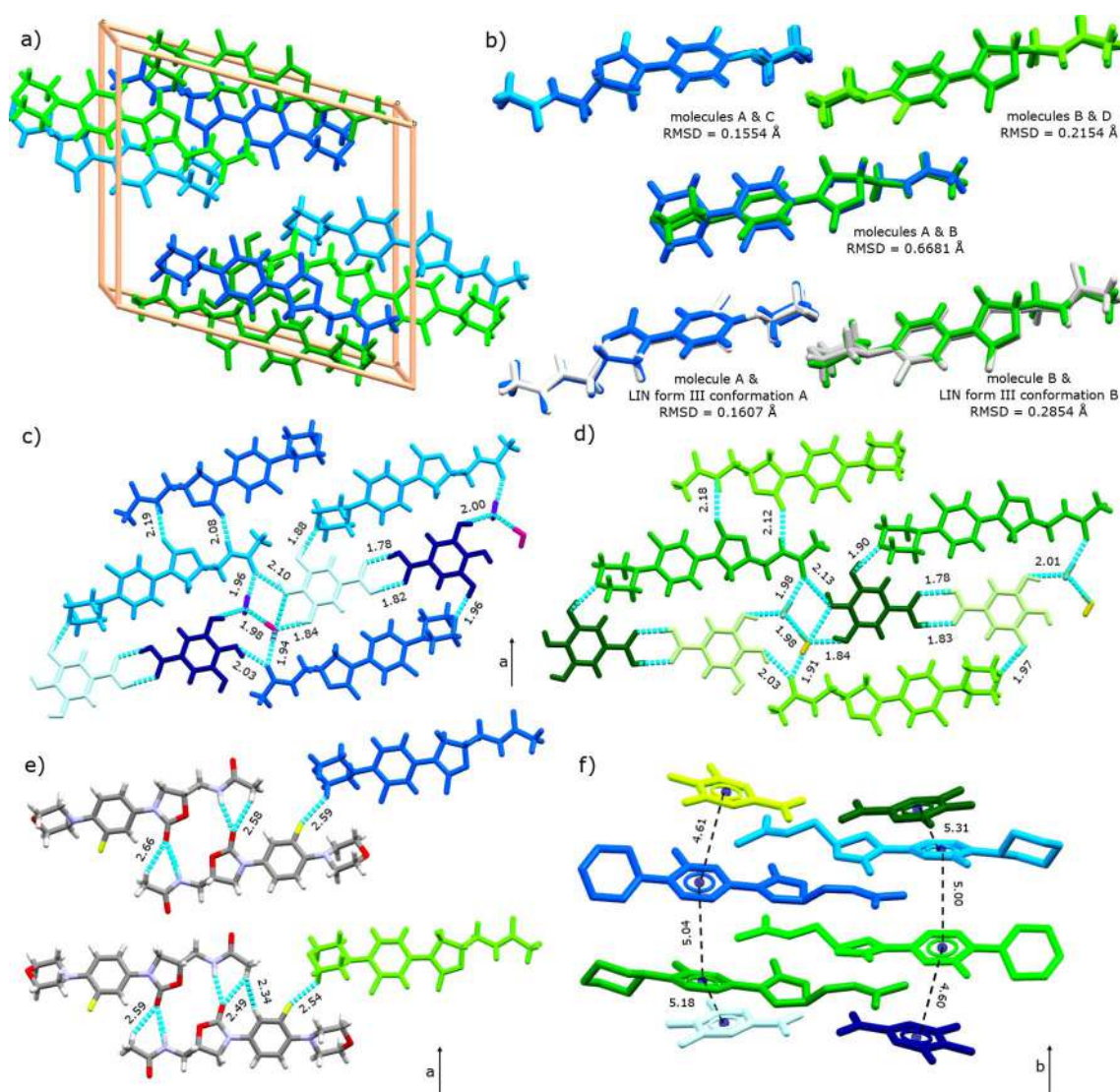


Figure 12

Packing arrangement, intermolecular interactions together with the distances between the interacting atoms and molecular conformations of LIN found in LIN:GA:H₂O cocrystal hydrate (CCDC deposition number 1993999): (a) packing arrangement, (b) comparison of four conformations of LIN with each other and with the ones found in LIN form III, (c) and (d) hydrogen-bonding network, (e) selected CH...O and CH...F short contacts (van der Waals radii < −0.05 Å previously) (f) aromatic–aromatic interactions between LIN and GA molecules. Different colours denote non-symmetry equivalent molecules; in (f) hydrogen atoms are omitted for clarity. All distances are given in Å.

Table 2

Supramolecular synthons formed by LIN in its polymorphic forms II and III, as well as in the five analyzed cocrystals.

Interaction type	Synthon	Crystalline form in which the synthon is present
Hydrogen bonds	$\text{NH} \cdots \text{O}=\text{C}_{\text{ring}}$	II, III (dimers), LIN:2,6-DHBA, LIN:GA:H ₂ O (dimers)
	$\text{NH} \cdots \text{O}=\text{C}_{\text{amide}}$	LIN:3,4-DHBA:H ₂ O
	$\text{NH} \cdots \text{O}=\text{C}-\text{OH}$	LIN:BA, LIN:PHBA:H ₂ O
	$\text{C}=\text{O}_{\text{amide}} \cdots \text{OH}_{\text{carboxylic}}$	LIN:BA, LIN:PHBA:H ₂ O, LIN:2,6-DHBA
	$\text{C}=\text{O}_{\text{amide}} \cdots \text{OH}_{\text{phenol}}$	LIN:3,4-DHBA:H ₂ O, LIN:GA
	$\text{C}-\text{O}_{\text{morph}} \cdots \text{OH}$	LIN:PHBA:H ₂ O, LIN:3,4-DHBA:H ₂ O, LIN:GA:H ₂ O
	$\text{C}-\text{N}_{\text{morph}} \cdots \text{OH}$	LIN:PHBA:H ₂ O
	$\text{OH}_{\text{phenol}} \cdots \text{OH}_{\text{carboxylic}}$	LIN:2,6-DHBA
	$\text{OH}_{\text{phenol}} \cdots \text{O}=\text{C}_{\text{carboxylic}}$	LIN:2,6-DHBA
	$\text{OH}_{\text{carboxylic}} \cdots \text{O}=\text{C}_{\text{carboxylic}}$	LIN:3,4-DHBA:H ₂ O, LIN:GA:H ₂ O
	$\text{OH} \cdots \text{OH}_{\text{water}}$	LIN:PHBA:H ₂ O, LIN:GA:H ₂ O
	$\text{OH}_{\text{water}} \cdots \text{O}$	LIN:3,4-DHBA:H ₂ O, LIN:GA:H ₂ O
	$\text{CH}_{\text{Ar}} \cdots \text{O}=\text{C}/\text{O}-\text{C}$	III, LIN:BA, LIN:PHBA:H ₂ O
	$\text{CH}_2 \cdots \text{O}=\text{C}/\text{O}-\text{C}$	II, III, LIN:PHBA:H ₂ O, LIN:2,6-DHBA
CH \cdots O contacts	$\text{CH}_3 \cdots \text{O}=\text{C}/\text{O}-\text{C}$	LIN:2,6-DHBA, LIN:3,4-DHBA:H ₂ O, LIN:GA:H ₂ O
	$\text{CH}_{\text{Ar}} \cdots \text{F}-\text{C}$	II
CH \cdots F contacts	$\text{CH}_2 \cdots \text{F}-\text{C}$	III, LIN:BA, LIN:PHBA:H ₂ O, LIN:GA:H ₂ O
	Parallel	LIN:BA, LIN:PHBA:H ₂ O, LIN:2,6-DHBA
$\pi-\pi$		LIN:3,4-DHBA:H ₂ O, LIN:GA:H ₂ O
	T-shaped	LIN:2,6-DHBA

hydroxyl group of 3,4-DHBA at C3 and C=O amide group with the $D-\text{H} \cdots A$ distances of 1.92 and 1.95 Å. The carboxyl groups from 3,4-DHBA molecules form strong dimers with the $D-\text{H} \cdots A$ distances of 1.84 and 1.83 Å. The carboxylic OH and C=O groups of 3,4-DHBA forms an additional hydrogen bond with water molecules, which also interacts with each other [Fig. 11(b)]. The structure is additionally stabilized by aromatic–aromatic interactions between LIN molecules with the distances between the centroids of the interacting rings equal to 4.66 and 3.98 Å.

3.9. LIN:GA:H₂O cocrystal

The last of the analysed cocrystals comprises linezolid and gallic acid, and crystallizes in monoclinic space group $P2_1$ as a monohydrate, with four symmetry-independent molecules in the asymmetric unit [Fig. 12(a)]. The chiral centre of the linezolid molecule is located at its asymmetric carbon atom C4. In the non-centrosymmetric space group possessing two LIN molecules in an asymmetric unit the pairs of LIN molecules can be related by pseudo glide plane. Therefore, the crystal structure of LIN:GA:H₂O approximates the centrosymmetric space group $P2_1/n$ with two pairs of linezolid molecules acting as enantiomers. In such pseudo centrosymmetric space group, all atoms of the second LIN molecule can be superimposed on the pharmacologically active enantiomer with the exception of the chiral C4 atom and its hydrogen. The structure could have been solved in space group $P2_1/n$ with disordered C4 and C5 atoms (with attached hydrogens), but this space group does not correspond to the chemical nature of linezolid molecule and such structure's initial refinement parameters were significantly worse. This situation is similar to the one observed in the crystal of LIN form III, determined in the space group $P\bar{1}$ with two molecules in an asymmetric unit (CCDC refcode TIYQAU) (Tanaka & Hirayama, 2008).

In the analysed cocrystal there are two pairs of LIN with very similar conformations [Fig. 12(b)], and these pairs differ in the mutual orientation of the fluorophenyl and the morpholine rings, resulting in the RMSD values for the atomic positions calculated after molecule overlay in the range of 0.64–0.71 Å (depending on the regarded pair, for details see Table S6). As it was in the case of LIN:3,4-DHBA:H₂O, the two pairs of conformers are each very similar to one of the conformers found in LIN form III, with the RMSD values for atomic positions of only 0.16 and 0.29 Å, for molecules A and B, respectively. Interestingly, although ¹³C CPMAS solid-state NMR spectra recorded for this

cocrystal indicated the presence of more than one formula unit per asymmetric part of a unit cell, for none of the ¹³C sites four resonances were distinguishable. This is probably the result of conformational similarity of the symmetry independent molecules of LIN, as well as very similar intermolecular interactions found for each of the four molecules.

Figs. 12(c)–12(e) feature hydrogen-bonding network for each of the LIN molecules. In each pair of similar conformations, two molecules of LIN interact with each other through C=O \cdots H–N hydrogen bond, with the C=O group originating from the 2-oxazolidone ring. This synthon is therefore the same as the one observed in LIN form III. In addition to this interaction, there are two more hydrogen bonds for each LIN molecule, one bifurcated bond between the amide C=O_{LIN} group and either water molecule or the hydroxyl group at the C-4 position of gallic acid, the other between the morpholine oxygen atom and the hydroxyl group at the C-3 position of gallic acid. These interactions with gallic acid hydroxyl groups are the only hydrogen bonds observed between this coformer and LIN in LIN:GA:H₂O crystal. As it was observed for LIN:3,4-DHBA:H₂O cocrystal, carboxyl groups of gallic acid form strongly interacting dimers with each other, while the last hydroxyl group of gallic acid at the C-5 position is engaged in a hydrogen bond with water. There is also a hydrogen bond between symmetrically independent water molecules. The short CH \cdots O and CH \cdots F contacts of all LIN conformations in this cocrystal are also highly similar for each conformer [Fig. 12(e)]. The fluorine atom interacts with CH₂ group from the morpholine ring, just as it was observed also for LIN form III cocrystal, while the C=O group from the 2-oxazolidone ring forms a short contact with the methyl group. It is worth to notice, that all the interactions described so far are between similar conformations of LIN, as well as with the hydrogen-bonded to them GA and water molecules. Through these interactions the molecules form sheets

Table 3

Stabilization energies (E^{stab} , kJ mol⁻¹) of the formation of LIN cocrystals calculated under periodic boundary conditions at DFT-D2 level of theory and the conformational energies (E^{conf} , kJ mol⁻¹) of LIN molecules found within each of the cocrystals in respect to the lowest value of the conformational energy found for molecule A in LIN:3,4-DHBA:H₂O.

See text of the manuscript for the explanation of the E^{stab} of LIN:PHBA:H₂O and LIN:3,4-DHBA:H₂O being given as a range of values, rather than a single value.

Cocrystal	LIN:BA	LIN:PHBA:H ₂ O	LIN:2,6-DHBA	LIN:3,4-DHBA:H ₂ O	LIN:GA:H ₂ O
Formula unit	LIN + BA	LIN + PHBA + H ₂ O	LIN + + 2,6-DHBA	LIN + 3,4-DHBA + 0.5 H ₂ O†	LIN + GA + H ₂ O
E^{stab} (of formula unit)	-0.11	-8.93 to -5.43	-24.34	-22.31 to -20.56	-8.34
E^{stab} (of molecules)	-0.05	-2.98 to -1.81	-12.17	-8.92 to -8.22	-2.78
E^{conf}	+6.38	+9.67	+17.91	0.00 (mol. A) +4.55 (mol. B)	+4.50 (mol. A) +8.93 (mol. B) +4.19 (mol. C) +4.98 (mol. D)

† Note, that the structure of this cocrystal determined from X-ray diffraction results has 0.625 H₂O in a formula unit.

[Fig. 12(c) and 12(d)] propagating in the *a* direction, and aligned in turns in the *b* direction. Interestingly, there are no significant interactions between the sheets, apart from aromatic–aromatic contacts shown in Fig. 12(f). Overall, the supramolecular synthons of LIN and its molecular conformation found in this cocrystal are both very similar to those present in LIN form III and LIN:3,4-DHBA:H₂O cocrystal.

3.10. Supramolecular synthons observed in crystalline forms of LIN – a summary

Table 2 features a list of the intermolecular interactions present in the seven analyzed crystalline forms of LIN, while the lengths and angles of all hydrogen bonds can be found in Table S5. In each of the crystals NH group is engaged in a hydrogen bond, most preferably with the carbonyl group from 2-oxazolidone ring of the other LIN molecule. Only in one case (LIN:3,4-DHBA:H₂O) does the amide H atom form a hydrogen-bonding interaction with the amide C=O group from the second molecule of LIN. Instead, this amide C=O group is readily engaged in a hydrogen bond with either phenolic or carboxylic hydroxyl group, a synthon observed in all five cocrystals. Less preferred hydrogen-bonding interactions are those formed between morpholine oxygen or nitrogen atoms and a hydrogen-bond donor. The one with the morpholine oxygen atom is present in three cocrystals, whereas the latter one only in LIN:PHBA:H₂O cocrystal. An additional role in stabilizing cocrystal hydrates is played by the hydrogen bonds formed by water molecules, acting as both hydrogen-bond acceptors and donors. Finally, in neither of the crystals was hydrogen-bonding interaction observed for the C—O—C oxygen atom from the 2-oxazolidone ring. In the case of short CH...O contacts, there is a larger variability among the analyzed crystals, with none of the observed interactions clearly being more frequent than the others. In contrast, among the CH...F short contacts, if present at all, the most frequent ones are those between methylene protons from the morpholine ring and the fluorine atom. Surprisingly, the CH_{Ar}...F synthon, commonly found in many fluorophenyl derivatives, in the case of the crystalline forms of LIN is present only in LIN form II. On the whole, it seems that the CH...F contacts are not the most important ones in the crystal structures of LIN. Finally, it is interesting to note that aromatic–aromatic interactions are present in all analyzed

cocrystals. It may be therefore conclude that aromatic entities possessing capability to form hydrogen bonds constitute preferred coformers to form cocrystals with LIN. However, what should also be stressed at this point, the number, localization and strength of the interactions present in each of the cocrystals are different, despite structural similarity of the coformers. This may well translate to the differences in energetic stability of the cocrystals. It may also indicate that it will not be feasible to create the cocrystals of LIN with all aromatic acid derivatives and further studies are needed to fully recognize the factors influencing the formation of LIN cocrystals.

3.11. Energetic stability of the cocrystals of LIN

To evaluate the energetic stability of the analyzed cocrystals the respective stabilization energies were calculated under periodic boundary conditions at the PBE-D2 level of theory. Table 3 shows the obtained values of E^{stab} in respect to the parent crystalline forms taking part in the cocrystals formation. Two of the analyzed cases, namely LIN:PHBA and LIN:3,4-DHBA, require additional comments as to the method used to calculate E^{stab} .

In the case of LIN:PHBA:H₂O, the crystal form of the starting material of PHBA is its anhydrous form, but LIN:PHBA:H₂O cocrystal is a monohydrate. The mechanochemical grinding of starting PHBA with water or methanol did not yield PHBA hydrate, and therefore, anhydrous form of PHBA should be accounted for in the calculations. As a result, in order to calculate the E^{stab} value for this cocrystal, an estimation of the energy contribution originating from water molecule is required, both in terms of intra- and intermolecular energy. In our calculations, the intramolecular energy of water was calculated by placing the molecule of water extracted from the geometry optimized structure of LIN:PHBA:H₂O in a 20 Å box and calculating its energy at the same level of theory as for all conducted calculations under periodic boundary conditions. To account for the intermolecular energy of pure water, we used the lattice energy of ice calculated before by Braun *et al.* (2011). This lattice energy, calculated for different polymorphic forms of ice, was determined to be in the range of -70.11 and -66.61 kJ mol⁻¹. As a consequence, the E^{stab} for LIN:PHBA:H₂O cocrystal will not be given as a single value, but

rather by a range of values. Finally, to account for the change in internal energy of water caused by the change of its phase from liquid to solid, a correction equal to $3/2 RT$ (where R is a gas constant and T is temperature) at 298 K was deducted from the obtained sum of the energy contribution of water (McMahon *et al.*, 2018; Dudek & Day, 2019).

LIN:3,4-DHBA:H₂O cocrystal is a hydrate with a variable amount of water. The diffraction data acquired for the freshly crystallized sample indicated that there is 0.625 H₂O molecule per 1 molecule of LIN and 3,4-DHBA. In our calculations, we decided to account only for 0.5H₂O molecule per linezolid molecule, which is a good estimation of the real amount of water present in the cocrystal and allows for significant savings in the computational time and resources. In addition, as one of the molecules of LIN is disordered, only the atomic positions corresponding to the higher occupancy was employed in the calculations. Finally, to estimate the value of E^{stab} for this cocrystal, we calculated the energy of 3,4-DHBA mono-

hydrate and then deducted from this value half of the energy contribution of inter- and intramolecular energy of water, calculated in the same manner as in the case of the PHBA:LIN:H₂O cocrystal. As a result, the E^{stab} for this cocrystal is also a range of values, rather than a single value.

In all five cases, the calculated stabilization energies are negative, suggesting that the formation of LIN:BA, LIN:2,6-DHBA, LIN:3,4-DHBA:H₂O, LIN:PHBA:H₂O and LIN:GA:H₂O is energetically favourable. A recently conducted survey of a 350-component set of organic cocrystals has shown that the stabilization energies of the cocrystals is $-24.6 \text{ kJ mol}^{-1}$ to $+10.2 \text{ kJ mol}^{-1}$ of molecules (Taylor & Day, 2018). Our results of stabilization energies of LIN cocrystals are in agreement with these observations, with all values falling within the ranges found in the cited survey. The lowest stabilization energy was found for LIN:BA cocrystal, and the highest for LIN:2,6-DHBA. It is worth to note that in this latter case the conformation of LIN is highly unfavourable energetically, in comparison to this energy in other cocrystals. This means that the intermolecular energy contribution to the lattice energy of this cocrystal have to be significant in order to overcome such unfavourable E^{conf} and yield so high E^{stab} value.

Finally, we point out that despite favourable energetics of the LIN cocrystals, their recrystallization from methanol solution was not an easy task (with numerous attempts resulting in the formation of crystalline forms of the parent compounds) and required seeding. Also, in order to obtain LIN:PHBA:H₂O cocrystal without any impurities from the starting materials by mechanochemistry, as much as 3 h of grinding was required, in addition to a considerable amount liquid assistant. This may indicate that the parent compounds are kinetically favoured over the cocrystals. However, one should also consider a possibility of the entropy change upon the formation of the cocrystals. The entropy term is usually not significant and therefore is often neglected in the calculation of stabilization energies. However, in the case of LIN this entropy change may be larger than usual, because of the change in the dynamics of the morpholine ring upon cocrystallization indicated by the solid-state NMR measurements.

3.12. Thermal properties of the cocrystals of LIN

The DSC curve for commercially available LIN form II features two endothermic transitions [Fig. 13(a)]. The first of these events at 154.44°C corresponds to the phase change from LIN form II to LIN form III, which is followed by the melting event of form III at 179.06°C (Aronhime *et al.*, 2008). In contrast, for LIN form III only the endotherm corresponding to the melting point of this form is visible. The thermograms obtained for the LIN cocrystals are shown in Fig. 13(b), while Table 4 compares the melting temperatures of the parent forms of the coformers and the respective cocrystals with LIN (for the DSC curves of the parent crystalline forms of the coformers supporting information, Figs. S5–S9). In the case of LIN:PHBA:H₂O and LIN:GA:H₂O cocrystals two endothermic events are visible, the first one associated

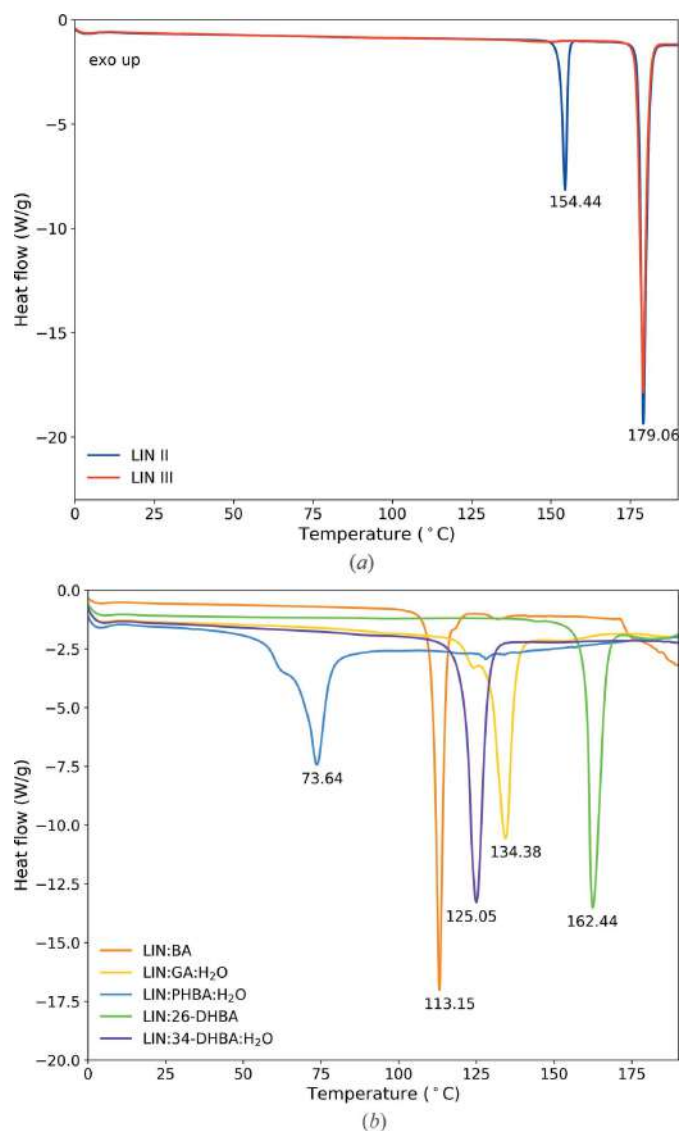


Figure 13
DSC curves for form II of LIN (upper) and five LIN cocrystals obtained in this work (lower).

Table 4

Melting temperatures (in °C) of the starting crystalline forms of the coformers used to prepare cocrystals with LIN and of the respective cocrystals.

	BA	PHBA	2,6-DHBA	3,4-DHBA	GA
T_{parent}	122.67	217.67	164.01	205.49	262.06
$T_{\text{cocrystal}}$	113.15	73.64	162.44	125.05	134.38

with the dehydration of the cocrystals, whereas the second one with the melting events. For LIN:3,4-DHBA:H₂O the dehydration process is not visible as a separate event, but the observed melting event is characterized by noticeably broader peak, possibly due to the overlap of both events.

In all cases the melting points of the cocrystals are lower than the melting points of both LIN and each of the coformers. However, in the case of LIN:2,6-DHBA the melting event takes place at a higher temperature than the LIN II → LIN III phase transition. This might pose a risk for the application of the thermal method of introducing LIN into mesoporous silica nanoparticles, associated with the possibility of the recrystallization of form III inside the pores. For the rest of the cocrystals such a risk is minimal.

3.13. Solubility measurements

Aware of the fact that in the majority of studies the design and synthesis of the cocrystals of APIs is performed in order to enhance water solubility of a drug, we decided to test the obtained cocrystal for this physicochemical parameter for the comparison purposes. According to the literature water solubility of LIN form II at 298 K is equal to 2.42 mg ml⁻¹ after 12 h equilibration of the supersaturated solution (Zheng *et al.*, 2017), which is in excellent agreement with our measurements, which yielded 2.55 mg ml⁻¹ at the 12 h point (Fig. 14). At other measurement points, only small differences in LIN concentration were observed, with a peak concentration of 2.94 mg ml⁻¹ after 24 h (which constitute 15% increase in respect to the first value). Fig. 14 shows data obtained for all

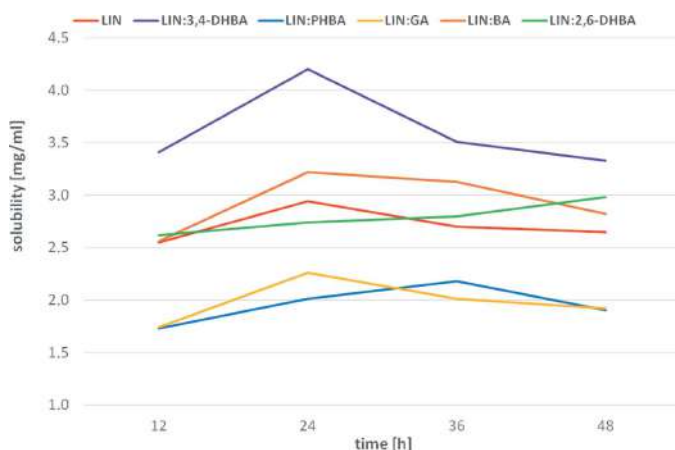


Figure 14

Results of water solubility measurements of LIN form II and its cocrystals with BA, 2,6-DHBA, 3,4-DHBA, PHBA and GA.

tested cocrystals after 12 h, 24 h, 36 h and 48 h equilibration of the analysed solutions. In the majority of cases, the highest concentration of LIN was observed for samples after 24 h equilibration, with the maximum change in the water solubility observed for LIN:3,4-DHBA:H₂O cocrystal and equal to 23% of the 12 h value. Due to the presence of this peak after 24 h for the majority of samples, we will directly compare the results obtained for all studied crystals at this measurement point.

In contrast to what could be expected from the melting point changes, upon cocrystallization not all cocrystals of LIN exhibit better water solubility than its form II. In fact, only two out of five cocrystals have better solubility than LIN form II after 24 h, *i.e.* LIN:3,4-DHBA:H₂O and LIN:BA. For the first of these two the observed improvement in solubility is significant and equal to 43% in respect to the value for LIN form II, whereas for LIN:BA cocrystal this improvement is equal to 10%. The three remaining cocrystals, LIN:2,6-DHBA, LIN:GA:H₂O and LIN:PHBA:H₂O show 7%, 23% and 32%, respectively, worse solubility than LIN form II.

Finally, we comment on the apparent lack of correlation of water solubility results with the calculated stabilization energies for the obtained cocrystals. Usually, a more thermodynamically stable cocrystal (*i.e.* with more negative stabilization energy) should be less soluble in the same solvent in comparison with a cocrystal less thermodynamically stable (although it also depend significantly on the solubility of a given coformer in this solvent). This is not the case of the analyzed cocrystals of LIN. For example, the calculated lattice energy for LIN:2,6-DHBA is as low as -12.17 kJ mol⁻¹ of molecules, which is even more negative than the average of -8 kJ mol⁻¹ of molecules (Taylor & Day, 2018), but its water solubility is lower than LIN:BA cocrystal having much less negative stabilization energy of -0.11 kJ mol⁻¹ of molecules. These discrepancies may suggest that entropic contribution to the overall stabilization energy, despite being usually very small, could in this case tip the scales of thermodynamic stability, as was observed earlier for a cocrystal of apremilast and picolinamide (Dudek *et al.*, 2019). As a result, the calculated stabilization energy values may be overestimated, as they do not account for the entropy change upon cocrystallization. On the other hand, the presented data does not include differences in the water solubilities of coformers alone, which may also result in the observed discrepancies. Still, it seems that caution is advisable when drawing conclusions on the thermodynamic stability of the cocrystals basing on the calculated E^{stab} values alone.

4. Conclusions

In this work, the crystal structures of two cocrystals of linezolid (LIN) with benzoic acid (BA) and *p*-hydroxybenzoic acid (PHBA) were determined, in order to recognize the synthon preferences exhibited by linezolid molecule. In both structures the $\text{NH}_{\text{LIN}} \cdots \text{O}=\text{C}-\text{OH}_{\text{coformer}}$ and $\text{C}=\text{O}_{\text{amide-LIN}} \cdots \text{OH}_{\text{coformer}}$ synthons were identified, with aromatic-aromatic interactions between benzoic acid deriva-

tives and LIN molecules further stabilizing the structures. It was also found that the additional hydroxyl group of PHBA offers a possibility of saturating more hydrogen-bond acceptor sites, abundant in LIN molecules, in contrast to only one hydrogen-bond donating site. As a result, hydroxylated aromatic acid derivatives were designated as promising cofomers for LIN and three new cocrystals of this API with 2,6-dihydroxybenzoic acid (2,6-DHBA), 3,4-dihydroxybenzoic acid (3,4-DHBA) and gallic acid (GA) were designed and synthesized. Their crystal structures revealed even more diverse range of supramolecular synthons formed by LIN. Basing on the frequency of the observed supramolecular synthons, the proposed hierarchy of the hydrogen-bond acceptor sites of LIN is $\text{C}=\text{O}_{\text{amide}} > \text{C}=\text{O}_{\text{oxazolidone}} > \text{C}-\text{O}-\text{C}_{\text{morpholine}} > \text{C}-\text{N}-\text{C}_{\text{morpholine}} > \text{C}-\text{O}-\text{C}_{\text{oxazolidone}}$. Among the weaker $\text{CH}\cdots\text{O}$ and $\text{CH}\cdots\text{F}$ interactions, the previous ones seem to be favoured, with $\text{CH}_{\text{Ar}}\cdots\text{F}$ synthon, common in fluorophenyl derivatives, found only in the crystal structure of LIN form II. In all cocrystals aromatic–aromatic interactions were formed, suggesting that indeed this is an important stabilizing factor for the analyzed structures.

All five cocrystals were evaluated for their energetic stability, thermal properties and water solubility. In all cases, negative stabilization energies were obtained from the performed quantum–chemical calculations, which suggests that formation of the cocrystals is energetically favourable. However, it should be noted that in the case of LIN:BA cocrystal the obtained stabilization energy was equal to only $-0.05 \text{ kJ mol}^{-1}$ of molecules. The new solids exhibited modified thermal properties in comparison with the parent crystal structures. Importantly, in all cases lower melting temperature than the melting point of linezolid form III was found, while four cocrystals had the melting point below the phase transition from LIN form II to LIN form III. This change in melting temperature is beneficial for the possible application of thermal-based methods to introduce the new solids into mesoporous silica nanoparticles. Water solubility measurements showed that only in two cases an enhancement in this physicochemical parameter was obtained. This concerns primarily LIN:3,4-DHBA:H₂O cocrystal, for which a 43% increase in water solubility was observed, while for LIN:BA cocrystal this increase was equal to only 10%.

Acknowledgements

The Polish Infrastructure for Supporting Computational Science in the European Research Space (PL-GRID) is gratefully acknowledged for providing computational resources.

Funding information

The following funding is acknowledged: Narodowe Centrum Nauki (grant No. UMO-2017/25/B/ST4/02684); Polish Infrastructure for Supporting Computational Science.

References

- Abou Hassan, O. K., Karnib, M., El-Khoury, R., Nemer, G., Ahdab-Barmada, M. & BouKhalil, P. (2016). *Front. Pharmacol.* **7**, 325.
- Aronhime, J., Koltai, T., Braude, V., Fine, S. & Niddam, T. (2008). United States Patent US 2008/0319191 A1.
- Bergren, M. S. (2003). US Patent 6559305 B1.
- Bharti, C., Nagaich, U., Pal, A. K. & Gulati, N. (2015). *Int. J. Pharm. Investig.* **5**, 124–133.
- Braun, D. E. & Griesser, U. J. (2018). *Front. Chem.* **6**, 31.
- Braun, D. E., Karamertzanis, P. G. & Price, S. L. (2011). *Chem. Commun.* **47**, 5443–5445.
- Burley, S. K. & Petsko, G. A. (1985). *Science*, **229**, 23–28.
- Cai, W. & Katrusiak, A. (2012). *CrystEngComm*, **14**, 4420–4424.
- Clark, S. J., Segall, M. D., Pickard, C. J., Hasnip, P. J., Probert, M. J., Refson, K. & Payne, M. C. (2005). *Z. Kristallog.* **220**, 567–570.
- Devarakonda, S. N., Thaimattam, R., Muppidi, V. K., Kanniah, S. L. & Duggirala, N. K. (2009). International Patent WO 2009/140466 A2.
- Do, J.-L. & Friščić, T. (2017). *ACS Cent. Sci.* **3**, 13–19.
- Dolomanov, O. V., Bourhis, L. J., Gildea, R. J., Howard, J. A. K. & Puschmann, H. (2009). *J. Appl. Cryst.* **42**, 339–341.
- D’Oria, E. & Novoa, J. J. (2008). *CrystEngComm*, **10**, 423–436.
- Douroumis, D., Ross, S. A. & Nokhodchi, A. (2017). *Adv. Drug Deliv. Rev.* **117**, 178–195.
- Du, J. J., Stanton, S. A., Williams, P. A., Ong, J. A., Groundwater, P. W., Overgaard, J., Platts, J. A. & Hibbs, D. E. (2018). *Cryst. Growth Des.* **18**, 1786–1798.
- Dudek, M. K. & Day, G. M. (2019). *CrystEngComm*, **21**, 2067–2079.
- Dudek, M. K., Jeziorna, A. & Potrzebowski, M. J. (2016). *CrystEngComm*, **18**, 5267–5277.
- Dudek, M. K., Wielgus, E., Paluch, P., Śniechowska, J., Kostrzewa, M., Day, G. M., Bujacz, G. D. & Potrzebowski, M. J. (2019). *Acta Cryst. B75*, 803–814.
- Food and Drug Administration (2019). Regulatory Classification of Pharmaceutical Co-Crystals. Guidance for Industry. <https://www.fda.gov/food/food-ingredients-packaging/generally-recognized-safe-gras>.
- Frelek, J., Górecki, M., Łaszcz, M., Suszczyńska, A., Vass, E. & Szczepek, W. J. (2012). *Chem. Commun.* **48**, 5295–5297.
- Fung, B. M., Khitrin, A. K. & Ermolaev, K. (2000). *J. Magn. Reson.* **142**, 97–101.
- Gottlieb, H. E., Kotlyar, V. & Nudelman, A. (1997). *J. Org. Chem.* **62**, 7512–7515.
- Grimme, S. (2006). *J. Comput. Chem.* **27**, 1787–1799.
- Horneffer, V., Dreisewerd, K., Lüdemann, H.-C., Hillenkamp, F., Läge, M. & Strupat, K. (1999). *Int. J. Mass Spectrom.* **185–187**, 859–870.
- Jafari, S., Derakhshankhah, H., Alaei, L., Fattahi, A., Varnamkhasti, B. S. & Saboury, A. A. (2019). *Biomed. Pharmacother.* **109**, 1100–1111.
- Jain, S., Patel, N. & Lin, S. (2015). *Drug Dev. Ind. Pharm.* **41**, 875–887.
- Karki, S., Friščić, T., Fábíán, L., Laity, P. R., Day, G. M. & Jones, W. (2009). *Adv. Mater.* **21**, 3905–3909.
- Kaur, R., Cavanagh, K. L., Rodríguez-Hornedo, N. & Matzger, A. J. (2017). *Cryst. Growth Des.* **17**, 5012–5016.
- Limnell, T., Santos, H. A., Mäkilä, E., Heikkilä, T., Salonen, J., Murzin, D. Y., Kumar, N., Laaksonen, T., Peltonen, L. & Hirvonen, J. (2011). *J. Pharm. Sci.* **100**, 3294–3306.
- Lipinski, C. A. (2001). *Curr. Drug. Discov.* **4**, 17–19.
- Maccaroni, E., Alberti, E., Malpezzi, L., Masciocchi, N. & Vladiskovic, C. (2008). *Int. J. Pharm.* **351**, 144–151.
- MacGillivray, L. R. & Zaworotko, M. J. (1994). *J. Chem. Crystallogr.* **24**, 703–705.
- Manzano, M. & Vallet-Regí, M. (2019). *Chem. Commun.* **55**, 2731–2740.

- McMahon, D. P., Stephenson, A., Chong, S. Y., Little, M. A., Jones, J. T. A., Cooper, A. I. & Day, G. M. (2018). *Faraday Discuss.* **211**, 383–399.
- Mellaerts, R., Jammaer, J. A. G., Van Speybroeck, M., Chen, H., Humbeeck, J. V., Augustijns, P., Van den Mooter, G. & Martens, J. A. (2008). *Langmuir*, **24**, 8651–8659.
- Moellering, R. C. (2003). *Ann. Intern. Med.* **138**, 135–142.
- Narayan, R., Nayak, U. Y., Raichur, A. M. & Garg, S. (2018). *Pharmaceutics*, **10**, 118.
- Ninković, D. B., Blagojević Filipović, J. P., Hall, M. B., Brothers, E. N. & Zarić, S. D. (2020). *ACS Cent. Sci.* **6**, 420–425.
- Okabe, N., Kyoyama, H. & Suzuki, M. (2001). *Acta Cryst.* **E57**, o764–o766.
- Palanisamy, V., Sanphui, P., Prakash, M. & Chernyshev, V. (2019). *Acta Cryst.* **C75**, 1102–1117.
- Parsons, S., Flack, H. D. & Wagner, T. (2013). *Acta Cryst.* **B69**, 249–259.
- Perdew, J. P., Burke, K. & Ernzerhof, M. (1996). *Phys. Rev. Lett.* **77**, 3865–3868.
- Perlovich, G. L. (2017). *CrystEngComm*, **19**, 2870–2883.
- Pickard, C. J. & Mauri, F. (2001). *Phys. Rev. B*, **63**, 245101.
- Putra, O. D., Umeda, D., Nugraha, I. P., Furuishi, T., Nagase, H., Fukuzawa, K., Uekusa, H. & Yonemochi, E. (2017). *CrystEngComm*, **19**, 2614–2622.
- Rao, D. M. & Reddy, P. K. (2005). International Patent WO 2005/035530 A1.
- Rao, D. M. & Reddy, P. K. (2008). United States Patent US 2008/0091011 A1.
- Rigaku Oxford Diffraction (2020). *CrysAlis PRO*. Rigaku Oxford Diffraction, Yarnton, England.
- Schultheiss, N. & Newman, A. (2009). *Cryst. Growth Des.* **9**, 2950–2967.
- Sheldrick, G. M. (2008). *Acta Cryst.* **A64**, 112–122.
- Sheldrick, G. M. (2015). *Acta Cryst.* **C71**, 3–8.
- Skorupska, E., Jeziorna, A. & Potrzebowski, M. J. (2016). *J. Phys. Chem. C*, **120**, 13169–13180.
- Skorupska, E., Kaźmierski, S. & Potrzebowski, M. J. (2017). *Mol. Pharm.* **14**, 1800–1810.
- Skorupska, E., Paluch, P., Jeziorna, A. & Potrzebowski, M. J. (2015). *J. Phys. Chem. C*, **119**, 8652–8661.
- Stanton, M. K., Tufekcic, S., Morgan, C. & Bak, A. (2009). *Cryst. Growth Des.* **9**, 1344–1352.
- Sun, C. C. & Hou, H. (2008). *Cryst. Growth Des.* **8**, 1575–1579.
- Tanaka, R. & Hirayama, N. (2008). *Anal. Sci.* **X**, **24**, x43–x44.
- Taylor, C. R. & Day, G. M. (2018). *Cryst. Growth Des.* **18**, 892–904.
- Thakur, T. S., Kirchner, M. T., Bläser, D., Boese, R. & Desiraju, G. R. (2010). *CrystEngComm*, **12**, 2079–2085.
- Thalladi, V. R., Weiss, H.-C., Bläser, D., Boese, R., Nangia, A. & Desiraju, G. R. (1998). *J. Am. Chem. Soc.* **120**, 8702–8710.
- Tieger, E., Kiss, V., Pokol, G., Finta, Z., Dušek, M., Rohlíček, J., Skořepová, E. & Brázda, P. (2016). *CrystEngComm*, **18**, 3819–3831.
- Tröbs, L. & Emmerling, F. (2014). *Faraday Discuss.* **170**, 109–119.
- Vilas-Boas, S. M., Brandão, P., Martins, M. A. R., Silva, L. P., Schreiner, T. B., Fernandes, L., Ferreira, O. & Pinho, S. P. (2018). *J. Mol. Liq.* **272**, 1048–1057.
- Wielgus, E., Paluch, P., Frelek, J., Szczepek, W. J. & Potrzebowski, M. J. (2015). *J. Pharm. Sci.* **104**, 3883–3892.
- Yates, J. R., Pickard, C. J. & Mauri, F. (2007). *Phys. Rev. B*, **76**, 024401.
- Zheng, S., Han, Y., Zhang, J. & Li, W. (2017). *Fluid Phase Equilib.* **432**, 18–27.

Supporting Information

to

Structural variety of heterosynthons in linezolid cocrystals with modified thermal properties

Mehrnaz Khalaji,¹ Aneta Wróblewska,¹ Ewelina Wielgus,¹ Grzegorz Bujacz,² Marta K. Dudek,^{1,*} Marek J. Potrzebowski^{1,*}

¹*Centre of Molecular and Macromolecular Studies of Polish Academy of Sciences, Sienkiewicza 112, 90-363 Lodz, Poland*

²*Institute of Technical Biochemistry, Technical University of Lodz, Stefanowskiego 4/10, 90-924 Lodz, Poland.*

Item	page
Figures S1. ¹³ C CPMAS NMR spectra of 3,4-DHBA and its monohydrate before and after grinding with water.	2
Figure S2. ¹³ C CPMAS NMR spectra of coformers in their crystalline forms used for grinding with LIN.	3
Figure S3. Solution ¹ H NMR spectra in anhydrous acetone- <i>d</i> ₆ for the analyzed cocrystals.	4
Figure S4. PXRD diffractograms for the obtained cocrystals of LIN.	6
Figures S5-S9. DSC curves for pure coformers used to prepare cocrystals of LIN.	7
Figure S10. Calibration curves from MS measurements used for the calculations of water solubility of LIN.	10
Table S1. Numerical data from the MS measurements used to calculate water solubility of the analyzed cocrystals.	11
Table S2. Numerical data from the calculations of stabilization energies of the studied cocrystals.	12
Table S3. Experimental and theoretical ¹³ C chemical shifts for LIN form II and III.	13
Figure S11. Experimental ¹³ C chemical shifts vs. calculated shielding constants for LIN forms II and III.	13
Table S4. Experimental and theoretical ¹³ C chemical shifts for LIN cocrystals.	15
Figure S12. Experimental ¹³ C chemical shifts vs. calculated shielding constants for LIN cocrystals.	17
Table S5. Geometrical data for the observed hydrogen bonds	18
Table S6. A comparison of the torsion angle values for all conformations of LIN found in its crystal structures	19

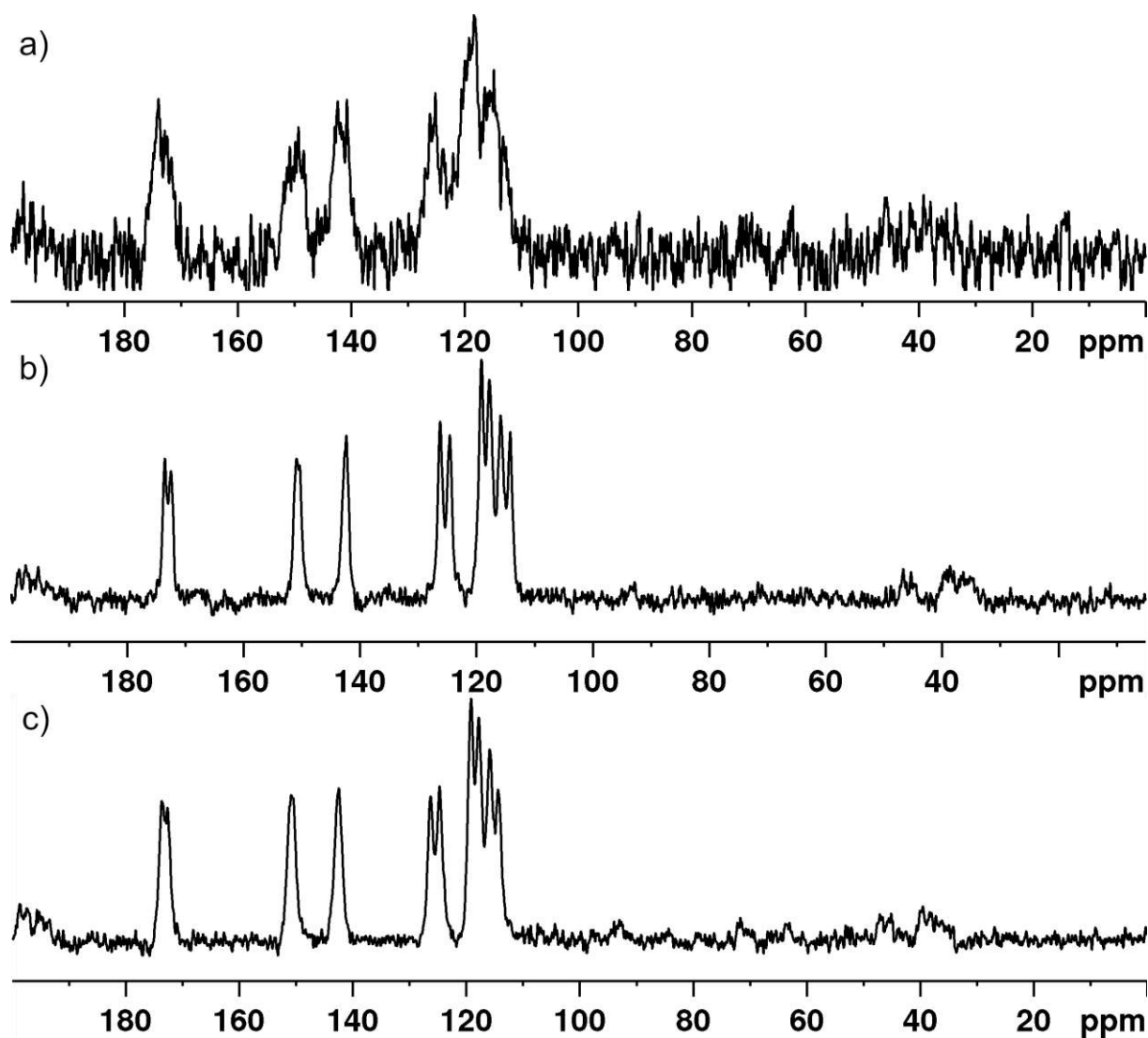


Figure S1. ^{13}C CPMAS spectra of 3,4-DHBA registered with a spinning speed of 8 kHz: (a) commercial, amorphous sample, (b) commercial sample recrystallized from water, corresponding to 3,4-DHBA monohydrate and (c) commercial sample ground for 1h with 100 μL of water.

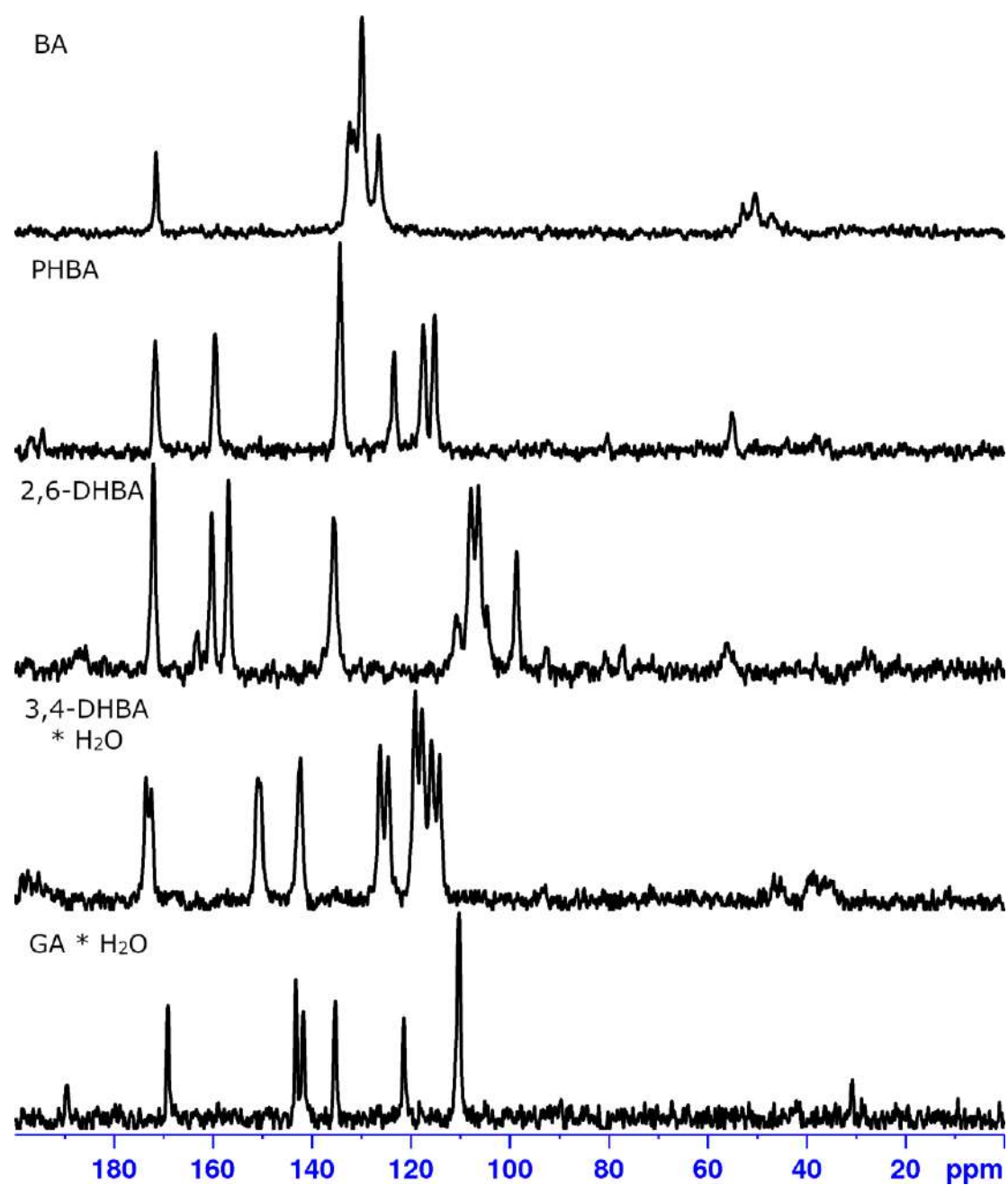
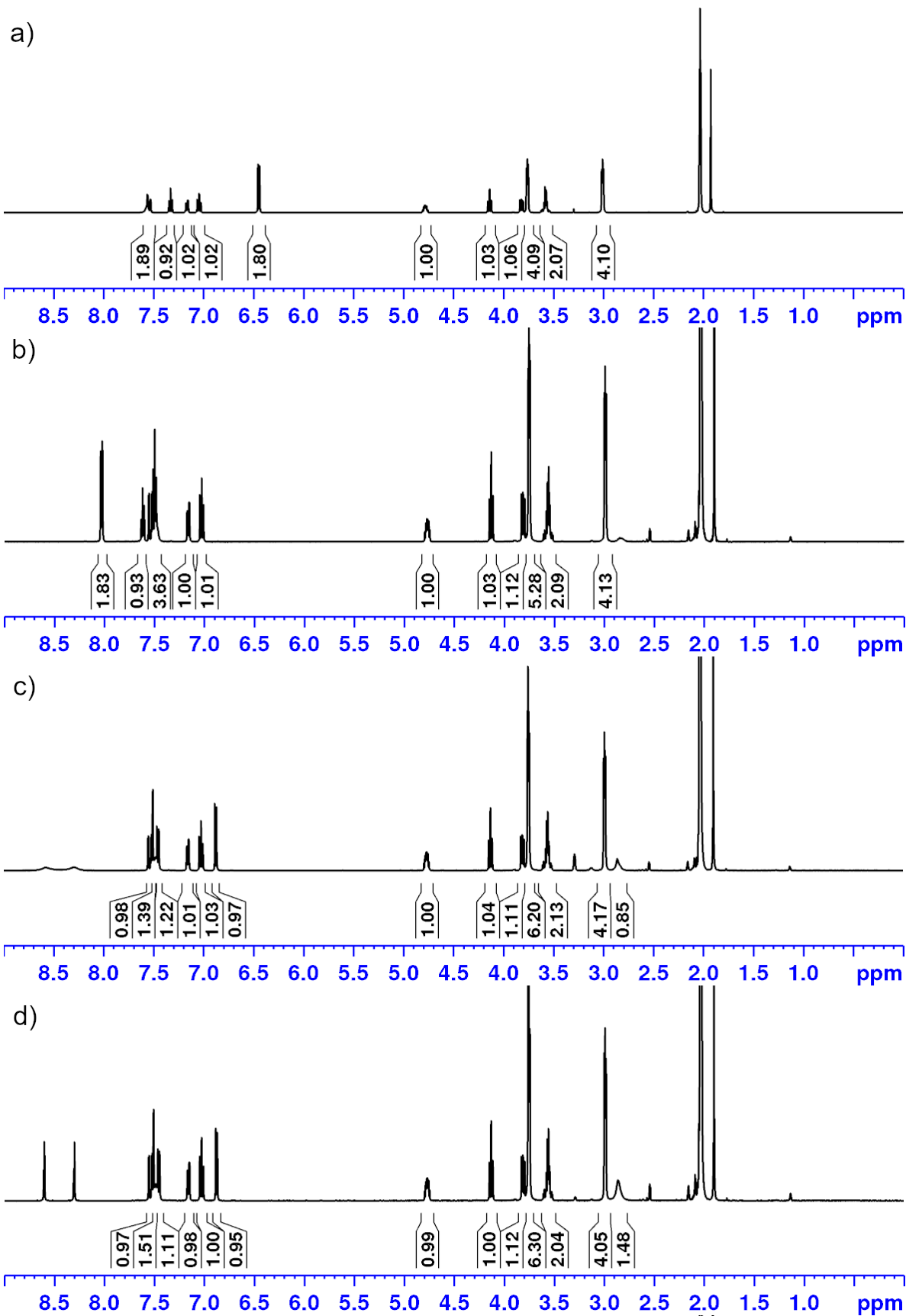


Figure S2. ^{13}C CPMAS spectra of coformers in their crystalline forms as used to obtained cocrystals with LIN.



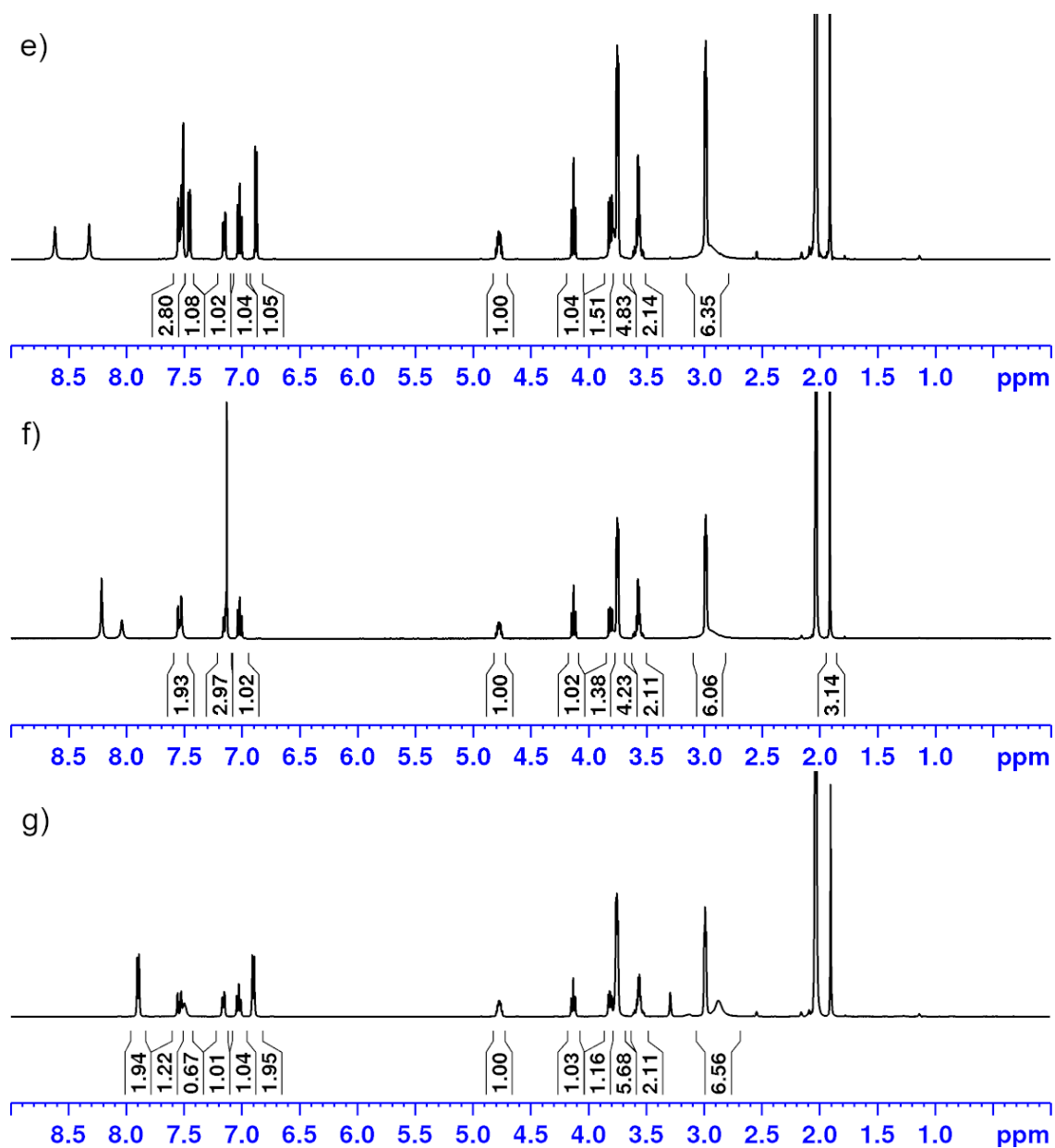


Figure S3. ^1H NMR spectra in anhydrous acetone- d_6 of cocrystals of LIN with 2,6-DHBA (a), BA (b), 3,4-DHBA (c, d, e), GA (f) and PHBA (g).

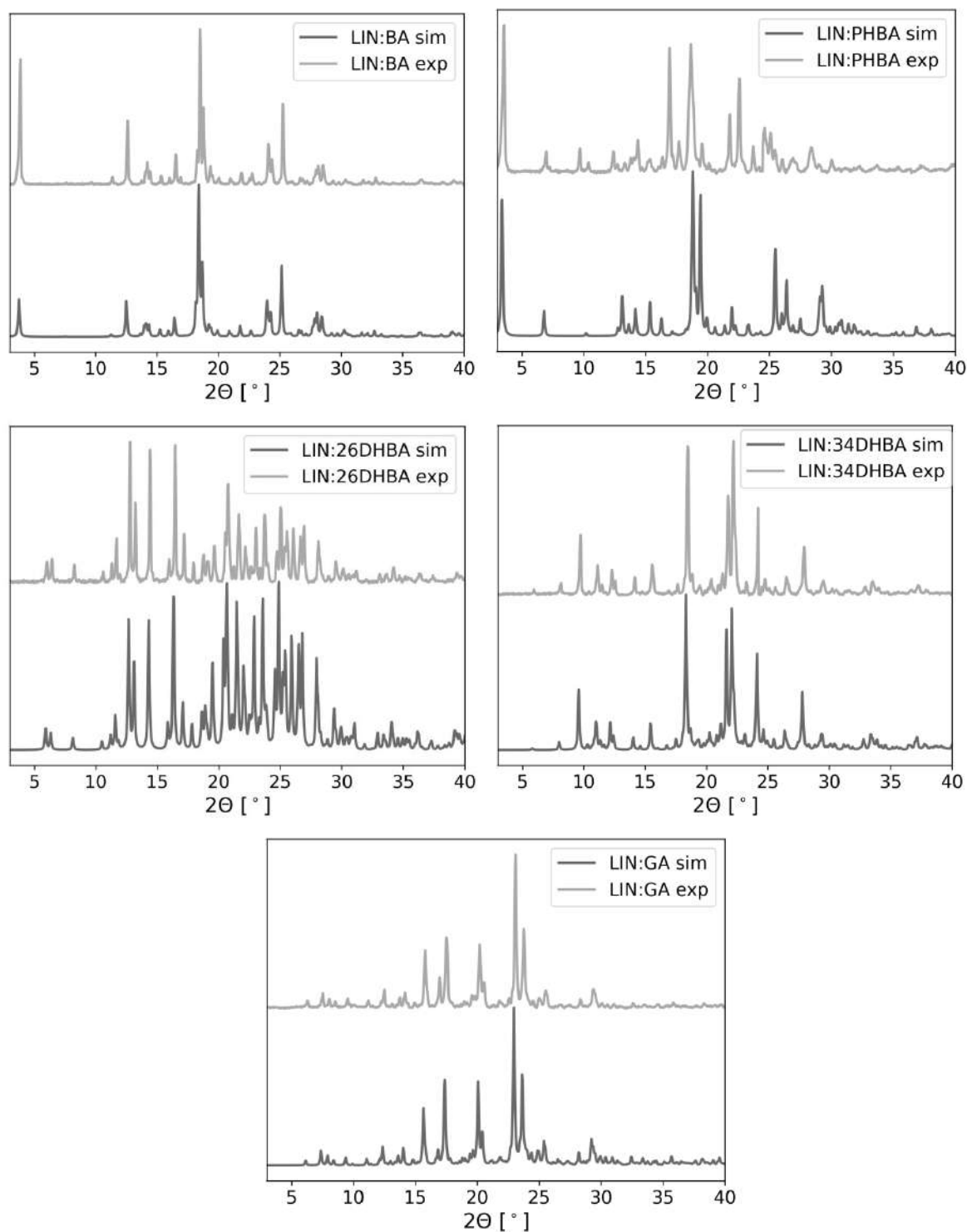


Figure S4. A comparison of the experimental powder X-Ray diffractograms for LIN:BA, LIN:PHBA:H₂O, LIN:2,6-DHBA, LIN:3,4-DHBA:H₂O and LIN:GA:H₂O samples obtained after mechanochemical grinding of LIN form II with appropriate coformers and simulated PXRD patterns for the crystallographic solutions from single crystal X-ray diffraction experiments.

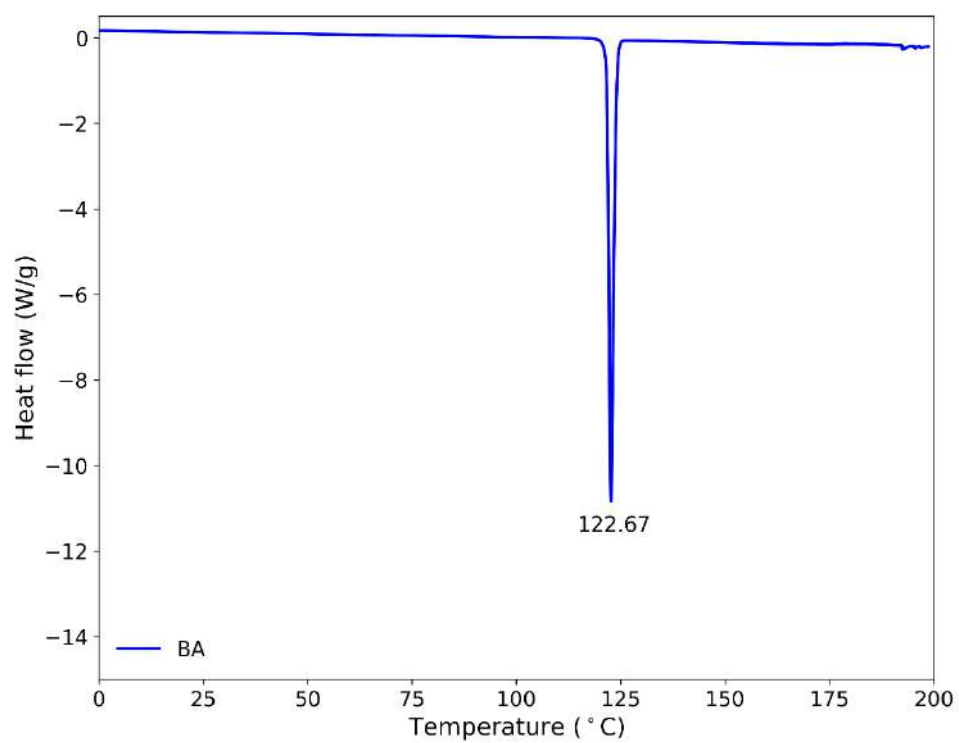


Figure S5. DSC curve for pure benzoic acid used for the mechanochemical preparation of LIN:BA cocrystal

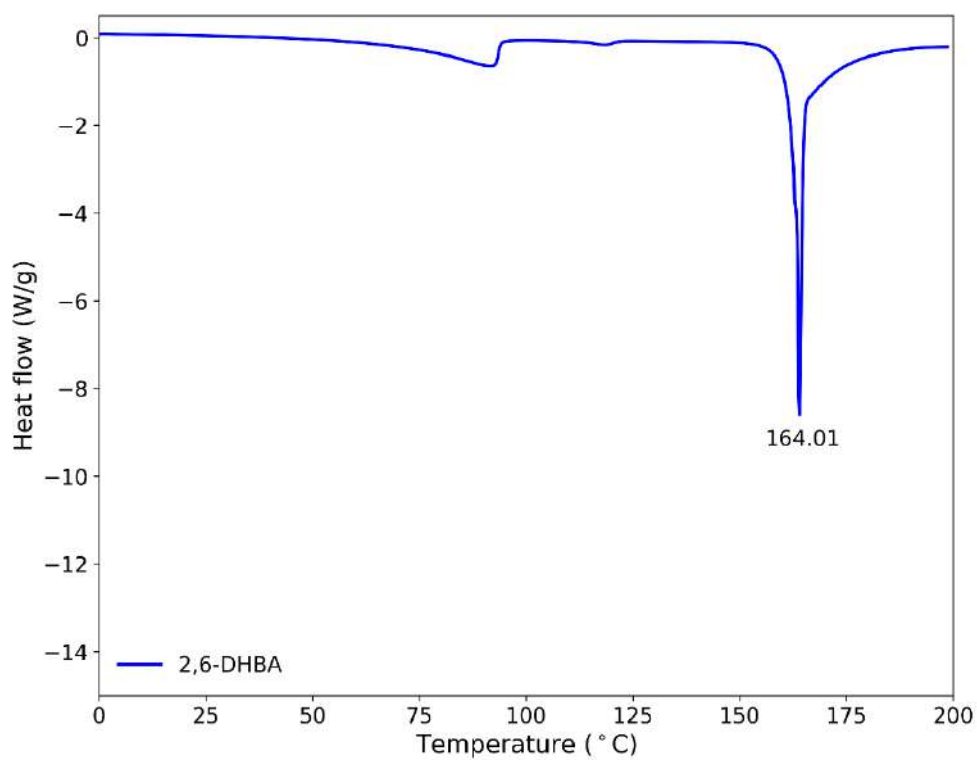


Figure S6. DSC curve for pure 2,6-dihydroxybenzoic acid used for the mechanochemical preparation of LIN:2,6-DHBA cocrystal

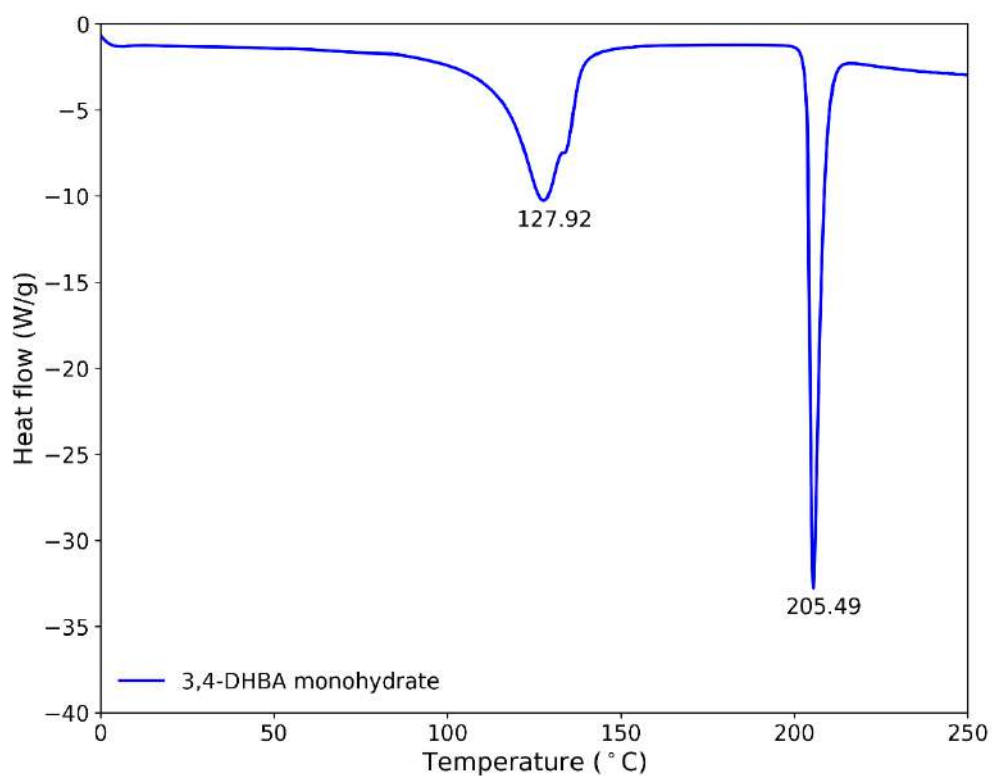


Figure S7. DSC curve for pure monohydrate of 3,4-dihydroxybenzoic acid used for the mechanochemical preparation of LIN:3,4-DHBA:H₂O cocrystal

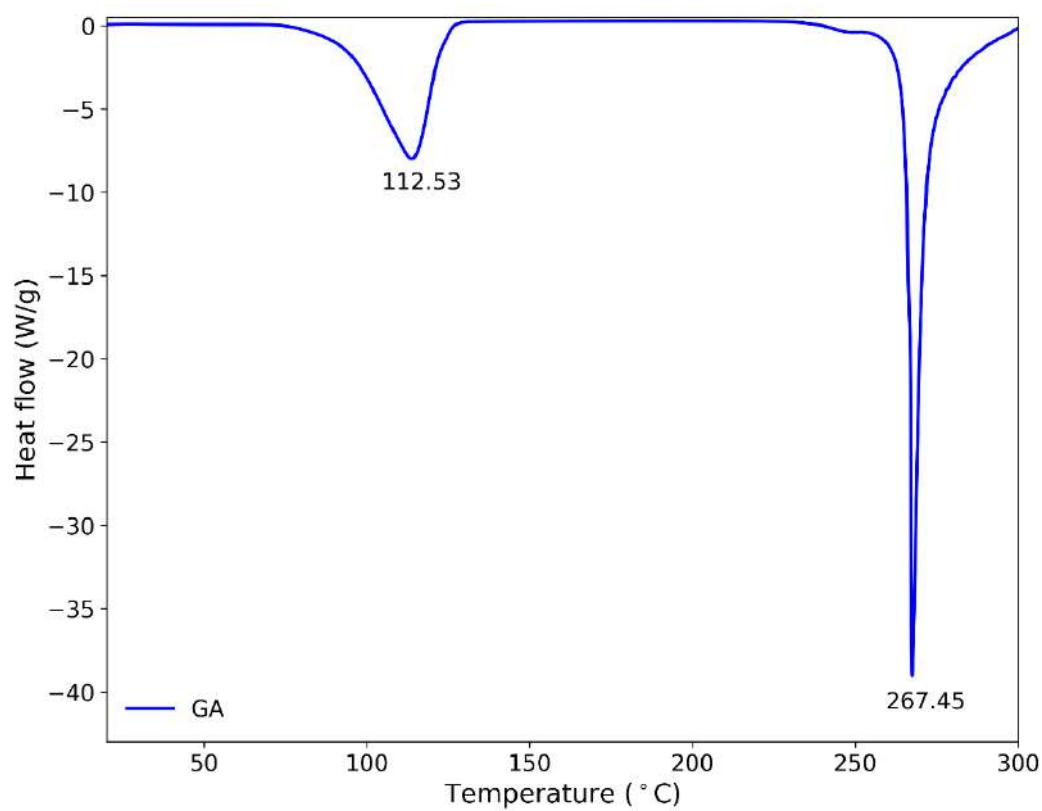


Figure S8. DSC curve for pure monohydrate of gallic acid used for the mechanochemical preparation of LIN:GA:H₂O cocrystal

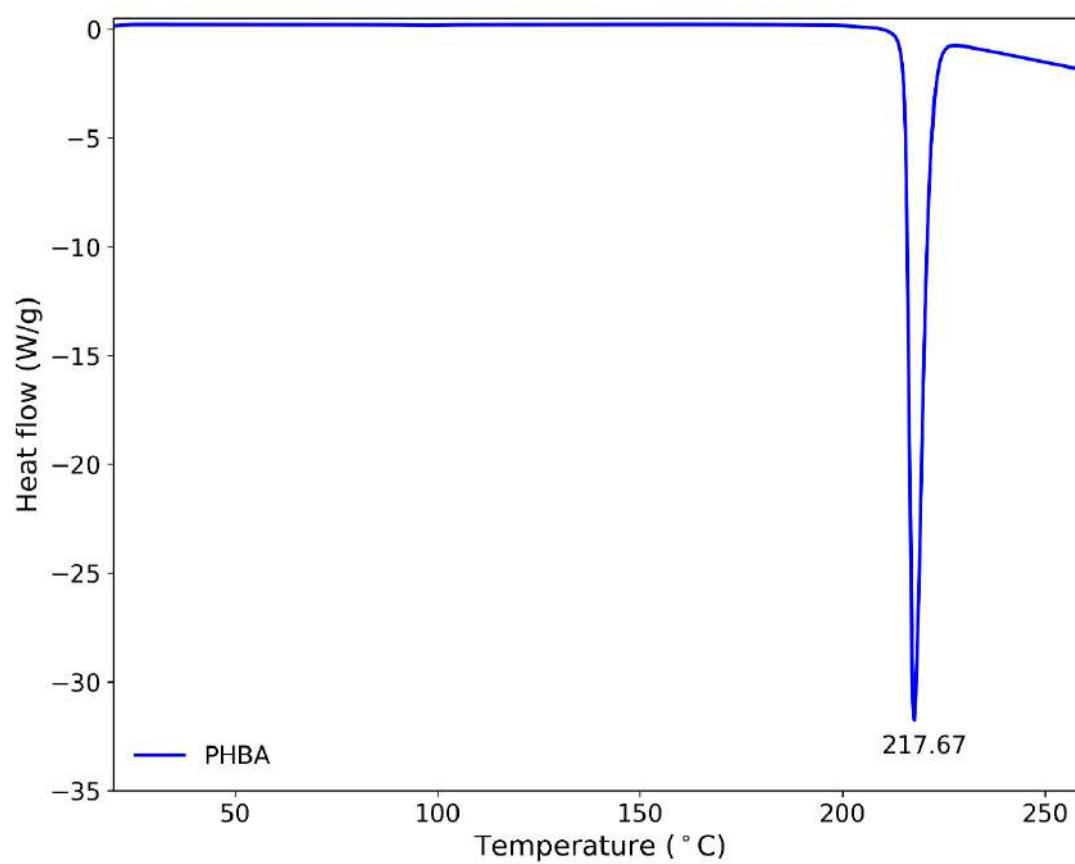


Figure S9. DSC curve for pure p-hydroxybenzoic acid used for the mechanochemical preparation of LIN:PHBA:H₂O cocrystal.

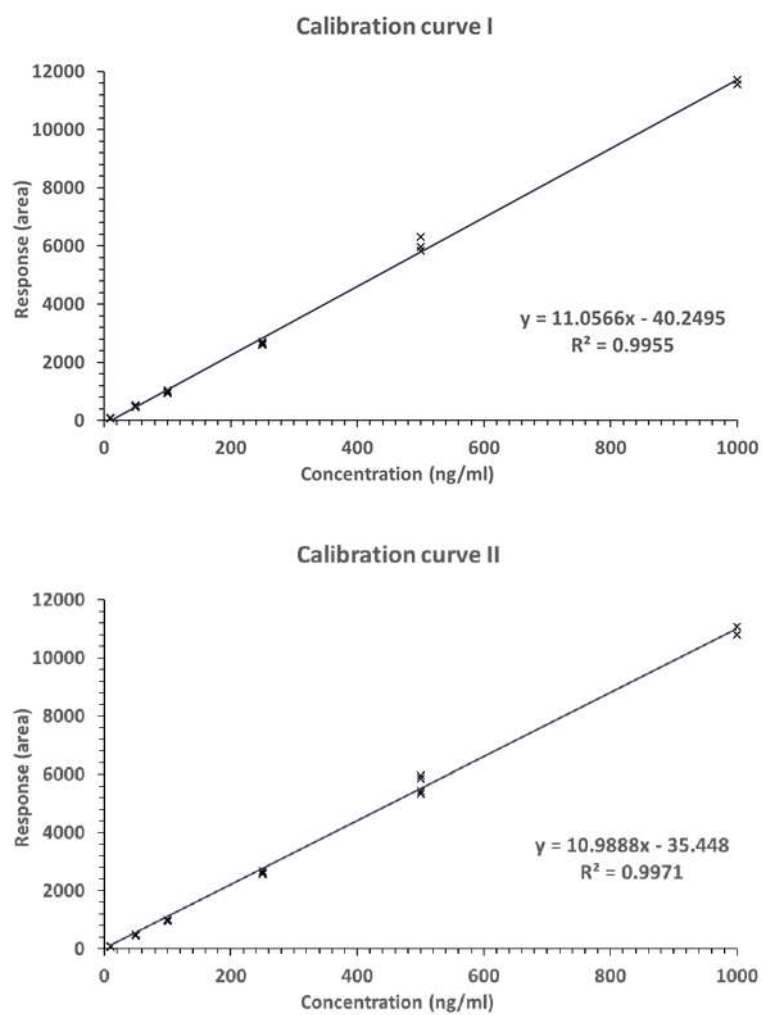


Figure S10. Calibration curves from MS measurements used for the calculations of water solubility of LIN.

Table S1. Numerical data used to calculate water solubility of the obtained cocrystals.

	time [h]	Concentration of LIN in each sample [ng/ml] ^a								Mean concentration [ng/ml]	Solubility [mg/ml]	RSD [%] ^b
LIN-II	12h	260.5	252.5	255.5	254.3	250.3	264.6	245.2	252.8	255.0	2.55	2.10
		259.7	251.1	256.0	254.8	250.8	265.7	252.9	253.3			
	24h	288.7	296.9	292.7	276.7	302.3	286.0	309.0	311.4	293.9	2.94	4.34
		290.7	286.9	275.9	274.5	302.4	286.5	310.8	310.3			
	36h	277.4	273.3	272.6	254.1	266.9	274.9	267.8	272.4	270.3	2.70	2.71
		278.7	275.2	273.6	255.0	264.0	275.3	267.8	275.0			
	48h	263.6	261.3	243.6	248.8	274.7	271.7	272.6	276.7	264.6	2.65	4.37
		265.5	260.3	244.0	253.5	274.3	272.3	274.0	276.2			
	12h	259.4	257.9	270.0	273.0	241.9	245.1	254.4	254.3	256.3	2.56	3.70
		259.8	258.3	263.4	269.3	244.9	245.6	250.3	252.9			
LIN:BA	24h	313.5	315.8	315.5	324.1	316.3	318.2	327.9	330.5	321.9	3.22	1.76
		320.5	326.1	315.9	324.5	321.0	322.4	327.5	330.8			
	36h	313.2	321.4	320.6	317.4	310.0	302.6	313.4	299.0	313.0	3.13	3.47
		333.2	328.1	317.7	321.7	310.4	303.0	294.5	301.7			
	48h	304.5	279.8	285.9	282.9	275.2	275.7	275.3	273.0	281.3	2.81	3.30
		301.2	281.7	282.5	281.8	275.6	276.1	275.7	273.4			
LIN:PHBA:H ₂ O	12h	176.9	177.3	170.4	172.0	174.8	174.0	170.3	170.0	173.3	1.73	1.71
		175.3	171.1	173.8	173.2							
	24h	205.0	205.8	208.2	203.1	197.1	198.0	194.4	201.0	201.1	2.01	2.09
		204.6	202.9	205.6	202.8	195.6	197.6	197.1	198.5			
	36h	221.5	213.2	216.4	223.0	215.0	208.0	227.4	219.6	217.8	2.18	2.72
		221.1	212.7	216.0	222.6	214.5	207.6	227.0	219.2			
	48h	198.1	198.8	195.4	192.4	190.2	187.7	179.4	185.0	190.3	1.90	3.43
		198.3	194.8	195.0	191.9	189.7	187.3	178.9	181.8			
LIN:2,6-DHBA	12h	248.4	260.8	262.2	266.6	266.0	269.4	259.9	262.9	262.2	2.62	2.35
		263.6	254.1	257.1	261.6	265.5	273.3	256.8	267.7			
	24h	257.7	269.2	268.2	277.5	281.1	274.3	278.4	277.2	273.8	2.74	2.31
		277.9	276.9	274.2	272.6							
	36h	280.0	284.8	278.0	280.6	282.3	284.5	278.5	282.3	280.5	2.80	0.97
		276.8	280.9	276.5	280.7							
	48h	286.7	293.2	294.3	298.4	313.3	306.8	289.0	297.6	298.0	2.98	2.46
		297.3	303.4	296.3	299.7							
LIN:3,4-DHBA:H ₂ O	12h	340.4	335.6	338.6	340.8	337.6	344.3	343.7	349.9	341.3	3.41	1.11
		341.8	338.9	339.5	343.9							
	24h	415.6	413.3	416.4	418.1	420.9	426.7	435.1	409.6	419.9	4.20	1.97
		415.6	410.0	425.6	431.7							
	36h	349.7	352.0	358.6	348.2	342.4	359.7	338.9	346.2	350.8	3.51	2.46
		350.1	332.0	357.8	363.6	353.7	357.6					
	48h	337.0	330.1	329.5	324.6	325.0	333.7	320.5	326.5	332.7	3.33	1.75
		338.1	337.2	334.4	339.2	335.6	333.0	341.3	337.2			
LIN:GA:H ₂ O	12h	174.3	173.8	179.8	178.4	167.4	160.1	164.9	165.1	173.7	1.74	4.14
		179.8	179.3	185.5	184.1	172.7	170.4	172.8	170.3			
	24h	231.7	227.4	218.4	215.7	227.7	234.2	224.6	224.5	226.2	2.26	2.59
		224.1	227.9	225.4	222.6	235.1	235.9	220.4	222.8			
	36h	212.7	215.0	212.2	203.3	183.8	185.0	189.8	188.8	200.4	2.00	6.36
		219.5	209.0	211.8	213.4	188.0	187.0	192.2	194.9			
	48h	188.5	189.9	187.1	186.8	194.9	192.4	194.5	190.5	192.3	1.92	2.20
		191.6	193.0	201.1	197.5							

^a Concentration of linezolid in samples after dilution; ^b Relative Standard Deviation

Table S2. Numerical data from the calculations of stabilization energies of the studied cocrystals. N and n denote number of molecules in a crystallographic unit cell and number of molecules in a formula unit, respectively.

crystal structures	CCDC refcodes or deposition numbers	E^{total} (kJ/mol)	N	E^{total} / N (kJ/mol)	$E^{\text{coformer}} + E^{\text{LIN}} / n$
pure components	BA	BENZAC13	4	-200617.22	-394323.96
	PHBA	JOZZIH01	4	-242992.74	-292183.58 (max) -292184.74 (min)
	3,4-DHBA*H ₂ O	BIJDON03	4	-330881.33	-358458.22
	3,4-DHBA	WUYNUA	6	-285348.37	
	2,6-DHBA	LEZJAB01	4	-285350.37	-436690.53
	GA*H ₂ O	KONTIQ01	4	-373249.04	-320426.58
	LIN II	TIYQAU01	4	-588030.69	
					E^{stab} (kJ/ mol of molecules)
cocrystals	LIN:BA	1993998	4	-394324.01	-0.05
	LIN:PHBA:H ₂ O	1997194	12	-292191.51	-2.98 – -1.81
	LIN:3,4-DHBA:H ₂ O	1994000	21	-358465.34	-7.13
	LIN:2,6-DHBA	1994001	8	-436702.70	-12.17
	LIN:GA:H ₂ O	1993999	24	-320429.36	-2.78

Table S3. Experimental (δ_{exp}) and theoretical ^{13}C chemical shifts (δ_{calc}) and shielding constants (σ_{calc}) for LIN form II and III, together with the regression curve calculated after plotting δ_{exp} vs. σ_{calc} and RMSD values for (δ_{exp} and δ_{calc}) pairs.

LIN form II				LIN form III			
atom	δ_{exp} (ppm)	σ_{calc} (ppm)	δ_{calc} (ppm)	atom	δ_{exp} (ppm)	σ_{calc} (ppm)	δ_{calc} (ppm)
C1	23.75	149.87	22.37	C1A	21.44	152.52	18.78
C2	170.35	0.59	169.71	C2A	170.47	0.74	169.49
C3	43.63	128.27	43.69	C3A	42.95	128.26	42.87
C4	73.50	95.48	76.06	C4A	72.65	94.67	76.22
C5	48.59	122.89	49.00	C5A	47.81	122.19	48.89
C6	157.30	14.49	155.99	C6A	154.51	16.66	153.68
C7	134.13	38.04	132.75	C7A	133.28	38.43	132.06
C8	109.57	61.51	109.58	C8A	106.24	65.53	105.15
C9	157.30	9.84	160.58	C10A	136.00	33.85	136.61
C10	138.80	32.28	138.43	C11A	117.46	52.51	118.08
C11	119.93	51.55	119.41	C12A	113.86	55.27	115.34
C12	118.87	53.47	117.52	C1B	20.98	153.40	17.90
C13	52.52	122.71	49.18	C2B	170.94	-0.35	170.57
C14	67.01	104.9	66.76	C3B	42.85	128.69	42.44
C15	67.01	101.07	70.54	C4B	72.65	94.91	75.98
C16	52.52	118.64	53.20	C5B	47.81	122.09	48.99
				C6B	154.51	16.60	153.74
				C7B	133.28	38.04	132.45
				C8B	105.16	67.10	103.59
				C10B	136.00	34.03	136.43
				C11B	119.55	50.59	119.99
				C12B	112.93	56.75	113.87
regression curve		$\delta_{\text{calc}} = (\sigma_{\text{calc}} - 172.54) / -1.0132$				$\delta_{\text{calc}} = (\sigma_{\text{calc}} - 171.43) / -1.0071$	
RMSD		1.76				1.59	

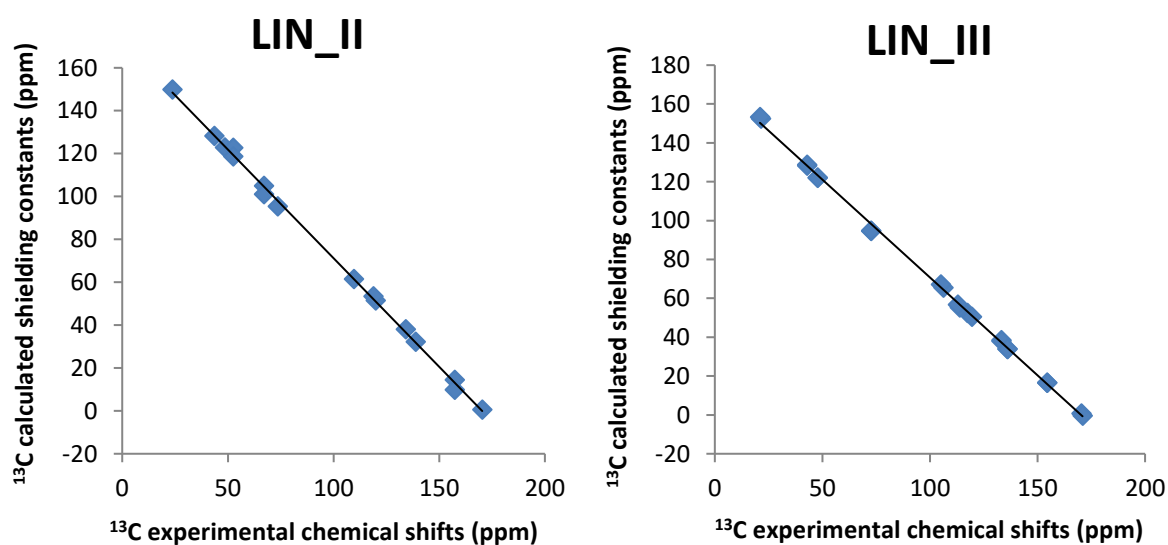


Figure S11. Experimental ^{13}C chemical shifts vs. calculated shielding constants for LIN forms II and III

Table S4. Experimental (δ_{exp}) and theoretical ^{13}C chemical shifts (δ_{calc}) and shielding constants (σ_{calc}) for the cocrystals of LIN, together with the regression curve calculated after plotting δ_{exp} vs. σ_{calc} and RMSD values for (δ_{exp} and δ_{calc}) pairs.

	LIN:BA			LIN:PHBA:H ₂ O			LIN:2,6-DHBA:H ₂ O		
atom	δ_{exp} (ppm)	σ_{calc} (ppm)	δ_{calc} (ppm)	δ_{exp} (ppm)	σ_{calc} (ppm)	δ_{calc} (ppm)	δ_{exp} (ppm)	σ_{calc} (ppm)	δ_{calc} (ppm)
C1	21.54	152.00	19.33	22.04	151.80	19.30	22.09	152.48	20.12
C2	175.37	-5.22	173.66	175.54	-5.76	174.08	174.93	-3.54	172.47
C3	42.89	127.57	43.31	43.04	127.52	43.15	46.76	124.87	47.09
C4	67.73	100.54	69.84	68.2	99.32	70.85	70.41	98.60	72.74
C5	47.41	123.32	47.48	47.11	123.83	46.78	48.88	122.36	49.54
C6	153.02	17.97	150.90	152.93	17.17	151.55	153.3	16.73	152.68
C7	133.1	36.65	132.56	135.09	33.61	135.40	130.27	41.48	128.51
C8	105.16	66.37	103.39	105.67	64.59	104.97	106.71	64.94	105.60
C9	156.3	10.10	158.62	156.5	9.52	159.07	155.65	10.62	158.65
C10	134.15	35.39	133.80	130.57	38.62	130.48	136.99	33.35	136.45
C11	118.35	51.74	117.75	118.8	50.08	119.22	119.42	51.33	118.89
C12	112.42	57.31	112.28	113.71	56.24	113.17	111.77	59.50	110.92
C13	53.27	117.01	53.68	51.26	118.32	52.19	52.22	121.62	50.26
C14	66.92	102.90	67.53	66.42	101.18	69.03	68.46	100.80	70.59
C15	68.71	98.80	71.55	66.42	100.91	69.29	68.46	100.41	70.97
C16	49.31	124.01	46.80	49.43	123.86	46.75	52.22	119.02	52.80
C1'	128.74	41.00	128.29	120.91	50.23	119.08	102.29	69.04	101.60
C2'	129.61	37.61	131.62	133.37	36.99	132.08	159.3	8.66	160.56
C3'	127.11	41.47	127.83	112.99	57.32	112.11	106.71	64.86	105.68
C4'	134.15	35.13	134.05	160.34	6.14	162.39	134.37	35.77	134.09
C5'	127.11	41.96	127.35	115.17	54.54	114.84	107.68	64.18	106.35
C6'	128.74	39.72	129.55	133.37	35.02	134.02	163.31	4.08	165.03
C7'	169.39	-0.77	169.29	169.21	0.05	168.37	171.19	-2.82	171.77
regression curve	$\delta_{\text{calc}} = (\sigma_{\text{calc}} - 171.69) / -1.0187$			$\delta_{\text{calc}} = (\sigma_{\text{calc}} - 171.45) / -1.0118$			$\delta_{\text{calc}} = (\sigma_{\text{calc}} - 173.09) / -1.0241$		
RMSD	1.42			1.62			1.53		

Table S4 continuation

LIN:3,4-DHBA:H ₂ O							LIN:GA:H ₂ O			
atom	δ_{exp} (ppm)	σ_{calc} (ppm)	δ_{calc} (ppm)	δ_{exp} (ppm)	σ_{calc} (ppm)	δ_{calc} (ppm)	atom	δ_{exp} (ppm)	σ_{calc} (ppm)	δ_{calc} (ppm)
C1A	23.99	149.31	23.28	21.36	152.56	19.30	C1C	21.73	151.17	20.67
C2A	173.44	-5.10	174.42	173.61	-2.29	171.55	C2C	173.61	-3.03	172.27
C3A	43.10	128.61	43.54	42.71	129.52	41.95	C3C	45.26	126.09	45.32
C4A	72.70	96.14	75.32	72.89	95.42	75.48	C4C	72.89	95.68	75.22
C5A	49.23	123.35	48.69	48.10	122.68	48.68	C5C	48.10	123.15	48.22
C6A	152.89	18.27	151.55	154.33	16.94	152.64	C6C	154.67	16.42	153.15
C7A	133.74	37.44	132.78	132.66	37.90	132.03	C7C	132.66	39.28	130.68
C8A	104.00	67.87	103.00	108.49	62.40	107.94	C8C	108.49	62.69	107.66
C9A	155.56	9.98	159.66	156.27	10.78	158.70	C9C	156.27	10.80	158.68
C10A	133.91	36.41	133.79	135.84	35.34	134.55	C10C	136.10	34.05	135.82
C11A	117.97	52.33	118.21	118.48	52.59	117.59	C11C	115.88	54.36	115.85
C12A	110.35	59.92	110.78	111.19	58.73	111.55	C12C	111.19	59.07	111.22
C13A	51.17	121.25	50.74	54.33	118.28	53.00	C13C	54.60	117.86	53.42
C14A	66.81	102.88	68.73	67.23	102.11	68.90	C14C	66.91	102.62	68.40
C15A	67.08	101.25	70.32	66.91	102.35	68.67	C15C	67.23	101.99	69.02
C16A	46.39	126.88	45.23	48.10	124.55	46.84	C16C	48.10	124.27	47.11
C1'A	122.17	47.94	122.50	118.29	52.80	117.38	C1'C	118.49	52.46	117.72
C2'A	115.61	55.16	115.44	110.50	60.66	109.65	C2'C	110.50	60.13	110.18
C3'A	143.76	23.54	146.39	145.79	21.80	147.86	C3'C	145.42	21.91	147.75
C4'A	153.18	16.16	153.61	139.04	27.87	141.89	C4'C	139.04	28.13	141.64
C5'A	116.55	52.56	117.98	145.24	22.52	147.15	C5'C	145.42	21.94	147.72
C6'A	127.02	42.64	127.69	107.96	64.04	106.33	C6'C	108.22	63.02	107.33
C7'A	173.72	-5.21	174.53	176.61	-5.04	174.25	C7'C	176.61	-4.79	174.00
C1B	23.20	150.60	22.01	21.73	151.41	20.43	C1D	21.73	151.60	20.24
C2B	177.44	-6.81	176.10	177.09	-6.48	175.67	C2D	173.61	-3.08	172.32
C3B	44.10	127.52	44.61	44.21	127.38	44.06	C3D	44.21	127.56	43.88
C4B	72.70	96.33	75.14	73.29	94.77	76.12	C4D	72.89	95.43	75.47
C5B	47.50	124.22	47.84	48.10	124.83	46.56	C5D	48.10	123.20	48.17
C6B	151.70	20.59	149.28	154.67	16.66	152.92	C6D	154.33	17.04	152.54
C7B	132.24	39.27	130.99	132.66	38.95	131.00	C7D	132.66	38.47	131.47
C8B	104.53	66.78	104.06	108.22	63.59	106.77	C8D	107.42	64.85	105.54
C9B	155.56	10.68	158.98	156.27	9.92	159.54	C9D	156.27	10.05	159.41
C10B	134.16	35.89	134.30	136.10	34.15	135.72	C10D	136.10	34.25	135.62
C11B	116.02	53.61	116.95	115.88	54.36	115.85	C11D	118.49	52.01	118.16
C12B	111.19	59.69	111.00	111.19	58.83	111.45	C12D	111.19	58.77	111.51
C13B	50.64	123.56	48.48	54.60	117.68	53.59	C13D	54.60	117.25	54.02
C14B	66.81	102.97	68.64	66.12	103.50	67.54	C14D	67.59	101.20	69.80
C15B	67.08	102.06	69.53	67.59	100.99	70.00	C15D	66.91	102.57	68.45
C16B	47.50	126.36	45.74	48.10	124.26	47.12	C16D	48.10	123.72	47.66
C1'B	120.62	50.57	119.93	117.75	53.20	116.99	C1'D	118.29	52.82	117.36
C2'B	116.02	53.21	117.35	110.05	61.37	108.96	C2'D	110.50	60.18	110.13
C3'B	143.53	23.70	146.23	145.42	21.99	147.67	C3'D	145.24	22.39	147.28
C4'B	153.18	14.28	155.45	139.04	27.53	142.23	C4'D	139.04	28.15	141.62
C5'B	116.55	53.00	117.55	145.79	21.63	148.03	C5'D	145.24	22.95	146.73
C6'B	125.97	44.26	126.11	107.42	64.80	105.58	C6'D	107.96	64.04	106.33

C7'B	175.13	-5.29	174.61	176.87	-5.35	174.56	C7'D	176.87	-5.31	174.52
regression										
curve	$\delta_{\text{calc}} = (\sigma_{\text{calc}} - 173.09) / -1.0261$					$\delta_{\text{calc}} = (\sigma_{\text{calc}} - 172.19) / -1.0171$				
RMSD	1.61					1.65				

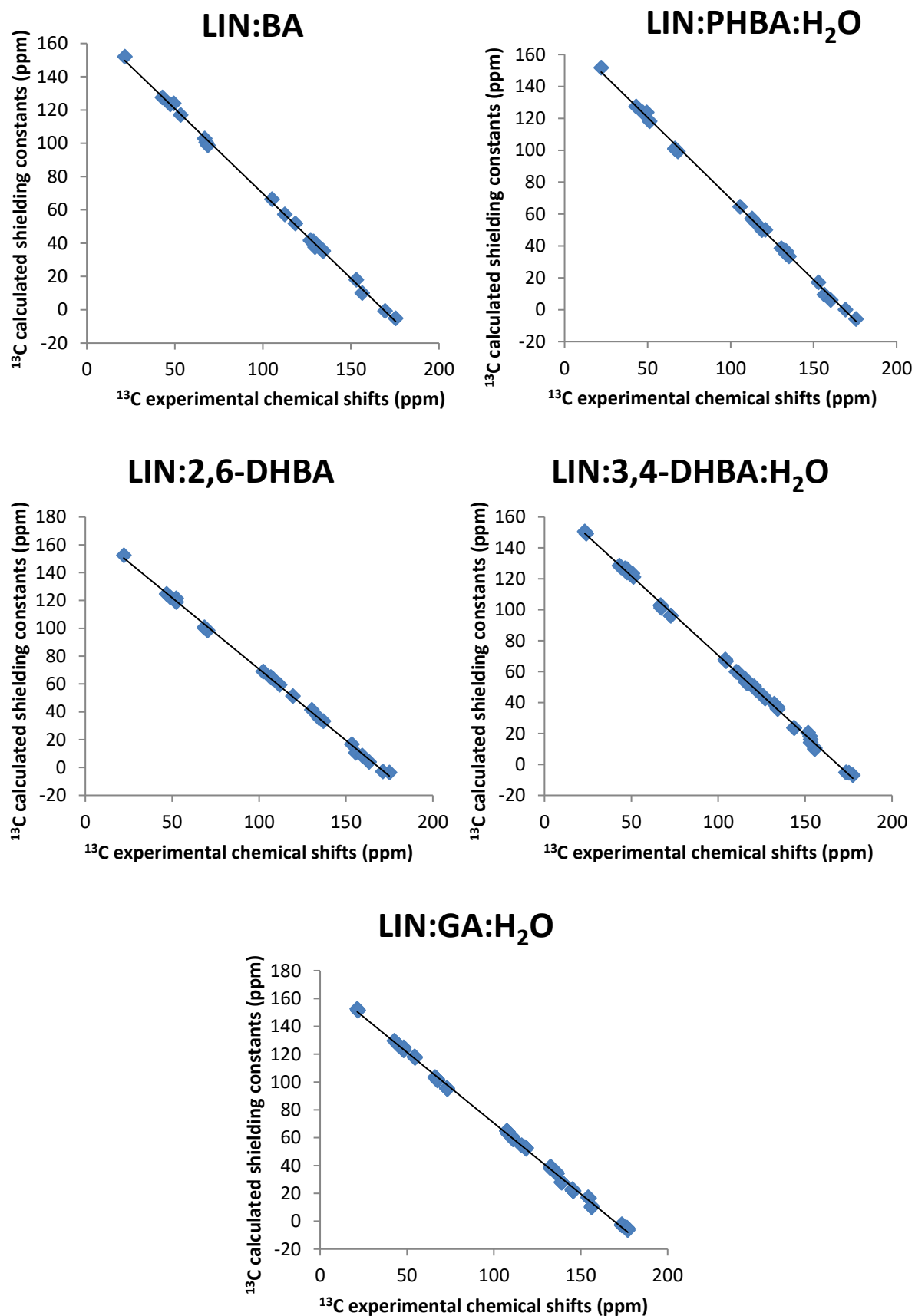


Figure S12. Experimental ^{13}C chemical shifts vs. calculated shielding constants for the cocrystals of LIN.

Table S5. D...A and D-H...A distances (in Å), as well as D-H...A angle values (in °) observed in the analyzed crystal structures of LIN.

Crystal structure	HB interaction	D...A distance	D-H...A distance	D-H...A angle
LIN_II	NH...O=C _{ring}	2.995	2.214	176.23
LIN_III	NH...O=C _{ring} (1)	2.970	2.068	167.46
	NH...O=C _{ring} (2)	2.972	2.040	149.12
LIN:BA	NH...O=C _{carboxylic}	2.834	2.039	153.27
	OH _{carboxylic} ...O=C _{amide}	2.618	1.808	168.74
LIN:PHBA:H ₂ O	NH...O=C _{carboxylic}	2.809	2.021	148.36
	OH _{carboxylic} ...O=C _{amide}	2.601	1.794	160.70
	OH _{phenol} ...OH _{water}	2.683	1.981	140.52
	OH _{water} ...O _{morph}	2.825	2.120	137.99
	OH _{water} ...N _{morph}	2.971	2.122	165.81
LIN:2,6-DHBA	NH...O=C _{ring}	2.922	2.064	175.07
	OH _{carboxylic} ...O=C _{amide}	2.564	1.745	175.41
	OH _{phenol} ...OH _{carboxylic}	2.608	1.902	143.55
	OH _{phenol} ...O=C _{carboxylic}	2.567	1.877	141.19
LIN:3,4-DHBA:H ₂ O	NH...O=C _{amide} (1)	3.092	2.279	157.74
	NH...O=C _{amide} (2)	3.056	2.235	159.83
	OH _{phenol} ...O=C _{amide} (1)	2.713	1.950	154.56
	OH _{phenol} ...O=C _{amide} (2)	2.689	1.911	158.13
	OH _{phenol} ...O _{morph} (1)	2.684	1.915	155.80
	OH _{phenol} ...O _{morph} (2)	2.739	2.011	147.53
	OH _{carboxylic} ...O=C _{carboxylic} (1)	2.615	1.830	159.72
	OH _{carboxylic} ...O=C _{carboxylic} (2)	2.638	1.842	163.33
	OH _{water} ...O=C _{carboxylic}	2.905	2.075	165.01
	OH _{water} ...OH _{water}	2.915	2.117	155.95
	OH _{water} ...OH _{carboxylic}	3.198	2.546	134.37
LIN:GA:H ₂ O	NH...O=C _{ring} (1)	2.931	2.081	150.69
	NH...O=C _{ring} (2)	3.031	2.188	166.47
	NH...O=C _{ring} (3)	2.973	2.124	169.38
	NH...O=C _{ring} (4)	3.270	2.182	147.55
	OH _{phenol} ...O=C _{amide} (1)	2.728	2.031	142.61
	OH _{phenol} ...O=C _{amide} (2)	2.719	2.032	141.12
	OH _{phenol} ...O=C _{amide} (3)	2.793	2.095	142.86
	OH _{phenol} ...O=C _{amide} (4)	2.830	2.134	142.64
	OH _{phenol} ...O _{morph} (1)	2.765	1.962	166.30
	OH _{phenol} ...O _{morph} (2)	2.759	1.969	161.80
	OH _{phenol} ...O _{morph} (3)	2.699	1.882	173.97
	OH _{phenol} ...O _{morph} (4)	2.701	1.904	163.78
	OH _{water} ...O=C _{amide} (1)	2.763	1.940	162.73
	OH _{water} ...O=C _{amide} (2)	2.753	1.909	172.46
	OH _{water} ...O=C _{amide} (3)	2.787	1.956	165.52
	OH _{water} ...O=C _{amide} (3')	2.863	2.020	171.86
	OH _{water} ...O=C _{amide} (4)	2.823	1.975	174.09
	OH _{water} ...O=C _{amide} (4')	2.828	1.860	177.47
	OH _{carboxylic} ...O=C _{carboxylic} (1)	2.594	1.777	173.70
	OH _{carboxylic} ...O=C _{carboxylic} (2)	2.638	1.821	174.71
	OH _{carboxylic} ...O=C _{carboxylic} (3)	2.598	1.782	173.99
	OH _{carboxylic} ...O=C _{carboxylic} (4)	2.646	1.831	172.81
	OH _{phenol} ...OH _{water} (1)	2.749	2.000	151.62
	OH _{phenol} ...OH _{water} (2)	2.624	1.836	160.77
	OH _{phenol} ...OH _{water} (3)	2.617	1.840	157.79

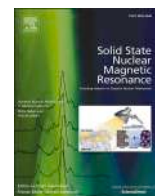
OH _{phenol} ...OH _{water} (4)	2.786	2.013	156.87
OH _{water} ...OH _{water} (1)	2.824	1.975	178.37
OH _{water} ...OH _{water} (2)	2.825	1.989	167.70

Table S6. A comparison of the torsion angle values (in °) for all conformations of LIN found in the analysed crystal structures.

	NH _{amide} -C3-C4-O	C6-N _{oxa} -C7-C8	C9-C10-N _{morph} -C13
LIN_II	-63.23	-134.16	-68.77
LIN_III mol A	-61.31	-5.51	-65.32
LIN_III mol B	-61.72	+20.91	+61.20
LIN:BA	-173.07	-20.06	+69.25
LIN:PHBA:H ₂ O	-172.95	-20.16	-65.34
LIN:2,6-DHBA	-65.18	+179.85	+57.05
LIN:3,4-DHBA:H ₂ O mol A	-63.30	+12.28	-67.27
LIN:3,4-DHBA:H ₂ O mol B	-70.79	-2.08	+60.42
LIN:GA:H ₂ O mol A	-66.39	-8.77	-68.66
LIN:GA:H ₂ O mol B	-60.01	+20.71	+63.48
LIN:GA:H ₂ O mol C	-67.43	-13.75	-63.97
LIN:GA:H ₂ O mol D	-60.27	+21.95	+66.97

T3:

Narrowing down the conformational space with solid-state NMR in crystal structure prediction of linezolid cocrystals, Khalaji, M., Paluch, P., Potrzebowski, M.J., Dudek, M.K., Solid State Nuclear Magnetic Resonance, 2022, 121, 101813



Narrowing down the conformational space with solid-state NMR in crystal structure prediction of linezolid cocrystals

Mehrnaz Khalaji, Piotr Paluch, Marek J. Potrzebowski, Marta K. Dudek^{*}

Centre of Molecular and Macromolecular Studies, Polish Academy of Sciences, Sienkiewicza 112, Lodz, 90-363, Poland

ARTICLE INFO

Keywords:

solid-State NMR
Pharmaceutical cocrystals
CSP calculations
NMR crystallography
Linezolid

ABSTRACT

Many solids crystallize as microcrystalline powders, thus precluding the application of single crystal X-Ray diffraction in structural elucidation. In such cases, a joint use of high-resolution solid-state NMR and crystal structure prediction (CSP) calculations can be successful. However, for molecules showing significant conformational freedom, the CSP-NMR protocol can meet serious obstacles, including ambiguities in NMR signal assignment and too wide conformational search space to be covered by computational methods in reasonable time. Here, we demonstrate a possible way of avoiding these obstacles and making as much use of the two methods as possible in difficult circumstances. In a simple case, our experiments led to crystal structure elucidation of a cocrystal of linezolid (LIN), a wide-range antibiotic, with 2,3-dihydroxybenzoic acid, while a significantly more challenging case of a cocrystal of LIN with 2,4-dihydroxybenzoic acid led to the identification of the most probable conformations of LIN inside the crystal. Having four rotatable bonds, some of which can assume many discreet values, LIN molecule poses a challenge in establishing its conformation in a solid phase. In our work, a set of 27 conformations were used in CSP calculations to yield model crystal structures to be examined against experimental solid-state NMR data, leading to a reliable identification of the most probable molecular arrangements.

1. Introduction

Crystal Structure Prediction (CSP) is one of the most alluring concepts in modern computational chemistry, due to a promise of being able to predict *a priori* (without any experimental knowledge) how a given molecule will crystallize and which crystal forms are the most plausible ones [1–3]. Due to an excellent progress made in this area over the period of the last 30 years, we are currently able to conduct reliable predictions for fairly large and complex systems, including large organic cages [4], pharmaceutical-like molecules [5,6], and multi-component systems [7–10]. Despite these successes, CSP still has its own weak spots, especially when dealing with flexible molecules, due to a very large search space that has to be accounted for in a successful prediction [11,12]. This is crucial especially when dealing with a system in which molecule(s) building it can assume numerous conformations. In cocrystals, by definition composed of at least two components, this is even more severe. In rigid CSP searches, *i.e.* the ones that consider rigid molecules at the stage of crystal structure generation, each combination of each conformation of each of the components of a cocrystal has to be

considered independently, which for highly flexible molecules can quickly become unfeasible.

In the context of using CSP in crystal structure determination, these challenges can be mitigated by experimental techniques, which can narrow down the search space. To that purpose, mainly solid-state NMR and powder X-ray diffraction (PXRD) techniques have been used, as a part of the so-called NMR crystallography approach [13–15]. In its most classical version, this approach consists of advanced solid-state NMR and diffraction-based experiments, combined with quantum-mechanical calculations to build, refine and/or validate the best structural model corresponding to the experimental data. Each of the three methods involved serves a different purpose. PXRD primarily delivers information on the long-range order present in the analyzed solid (unit cell parameters, crystal system, space group), while solid-state NMR data are more sensitive to a local environment of given nuclei, and therefore can be a source of data on the number of molecules present in an asymmetric part of the crystallographic unit cell, molecular conformation present in a crystal, local disorder, as well as atom-atom proximity arising from intermolecular interactions [16–18]. Together, these experimental data

^{*} Corresponding author.

E-mail address: mdudek@cbmm.lodz.pl (M.K. Dudek).

<https://doi.org/10.1016/j.ssnmr.2022.101813>

Received 30 April 2022; Received in revised form 28 July 2022; Accepted 28 July 2022

Available online 8 August 2022

0926-2040/© 2022 The Authors. Published by Elsevier Inc. This is an open access article under the CC BY-NC-ND license (<http://creativecommons.org/licenses/by-nc-nd/4.0/>).

can be used to build a structural model which then can be refined by computational methods and validated against the experiment. However, in many cases a number of ambiguities in the interpretation of the experimental data may arise, for example because of the overlap of NMR signals or low crystallinity of a sample. As a result, the extracted constraints are not conclusive enough to build a reliable structural model. Then, CSP calculations are especially valuable, as in principle they can deliver structural models regardless of the experimental data. In this sense, the experimental part of NMR crystallography and CSP calculations complement each other and remedy each others weaknesses.

In our previous work we have shown the benefits of CSP-NMR protocol in crystal structure determination of two polymorphs of relatively simple molecule, furazidin. Despite having only three rotatable bonds, furazidin proved to be a challenge in terms of establishing the crystal structure of its $Z' = 2$ polymorph, and required using both CSP calculations and experimental techniques (solid-state NMR and PXRD) [19]. Similarly, solid-state NMR data were used to indicate a correct tautomer of mebendazole present in each of its three polymorphic forms, leading to significant saving in computational time and enabling successful prediction of all three polymorphs [20]. Recently, also Hofstetter et al. [21] have demonstrated a smart way of exploiting structural constraints extracted from solid-state NMR HETCOR experiments in order to eliminate those conformations of ampicillin, which were not in agreement with the observed correlation signals. This elimination, however, was based on a lack, rather than a presence of the ^1H - ^{13}C correlation cross-peaks. This is because in the case of molecular crystals it is impossible to differentiate between inter- and intramolecular interactions in the NMR experiment, and the presence of certain correlation signals may arise from either of these, which inhibits the selection of a correct conformation. Instead, for some molecular conformations resulting in in-space proximities of otherwise distanced ^1H and ^{13}C pairs, the presence of correlation cross-peaks can justifiably be expected, while their lack indicates that a given conformation may be excluded from the pool of possible structures [21]. A concept of narrowing down the number of possible candidate crystal structures was also demonstrated by Brus et al., using the analysis of ^1H - ^1H double quantum - single quantum correlations [22] and ^1H - ^{15}N dipolar couplings [23]. Another way of indicating the most probable conformer inside an analyzed crystal in the case of a complex, multi-component system is based on the fact that NMR chemical shifts are the most sensitive to the local environment of a molecule and less so to the long range order of a crystal. Therefore, as has been shown in our recent work for methanol solvate-hydrate of catechin [24], it is possible to use the calculated NMR chemical shifts for the CSP-created crystal structures of a simple system, which is similar to the investigated one, to indicate the most likely molecular conformation present in the latter.

In this work, we extend our previous approach to two binary systems of an antibiotic, linezolid (LIN, Fig. 1a). We have shown that this molecule is prone to form cocrystals and cocrystal hydrates with dihydroxybenzoic acids [25,26], yet, some of these systems crystallized only in the form of microcrystalline powder, thus precluding the use of single crystal X-ray diffraction in structure determination. On the other hand, a full CSP search of such complex systems, comprising two different molecules each of which can assume numerous conformations, seems unfeasible. Here, we test to what extent solid-state NMR-derived data can help in crystal structure determination of two LIN cocrystals: with 2,3-dihydroxybenzoic acid (2,3-DHBA, Figs. 1b) and 2,4-dihydroxybenzoic acid (2,4-DHBA, Fig. 1c), and demonstrate the usefulness of the combined CSP-NMR approach. The two examined cases can be viewed as a straightforward one (LIN:2,3-DHBA), for which the experimental data indicated high degree of similarity of this structure with the one of known LIN:2,6-DHBA cocrystal, and a much more demanding one (LIN:2,4-DHBA), with no counterparts in any of the known crystal forms of LIN.

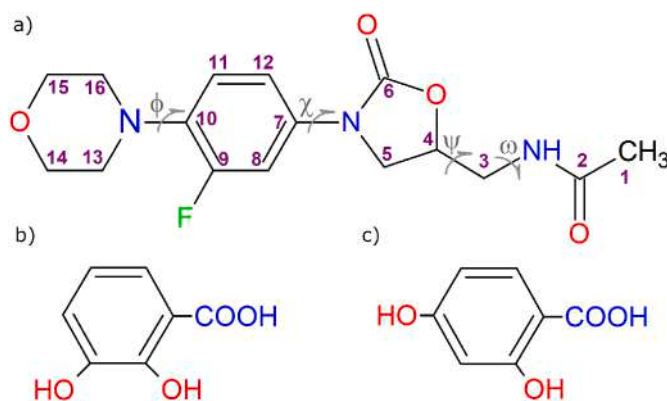


Fig. 1. (a) Molecular structure of LIN with carbon atom numbering, (b) molecular structure of 2,3-DHBA, (c) molecular structure of 2,4-DHBA. Grey arrows indicate rotatable bonds of LIN included in the conformational search, designated as φ , χ , ψ , and ω torsions.

2. Materials and methods

2.1. Materials

LIN was purchased from ABCR GmbH (Germany), 2,6-, 2,3- and 2,4-DHBA were purchased from Sigma Aldrich. LIN:2,3-DHBA, LIN:2,6-DHBA and LIN:2,4-DHBA cocrystals were obtained as described previously [26]. Briefly, 100 mg of LIN was placed in an agate jar together with 46 mg of a given DHBA (which corresponds to 1:1 molar ratio), one agate ball and 60–80 μL of methanol to create liquid-assisted grinding conditions. The samples were ground in a ball mill for 1 h, using 25 Hz frequency. The phase purity and identity of the formed cocrystals was confirmed by PXRD and ^{13}C solid-state NMR experiments.

2.2. Solid-state NMR experiments

All ^{13}C CPMAS NMR experiments were acquired with a Bruker Avance III 400 spectrometer, which operates at 100.90 and 400.13 MHz frequencies for ^{13}C and ^1H , respectively. In each case sample spinning speed was set to 8 kHz, cross-polarization contact time was 2.5 ms, and a relaxation delay at least 10 s.

VF-MAS (very fast magic angle spinning) experiments were carried out on a Bruker Avance III 600 spectrometer, operating at 43.35, 150.92, and 600.13 MHz for ^{14}N , ^{13}C and ^1H , respectively. Samples were spun at 62.5 kHz in 1.3 mm ZrO_2 rotors, with long term stability better than 10 Hz controlled by a MAS-II Bruker pneumatic unit. ^1H Bloch decay, ^1H - ^{13}C inverse detected HETCOR [27,28] and ^1H DQ experiments with Back-to-Back (BaBa) recoupling were carried out using a triple channel $^1\text{H}/^{13}\text{C}/^{15}\text{N}$ standard bore 1.3 mm Bruker probe head. Experiments involving ^{14}N (D-HMQC [29,30]) have been carried out using a dual channel 1.3 mm $^1\text{H}/^{14}\text{N}$ standard bore Bruker probe head. ^1H and ^{13}C chemical shifts were referenced with respect to a finely powdered solid adamantane (1.8 ppm for ^1H and 38.5 ppm for ^{13}C), while ^{14}N chemical shifts were referenced indirectly, using ^1H NMR frequency and x_{ref} referencing macro provided by Bruker. Temperature inside 1.3 mm rotor was estimated to be 50 $^\circ\text{C}$ by measuring ^{79}Br chemical shift at the same spinning speed, according to a paper published by Tycko [31]. All 2D correlations were carried out with a repetition rate equal to 1.3 ^1H T_1 relaxation time measured by saturation recovery experiment (^1H T_1 was found to be equal to 27 and 15 s, respectively, for LIN:2,3-DHBA, and LIN:2,4-DHBA cocrystals).

^1H - ^{13}C inverse detected HETCOR experiments were carried using a pulse sequence proposed by Pruski et al. [27,28]. For all samples a set of two spectra were collected with a different second contact time equal to

50 and 3000 μ s, respectively. In the first case (short second contact time), the correlation signals arising from carbon atoms directly connected to at least one proton were visible (^{13}C - ^1H pairs), while whenever longer second contact time was used, remote ^{13}C - ^1H correlations were visible as well. In both cases the first contact time was equal to 2000 μ s. Both cross-polarization steps were performed with a ramp-shaped pulse from 90 to 100% on the ^1H channel with a precisely optimized RF (radio-frequency) field at around 160 kHz (using ^{13}C , ^{15}N -labeled histidine hydrochloride). The RF field on the ^{13}C channel was kept constant during the CP steps and 90° pulses, with an RF equal to 100 kHz. Low power swept-frequency two-pulse phase modulation (SWf-TPPM) [32] was used on both channels with an RF equal to 10 kHz. The spectral window in an indirect ^{13}C dimension was set to 31.25 kHz (207 ppm) and between 270 and 313 complex points were recorded (depending on the required resolution to resolve all ^{13}C sites) giving $t_{1\text{max}}$ ranging from 8.64 to 10 ms. For a ^1H direct dimension the acquisition time was set to 10 ms with a spectral window equal to 62.5 kHz, and further data was truncated during processing to $3 \times T_2^*$ of the sharpest ^1H line, which was estimated from data processed with a not-truncated ^1H FID. No line broadening was used in the ^1H dimension, and 8 to 12 scans per t_1 -increment were coherently added depending on a signal-to-noise ratio.

^1H - ^1H double quantum - single quantum (DQ-SQ) Back-to-Back experiments were acquired with a spectral window in a DQ dimension equal to 31.25 kHz (rotor synchronized with a half of the spinning speed). 128 complex t_1 points were collected, resulting in indirect acquisition times equal to 4 ms.

^1H - ^{14}N D-HMQC experiments were performed with a SR421 recoupling sequence, with a precisely optimized ^1H RF on an unlabeled L-histidine hydrochloride sample. A recoupling time was set to 128 μ s, so that only directly bonded ^1H - ^{14}N pairs were visible. On a ^{14}N channel selective long pulses (SLP) [30,33,34] lasting 24 μ s (1.5 of a rotor period) were applied, with an RF equal to 42 kHz (2/3 of a spinning speed). A ^{14}N RF power was calibrated using NH_4Cl . A spectral window in an indirect ^{14}N dimension was set to 62.5 kHz (to achieve rotor synchronization) which was equal to 1441 ppm and 16 complex points were collected, giving an indirect acquisition time equal to 256 μ s. 256 scans were coherently added, and no apodization was applied in a ^{14}N indirect dimension. A ^1H direct dimension was processed in the same manner as in the case of ^1H - ^{13}C HETCOR experiments.

2.3. Powder X-ray diffraction

For PXRD measurements a Panalytical Empyrean diffractometer was used. The samples were analyzed in Bragg-Brentano reflection mode, using Cu-K α radiation ($\lambda = 1.5419 \text{ \AA}$), the 2θ range of $5\text{--}50^\circ$ and a 0.0131° step size. For the incident beam a fixed divergence slit of $1/8^\circ$ and a fixed mask of 10 mm were used.

2.4. Conformational search

Conformational search for 2,3- and 2,4-DHBA was performed by generating a set of 8 conformations, accounting for all possible combinations of the most plausible orientations of all OH groups. It was assumed that OH groups will all be in a plane of the aromatic ring, as the energetic penalty for distortion from this plane is usually high and in the majority of crystal forms of hydroxybenzoic acids such distortion is not observed. Each conformation was then geometry optimized in a gas phase using Gaussian16 software [35], B3LYP DFT functional with GD3-BJ dispersion correction and 6-311G(d,p) basis set.

In the case of LIN, its molecule has in principle four rotatable bonds, assuming that $\text{NH}\cdots\text{C}=\text{O}$ amide bond can be treated as planar, with only one preferred orientation. This assumption was later checked against the

NMR experimental data. Some of the rotatable bonds, marked in Fig. 1 with light-grey arrows, can be treated independently in the conformational search. In particular, the mutual orientation of morpholine and fluorophenyl rings (described by a φ torsion) can be examined independently of the mutual orientation of fluorophenyl and oxazolidone rings (χ torsion). On the other hand, two rotatable bonds in a side chain (described by ψ and ω torsions) should not be considered independently. With that in mind, three relaxed scan calculations were performed for LIN molecule, using Gaussian16 software and the level of theory specified above. A geometry-optimized molecule of LIN from the crystal structure of its form II was taken as a starting point. In the first two scans, each performed independently, φ or χ torsion was varied using 12 step of 30° . In the third scan, both ψ and ω were varied using 45° step and 8 steps, which resulted in 81 independent geometry optimizations for the given fixed values of the varied torsions.

The performed calculations indicate the most energetically favourable conformations of LIN. However, to look at the molecule of LIN from the perspective of its plausible conformation in a crystal, which does not necessarily coincides with any of the gas phase minimum, we also checked the incidence of typical arrangements of the functional groups of LIN in the Cambridge Structural Database (CSD). This can be easily done with a Mogul software for a user defined fragments of the analyzed molecule [36]. The results obtained from Mogul analysis, together with the ones from DFT conformational search were used at the further stages of conformers selection. All detailed results can be found in Supporting Information.

2.5. Crystal structure prediction calculations

In all CSP searches crystal structures were generated for the selected conformations of LIN and 2,3-DHBA or LIN and 2,4-DHBA, treating both molecules at the first stage of calculations as rigid entities. To that purpose Global Lattice Energy Explorer was used to generate trial crystal structures [37], which were then energy minimized with respect to intermolecular interactions employing DMACRYS software [38] and FIT potential [39] to model repulsion-dispersion interactions. The cut-off value for the van der Waals interactions used in these calculations was equal to 25 \AA , and the atom centered multipoles were generated by GDMA 2.2.11 software [40], from electron density as calculated by Gaussian16 [35] at B3LYP-D3BJ/6-311G(d,p) level of theory. For LIN:2,3-DHBA only two space groups were tested, namely $P2_12_12_1$ and $P2_1$, and the search was continued until 10000 successfully energy-minimized structures were obtained in each space group. These space groups were selected because of the observed structural similarity of the investigated structure to that of LIN:2,6-DHBA cocrystal (see section 3). In the case of LIN:2,4-DHBA four space groups in which chiral molecules can crystallize were tested, $P2_12_12_1$, $C2$, $P2_1$, and $P1$. These space groups were selected as the four most common space groups for organic chiral molecules, as they account for over 85% of crystal structures of pure enantiomers [41]. The search was continued until 5000 successfully energy-minimized structures were obtained in each tested space group and for each combination of the selected conformations. For both systems, all generated structures were examined for duplicates, by comparing their PXRD patterns, energy and density data, using an in-house Python script and the following cut-off values: 1.0 kJ/mol for energy, 0.05 g/cm 3 for density, and 0.1° for PXRD pattern similarity measured by the constrained dynamic time warping method.

2.6. DFT-D geometry optimization and NMR calculations

The selected low-energy structures of both systems generated in CSP searches, usually the ones found within 15–20 kJ/mol above the global minimum structure, were further geometry optimized with CASTEP19 code [42], this time allowing all atoms to relax and therefore, the conformation of components to change. In the first step only atomic positions were allowed to relax, in the second step, also unit cell

parameters were varied. The energy cut-off of 1000 eV and a k-points separation of 0.07^{-1} \AA were used, together with the PBE functional [43], and many-body dispersion-correction scheme (MBD) [44]. After successful geometry optimization NMR parameters were calculated under periodic boundary conditions using GIPAW approach [45] and the same level of theory as specified above. The calculated shielding constants (σ_{calc}) were compared with the experimental chemical shifts (δ_{exp}) and for each structure a linear regression curve was calculated. Subsequently, the calculated shielding constants were transformed to the chemical shifts (δ_{calc}) using the obtained equations according to a formula:

$$\delta_{\text{calc}} = \frac{(\sigma_{\text{calc}} - b)}{a} \quad (1)$$

where a and b are the slope and intercept, respectively, calculated from a given linear regression curve. The obtained δ_{calc} values were then used together with the δ_{exp} values to calculate root-mean-square deviation (RMSD) values (expressed in ppm) for each set of data. Table S5 (Supporting Information) shows a , b , and a correlation coefficient R^2 values obtained in each case, together with the corresponding RMSD values. For LIN:2,4-DHBA we also wanted to examine whether it suffice to calculate NMR parameters for structures subjected only to geometry optimization with a fixed unit cell (first step of CASTEP calculations). Usually, the first step of the calculations requires much shorter computational time and less CPU resources, so it could be advantageous to be able to check the agreement in terms of NMR data at this stage and re-optimized only the most promising structures. We refer to these results as the ones obtained for partially optimized crystal structures.

3. Results and discussion

3.1. A straightforward case of LIN:2,3-DHBA

3.1.1. Primary structural characteristic

One of the ways to confirm the formation of a cocrystal is through solid-state NMR measurements. In our case, ^{13}C CPMAS, ^1H DQ MAS with ^1H - ^1H Back-to-Back (BaBa) recoupling, and ^1H - ^{13}C HETCOR NMR spectra were recorded for a sample containing LIN and 2,3-DHBA after grinding in a ball mill for 1h in the presence of methanol. In the ^{13}C CPMAS spectrum recorded for the ball-milled sample the chemical shifts originating from LIN and 2,3-DHBA are different from those of the parent components and in agreement with those previously published for LIN:2,3-DHBA cocrystal [26]. In addition, in the 2D NMR spectra, the presence of the correlation signals originating from intermolecular interactions of LIN with 2,3-DHBA is a proof that both molecules are bound together in one crystal lattice, thus confirming the formation of a cocrystal. This conclusion is further corroborated by the results of DSC and TGA analysis, showing a lack of additional species (e.g. solvents) present in a system, as well as PXRD data (see Supporting Information). The 2D NMR correlation spectra were first used to assign ^{13}C and ^1H signals to particular nuclei of LIN and 2,3-DHBA, and then to identify intermolecular interactions present in the analyzed cocrystal. Fig. 2a features ^1H - ^{13}C *inv*HETCOR spectrum recorded with a relatively long contact time, allowing for the recognition of these interactions, as well as for the assignment of the resonances. For example, a correlation signal between C1 carbon atom of LIN resonating at 21.9 ppm with a proton signal at ca. 8.8 ppm, which further correlates with a carbonyl atom signal at 174.2 ppm, assignable to C2 carbon of LIN, allowed for a putative assignment of the 8.8 ppm ^1H resonance to NH group of LIN (each of the two correlation signals is marked with a red triangle in Fig. 2a). This assignment was further confirmed by ^1H - ^{14}N D-HMQC

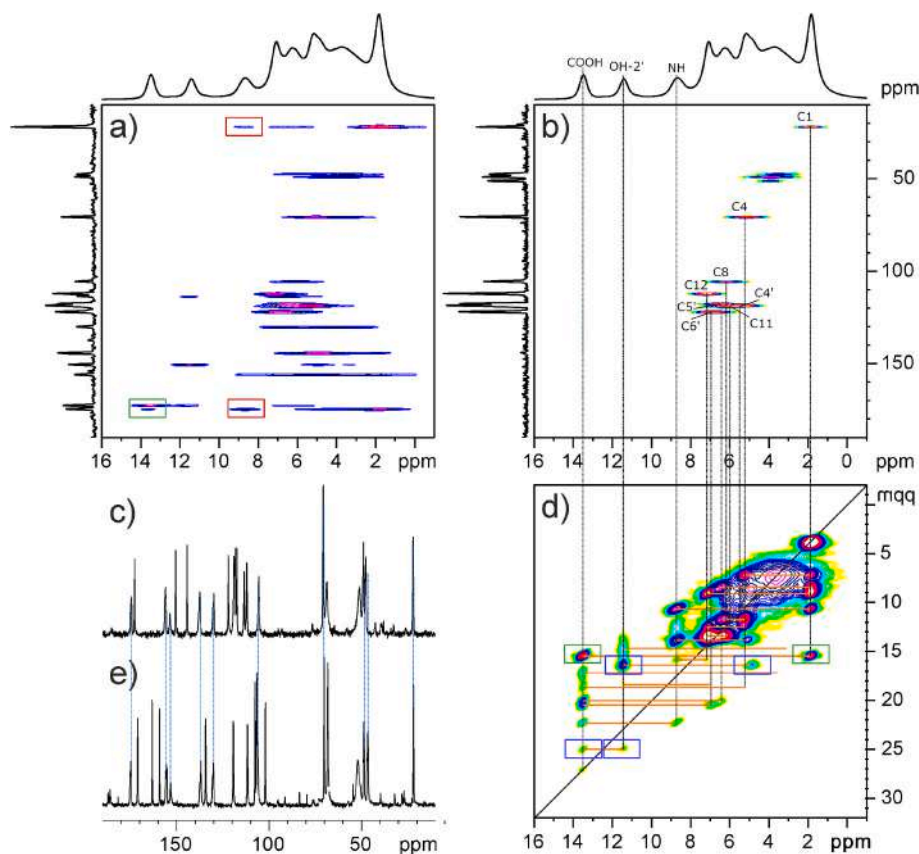


Fig. 2. (a) and (b) ^1H - ^{13}C *inv*HETCOR NMR spectrum recorded with a contact time of 3 ms (a) and 100 μs (b), and (d) ^1H DQ MAS with ^1H - ^1H Back-to-Back (BaBa) recoupling spectrum for LIN:2,3-DHBA cocrystal; (c) and (e) a comparison of the ^{13}C CPMAS NMR spectra recorded for LIN:2,3-DHBA and LIN:2,6-DHBA cocrystals. The 2D spectra were recorded with a sample spinning speed of 62.5 kHz; color rectangles mark some of the main correlation signals (see text for a detailed explanation). In 1D spectra the dotted light blue lines correspond to the resonances originating from LIN and indicate the similarity of chemical environment of LIN molecules in both crystals.

spectrum (see Supporting Information). Similarly, it is possible to recognize intermolecular interactions between LIN and 2,3-DHBA. For instance, a correlation signal between C2 carbon atom of LIN resonating at 174.2 ppm with a proton signal at ca. 13.60 ppm, which further correlates with a C7' atom of 2,3-DHBA signal at 172.5 ppm, confirmed the intermolecular interaction inside the cocrystal lattice (green rectangle in Fig. 2a).

Fig. 2b shows ^1H - ^{13}C *inv*HETCOR spectrum recorded with a short second contact time, resulting in the correlation signals originating only from directly bonded C–H pairs. All these pairs are assigned in the figure to the respective C–H sites of the molecules forming the cocrystal. Collating this spectrum together with a ^1H - ^1H SQ-DQ MAS spectrum with BaBa recoupling, shown in Fig. 2d, allows for recognizing further intermolecular and intramolecular contacts. In general, ^1H - ^1H SQ-DQ MAS spectrum with BaBa recoupling presents the dipolar interactions between hydrogen atoms that are close enough in space (i.e. separated by the distance of less than 3.5 Å) [46,47]. Here, an indirect dimension is a double-quantum axis, which means that a given ^1H signal is seen at the chemical shift value corresponding to the double of its normal chemical shift. As a result, greater separation of the correlation signals is possible in comparison to single quantum – single quantum experiments. An analysis of ^1H - ^1H dipolar correlations revealed the chemical shift of OH-3' proton to be 4.88 ppm (see blue rectangles marking correlation signals between this signal and the OH-2' signal at 11.55; none of these signals have their corresponding correlation arising from CH pair in the above HETCOR spectrum), which is a rather uncommon value for a hydrogen bonded OH group. This would suggest that this proton is not actually engaged in any strong hydrogen bond, probably only in an intramolecular hydrogen bond between OH-3' and an oxygen atom of OH-2' with an estimated length of ca. 2.2–2.5 Å (this estimation comes from conformational analysis of 2,3-DHBA). Contrarily, OH-2' and COOH protons, with chemical shifts of 11.55 and 13.60 ppm, respectively, seem to be forming strong hydrogen bond having lengths of less than 1.9 Å. Apart from that, the dipolar interactions between methyl hydrogen atoms of LIN resonating at 1.96 ppm with a COOH hydrogen of 2,3-DHBA at 13.60 ppm, which are highlighted by a green rectangle shows an intramolecular interaction between acid COOH proton and LIN methyl group, indicating these groups has to be close in space. This is also corroborated by a correlation signals between COOH and NH protons. Finally, a strong correlation signals between NH and CH_3 signals from LIN indicate that these groups are very close in space, thus confirming our assumption about the trans conformation of the LIN amide bond.

A comparison of the ^{13}C CPMAS NMR spectra recorded for LIN:2,3-DHBA and LIN:2,6-DHBA cocrystals with a known crystal structure [25] (Fig. 2c and e) indicates that in both cases chemical shifts originating from LIN are similar. The similarity is also apparent for the ^1H NMR spectra recorded under very fast MAS conditions for both samples (see Supporting Information). Since NMR parameters are more sensitive to a local chemical environment and less so to a long-range order, these NMR results suggest that in both crystals conformation of LIN is the same or at least very similar. In addition, it also seems that there is a similarity in the local environment of the components, as evidenced from very similar pattern of the correlation signals in ^1H - ^1H SQ-DQ spectra with BaBa recoupling of both systems (Supporting Information). Finally, a comparison of PXRD diffractograms for both cocrystals (Fig. 3) suggests that they may share the same crystal packing and have similar lattice parameters. All the above evidence indicate a possibility of building a structural model of LIN:2,3-DHBA directly from LIN:2,6-DHBA cocrystal, or at least using the same conformation of LIN as the one present in the known crystal structure of LIN:2,6-DHBA.

3.1.2. Conformational search for 2,3-DHBA

As shown above, there is ample spectroscopic evidence that molecular conformation of LIN in its cocrystal with 2,3-DHBA is the same as

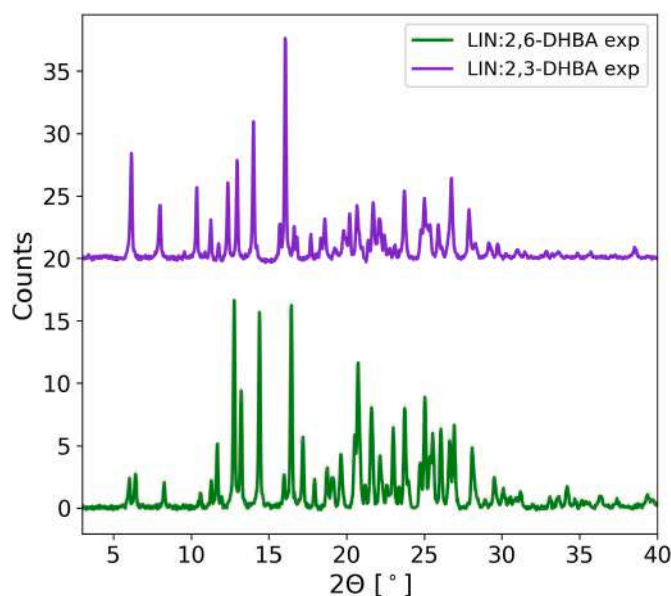


Fig. 3. A comparison of PXRD diffractograms recorded w for LIN:2,3-DHBA and LIN:2,6-DHBA cocrystals.

the one in LIN:2,6-DHBA cocrystal. This, however, cannot be said about the coformer, since the observed correlations can arise from both intra- and intermolecular interactions. Therefore, a conformational analysis of 2,3-DHBA was required. The performed conformational search yielded a set of eight different conformations of 2,3-DHBA, accounting for the most plausible orientations of the OH and COOH groups. Among these eight conformations, only one is significantly more stable than all the others, with the gas phase energy difference between this conformation and the next one equal to 15.91 kJ/mol. Hence, only the global gas phase minimum conformation of 2,3-DHBA was considered at further stages of crystal structure determination of LIN:2,3-DHBA system, with a possibility to include more conformations in the case of not finding a satisfactory enough structural model.

3.1.3. Crystal structure prediction calculations

To check whether our conformational guesses from the previous steps are correct for both molecules we took in the first approximation two most common chiral space groups (since LIN is a chiral molecule), $P2_12_12_1$ and $P2_1$ (number 19 and 4, respectively). This is a commonly used approach in CSP calculations to look only at those space groups which are the most frequent in the Cambridge Structural Database (CSD) and look for the crystal structure in other less common space groups only if no valid structural model can be found in the most common ones. In addition, LIN:2,6-DHBA cocrystal crystallizes in $P2_12_12_1$ space group, and from the PXRD data a strong similarity between this structure and LIN:2,3-DHBA may be suspected, which further confirms our first choice of the tested space groups.

To build a viable structural model of LIN:2,3-DHBA system two approaches were employed. First, we used LIN:2,6-DHBA crystal structure and simply replaced 2,6-DHBA with the gas phase global minimum conformation of 2,3-DHBA. The resulting structure, designated as model M – 1, was geometry optimized under periodic boundary conditions in CASTEP, followed by calculations of NMR parameters, which were then compared to the experimental NMR parameters obtained for LIN:2,3-DHBA. The second way of searching for viable structural model of LIN:2,3-DHBA comprised crystal structure prediction (CSP) calculations using molecular conformations as described above. In the obtained CSP energy landscape there were only three crystal structures found within the first 20 kJ/mol above the global minimum, and all of them were found in $P2_12_12_1$ space group (Fig. 4a). These structural models, named as CSP-1, CSP-2, CSP-3 (with numbers corresponding to their energy

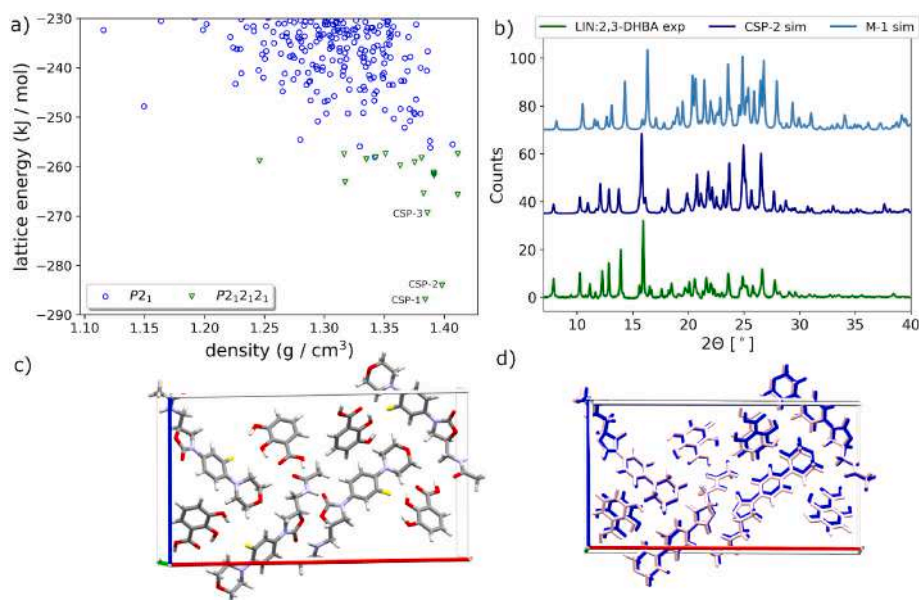


Fig. 4. (a) The low energy region of the CSP energy landscape for LIN:2,3-DHBA (b) A comparison of the experimental PXRD pattern for LIN:2,3-DHBA and simulated ones for CSP-2 and M – 1 models (c) The proposed crystal structure for LIN:2,3-DHBA, corresponding to CSP-2 model (d) A comparison of this structure with that of LIN:2,6-DHBA cocrystal.

rank according to the force field energy), were submitted to geometry optimization and NMR parameters calculations in CASTEP.

Table 1 shows ^{13}C and ^1H root-mean-square deviation (RMSD) values (expressed in ppm) for each set of data obtained after comparison of the δ_{calc} values with the δ_{exp} ones. For the sake of having a frame of reference, data obtained for the geometry optimized crystal structure of LIN:2,6-DHBA are also included. In the analysis of the obtained results, we first look mainly at the agreement in terms of ^1H chemical shifts as they are the most sensitive to molecular conformation in a crystal [48–50]. Note, that here we understand molecular conformation not so much as an overall shape of a molecule, but rather as a set of local changes to structural parameters, resulting in a change of a local chemical environment of the ^1H nuclei. One of the reason for ^1H being more sensitive to such changes is that they are the ones being, so to say, ‘at the surface’ of a molecule and hence, their local environment is the most affected by any local structural change. Among the analyzed structural models, the CSP-2 one shows the best agreement in terms of ^1H RMSD value, with the second best being M-1. In fact, both of these models are similar, with an RMSD in terms of atomic positions obtained from the comparison of 20-molecule clusters by Crystal Packing Similarity Tool [51] equal to 0.44 Å. Therefore, in our further analysis we focused our attention to these two models of LIN:2,3-DHBA. In terms of ^{13}C RMSD values, the CSP-2 model is also the best one among the considered structures. The obtained level of agreement in terms of ^1H and ^{13}C RMSD values is slightly worse than that observed for LIN:2,6-DHBA but is satisfactory enough to warrant designating CSP-2 model as the one corresponding to the experimental structure of

LIN:2,3-DHBA. None of the calculated ^1H and ^{13}C chemical shifts deviate significantly from their experimental counterparts, while similar ^1H and ^{13}C RMSD values are considered good enough in the literature [21,52]. This conclusion is further supported by the comparison of the experimental and simulated PXRD diffractograms (Fig. 4b). As can be seen, there is apparent similarity between the experimental PXRD data and those for CSP-2 model, as opposed to the next-best model, namely M – 1, which shows noticeably worse agreement in terms of PXRD. In the case of CSP-2 model the observed differences in PXRD data can be ascribed to different temperatures corresponding to both sets of data (295 K for experimental data and 0 K for the simulated ones). Note, that PXRD data are simulated precisely for a given unit cell, so there is no computational error associated with the simulated diffractograms. Hence, the observed differences can only be the result of temperature differences and inaccuracy in structure determination. In our case, the observed agreement for the CSP-2 model in terms of both solid-state NMR and PXRD data was considered satisfactory enough to prevent us from searching for LIN:2,3-DHBA structural model any further. Finally, it is worth to mention that this very model, after DFT-MBD* optimization showed the lowest energy of all considered models.

The proposed crystal structure of LIN:2,3-DHBA cocrystal is shown in Fig. 4c. Its analysis reveals that it satisfy all structural constraints (in terms of intermolecular interactions) extracted from 2D NMR spectra and that it is indeed isostructural with LIN:2,6-DHBA (see Fig. 4d). In particular, the overlay of molecular conformations of LIN from both cocrystals yields an RMSD for atomic positions equal to only 0.0729 Å. The presented results demonstrate the benefit of using CSP calculations even in the cases of apparent isostructurality of the analyzed crystal structure with the known one, as they allow for finding a better structural model than the one obtain by a simple modification of a known crystal structure.

3.2. A difficult case of LIN:2,4-DHBA

3.2.1. Primary structural characteristic

Fig. 5 shows ^{13}C CPMAS and ^1H MAS NMR spectra, as well as PXRD diffractogram for LIN:2,4-DHBA. The displayed PXRD pattern is visibly different from the ones of LIN:2,3-DHBA and LIN: 2,6-DHBA cocrystals, indicating that this crystal is not isostructural with the other two. Also,

Table 1

The ^1H and root-mean-square deviation (RMSD) values in ppm for LIN:2,6-DHBA, as well as considered structural models of LIN:2,3-DHBA. Note that because of inaccuracy of PBE functional in evaluating chemical shifts of fluorinated atoms [53], C–F carbons were excluded from the analysis.

Structural model	LIN:2,6-DHBA	M-1	CSP-1	CSP-2	CSP-3
^1H RMSD	0.294	0.409	0.412	0.384	0.867
^{13}C RMSD	1.89	1.85	2.17	1.91	2.20
^{13}C RMSD without C–F	1.52	1.63	1.83	1.61	1.77

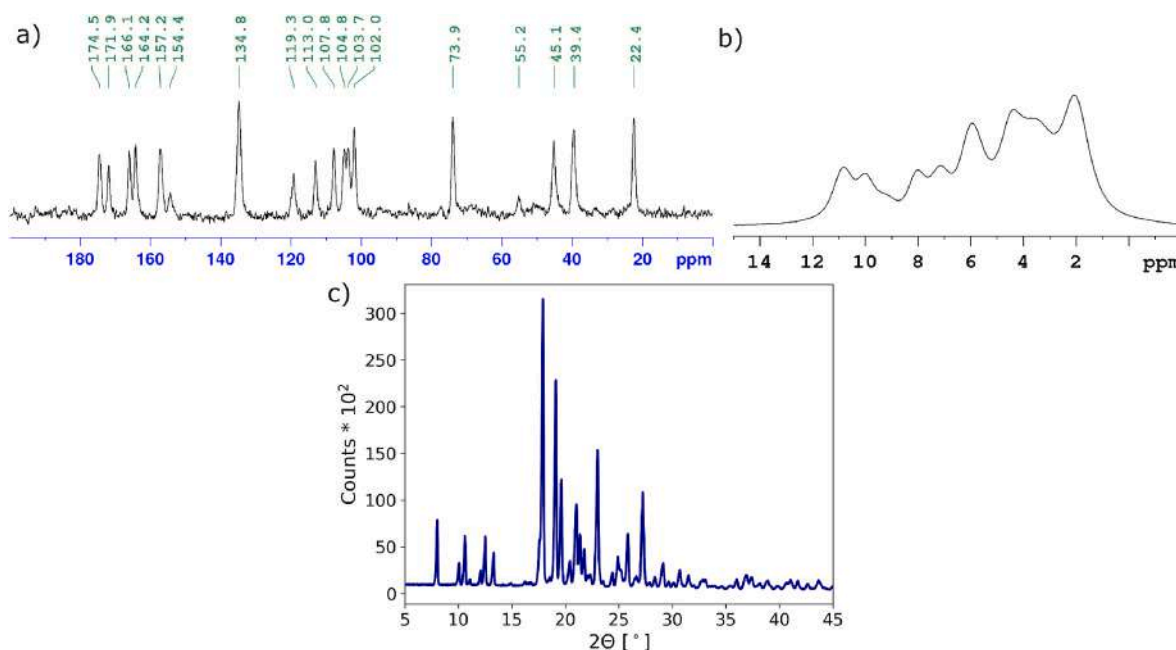


Fig. 5. (a) ^{13}C CPMAS and (b) ^1H MAS NMR spectra for LIN:2,4-DHBA cocrystal; proton spectrum was recorded with a sample spinning speed of 62.5 kHz, and (c) PXRD diffractogram for the same sample.

^1H and ^{13}C NMR data indicate significant differences in the local environment of the components, visible especially in the region of OH and COOH protons of 2,4-DHBA, thus precluding a possibility of building a structural model using either of the known structures. A detailed analysis of the NMR data for this sample is given in section 3.2.3.

3.2.2. Conformational search for LIN and 2,4-DHBA

Fig. 6 features the results of the performed relaxed scans calculations. As mentioned in Section 2, the three scans for LIN were done independently, and they show how the relative gas phase energy of LIN changes with a given torsion. To decide which of these conformations should be considered in a CSP search, two main criteria were employed. First of these is an energetic one. It has been shown that for single-component crystals a conformation of up to ca. 25 kJ/mol of molecules above the global gas phase minimum can be adopted by a molecule, in particular in the case of larger molecules, for which the global gas phase minimum structure has a folded conformation [54]. Since this is the case of LIN, it would be safe to suspect that considering all conformations within the specified range of energy above the global minimum is a justified approach. However, bearing in mind that in a formula unit of LIN:2,4-DHBA there are two molecules, it is possible that the considered energy window for one molecule should be doubled, if the second one assumes its gas phase minimum conformation. As a result, in principle all conformations with energy of up to 50 kJ/mol above the global gas phase minimum should be considered. Therefore, it is clear from Fig. 6, that all values of φ and χ torsions should be accounted for, but in the case of ψ and ω some combinations of these two torsions can be safely excluded.

The second criterion allowing for narrowing down the number of possible conformations of LIN is the incidence of the torsion angle values of similar structural elements in the CSD. The analysis performed in Mogul for four selected torsion angles indicated that there are two most common arrangements of the φ torsion in the range of 0–180°, namely around 60 and 150°. The first of these values corresponds to a local energy minimum in the relaxed scan plot, together with the other two values, i.e. –60 and –150°, whereas the second value, $\varphi = 150^\circ$, corresponds to an energy maximum in the relaxed scan plot for LIN. Although according to our earlier argument all conformations with

energy of up to 50 kJ/mol should be considered, we decided to exclude this one as being less likely than the remaining three for the sake of maintaining the balance between considering all possibilities and a limited amount of time and resources. Therefore, at further stages three out of four indicated values of the φ torsion were considered: 60, –60 and –150°. Similarly, in the case of χ torsion, its two most common orientations in the CSD peak at around 0 and 180°. These two values of χ correspond to two local energy minima found in the relaxed scan plot, and so the two orientations of fluorophenyl and oxazolidone rings described by the indicated values were considered at further stages. Finally, in the case of ω torsion, there is an almost even distribution of its value in the CSD, in the range of 60–180°, while for ψ again two main values can be indicated, i.e. around 60 and 180°. As a result, we decided to include five evenly distributed values of ω in the indicated range and two values of ψ in further considerations. To summarize, the performed analysis allowed us to indicate the most probable values of the flexible torsion angles, by narrowing them down to 3, 2, 2 and 5 discrete values for φ , χ , ψ and ω , respectively.

In the case of 2,4-DHBA, the conformational search yielded a set of ten different conformations of 2,4-DHBA, accounting for the most plausible orientations of the OH and COOH groups. Of these, two conformations have significantly lower intermolecular energy, one being a global minimum conformation and the other having its energy only 2 kJ/mol above the global minimum. In addition, there are two other conformations of 2,4-DHBA with relative intermolecular energies of 15.9 and 17.2 kJ/mol above the global minimum, so these also should be taken into account, while the remaining conformations have their relative energy higher than 50 kJ/mol and thus may be safely excluded from further considerations.

3.2.3. Structural constraints from solid-state NMR data

The assignment of ^1H and ^{13}C resonances of LIN:2,4-DHBA was done on the basis of *inv*HETCOR recorded with long and short contact time, as well as ^1H - ^1H SQ-DQ spectrum with BaBa recoupling (all shown in Fig. 7). All values of chemical shifts are given in Supporting Information.

Because thermal analysis by TGA and DSC indicates that the analyzed crystal is not a solvate, it can be concluded from the ^{13}C CPMAS NMR spectrum of LIN:2,4-DHBA that there is one molecule of

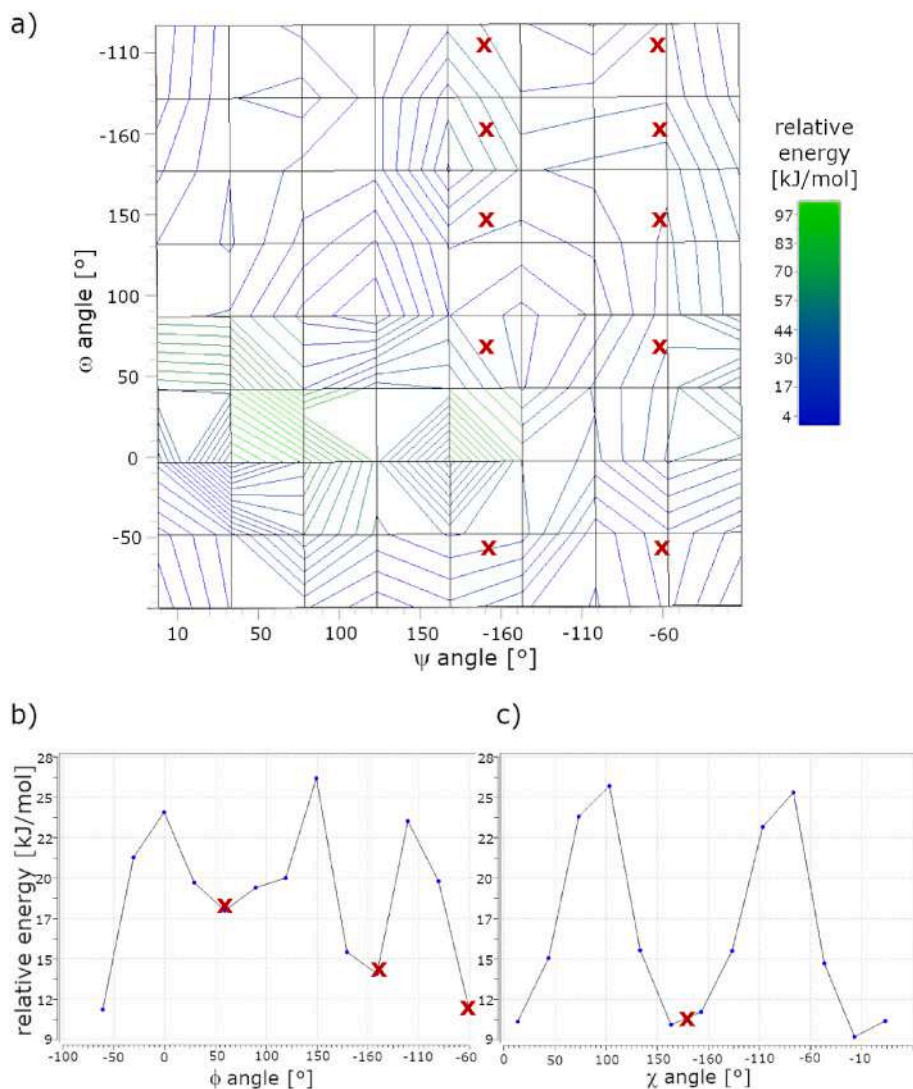


Fig. 6. The gas phase energy dependence calculated at the B3LYP/6-311g(d,p) level of theory on the values of the selected torsion angles of LIN: the evaluation was performed independently for (a) a pair of ψ and ω , (b) ϕ , and (c) χ . For the definitions of the used angles, see Fig. 1. Red crosses mark conformations selected for CSP calculations.

LIN and one molecule of 2,4-DHBA in an asymmetric part of a crystallographic unit cell. In addition, no ^{13}C signals originating from morpholine ring are detectable in the NMR spectrum, indicating significant mobility of this fragment of molecule, as was also observed for neat polymorphs of LIN [55], as well as for some other previously characterized cocrystals [25]. This could suggest that neither oxygen nor nitrogen atoms from the ring itself are not engaged in strong, directional intermolecular interactions, as these would restrict the ring's mobility. The comparison of this spectrum to the ^{13}C CPMAS NMR spectra recorded for all known crystal forms of LIN, including its two neat forms and four cocrystals and cocrystal hydrates, suggests that the arrangement of fluorophenyl and 2-oxazolidone rings is such that the fluorine atom from the first ring and C=O group from the second ring are in a *trans* position. This mutual arrangement of the two rings influences the chemical shifts of C-6 and C-9 carbon atoms: for the *trans* arrangement it appears that the chemical shift for C-9 carbon is 2–3 ppm lower than for C-6 carbon atom, whereas for *cis* configuration of the rings the ordering of these two signals is reversed. The *trans* arrangement of the rings is confirmed by the correlation signal between ^1H -12 resonance from fluorophenyl ring (at 8.04 ppm) and C-6 resonance from carbonyl group of 2-oxazolidone ring (at 157.2 ppm), observed in the *inv*HETCOR experiment and assigned in Fig. 7c. This observation allows us to limit

the number of considered values of χ torsion to only one discrete value of -170° . In the case of the mutual arrangement of fluorophenyl and morpholine rings, no definite structural constraints could be extracted from the NMR spectra, mainly because the NMR signals originating from morpholine ring are hardly observable due to a fast dynamics of this ring [25]. The 2D correlation NMR spectra allowed us also to confirm the arrangement of the amide bond. The chemical shift of the NH proton was determined to be 9.33 ppm, on the basis of ^1H - ^{14}N HMQC spectrum (Fig. 7a). In both ^1H - ^{13}C HETCOR spectrum and ^1H - ^1H SQ-DQ spectrum with BaBa recoupling this proton signal clearly correlates with ^1H and ^{13}C signals from CH_3 group, confirming the *trans* configuration of the NH-CO moiety. However, the arrangement of the ψ and ω torsions could not be definitely determined. This is because it is impossible to differentiate between intra- and intermolecular interactions and so many of the observed correlations may arise from both. Similarly, no definite conclusions could be drawn as to the orientation of hydroxyl groups in 2,4-DHBA. This is mainly because there are some ambiguities in the assignment of the OH protons to COOH, C-2' and C-4' sites, as these resonances overlap in the correlation spectra. As a result, no constraints could be put on a 2,4-DHBA molecule. This also hindered the identification of LIN - 2,4-DHBA contacts. For example, there is a clear

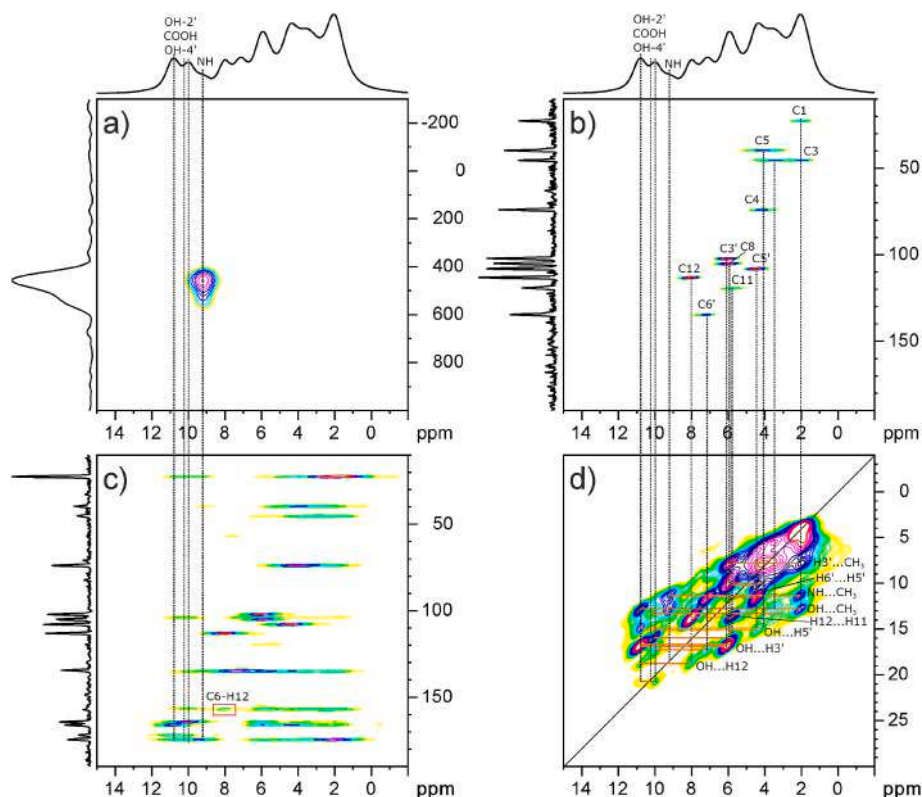


Fig. 7. (a) ^1H - ^{14}N D-HMQC, (b), (c) ^1H - ^{13}C invHETCOR NMR with short (100 μs) (b) and long (3 ms) (c) second contact time, and (d) ^1H - ^1H SQ-DQ with Back-to-Back recoupling NMR spectra for LIN:2,4-DHBA cocrystal recorded with a spinning speed of 62.5 kHz; red rectangle marks one of the key ^1H - ^{13}C correlation; the C-H pairs are assigned in the HETCOR spectrum with short contact time.

correlation in the ^1H - ^1H SQ-DQ spectrum with BaBa recoupling between LIN methyl group and one of the C-OH resonances, but it is not clear whether this is OH-2' or OH-4' site.

The conformational search and the analysis of solid-state NMR spectra allowed us for the selection of 27 conformations of LIN for CSP calculations, which is still a lot, but seems to be computationally manageable. In addition, we also included gas phase global minimum conformation of LIN, even though it is not in agreement with the structural constraints observed in the NMR spectra. This was done for the sake of comparison of the ability of low and high energy conformations to build energetically feasible crystal structures. In the case of 2,4-DHBA two conformations were selected to be used in CSP calculations. Note that here we limited ourselves to two lowest-energy conformations, keeping in mind that this may lead to unsuccessful overall predictions. At the same time, such a CSP search still offers a possibility to at least indicate the correct conformation of LIN present in the crystal structure.

3.2.4. Crystal structure prediction calculations

The final set of selected conformations of LIN and 2,4-DHBA amount together to 56 combinations of the possible arrangements of these two molecules. A full CSP search for each of the combinations is computationally very expensive, in particular in respect to DFT optimization of the CSP-generated structures. Therefore we decide to include our previously developed short-cut, which allows for significant savings in computational time. The idea standing behind this short-cut is that NMR parameters are sensitive primarily to a local structure and less so to a long-range order of the crystal. What is more, molecules tend to form similar arrangements (involving similar intermolecular interactions) in different crystal structures. The idea then is to take a set of crystal structures built by different conformations and compare chemical shifts calculated for each such crystal with the experimental NMR parameters.

In such a case one should be fully aware that we do not expect a perfect agreement between the calculated and the experimental chemical shifts, but a certain level of the agreement observed at this stage is with all probability indicative of a conformation of a molecule present in a crystal. In the case of LIN:2,4-DHBA system we are primarily mainly interested in the conformation of LIN and so only chemical shifts of this molecule are of interest at this point.

The first step of selection of the most promising conformers is energetic consideration, i.e. establishing which conformers of LIN are at all capable to pack efficiently into energetically favourable crystal structures. Our 56 CSP searches conducted in 4 most common space groups for chiral molecules resulted in a very crowded crystal energy landscape (see Supporting Information), but not all conformers were able to form structures found within the first 20 kJ/mol of this landscape. Fig. 8 features this energy region of the landscape, with legend showing only these conformations, which have representative crystal structure in this region. Note that this landscape refers to force field energies before DFT re-ranking. According to this, the lowest energy structures are the ones built by a conformation corresponding to the gas phase minimum of LIN, which has to be considered with caution. It was already reported, that inaccurately determined energies of molecular conformations are able to hinder identification of the most energetically favourable structures [56]. In addition, the CSP searches treated LIN molecules as rigid entities, and so we may expect some conformational adjustments upon DFT geometry optimizations [57]. Nevertheless, some conformer selection can be made at this point, excluding those which do not build structures found within the presented energy region. In particular, none of the conformations of LIN having its gas phase energy more than 30 kJ/mol above the global minimum was found in the energetically feasible crystal structures and therefore were not considered at the further stages.

As already mention, the most computationally expensive stage of the

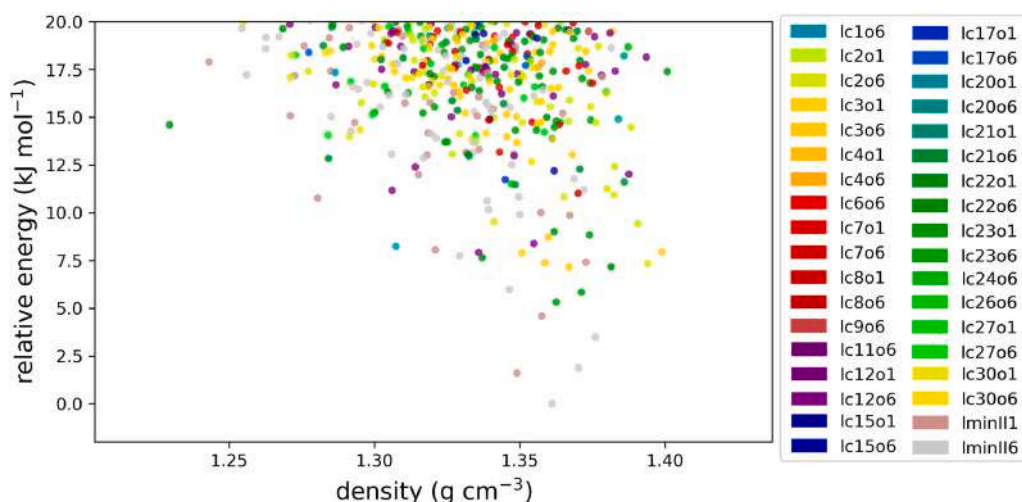


Fig. 8. The first 20 kJ/mol region of the CSP-generated crystal energy landscape for different conformations of LIN and two selected conformations of 2,4-DHBA. Conformations of LIN, denoted as lc[NUMBER] are numbered according to their respective values of the varied torsion angles (see Supporting Information), two conformations of 2,4-DHBA are represented by 'o6' or 'o1' notation, with 'o6' being gas phase global minimum conformation.

CSP protocol is DFT re-optimization of the generated crystal structures. As our primary aim is to indicate the conformation of LIN building the experimental crystal structure of LIN:2,4-DHBA, we do not need to geometry optimize all lowest energy structures. According to our short-cut, it suffices to select the representative structures built by different conformations in order to check which of them would yield the NMR parameters closest to the experimental data. In the lowest energy region of the generated CSP energy landscape, crystal structures built by 21 different conformations of LIN can be found. For the next stage we selected their lowest-energy representatives from each of the tested space groups and performed DFT optimization and calculations of NMR parameters. This resulted in 84 independent CASTEP geometry optimizations. Fig. 9 presents the obtained ^1H RMSD values (calculated only for LIN chemical shifts). Its analysis reveals that six conformations can immediately be excluded from further considerations as none of the crystal structures formed by them yielded an RMSD value lower than arbitrarily chosen threshold of 0.7 ppm. In addition, a number of conformations have only one structure falling beyond this threshold. As we showed before for furazidin [19] a serendipitous agreement in terms of ^1H NMR parameters is not uncommon, and therefore we decided to consider at the final stage only these conformations which form at least two crystal structures falling beyond the 0.7 ppm threshold. This resulted in the selection of five conformations: lc2, lc7, lc12, lc22 and lc27. Importantly, all of them have the same torsion angle value of 95° for the ω torsion (see Supporting Information), which showed the highest variability in the conformational search. This finding alone already allows for significant narrowing of the considered conformational space. The differences between the selected conformations concern φ and ψ torsion angles, the first of which defines mutual arrangement of phenyl and morpholine ring, while the second one defines the position of the side chain together with ω torsion.

As a side note, it is worth to mention the differences in energetic ranking of the structures after DFT optimization. In particular, none of the structures built by the gas phase minimum conformation of LIN was found within the first 10 kJ/mol from the global minimum structure. Instead, the most stable structures were built by conformations having gas phase energies in the range of 17–29 kJ/mol above the global gas phase minimum. This is partly in agreement with the results reported before by Thompson and Day [54], which indicated that energetically favourable structures are often formed by conformations higher in gas phase energy when molecules building them are capable of assuming more extended conformations. This is also true for LIN, for which gas phase minimum conformation is a bent one, whereas all conformations

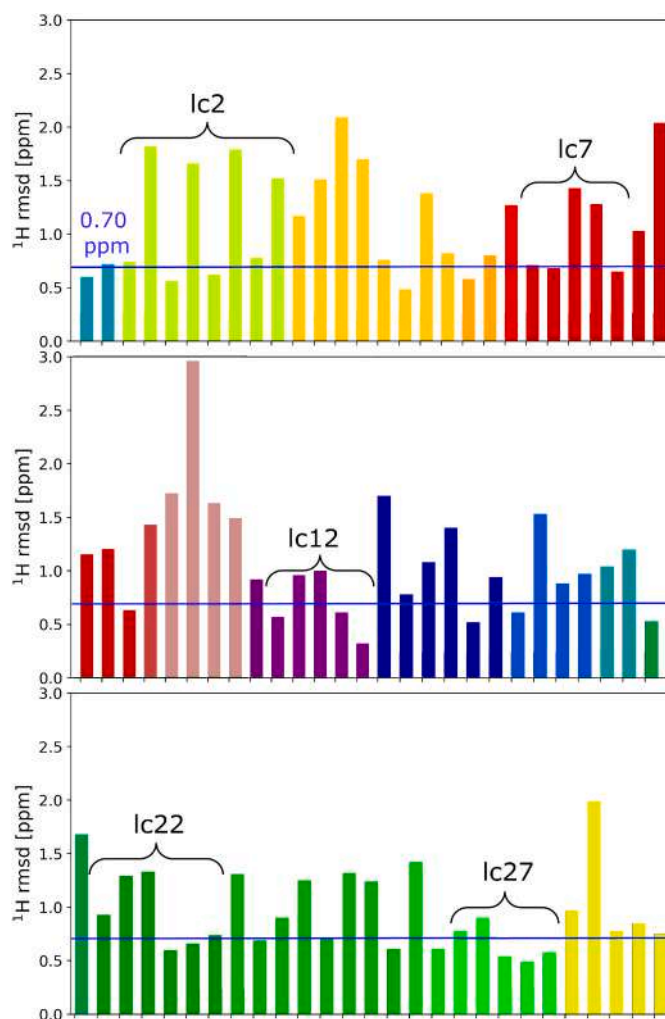


Fig. 9. ^1H RMSD values for each of the representative 84 lowest-energy model crystal structures of LIN:2,4-DHBA built by different conformations of LIN. The conformations are color-coded according to the legend presented in Fig. 8. For the indicated conformations at least two structures falling below the arbitrarily selected cut-off value, marked by a blue line, were found (see text for details).

building energetically favourable structures are extended. On the other hand, we found higher energy threshold for the conformations capable of building energetically favourable structures than the one reported before (29 kJ/mol against 25 kJ/mol), possibly because we are looking at the structures of a cocrystal, while before only single component crystals were considered. In our case the coformer (2,4-DHBA) is much smaller molecule than LIN and it is able to pack more efficiently, leading to the formation of more stabilizing intermolecular interactions, satisfying all possible hydrogen bond acceptors and donors. Similar observations were made before for catechin methanol solvate [9].

The final stage of our calculations included DFT geometry optimization of all crystal structures built by the five selected conformers and found within the lowest (20 kJ/mol) energy region of the force field crystal energy landscape (122 crystal structures). The final results in terms of relative energy (for the lowest energy structures found within the first 20 kJ/mol above the global minimum), as well as ^1H and ^{13}C RMSD values are shown in Fig. 10. Note, that the presented plots include also structures optimized at the first stage of DFT optimization, but only those which are built by one of the five selected conformations of LIN. The global minimum in the presented landscape belongs to a structure built by conformation lc12, but its agreement with the NMR data is far from being acceptable. In fact, this conformation was found in only two lowest-energy structures, none of which show good agreement with NMR data. In contrast, conformations lc22 and lc27 are the ones most frequently found among the structures yielding the best agreement with

the experiment. Altogether, there are 6 crystal structures yielding a ^1H RMSD value below 0.55 ppm, half of them are built by conformation lc22 and the other half - by lc27. Of these only one crystal structure show also one of the best agreements in terms of ^{13}C NMR data with a ^{13}C RMSD value of 1.49 ppm. This structure, built by conformation lc22, is marked by a red rectangle in Fig. 10. As a result, it can be concluded that the most probable conformations of LIN present in the crystal structure of LIN:2,4-DHBA cocrystal are lc22 and lc27 shown in Fig. 11, with the previous one being the best candidate. Interestingly, lc22 is very similar to the conformation found in the experimental crystal structure of neat form II of LIN, whereas lc27 resembles a conformation found in LIN: PHBA cocrystal hydrate [25]. This similarity adds merit to our selection of the most probable candidates for LIN:2,4-DHBA cocrystal. Finally, we would like to point out that in this work only ^1H NMR data similarity was considered as a main criterion for a preliminary selection of the most plausible conformations of LIN, while ^{13}C NMR data were used as a final verification. Our experience shows that such a selection would not work if the process would be reversed, i.e. using ^{13}C chemical shifts similarity as a selection criterion, followed by a final verification with ^1H chemical shift similarity. The problem with ^{13}C chemical shifts is that there are many more candidate structures indicated to be in agreement with an experiment in terms of this parameter and therefore ^1H chemical shifts are deemed to be more discriminating and insightful.

The next step of finding a suitable model for experimental crystal structure of LIN:2,4-DHBA could comprise further CSP calculations using selected conformations of LIN with all possible conformations of 2,4-DHBA and/or an attempt to solve this structure using high resolution powder X-Ray diffraction data and Rietveld refinement, which can also make use of the selected conformations of LIN. This, however, is beyond the scope of our current work. Note, that due to ambiguities in the NMR signal assignment for 2,4-DHBA, it is difficult to make further use of the calculated vs experimental NMR data in establishing the most probable packing arrangement or the conformation of this molecule.

It is also worth to mention about two other obstacles encountered in crystal structure determination of LIN:2,4-DHBA cocrystal. First, one should be cautious in respect to the mutual arrangement of the fluorophenyl and morpholine rings of LIN. Although in both selected conformations this arrangement is similar, it was established on the basis of rather limited experimental data, namely only these originating from

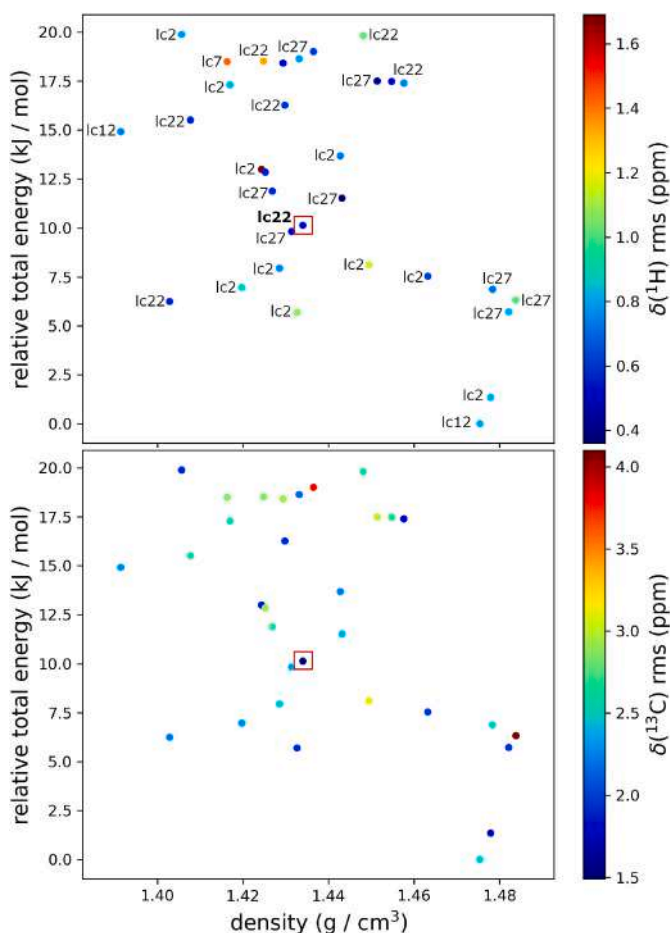


Fig. 10. Final DFT-MBD crystal energy landscape including the lowest energy structures (below 20 kJ/mol) built by five selected conformations of LIN with ^1H and ^{13}C RMSD values plotted as colormaps. The upper plot features conformations building particular structures. A red rectangle marks the only structure showing sufficiently good agreement in terms of both considered NMR parameters.

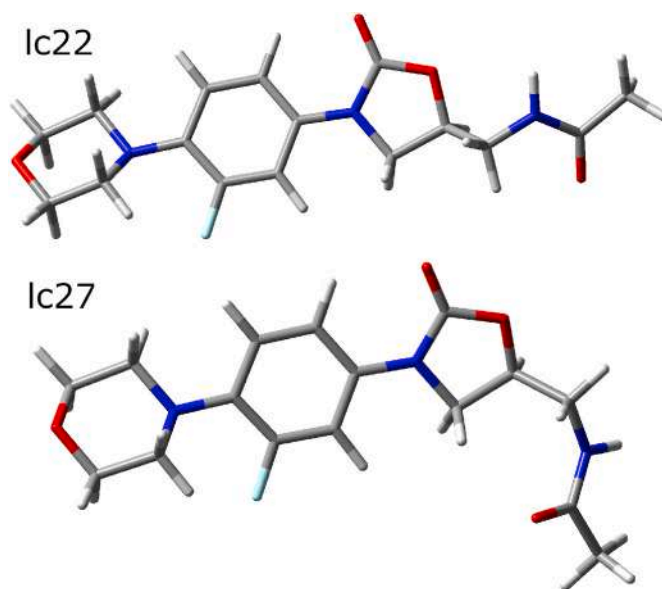


Fig. 11. Two most probable conformations of LIN present in LIN:2,4-DHBA cocrystal, with lc22 being the best candidate according to ^1H and ^{13}C RMSD values.

the fluorophenyl ring. As mentioned before, the morpholine ring exhibits significant dynamics in this crystal, resulting in NMR signals originating from this ring hardly detectable, both in 1D and 2D NMR spectra. In order not to introduce any ambiguities into our comparison of the calculation results with the experimental ones, we did not include any chemical shifts originating from the morpholine ring in this comparison.

Secondly, maybe more as a side note, although in our eyes rather an important one, we advise caution when comparing the experimental NMR data with the ones obtained for partially DFT-optimized crystal structures (see section 2 for explanation of this term). Our calculations indicate that in some cases a significant change in conformation is possible at the second stage of DFT optimization, leading to significant changes in the obtained ^1H RMSD values for two sets of data (partially optimized vs fully optimized). In particular, there were two out of the tested 44 model crystal structures, for which the RMSD values changed in one case from 1.26 ppm (partial optimization) to 0.69 ppm (full optimization), and in the other from 1.62 ppm (partial optimization) to 0.58 ppm (full optimization). These changes in the ^1H RMSD values were associated with significant changes to conformations of LIN inside these particular crystals, expressed in changes to the RMSD values calculated for atomic positions (0.101 Å in the first case and as much as 0.624 Å in the second case). Therefore, using such partially optimized structures may in some cases lead to omission of relevant crystal structures and should be used only in justified cases. Clearly, only partial re-optimizing of model crystal structures after rigid CSP searches is not one of such cases, despite a promise of significant savings to computational time and resources.

4. Conclusions

A joint use of solid-state NMR experiments recorded under very fast magic angle spinning and crystal structure prediction calculations led us to the determination of the crystal structure of microcrystalline LIN:2,3-DHBA cocrystal. This case, however, can be considered as a small challenge because gathered experimental data indicated structural similarity of this crystal structure to that of the known cocrystal of LIN with 2,6-DHBA. The other examined case of a cocrystal of LIN with 2,4-DHBA posed a much greater challenge, so much so that it was not possible so fully solve this crystal structure using NMR crystallography approach within the framework of our studies. This was mainly because of significant conformational flexibility of LIN, having a ‘floppy’ side-chain able to assume numerous conformations. As a result, a number of possible conformations of LIN to be considered in CSP is very significant. When we add to that the fact that 2,4-DHBA can also assume several possible conformations and that each combination of each possible conformations of the two molecules should be considered to cover the entire search space, the task quickly becomes unfeasible. In addition, some ambiguities in the NMR signal assignment for 2,4-DHBA prevented us from finding relevant structural constraints which could be used to limit the search space. To overcome these difficulties we proposed here a way of establishing molecular conformation found within the examined crystal even without the necessity of finding a structural model precisely corresponding to the experimental crystal structure. Our approach make use of knowledge-based data (Mogul search), conformational search and structural constraints extracted from solid-state NMR spectra to tentatively limit the search space and select a set of conformations to be used in CSP calculations. In our case the selected set comprised 27 conformations used in CSP calculations with two possible conformations of 2,4-DHBA. The comparison of the theoretical NMR data obtained for this set of conformations with the experimental ones for LIN led us to narrowing down the number of possible conformations of LIN to five. Finally, all relevant crystal structures built by the selected conformations were used to indicate the most probable ones, resulting in the identification of two molecular arrangements of LIN, one

of which showed an excellent agreement with the experiment in terms of both considered NMR parameters, i.e. ^1H and ^{13}C chemical shifts. Lastly, we would like to point out again that in the case of rigid CSP searches a full geometry optimization of the generated structures seems to be a prerequisite before comparison of the calculated and experimental NMR data. Otherwise, one risks omitting relevant crystal structures.

Declaration of competing interest

The authors declare that they have no known competing financial interests or personal relationships that could have appeared to influence the work reported in this paper.

Data availability

Data will be made available on request.

Acknowledgements

This work was financially supported by Polish National Science Centre under Sonata 14 grant No. UMO-2018/31/D/ST4/01995. The Polish Infrastructure for Supporting Computational Science in the European Research Space (PL-GRID) is gratefully acknowledged for providing computational resources. A purchase of a Panalytical powder X-Ray diffractometer used to obtain results included in this publication was supported by the funds from the EU Regional Operational Program of the Lodz Region, RPLD.01.01.00-10-0008/18.

Appendix A. Supplementary data

Supplementary data to this article can be found online at <https://doi.org/10.1016/j.ssnmr.2022.101813>.

References

- [1] S.L. Price, Predicting crystal structures of organic compounds, *Chem. Soc. Rev.* 43 (2014) 2098–2111, <https://doi.org/10.1039/C3CS60279F>.
- [2] S.M. Woodley, R. Catlow, Crystal structure prediction from first principles, *Nat. Mater.* 7 (2008) 937–946, <https://doi.org/10.1038/nmat2321>.
- [3] G.M. Day, Current approaches to predicting molecular organic crystal structures, *Crystallogr. Rev.* 17 (2011) 3–52, <https://doi.org/10.1080/0889311X.2010.517526>.
- [4] A. Pulido, L. Chen, T. Kaczorowski, D. Holden, M.A. Little, S.Y. Chong, B.J. Slater, D.P. McMahon, B. Bonillo, C.J. Stackhouse, A. Stephenson, C.M. Kane, R. Clowes, T. Hasell, A.I. Cooper, G.M. Day, Functional materials discovery using energy–structure–function maps, *Nature* 543 (2017) 657–664, <https://doi.org/10.1038/nature21419>, doi:10.1038/nature21419.
- [5] J. Hoja, H.-Y. Ko, M.A. Neumann, R. Car, R.A. DiStasio, A. Tkatchenko, Reliable and practical computational description of molecular crystal polymorphs, *Sci. Adv.* 5 (2019), <https://doi.org/10.1126/sciadv.aau3338>, eaa3338.
- [6] R.M. Bhardwaj, J.A. McMahon, J. Nyman, L.S. Price, S. Konar, I.D.H. Oswald, C. R. Pulham, S.L. Price, S.M. Reutzel-Edens, A prolific solvate former, galunisertib, under the pressure of crystal structure prediction, produces ten diverse polymorphs, *J. Am. Chem. Soc.* 141 (2019) 13887–13897, <https://doi.org/10.1021/jacs.9b06634>, 10.1021/jacs.9b06634.
- [7] D.E. Braun, P.G. Karamertzanis, S.L. Price, Which, if any, hydrates will crystallise? Predicting hydrate formation of two dihydroxybenzoic acids, *Chem. Commun.* 47 (2011) 5443–5445, <https://doi.org/10.1039/c1cc10762c>, 10.1039/c1cc10762c.
- [8] D.E. Braun, M. Orlova, U.J. Griesser, Creatine: polymorphs predicted and found, *Cryst. Growth Des.* 14 (2014) 4895–4900, <https://doi.org/10.1021/cg501159c>, doi:10.1021/cg501159c.
- [9] M.K. Dudek, G.M. Day, Explaining crystallization preferences of two polyphenolic diastereoisomers by crystal structure prediction, *CrystEngComm* 21 (2019) 2067–2079, <https://doi.org/10.1039/C8CE01783B>, 10.1039/C8CE01783B.
- [10] M. Pakhnova, I. Kruglov, A. Yamilkin, A.R. Oganov, Search for stable cocrystals of energetic materials using the evolutionary algorithm USPEX, *Phys. Chem. Chem. Phys.* 22 (2020) 16822–16830, <https://doi.org/10.1039/D0CP03042B>, doi:10.1039/D0CP03042B.
- [11] D.E. Braun, J.A. McMahon, R.M. Bhardwaj, J. Nyman, M.A. Neumann, J. van de Streek, S.M. Reutzel-Edens, Inconvenient truths about solid form landscapes revealed in the polymorphs and hydrates of gandotinib, *Cryst. Growth Des.* 19 (2019) 2947–2962, <https://doi.org/10.1021/acs.cgd.9b00162>, doi:10.1021/acs.cgd.9b00162.

- [12] M.K. Dudek, K. Druzbicki, Along the road to crystal structure prediction (CSP) of pharmaceutical-like molecules, *CrystEngComm* 24 (2022) 1665–1678, <https://doi.org/10.1039/d1ce01564h>, doi:10.1039/d1ce01564h.
- [13] D.L. Bryce, NMR crystallography: structure and properties of materials from solid-state nuclear magnetic resonance observables, *IUCr* 4 (2017) 350–359, <https://doi.org/10.1107/s2052252517006042>, doi:10.1107/s2052252517006042.
- [14] S.E. Ashbrook, D. McKay, Combining solid-state NMR spectroscopy with first-principles calculations – a guide to NMR crystallography, *Chem. Commun.* 52 (2016) 7186–7204, <https://doi.org/10.1039/c6cc02542k>, doi:10.1039/c6cc02542k.
- [15] P. Hodgkinson, NMR crystallography of molecular organics, *Prog. Nucl. Magn. Reson. Spectrosc.* 118–119 (2020) 10–53, <https://doi.org/10.1016/j.pnmrs.2020.03.001>, doi:10.1016/j.pnmrs.2020.03.001.
- [16] C.M. Widdifield, H. Robson, P. Hodgkinson, Furosemide's one little hydrogen atom: NMR crystallography structure verification of powdered molecular organics, *Chem. Commun.* 52 (2016) 6685–6688, <https://doi.org/10.1039/c6cc02171a>, doi:10.1039/c6cc02171a.
- [17] L. Mafra, S.M. Santos, R. Siegel, I. Alves, F.A.A. Paz, D. Dudenko, H.W. Spiess, Packing interactions in hydrated and anhydrous forms of the antibiotic ciprofloxacin: a solid-state NMR, X-ray diffraction, and computer simulation study, *J. Am. Chem. Soc.* 134 (2011) 71–74, <https://doi.org/10.1021/ja208647n>, doi:10.1021/ja208647n.
- [18] A.S. Tatton, H. Blade, S.P. Brown, P. Hodgkinson, L.P. Hughes, S.O.N. Lill, J. R. Yates, Improving confidence in crystal structure solutions using NMR crystallography: the case of β -piroxycam, *Cryst. Growth Des.* 18 (2018) 3339–3351, <https://doi.org/10.1021/acs.cgd.8b00022>, doi:10.1021/acs.cgd.8b00022.
- [19] M.K. Dudek, P. Paluch, E. Pindelska, Crystal structures of two furazidin polymorphs revealed by a joint effort of crystal structure prediction and NMR crystallography, *Acta. Crystallogr. B. Struct. Sci.* 76 (2020) 322–335, <https://doi.org/10.1107/S205252062000373X>, doi:10.1107/S205252062000373X.
- [20] F. Bravetti, S. Bordignon, E. Allig, D. Eisenbeil, L. Fink, C. Nervi, R. Gobetto, M. U. Schmidt, M.R. Chierotti, Solid-state NMR-driven crystal structure prediction of molecular crystals: the case of mebendazole, *Chem. Eur J.* (2021), <https://doi.org/10.1002/chem.202103589>, doi:10.1002/chem.202103589.
- [21] A. Hofstetter, M. Balodis, F.M. Paruzzo, C.M. Widdifield, G. Stevanato, A.C. Pinon, P.J. Bygrave, G.M. Day, L. Emsley, Rapid structure determination of molecular solids using chemical shifts directed by unambiguous prior constraints, *J. Am. Chem. Soc.* 141 (2019) 16624–16634, <https://doi.org/10.1021/jacs.9b03908>, doi:10.1021/jacs.9b03908.
- [22] J. Brus, J. Czernek, L. Kobera, M. Urbanova, S. Abbrent, M. Husak, Predicting the crystal structure of decitabine by powder NMR crystallography: influence of long-range molecular packing symmetry on NMR parameters, *Cryst. Growth Des.* 16 (2016) 7102–7111, <https://doi.org/10.1021/acs.cgd.6b01341>, doi:10.1021/acs.cgd.6b01341.
- [23] J. Brus, J. Czernek, M. Hruby, P. Svec, L. Kobera, S. Abbrent, M. Urbanova, Efficient strategy for determining the atomic-resolution structure of micro- and nanocrystalline solids within polymeric microbeads: domain-edited NMR crystallography, *Macromolecules* 51 (2018) 5364–5374, <https://doi.org/10.1021/acs.macromol.8b00392>, doi:10.1021/acs.macromol.8b00392.
- [24] M.K. Dudek, P. Paluch, J. Sniechowska, K.P. Nartowski, G.M. Day, M. J. Potrzebowski, Crystal structure determination of an elusive methanol solvate-hydrate of catechin using crystal structure prediction and nmr crystallography, *CrystEngComm* 22 (2020) 4969–4981, <https://doi.org/10.1039/D0CE00452A>, doi:10.1039/D0CE00452A.
- [25] M. Khalaji, A. Wróblewska, E. Wielgus, G.D. Bujacz, M.K. Dudek, M. J. Potrzebowski, Structural variety of heterosynthons in linezolid cocrystals with modified thermal properties, *Acta. Crystallogr. B. Struct. Sci.* 76 (2020) 892–912, <https://doi.org/10.1107/s2052520620010896>, doi:10.1107/s2052520620010896.
- [26] M. Khalaji, M.J. Potrzebowski, M.K. Dudek, Virtual cocrystal screening methods as tools to understand the formation of pharmaceutical cocrystals—a case study of linezolid, a wide-range antibacterial drug, *Cryst. Growth Des.* 21 (2021) 2301–2314, <https://doi.org/10.1021/acs.cgd.0c01707>, doi:10.1021/acs.cgd.0c01707.
- [27] J.W. Wiench, C.E. Bronnimann, V.S.-Y. Lin, M. Pruski, Chemical shift correlation NMR spectroscopy with indirect detection in fast rotating solids: studies of organically functionalized mesoporous silicas, *J. Am. Chem. Soc.* 129 (2007) 12076–12077, <https://doi.org/10.1021/ja074746+>, doi:10.1021/ja074746+.
- [28] K. Mao, J.W. Wiench, V.S.-Y. Lin, M. Pruski, Indirectly detected through-bond chemical shift correlation NMR spectroscopy in solids under fast MAS: studies of organic-inorganic hybrid materials, *J. Magn. Reson.* 196 (2009) 92–95, <https://doi.org/10.1016/j.jmr.2008.10.010>, doi:10.1016/j.jmr.2008.10.010.
- [29] S. Cavadini, S. Antonijevic, A. Lupulescu, G. Bodenhausen, Indirect detection of nitrogen-14 in solids via protons by nuclear magnetic resonance spectroscopy, *J. Magn. Reson.* 182 (2006) 168–172, <https://doi.org/10.1016/j.jmr.2006.06.003>, doi:10.1016/j.jmr.2006.06.003.
- [30] A.G. Rankin, J. Trébosc, P. Paluch, O. Lafon, J.-P. Amoureux, Evaluation of excitation schemes for indirect detection of ^{14}N via solid-state HMQC NMR experiments, *J. Magn. Reson.* 303 (2019) 28–41, <https://doi.org/10.1016/j.jmr.2019.04.004>, doi:10.1016/j.jmr.2019.04.004.
- [31] K.R. Thurber, R. Tycko, Measurement of sample temperatures under magic-angle spinning from the chemical shift and spin-lattice relaxation rate of ^{79}Br in KBr powder, *J. Magn. Reson.* 196 (2009) 84–87, <https://doi.org/10.1016/j.jmr.2008.09.019>, doi:10.1016/j.jmr.2008.09.019.
- [32] C. Vinod Chandran, P.K. Madhu, N.D. Kurur, T. Bräuniger, Swept-frequency two-pulse phase modulation (SWF-TPPM) sequences with linear sweep profile for heteronuclear decoupling in solid-state NMR, *Magn. Reson. Chem.* 46 (2008) 943–947, <https://doi.org/10.1002/mrc.2285>, doi:10.1002/mrc.2285.
- [33] M. Shen, J. Trébosc, O. Lafon, Z. Gan, F. Pourpoint, B. Hu, Q. Chen, J.-P. Amoureux, Solid-state NMR indirect detection of nuclei experiencing large anisotropic interactions using spinning sideband-selective pulses, *Solid State Nucl. Magn. Reson.* 72 (2015) 104–117, <https://doi.org/10.1016/j.snmr.2015.09.003>, doi:10.1016/j.snmr.2015.09.003.
- [34] P. Paluch, A.G. Rankin, J. Trébosc, O. Lafon, J.-P. Amoureux, Analysis of HMQC experiments applied to a spin $\frac{1}{2}$ nucleus subject to very large CSA, *Solid State Nucl. Magn. Reson.* 100 (2019) 11–25, <https://doi.org/10.1016/j.snmr.2019.03.001>, doi:10.1016/j.snmr.2019.03.001.
- [35] M. J. Frisch, G. W. Trucks, H. B. Schlegel, G. E. Scuseria, M. A. Robb, J. R. Cheeseman, G. Scalmani, V. Barone, G. A. Petersson, H. Nakatsuji, X. Li, M. Caricato, A. V. Marenich, J. Bloino, B. G. Janesko, R. Gomperts, B. Mennucci, H. P. Hratchian, J. V. Ortiz, A. F. Izmaylov, J. L. Sonnenberg, D. Williams-Young, F. Ding, F. Lipparini, F. Egidi, J. Goings, B. Peng, A. Petrone, T. Henderson, D. Ranasinghe, V. G. Zakrzewski, J. Gao, N. Rega, G. Zheng, W. Liang, M. Hada, M. Ehara, K. Toyota, R. Fukuda, J. Hasegawa, M. Ishida, T. Nakajima, Y. Honda, O. Kitao, H. Nakai, T. Vreven, K. Throssell, J. A. Montgomery, Jr., J. E. Peralta, F. Ogliaro, M. J. Bearpark, J. J. Heyd, E. N. Brothers, K. N. Kudin, V. N. Staroverov, T. A. Keith, R. Kobayashi, J. Normand, K. Raghavachari, A. P. Rendell, J. C. Burant, S. S. Iyengar, J. Tomasi, M. Cossi, J. M. Millam, M. Klene, C. Adamo, R. Cammi, J. W. Ochterski, R. L. Martin, K. Morokuma, O. Farkas, J. B. Foresman, D. J. Fox, Gaussian16 Revision C.01, 2016. Gaussian Inc. Wallingford CT.
- [36] I.J. Bruno, J.C. Cole, M. Kessler, J. Luo, W.D.S. Motherwell, L.H. Purkis, B.R. Smith, R. Taylor, R.I. Cooper, S.E. Harris, A.G. Orpen, Retrieval of crystallographically-derived molecular geometry information, *J. Chem. Inf. Comput. Sci.* 44 (2004) 2133–2144, <https://doi.org/10.1021/ci049780b>, doi:10.1021/ci049780b.
- [37] D.H. Case, J.E. Campbell, P.J. Bygrave, G.M. Day, Convergence properties of crystal structure prediction by quasi-random sampling, *J. Chem. Theor. Comput.* 12 (2016) 910–924, <https://doi.org/10.1021/acs.jctc.5b01112>, doi:10.1021/acs.jctc.5b01112.
- [38] S.L. Price, M. Leslie, G.W.A. Welch, M. Habgood, L.S. Price, P.G. Karamertzanis, G. M. Day, Modelling organic crystal structures using distributed multipole and polarizability-based model intermolecular potentials, *Phys. Chem. Chem. Phys.* 12 (2010) 8478, <https://doi.org/10.1039/c004164e>, doi:10.1039/c004164e.
- [39] D.S. Coombes, S.L. Price, D.J. Willock, M. Leslie, Role of electrostatic interactions in determining the crystal structures of polar organic molecules. A distributed multipole study, *J. Phys. Chem. A* 100 (1996) 7352–7360, <https://doi.org/10.1021/jp960333b>, doi:10.1021/jp960333b.
- [40] A.J. Stone, Distributed multipole analysis: stability for large basis sets, *J. Chem. Theor. Comput.* 1 (2005) 1128–1132, <https://doi.org/10.1021/ct050190+>, doi:10.1021/ct050190+.
- [41] CCDC, CSD Space Group Statistics, 2021. <https://www.ccdc.cam.ac.uk/support-and-resources/ccdcresources/>.
- [42] S.J. Clark, M.D. Segall, C.J. Pickard, P.J. Hasnip, M.L.J. Probert, K. Refson, M. C. Payne, First principles methods using CASTEP, *Z. für Kristallogr. - Cryst. Mater.* 220 (2005) 567–570, <https://doi.org/10.1524/zkri.220.5.567.65075>, doi:10.1524/zkri.220.5.567.65075.
- [43] J.P. Perdew, K. Burke, M. Ernzerhof, Generalized gradient approximation made simple, *Phys. Rev. Lett.* 77 (1996) 3865–3868, <https://link.aps.org/doi/10.1103/PhysRevLett.77.3865>, doi:10.1103/PhysRevLett.77.3865.
- [44] L. Kronik, A. Tkatchenko, Understanding molecular crystals with dispersion-inclusive density functional theory: pairwise corrections and beyond, *Acc. Chem. Res.* 47 (2014) 3208–3216, <https://doi.org/10.1021/ar500144s>, doi:10.1021/ar500144s.
- [45] J.R. Yates, C.J. Pickard, F. Mauri, Calculation of NMR chemical shifts for extended systems using ultrasoft pseudopotentials, *Phys. Rev. B* 76 (2007), <https://doi.org/10.1103/physrevb.76.024401>, doi:10.1103/physrevb.76.024401.
- [46] M. Zilka, J.R. Yates, S.P. Brown, An NMR crystallography investigation of furosemide, *Magn. Reson. Chem.* 57 (2018) 191–199, <https://doi.org/10.1002/mrc.4789>, doi:10.1002/mrc.4789.
- [47] K. Maruyoshi, D. Iuga, A.E. Watts, C.E. Hughes, K.D. Harris, S.P. Brown, Assessing the detection limit of a minority solid-state form of a pharmaceutical by ^1H double-quantum magic-angle spinning nuclear magnetic resonance spectroscopy, *J. Pharmacol. Sci.* 106 (2017) 3372–3377, <https://doi.org/10.1016/j.xphs.2017.07.014>, doi:10.1016/j.xphs.2017.07.014.
- [48] E. Salager, G.M. Day, R.S. Stein, C.J. Pickard, B. Elena, L. Emsley, Powder crystallography by combined crystal structure prediction and high-resolution ^1H solid-state NMR spectroscopy, *J. Am. Chem. Soc.* 132 (2010) 2564–2566, <https://doi.org/10.1021/ja909449k>, doi:10.1021/ja909449k.
- [49] M. Baías, J.-N. Dumez, P.H. Svensson, S. Schantz, G.M. Day, L. Emsley, De novo determination of the crystal structure of a large drug molecule by crystal structure prediction-based powder NMR crystallography, *J. Am. Chem. Soc.* 135 (2013) 17501–17507, <https://doi.org/10.1021/ja4088874>, doi:10.1021/ja4088874.
- [50] M.K. Dudek, G. Bujacz, M.J. Potrzebowski, Experimental tests for quality validation of computationally predicted crystal structures – a case of a conformationally flexible procyanidin A-2 dihydrate, *CrystEngComm* 19 (2017) 2903–2913, <https://doi.org/10.1039/c7ce00618g>, doi:10.1039/c7ce00618g.
- [51] J.A. Chisholm, S. Motherwell, COMPACT: a program for identifying crystal structure similarity using distances, *J. Appl. Crystallogr.* 38 (2005) 228–231, <https://doi.org/10.1107/s0021889804027074>, doi:10.1107/s0021889804027074.
- [52] C.M. Widdifield, S.O.N. Lill, A. Broo, M. Lindkvist, A. Pettersen, A.S. Ankarberg, P. Aldred, S. Schantz, L. Emsley, Does Z prime equal 1 or 2? Enhanced powder NMR crystallography verification of a disordered room temperature crystal

- structure of a p38 inhibitor for chronic obstructive pulmonary disease, *Phys. Chem. Chem. Phys.* 19 (2017) 16650–16661, doi:10.1039/c7cp02349a.
- [53] F. Alkan, S.T. Holmes, C. Dybowski, Role of exact exchange and relativistic approximations in calculating ^{19}F magnetic shielding in solids using a cluster ansatz, *J. Chem. Theor. Comput.* 13 (2017) 4741–4752, doi:10.1021/acs.jctc.7b00555.
- [54] H.P.G. Thompson, G.M. Day, Which conformations make stable crystal structures? Mapping crystalline molecular geometries to the conformational energy landscape, *Chem. Sci.* 5 (2014) 3173–3182, <https://doi.org/10.1039/C4SC01132E>, doi: 10.1039/C4SC01132E.
- [55] E. Wielgus, P. Paluch, J. Frelek, W.J. Szczepek, M.J. Potrzebowski, Full characterization of linezolid and its synthetic precursors by solid-state nuclear magnetic resonance spectroscopy and mass spectrometry, *J. Pharmacol. Sci.* 104 (2015) 3883–3892, <https://doi.org/10.1002/jps.24606>, doi:10.1002/jps.24606.
- [56] C. Greenwell, G.J.O. Beran, Inaccurate conformational energies still hinder crystal structure prediction in flexible organic molecules, *Cryst. Growth Des.* 20 (2020) 4875–4881, doi:10.1021/acs.cgd.0c00676.
- [57] A.J. Cruz Cabeza, G.M. Day, W.D.S. Motherwell, W. Jones, Amide pyramidalization in carbamazepine: a flexibility problem in crystal structure prediction? *Cryst. Growth Des.* 6 (2006) 1858–1866, doi:10.1021/cg0601756.

Supporting Information

to

**Narrowing down the conformational space with solid-state NMR in Crystal Structure
Prediction of linezolid cocrystals**

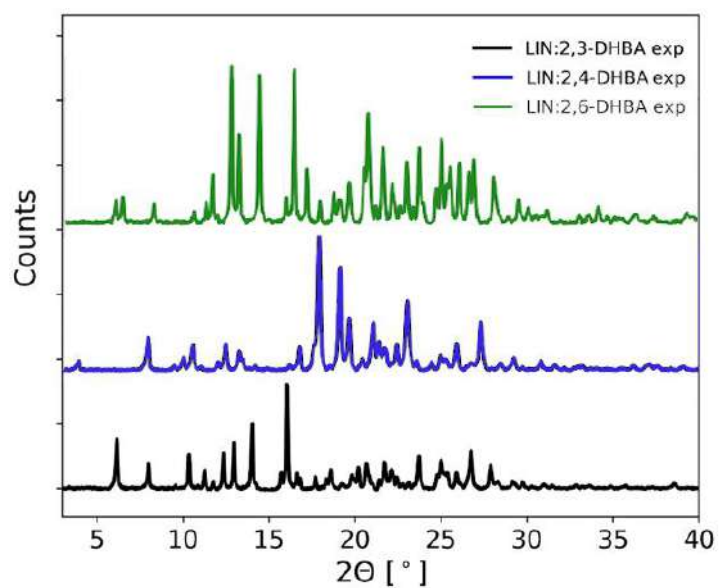
Mehrnaz Khalaji, Piotr Paluch, Marek J. Potrzebowski, Marta K. Dudek

Centre of Molecular and Macromolecular Studies, Polish Academy of Sciences, Sienkiewicza 112, 90-363 Lodz, Poland, e-mail: mdudek@cbmm.lodz.pl

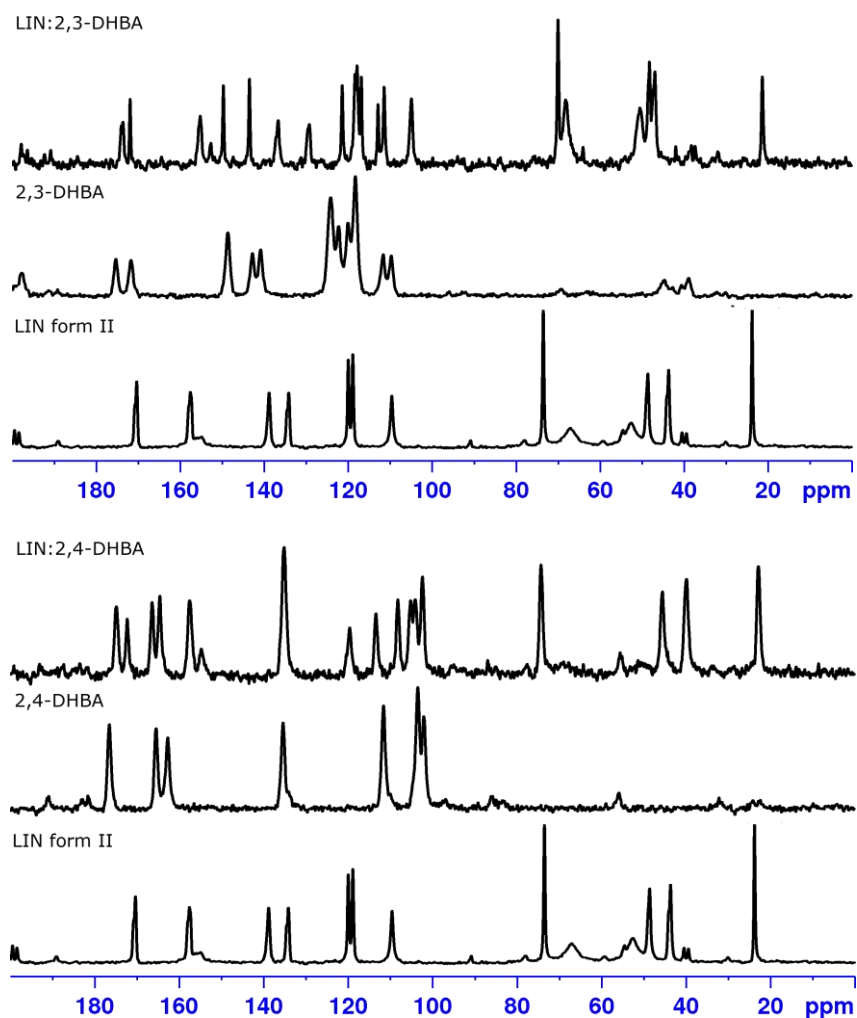
Content

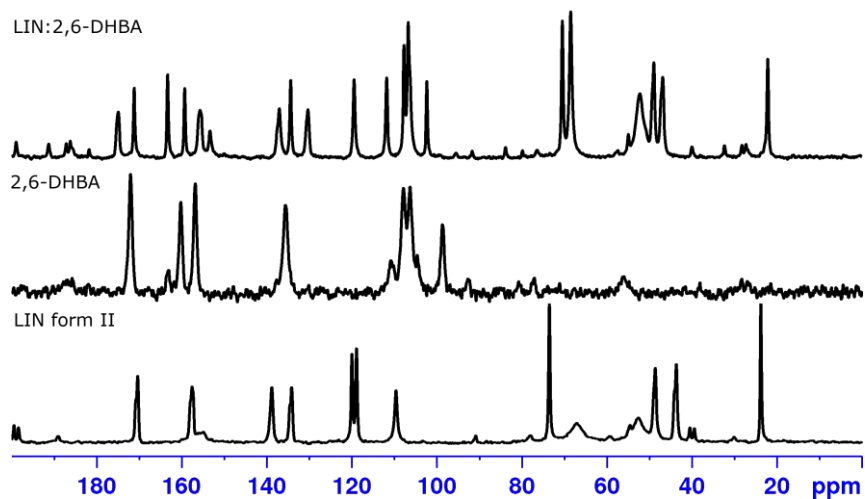
1. PXRD data for three cocrystals of LIN
2. ^{13}C CPMAS NMR spectra for pure components and three cocrystals of LIN
3. DSC and TGA plots for LIN:2,3-DHBA and LIN:2,4-DHBA cocrystals
4. Mogul search results
5. Conformational search results and list of considered conformations
6. ^1H - ^{14}N D-HMQC NMR spectrum for LIN:2,3-DHBA
7. Comparison of ^1H MAS and ^1H - ^1H SQ-DQ NMR spectra for LIN:2,3-DHBA and LIN:2,6-DHBA
8. Table S4. Calculated and experimental values of the chemical shifts for the three cocrystals and for structural models of 2,3-DHBA
9. Table S5. a, b, and a correlation coefficient (R^2) values obtained for LIN:2,3-DHBA models, together with the corresponding RMSD value and ^1H and ^{13}C RMSD values for LIN:2,4-DHBA models.
10. Table S6. Comparison of ^1H RMSD values calculated for chemical shift of LIN only for selected model structures of LIN:2,4-DHBA fully optimized (first column) and partially optimized (second column).
11. A full CSP energy landscape obtained for LIN:2,4-DHBA (CSP search in 4 most common chiral space groups, 56 combinations of conformations of LIN and 2,4-DHBA)

1. PXRD data for three cocrystals of LIN

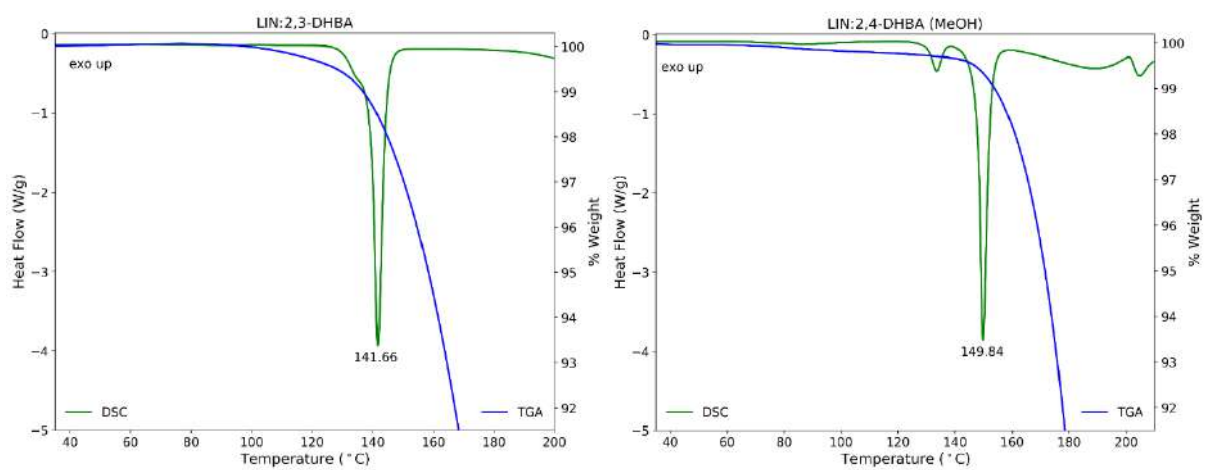


2. ^{13}C CPMAS NMR spectra for pure components and three cocrystals of LIN



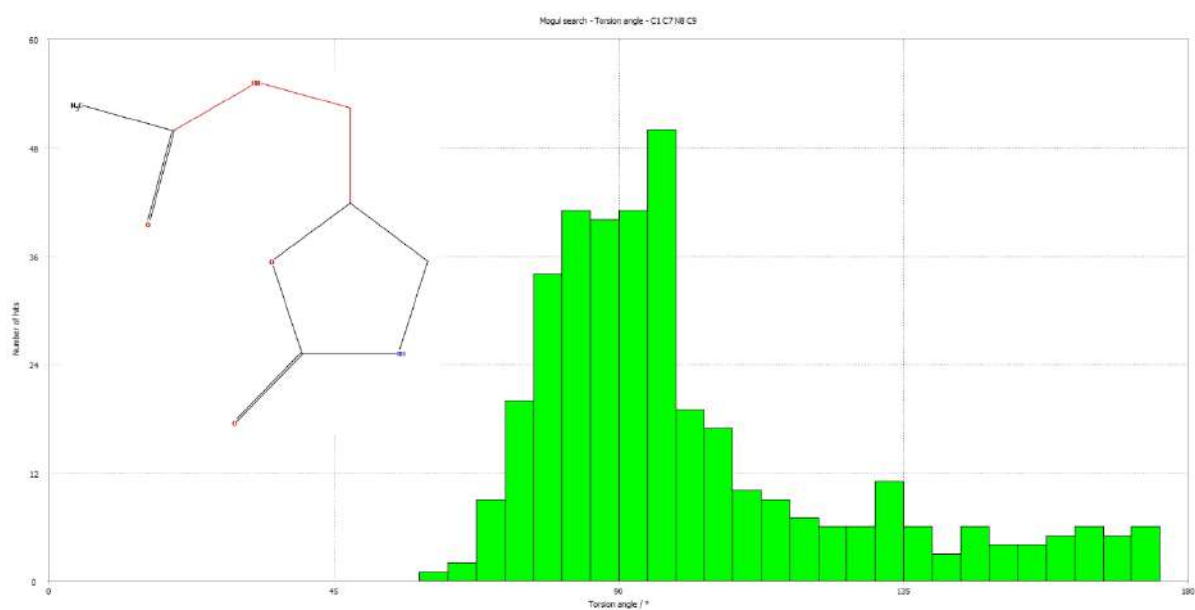


3. DSC and TGA plots for LIN:2,3-DHBA and LIN:2,4-DHBA cocrystals

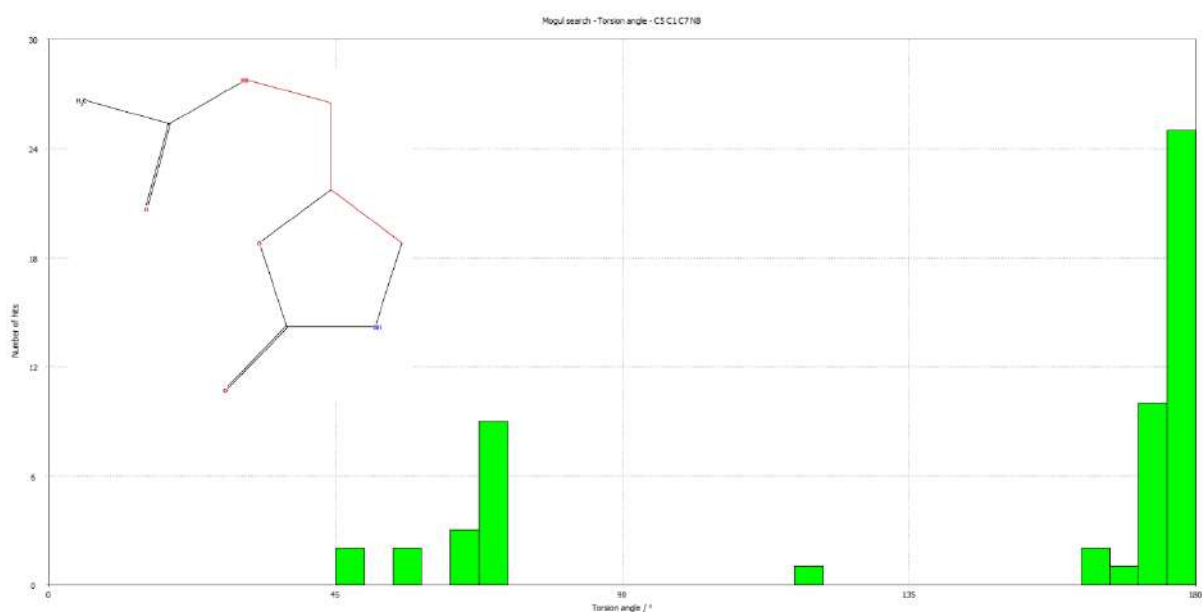


4. Mogul search results for four torsions of LIN

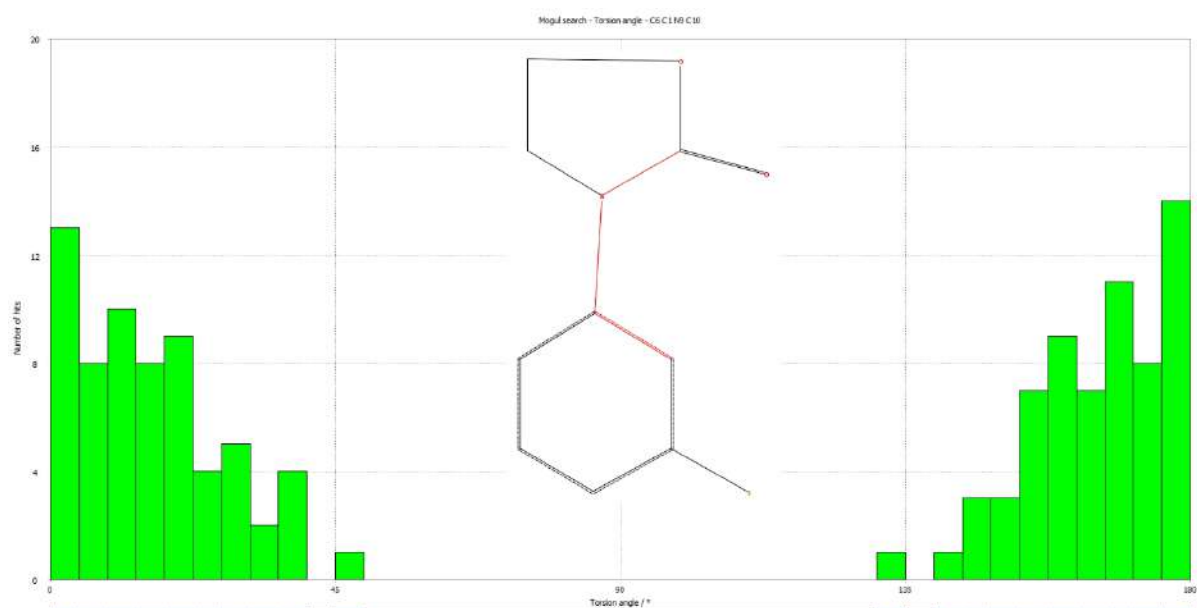
omega (C4-C3-NH-C2)



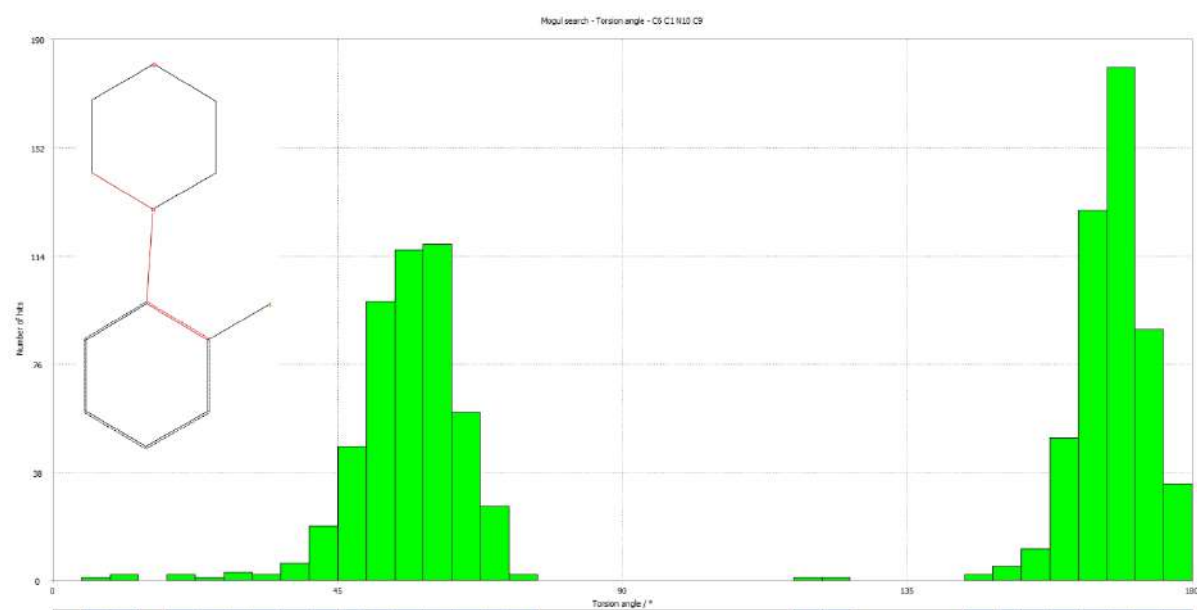
psi (NH-C3-C4-O2)



chi (C6-N2-C7-C8)



phi (C9-C10-N3-C13)



5. Conformational search results and list of considered conformations

Table S1. Gas phase energies obtained for 8 conformations of 2,3-DHBA. Bolded conformation is the one considered in a CSP search. Varied torsions are marked with grey arrows.

	E(Hartree)	E(kJ/mol)	relativeE(kJ/mol)
1	-571.4707	-1500396.202	0.00
2	-571.4646	-1500380.292	15.91
3	-571.4621	-1500373.707	22.50
4	-571.4564	-1500358.650	37.55
5	-571.4517	-1500346.525	49.68
6	-571.4508	-1500343.973	52.23
7	-571.4386	-1500311.994	84.21
8	-571.4383	-1500311.178	85.02



Table S2. Gas phase energies obtained for 10 conformations of 2,4-DHBA. Bolded conformations are the ones considered in a CSP search. Varied torsions are marked with grey arrows. In addition also hydroxyl proton position of COOH group was varied.

	E(Hartree)	E(kJ/mol)	relativeE(kJ/mol)
1	-571.4716	-1500398.706	2.03
2	-571.4658	-1500383.494	17.24
3	-571.4533	-1500350.671	50.06
4	-571.4521	-1500347.554	53.18
5	-571.4663	-1500384.837	15.90
6	-571.4724	-1500400.734	0.00
7	-571.4515	-1500345.835	54.90
8	-571.4525	-1500348.466	52.27
9	-571.455	-1500354.989	45.75
10	-571.4533	-1500350.606	50.13

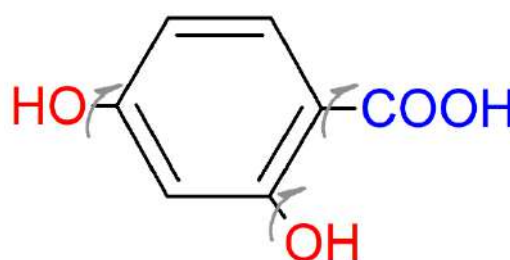
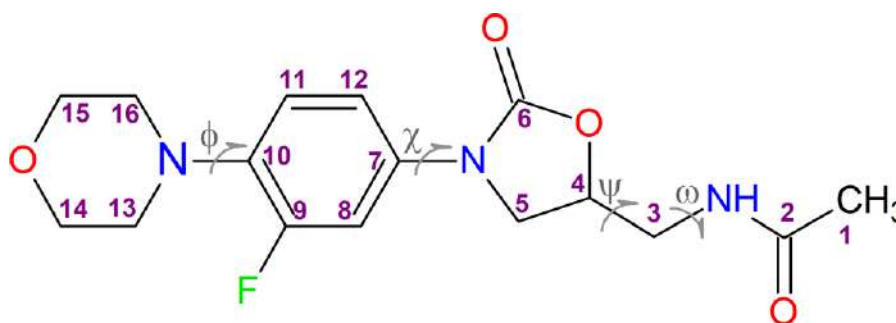


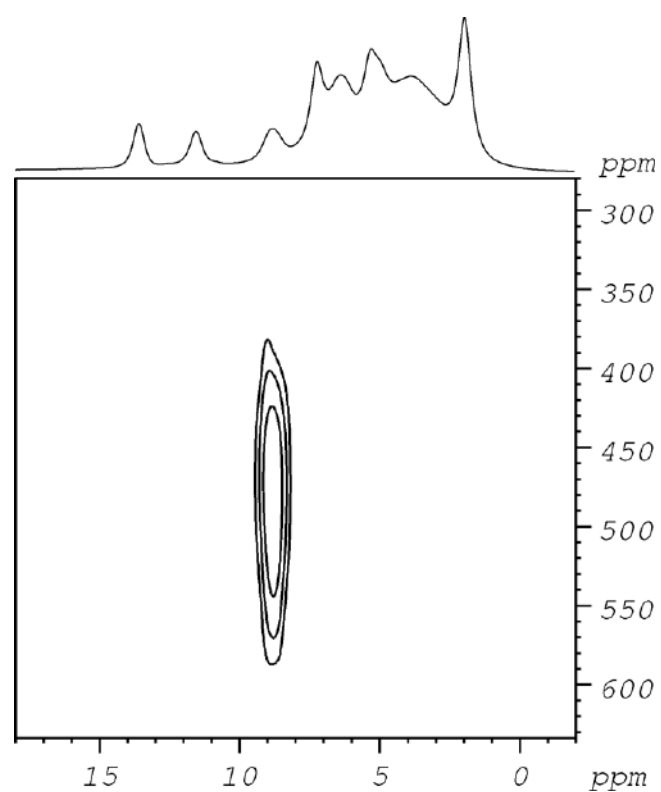
Table S3. List of ω , ψ , χ and ϕ values in considered in a CSP search conformations of LIN together with gas phase energies (for the definition of the torsions see figure below). Bolded conformations are those selected for the final stage of calculations.



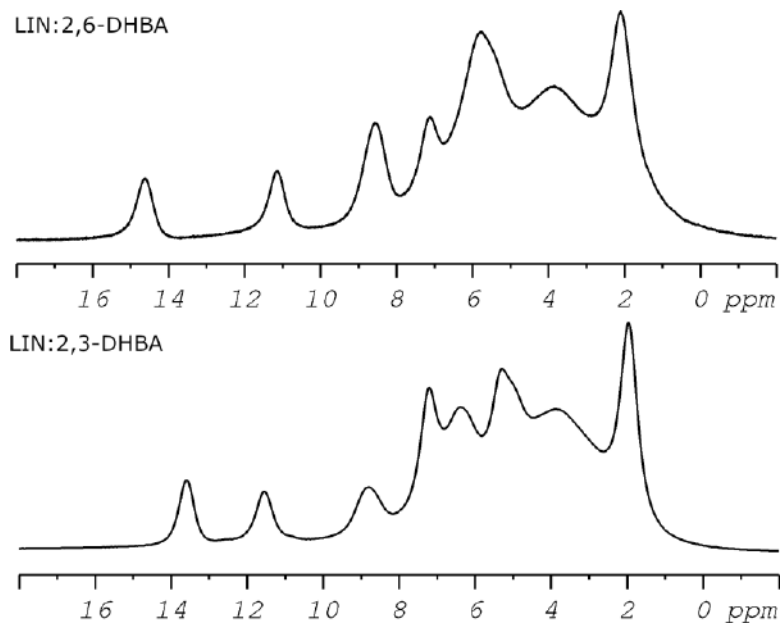
conformation	E(Hartree)	E(kJ/mol)	relative (kJ/mol)	ω	ψ	χ	ϕ
lc1	-1187.149366	-3116861	24.73	-50	-60	-170	-60

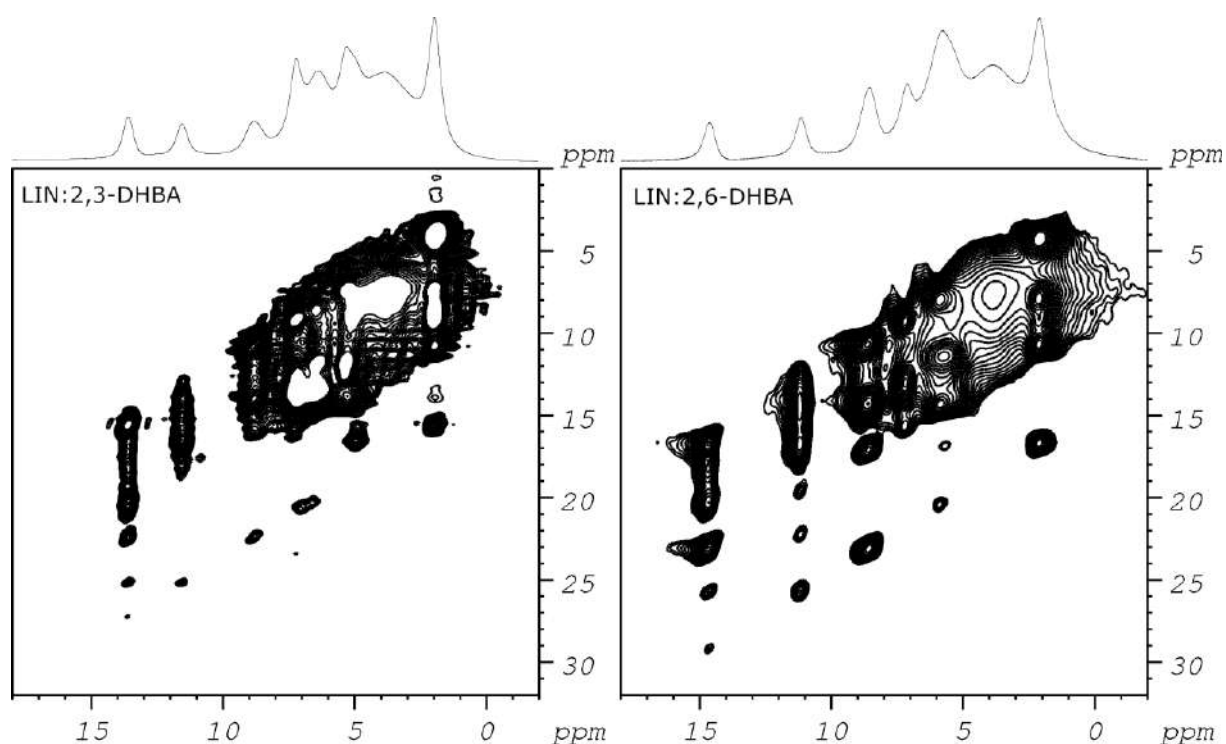
lc2	-1187.152272	-3116868	17.10	-95	-60	-170	-60
lc3	-1187.15163	-3116867	18.79	-140	-60	-170	-60
lc4	-1187.148929	-3116860	25.88	175	-60	-170	-60
lc5	-1187.145321	-3116850	35.35	85	-60	-170	-60
lc6	-1187.148509	-3116858	26.98	-50	-60	-170	-150
lc7	-1187.151403	-3116866	19.38	-95	-60	-170	-150
lc8	-1187.15076	-3116864	21.07	-140	-60	-170	-150
lc9	-1187.148062	-3116857	28.15	175	-60	-170	-150
lc10	-1187.144479	-3116848	37.56	85	-60	-170	-150
lc11	-1187.14829	-3116858	27.55	-50	-170	-170	-60
lc12	-1187.151539	-3116866	19.02	-95	-170	-170	-60
lc13	-1187.063958	-3116636	248.97	-140	-170	-170	-60
lc14	-1187.144482	-3116848	37.55	175	-170	-170	-60
lc15	-1187.148811	-3116859	26.19	85	-170	-170	-60
lc16	-1187.147451	-3116856	29.76	-50	-170	-170	-150
lc17	-1187.150755	-3116864	21.08	-95	-170	-170	-150
lc18	-1187.146995	-3116854	30.95	-140	-170	-170	-150
lc19	-1187.143633	-3116846	39.78	175	-170	-170	-150
lc20	-1187.147951	-3116857	28.45	85	-170	-170	-150
lc21	-1187.149448	-3116861	24.51	-50	-60	-170	60
lc22	-1187.152324	-3116868	16.96	-95	-60	-170	60
lc23	-1187.151678	-3116867	18.66	-140	-60	-170	60
lc24	-1187.148969	-3116860	25.77	175	-60	-170	60
lc25	-1187.145446	-3116850	35.02	85	-60	-170	60
lc26	-1187.148331	-3116858	27.45	-50	-170	-170	60
lc27	-1187.151681	-3116867	18.65	-95	-170	-170	60
lc28	-1187.147889	-3116857	28.61	-140	-170	-170	60
lc29	-1187.144566	-3116848	37.33	175	-170	-170	60
lc30	-1187.148865	-3116859	26.05	85	-170	-170	60
lmin	-1187.158785	-3116885	0.00	90	60	0	60

6. ^1H - ^{14}N D-HMQC NMR spectrum for LIN:2,3-DHBA



7. Comparison of ^1H MAS and ^1H - ^1H SQ-DQ MAS NMR spectra for LIN:2,3-DHBA and LIN:2,6-DHBA





8. Table S4. Experimental and calculated ^1H and ^{13}C chemical shift values for LIN:2,6-DHBA, LIN:2,3-DHBA and LIN:2,4-DHBA

LIN:2,6-DHBA				
experiment			calculations	
site	$\delta(^{13}\text{C})$	$\delta(^1\text{H})$	$\delta(^{13}\text{C})^*$	$\delta(^1\text{H})^{**}$
C1	21.82	2.10	19.59	2.53
C2	174.59	8.74 (NH)	172.83	8.99
C3	46.48	3.49	46.70	3.88
C4	70.13	5.35	72.51	5.66
C5	48.60	4.39	49.17	4.18
C6	155.40		152.92	
C7	129.97		128.61	
C8	106.17	6.20	105.57	6.05
C9	153.01		158.36	
C10	136.70		136.60	
C11	119.13	6.10	118.94	5.72
C12	111.49	7.12	110.91	6.78
C13	52.02	3.23	49.90	3.27
C14	68.18	4.10	70.73	4.05
C15	68.18	4.60	70.35	4.77
C16	52.02	4.00	52.45	4.22
C1'	102.03		101.54	
C2'	163.01	11.51 (OH)	165.35	11.53

C3'	107.40	5.71		106.32	5.32
C4'	134.07	5.65		134.22	5.29
C5'	106.42	5.84		105.65	5.62
C6'	159.01	8.59 (OH)		160.85	8.60
C7'	170.89	14.63 (COOH)		172.12	14.70
* $\delta(^{13}\text{C})_{\text{calc}} = (\sigma(^{13}\text{C})_{\text{calc}} - 172.42) / -1.0181$					
** $\delta(^1\text{H})_{\text{calc}} = (\sigma(^1\text{H})_{\text{calc}} - 30.923) / -1.1156$					
LIN:2,3-DHBA					
experiment					
site	$\delta(^{13}\text{C})$	$\delta(^1\text{H})$			
C1	21.94	1.96			
C2	174.34	8.79 (NH)			
C3	47.5	3.74			
C4	70.60	5.25			
C5	48.78	4.32	3.75		
C6	155.85				
C7	129.87				
C8	105.54	6.29			
C9	153.43				
C10	137.26				
C11	118.93	6.22			
C12	112.00	7.21			
C13	49.12	3.98			
C14	68.69				
C15	68.69				
C16	51.11	3.98			
C1'	113.46				
C2'	150.29	4.88 (OH)			
C3'	144.10	11.55 (OH)			
C4'	118.45	5.35			
C5'	117.47	6.52			
C6'	122.01	7.03			
C7'	172.51	13.60 (COOH)			
calculated $\delta(^1\text{H})$ values					
	CSP-1	CSP-2	CSP-3	M-1	
H1	2.08	2.42	1.36	2.35	
H3a	3.97	4.12	3.80	4.08	
H3b	3.63	3.89	3.50	4.06	
H4	5.58	5.48	5.69	5.60	
H5a	4.27	4.33	4.01	4.29	
H5b	4.06	4.06	3.80	4.16	
H8	5.90	5.87	6.17	5.87	
H11	5.91	5.78	6.33	5.73	
H12	7.20	6.63	7.31	6.67	
NH	9.51	9.16	10.05	9.10	

H2'(OH)	11.94	12.19	13.57	12.25
H3'(OH)	5.38	4.87	4.78	4.82
H4'	5.38	5.13	5.76	5.00
H5'	5.50	6.12	5.89	6.06
H6'	6.50	6.43	6.81	6.43
H7'(COOH)	13.48	13.73	11.36	13.72
calculated $\delta(^{13}\text{C})$ values				
	CSP-1	CSP-2	CSP-3	M-1
C1	21.68	21.25	23.82	20.45
C2	173.93	172.17	176.05	172.24
C3	49.96	47.04	47.43	46.09
C4	71.59	73.47	72.23	73.46
C5	49.63	49.44	49.30	49.71
C6	152.76	153.04	152.21	153.44
C7	129.19	127.78	129.61	127.48
C8	103.62	104.61	103.44	105.24
C9	158.86	158.43	159.51	157.77
C10	134.61	135.76	134.88	135.44
C11	118.11	117.97	118.71	118.37
C12	113.66	111.42	112.79	111.72
C13	50.22	47.70	48.21	47.63
C14	69.53	70.67	70.78	71.07
C15	68.62	69.62	68.80	70.02
C16	49.55	51.42	50.57	52.02
C1'	111.58	112.25	110.98	112.47
C2'	152.94	152.53	152.54	152.37
C3'	147.30	145.88	146.59	145.84
C4'	115.87	116.04	116.57	117.07
C5'	115.05	117.55	113.99	117.26
C6'	119.42	121.21	120.45	120.50
C7'	174.17	174.74	172.67	174.38
LIN:2,4-DHBA				
experiment				
site	$\delta(^{13}\text{C})$	$\delta(^1\text{H})$		
C1	22.42	2.04		
C2	174.46	9.33 (NH)		
C3	45.14	2.04	3.45	
C4	73.93	4.22		
C5	39.45	4.10	3.90	
C6	157.18			
C7	134.78			
C8	104.82	5.92		
C9	154.40			
C10	134.78			
C11	119.25	5.76		

C12	113.01	8.04	
C13			
C14			
C15			
C16			
C1'	103.72		
C2'	166.07	10.9* (OH)	
C3'	102.00	6.07	
C4'	164.22	10.0* (OH)	
C5'	107.82	4.49	
C6'	134.78	7.13	
C7'	171.93	10.3* (COOH)	

* these signals are interchangeable

9. **Table S5.** a, b, and a correlation coefficient (R^2) values obtained for LIN:2,3-DHBA models, together with the corresponding RMSD value and ^1H and ^{13}C RMSD values for LIN:2,4-DHBA models.

LIN:2,3-DHBA				
model	a	b	R^2	RMSD
^1H data				
CSP-1	-1.1111	-31.01	0.9802	0.412
CSP-2	-1.2264	-31.555	0.9828	0.384
CSP-3	-0.9435	-30.129	0.9180	0.867
M-1	-1.2151	-31.527	0.9806	0.409
^{13}C data				
CSP-1	-1.0242	173.52	0.9975	2.17
CSP-2	-1.0239	173.44	0.9981	1.91
CSP-3	-1.0242	173.29	0.9975	2.20
M-1	-1.0265	173.72	0.9982	1.85
LIN:2,4-DHBA first step				
model	^1H RMSD (for LIN $\delta^1\text{H}$ only)		relative DFT energy (kJ/mol)	
lc11o6s1n_4	0.92		58.27	
lc12o1s1_19	0.57		23.98	
lc12o1s1_4	0.96		32.45	
lc12o1s1_5	1.00		31.50	
lc12o6s1_19	0.61		32.03	
lc12o6s1n_4	0.32		41.55	
lc15o1s1_19	0.78		9.28	
lc15o1s1_5	1.40		10.01	
lc15o1s1n_1	1.70		19.99	
lc15o1s1n_4	1.08		21.79	
lc15o6s1_19	0.52		7.44	
lc15o6s1_4	0.94		22.80	
lc17o1s1_19	0.61		19.75	

lc17o1s1_4	1.53	23.71
lc17o6s1_19	0.88	10.33
lc17o6s1n_4	0.97	21.84
lc1o6s1_19	0.60	20.89
lc1o6s1n_4	0.72	22.05
lc20o1s1n_4	1.04	16.65
lc20o6s1_19	1.20	35.79
lc21o6s1_19	0.53	15.70
lc21o6s1_4	1.68	22.07
lc22o1s1_19	0.93	22.15
lc22o1s1_5	1.33	18.06
lc22o1s1n_4	1.29	42.19
lc22o6s1_19	0.60	15.81
lc22o6s1_5	0.74	16.95
lc22o6s1n_4	0.66	38.39
lc23o1s1_19	0.69	9.18
lc23o1s1_4	0.90	39.85
lc23o1s1_5	1.25	37.47
lc23o1s1n_1	1.31	11.75
lc23o6s1_19	1.32	11.05
lc23o6s1_5	0.61	5.22
lc23o6s1n_1	0.70	13.08
lc23o6s1n_4	1.24	28.04
lc24o6s1_19	1.42	39.46
lc26o6s1_4	0.61	1.17
lc27o1s1_19	0.78	18.85
lc27o1s1_5	0.90	24.76
lc27o6s1_19	0.54	36.29
lc27o6s1_5	0.58	11.42
lc27o6s1n_4	0.49	48.58
lc2o1s1_19	1.82	35.31
lc2o1s1_5	1.66	33.98
lc2o1s1n_1	0.74	25.73
lc2o1s1n_4	0.56	12.39
lc2o6s1_19	1.79	22.82
lc2o6s1_4	0.78	39.52
lc2o6s1_5	1.52	45.25
lc2o6s1n_1	0.62	7.08
lc30o1s1_19	0.97	5.50
lc30o1s1_4	1.99	20.11
lc30o1s1_5	0.78	12.29
lc30o6s1_19	0.85	2.70
lc30o6s1_4	0.75	20.30
lc3o1s1_19	1.51	10.46
lc3o1s1_4	2.09	40.18

lc3o1s1_5	1.70	16.77	
lc3o1s1n_1	1.17	25.96	
lc3o6s1_19	0.48	33.41	
lc3o6s1_5	0.82	9.80	
lc3o6s1n_1	0.76	5.10	
lc3o6s1n_4	1.38	30.82	
lc4o1s1_19	0.58	0.00	
lc4o6s1_4	0.80	26.04	
lc6o6s1_19	1.27	15.48	
lc7o1s1_19	0.71	29.58	
lc7o1s1_5	1.43	18.04	
lc7o1s1n_4	0.68	34.62	
lc7o6s1_19	1.28	34.04	
lc7o6s1_4	0.65	40.47	
lc8o1s1_19	1.03	14.74	
lc8o1s1n_4	2.04	28.66	
lc8o6s1_19	1.15	26.73	
lc8o6s1_5	0.63	5.00	
lc8o6s1n_4	1.20	28.27	
lc9o6s1_19	1.43	39.86	
lmin1s1_19	1.72	17.54	
lmin1s1_4	2.96	22.72	
lmin6s1_19	1.63	15.51	
lmin6s1_4	1.49	13.38	
LIN:2,4-DHBA second step			
model	¹ H RMSD (for LIN δ ¹ H only)	¹³ C RMSD (for LIN δ ¹³ C only)	relative DFT energy (kJ/mol)
lc12o1s10_19	0.67	2.92	47.10
lc12o1s11_19	0.86	2.53	50.66
lc12o1s12_19	0.64	2.23	33.77
lc12o1s13_19	0.73	2.24	14.92
lc12o1s2_19	0.89	3.09	38.85
lc12o1s2n_4	0.84	1.82	37.68
lc12o1s2nr_5	0.7	2.91	27.33
lc12o1s3_19	0.73	2.5	27.01
lc12o1s3n_4	0.99	2.82	41.33
lc12o1s4_19	0.57	3.15	26.89
lc12o1s4_4	0.79	2.44	0.00
lc12o1s5_19	0.74	2.28	31.72
lc12o1s6_19	1.07	1.68	41.11
lc12o1s7_19	0.82	3.14	27.71
lc12o1s8_19	0.48	2.83	31.25
lc12o1s9_19	0.6	2.61	43.68
lc12o6s10_19	0.96	2.76	40.15
lc12o6s2_19	0.78	1.62	29.64

lc12o6s2n_4	0.53	2.42	28.83
lc12o6s3_19	0.75	2.50	26.79
lc12o6s3n_4	1.08	3.50	57.38
lc12o6s4_19	0.66	3.38	30.57
lc12o6s4_4	0.8	1.70	35.76
lc12o6s5_19	0.45	2.78	31.68
lc12o6s5_4	1.08	2.61	60.05
lc12o6s6_19	0.49	1.62	27.44
lc12o6s7_19	0.78	2.04	28.93
lc12o6s8_19	0.5	2.69	41.63
lc12o6s9_19	0.65	2.24	34.70
lc22o1s10_4	1.75	2.25	42.89
lc22o1s2_19	1.82	1.98	31.28
lc22o1s2_4	0.86	1.69	27.82
lc22o1s2n_5	1.66	3.03	72.31
lc22o1s3_19	0.57	2.63	15.51
lc22o1s3n_4	0.68	2.24	33.80
lc22o1s3n_5	2.41	3.77	77.16
lc22o1s4_19	0.99	1.18	45.44
lc22o1s4n_4	0.7	1.8	49.39
lc22o1s5n_4	2.24	2.75	35.13
lc22o1s6_4	0.52	1.49	10.13
lc22o1s7n_4	0.51	2.27	49.76
lc22o1s8_4	0.53	2.70	17.48
lc22o1s9n_4	0.93	2.45	29.06
lc22o6s2_19	1.12	2.30	22.21
lc22o6s2_5	0.56	2.18	6.24
lc22o6s2n_4	0.8	3.07	30.34
lc22o6s3_19	0.95	2.43	28.18
lc22o6s3_4	0.59	2.79	48.64
lc22o6s4_19	1.01	2.64	19.82
lc22o6s4_4	0.81	2.48	22.58
lc22o6s5_19	1.43	1.96	21.91
lc27o6s2_19	0.61	3.82	19.01
lc27o6s2_5	0.8	1.96	5.72
lc27o6s2n_4	1	1.52	24.13
lc27o6s3_19	0.36	2.38	11.52
lc27o6s3_4	0.4	3.02	17.50
lc27o6s3_5	1.6	2.26	33.64
lc27o6s4_19	0.53	2.93	18.42
lc27o6s4_4	0.99	4.1	6.32
lc27o6s5n_4	0.52	2.30	9.82
lc27o6s6n_4	0.71	2.52	6.86
lc27o6s7_4	0.69	2.7	32.18
lc27o6s8_4	1.14	2.94	21.69

lc27o6s9_4	0.7	1.63	21.62
lc2o1s2_19	0.81	1.69	1.34
lc2o1s2_4	1.63	1.37	30.53
lc2o1s2_5	0.72	2.41	34.13
lc2o1s2n_1	1.62	1.92	38.25
lc2o1s3_5	1.51	2.09	48.09
lc2o1s3n_1	1.27	1.79	52.86
lc2o1s3n_4	1.24	2.91	23.65
lc2o1s4_19	0.87	2.27	6.96
lc2o1s4_5	1.48	1.91	44.30
lc2o1s4n_1	0.77	1.92	19.89
lc2o1s4n_4	1.28	2.36	34.51
lc2o1s5_19	0.78	2.64	35.19
lc2o1s5n_1	1.51	2.49	46.47
lc2o1s6_19	0.72	2.23	13.68
lc2o1s6n_1	0.8	1.86	25.83
lc2o1s7_19	1.23	1.85	20.56
lc2o1s8_19	0.99	2.35	34.33
lc2o6s10_19	0.53	1.49	53.19
lc2o6s10_4	0.97	2.26	35.60
lc2o6s11_4	1.46	1.51	41.35
lc2o6s2_19	1.14	3.11	8.11
lc2o6s2_4	0.95	2.64	33.08
lc2o6s2_5	1.46	1.62	45.23
lc2o6s2n_1	1.69	1.88	12.99
lc2o6s3_19	0.76	2.39	30.39
lc2o6s3_4	0.82	1.31	23.00
lc2o6s3_5	0.75	2.48	34.74
lc2o6s3n_1	1.49	1.98	53.05
lc2o6s4_19	0.87	1.71	26.77
lc2o6s4_4	2.14	2.27	31.01
lc2o6s4_5	1.06	1.98	23.80
lc2o6s4n_1	0.58	1.99	25.01
lc2o6s5_19	0.72	3.21	31.85
lc2o6s5_4	1.79	2.59	28.42
lc2o6s5_5	1.06	1.93	5.69
lc2o6s5n_1	1.51	2.41	59.55
lc2o6s6_1	0.67	1.98	39.81
lc2o6s6_19	0.7	2.13	27.17
lc2o6s6_4	0.7	3.12	24.64
lc2o6s6_5	1.48	2.25	31.72
lc2o6s7_19	0.74	2.44	7.94
lc2o6s7_4	1.86	2.11	30.46
lc2o6s7nr_5	0.8	2.06	26.63
lc2o6s8_19	0.82	2.60	17.30

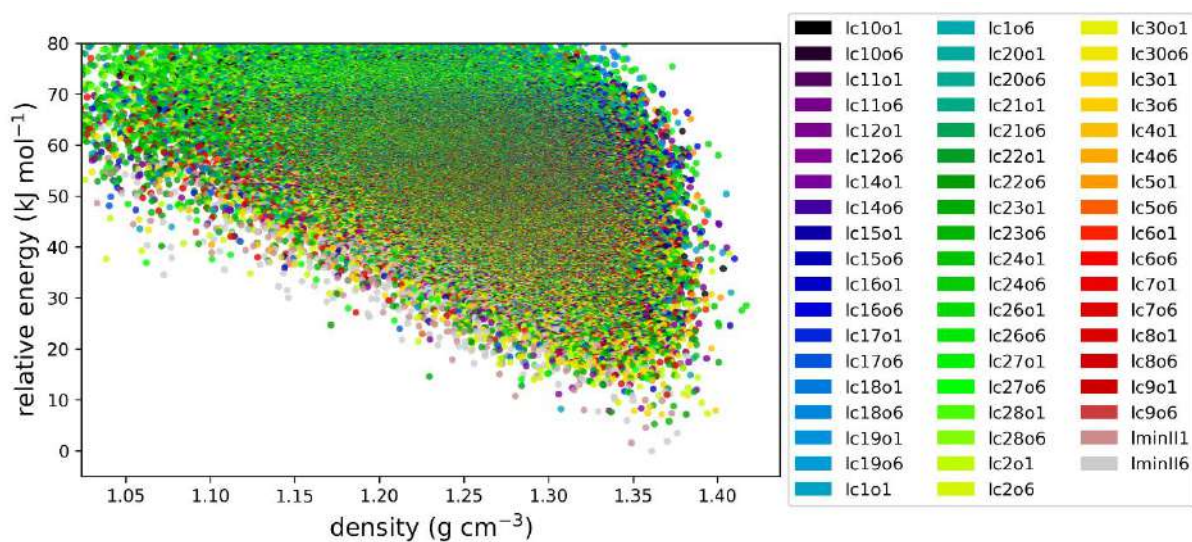
lc2o6s8_4	1.2	1.43	21.97
lc2o6s9_19	0.77	2.44	30.21
lc2o6s9_4	1.56	2.75	27.32
lc7o1s2_19	1.48	1.61	31.29
lc7o1s2n_4	1.02	3.09	54.49
lc7o1s3_4	1.25	1.78	42.95
lc7o1s4n_4	1.34	1.87	42.20
lc7o1s5_4	0.54	2.19	49.36
lc7o1s6_4	2.37	2.56	34.87
lc7o6s2_19	0.93	2.24	26.93
lc7o6s2_4	1.84	2.76	24.89
lc7o6s3n_4	0.54	2.14	33.15
lc7o6s4n_4	0.6	2.77	48.62

10. Table S6. Comparison of ^1H RMSD values calculated for chemical shift of LIN only for selected model structures of LIN:2,4-DHBA fully optimized (first column) and partially optimized (second column). Bolded font mark two structures for which the largest differences between two sets of data were noticed.

model	^1H RMSD	
	fully optimized	partially optimized
lc12o1s1_19	0.57	0.67
lc12o1s1_4	0.96	0.91
lc12o6s1_19	0.61	0.66
lc12o6s1n_4	0.32	0.36
lc15o1s1_19	0.78	0.77
lc15o6s1_19	0.52	0.58
lc17o1s1_19	0.61	0.66
lc17o6s1n_4	0.97	0.99
lc1o6s1_19	0.60	0.68
lc1o6s1n_4	0.72	0.7
lc20o1s1n_4	1.04	1.08
lc21o6s1_19	0.53	0.63
lc21o6s1_4	1.68	1.69
lc22o1s1n_4	1.29	1.08
lc22o6s1_19	0.60	0.55
lc22o6s1_5	0.74	0.78
lc22o6s1n_4	0.66	0.64
lc23o1s1_19	0.69	1.26
lc23o6s1_5	0.61	0.75
lc23o6s1n_1	0.70	0.72
lc23o6s1n_4	1.24	1.2
lc26o6s1_4	0.61	0.57
lc27o6s1_19	0.54	0.48
lc27o6s1_5	0.58	0.48

lc27o6s1n_4	0.49	0.37
lc2o1s1n_1	0.74	0.64
lc2o1s1n_4	0.56	0.56
lc2o6s1_4	0.78	0.75
lc2o6s1_5	1.52	1.46
lc2o6s1n_1	0.62	0.67
lc30o6s1_4	0.75	0.81
lc3o1s1_4	2.09	2.02
lc3o1s1n_1	1.17	1.17
lc3o6s1n_1	0.76	0.89
lc3o6s1n_4	1.38	1.2
lc4o1s1_19	0.58	1.62
lc7o1s1_19	0.71	0.73
lc7o1s1n_4	0.68	0.67
lc7o6s1_4	0.65	0.56
lc8o1s1_19	1.03	1.07
lc8o6s1_19	1.15	1.11
lc8o6s1_5	0.63	0.85
lmin1s1_19	1.72	1.92
lmin1s1_4	2.96	2.86

11. A full CSP energy landscape obtained for LIN:2,4-DHBA (CSP search in 4 most common chiral space groups, 56 combinations of conformations of LIN and 2,4-DHBA)



T4:

Narrowing down the conformational space with solid-state NMR in crystal structure prediction of linezolid cocrystals, Khalaji, M., Paluch, P., Potrzebowski, M.J., Dudek, M.K., Solid State Nuclear Magnetic Resonance, 2022, 121, 101813

Unexpected Factors Affecting the Kinetics of Guest Molecule Release from Investigation of Binary Chemical Systems Trapped in a Single Void of Mesoporous Silica Particles

Katarzyna Trzeciak,^[a] Ewelina Wielgus,^[a] Sławomir Kaźmierski,^[a] Mehrnaz Khalaji,^[a] Marta K. Dudek,^{*,[a]} and Marek J. Potrzebowski^{*,[a]}

In this work, we present results for loading of well-defined binary systems (cocrystal, solid solution) and untreated materials (physical mixtures) into the voids of MCM-41 mesoporous silica particles employing three different filling methods. The applied techniques belong to the group of “wet methods” (diffusion supported loading – DiSupLo) and “solvent-free methods” (mechanical ball-mill loading – MeLo, thermal solvent free – TSF). As probes for testing the guest1-guest2 interactions inside the MCM-41 pores we employed the benzoic acid (BA), perfluorobenzoic acid (PFBA), and 4-fluorobenzoic acid (4-FBA).

The guests intermolecular contacts and phase changes were monitored employing magic angle spinning (MAS) NMR Spectroscopy techniques and powder X-ray diffraction (PXRD). Since mesoporous silica materials are commonly used in drug delivery system research, special attention has been paid to factors affecting guest release kinetics. It has been proven that not only the content and composition of binary systems, but also the loading technique have a strong impact on the rate of guests release. Innovative methods of visualizing differences in release kinetics are presented.

Introduction

Mesoporous silica particles (MSPs) have recently gained much attention as catalyst carriers,^[1] drug transport systems,^[2] and even as effective nanoreactors.^[3] Originally, MSPs were introduced by Mobil Corporation in 1992 as catalysts and catalyst supports. Over the past three decades, they have found a plethora of applications in this field due to their exceptional physical properties and high chemical stability. Recent review of Singh *et al.* summarizes progress and achievements in this branch of chemistry.^[4]

Very quickly, MSPs also became an attractive drug delivery vehicle offering decreased drug precipitation, improved solubility, and a choice of several different administration paths. The field of drug delivery systems (DDSs) is growing very quickly, becoming one of the most profitable areas in the pharmaceutical industry. MSPs offer unique geometrical features, such as high surface area and large pore size and volume, that can be further adapted to meet specific needs.^[5] Recently, MSPs have been approved as GRAS (generally recognized to be safe) drug carriers by the Food and Drug Administration (FDA).^[6]

The aim of our work is to answer the question whether it is possible to load two (or more) components into one MSP pore,

as well as to explore the influence of the loading method on the localization, interactions, and release ratio of the embedded guests. Recently, Gašperlin and coworkers have presented an overview of different loading techniques into the mesoporous silica nanoparticles.^[7] Generally, these techniques can be divided into two groups; solvent-free (SF) methods and methods using solvents (so-called wet methods). The SF methods offer several advantages. The filling factor in the final formulation is easily predicted, as it is directly influenced by the weight ratio between the compound used for loading and mesoporous materials. The concentrations of up to 50% are not unusual. Among the various SF techniques in laboratory practice, physical mixing,^[8] co-grinding,^[9] melting,^[10] and microwave irradiation^[11] are commonly used. The loading procedure employing solvent methods is more challenging. A crucial problem is a choice of a proper solvent for loading. The use of non-polar solvents (such as hexane) has been shown to result in a higher filling factor compared to polar solvents (such as dimethyl sulfoxide or methanol), regardless of the solubility of the chemicals under investigation.^[12] Among the wet methods, in particular the incipient wetness impregnation,^[13] solvent evaporation,^[14] supercritical and liquid carbon dioxide (CO₂) technology^[15] have found a plethora of applications. Their advantages and disadvantages (multi-stage and long-term processes, large amount of solvents used, difficult to control filling factor) have been exhaustively discussed in many articles.^[16]

Recently, in our laboratory, we have tested the effectiveness of various loading approaches, paying particular attention to the economic and ecological aspects of the process, with the intention of using laboratory solutions in future large-scale technologies. For obvious reasons the solvent-free methods

[a] Dr. K. Trzeciak, Dr. E. Wielgus, Dr. S. Kaźmierski, M. Khalaji, Prof. Assoc. M. K. Dudek, Prof. Dr. M. J. Potrzebowski
Centre of Molecular and Macromolecular Studies
Polish Academy of Sciences
Sienkiewicza Łódź, 112, 90-363 Łódź, Poland
E-mail: mdudek@cbmm.lodz.pl
marekpot@cbmm.lodz.pl



Supporting information for this article is available on the WWW under <https://doi.org/10.1002/cphc.202200884>

which fulfill the given supra requirements are the first choice. Our preliminary results showing the power of the melting method (which we called Thermal Solvent Free) and mechanochemical loading (acronym MeLo) with the use of shaking and planetary ball-mills were published elsewhere.^[17] Very recently we also reported a significant improvement of the wet method. The technique, which we called DiSupLo (Diffusion Supported Loading), employs and strengthens the advantages of wet methods and eliminates their drawbacks.^[18] DiSupLo is a fast, one-step process and requires a minimal amount of solvent. In the current contribution we are evaluating whether the loading method influences the behavior and interactions of the guest(s) trapped inside the pores of MCM-41, and demonstrating that, quite unexpectedly, they can have a decisive influence on the release ratio of the guest molecules. So far, in most of the projects related to the use of MSPs as carriers of chemical media, researchers have focused attention on embedding only one component into the pores. Attempts to introduce cocrystals or more complex ternary systems are relatively rare.^[18,19] Nevertheless, there are a number of publications showing binary systems loaded into mesoporous silica materials.^[20]

Among the various mesoporous silica particles, MCM-41 is the most widely studied material.^[21] It is often used as a model to compare with other particles or to study fundamental aspects in sorption, catalysis, drug delivery, etc. This mesoporous material is also a convenient object for studying thermal processes in a broad temperature range and analyzing phase transitions as well as the dynamics of guest molecules in a confined space.^[22] Such a wide range of applications is possible thanks to the unique features and simplicity and ease of preparation of the MCM-41. MCM-41 has a high surface area of up to 1200 m²/g and large pore volumes. The pores are very uniform causing narrow pore size distributions to be unidirectional and arranged in a honeycomb structure over micrometer length scales. The pore walls are quite thin with a thickness between 1 and 1.5 nm.^[23] The presence of these thin pore walls leads to low chemical and hydrothermal stabilities.

In this work, we also wish to check and test the possibility of trapping two (or more) components in one pore (common space) of MCM-41 employing three different loading methods discussed above; TSF, MeLo, and DiSupLo. Our studies are extended to the analysis of spontaneous solid state surface processes taking place without external stimuli. As model binary systems (guest molecules) we chose two well-defined, chemically similar binary systems; Benzoic Acid (BA) with Perfluoro Benzoic Acid (PFBA) and Benzoic Acid with 4-Fluor Benzoic Acid (4-FBA). The X-ray structures of both binaries BA:PFBA and BA:4-FBA were refined using single-crystals studies (sc X-ray). The choice of such systems for studying the loading process is motivated by the planned use of NMR spectroscopy as a primary tool for exploring guest behavior and controlling guest-guest as well guest-host interactions. In this case, as an analytical probe, we have in hand three $I = 1/2$ spins (¹H, ¹⁹F, ¹³C) which are sensitive and diagnostic markers of guest localization and dynamic processes inside the pores. Special attention was paid to the analysis of factors affecting dissolution and the

kinetics of guests release. Innovative methods of visualizing differences in release kinetics are shown and discussed.

Results and Discussion

Structure and Stability of BA:PFBA and BA:4-FBA Binaries in the Solid State

The solid state NMR study of BA:PFBA cocrystal employing ¹H, ¹⁹F, and ¹³C nuclei as diagnostic probes was reported in our previous paper.^[17b] Benzoic acid and pentafluorobenzoic acid readily form a cocrystal stabilized by two symmetry-unrelated heterodimers and strong face-to-face stacking interactions between BA and PFBA rings, propagating infinitely along the b direction (Figure 1a). Such stacking interaction between aryl and perfluoroaryl has been established as one of the important synthons in crystal engineering, due to an observed tendency to form such an arrangement in a variety of systems.^[24] 4-FBA forms with BA a solid solution rather than a cocrystal, in varying stoichiometric ratios, depending on the ratio of pure components taken for the crystallization experiments. This solid solution morphology is unique, and its crystal structure is different from the parent crystal structures.^[25] In our case, the crystallization experiments were carried out using a 1:1 BA:4-FBA stoichiometric ratio, and yielded a crystal structure with approximately 0.53:0.47 F/H occupancy at the C-4 site, as indicated by single crystal X-Ray measurements, PXRD and DSC data. Similarly, as in the case of BA:PFBA cocrystal, this solid solution structure is stabilized mainly by dimeric interactions between BA and 4-FBA molecules, but an additional stabilization seems to be provided primarily by directional C–H...F interactions between 4-F and 3-H site, instead of aromatic – aromatic stacking interactions (Figure 1b).

To the best of our knowledge solid solution of BA:4-FBA has never been investigated employing solid state NMR spectroscopy. Figure 2a depicts the spectra recorded with a different spinning rate under the magic angle; 60 kHz (¹H MAS), 25 kHz (¹⁹F MAS), and 8 kHz (¹³C CP/MAS). In particular, the ¹⁹F MAS spectra were found to provide important information

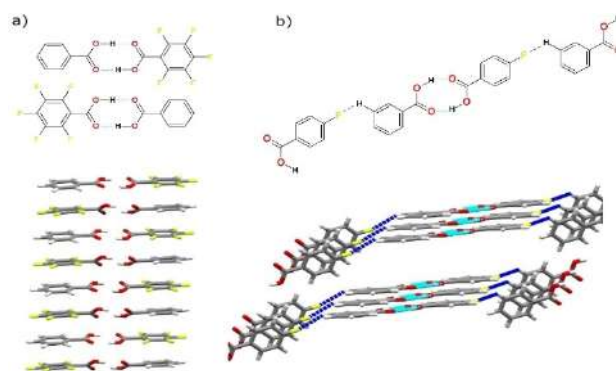


Figure 1. a) Aromatic – aromatic interactions stabilizing the crystal structure of BA:PFBA cocrystal and b) C–H...F interactions (marked with navy dashed lines) found in the crystal structure of 0.53:0.47 solid solution of BA:4-FBA.

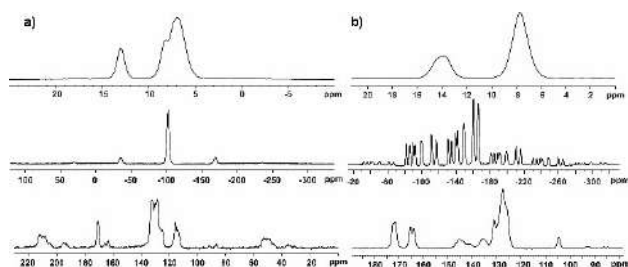


Figure 2. a) The Solid State NMR spectra: ^1H MAS (top), ^{19}F MAS (middle), and ^{13}C CP MAS (bottom) of BA:4-FBA solid solution recorded with a spinning rate of 60 kHz, 25 kHz, and 8 kHz, respectively. b) ^1H MAS (top), ^{19}F MAS (middle), and ^{13}C CP MAS (bottom) NMR spectra of BA:PFBA cocrystal, adapted with permission from Ref. [17b]. Copyright (2015) American Chemical Society.

and revealed significant differences between the two binaries, BA:PFBA^[17b] and BA:4-FBA.

BA:PFBA and BA:4-FBA Binaries Embedded into MCM-41 Employing TSF, MeLo, and DiSupLo Methods

In our recent work, we paid attention to a bi-modal nature of MCM-41 in mechano-loading (MeLo) of solid guest molecules, employing the BA and 4-FBA as reference samples.^[17c] It was found that depending on the host/guest ratio (weight to weight), guest molecules were embedded in different MCM-41 voids, including the internal space in the pores as well as an interstitial space. In this paper, checking the applicability of the three methods of loading (DiSupLo, MeLo, and TSF) and trying to provide the clear and concise description of loading processes, we limited the ratio of guests/MCM-41 to 1:2 (weight to weight).

Figure 3a (left) shows the ^{19}F MAS spectra recorded with a spinning rate of 24 kHz for BA:PFBA cocrystals embedded into MCM-41 pores with TSF, MeLo (without LA and with LA), and DiSupLo methods. The loading process was also controlled by ^1H MAS measurements (Figure 3b, right) which allows to follow the behavior of BA co-former. Analysis of ^1H and ^{19}F spectra clearly proves that in each procedure the guest ingredients are

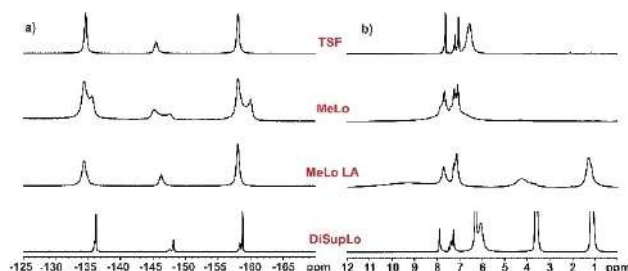


Figure 3. a) ^{19}F and b) ^1H MAS NMR spectra of BA:PFBA cocrystal embedded in MCM-41 (1:2 by weight) using TSF (top), MeLo (without LA and with LA – middle), and DiSupLo (bottom) methods. Spectra were recorded with a spinning rate of 24 kHz.

trapped inside the voids, which is also confirmed by the data from nitrogen adsorption-desorption measurements (specific surface area, porous volume, and average pore diameter) shown in Table S1 in Supporting Materials. Significant narrowing of ^1H resonances results from increased dynamics and decreased intermolecular interactions of molecules embedded into the MSPs. In particular, the ^1H resonance originating from carboxyl group is no longer visible when the studied acids are located inside the voids. However, it is worthy to note that the spectra are not identical. TSF gives the most homogeneous system which is represented by three relatively sharp lines (^{19}F ortho, meta, para positions). In the case of the sample obtained by the MeLo method, two different systems of both guest molecules, system X and system Y, are clearly visible. It should be noted, that both systems comprise both guest molecules each. The situation is different when ethanol is used as a LA in MeLo. Then, this ternary system becomes homogeneous and we observe the three ^{19}F lines again. Finally, DiSupLo gives very sharp resonance lines with two different systems visible. As can be seen, one system dominates, but traces of the other are also visible. The ^1H MAS spectra correlate very well with ^{19}F data. In addition, for samples after MeLo with LA and DiSupLo ^1H signals from ethanol are detectable.

The question that appears to be an intellectual and practical challenge concerns two problems. The first problem is associated with the location of the X and Y systems and determining whether these components are in one domain or in different spaces. This problem is particularly visible for BA:PFBA guest in a sample obtained by MeLo. The second problem concerns the nature of BA and PFBA contact in the MCM-41 voids (tight pair or split) and their arrangement to one another (similar to X-ray structure or different). To answer these questions we have carried out 2-dimensional NMR correlation experiments in homo- and hetero-nuclear modes based on Nuclear Overhauser Effect (NOESY).

Figure 4a shows ^{19}F - ^{19}F NOESY experiment for the sample obtained by the MeLo method. The measurements were performed with a broad range of mixing times, from 10 ms to 300 ms. There were no cross-peaks between the X and Y systems in any of the cases. It means that X and Y are located in separated domains of MCM-41 with distances larger than 10 Å.

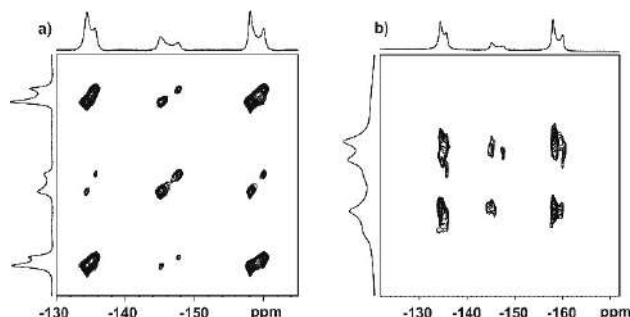


Figure 4. a) ^{19}F - ^{19}F NOESY MAS and b) ^1H - ^{19}F HOESY MAS spectra of BA:PFBA cocrystal embedded in MCM-41 (1:2 by weight) using the MeLo method (without LA) recorded at 12.5 kHz MAS with a mixing time of 20 ms and 350 ms, respectively.

The X and Y units are both composed of BA and PFBA components, and solving the problem of the structure of such a composite inside the pore requires the use of a different NMR tool. Figure 4b depicts the ^1H - ^{19}F HOESY spectrum for the same sample as shown in Figure 4a. The vertical axis shows the ^1H MAS spectrum representing the BA co-former while the horizontal axis displays the ^{19}F MAS spectrum for PFBA. The analysis of the ^1H - ^{19}F dipolar coupling constants shows that the range of observable distances for this pair of spins should be similar to that for the homonuclear systems (^1H - ^1H and ^{19}F - ^{19}F). The strong correlation peaks seen in the contour plot provide unambiguous evidence that BA and PFBA are in a close contact in both cases (X and Y). Moreover, the pattern of cross-peaks suggests a layered arrangement of both molecules in a similar alignment as seen in the crystal lattice. These conclusions regarding the structure of BA:PFBA inside the MCM-41 pores are also valid for samples obtained by TSF and DiSupLo methods.

In the next step, we have tested a similar system, BA:4-FBA solid solution with MCM-41. As in the case of BA:PFBA we have investigated the method of loading for samples with a guest:host ratio of 1:2 (weight to weight). Our previous research for an isolated particle, 4-FBA with MCM-41, showed that this ratio of components produces a homogeneous system with a well-defined guest localization, in one domain.^[17c]

Figure 5a (left column) depicts the ^{19}F MAS spectra for samples prepared employing MeLo (with LA and without LA), DiSupLo, and TSF methods. The corresponding ^1H MAS spectra are shown in the right column (Figure 5b). From the data analysis, we can conclude that for each method used, components of BA:4-FBA solid solution are embedded in the voids, while the presence of only one dominating ^{19}F resonance suggests that 4-FBA is preferably located in only one domain, in contrast to PFBA/MCM-41 sample obtained by MeLo, in which the guest clearly occupied two different domains. Unfortunately, the ^1H and ^{19}F 1D MAS spectra do not answer the question of whether the individual co-formers, BA and 4-FBA, are in a close contact or separate spaces. Moreover, it was found that the ^1H - ^{19}F HOESY experiment is not diagnostic because strong intra-molecular hetero-nuclear contacts dominate the spectral pattern. Thus, in this particular case, the ^1H - ^1H

NOESY correlation, due to the well-separated ^1H components for BA and 4-FBA particles in the 1D NMR spectra, is more informative. The ^1H resonances for ortho and meta positions of 4-FBA are found at $\delta=7.13$ ppm and $\delta=6.10$ ppm. For BA component the ortho, meta, and para signals are respectively at $\delta=7.13$ ppm, $\delta=6.48$ ppm, and $\delta=6.61$ ppm. As can be seen, the ortho signals for both components overlap, while the meta signal of 4-FBA is separated.

Figure 6a shows the expanded part of the ^1H - ^1H NOESY spectrum recorded with a spinning rate of 10 kHz and a mixing time of 750 ms for DiSupLo sample. From the analysis of correlation peaks, the interaction between meta protons of BA and meta protons of 4-FBA is apparent. The contact between the ortho protons BA and meta 4-FBA is not so obvious due to the overlapping of the ortho signals of both components, but we cannot exclude such interactions. Apparently, there is no cross-peak between the para proton of BA and the meta proton of 4-FBA. The study of the pattern of correlation peaks proves that both molecules are in one space, although their mutual arrangement is not easy to define. It is worth noting that both acids strongly interact with ethanol forming ternary system (Figure 6b). Ethanol was used as a transport medium in the DiSupLo procedure. NOESY cross-peak intensities do not provide accurate quantitative information on nuclei distances for dynamic systems with limited molecular motion, but in a semi-quantitative manner it can be assumed that 4-FBA is in a closer contact with ethanol. The NOESY cross-peaks pattern for sample obtained by means of TSF method is slightly different. In this case, we also see strong interaction between meta protons of 4-FBA and para protons of BA (Figure 6c). This means

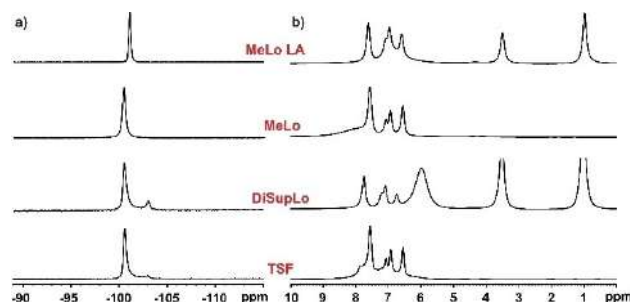


Figure 5. a) ^{19}F and b) ^1H MAS NMR spectra of BA:4-FBA solid solution embedded in MCM-41 (1:2 by weight) using TSF (bottom), DiSupLo (middle), MeLo (without LA – middle and with LA – top) methods. Spectra were recorded with a spinning rate of 24 kHz.

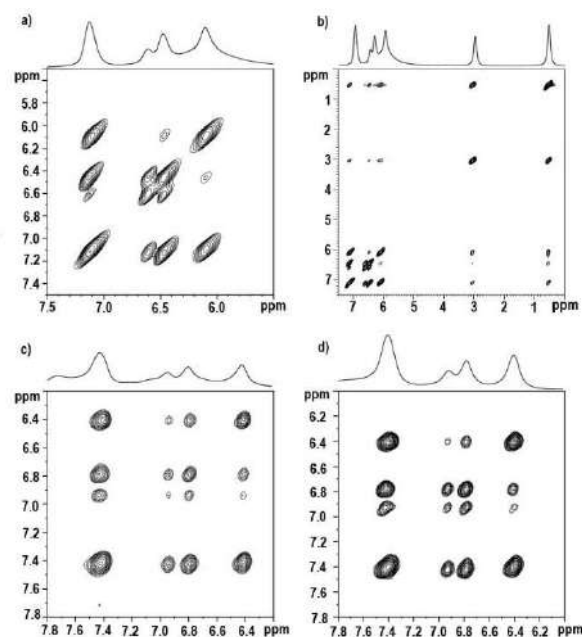


Figure 6. ^1H - ^1H NOESY MAS spectra of BA:4-FBA solid solution embedded in MCM-41 (1:2 by weight) using: a) DiSupLo (expanded part of the spectrum), b) DiSupLo (full range of the spectrum), c) TSF and d) MeLo (without LA) methods. Spectra were recorded with a spinning rate of 10 kHz and a mixing time equal to 750 ms.

that both BA/4-FBA co-formers are located in one pore and interact with each other, but the two molecules are positioned differently than in the sample obtained by DiSupLo method. Figure 6d depicts the NOESY spectrum for the sample prepared by means of MeLo procedure. The resemblance between the cross-peaks pattern for samples prepared employing the TSF and MeLo methods is seen.

Summarizing the results presented in this section, it can be concluded that the co-formers of BA:4-FBA solid solution are located in a joint space, regardless of the loading method used (TSF, DiSupLo, MeLo), but there is one preferred domain for both of them. It is also highly probable, that the mutual orientation of the co-formers embedded in the voids can be different from what is observed in a crystal structure of this system and different structural motifs should be considered. In contrast, BA:PFBA system in the MCM-41 can occupy more than one domain, depending on the method of sample loading, but in all cases both components appear to be located in the same space, exhibiting intermolecular interactions similar to those found in BA:PFBA cocrystal.

Loading of Physical Mixtures of BA:PFBA and BA:4-FBA into MCM-41

So far we have studied the loading into the voids of MCM-41 of pre-organized binary systems, which, according to NMR data, retained their initial interactions, better or worse. There is no doubt, however, that in both cases the co-formers (BA:FBA and BA:4-FBA) in MCM-41 are in a close contact. This conclusion is not obvious for a physical mixture of components with undefined intermolecular interactions in the solid state at the start of the experiments. To answer the question of what is the organization of the particles inside the pores, as in the previous section, we used 1D and 2D NMR techniques. Physical mixtures of ingredients (BA, PFBA, and BA, 4-FBA) with MCM-41 in a weight ratio of 1:2 were prepared. MeLo and DiSupLo loading methods were used to deposit guest particles in the pores.

Figure 7 shows the ^{19}F MAS and ^1H MAS spectra for a mixture of BA and PFBA with MCM-41 treated according to the methods described in the legend and experimental. The spectral pattern is very similar to that observed for BA:PFBA

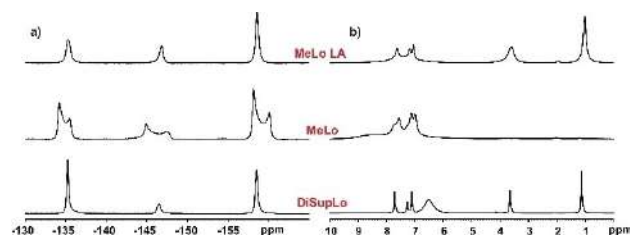


Figure 7. a) ^{19}F and b) ^1H MAS NMR spectra of BA:PFBA physical mixtures loaded to MCM-41 (1:2 by weight) using DiSupLo (bottom), MeLo (without LA – middle and with LA – top) methods. Spectra were recorded with a spinning rate of 24 kHz.

cocrystals. Moreover, the 2D ^1H - ^{19}F HOESY spectra prove the close contact between BA and PFBA co-formers.

Figure 8 depicts the ^{19}F MAS and ^1H MAS spectra for a mixture of BA and 4-FBA with MCM-41. As one can see, each of the loading methods used gives very well-organized systems, without a trace of either of the components being located in more than one space. This result contradicts the data recorded for the mixture of BA and PFBA, where two different BA/PFBA systems were observed. The ^1H - ^{19}F NOESY spectra prove that both co-formers; BA and 4-FBA are in close contact and very likely are located in a common space. The NOESY experiment on a sample obtained by means of MeLo with LA, containing ethanol in the pores along with BA and 4-FBA particles, requires a short comment. One can see that ethanol interacts with both particles forming ternary system. The correlation peaks are clearly visible. The cross-peaks showing the interactions between BA and 4-FBA are less intense compared to the sample obtained with MeLo and without LA. This observation can be explained if we assume that the solvated molecules are more mobile and more distant compared to the solvent free system. In this case, the dipolar interactions are reduced.

In the final stage, we tested physical mixtures of three independent components BA and PFBA with MCM-41 and BA and 4-FBA with MCM-41 in an environment free from any external stimuli. The samples were stored in closed vessels at ambient temperature, the only factor that varied was the storage time. We tested freshly prepared samples (measured immediately after mixing the ingredients by hand) and samples stored for three months.

Figure 9a shows the ^{19}F NMR spectrum of a BA:PFBA/MCM-41 mixture, prepared just prior to the NMR measurement and spun at 24 kHz. The total measurement time, from placing the rotor inside the magnet, achieving spinning stability, and data acquisition is approx. 1 hour. Surprisingly, the ^{19}F NMR spectral

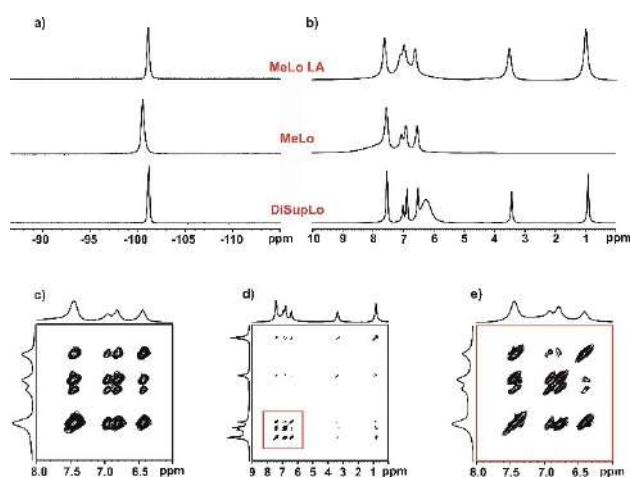


Figure 8. a) ^{19}F and b) ^1H MAS NMR spectra of BA:4-FBA physical mixtures loaded in MCM-41 (1:2 by weight) using DiSupLo (bottom), MeLo (without LA – middle and with LA – top) methods recorded with a spinning rate of 24 kHz; ^1H - ^{19}F NOESY spectra of BA:4-FBA physical mixtures loaded into MCM-41 (1:2 by weight) using: c) MeLo (without LA), d) MeLo (with LA) and e) MeLo (with LA, expanded part of the spectrum) methods recorded with a spinning rate of 10 kHz and a mixing time equal to 750 ms.

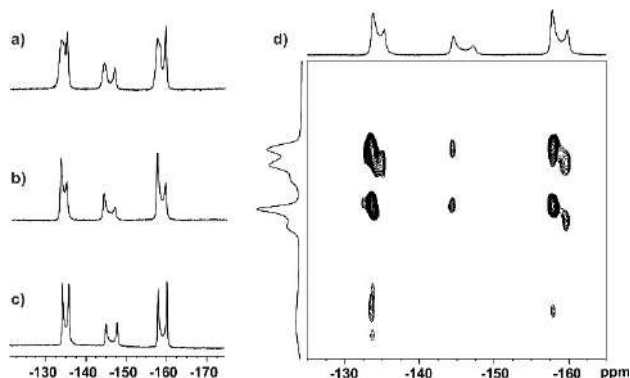


Figure 9. a) ^{19}F MAS NMR spectrum of physical mixture BA, PFBA, and MCM-41 recorded immediately after mixing of components, b) ^{19}F MAS NMR spectrum of a physical mixture of BA, PFBA, and MCM-41 recorded after spinning the sample overnight in a magnet, c) ^{19}F MAS NMR spectrum of a physical mixture of BA, PFBA, and MCM-41 recorded after three months, d) ^1H - ^{19}F HOESY MAS NMR spectra of BA, PFBA, and MCM-41 physical mixture recorded at 24 kHz MAS with a mixing time of 350 ms.

pattern is very similar to that observed for the sample prepared by the MeLo method. It is worth emphasizing that after a long measurement (acquisition overnight), the sample undergoes further transformations (Figure 9b). A sample stored for three months has a different spectral pattern, although two systems, X and Y, are still visible. Trying to explain these results, we suggest that ^{19}F NMR spectra visualize processes occurring in the outer and/or interstitial space. An intriguing question concerns the self-assembly of BA and PFBA components at MCM-41 space locations. Such a process has been recently proven by Bobrovs et al. who, while studying the prenucleation mechanism by means of HOESY NMR measurements, showed a high affinity of both co-formers for the formation of binary systems.^[26] Figure 9d depicts the ^1H - ^{19}F HOESY spectrum of a freshly prepared BA:PFBA/MCM-41 sample. The 2D NMR correlation takes 4 hours to acquire an appropriate number of serial files to achieve an acceptable resolution in an indirect dimension. A close contact between BA and PFBA components is apparent.

An identical procedure was applied for BA, 4-FBA, and MCM-41 mixture. As in the previous case, we monitored interaction of BA and 4-FBA components in contact with MCM-41 (Figure 10). Figure 10a depicts the ^1H - ^1H NOESY MAS NMR spectra for freshly prepared physical mixtures BA, 4-FBA, and MCM-41. Having in mind the spectral pattern shown in Figure 8, we can conclude that for this sample the arrangement of benzoic acid molecules is more complex compared to the samples prepared using the discussed supra loading techniques. It is clear from the analysis of the correlation peaks that there is no close contact between BA and 4-FBA. A sample stored for several days at ambient temperature in a closed vessel undergoes transformation. New cross-peaks which are clearly seen in Figure 10b prove the close distance between BA and 4-FBA molecules which suggests the formation of a binary system between the two molecules.

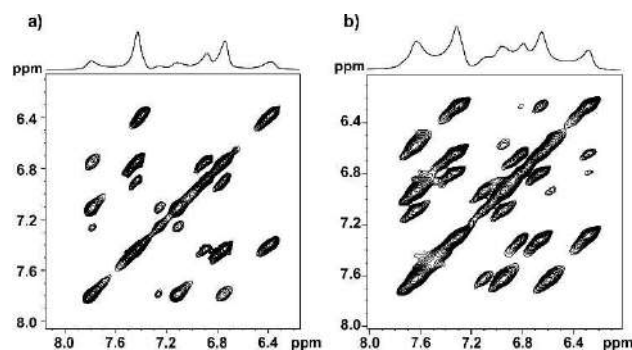


Figure 10. ^1H - ^1H NOESY MAS NMR spectra for physical mixtures BA, 4-FBA, and MCM-41 (0.5:0.5:2 by weight) a) freshly prepared sample b) sample kept for three days at ambient temperature. Spectra were recorded with a spinning rate of 24 kHz and a mixing time of 500 ms.

Summarizing the results shown in the last paragraph, we cannot exclude that the Magic Angle Spinning technique should be considered as one of the loading techniques, in particular when fast sample rotation is employed during measurement. Both the thermal effect associated with rotation and the centrifugal force accompanying rotation can be treated as external stimuli facilitating the loading of media to the voids of MCM-41.

Powder X-ray Diffraction Studies of Solid State Processes for Physical Mixtures of BA and PFBA, BA, and 4-FBA as Well as Their Interactions with MCM-41

The rather unexpected NMR results, which we noted for the physical mixture of co-formers in contact with MCM-41, prompted us to investigate these systems with a particular focus on pre-loading processes. For this purpose, the powder X-ray diffraction technique proved to be the optimal tool.

There is no surprise that both studied binary systems, BA:4-FBA and BA:PFBA can be easily obtained via mechanochemical grinding. It is evident from the inspection of the powder X-Ray diffractograms registered for the respective freshly prepared physical mixtures and the ones registered for the solids obtained after grinding (Figure 11). In this latter case, reflexes originating from a physical mixture are no longer detectable in the diffractograms, indicating a full conversion to the binaries. Surprisingly, we also observed that both BA:4-FBA solid solution and BA:PFBA cocrystal are formed spontaneously while storing the respective physical mixtures at ambient conditions. Figure 12 shows the diffractograms collected for fresh and one month old physical mixtures of both systems, together with the diffractogram for the binaries. In both systems reflexes originating from the binaries are clearly visible in the stored physical mixtures, and in the case of BA:4-FBA system the conversion to solid solution is almost complete, whereas for BA:PFBA system a significant portion of the physical mixture remained intact after the storing period.

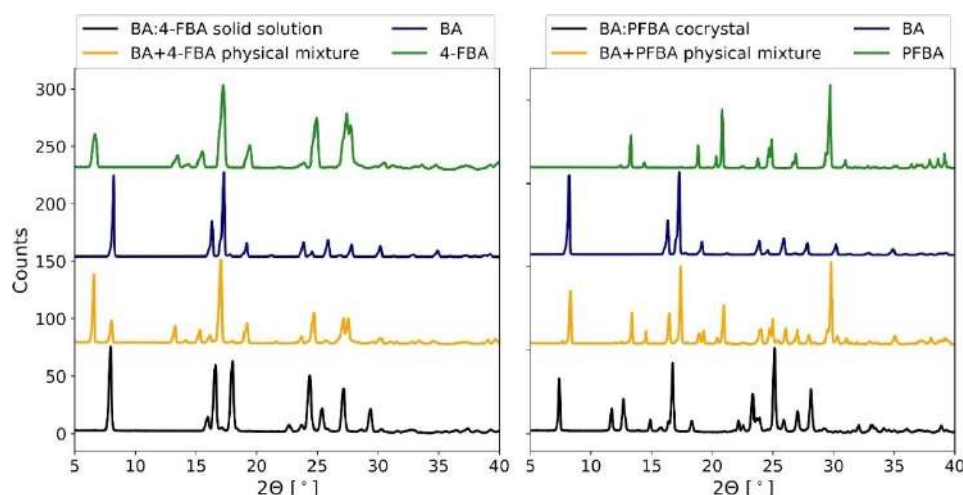


Figure 11. A comparison of the powder X-Ray diffractograms collected for the starting components (BA, 4-FBA, and PFBA), their freshly prepared physical mixtures (BA + 4-FBA and BA + PFBA), and the mechanochemically obtained binaries (BA:4-FBA and BA:PFBA).

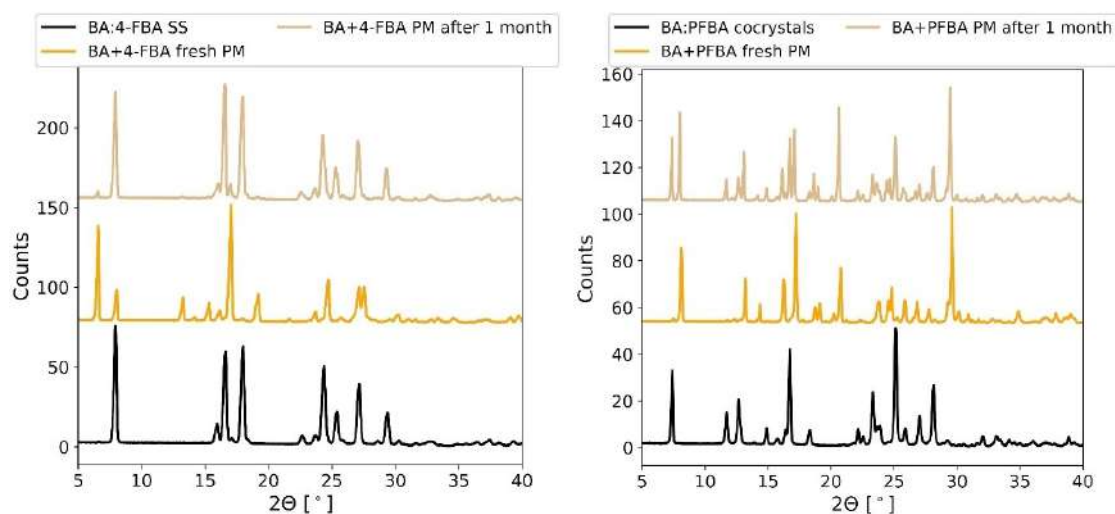


Figure 12. A comparison of the powder X-ray diffractograms collected for the freshly prepared physical mixtures, the same mixtures after one month of storage at ambient conditions, and the respective binaries prepared via mechanochemical grinding: BA:4-FBA (left) and BA:PFBA (right).

To gain an additional insight into energetic stabilization of the two studied systems, we calculated stabilization energies (E^{stab}) for both binaries under periodic boundary conditions (see Supporting Materials, Table S2.) The value of E^{stab} indicates whether a formation of a particular crystal system is energetically favorable in terms of the enthalpy differences between pure parent crystal structures and a binary system, but it does not account for the entropy change upon formation of this system. In the majority of cases of cocrystals published in the Cambridge Structural Database (CSD), the E^{stab} value is negative, indicating a gain in enthalpy upon cocrystallization.^[27] This is also the case of BA:PFBA system, for which the E^{stab} value was found to be equal to -0.12 kJ/mol of molecules. In contrast, the E^{stab} value calculated for 0.5:0.5 BA:4-FBA system was positive and equal to $+2.07$ kJ/mol of molecules. This would suggest that the formation of BA:4-FBA solid solution is not favorable in

terms of crystal enthalpy. In this case, however, a gain in the entropy may be responsible for the formation of this structure. This is corroborated by the observed spontaneity of the formation of this solid solution, which suggest that for both systems, BA:4-FBA and BA:PFBA, the Gibbs free enthalpy of formation is negative, otherwise they could not have been formed. Since for BA:4-FBA system the calculated stabilization energy was positive, it is the entropy that has to be responsible for the energetic favorability of this reaction.

In the next step, we tested the behavior of the physical mixtures of the studied solids in the presence of MCM-41. In these experiments, each solid (excluding MCM-41) was separately ground before mixing. All separated components were put together in one pot and homogenized. The changes in the prepared physical mixtures were tested over a period of about one month. The preliminary grinding of the components was

done to ensure an appropriate quality of powder X-Ray diffractograms, for which uniform size of the crystallites is a prerequisite. After mixing the three components together, the first diffractograms were collected almost immediately.

Figure 13 shows the changes in the diffractograms collected for the prepared physical mixtures of BA, 4-FBA, and MCM-41, as well as of BA, PFBA and MCM-41 stored at ambient conditions for a period of over one month. During this time, at least two processes take place. The first one is associated with the previously described spontaneous formation of the binary systems. In the case of BA:4-FBA the reflexes originating from solid solution are visible already after one hour of storage.

At the same time, another very fast process occurs, possibly associated with the crystalline components spontaneously entering the voids of the silica nanoparticles, with their amorphization, or with both of these processes. The amorphization/entering the pores of MCM-41 is visible after a closer inspection of the reflexes originating from BA:4-FBA. In the freshly prepared material very sharp and intense reflexes are visible, but their intensity drops significantly after one hour of storage and this observation cannot be ascribed only to the formation of a solid solution. After 3 hours the reflexes originating from parent BA and 4-FBA crystals do not appear as sharp signals anymore and their intensity is significantly lower.

Somewhat similar phenomena are observed for BA:PFBA system, although their rates seem to be different. Here, the reflexes originating from the spontaneously formed cocrystal start to appear after 1–2 hours of storage and their intensity increases with elapsing time. This increase however, seems to be decidedly slower than the observed decrease in the intensity of reflexes originating from parent components, which is visible after observing the plots showing intensity changes in particular reflexes shown in Figure 14 (in particular, see changes in the intensities of characteristic reflexes originating from BA, PFBA, and BA:PFBA during the first 15 hours of storage in Figure 14c; a similar phenomenon is observed for BA:4-FBA, see Figure 14a).

The most significant drop in the intensities of the reflexes from BA and PFBA takes place during the first 3 hours, a period

of time in which the reflexes from BA:PFBA phase are barely seen. Such a fast decrease may be caused by several factors. First, both parent components (BA and PFBA) spontaneously enter the mesopores of MCM-41 with a more or less equal rate. It is also possible, that they simply undergo amorphization in contact with the silica nanoparticles. On the other hand, this should result in the elevated background of the PXRD pattern, an effect which is not observed. Finally, the observed dissonance between the rate of decrease in the reflexes intensities of BA and PFBA and the rate of increase in the reflexes intensities of BA:PFBA could be the result of a fast formation of the binary system and entering the mesopores of MCM-41 by BA:PFBA together. This, however, seems to be the least probable, if we consider that the rate of formation of a binary system from a physical mixture of BA and PFBA without the presence of MCM-41 was not observed to be that fast. In addition, in Figure 14d a decrease in the intensities of reflexes originating from the formed BA:PFBA cocrystal, most probably associated with this cocrystal entering the pores of MCM-41, starts to be visible after ca. 3 days of storage and is a rather slow process lasting for 29 days. After this period there are no reflexes originating from any crystalline phase visible in the PXRD pattern. In contrast, in the case of BA:4-FBA such a disappearance of all reflexes from crystalline phases is not observed, which may suggest that the formed solid solution is less prone (if at all) to enter the MCM-41 pores than the single components.

Concluding this part, it seems that the most significant difference in the interactions between MCM-41 and physical mixtures of BA:4-FBA and BA:PFBA is that the latter system enters easily and spontaneously the silica mesopores (BA and PFBA enter the pores together), whereas in the case of the solid solution, this effect is apparent only for single components. From the performed NMR experiments it was evident that physical mixtures of BA and PFBA, as well as BA and 4-FBA can enter the pores of MSPs and show similar interactions as upon using some of the loading methods. It was not clear, however, whether this was because of the sample rotation or because this process can be spontaneous. The results from PXRD

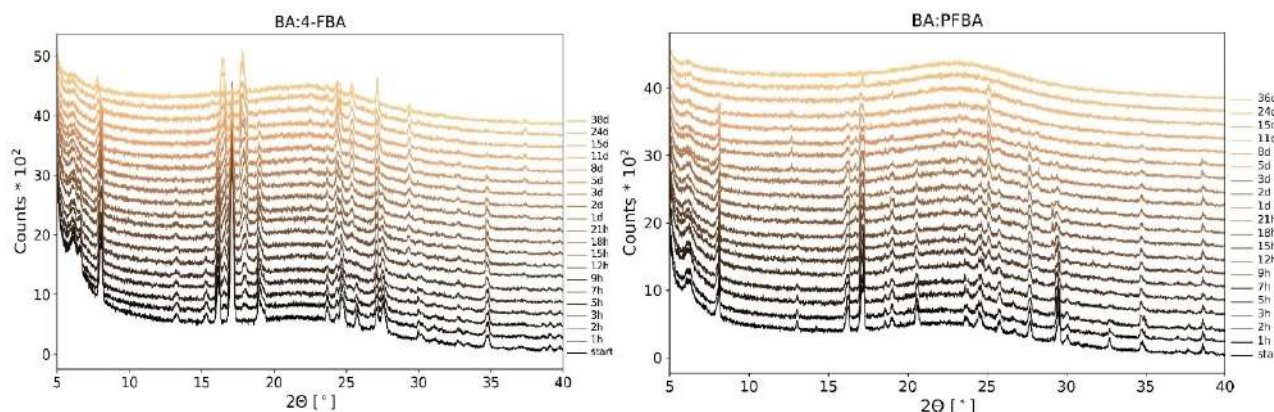


Figure 13. A comparison of powder X-ray diffractograms collected for a physical mixture of BA, 4-FBA, and MCM-41 (left) and BA, PFBA, and MCM-41 (right) upon storage of the samples at ambient conditions for over one month.

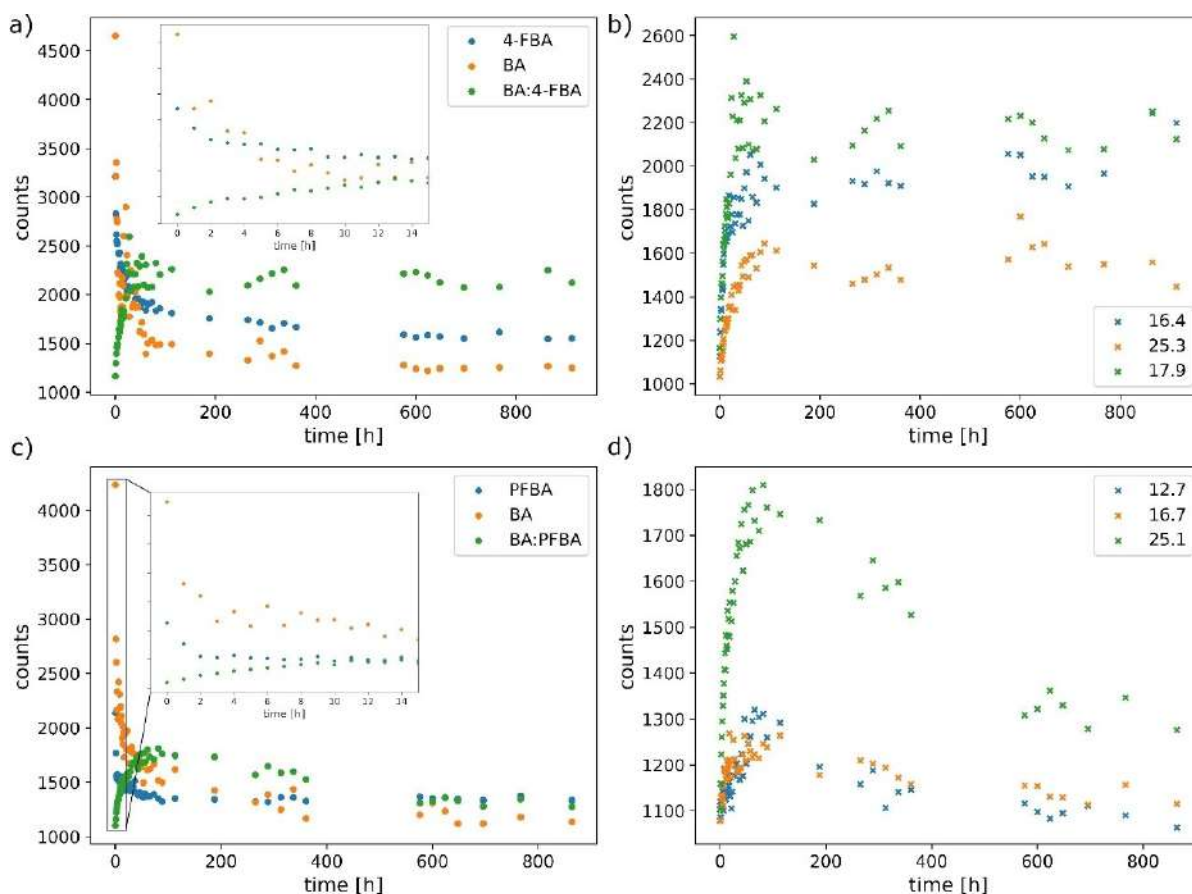


Figure 14. Changes in the intensities (INT) of characteristic reflexes in powder X-Ray diffractograms collected for a physical mixture of BA, PFBA, 4-FBA, and MCM-41 upon storage of the samples at ambient conditions for over one month: a) INT(t) for the selected representative reflexes of each crystal ($2\theta = 17.2^\circ$, 6.6° and 17.9° for BA, 4-FBA and BA:4-FBA, respectively); b) INT(t) for three characteristic reflexes of BA:4-FBA solid solution (the values given in the legend are the respective 2θ values of the reflexes); c) INT(t) for the selected representative reflexes of each crystal ($2\theta = 17.2^\circ$, 20.5° , and 25.1° for BA, PFBA, and BA:PFBA, respectively); d) INT(t) for three characteristic reflexes of BA:PFBA cocrystal (the values given in the legend are the respective 2θ values of the reflexes).

experiments indicate that indeed the process of entering of the studied components into the pores of MCM-41 is spontaneous, but a full incorporation of the ingredients can take a long time. In addition, it is not clear what is the location of the components, which spontaneously entered the pores of MCM-41 and this question cannot be easily answered by solid-state NMR studies, because the sample rotation necessary to perform the experiments can influence this location.

Study of Dissolution and Release Rate of Binary Systems Embedded in MCM-41 Voids

As we highlighted in the Introduction one of the most important applications of mesoporous silica is their use as drug delivery systems. Thus, the knowledge about the release rate of drugs embedded in such systems is crucial for future treatment strategy.

In addition, in a previous article we showed that the kinetics of an active pharmacological ingredient (API) release can be controlled by the appropriate choice of co-formers.^[19b] Here, we

wanted to examine how the fact of possible localization of components in different sites of MSPs can influence their release ratio and dissolution profiles. This could also provide an additional evidence as to the location of components after using different loading techniques, as well as after spontaneous process of entering the MCM-41 pores. The experimental data obtained so far indicate that the studied systems differ significantly in terms of the chemical environment and interactions of the guest molecules depending on the loading method, which should also have a decisive influence on the kinetics of guests release. The measurements were carried out in water (pH=5.7) at a temperature of 8°C . In order to have a complete picture of the dissolution processes for all tested ingredients, we measured pure co-formers, binaries, and all these systems embedded in the MCM-41 mesoporous silica support using three different loading methods. The corresponding N_2 data, profiles for all components separately and embedded in the pores of MCM-41 are attached in Supporting Materials (see Figures S4–S5, Table S1).

Spectacular differences between samples and loading methods were observed when the dissolution and release

results were presented in the form of inverse values $1/CR_t$ (CR – Cumulative Release in %) in the function of the release time t . The appropriate profiles (Figure 15) are shown in the mode of normalized intensity, expressed by the equation, (It/I_{max}) were I_{max} represents the maximal value of cumulative release ($1/CR_{max}$), while It is the value at time t ($1/CR_t$). Figure 15a shows the dissolution profiles for pure BA (grey line), pure PFBA (blue line), and BA, PFBA in BA:PFBA cocrystal (yellow/orange lines) in the range from 1 min to 20 min. In order to quantitatively describe these processes, we introduced a parameter that determines the point of intersection of the ordinate axes. The value of η was determined by linear regression of the plateau using the equation $y = \alpha x + \eta$ assuming that α must be in the range from 0 to -0.008 .

The η parameter for BA is equal to 0.02, for PFBA 0.54 while for BA:PFBA cocrystal 0.11. This means that by forming BA:PFBA cocrystal the solubility of BA co-former was slightly improved but the solubility of PFBA was significantly decreased. Figure 15b features the dissolution profiles for BA and PFBA of BA:PFBA cocrystal loaded into the MCM-41 pores employing three methods. The η parameter for the TSF method is equal to 0.89 and 0.85, for DiSupLo is 0.78 and 0.75 while for MeLo only 0.43 and 0.42, given for BA and PFBA, respectively. The differences between the profiles are obvious and it is clear that the MeLo method does not follow the trend observed for TSF and DiSupLo. This observation agrees well with the results from solid state NMR spectra, which suggested different localization and/or interactions of guests inside MCM-41 after using MeLo loading. A similar analysis was done for all other systems (Figure 15). The appropriate η values are collected in Table 1.

The full profile of dynamics of dissolution and release processes can be also analyzed by testing the amount of released substances in a given time unit employing equation $[xt - x(t-1)]$, where x is a cumulative release given in percentages (for values of CRs see Supporting Materials, Figures S7–S8).

Table 1. The collected values of η parameters for systems shown in Figure 15.

Systems under investigation	Parameter η		
	BA	PFBA	4-FBA
Pure components	0.02	0.54	0.04
BA:PFBA cocrystal	0.11	0.11	–
BA:4-FBA solid solution with 1:1 ratio	0.035	–	0.13
BA:PFBA/MCM-41 TSF	0.89	0.85	–
BA:PFBA/MCM-41 DiSupLo	0.78	0.75	–
BA:PFBA/MCM-41 MeLo	0.43	0.42	–
BA:4-FBA/MCM-41 TSF	0.43	–	0.40
BA:4-FBA/MCM-41 DiSupLo	0.40	–	0.36
BA:4-FBA/MCM-41 MeLo	0.06	–	0.04
BA, PFBA, MCM-41	0.39	0.61	–
Physical mixture fresh			
BA, PFBA, MCM-41	0.85	0.85	–
Physical mixture			
Stored three months			
BA, 4-FBA, MCM-41	0.20	–	0.30
Physical mixture fresh			
BA, 4-FBA, MCM-41	0.40	–	0.38
Physical mixture			
Stored three months			

Figure 16 a shows the dissolution curves for pure BA (grey line), pure PFBA (blue line), and BA and PFBA from BA:PFBA cocrystal (yellow/orange lines) in the range from 1 min to 15 min. It is clear that the dynamics of dissolution of PFBA changes significantly upon formation of a cocrystal with BA, delaying a peak in the released amount and somewhat decreasing its intensity. To a lesser extent changes in the amount of released substance are also visible for BA from BA:PFBA cocrystal, but they concern mostly the amount of released substance and not the peak position. This means that by forming BA:FBA cocrystal the solubility of BA co-former was improved, while the solubility of PFBA was significantly decreased. It is worth to stress that such changes to the dissolution profile of a molecule as those observed for PFBA are usually very advantageous, because a burst release (high amount of a substance released in a short time) may increase a risk of side effects incidence. Figure 16b features the release profiles for BA and PFBA of BA:PFBA cocrystal loaded into the MCM-41 pores employing three studied methods. The differences between the profiles are obvious and clearly demonstrate that by using each method of loading the dissolution rates can be significantly influenced. Noteworthy, the release ratio of both substances loaded using a given method are very similar, indicating that indeed each method may lead to different location of guest compounds. This is particularly visible for MeLo method, which clearly does not follow the trend observed for TSF and DiSupLo. It was also evident when the η values were analyzed. In the MeLo case, the release ratio is much closer to constant over the first minutes, in contrast to the two latter methods, for which a very intense peak is observed in the first minute, followed by a remarkable drop in the release ratio.

A similar analysis was done for BA and 4-FBA co-formers, these components in BA:4-FBA solid solution, and the solid solution loaded into MCM-41 using the three loading methods. Figure 16c shows the dissolution rate profiles for BA (blue), 4-FBA (grey), BA from BA:4-FBA solid solution (orange), and 4-FBA from BA:4-FBA solid solution (yellow). In this case, the formation of solid solution did not influence the release ratio significantly, and it is clear that both components are poorly water soluble, regardless of their crystal form. Figure 16d features curves for BA and 4-FBA of BA:4-FBA solid solution loaded into MCM-41 pores using TSF, DiSupLo, and MeLo methods. In all cases the dissolution profiles changed remarkably in comparison to pure solid solution samples. As in the case of BA:PFBA, the MeLo method is represented by a different profile compared to TSF and DiSupLo.

Again, in this case a more or less equal amount of both components is released over an extended period of time, while for samples from DiSupLo and TSF methods, a burst release is observed in the first 5 minutes of measurements. Nevertheless, it is worth to note, that the amount of released substances is significantly higher in case of samples loaded into MCM-41 in comparison to pure solid solution.

In the final stage of dissolution studies, we have investigated the physical mixture of three components prepared employing the method described earlier. Measurements were carried out for freshly prepared samples and samples kept for

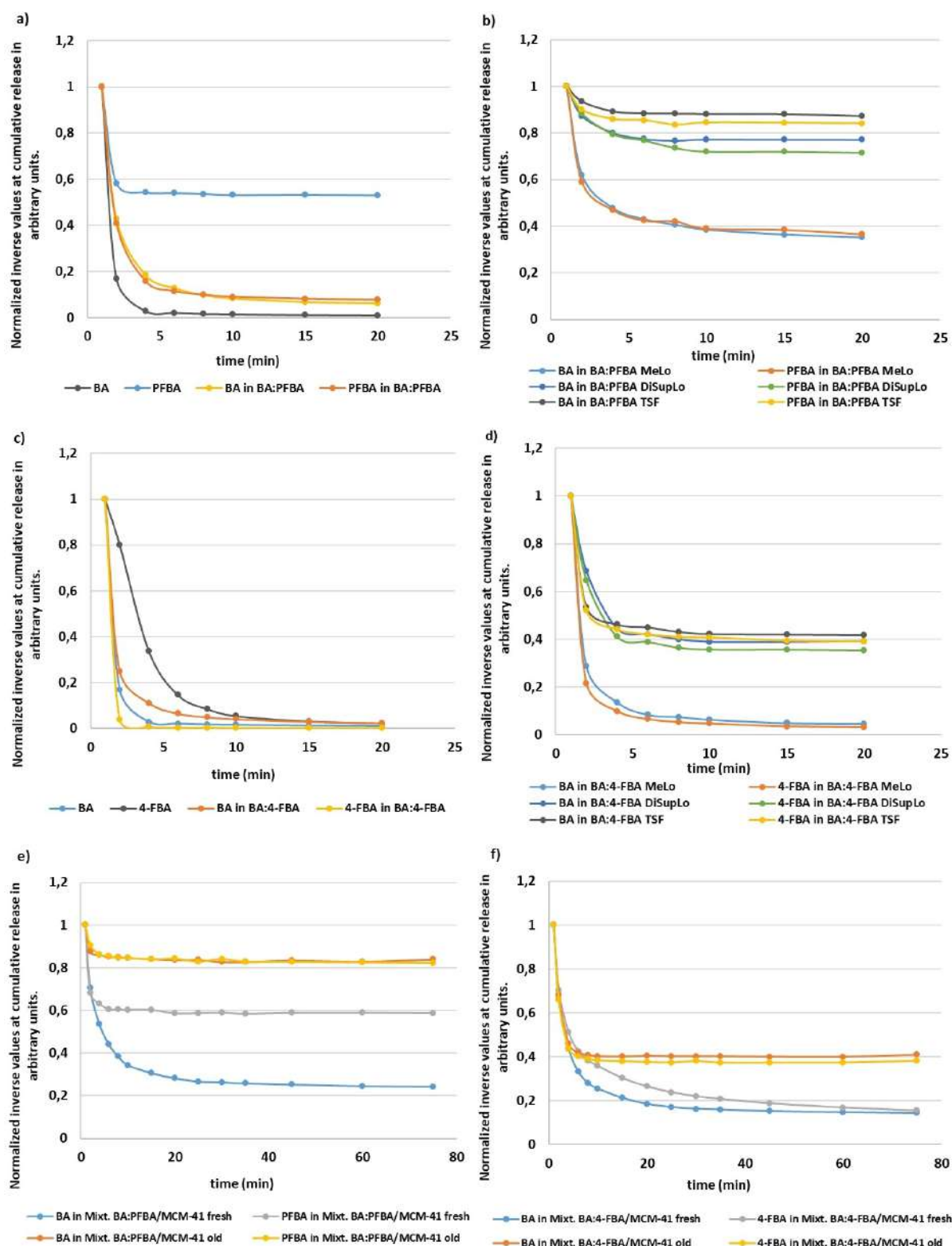


Figure 15. Profiles of dissolution for pure components and release of components embedded into the MCM-41 voids shown as normalized inverse values at cumulative release in arbitrary units: a) BA, PFBA, and BA:PFBA cocrystal, b) component BA and PFBA of BA:PFBA cocrystal embedded into MCM-41 employing DiSupLo, TSF, and MeLo loading methods, c) BA, 4-FBA and BA:4-FBA solid solution 1:1, d) component BA and 4-FBA of BA:4-FBA solid solution embedded into MCM-41 employing DiSupLo, TSF, and MeLo loading methods, e) BA, PFBA, and MCM-41 physical mixture analyzed immediately after preparation and stored at ambient temperature three months in a closed vessel, f) BA, 4-FBA and MCM-41 physical mixture analyzed immediately after preparation and stored at ambient temperature three months in a closed vessel. Each component is marked by different color specified in the legend below the plots.

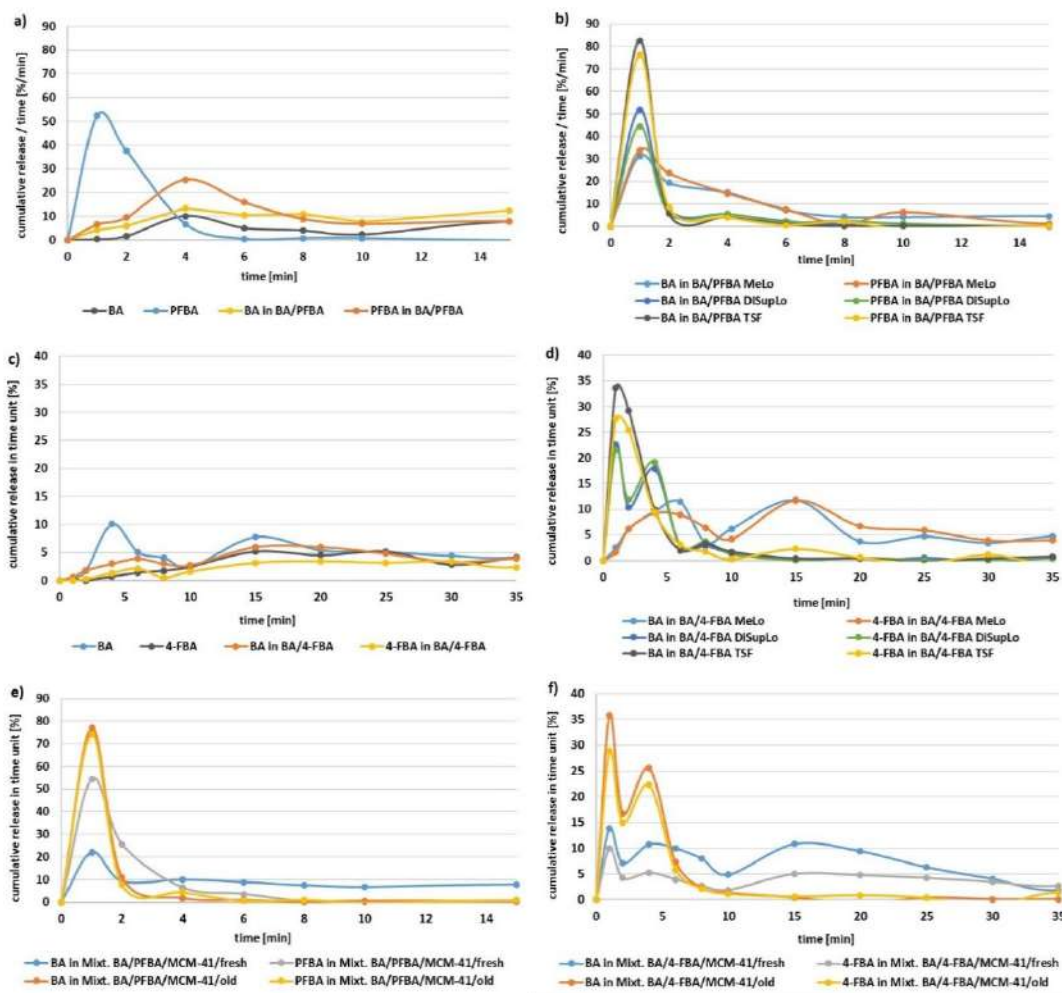


Figure 16. Visualization of the dissolution and release profiles for a) BA, PFBA, and BA, PFBA in BA:PFBA cocrystal, b) component BA and PFBA of BA:PFBA cocrystal loaded into MCM-41 pores employing the three loading methods, c) BA and 4-FBA in BA:4-FBA solid solution (1:1), d) component BA and 4-FBA of BA:4-FBA solid solution loaded into MCM-41 pores employing the three loading methods, e) physical mixture of BA, PFBA, and MCM-41, f) physical mixture of BA, 4-FBA, and MCM-41. Measurements shown in Figures (e) and (f) were carried out for samples freshly prepared and stored for three months. Each component is marked by different color specified in the legend below the plots.

three months. Figure 16e shows the dissolution profiles for BA and PFBA from BA:PFBA/MCM-41 mixture. The weight to weight ratio of acids (BA and PFBA) *versus* MCM-41 is equal to 1:2. The analysis of the curves revealed some important features showing the differences between the freshly prepared samples and the samples stored for three months. In the first case, the BA (blue) and PFBA (grey) components show clearly different trends, similarly as it was observed for pure samples. This proves that both components should be treated as separate species and not as an integrated binary system. A dramatically different situation is observed in the case of a mixture stored for three months. For this sample, BA and PFBA components (orange, yellow) show the same trend, similar to those observed for cocrystal samples loaded into MCM-41 by DiSupLo and TSF method. Such results confirm that the long storage of the physical mixture promotes the formation of the BA:PFBA binary system and its spontaneous entering the pores of the MCM-41 carrier. Figure 16f shows the release profiles for

BA and 4-FBA from the physical mixture of BA:4-FBA/MCM-41 measured immediately after the preparation and for the sample stored for three months. The conclusions are very similar to those for the BA:PFBA/MCM-41 mixture. For a freshly prepared sample, the dissolution profiles of BA and 4-FBA are somewhat different, while for sample stored for three months they are almost exactly the same and very similar to the dissolution profiles obtained for BA:4-FBA solid solution loaded employing DiSupLo and TSF methods. As in the previous case, we can conclude that long storage of the mixture promotes entering of BA and 4-FBA into the pores of MCM-41 carrier. It may be also suggested, that upon such entering the components are located in similar spaces as after DiSupLo and TSF loading, while after MeLo guest molecules are either located deeper inside the MCM-41 pores or are interacting more strongly, for example with silanol groups located at the inner pore surface.

Conclusions

Our studies confirm the complex nature of MCM-41 porosity. This material has at least two different areas with free spaces (voids) where guest particles can be located, namely interstitial space and internal pore space.^[17c,21d] For chemical individuals with a high affinity for the formation of binary systems (BA and PFBA as well as BA and 4-FBA), which can create such systems spontaneously without the participation of external stimuli, the presence of MCM-41 does not block this process. Two-component systems located in MCM-41 voids retain a subtle binary structure, stabilized by non-covalent interactions (aromatic-aromatic interactions, hydrogen bonds). This is confirmed by two-dimensional NMR correlations (NOESY, HOESY). When molecules of ethanol are introduced to the system, the tight ternary guests assembly inside the void is formed. In the case of materials with a high affinity for interaction with MCM-41, the measurement technique can be treated as a method of packing guests into MCM-41 voids. It is especially visible in the MAS NMR technique, where the centrifugal forces and the thermal effect stimulate the loading process. The process of loading the guest molecules in the free spaces of MCM-41 can take place spontaneously, without the participation of external stimuli. Our study confirms that the selection of co-formers has a significant impact on the release rates of media located in MCM-41 voids, since the release profiles for the BA:PFBA and BA:4-FBA systems are apparently different. However, the most unexpected results were found after the analysis of the release ratio of guests loaded using different loading methods, indicating that the selected method can greatly influence the release profile of the guest particles located in the voids of MCM-41. This effect is visible when we compare the TSF and DiSupLo methods with the MeLo method and is also consistent with solid-state NMR data showing different spectral picture for species loaded by mechanochemistry, melting or diffusion-enhanced processes. One of the explanations may be the assumption that in the case of the mechanical method, the particles are located deeper in specific spaces from which it is more difficult for them to get out. This process requires further studies.

Finally, we would like to point out that apart from coformer selection, there is one more way to tune the kinetics of release of guest molecules from MCM-41, i.e. the method used for loading. This observation is of significant importance, as it seems that the loading method may have even more decisive impact on the release, that the composition of binary systems used for the loading. Regardless whether this is true, both factors together, i.e. binary system composition and a loading method, create a powerful tool for steering the amount and rate of release.

Experimental Section

Materials

MCM-41 (hexagonal) silica purchased from Sigma-Aldrich was calcined at 300 °C for 1 h to remove water. The BA, 4-FBA, and PFBA were obtained from Tokyo Chemical Industry (TCI) and used without further purification.

Loading Procedure

The weight ratio of BA:PFBA, BA:4-FBA binaries, and BA, 4-FBA, PFBA acids to MCM-41 in the samples prepared by all loading methods was 1:2. All samples after the loading were characterized by DSC, TGA, adsorption-desorption of nitrogen, as well as by SEM analyses (see Supporting Materials for the detailed results, Figures S1–S6).

MeLo Method

The samples obtained by the MeLo method using planetary ball mill PM 200 were prepared according to the procedure described earlier.^[17c] The samples were prepared with the addition of ethanol (20 μ l) as a liquid assistant (LA) and without LA.

TSF Method

A physical mixture of selected acids or binaries and MCM-41 was heated at a temperature approximately 7 Celsius degrees above the melting point of the starting components for 70 minutes. The heating temperature for BA:4-FBA and BA:PFBA binaries was 157 °C and 97 °C, respectively.

DiSupLo Method

The samples were prepared according to the DiSupLo procedure described previously.^[18]

Binaries Preparation

The BA:4-FBA and BA:PFBA binaries were prepared by grinding procedure using the MM200 mixing mill. The physical mixture of BA and 4-FBA in a 1:1 molar ratio with 20 μ l of methanol as LA was mechanically ground in an agate jar (5 ml) with one ball (\varnothing = 5 mm) for 20 min at an oscillation rate of 25 Hz. Cocrystal BA:PFBA was prepared by grinding the components for 15 min without LA addition. Both binaries were then crystallized from the ethanol:m-xylene mixture (1:1 v/v) at room temperature. The formation of respective binaries was confirmed by PXRD and thermal analyses.

Preparation of Physical Mixtures

All separated components were placed together in one pot and homogenized. The BA, 4-FBA, and PFBA acids used in the samples of the physical mixtures with MCM-41 were separately homogenized before mixing. The weight ratio of acids to MCM-41 was 1:2. The molar ratio of BA:4-FBA and BA:PFBA was 1:1. Freshly prepared physical mixtures and samples stored for one and three months were measured.

NMR Measurements

^{13}C CP MAS spectra were recorded on a BRUKER Avance III 400WB spectrometer, operating at 400.16 for ^1H and 100.62 MHz for ^{13}C , equipped with a MAS probe head using 4 mm ZrO_2 rotors. Spectra were recorded with MAS frequency of 8000 Hz and a proton 90° pulse of 6.0 μs in length and a contact time of 4 ms. The repetition delay (D1) was 4 s, and the spectral width was 48.0 kHz. Depending on the sample, the FIDs were accumulated with 512 to 1024 scans and time domain size of 2 K data points with SPINAL16 decoupling sequence during the acquisition time. A sample of native glycine (α -form) was used for setting the Hartmann-Hahn condition and as an external chemical shift reference ($\delta_{(\text{C}=\text{O})} = 176.50$ ppm).

^1H and ^{19}F spectra were recorded on a Bruker Avance III 600 spectrometer operating at 600.15 MHz for ^1H and 564.71 MHz for ^{19}F , employing a triple-channel $^1\text{H}/^{19}\text{F}/^{13}\text{C}$ 2.5 mm MAS probe head and ZrO_2 rotors at MAS spinning rate of 24 kHz.

To eliminate probe head background signal, ^{19}F MAS spectra were recorded using zg-echo pulse sequence with pulse timing synchronized with rotor rotation. Spectra were acquired with relaxation delay (D1) of 3 and 600 seconds.

^1H - ^1H NOESY spectra were recorded in $4\text{K} \times 256$ ($\text{F}_2 \times \text{F}_1$) data point matrix with 8 or 16 scans each and relaxation delay of 1.6 s. Spectral width (SW) was 16 ppm (9800 Hz) in both dimensions. Usually, spectra were recorded with a mixing time of 300 ms.

^{19}F - ^{19}F NOESY MAS spectra were acquired in $4\text{K} \times 256$ ($\text{F}_2 \times \text{F}_1$) data point matrix with 16 scans each and relaxation delay of 3 s. Spectral width (SW) was 63 ppm (35 500 Hz) in both dimensions. Spectra were recorded with two different mix times: 50 and 300 ms.

^{19}F - ^1H HOESY MAS spectra were recorded in $1\text{K} \times 256$ ($\text{F}_2 \times \text{F}_1$) data point matrix with a number of scans between 40 and 160, depending on the sample. Relaxation delay was set to 1 or 3 seconds. Spectral widths were set to 35 500 Hz (63 ppm) and 13 200 Hz (22 ppm) in F_2 and F_1 dimension, respectively. Spectra were recorded with two mixing times: 350 and 750 ms.

Very Fast MAS (VF MAS) NMR spectrum was recorded on a Bruker Avance III 600 spectrometer operating at 600.13 MHz for ^1H , equipped with a 1.3 mm MAS probe head utilizing 1.3 mm ZrO_2 rotor with applied MAS rotation frequency of 60 kHz.

For ^1H VF NMR MAS spectrum 5432 data points were collected with a spectral width of 27 kHz (giving a total acquisition time equal to 100 ms) and a 90° pulse of 2.5 μs . 32 scans were accumulated per experiment with a relaxation delay of 3 s. Spectrum was externally referenced to TSP (trimethylsilylpropanoic acid) (0 ppm).

All spectra were recorded and processed with a Bruker TopSpin 3.1 program.

Powder X-ray Diffraction

Powder X-Ray diffraction experiments were acquired with a Panalytical Empyrean diffractometer in Bragg-Brentano reflection mode using zero-background silicon sample holders. The diffractometer was equipped with a PIXcel^{3D} detector with all 255 active channels and $\text{Cu K}\alpha$ radiation was used ($\lambda = 1.541874$ Å). For the incident beam 0.02 Soller slits, $1/8^\circ$ divergence slit, and a 10 mm beam mask were used. For the diffraction beam 0.02 large Soller slits and 7.5 mask were used. The diffractograms were registered in a 2Θ range of 5.0000 – 49.9975° , using a step size of 0.0131° .

For studying spontaneous changes to the samples during storage, an automatic program measuring diffractograms under the same conditions was used. Typically, the samples were kept inside the

diffractometer and were not displaced from their respective sample holders. The measurement times and intervals were the same for all compared samples. For the analysis of intensity changes to the selected reflexes and in-house Python script was used, utilizing a Matplotlib library^[28] to produce the plots showing the intensity changes with elapsing time.

Differential Scanning Calorimetry (DSC)

Calorimetric measurements were performed using a DSC 2920 from TA Instrument. Samples were heated from room temperature to 200°C with a heating rate of $10^\circ\text{C}/\text{min}$ under a nitrogen flow of 50 ml/min.

Adsorption–Desorption of Nitrogen

Nitrogen adsorption-desorption isotherms were recorded at -196°C using the Micromeritics ASAP 2020 Plus apparatus. Before measurements, the MCM-41 and loaded samples were vacuum degassed at 110°C and room temperature for 48 h, respectively. The specific surface areas were calculated according to the standard Brunauer-Emmet-Teller (BET) method. The pore size distributions were determined using the Barret-Joyner-Hallenda (BJH) method at desorption.

Study of Dissolution and Release Rate of Binary Systems Embedded in MCM-41 Voids

In vitro dissolution studies were carried out using a USP II paddle method on a dissolution tester (model – Vision G2 Classic 6, Hanson). Pure components, BA:PFBA and BA:4-FBA binaries, samples of BA:PFBA/MCM-41, BA:4-FBA/MCM-41 prepared by three methods were immersed in 1000 ml of distilled water ($\text{pH} = 5.7$).

The temperature of the dissolution medium was maintained at $8^\circ\text{C} \pm 0.5$ and the rotation speed was kept at 25 rpm. Aliquot samples of 1 ml were withdrawn at predetermined time intervals (1, 2, 4, 6, 8, 10, 15, 20, 35, 30, 45, 60, 75, 90, 105, 135, 165, and 195 min) and equivalent volumes of fresh dissolution medium were added to keep a constant dissolution volume. Samples were filtered using a 0.45 μm PTFE syringe filter.

The quantification of the dissolved components was carried out with the use of an ACQUITY UPLC I-Class chromatography system equipped with a binary solvent pump and a photodiode array detector (Waters Corp., Milford, MA, USA). Separation of the compounds was achieved using an ACQUITY UPLCTM BEH C18 column (100×2.1 mm, 1.7 μm). The mobile phase was composed by mixing 0.05% acetic acid (A) and 0.05% acetic acid in acetonitrile (B). The elution gradient was: 27% B (0–1.0 min), 27–60% B (1.0–3.5 min), 60–60% B (3.0–3.5 min), 60–27% B (3.5–3.51 min) and 27–27% B (3.51–7 min). The flow rate was 0.45 mL/min, the column temperature was 45°C . The optimal absorption wavelengths for all components were determined and were set at 265 nm for PFBA and 230 nm for BA and 4-FBA. The initial stock calibration solution of standards was created with a concentration of approximately 10 mg/ml in methanol. The stock solutions were serially diluted with water to obtain working solutions at several concentration levels. Two calibration curves were prepared at six different concentrations of standards solutions in the range from 0.5 to 25 mg/L with correlation coefficients above 0.998 for all compounds. The system was controlled by using a MassLynx software (Version 4.1) and data processing (peak area integration, construction of the calibration curve) was performed by a TargetLynxTM program.

Castep Calculations

Stabilization energies for the studied binary systems were calculated from the differences between the energy obtained for a DFT–D optimized binary structure and a sum of DFT–D optimized structures of respective components. The calculations were performed under periodic boundary conditions using CASTEP code,^[29] with PBE functional^[30] and MDB dispersion correction scheme.^[31] An energy cut-off value of 1000 eV and a k-point separation of 0.07 \AA^{-1} were used. For the calculation of intramolecular energy contribution to the total energies of the studied systems, a given molecule was placed in a 30 \AA box and its energy was calculated at the same level of theory. The intermolecular energy contribution was calculated from the difference between a total energy and an intramolecular energy.

Supporting Information Summary

DSC and TGA curves, adsorption-desorption of nitrogen, Scanning Electron Microscopy (SEM) images, release profiles, and calculation of stabilization energies can find in the Supporting Information.^[32–34]

Acknowledgements

The purchase of a Panalytical Empyrean diffractometer and dissolution tester model-Vision G2 Classic 6, Hanson used to obtain results included in this publication was supported by the funds from the EU Regional Operational Program of the Lodz Region, RPLD.01.01.00-10-0008/18. This work was financially supported by Polish National Science Centre under Opus grant No. 2018/31/B/ST4/01973. The Polish Infrastructure for Supporting Computational Science in the European Research Space (PL-GRID) is gratefully acknowledged for providing computational resources.

Conflict of Interest

The authors declare no conflict of interest.

Data Availability Statement

The data that support the findings of this study are available from the corresponding author upon reasonable request.

Keywords: drug delivery systems · loading methods · mesoporous silica particles · powder X-ray diffraction · solid state NMR

- [1] a) H. Yan, H. Qin, W. Liang, X. Jin, Y. Zhang, X. Feng, Y. Liu, X. Chen, C. Yang, *Catal. Sci. Technol.* **2019**, *9*, 4909–4919; b) Y. Wu, Y. Zhang, J. Zhou, D. Gu, *Emergent Mater.* **2020**, *3*, 247–266.
- [2] a) M. Manzano, M. Vallet-Regí, *Adv. Funct. Mater.* **2020**, *30*, 1902634; b) B. Murugan, S. Sagadevan, A. L. J. I. Fatimah, K. N. Fatema, W.-C. Oh, F. Mohammad, M. R. Johan, *Mater. Res. Express* **2020**, *7*, 102002; c) R. Narayan, U. Y. Nayak, A. M. Raichur, S. Garu, *Pharmaceutics* **2018**, *10*, 102.

- 118; d) M. Gisbert-Garzaran, M. Manzano, M. Vallet-Regí, *Pharmaceutics* **2020**, *12*, 83; e) V. Selvarajan, S. Obuobi, P. L. R. Ee, *Front. Chem.* **2020**, *8*, 602; f) M. Colilla, M. Vallet-Regí, *Int. J. Mol. Sci.* **2020**, *21*, 8605; g) R. Diab, N. Canilho, I. A. Pavel, F. B. Haffner, M. Girardon, A. Pasc, *Adv. Colloid Interface Sci.* **2017**, *249*, 346–362; h) M. Vallet-Regí, *Acta Biomater.* **2022**, *137*, 44–52.
- [3] a) L. Long, M. Zong, Y. Xie, Q. Chai, J. Liu, X. Wu, *ACS Appl. Nano Mater.* **2022**, *5*, 1553–1561; b) M. Choi, F. Kleitz, D. Liu, H. Y. Lee, W.-S. Ahn, R. Ryoo, *J. Am. Chem. Soc.* **2005**, *127*, 1924–1932; c) K. Moller, T. Bein, R. X. Fischer, *Chem. Mater.* **1998**, *10*, 1841–1852.
- [4] B. Singh, J. Na, M. Konarova, T. Wakihara, Y. Yamauchi, C. Salomon, M. B. Gawande, *Bull. Chem. Soc. Jpn.* **2020**, *93*, 1459–1496.
- [5] a) M. Vallet-Regí, M. Colilla, I. Izquierdo-Barba, M. Manzano, *Molecules* **2018**, *23*, 47–65; b) X. Hong, X. Zhong, G. Du, Y. Hou, Y. Zhang, Z. Zhang, T. Gong, L. Zhang, X. Sun, *Sci. Adv.* **2020**, *6*, eaaz4462.
- [6] a) <https://www.fda.gov/food/food-ingredients-packaging/generally-recognized-safe-gras>; b) T. I. Janjua, Y. Cao, C. Yu, A. Popat, *Nat. Rev. Mater.* **2021**, *6*, 1072.
- [7] K. B. Seljak, P. Kocbek, M. Gašperlin, *J. Drug Delivery Sci. Technol.* **2020**, *59*, 101906.
- [8] S. C. Shen, W. K. Ng, L. Chia, Y. C. Hong, R. B. Tan, *J. Pharm. Sci.* **2010**, *99*, 1997–2007.
- [9] B. Malfait, N. T. Correia, A. Mussi, L. Paccou, Y. Guinet, A. Hédoux, *Microporous Mesoporous Mater.* **2019**, *277*, 203–207.
- [10] F. Uejo, Y. Limwikrant, K. Moribe, K. Yamamoto, *Asian J. Pharm. Sci.* **2013**, *8*, 329–335.
- [11] L. J. Waters, T. Hussain, G. Parkes, J. P. Hanrahan, J. M. Tobin, *Eur. J. Pharm. Biopharm.* **2013**, *85*, 936–941.
- [12] C. Charnay, S. Bégu, C. Tourné-Péteilh, L. Nicole, D. A. Lerner, J. M. Devoisselle, *Eur. J. Pharm. Biopharm.* **2004**, *57*, 533–540.
- [13] R. Mellaerts, K. Houthoofd, K. Elen, H. Chen, M. Van Speybroeck, J. Van Humbeeck, P. Augustijns, J. Mullens, G. Van den Mooter, J. A. Martens, *Microporous Mesoporous Mater.* **2010**, *130*, 154–161.
- [14] R. Mellaerts, J. A. G. Jammaer, M. Van Speybroeck, H. Chen, J. Van Humbeeck, P. Augustijns, G. Van den Mooter, J. A. Martens, *Langmuir* **2008**, *24*, 8651–8659.
- [15] a) A. Bouledjoudja, Y. Masmoudi, M. Van Speybroeck, L. Schueller, E. Badens, *Int. J. Pharm.* **2016**, *499*, 1–9; b) R. J. Ahern, J. P. Hanrahan, J. M. Tobin, K. B. Ryan, A. M. Crean, *Eur. J. Pharm. Sci.* **2013**, *50*, 400–409.
- [16] a) K. Trzeciak, A. Chotera-Ouda, I. I. Bak-Sypien, M. J. Potrzebowski, *Pharmaceutics* **2021**, *13*, 950; b) V. P. Lehto, J. Riikonen, in *Porous Silicon for Biomedical Applications*, Ed., Woodhead Publishing: Cambridge, UK, **2014**, pp. 337–355; c) C. A. McCarthy, R. J. Ahern, R. Döntireddy, K. B. Ryan, A. M. Crean, *Expert Opin. Drug Delivery* **2016**, *13*, 93–108; d) Z. Li, Y. Zhang, N. Feng, *Expert Opin. Drug Deliv.* **2019**, *16*, 219–237.
- [17] a) E. Skorupska, A. Jeziorna, P. Paluch, M. J. Potrzebowski, *Mol. Pharm.* **2014**, *11*, 1512–1519; b) E. Skorupska, P. Paluch, A. Jeziorna, M. J. Potrzebowski, *J. Phys. Chem. C* **2015**, *119*, 8652–8661; c) K. Trzeciak, S. Kaźmierski, K. Drużbicki, M. J. Potrzebowski, *J. Phys. Chem. C* **2021**, *125*, 10096–10109.
- [18] K. Trzeciak, S. Kaźmierski, E. Wielgus, M. J. Potrzebowski, *Microporous Mesoporous Mater.* **2020**, *308*, 110506.
- [19] a) E. Skorupska, A. Jeziorna, M. J. Potrzebowski, *J. Phys. Chem. C* **2016**, *120*, 13169–13180; b) E. Skorupska, S. Kaźmierski, M. J. Potrzebowski, *Mol. Pharm.* **2017**, *14*, 1800–1810.
- [20] a) Q. Liu, J. Zhang, W. Sun, Q. R. Xie, W. Xia, H. Gu, *Int. J. Nanomed.* **2012**, *7*, 999–1013; b) J. M. Rosenholm, E. Peuhu, J. E. Eriksson, C. Sahlgren, M. Lindén, *Nano Lett.* **2009**, *9*, 3308–3311; c) A. Vyalkha, Th. Emmler, E. Gedata, I. Shenderovich, G. H. Findenegg, H.-H. Limbach, G. Buntkowsky, *Solid State Nucl. Magn. Reson.* **2005**, *28*, 117–124; d) S. Schneider, M. Brodrecht, H. Breitzke, T. Wissel, G. Buntkowsky, H. S. Varol, R. Brilmayer, A. Andrieu-Brunsen, M. Vogel, *J. Chem. Phys.* **2022**, *157*, 034503; e) M. Reuhl, P. Monnard, M. Vogel, *J. Chem. Phys.* **2022**, *156*, 084506; f) M. F. Harrach, B. Drossel, W. Winschel, T. Gutmann, G. Buntkowsky, *J. Phys. Chem. C* **2015**, *119*, 28961–28969; g) B. Kumari, M. Brodrecht, H. Breitzke, M. Werner, B. Grünberg, H.-H. Limbach, S. Forg, E. P. Sanjon, B. Drossel, T. Gutmann, G. Buntkowsky, *J. Phys. Chem. C* **2018**, *122*, 19540–19550.
- [21] a) F. Habache, M. Hachemaoui, A. Mokhtar, K. Chikh, F. Benali, A. Mekki, F. Zaoui, Z. Cherif, B. Boukoussa, *J. Inorg. Organomet. Polym. Mater.* **2020**, *30*, 4245–4268; b) D. M. Oliveira, A. S. Andrada, *Ceramica* **2019**, *65*, 170–179; c) C. Liu, Q. Li, D. Zhang, Y. Li, J. Liu, X. Xiao, *Prog. Med. Chem.* **2021**, *33*, 2085–2102; d) V. Torres-Barthelemy, N. Pérez-Hernández, I. G. Shenderovich, P. M. Tolstoy, G. S. Denisov, H.-H. Limbach, *J. Phys. Chem. C* **2020**, *124*, 22082–22095; e) Ch. Balzer, A. M. Waag, S. Gehret, G.

- Reichenauer, F. Putz, N. Hüsing, O. Paris, N. Bernstein, G. Y. Gor, A. V. Neimark, *Langmuir* **2017**, *33*, 5592–5602.
- [22] a) S. Jahnert, F. Vaca Chavez, G. E. Schaumann, A. Schreiber, M. Schonhoff, G. H. Findenegg, *Phys. Chem. Chem. Phys.* **2008**, *10*, 6039–6051; b) E. Gedat, A. Schreiber, J. Albrecht, Th. Emmeler, I. Shenderovich, G. H. Findenegg, H.-H. Limbach, G. Buntkowsky, *J. Phys. Chem. B* **2002**, *106*, 1977–1984; c) Y. Xia, G. Dosseh, D. Morineau, Ch. Alba-Simionesco, *J. Phys. Chem. B* **2006**, *110*, 19735–19744; d) T. Azais, G. Hartmeyer, S. Quignard, G. Laurent, F. Babonneau, *J. Phys. Chem. C* **2010**, *114*, 8884–8891; e) S. Z. Qiao, S. K. Bhatia, D. Nicholson, *Langmuir* **2004**, *20*, 389–395; f) S. Kittaka, S. Takaharam, H. Matsumoto, Y. Wada, T. J. Satoh, T. Yamaguchi, *J. Chem. Phys.* **2013**, *138*, 204714.
- [23] L. A. Solov'yov, O. V. Belousov, R. E. Dinnebier, A. N. Shmakov, S. D. Kirik, *J. Phys. Chem. B* **2005**, *109*, 3233–3237.
- [24] M. Gdaniec, W. Jankowski, M. J. Milewska, T. Półniński, *Angew. Chem. Int. Ed.* **2003**, *42*, 3903–3906; *Angew. Chem.* **2003**, *115*, 4033–4036.
- [25] S. Chakraborty, G. R. Desiraju, *Cryst. Growth Des.* **2018**, *18*, 3607–3615.
- [26] R. Bobrovs, A. A. Auzins, L. Drunka, R. Metlans, R. Muhamadejevs, K. Jaudzems, *Cryst. Growth Des.* **2021**, *21*, 6166–6172.
- [27] C. R. Taylor, G. M. Day, *Cryst. Growth Des.* **2018**, *18*, 892–904.
- [28] J. D. Hunter, *Comput. Sci. Eng.* **2007**, *9*, 90–95.
- [29] S. J. Clark, M. D. Segall, C. J. Pickard, P. J. Hasnip, M. I. J. Probert, K. Refson, M. C. Payne, *Z. Kristallogr.* **2005**, *220*, 567–570.
- [30] J. P. Perdew, K. Burke, M. Ernzerhof, *Phys. Rev. Lett.* **1996**, *77*, 3865–3868.
- [31] L. Kronik, A. Tkatchenko, *Acc. Chem. Res.* **2014**, *47*, 3208–3216.
- [32] M. Nieger, *CSD Communication* **2010**.
- [33] V. Benghiat, L. Leiserowitz, *J. Chem. Soc. Perkin Trans. 2* **1972**, 1778–1785.
- [34] V. R. Hathwar, T. S. Thakur, R. Dubey, M. A. Pavan, T. N. G. Row, G. R. Desiraju, *J. Phys. Chem. A* **2011**, *115*, 12852–12863.

Manuscript received: November 30, 2022

Revised manuscript received: December 9, 2022

Accepted manuscript online: December 12, 2022

Version of record online: January 5, 2023

Unexpected Factors Affecting the Kinetics of Guest Molecule Release from Investigation of Binary Chemical Systems Trapped in a Single Void of Mesoporous Silica Particles.

Katarzyna Trzeciak, Ewelina Wielgus, Sławomir Kaźmierski, Mehrnaz Khalaji, Marta K. Dudek
and Marek J. Potrzebowski.

Contents:

- I. DSC and TGA curves.**
- II. Adsorption-Desorption of Nitrogen.**
- III. Scanning Electron Microscopy (SEM) images.**
- IV. Release profiles**
- V. Calculation of stabilization energies**

I. DSC and TGA curves.

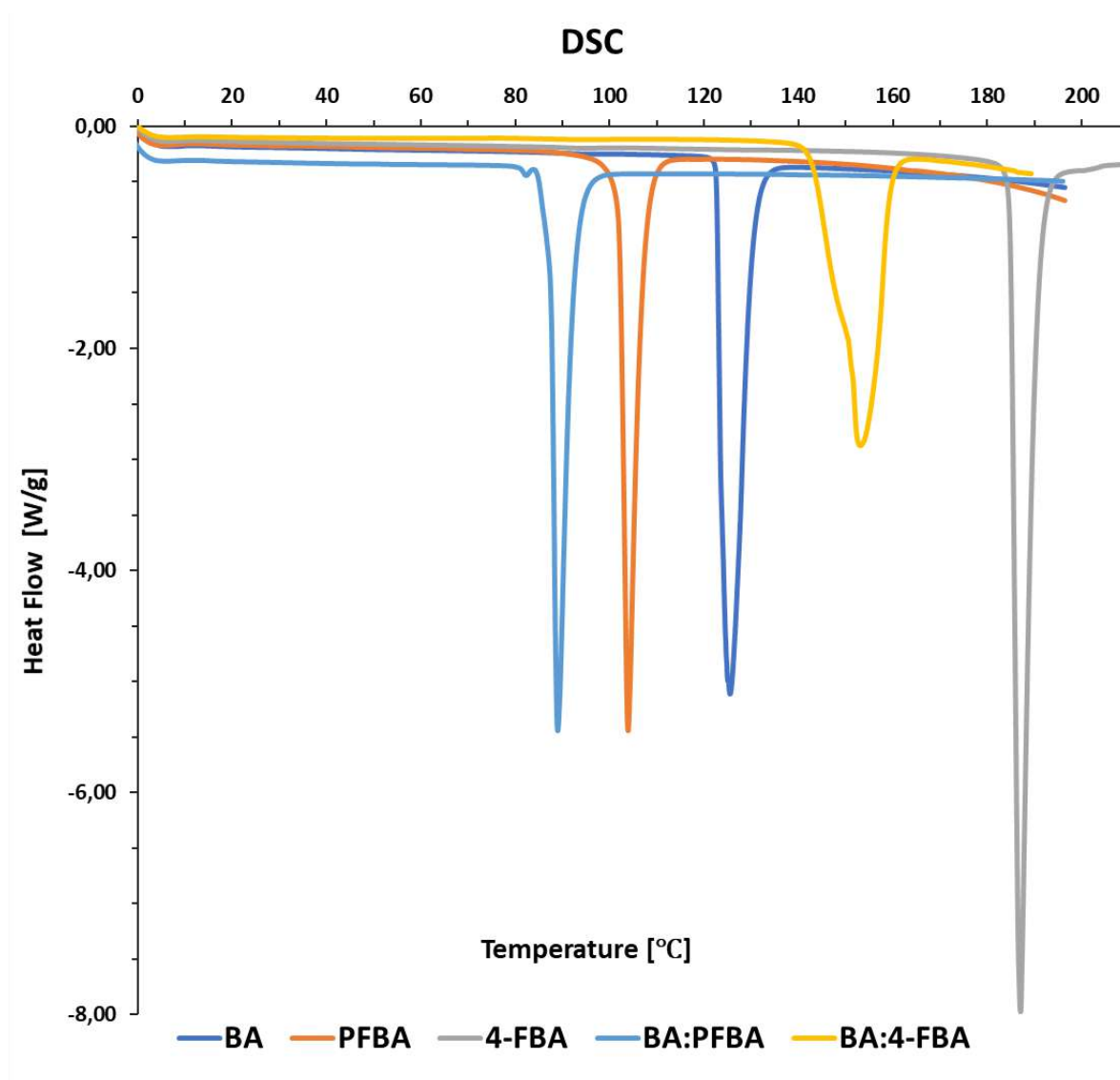


Figure S1. DSC curves of crystalline BA, PFBA, 4-FBA and binaries BA:PFBA and BA:4-FBA.

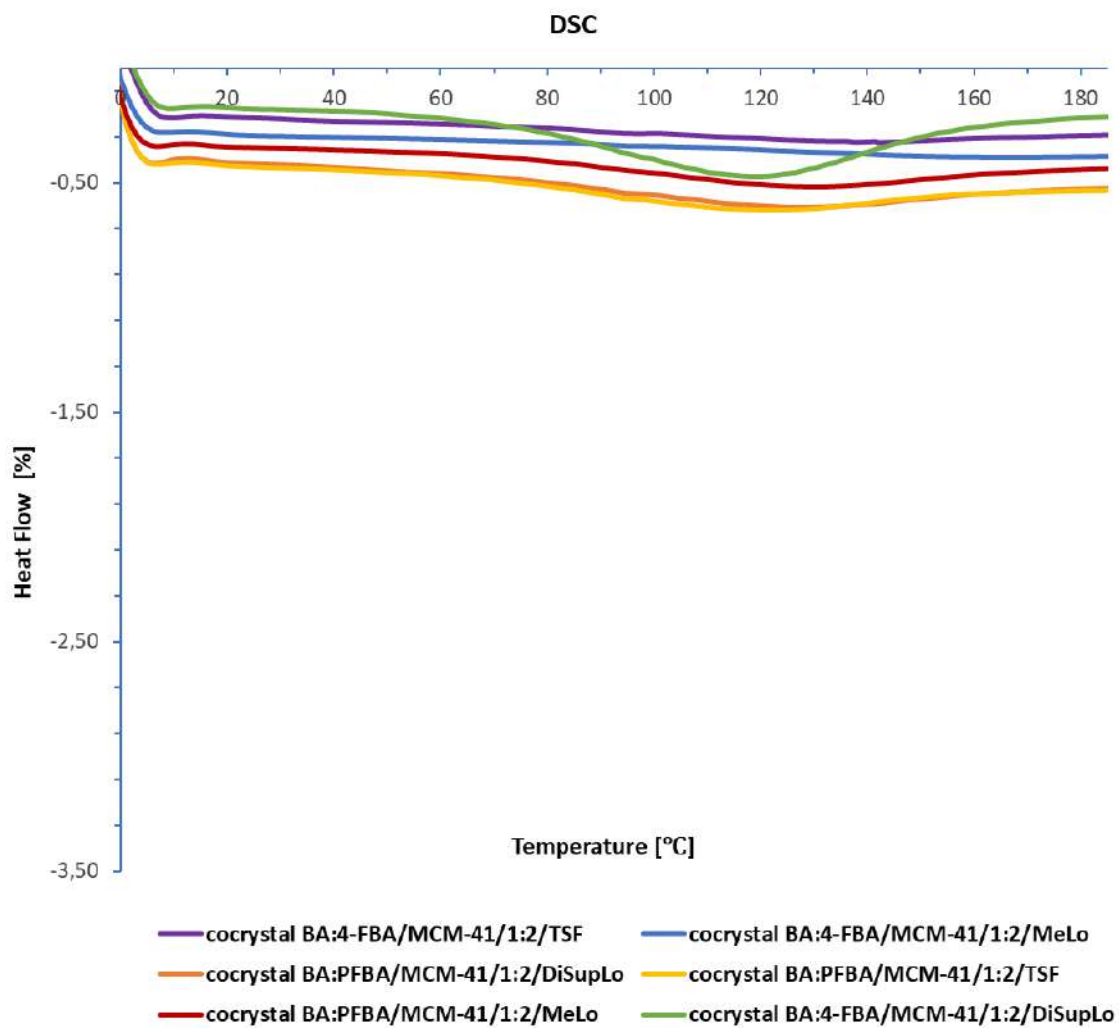


Figure S2. DSC curves of BA:PFBA and BA:4-FBA cocrystals embedded in MCM-41 (1:2) by TSF, DiSupLo, and MeLo methods.

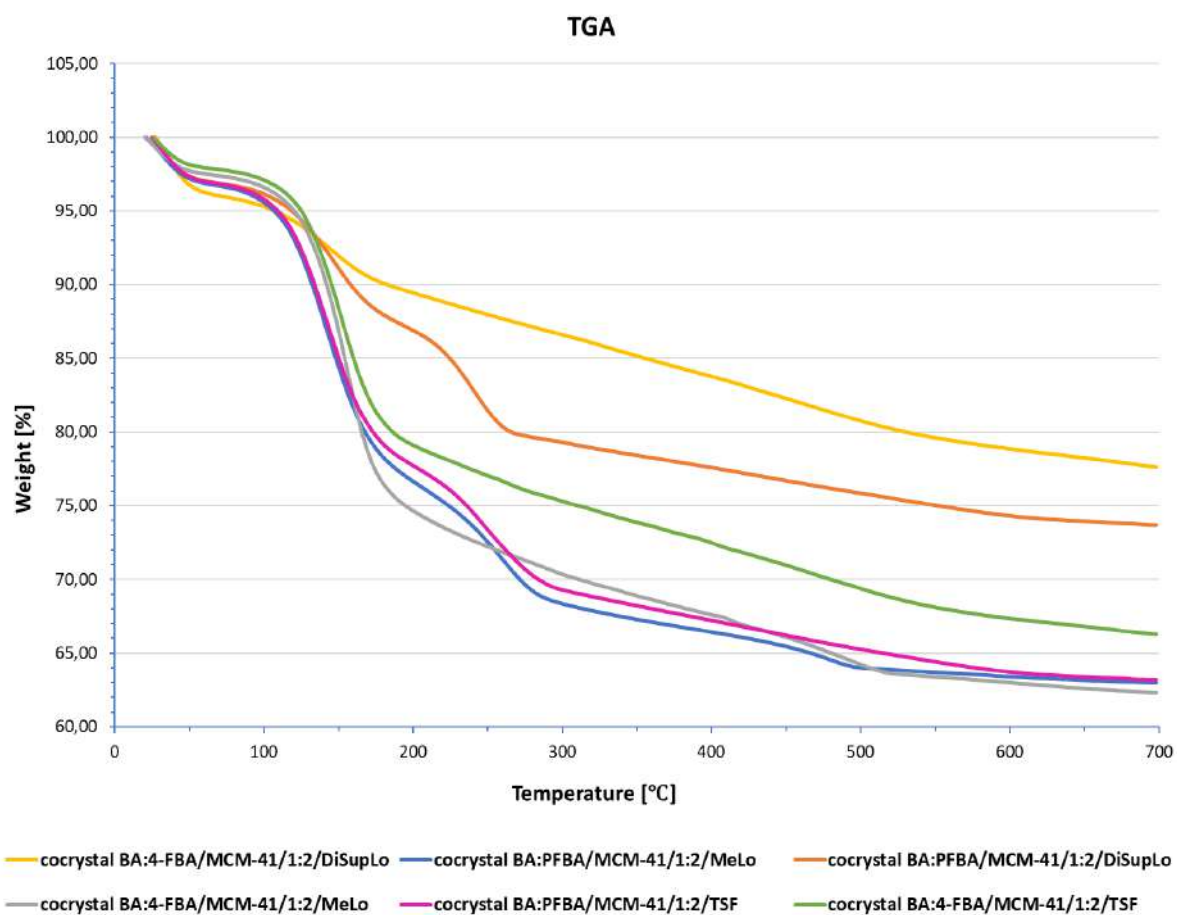


Figure S3. TGA curves of BA:PFBA and BA:4-FBA cocrystals embedded in MCM-41 (1:2) by TSF, DiSupLo, and MeLo methods.

II. Adsorption-Desorption of Nitrogen.

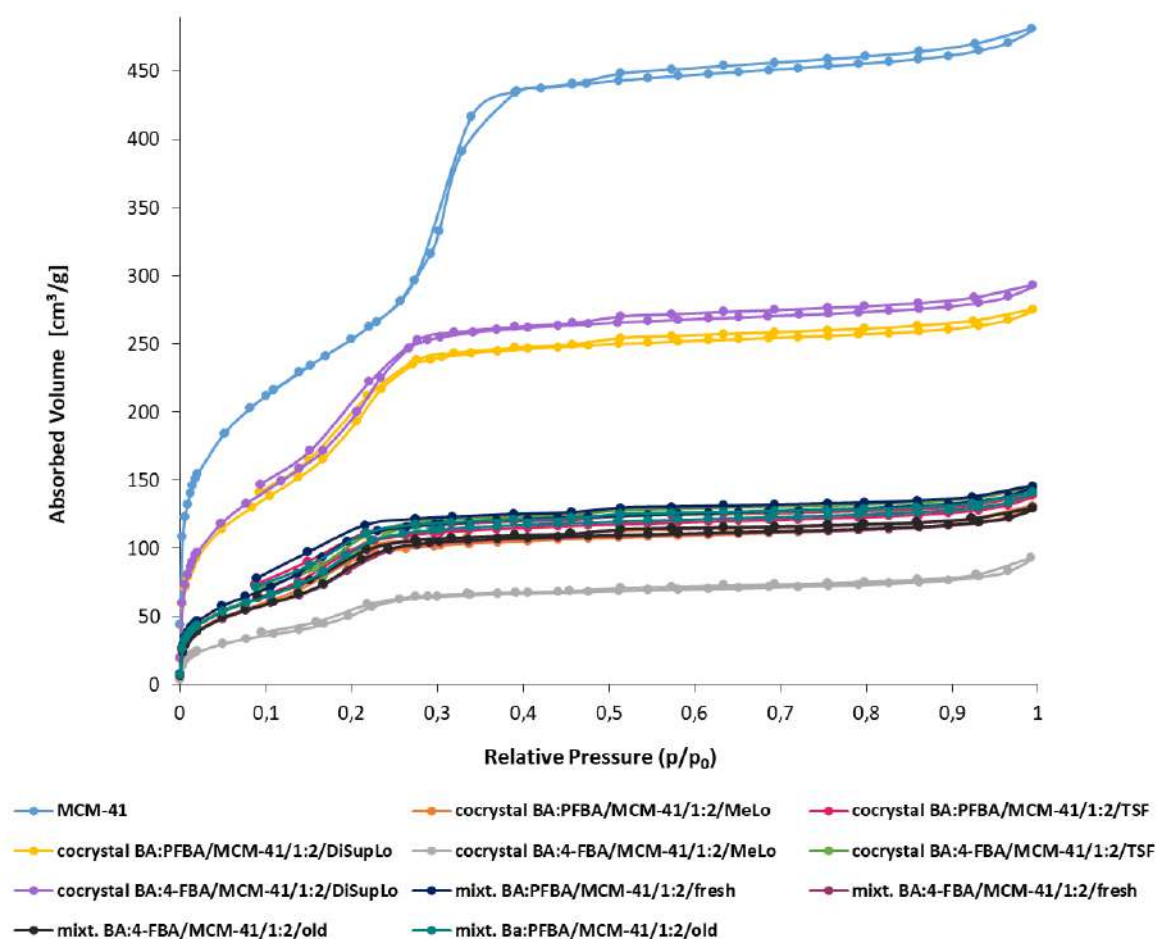


Figure S4. Nitrogen adsorption-desorption isotherms for MCM-41, mixtures of pure components, and loaded samples prepared by three methods.

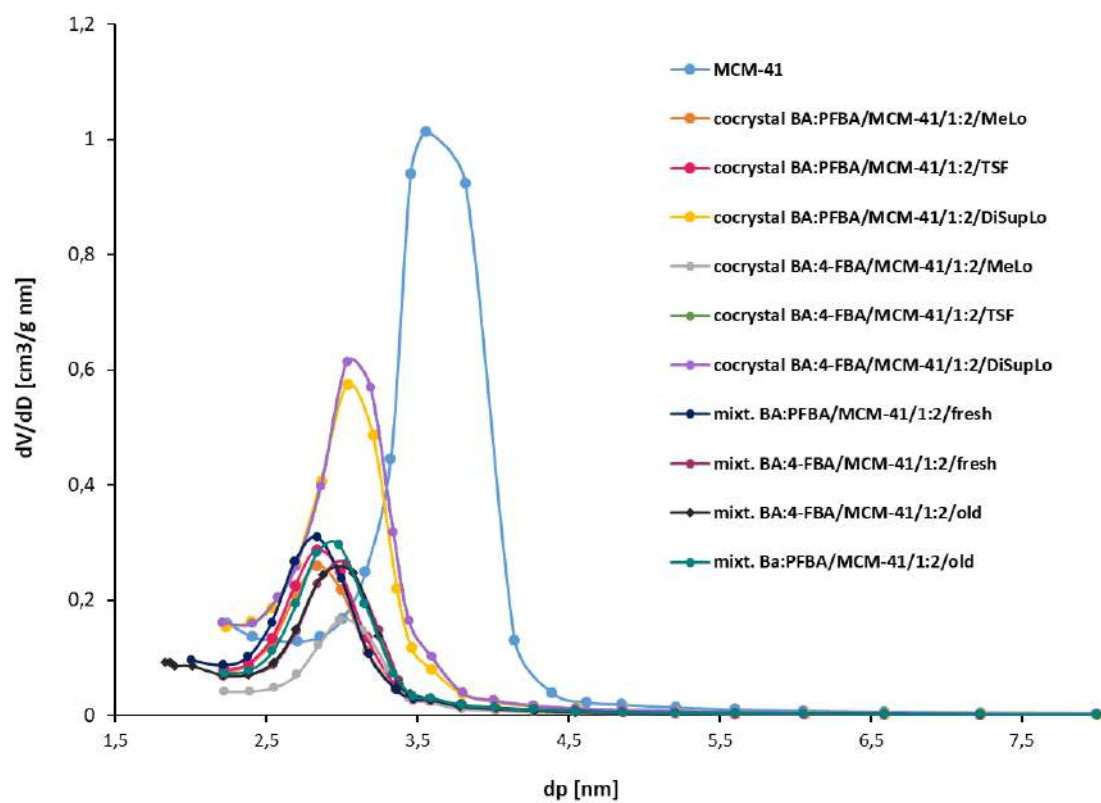


Figure S5. Nitrogen adsorption-desorption isotherms for MCM-41, mixtures of pure components, and loaded samples prepared by three methods.

Table S1. Textural characterization of MCM-41, mixtures of pure components, and loaded samples prepared by three methods.

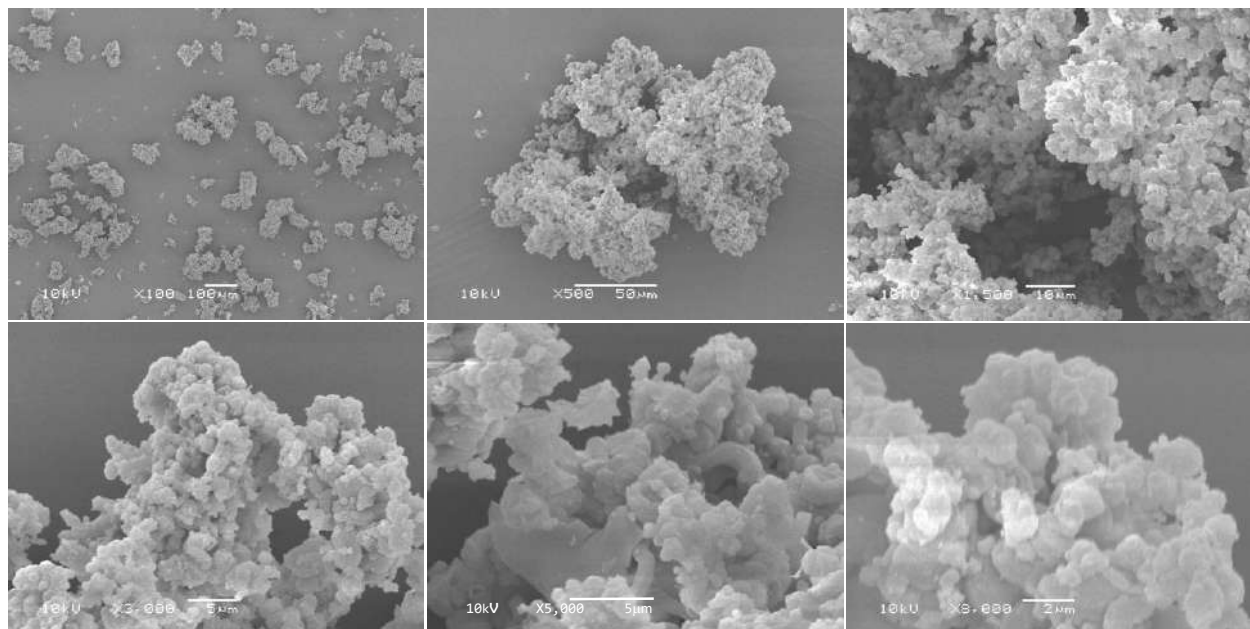
Sample	Specific surface area [m ² /g]	Pore volume [cm ³ /g]	Pore diameter [nm]	V _p /V _{MCM-41}
MCM-41	930	0,91	3,6	-
cocrystal BA:PFBA/MCM-41/1:2/DiSupLo	778	0,57	3,1	0,63
cocrystal BA:PFBA/MCM-41/1:2/TSF	484	0,29	2,9	0,32
cocrystal BA:4-FBA/MCM-41/1:2/TSF	479	0,29	3,0	0,32
cocrystal BA:4F-BA/MCM-41/1:2/ DiSupLo	793	0,63	3,1	0,69
cocrystal BA:4-FBA/MCM-41/1:2/MeLo	298	0,19	3,1	0,21
cocrystal BA:PFBA/MCM-41/1:2/MeLo	437	0,27	2,9	0,30
mixt. Ba:PFBA/MCM-41/1:2/fresh	429	0,29	2,8	0,32
mixt. Ba:PFBA/MCM-41/1:2/old	472	0,30	2,9	0,33
mixt. Ba:4-FBA/MCM-41/1:2/fresh	295	0,32	3,0	0,35
mixt. Ba:4-FBA/MCM-41/1:2/old	315	0,26	3,0	0,29

V_p – pore volume with components loaded into the pores

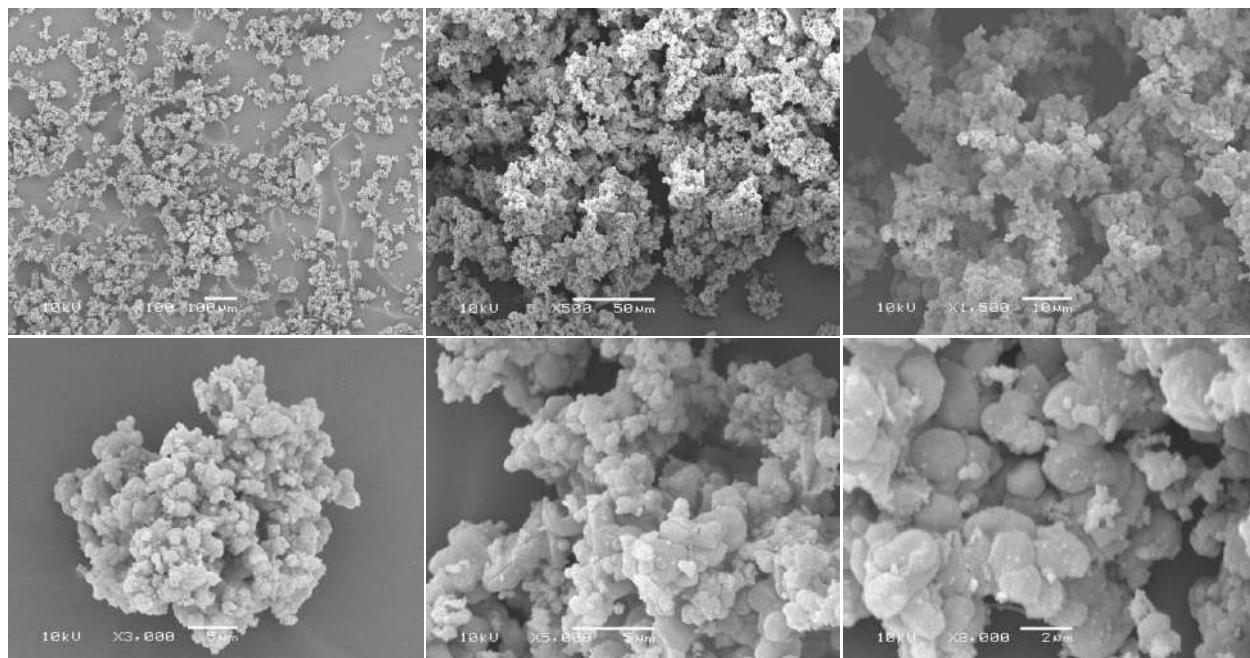
V_{MCM-41} - pore volume without components

III. Scanning Electron Microscopy (SEM) images.

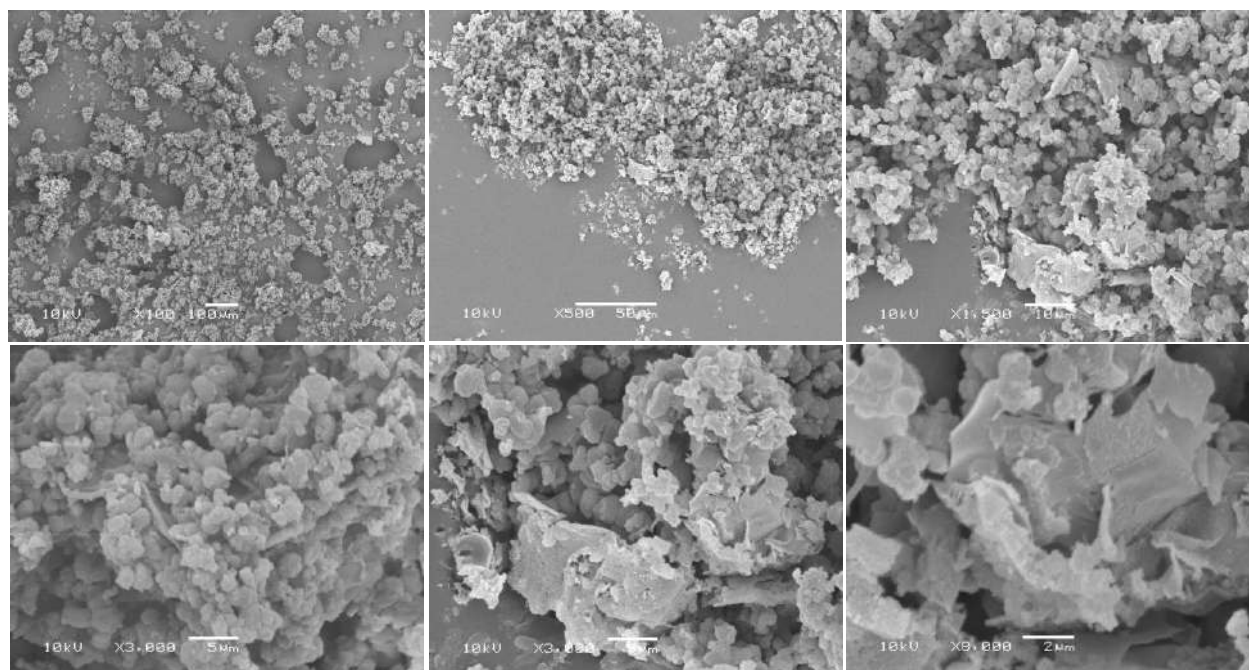
a)



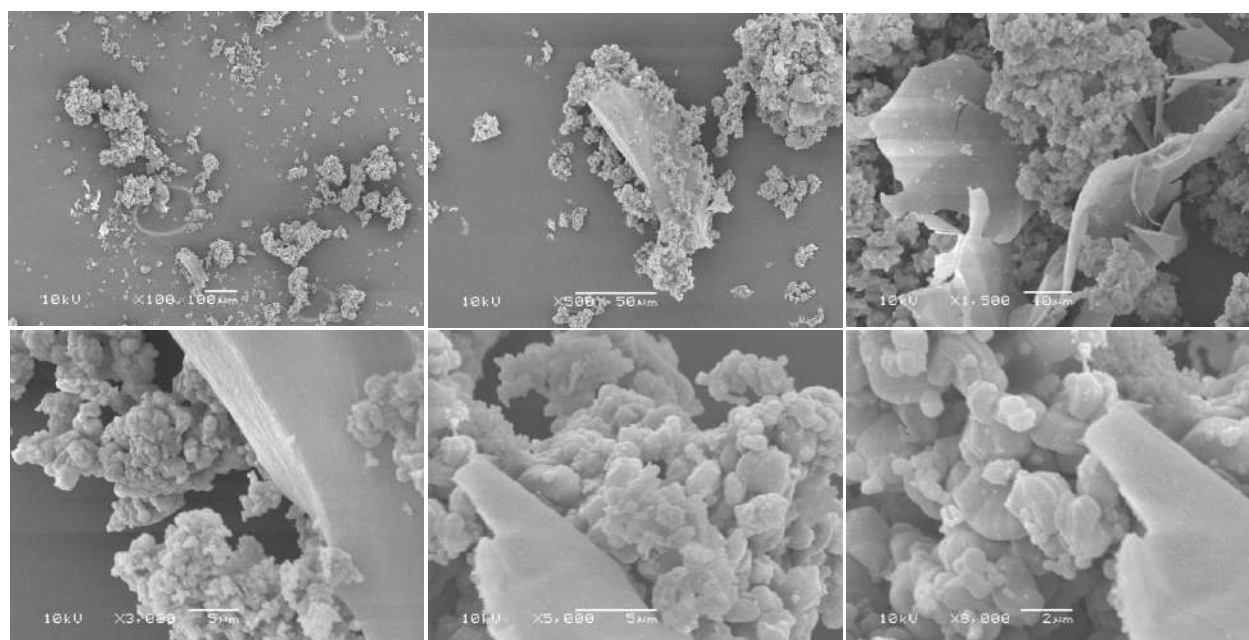
b)



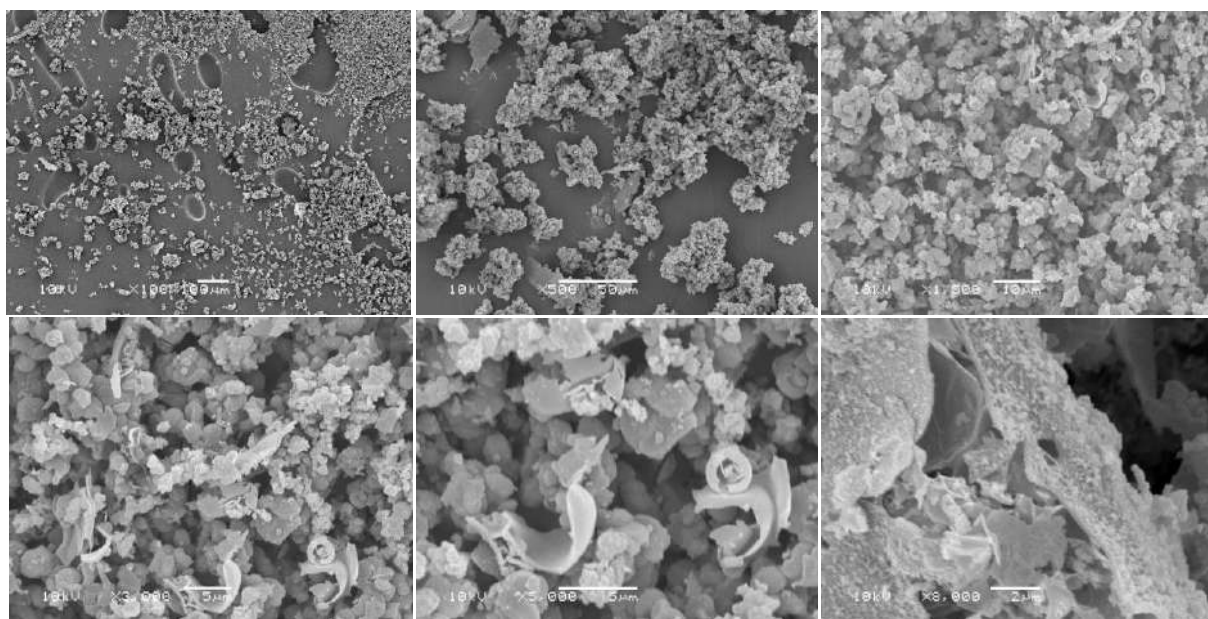
c)



d)



e)



f)

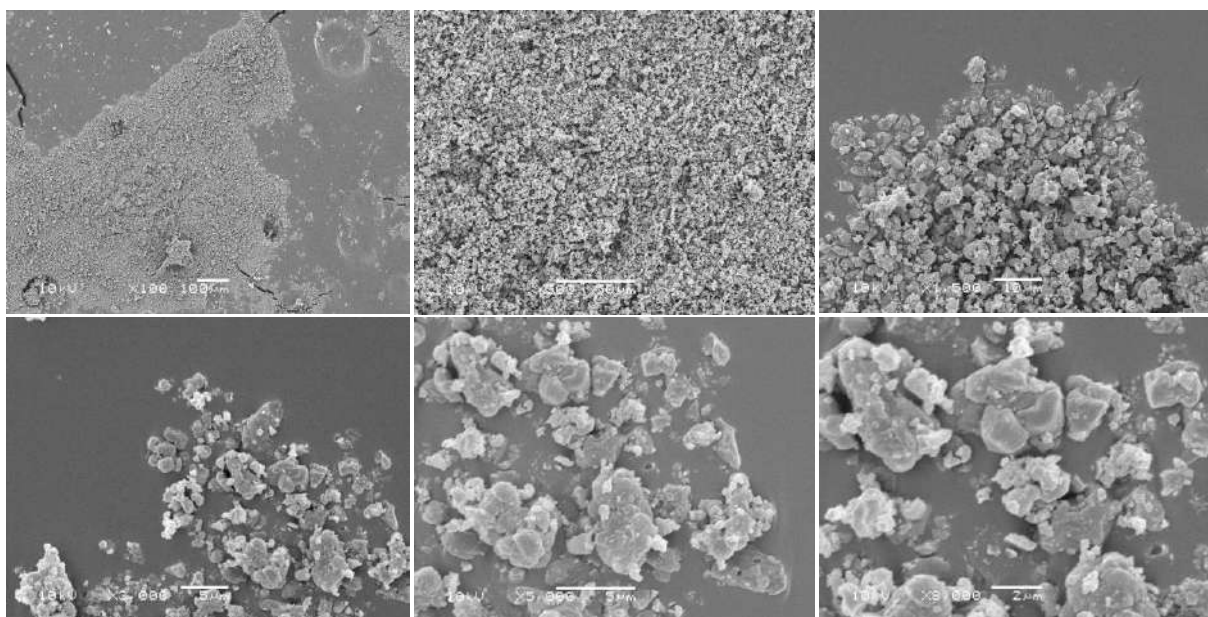


Figure S6. SEM images of MCM-41 **(a)** and physical mixture of BA:4-FBA/MCM-41/1:2/old **(b)**, Ba:PFBA/MCM-41/1:2/old **(c)**, Ba:PFBA/MCM-41/1:2/fresh **(d)**, Ba:4-FBA/MCM-41/1:2/ fresh **(e)**, Ba:PFBA/MCM-41/1:2 after MeLo method **(f)**.

IV. Release profiles

Figure S7a features the curves showing the BA component while Figure S7b represents PFBA. The qualitative analysis of these curves proves the significantly different behavior of benzoic acid which solubility is much worse compared to other specimens. The release profiles of BA and PFBA in BA:PFBA cocrystal incorporated into MCM-41 by the DiSupLo method plateaued at 60%. These unexpected values require some comment. The answer explaining the discrepancy between TSF, MELO, and DiSupLo comes from the analysis of the ethanol content, which in the DiSupLo method serves as an external bath. The ethanol in the diffusion vessel has been found to contain both BA and PFBA components, which means that the co-formers diffuse into the outer bath during loading.

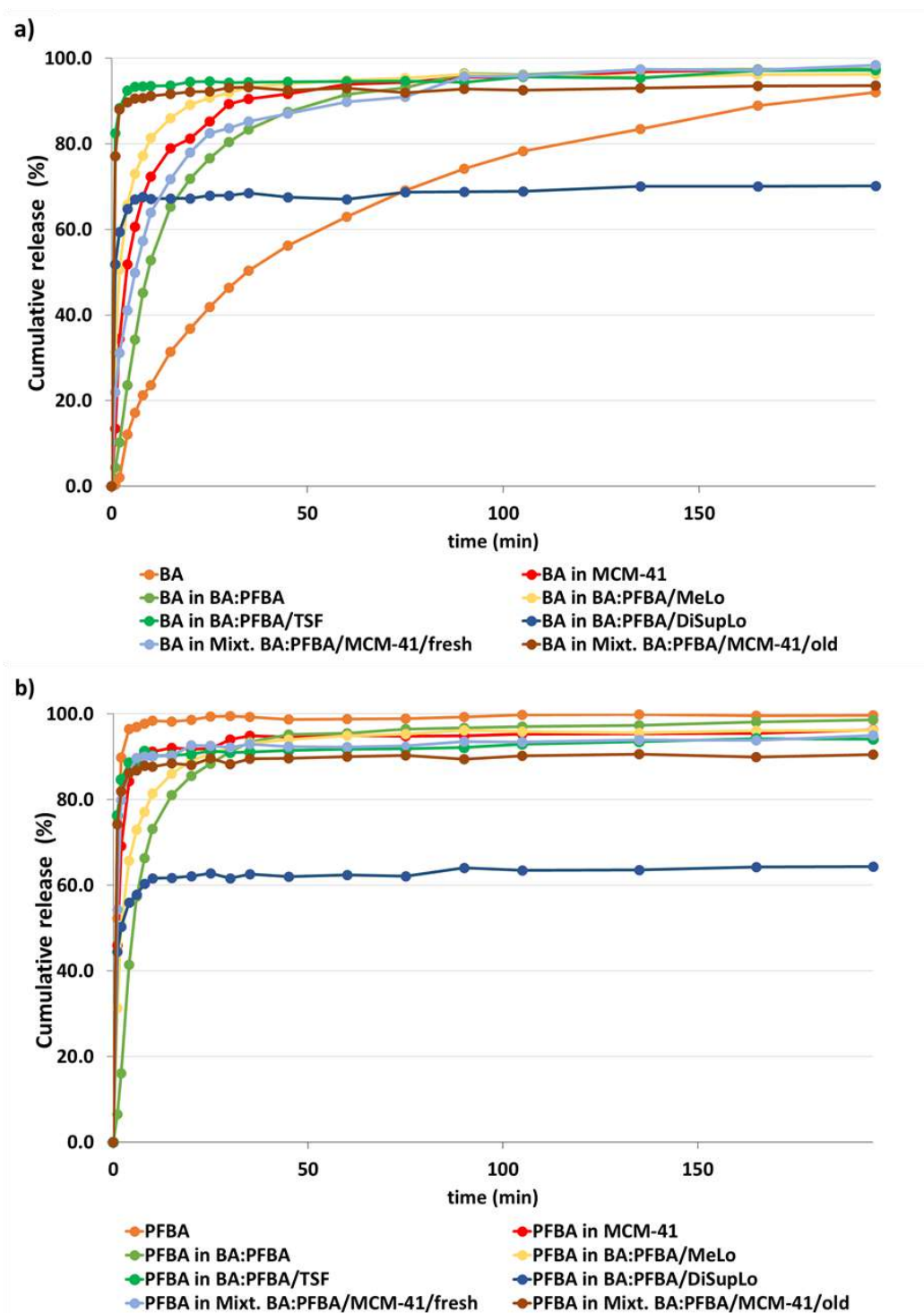


Figure S7. Powder dissolution profiles of a) BA and BA in BA:PFBA cocrystal and MCM-41, b) PFBA and PFBA in BA:PFBA cocrystal and MCM-41, and component BA and PFBA of BA:PFBA cocrystal loaded into MCM-41 pores employing three methods as described in Legend. Water with pH 5.7 was used as a dissolution medium.

Figure S8a shows the profiles for BA co-former while 8b for 4-FBA. Visual analysis of these curves suggests that both BA and 4-FBA components interact differently with water during the dissolution process. As in the previous case for DiSupLo method the plateau is reached at value ca 60%.

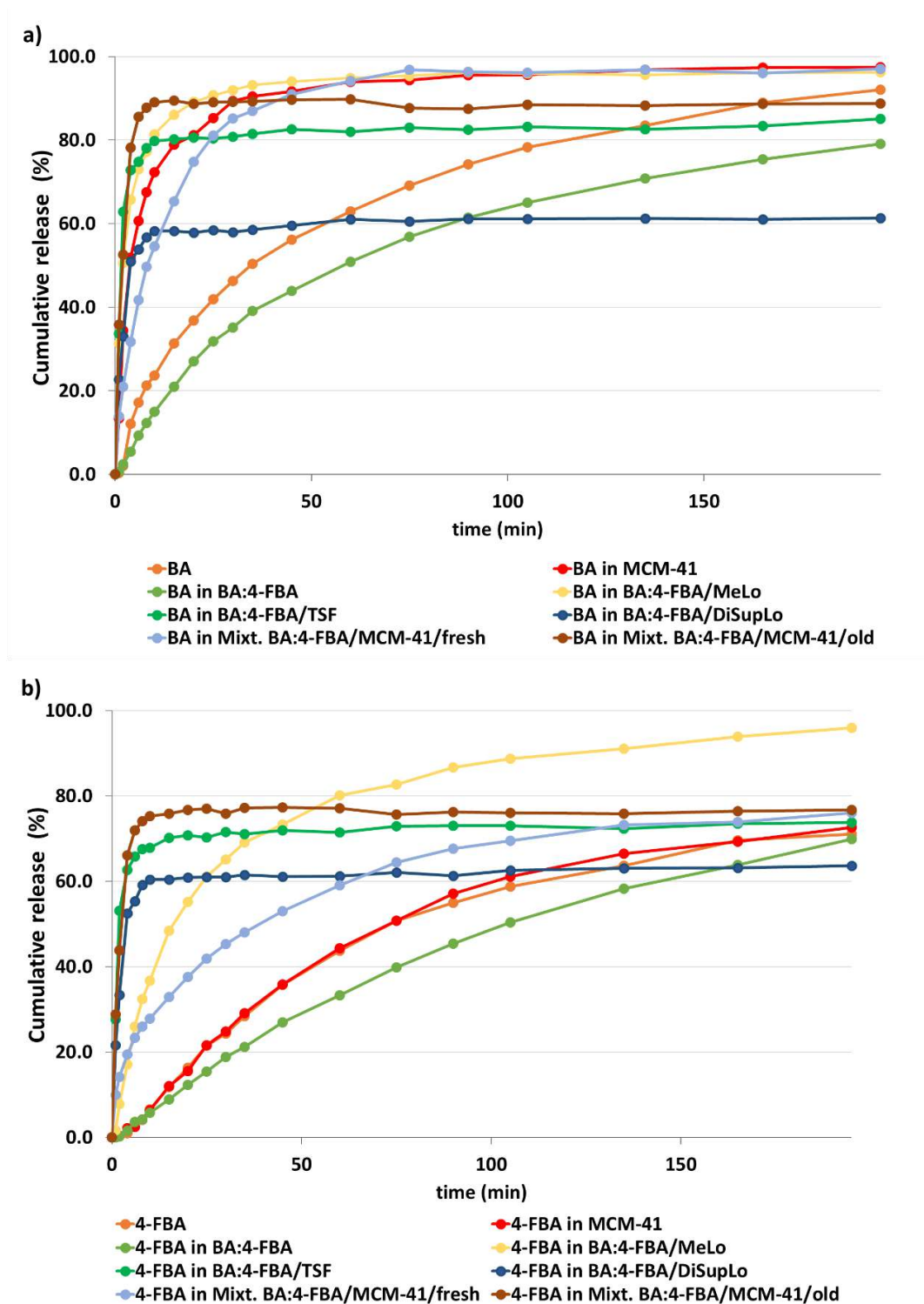


Figure S8. Powder dissolution profiles of a) BA and BA in BA:4-FBA cocrystal and MCM-41, b) 4-FBA and 4-FBA in BA:4-FBA cocrystal and MCM-41, and component BA and 4-FBA of BA:4-FBA/MCM-41 cocrystal loaded into MCM-41 pores employing three methods as described in Legend. Water with pH 5.7 was used as a dissolution medium.

V. Calculation of stabilization energies

Table S2.

	Structure (CSD refcode)	composition	E [ev /unit cell]	number of symmetry operations	E ^{stab} [kJ/mol of molecules]
binaries	SATHOK01 ¹ _F1F2	BA:4-FBA 0.5:0.5	-9610.5750		
	SATHOK01_F2F3	BA:4-FBA 0.5:0.5	-9610.5945		
	SATHOK01_F3F4	BA:4-FBA 0.5:0.5	-9610.5822		
	SATHOK01_F1F3	BA:4-FBA 0.5:0.5	-9610.5773		
	SATHOK01_F1F4	BA:4-FBA 0.5:0.5	-9610.6002		
	mean		-9610.5858	4	2.07
	UKOKIO ²	BA:PFBA 0.5:0.5	-59087.3573	16	-0.12
pure components	BENZAC12 ³	BA	-8319.5920	4	
	PFBZAC ⁴	PFBA	-10612.0382	2	
	PFBZAD15 ⁵	4-FBA	-10901.7516	4	

Stabilization energies in kJ/mol were calculated according to the equation:

$$E^{stab} = \frac{E_{binary}^{total}}{N_{symm_{op}}} - (0.5 * \frac{E_{component1}^{total}}{N_{symm_{op}}} + 0.5 * \frac{E_{component2}^{total}}{N_{symm_{op}}})$$

In the case of BA:4-FBA solid solution, the unit cell was converted to P1 space group, so that the H/F occupancy could be accounted for. We considered the structures with 0.5 H/F occupancy, which means that out of 4 BA/4-FBA molecules present in a unit cell, two of them

contained hydrogen atom and the other two – fluorine. Each possible combination of fluorine atom locations was considered and stabilization energy was calculated from the mean value obtained from five separate calculations.

References:

-
- ¹ S. Chakraborty, G. R. Desiraju, *Cryst. Growth Des.* (2018), **18**, 3607, doi: [10.1021/acs.cgd.8b00395](https://doi.org/10.1021/acs.cgd.8b00395)
- ² M. Gdaniec, W. Jankowski, M. J. Milewska, T. Polonski, *Angew. Chem., Int. Ed.* (2003), **42**, 3903, doi: [10.1002/anie.200351432](https://doi.org/10.1002/anie.200351432)
- ³ M. Nieger, *CSD Communication* (2010)
- ⁴ V. Benghiat, L. Leiserowitz, *J. Chem. Soc., Perkin Trans. 2* (1972), 1778, doi: [10.1039/p29720001778](https://doi.org/10.1039/p29720001778)
- ⁵ V. R. Hathwar, T. S. Thakur, R. Dubey, M. A. Pavan, T. N. G. Row, G. R. Desiraju, *J. Phys. Chem. A* (2011), **115**, 12852, doi: [10.1021/jp2039866](https://doi.org/10.1021/jp2039866)

Appendix II

Declaratory statement from co-authors of the published results

Łódź, 22/11/2023

Dr Sławomir Kaźmierski
Center of Molecular and Macromolecular Studies,
Polish Academy of Sciences
90-636 Łódź, Poland
E-mail: slawomir.kazmierski@cbmm.lodz.pl

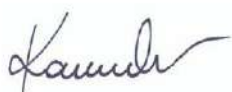
Declaration

I hereby declare that in the preparation of publications:

Unexpected Factors Affecting the Kinetics of Guest Molecule Release from
Investigation of Binary Chemical Systems Trapped in a Single Void of Mesoporous Silica
Particles, Trzeciak, K., Wielgus, E., Kaźmierski, S., Khalaji M., Dudek, M.K., Potrzebowski,
M.J., ChemPhysChem, 2023, 24(7), e202200884, DOI: 10.1002/cphc.202200884.

my contribution was: NMR experiment set-up and NMR measurements.

Dr Sławomir Kaźmierski



Dr Piotr Paluch

Łódź, 22/11/2023

Center of Molecular and Macromolecular Studies,

Polish Academy of Sciences

90-636 Łódź, Poland

E-mail: piotr.paluch@cbmm.lodz.pl

Declaration

I hereby declare that in the preparation of publications:

Narrowing down the conformational space with solid-state NMR in crystal structure prediction of linezolid cocrystals, Khalaji, M., Paluch, P., Potrzebowski, M.J., Dudek, M.K., Solid State Nuclear Magnetic Resonance, 2022, 121, 101813, DOI: 10.1016/j.ssnmr.2022.101813.

my contribution was measurement of NMR spectra at Fast MAS condition

Dr Piotr Paluch



Dr Aneta Wróblewska
Center of Molecular and Macromolecular Studies,
Polish Academy of sciences
90-636 Łódź, Poland
E-mail: aneta.wroblewska@chemia.uni.lodz.pl

Łódź, 22/11/2023

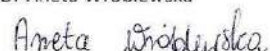
Declaration

I hereby declare that in the preparation of publications:

Structural variety of heterosynthons in linezolid cocrystals with modified thermal properties,
Khalaji, M., Wróblewska, A., Wielgus, E., Bujacz, G.D., Dudek, M.K., Potrzebowski, M.J., Acta
Crystallographica Section B: Structural Science, Crystal Engineering and Materials, 2020, 76, pp.
892–912, DOI: 10.1107/S2052520620010896.

my contribution included participating in the initial cocrystallization experiments using
mechanochemistry, conducted jointly with Mehrnaz Khalaji. Additionally, I provided supervision
and scientific guidance during the early phase of the research on linezolid cocrystals.

Dr Aneta Wróblewska



Dr hab. Marta Dudek, prof. CBMM
Center of Molecular and Macromolecular Studies,
Polish Academy of Sciences
90-363 Łódź, Poland
E-mail: marta.dudek@cbmm.lodz.pl

Łódź, 28/05/2025

Declaration

I hereby declare that in the preparation of publications:

1. Narrowing down the conformational space with solid-state NMR in crystal structure prediction of linezolid cocrystals, Khalaji, M., Paluch, P., Potrzebowski, M.J., Dudek, M.K., Solid State Nuclear Magnetic Resonance, 2022, 121, 101813, DOI: 10.1016/j.ssnmr.2022.101813.

my contribution was planning the experiments, running crystal structure prediction calculations, taking part in spectral assignment, analyzing results and writing the manuscript. I am the corresponding author of this paper.

2. Virtual Cocrystal Screening Methods as Tools to Understand the Formation of Pharmaceutical Cocrystals - A Case Study of Linezolid, a Wide-Range Antibacterial Drug, Khalaji, M., Potrzebowski, M.J., Dudek, M.K., Crystal Growth and Design, 2021, 21(4), pp. 2301–2314, DOI: 10.1021/acs.cgd.0c01707.

my contribution was planning the experiments, running some of the solid-state and PXRD measurements, taking part in spectral assignment, running DFT calculations and analyzing all results and writing the manuscript. I am the corresponding author of this paper

3. Structural variety of heterosynthons in linezolid cocrystals with modified thermal properties, Khalaji, M., Wróblewska, A., Wielgus, E., G.D., Bujacz, Dudek, M.K., Potrzebowski, M.J., Acta Crystallographica Section B: Structural Science, Crystal Engineering and Materials, 2020, 76, pp. 892–912, DOI: 10.1107/S2052520620010896.

my contribution was planning the experiments, running crystal structure prediction calculations, taking part in spectral assignment, analyzing results and writing the manuscript. I am the corresponding author of this paper

4. Unexpected Factors Affecting the Kinetics of Guest Molecule Release from Investigation of Binary Chemical Systems Trapped in a Single Void of Mesoporous Silica Particles, Trzeciak, K. Wielgus, E. Kaźmierski, S., Khalaji, M., Dudek, M.K., Potrzebowski, M.J., ChemPhysChem, 2023, 24(7), e202200884, DOI: 10.1002/cphc.202200884.

my contribution was running DFT calculations, taking part in analyzing and interpreting the results and in writing the manuscript.



Marta Dudek



Lodz University of Technology
Institute of Molecular and Industrial Biotechnology

Łódź, 2.06.2025 r.

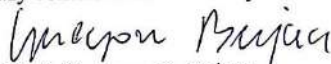
Prof. dr hab. inż. Grzegorz D. Bujacz
E-mail: grzegorz.bujacz@p.lodz.pl

Declaration

I hereby declare that in the preparation of publications:

Khalaji, M., Wróblewska, A., Wielgus, E., Bujacz, G.D., Dudek, M.K., Potrzebowski, M.J. Structural variety of heterosynthons in linezolid cocrystals with modified thermal properties. *Acta Crystallographica Section B: Structural Science, Crystal Engineering and Materials* (2020) **76**, pp. 892–912. DOI: 10.1107/S2052520620010896.

My contribution was in crystal structure determination of obtained cocrystals.


Prof. Grzegorz D. Bujacz

Institute of Molecular and Industrial Biotechnology
90-537 Łódź, Stefanowskiego 2/22
Phone +48 42 631 34 42, email: w5i51@adm.p.lodz.pl, www.binoz.p.lodz.pl
Correspondence address:
90-924 Łódź, Żeromskiego 116



Dr Katarzyna Trzeciak
Center of Molecular and Macromolecular Studies,
Polish Academy of Sciences
90-636 Łódź, Poland
E-mail: katarzyna.trzeciak@cbmm.lodz.pl

Łódź, 22/11/2023

Declaration

I hereby declare that in the preparation of publications:

Unexpected Factors Affecting the Kinetics of Guest Molecule Release from Investigation of Binary Chemical Systems Trapped in a Single Void of Mesoporous Silica Particles, Trzeciak, K. Wielgus, E. Kaźmierski, S., Khalaji M., Dudek, M.K., Potrzebowski, M.J., ChemPhysChem, 2023, 24(7), e202200884, DOI: 10.1002/cphc.202200884.

My contribution was:

- preparation of binary systems (cocrystals and solid solution) and physical mixtures in different molar ratios
- incorporation of model systems into MCM-41 pores using three methods: TSF, DiSuplo, MeLo
- performing SSNMR measurements
- writing
- preparing figures
- preparing samples for solubility and release rate studies of binary systems embedded in MCM-41 pores and performing these studies
- preparing samples and performing nitrogen adsorption-desorption measurements and their analysis
- preparing Supporting Information and graphical abstract
- taking SEM images
- corrections after reviews



Dr Katarzyna Trzeciak

Prof Marek Potrzebowski
Center of Molecular and Macromolecular Studies,
Polish Academy of Sciences
90-636 Łódź, Poland
E-mail: marek.potrzebowski@cmm.lodz.pl

Łódź, 30/05/2025


Declaration

I hereby declare that in the preparation of publications:

1. Narrowing down the conformational space with solid-state NMR in crystal structure prediction of linezolid cocrystals, Khalaji, M., Paluch, P., Potrzebowski, M.J., Dudek, M.K., Solid State Nuclear Magnetic Resonance, 2022, 121, 101813, DOI: 10.1016/j.ssnmr.2022.101813.
2. Virtual Cocrystal Screening Methods as Tools to Understand the Formation of Pharmaceutical Cocrystals – A Case Study of Linezolid, a Wide-Range Antibacterial Drug, Khalaji, M., Potrzebowski, M.J., Dudek, M.K., Crystal Growth and Design, 2021, 21(4), pp. 2301–2314, DOI: 10.1021/acs.cgd.0c01707.
3. Structural variety of heterosynthons in linezolid cocrystals with modified thermal properties, Khalaji, M., Wróblewska, A., Wielgus, E., G.D., Bujacz, Dudek, M.K., Potrzebowski, M.J., Acta Crystallographica Section B: Structural Science, Crystal Engineering and Materials, 2020, 76, pp. 892–912, DOI: 10.1107/S2052520620010896.
4. Unexpected Factors Affecting the Kinetics of Guest Molecule Release from Investigation of Binary Chemical Systems Trapped in a Single Void of Mesoporous Silica Particles, Trzeciak, K. Wielgus, E. Kaźmierski, S., Khalaji, M., Dudek, M.K., Potrzebowski, M.J., ChemPhysChem, 2023, 24(7), e202200884, DOI: 10.1002/cphc.202200884.

my contribution was about the discussion of results, mentoring, improving manuscripts, and support in solid-state NMR measurements.

Prof Marek J. Potrzebowski



Dr Ewelina Wielgus

Łódź, 22/11/2023

Center of Molecular and Macromolecular Studies,

Polish Academy of Sciences

90-636 Łódź, Poland

E-mail: ewelina.wielgus@cbmm.lodz.pl

Declaration

I hereby declare that in the preparation of publications:

1. Structural variety of heterosynthons in linezolid cocrystals with modified thermal properties, Khalaji, M., Wróblewska, A., Wielgus, E., Bujacz, G.D., Dudek, M.K., Potrzebowski, M.J., Acta Crystallographica Section B: Structural Science, Crystal Engineering and Materials, 2020, 76, pp. 892–912, DOI: 10.1107/S2052520620010896.

2. Unexpected Factors Affecting the Kinetics of Guest Molecule Release from Investigation of Binary Chemical Systems Trapped in a Single Void of Mesoporous Silica Particles, Trzeciak, K., Wielgus, E., Kaźmierski, S., Khalaji, M., Dudek, M.K., Potrzebowski, M.J., ChemPhysChem, 2023, 24(7), e202200884, DOI: 10.1002/cphc.202200884.

my contribution was to perform the measurements of water solubility of linezolid cocrystals with aromatic acids (paper 1) and measurement of dissolution and rate of binary systems (cocrystal, solid solution) release embedded into mesoporous silica particles (paper 2).

Dr Ewelina Wielgus

